THE UNIVERSITY *of* EDINBURGH

DOCTOR OF PHILOSOPHY THESIS

MODELLING OF FAILURES IN THIN-WALLED METAL SILOS UNDER ECCENTRIC DISCHARGE

THE UNIVERSITY OF EDINBURGH
AUGUST 2010

Author: Adam Jan Sadowski

Supervisor: Professor J. Michael Rotter

Declaration

This thesis carrying the title 'Modelling of Failures in Thin-Walled Metal Silos under Eccentric Discharge' has been submitted to the Institute for Infrastructure and Environment of the School of Engineering of the University of Edinburgh for the degree of Doctor of Philosophy.

It is hereby declared that the work presented in this thesis is the sole work of the author except where otherwise acknowledged and has not formed the basis of submission for any other degree.

The publications based on this thesis are as follows:

Sadowski A.J. & Rotter J.M. (2010). "A Study of Buckling in Steel Silos under Eccentric Discharge Flows of Stored Solids." *Jrnl. of Eng. Mech.*, ASCE, 136(6), 769-776.

Sadowski A.J. & Rotter J.M. (2009). "Eccentric discharge buckling of a very slender silo." *Proc. IASS 2009 Symposium*, 28 September – 2 October, Valencia, Spain.

Sadowski A.J. & Rotter J.M. (2008). "A Study of Buckling in Steel Silos under Eccentric Discharge Flows of Stored Solids." *Proc. Eurosteel 2008 Conference*, 3-5 September, Graz, Austria, 1509-1514.

Abstract

Eccentric discharge of granular solids is widely considered one of the most serious design conditions for thin-walled metal silos, and one which has been the cause of very many silo disasters in the past. Yet the reasons for these consequences have not been very well understood, given the serious difficulties inherent in measuring or modelling flow patterns of granular solids, wall pressures and the associated structural response.

To this end, this thesis presents a programme of theoretical and computational analyses which investigate the effects of a very wide range of different discharge flow patterns from silos, including both concentric and eccentric flows. The critical effects of changes of flow channel geometry, silo aspect ratio, changes of plate thickness and geometric and material nonlinearity are explored in detail.

The codified procedures and pressure distributions for concentric and eccentric discharge of the EN 1991-4 (2007) European Standard are analysed first on a number of example silos custom-designed according to EN 1993-1-6 (2007) and EN 1993-4-1 (2007), followed by the development and investigation of a more complete mixed flow pressure theory. The computational analyses presented in this thesis are thought to be the first of their kind.

Acknowledgements

My infinite gratitude goes to my supervisor and mentor Professor Michael Rotter for his equally infinite patience and wisdom, who could easily produce a doctoral thesis every week and who was kind enough to let me study with him.

I would also like to thank my parents Ewa and Piotr, both academics in some form at some point in their careers, who fostered in me a strive for knowledge as a child (despite serious protests on my part - what can I say, I was young and foolish) and I owe my academic enthusiasm to them.

I would finally like to thank my dear wife Tatiana who took the plunge and came to me all the way from her homeland. It is thanks to her that I was inspired to finish on time and on budget. I dedicate this thesis to her and I wish her all the best in her own work and studies.

Table of Contents

Chapter 1 – Introduction and literature review

1.1 Introduction

Silos are storage structures, capable of retaining tens of thousand of tonnes of different granular materials, and are vital to industry and the economy. They are, in many respects, under-appreciated by the general public due to their absence from city landscapes, usually banished to bleak industrial complexes or farms. Yet a silo disaster is a significant financial burden, both in terms of the destruction of the structure, the loss of the material stored inside and the halt in productivity at the facility. This field, therefore, merits considerable study.

The aim of this thesis is to develop an improved understanding of the structural behaviour of a silo and its contents during discharge, especially under non-axisymmetric (eccentric) flow patterns. Eccentric flows have been directly responsible for a great number of catastrophic silo failures leading to high economic, material and, regrettably, sometimes human losses. Progress in understanding these structural failures has been slow due to the highly unpredictable nature of eccentric discharge and the complexity of the mechanics involved.

Silos are built either of reinforced concrete or sheet metal, the two different methods of construction greatly influencing the behaviour of the silo. A concrete silo will not buckle in the same way as a metal silo, nor will a metal silo burst or suffer the same cracking effects as a concrete one under bending and tensile forces. A concrete silo is, however, significantly more resistant to abrasive materials, such as coal and iron ore, but a metal silo is much more efficient in terms of material use for storing smaller-particle granular solids, such as cereals. Only thin-wall metal silos, specifically steel, are considered in this thesis since these are usually more common and have suffered numerous catastrophic buckling failures under eccentric flows in the past. An example of buckling failure in a full-scale and model silo is shown in Fig. 1.1.

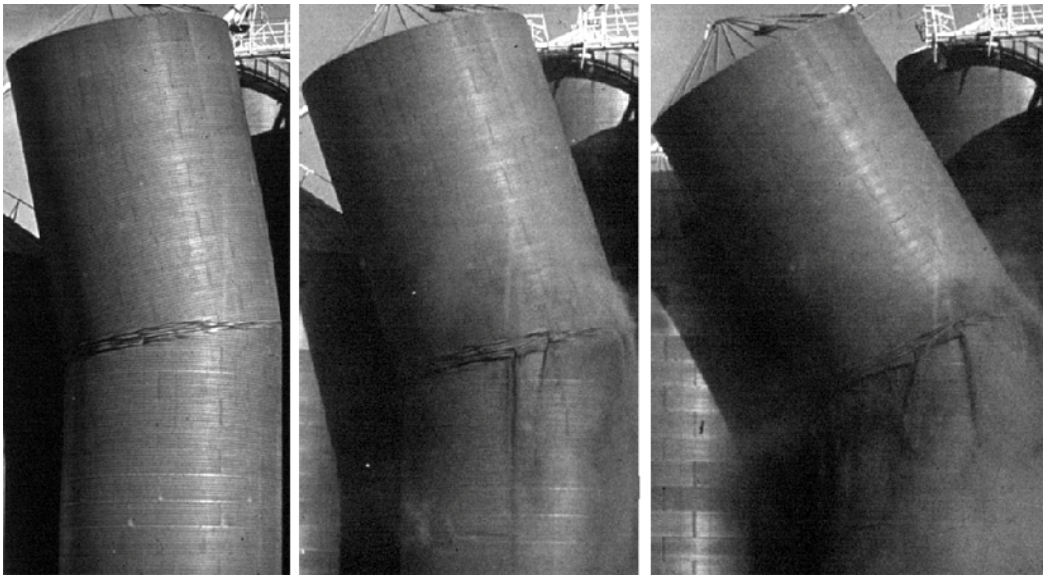

a) Progressive catastrophic collapse of a steel silo due to eccentric discharge (courtesy of J.M. Rotter)

b) Global overturning collapse of a model silo under fully eccentric discharge (after Watson, 2010)

Fig. 1.1 – Examples of collapse under eccentric discharge

Classical design of silo structures is based on the assumption that the normal pressure and frictional traction exerted by the granular solid on the silo wall are both

axisymmetric, resulting in a relatively simple linear behaviour of the structure. The critical failure mechanism of concrete silos has generally been assumed to be by bursting of the wall due to fracture or yielding of the reinforcement under high uniform internal pressure, while that of metal silos has generally been assumed to be through buckling due to high uniform axial compression (Rotter, 2001a). However, true pressure patterns in silos usually possess a significant degree of axial asymmetry, even under supposedly concentric filling or discharge procedures (Ooi *et al.*, 1990). Up to the release of the current European Standard on silo pressure (EN 1991-4, 2007), the only treatment of such asymmetries in silo loadings was the linear superposition of simple rectangular patches of additional normal pressure at arbitrary locations (e.g. DIN 1055-6, 1987; ISO 11697, 1995; AS 3774, 1996). It will be shown in this thesis that this approach is not at all satisfactory at emulating both the realistc behaviour of the granular solid and its effect on the structure.

To this end, the following literature review is split to follow two different, but related, areas of research. The first part introduces the literature on the discharge of granular solids in silos and hoppers, including flow patterns, wall pressures and structural effects. The second part covers the literature on the subject of structural analysis and design of shell structures for stability and plasticity, including computational analysis and the finite element method. Both of these topics are extremely broad and contain a voluminous range of publications. However, not all are relevant to the current thesis and there is no room to list them all. The focus will be on the most important ones which in some way have influenced the current work.

1.2 Literature on granular solids pressures in silos and structural consequences

1.2.1 Silo pressure theory

Contrary to the familiar frictionless hydrostatic pressure distribution of fluids, whereby the normal pressure exerted on a fluid-filled container depends uniquely on the head, pressures in silos are dominated by complex frictional phenomena (Rotter, 2007a) which are difficult to quantify. Similarly, where the Navier-Stokes equations have been around for nearly two hundred years (starting with Navier, 1822) to describe viscous heat-conducting fluid flow precisely, no corresponding set of complete equations yet exists for granular solid flow.

The foremost piece of work in the field of silo pressures in a uniformly-filled axisymmetric cylindrical vessel is the theory of Janssen (1895), a German engineer working on square wooden silos containing wheat, corn and dry sand. The fundamental assumptions in that theory have been used in all serious work of this nature ever since, and a summary of the derivation is appropriate here.

Consider an infinitesimally thin slice of a solid of bulk density γ at a depth z below the equivalent solid surface, shown in Fig. 1.2. The analysis presented here follows that of Rotter (2007a).

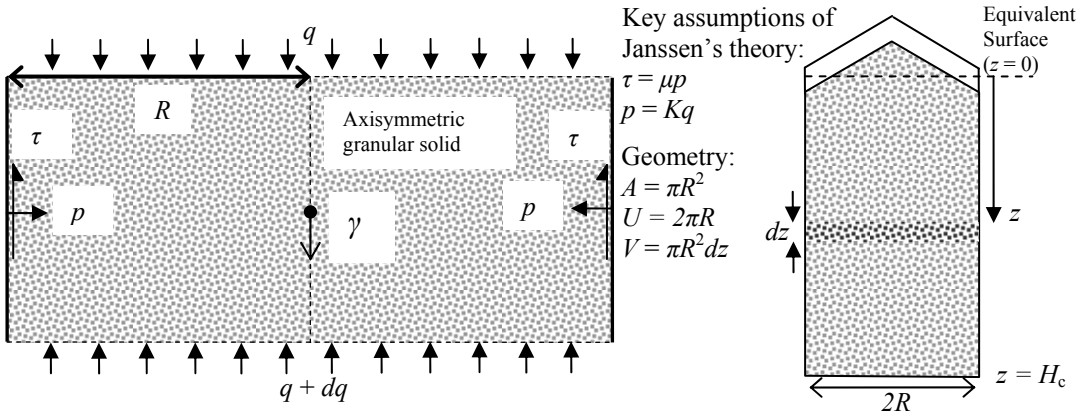

Fig. 1.2 – Derivation diagram for silo pressures, after Rotter (2007a)

The original assumptions made by Janssen are as follows. Firstly, the vertical stress q through the cross-section and the normal p and shear τ stresses on the circumferential boundary are taken to be the mean values at any level. Secondly, the mean normal wall pressure p is related to the mean vertical stress q through a lateral pressure ratio K which is deemed to be constant throughout the whole silo. Thirdly, full wall friction is assumed to have developed between the solid and the wall so that the mean frictional shear τ is related to the mean normal pressure p by the fully-developed wall friction coefficient μ, assumed to be constant throughout the silo. Lastly, the bulk solid density γ is also assumed to be constant.

Vertical equilibrium of the slice leads to the following differential equation:

$$\frac{dq(z)}{dz}A + U\tau(z) = \gamma A \tag{1.1}$$

Applying the boundary condition such that the vertical pressure is zero at the top surface $q(0) = 0$ and incorporating the above assumptions, the solution to Eq. 1.1 yields the famous Janssen equation for normal pressure on the silo wall:

$$p(z) = p_0\left(1 - e^{-\frac{z}{z_0}}\right) \text{ where } p_0 = K\gamma z_0 \text{ and } z_0 = \frac{A}{\mu K U} = \frac{R}{2\mu K} \tag{1.2}$$

Close to the surface ($z \to 0$), and thus $p(z) \approx K\gamma z_0$ which is analogous to hydrostatic pressure though reduced by the factor K. At great depth, $z \to \infty$ and hence $p(z) \to p_0$ meaning that the pressure tends to a single asymptotic value dependent only on the solid density, the silo radius and the frictional contact between the solid and the wall (i.e. the weight of the granular solid is being carried by friction). A typical shape of the Janssen distribution for a slender silo is shown in Fig. 1.3a. Replacing the expressions for the area and circumference of a circle in Eq. 1.2, A and U respectively, with those of a square yields instead the Janssen equation for silos of square cross-section.

The fact that the vertical pressures in the solid do not increase hydrostatically but tend to an asymptotic value at a certain depth had been known some years before Janssen. Indeed, the English engineer Roberts (1882, 1884) had reported that the pressure at the base of a grain silo did not increase any further when the height of the grain exceeded twice the width of the silo.

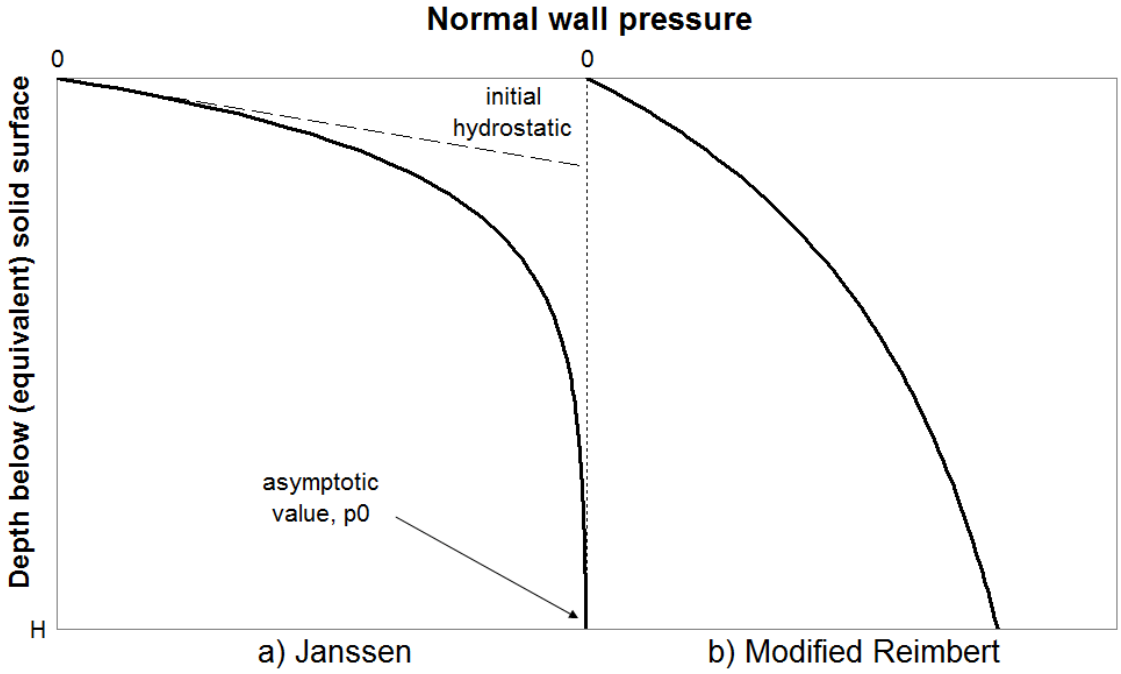

Fig. 1.3 – Variants of the Janssen and modified Reimbert pressure distribution

The origin of z in the Janssen equation is assumed to be at the top surface of the granular solid. Since these surfaces are almost always uneven, an equivalent surface usually needs to be defined to account for any variations from a perfectly level surface, an assumption that is more suitable for slender silos. For squat silos, there may be differences of several metres between the actual level of the solid-wall contact and the equivalent surface, so that the Janssen distribution would predict high pressures against the wall where there are none at all (Rotter, 2001a). A solution for this is found in the semi-empirical theory of M. and A. Reimbert (1976), modified by Rotter (1983b) to be in a more accessible form in line with Eq. 1.2, which is given in EN 1991-4 (2007) as:

$$p(z) = p_0 \left(1 - \left\{ \left(\frac{z - h_0}{z_0 - h_0} \right) + 1 \right\}^n \right) \tag{1.3}$$

where $h_0 = \frac{R}{3} \tan \phi_r$, $n = \frac{-(1 + \tan \phi_r)}{\left(1 - \frac{h_0}{z_0} \right)}$ and ϕ_r is the angle of repose of the granular solid while p_0 and z_0 are defined as before. A typical shape is shown in Fig. 1.3b.

The Janssen equation is usually a remarkably good approximation to the filling pressures in a silo and early experimental studies reported wall pressures that apparently correlated very closely with its predictions (e.g. Jamieson, 1903; Tolz, 1903; Bovey, 1904; Pleißner, 1906; Hoppe, 1979). However, Janssen's equation is naturally unable to capture many phenomena, such as the manner and eccentricity of filling and the packing of the granular material, which have been found to have a significant influence on the filling pressures within a silo. Early evidence of this was found by Takhtamishev (1953) during his experiments on model concrete silos who related lower wall pressures to a more tightly packed granular solid and higher wall pressures to a more loosely packed one. Other studies, including Otis and Pomroy (1957) and Aldrich (1963), have also shed doubt on the validity of assuming a constant bulk solid density throughout the silo. Many further studies by researchers, including Reimbert M. and Reimbert A. (1961), Borcz and Marcinkowski (1974), Nielsen and Kristiansen (1980), Kamiński (1981) and Kamiński and Zubrzycki (1981), have reported significantly higher filling pressures than those predicted by Janssen.

1.2.2 Hopper pressure theory

An analogous but more complex derivation exists for the normal pressures against the wall of a uniformly-loaded axisymmetric conical hopper, shown in Fig. 1.4 below. First thought to have been carried out by the Polish engineer Dąbrowski (1957), it is more commonly attributed to Walker (1966) and its derivation is presented in Arnold *et al.* (1980), Drescher (1991), Rotter (2007a) and many others. The assumptions are almost the same to those of the Janssen derivation, and the notation presented here follows that of Rotter (2007a).

The mean normal pressure p on the inclined wall is assumed to be related to the mean vertical stress q through a hopper pressure ratio F, and the mean frictional shear τ is related to the mean normal pressure p by the fully-developed wall friction coefficient for the hopper μ_h. Once again, F and μ_h are assumed to be constant throughout the hopper. The vertical coordinate of the hopper x is defined as upwards positive starting from the apex of the hopper cone which occurs below the outlet and is thus not physically a part of the hopper.

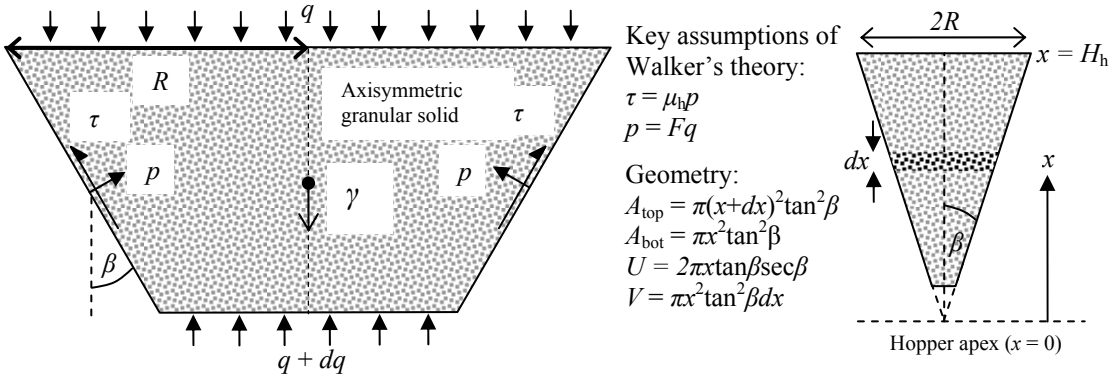

Fig. 1.4 – Derivation diagram for hopper pressures, after Rotter (2007a)

Vertical equilibrium leads to:

$$x\frac{dq(x)}{dx} - 2q(x)\left[F\left(1+\mu_h \cot\beta\right)-1\right] = -\gamma x \tag{1.4}$$

The solution to Eq. 1.4 assumes a top boundary condition of $q(H_h) = q_{vft}$ which is the vertical stress in the solid at the bottom of the silo. If there is no silo above the hopper, the top surface of the granular solid may be assumed to be free from stress, i.e. $q_{vft} = 0$. Thus, incorporating all of the above assumptions yields the equation for the normal wall pressure in the hopper:

$$p(x) = F\left[q_{vft}\left(\frac{x}{H_h}\right)^n + \frac{\gamma H_h}{n-1}\left\{\left(\frac{x}{H_h}\right) - \left(\frac{x}{H_h}\right)^n\right\}\right] \tag{1.5}$$

where n is the power of the distribution.

The above equation identifies two components of the hopper pressure; the weight of the solid in the hopper itself and the weight of the overlying solid in the silo, if present. The weight from the silo is maximised when the wall friction coefficient of the silo wall is lower, since less of the load will then be carried by friction. Steep or rough-wall hoppers usually have a high value of n which may result in a pressure distribution peaking sharply at the transition ($x = H_h$).

The EN 1991-4 (2007) standard differentiates between hoppers in which the wall friction is fully mobilised and those in which it is not. These are termed 'steep' and 'shallow' hoppers respectively. A hopper is deemed to be shallow if $\tan\beta > \frac{1}{2}(1 - K)/\mu_h$ (Rotter, 1999a; 2000). Steep hoppers thus use the fully-developed wall friction coefficient μ_h, while shallow hoppers use an effective wall friction coefficient based on the lateral pressure ratio of the solid and the hopper apex half-angle: $\mu_{eff} = \frac{1}{2}(1 - K)\cot\beta$. The typical shapes of steep and shallow hopper normal pressure distributions are shown in Fig. 1.5.

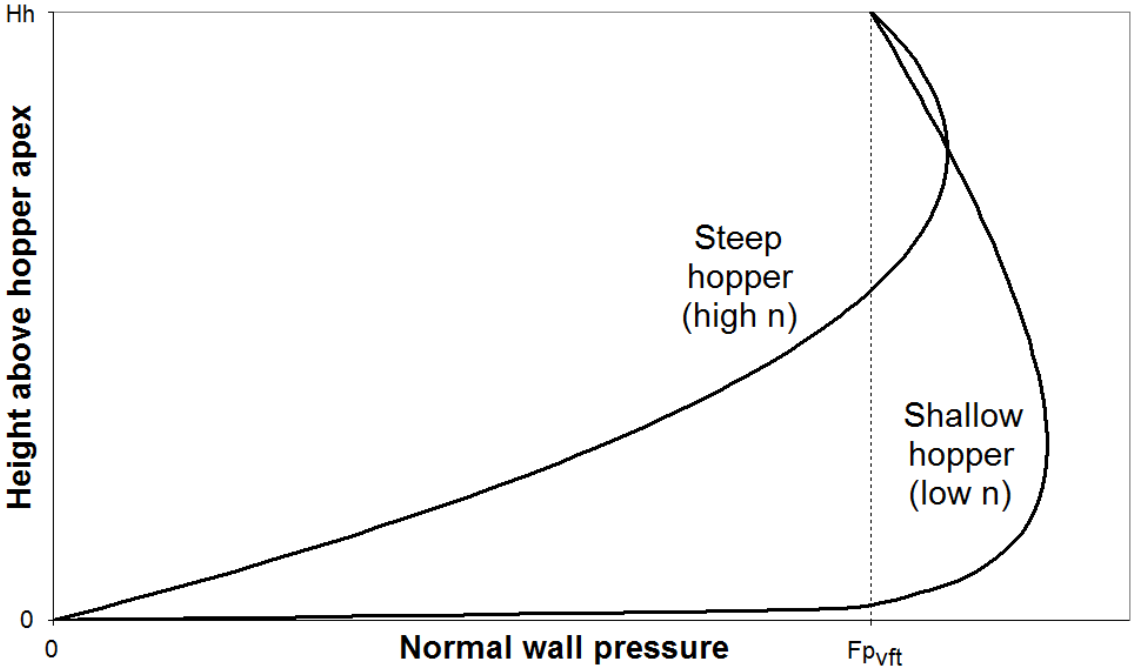

Fig. 1.5 – Normal wall pressure distributions for a steep and shallow hopper

1.2.3 The lateral pressure ratio

In both the Janssen and Dąbrowski/Walker theories, four specific granular solid parameters are required: γ, μ, K and F, the latter two usually being the most problematic to define. Though Janssen introduced the concept of the lateral pressure ratio in his derivation, he did not suggest any way of obtaining it. Koenen (1895) was the first to suggest a value based on the theory of Rankine (1857) for pressures in soils at failure. An in-depth discussion of K may be found in Blight (2006), though it is rather difficult to generalise his conclusions.

Rankine's theory defines two limiting values of K at which the solid is at plastic failure. These are the Rankine active (smallest, K_a) and passive (largest, K_p) limits, one the inverse of the other. Derivation of the two limits is based on the assumption that the solid is in a state of plastic failure dependent on the mean vertical and horizontal stresses alone. These are assumed to be principal stresses, which is not strictly true due to the friction acting on the wall (Blight, 2006). From a Mohr's circle analysis assuming fully-developed wall friction, one obtains:

$$K_a = \frac{1-\sin\phi_i}{1+\sin\phi_i} \text{ and } K_p = \frac{1+\sin\phi_i}{1-\sin\phi_i} \tag{1.6}$$

where ϕ_i is the angle of internal friction of the solid.

In the first application of Janssen's theory, Koenen (1895) used the Rankine definitions to assume that the solid in a silo after filling was in a Rankine active state, and hence had higher vertical pressures than horizontal.

The two Rankine states are reached when the solid can deform plastically, requiring the silo wall to move in (passive limit) or out (active limit). However, silo walls have significant rigidity and thus a different solid state referred to as K_0 exists during storage. This is significantly higher than the Rankine active limit, giving rise to higher filling pressures. The value of K_0 has long been approximated by (Jaky, 1948; Muir-Wood, 1990; Blight, 2006) as:

$$K_0 = 1-\sin\phi_i \tag{1.7}$$

More flexible walls, undergoing outward deformation, lead to slightly lower values than K_0, but still not as low as K_a. The value is based on soil mechanics theory and K_0 is often known as the coefficient of earth pressure at rest.

A more sophisticated treatment of the lateral pressure ratio came from Walker (1966), extended by Walters (1973), who recognised that the solid adjacent to the wall must be in a stress state corresponding to the wall friction shearing against its boundary with fully-mobilised friction. A similar Mohr's circle analysis yields a different relation, presented here in the form given in the Australian Standard for Loads in Bulk Solids Containers, AS 3774 (1996):

$$K = \frac{1+\sin^2\phi_i - 2\sqrt{\sin^2\phi_i - \mu_w^2\cos^2\phi_i}}{4\mu_w^2+\cos^2\phi_i} \tag{1.8}$$

where μ_w is the fully-developed wall friction coefficient of the solid.

This equation has two limiting values. As $\mu_w \rightarrow 0$ (perfectly smooth wall), $K \rightarrow K_a$ (Rankine Active state), and as $\mu_w \rightarrow \tan\phi_i$ (perfectly rough wall), K tends to the value:

$$K = \frac{1-\sin^2\phi_i}{1+\sin^2\phi_i} \tag{1.9}$$

The distribution of K with μ_w according to Eq. 1.8 is shown in Fig. 1.6. The lateral pressure ratio increases with the friction coefficient, gradually at first and then more steeply as $\mu_w \rightarrow \tan\phi_i$. In the Rankine active state, rough solids are predicted to have very low values of K indicating very low pressures near the surface, which is not true, and it was recognised that the Rankine active limit was an underestimate of filling pressures after extensive damage to many silos.

The current European Standard for loadings on silos, EN 1991-4 (2007), follows a different procedure and instead tabulates various mean values of K_m for different granular solids under different conditions. A conversion factor is also given, a_K (greater than unity), and through division or multiplication of K_m by a_K respectively one obtains the upper or lower characteristic design value of K. This semi-empirical approach attempts to accommodate the large statistical variations in granular solids' properties. The same method is also used to obtain characteristic design values of γ, μ and ϕ_i.

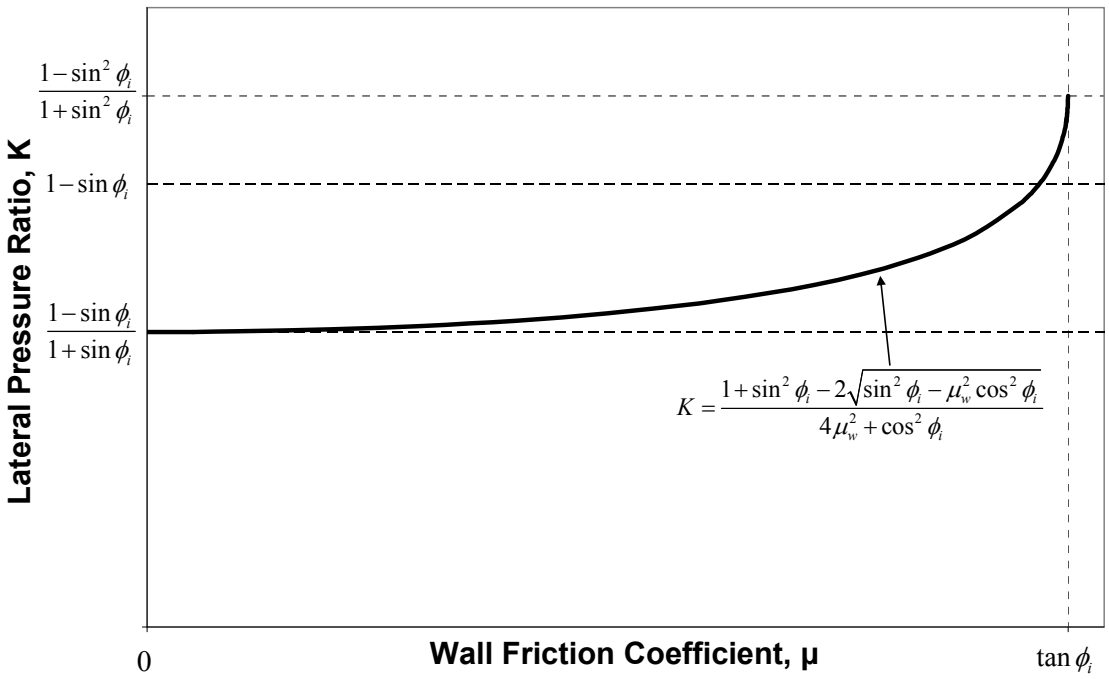

Fig. 1.6 – Variation of the lateral pressure ratio with the wall friction coefficient

It should finally be reminded that the Janssen and Walker pressure theories, on which all silo design is essentially based, assume constant values of K (however it is calculated) down the entire silo height. This is very unlikely to be the case in reality, and results from experimental studies (e.g. Reimbert, 1961; Blight, 2006) suggest that the lateral pressure ratio is dependent on the depth within the solid and on the height and cross-section of the silo. Other early researchers, including Ketchum (1907), Amundson (1945) and Saul (1953) also found considerable variations in K with depth, while others still, including Jaky, (1948) and Zakrzewski (1959) found very little. The experimental field of silo pressures is notoriously difficult and very many different authors often get conflicting results for the same apparent phenomenon. More research is needed to improve the understanding of the variation of the lateral pressure ratio in the silo.

1.2.4 The hopper wall pressure ratio

For the hopper wall pressure ratio under filling conditions, F_f, the empirical value of Rotter (1990), based on the experimental data of Motzkus (1974), is prescribed in EN 1991-4:

$$F_f = \frac{1+0.8\mu_h \cot\beta}{1+\mu_h \cot\beta} \tag{1.10}$$

where μ_h is the lower characteristic value of the wall friction coefficient (fully or partially-mobilised, depending on hopper steepness) of the hopper, and β is the hopper apex half-angle.

For the corresponding value of under discharge conditions, F_e, the theoretical value of Walker (1966), also based on a Mohr's circle analysis, is prescribed in EN 1991-4:

$$F_e = \frac{1+\sin\phi_i \cos\varepsilon}{1-\sin\phi_i \cos(2\beta+\varepsilon)} \text{ where } \varepsilon = \tan^{-1}\mu_h + \sin^{-1}\left\{\frac{1}{\sin\phi_i}\sqrt{\frac{\mu_h^2}{1+\mu_h^2}}\right\} \quad (1.11)$$

Neither of the above equations are used in the analyses presented in this thesis, and are thus not pursued further here.

1.2.5 Concentric discharge in silos

It was discovered early that the normal pressures may increase significantly during discharge (Prante, 1896; Jamieson, 1903; Bovey, 1904; Pleißner, 1906; Ketchum, 1907), yet it was not clear how large these increases were or for how long they persisted. Long term pressure rises were of the order of 30%, whilst very short term local rises were of the order of 300% (Rotter, 2007a). A significant attempt to explain these large increases was made by Nanninga (1956) who proposed, developing the idea of Koenen (1895), that in addition to a solid after filling being in a Rankine active state, during discharge it is in a Rankine passive state. The change from active to passive states during discharge was originally proposed to be gradual resulting in a much lower pressure increase (Fig. 1.7b), but this idea was adopted by others (Walker, 1966; Walters, 1973; Jenike *et al.*, 1973; Arnold and McLean, 1976; Arnold *et al.*, 1980) who postulated that this effect was quite sudden (Fig. 1.7c), leading to what become known as the 'switch' theory.

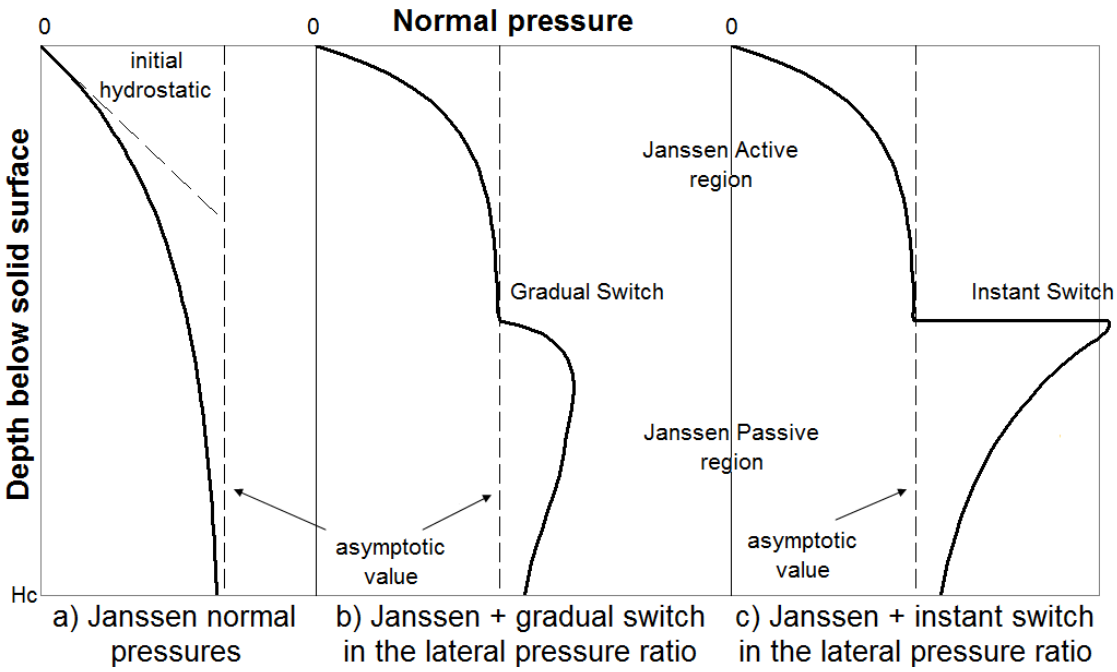

Fig. 1.7 – Illustration of the switch in Janssen normal wall pressure

For a typical solid, K_p/K_a is of the order of 10, yet such huge pressure jumps have never been reported during discharge (e.g. Frese, 1977), nor do many steel silos fail by bursting which is what one would expect if such an axisymmetric jump in pressure were present. Jenike *et al.* (1973) addressed this discrepancy by devising the 'minimum strain energy theory' which used the calculus of variations and the assumption of an elastic stored solid to deduce rather smaller pressure increases. This idea was followed by Arnold and McLean (1976) and Arnold *et al.* (1980), the results of which were adopted into the AS 3774 Standard. However, the basis of this theory is weak and it fails to address the problem of unsymmetrical pressures.

The 'switch' theory is now largely discredited (Rotter, 2007a). In design, the increase in pressures for concentric flow is normally accounted for by simple multiplication factors of the order of 1.8. However, these are also based on concepts from quite simple theories (Jenike *et al.*, 1973; Drescher, 1991; Nedderman, 1992), including that of the 'switch'. Other experimental studies which explored flow patterns during concentric discharge include Deutsch and Clyde (1967), McCabe (1974) and Chatlynne and Resnick (1973). An alternative and more robust theory, which predicts more modest and realistic pressure increases during discharge without relying on making questionable alterations to the lateral pressure ratio, is presented in this thesis.

1.2.6 The patch load concept

Since the Janssen derivation assumes axisymmetric pressures, it was naturally first thought that measured pressures would be axisymmetric too, and experimenters originally placed a single pressure cell at any vertical location (Pieper and Wenzel, 1964; Rotter, 2007a). Later experiments which included more pressure cells around the circumference revealed that even during storage there are significant differences in normal pressures at any level, and during discharge the pressures fluctuate wildly (Fig. 1.8). These variations are difficult to characterise with simple equations (Nielsen and Kristiansen, 1980; Gale *et al.*, 1986; Ooi *et al.*, 1990; 2005; Nielsen, 1998), and show that even concentric discharge is not very 'concentric' at all.

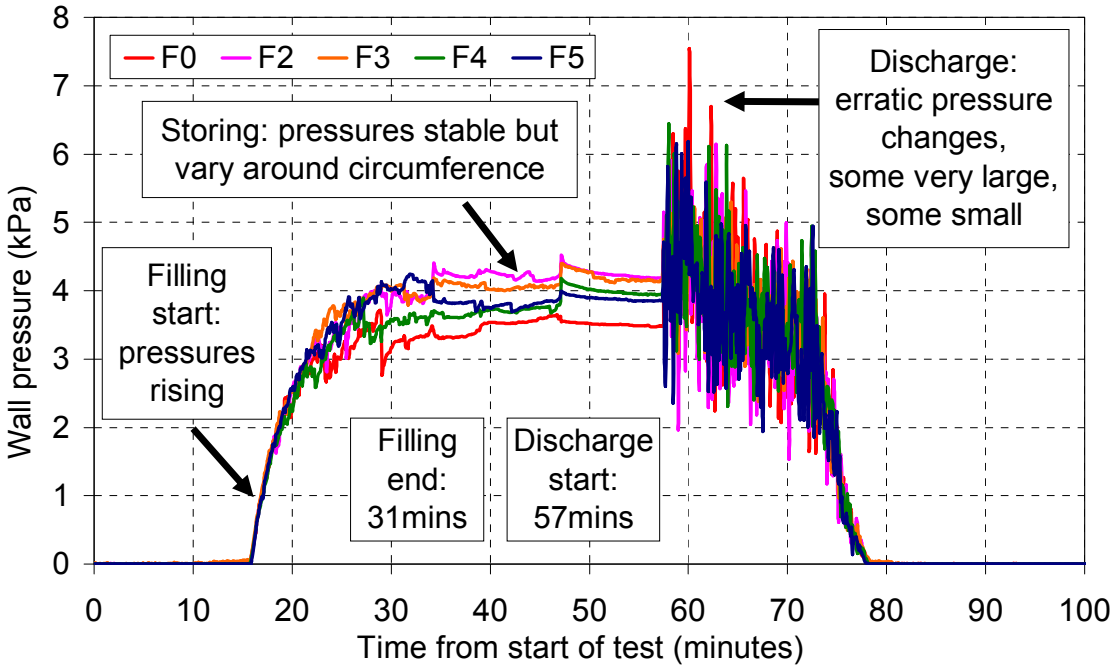

Fig. 1.8 – Example of the erratic variation of measured normal pressures during discharge (F0 – F5 are pressure cells around the circumference), after Rotter (2007a)

In older design standards (e.g. DIN 1005-6, 1987; ISO 11697, 1995; PN-B-03202, 1996), the effect of unsymmetrical pressures arising under notionally-symmetrical conditions of both filling and discharge was treated as an additional unsymmetrical component to the axisymmetric solid pressures. This attempted to account somewhat for the structural consequences of unsymmetrical loads on silos, as such loads are known to be highly damaging on shells (Calladine, 1983; Yamaki, 1984). The influence of this additional component was expressed through the application of a 'patch' of continuous

normal pressure with a prescribed magnitude and distribution at a location where its presence was thought to be most damaging (Fig. 1.9).

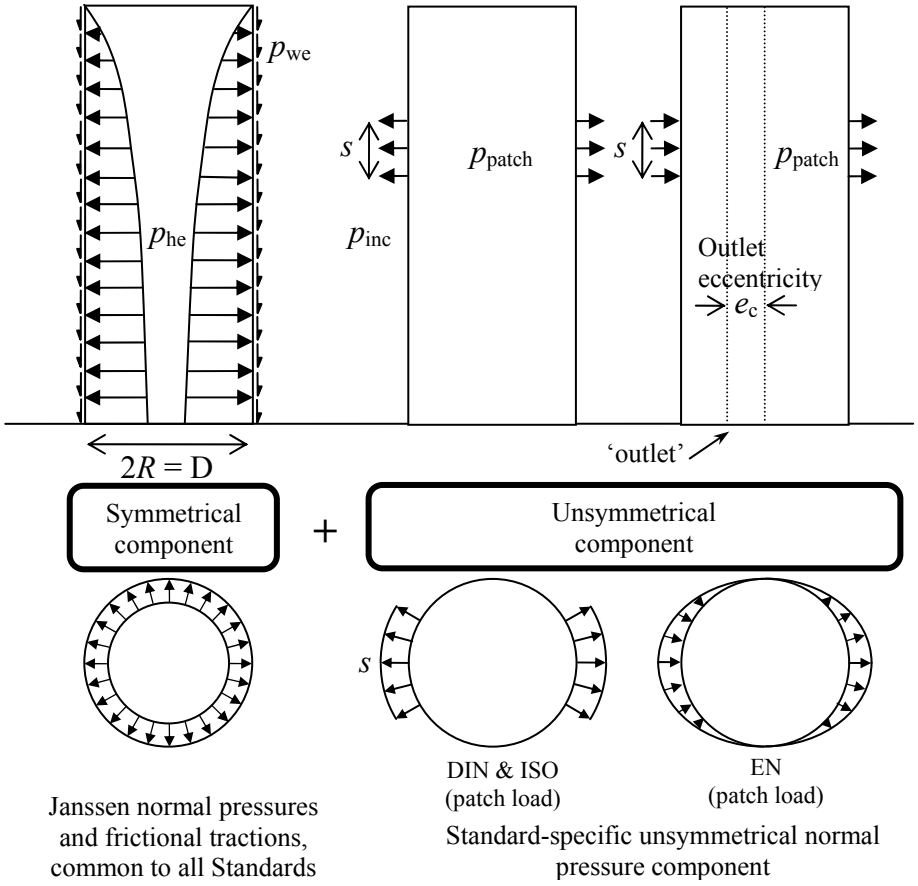

Fig. 1.9 – Schematics of normal pressure components for patch loads as defined by DIN 1055-6 (1987), ISO11697 (1995) and EN 1991-4 (2007)

Codified representations of patch loads differ considerably from one standard to another. For example, the German and ISO Standards (DIN 1055-6, 1987; ISO11697, 1995) define two rectangular patches of size $s \times s$ (s being a function of D, the silo diameter) of increased pressure at a prescribed height, both opposite each other. The patch load treatment in the new European Standard (EN 1991-4, 2007) is required if the outlet eccentricity e_c is considered to be less than $0.25D$, but the calculation must always be carried out except for the smallest of silos. A patch of normal pressure with a sinusoidal distribution is defined around the full circumference, with a pressure reduction nearest the outlet (if any) and a corresponding increase on the opposite side, both at a prescribed height and spanning a vertical distance of s. None of these Standards define an associated increase in frictional tractions for the patch load.

It may be argued that these are acceptable for use where minor eccentricities are expected, but unfortunately in all cases except EN 1991-4 (2007) and AS 3774 (1996) these are the *only* prescribed distributions to account for non-uniform pressures. The patch treatment, though rudimentary and not rigorously representative of a realistic pressure pattern (e.g. Hartlén *et al.*, 1984; Ooi *et al.*, 1990; Nielsen, 1998), did however correctly identify unsymmetrical normal pressures, rather than frictional tractions, as the main catalyst for failure of the silo.

In the earlier standards (DIN and ISO), the patch pressures were applied going outwards with the implication that failure would be through circumferential bending. This was based on the common misconception that failure in all silos is governed by material yielding due to circumferential bending and tension (Jenike, 1967; Emanuel *et al.*, 1983; Roberts and Ooms 1983; Wood, 1983) which influenced designers to treat the shell as a simple planar ring. This may be appropriate for thick-walled reinforced-concrete silos, but thin-walled metal silos behave entire differently. Bursting failure in metal silos is uncommon except where inadequate bolted joints are used (Rotter, 2006). By contrast, the single-harmonic patch load distribution of EN 1991-4 (2007) is designed to create a global overturning moment and an increase in axial compression on one side of the silo, with buckling of metal silos in mind.

Some research has since been done to investigate the effect of these patches of normal pressure on silo stability using both linear elastic and more sophisticated computational analyses. Gillie and Rotter (2002) and Song (2004) found that the size, magnitude and location of a patch may each have a deleterious effect on both the linear elastic membrane and bending stresses in the silo wall. Song and Teng (2003) and Song (2004) also showed, however, that although the patch load is indeed very detrimental in linear elastic and linear bifurcation finite element analyses of the structure, in geometrically nonlinear analyses the bifurcation loads were little different to those with no patch load. Geometric nonlinearity was found to make the influence of such patch loads negligibly small, and may therefore be said to have a beneficial effect. This, combined with the lack of consistency throughout these Standards with regard to the definitions of the unsymmetrical pressure distributions, strongly suggests that the patch load treatment is not satisfactory.

1.2.7 Flow patterns in silos

Many different types of flow patterns may occur in silos, each one constituting its own design condition with significantly different pressure distributions. The three basic flow patterns introduced in EN 1991-4 (2007) for the initial discharge of solids from a silo in the full condition are 'mass flow', 'mixed flow' and 'pipe flow', (Fig. 1.10). The following descriptions follow those found in Rotter (2001a), while a similar overview may also be found in Hampe (1987).

Mass flow occurs when the entire body of stored solid discharges simultaneously, with a 'first in-first out' flow order: there are no 'dead' zones of solid which fail to discharge. It is advantageous where prolonged storage of material is to be avoided, or a homogenous, non-segregated, well-controlled outflow stream is desired. However, a relatively steep hopper is required to ensure such flows, potentially raising the energy cost of elevating the solid to a higher level. Additionally, there is significant wear of the silo wall under full mass flow, exacerbated by more abrasive materials such as coal and metal ores. The solid itself may also become damaged after discharge due to a large drop height. Mass flow is most common for loosely-packed solids.

Funnel flow occurs when only a limited portion of the cross-section actually discharges, the remainder being initially stationary. The flow pattern thus follows a 'first in-last out' order. Such discharge often commences as an unstable narrow channel ('pipe flow') surrounded by stationary material which may extend all the way to the surface ('internal pipe flow'), and consequently spreads out into a wider, more stable form ('mixed flow'). In the later stages of the discharge, the surrounding stationary solid eventually also begins to move. Funnel flow significantly reduces abrasion against the silo wall and is easier on the stored material, but unless the solid is sufficiently free-flowing or the outlet is sufficiently large, it may fail to discharge completely leaving dead zones that must be removed manually, a dangerous process. This type of flow is very likely to occur for densely-packed solids, which require extensive dilation to flow that only a vertical free-fall through an outlet can provide (Zhong *et al.*, 1996; 2001). Conversely, flow of a loosely-packed granular solid does not require high dilation and wider channels are possible.

Flow patterns are influenced by a multitude of complex factors including granular solid solid properties (e.g. internal and wall friction, elasticity, dilation, cohesion, particle size distribution, moisture content and temperature), the filling process (e.g. segregation, packing, non-uniformities and eccentricities) and silo geometry (e.g. aspect ratio, presence of hopper and internal structures). The conditions under which mass flow occurs are relatively well understood and may be ensured through adequate hopper steepness, low wall friction and outlet size, but other flow patterns are significantly more difficult to guarantee. Additionally, it is known that the initial packing of some solids may have a radical effect on the flow pattern (e.g. Wright, 1979; Sugden, 1980; Munch-Andersen and Nielsen, 1990; Zhong *et al.*, 1996; 2001). Specifically, the development of mass or pipe flow is suggested to be closely dependent on the manner (distributed or concentrated) and eccentricity of the initial filling (e.g. Takhtamisev, 1953; Nielsen and Kristiansen, 1980).

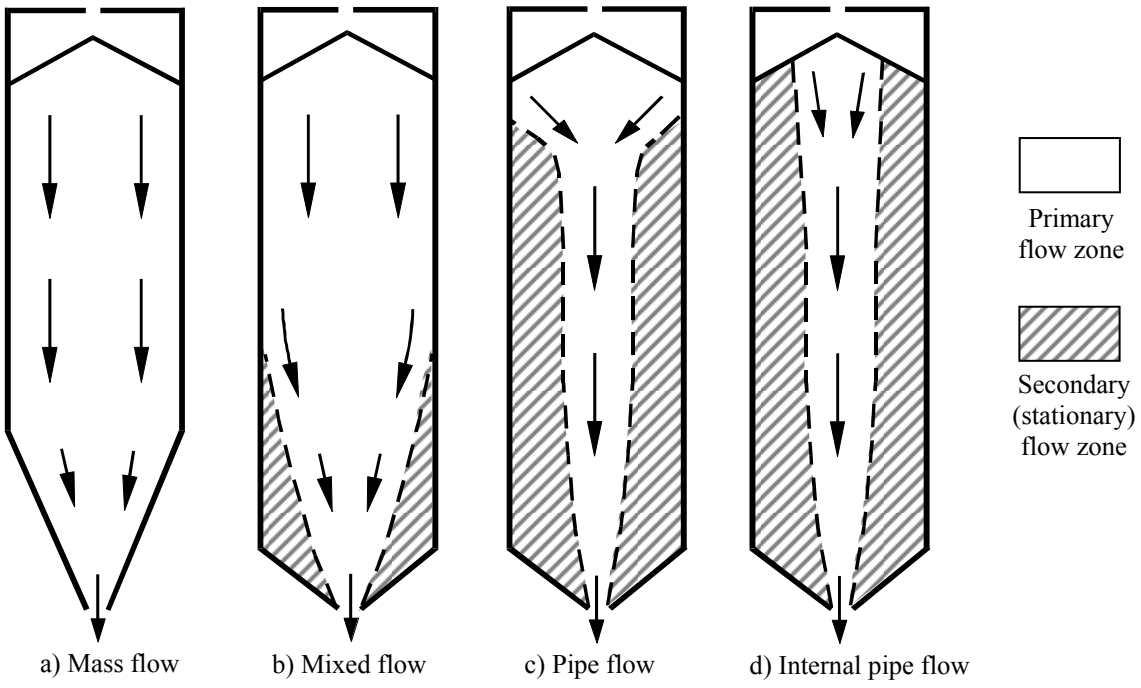

Fig. 1.10 – A selection of typical axisymmetric flow patterns, after EN 1991-4 (2007)

Unsymmetrical flow patterns are present under notionally concentric conditions more often than they are absent, leading to patterns akin to Fig. 1.11a, and are the justification behind the patch load treatment presented previously. Granular solids flows which can no longer be idealised as concentric are named ‘eccentric’, and are the central focus of this thesis. Highly eccentric discharge in dense solids leads to a much more clearly

differentiated pressure pattern associated with the formation of an unsymmetrical pipe flow channel, shown in Fig. 1.11b, c and d below. Such flows may occur either accidentally, or may be a design feature of the silo for operational reasons.

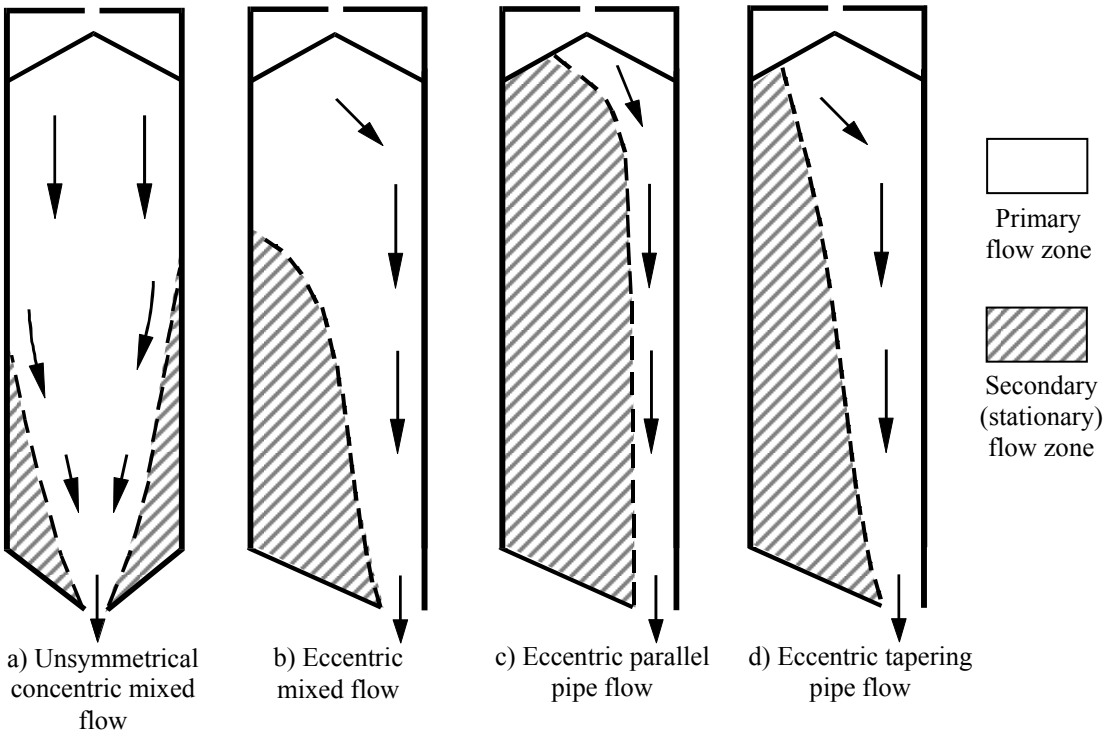

Fig. 1.11 – A selection of typical unsymmetrical flow patterns, after EN 1991-4 (2007)

1.2.8 Eccentric discharge in silos

The first known experiment dealing with eccentric unloading of grain bins was performed by the German engineer Prante (1896) who determined that the lateral pressures on the silo wall opposite the outlet increased by 2 to 4 times the static lateral pressures. Though Prante's results were apparently considered unreliable at the time (Bucklin *et al.*, 1990), they provided an early indication of the problems associated with eccentric discharge. One of the first recommendations warning against the practice of eccentric discharge, by Ketchum (1907), was based on Prante's work.

Very many experiments and some computational studies have since been conducted on silos under eccentric discharge, e.g. Pieper and Wenzel (1964), Pieper and Wagner (1969), Ravanet (1976), Nielsen and Kristiansen (1979), Ross *et al.* (1980), Nielsen and Andersen (1981), Britton and Hawthorne (1984), Hampe and Kamiński (1984a,b), Hartlén *et al.* (1984), McLean and Bravin (1985), Gale *et al*. (1986), Carson *et al.* (1991), Chen (1996), Chen *et al*. (1998), Ayuga *et al.* (2001), Vidal *et al.* (2006) and

many more. These studies produced highly varied outcomes which are extremely difficult to generalise. This is not an unexpected outcome given the difficult nature of the problem. Other authors, including Jenike (1967), NRCC (1969), Colijn and Peschl (1981), FBIC (1981), Wood (1983), Roberts and Ooms (1983), Emanuel *et al.* (1983), Rotter (1985a), Safarian and Harris (1985), Gorenc *et al.* (1986), Ooms and Roberts (1986), DIN 1055-6 (1987), ACI 313-77 (1983), ACI ADP (1989) and Blight (2006), proposed a vast array of different pressure distributions or failure criterions under eccentric discharge. However, most of these were generally not successful in closely reproducing what had been observed in experiments or in the field.

An important step in understanding came some twenty years ago with Rotter's theory (1986) for the pressures in a silo with a parallel-sided flow channel developing adjacent to a crescent-shaped body of stationary solid. The derivation follows the same structure and assumptions of mean pressure values as Janssen's slice analysis, but with more complex boundary conditions. A marginally-simplified version (Rotter, 2001b) is summarised in Fig. 1.12. The assumption of a parallel-sided flow channel allows the solution to be written in closed form.

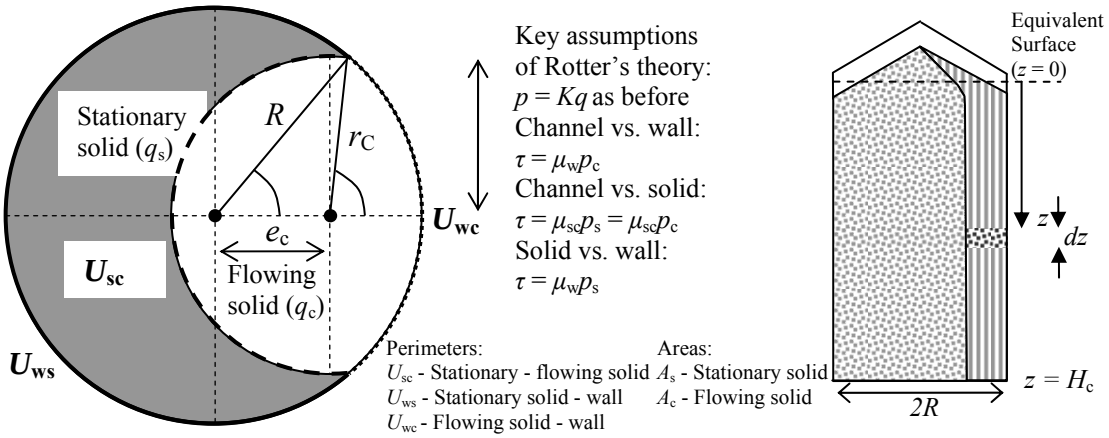

Fig. 1.12 – Derivation diagram for Rotter's original eccentric discharge theory (1986)

The respective expressions for the areas of the flowing and stationary solids, A_c and A_s, as well as the perimeters, may be derived using basic geometry. Vertical equilibrium of a slice through the truncated flow channel circle leads to the following ordinary differential equation:

$$A_c \frac{dq_c(z)}{dz} + q_c(z) K \left(\mu_w U_{wc} + \mu_{sc} U_{sc} \right) = \gamma A_c \tag{1.12}$$

The solution to Eq. 1.12 assumes the boundary condition of zero stress at the solid surface $q_c(0) = 0$, and yields the equation for the pressure normal to the silo wall within the flow channel:

$$p_c(z) = p_{c0}\left(1 - e^{-\frac{z}{z_{c0}}}\right) \text{ where } p_{c0} = K\gamma z_{c0} \text{ and } z_{c0} = \frac{1}{K}\left(\frac{A_c}{\mu_w U_{wc} + \mu_{sc} U_{sc}}\right) \tag{1.13}$$

Similarly, vertical equilibrium of a slice through the crescent-shaped stationary solid, with the condition that the shears on the perimeter with the flow channel must be in equilibrium with those in the flow channel (Eq. 1.13), leads to the following ordinary differential equation:

$$A_s \frac{dq_s(z)}{dz} + q_s(z) K \mu_w U_{ws} = \gamma A_s + \mu_{sc} U_{sc} p_{c0}\left(1 - e^{-\frac{z}{z_{c0}}}\right) \tag{1.14}$$

The solution to Eq. 1.14 also assumes the boundary condition of zero vertical stress at the solid surface $q_s(0) = 0$. The equation for the pressure normal to the silo wall in the stationary solid is thus:

$$p_s(z) = p_{s0}\left(1 + w + wue^{-\frac{z}{z_{c0}}} - (1 + w + wu)e^{-\frac{z}{z_{s0}}}\right) \tag{1.15}$$

where

$$p_{s0} = K\gamma z_{s0}\,;\, z_{s0} = \frac{A_s}{\mu_w K U_{ws}}\,;\; w = \left(\frac{A_c}{A_s}\right)\left(\frac{U_{sc}\sin\phi_i}{\mu_w U_{wc} + U_{sc}\tan\phi_i}\right) \text{ and } u = \frac{z_{c0}}{z_{c0} + z_{s0}}$$

It is clear that as $A_c \to 0$, $w \to 0$, $z_{c0} \to 0$, $u \to 0$ and therefore $p_s \to$ Janssen Eq. 1.2.

Rotter's original working of this theory (1986) continued with further assumptions about the lateral pressure ratio based on the Walker and Rankine theories, but these are not critical to the derivation. A more powerful version of this theory is developed in this thesis assuming curved parabolic flow channel sides, rather than parallel sides. The resulting differential equations may only be solved by numerical integration, but the range of flow channel geometries which may be modelled is almost unlimited. The first investigation of a similar theory was only made in the relatively unknown undergraduate thesis of Barry (1988).

The vertical pressure in the flow channel is always predicted to be significantly lower than in the stationary solid and, consequently, so are the normal pressure and frictional

traction exerted by this low pressure on the silo wall. An example of typical pressure distributions predicted by Rotter's (1986) eccentric discharge pressure theory is shown in Fig. 1.13 below.

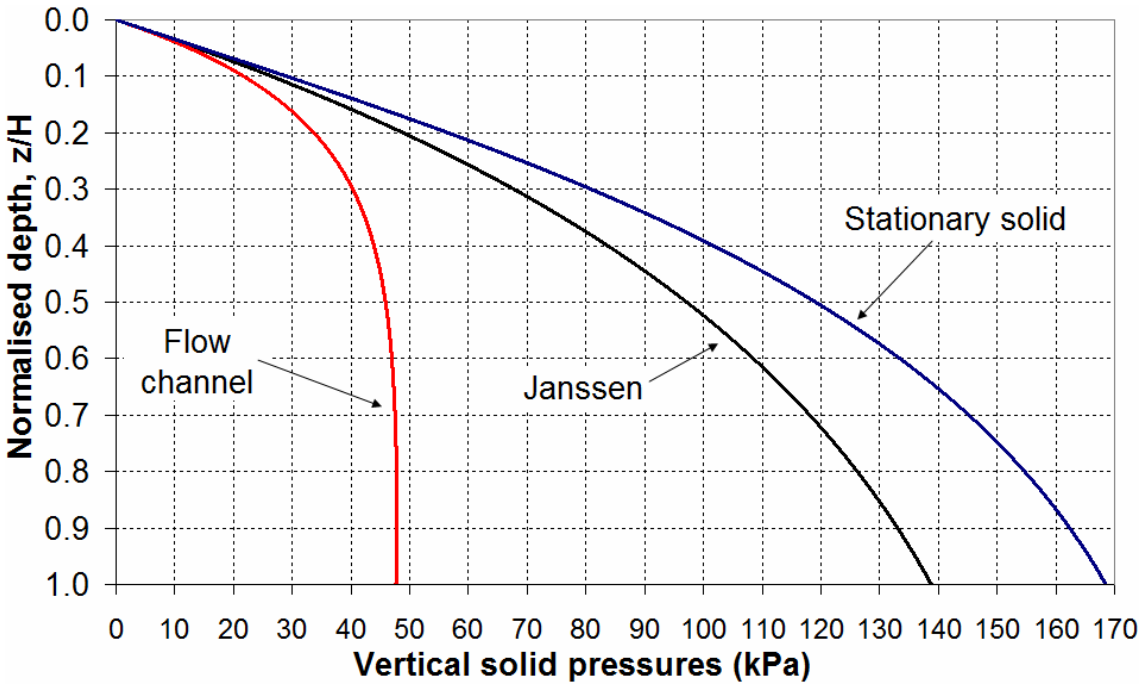

Fig. 1.13 – Example of typical vertical solid pressures according to Rotter (1986)

The evidence about whether the pressure in the flow channel should be lower or higher than that in the stationary solid is conflicting. The experiments of Pieper and Wagner (1969) on model bins containing sand reported apparent increases in lateral pressure on the side of the outlet, while Thompson *et al.* (1986) determined that the largest vertical loads during eccentric discharge of wheat from corrugated model steel bins also occurred adjacent to the outlet. An equivalent conclusion was reached by Horabik *et al.* (1987), based on observations of eccentric discharge of wheat from a smooth-walled model bin, and by Gopalakrishnan (1978) in his experiments on eccentric discharge of rice (but *not* wheat, which found pressure decreases adjacent to the outlet) from square silos. Bucklin *et al*. (1980), Colijn and Peschl (1981) and Safarian and Harris (1985) all proposed design models based on the assumption of increased pressures in the flow channel and a failure mode through circumferential plastic collapse. However, it is difficult to rely on the accuracy on many of these findings given the relatively crude experimental techniques and philosophies that were often employed, including the use of a single pressure cell at any level and the focus on the highest recorded pressure values, regardless of location or duration. As noted at the start of this section, pressure

models based on observations made from unwise experimental procedures are rarely founded on sound mechanics and generally unsuccessful in analytically reproducing observations in the field.

Experimental evidence that directly supports reduced flow channel pressures may be found in the full-scale Swedish grain silo tests at Karpalund which are widely reported in, amongst others, Nielsen and Askegaard (1977), Nielsen and Kristiansen (1980), Nielsen and Andersen (1980; 1982), Nielsen (1983; 1998), Hartlén *et al.* (1984) and Ooi *et al.* (1990; 2005). This experimental program was pioneering in its use of multiple pressure cells down at least four meridional generators, all at different circumferential positions. The results and conclusions derived from these tests may therefore be considered more reliable than much of what came before. Other experimental studies which found a reduction in wall pressures adjacent to an eccentric outlet include Jamieson (1904), Ravenet (1976), Frese (1977), Gale *et al.* (1986), Ooms and Roberts (1986) and Blight (2006). However, where the Rotter (1986) theory predicts a progressive growth in flow channel pressures with depth down to an asymptotic value (Fig. 1.13 and Eq. 1.13), the results of the Karpalund tests, and both Ravenet (1976) and Gale *et al.* (1986) suggest the reverse whereby the channel pressures start at zero at the outlet and grow progressively with height.

A cruder version of Rotter's 1986 work has been adopted, for the first time as a codified procedure, into the Section 5.2.4.3 of EN 1991-4 (2007) for Action Assessment Class 3 silos with large anticipated eccentricities or very slender aspect ratios. This Standard uses the Janssen distribution, Eq. 1.2, rather than the significantly more complex distribution from Eq. 1.15, for the pressure in the stationary solid. This purposeful simplification is not based on sound mechanics and was made because the theory was being introduced into a Standard for the first time. The Janssen values (Eq. 1.2 and Fig. 1.13), are quite a bit lower than what Eq. 1.15 predicts and it is not yet known what structural effect this change may have.

An additional consideration in the original theory was the possibility that high normal pressures might develop against the wall in the zone immediately inside the static solid (Jenike, 1967; Wood, 1983; Rotter, 1986; Chrisp *et al.*, 1988; Chen, 1996). Such a rise occurs due to the arching effect of the ring of static material immediately adjacent to the

flowing material (Fig. 1.14a). It is required in order to maintain horizontal pressure equilibrium at any level, since it must counter the drop in pressures that occurs in the wall against the flow channel, but the form that it must take is not yet understood.

Due to the strive for a universally conservative design procedure for this dangerous and poorly-understood phenomenon, the zones of high pressures in the stationary solid immediately adjacent to the channel were assigned an almost belligerently severe form by EN 1991-4, illustrated in Fig. 1.14b below. This form does indeed respect horizontal equilibrium, but is very damaging to the structure. An study of more realistic circumferential distributions of normal pressures (Fig. 1.14c), based on a stricter analytical derivation using elasticity theory of Timoshenko and Goodier (1970), is presented in Appendix B of this thesis.

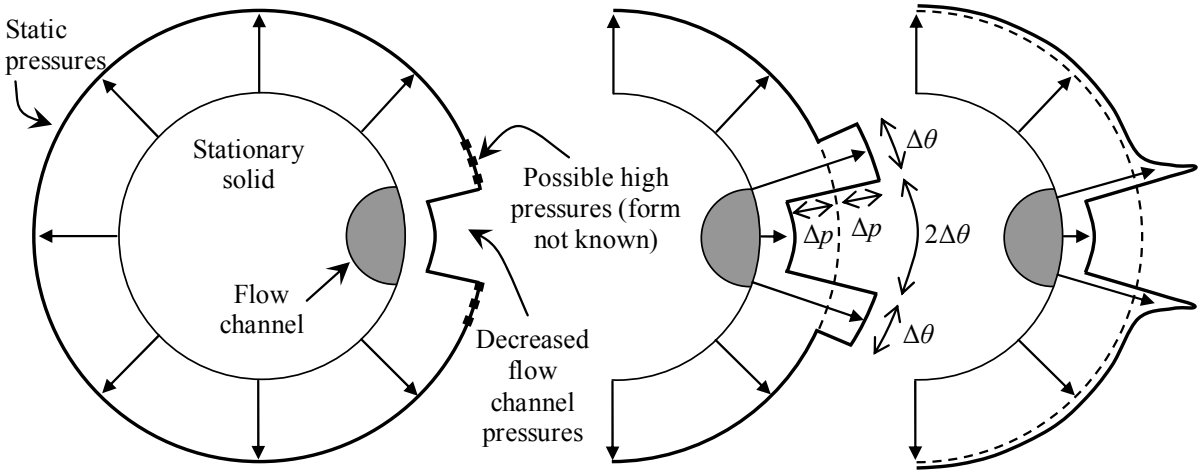

Fig. 1.14 – Suggestions for the form of normal pressures against the wall of an eccentrically discharging silo

Aside from Rotter's initial studies (1986, 2001b) which probed the structural effects of the original form of the pressure distribution using a linear elastic finite element analysis with encouraging results, and a very short discussion by Kaldenhoff (2008), no other related studies of this pressure model are known. The author's own work to date has explored the structural consequences of the EN 1991-4 implementation of this theory (Sadowski and Rotter, 2008; 2009; 2010), and has revealed many crucial aspects of silo behaviour under eccentric discharge which correspond very closely to observations made in practice. These are explored in full in this thesis.

1.3 Literature on shell structures, stability, computational analysis and design

1.3.1 Shell theory

A cylindrical metal silo is a highly efficient shell structure. Stresses in thin-walled shells of revolution may be calculated by two different methods. Firstly, a simpler treatment is given by shell membrane theory, which uses local static equilibrium to consider only in-plane 'membrane' stresses constant through the shell thickness (Rotter, 1987a). The theory ignores out-of-plane stresses, bending or twisting moments, material stiffness or changes of geometry. Secondly, a complete but significantly more complex treatment is given by shell bending theory, which includes all of the above omissions (Rotter, 1987b).

Both theories are treated in considerable depth by texts such as Timoshenko and Woinowsky-Krieger (1959), Flügge (1960), Budiansky and Sanders (1963), Kraus (1967), Seide (1975), Gould (1977), Calladine (1983) and many others. These classical texts present very meticulous and mathematically complicated derivations of the governing equations, giving several helpful examples for load patterns and geometries which have some form of symmetry. Such load patterns include uniform axial compression, torsion, internal pressure and external pressure. These are applied predominantly to uniform thickness shells in the form of spheres, hemispheres, cones, cylinders, plates and other such axisymmetric shapes. It is usually due to assumptions of axisymmetry that the governing differential equations may be solved, and this makes the above theoretical treatments of limited use when attempting to solve algebraically for the highly complex, but more realistic, load patterns and varying-thickness shell designs.

The treatment of non-uniform loads is mostly limited to membrane theory treatments of the 'simpler' cases, also due to the mathematical complexity. These include local supports at regular intervals, axisymmetric bands of pressure, axisymmetric hydrostatic loads and so on. For localised or wind loads, a Fourier series expansion is usually used (e.g. Rotter, 1987a; 1987b; Ansourian, 2004).

Algebraic bending theory solutions for problems on non-axisymmetric systems are rarely available. Indeed, bending theory is usually avoided even for axisymmetric

systems except at locations where localised bending is anticipated to occur and to be of significance, such as near certain boundary conditions. The difference between the two shell theories is illustrated in Fig. 1.15 below, which shows the bending and membrane theory solution for axial stresses in two silos: a slender silo (H/D = 3) under Janssen pressures and a squat silo (H/D = 0.5) under modified Reimbert pressures. The shell wall bends to satisfy a restrained boundary condition and in doing so introduces high local bending stresses, an effect not captured by membrane theory. For squatter silos, bending effects protrude significantly further into the shell and a membrane theory solution may become significantly less accurate.

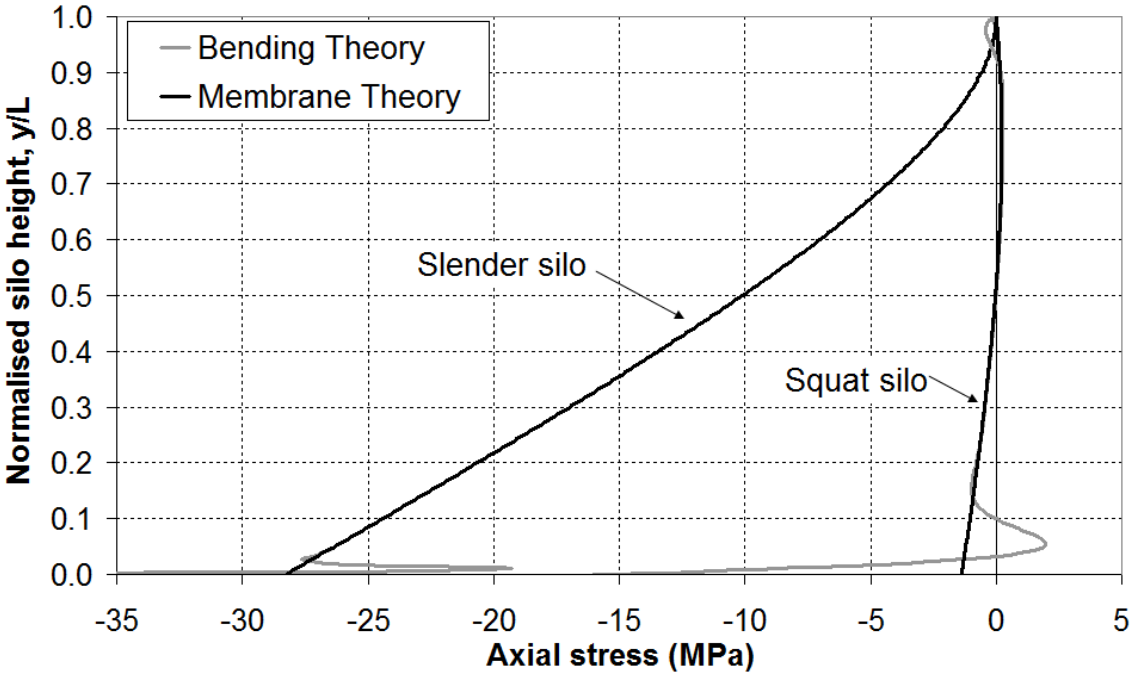

Fig. 1.15 – Comparison of membrane and bending theory solutions for the axial stresses in the silo under Janssen and modified Reimbert silo pressures

For thick-walled shells such as pipes, where shear strains and stresses acting normal to the plane of the shell may no longer be ignored or assumed constant throughout the thickness of the shell, it is necessary to perform an elastic solid analysis. This results in different phenomena and is beyond the scope of this thesis. Elasticity theory is treated in many classical texts including Muskhelishvili (1953), Timoshenko and Goodier (1970) and Ugural and Fenster (1977).

1.3.2 Stability of silo shell structures

Shells are three-dimensional structures which exhibit extremely complex buckling behaviour in the form of snap-through and bifurcation buckling, usually with highly unstable post-buckling paths. This behaviour is significantly more complex than the 'simpler' (usually two-dimensional) lateral-torsional buckling of beams, columns or plates which exhibit stable or neutral post-buckling paths. The latter are covered in depth by many university course texts, the definitive reference being perhaps Timoshenko and Gere (1963).

Silos are slender, thin-walled shell structures and are very susceptible to stability failures (i.e. buckling) at stresses and load levels well below those which would cause plastic collapse. The first theoretical shell buckling problem to be solved was the uniform-thickness cylinder under axial compression, the load case associated with the most common silo failure mode (Rotter, 2004). This was solved independently and almost simultaneously by three authors (Lorenz, 1908; Timoshenko, 1910; Southwell, 1914), which led to the theoretical 'classical elastic critical buckling stress'. It is usually denoted as σ_{cl} or σ_{cr}, depending on the source, but is presented in Eq. 1.16 using the notation σ_{cl}. This equation has been used as a reference benchmark for the analysis of cylindrical shells ever since.

$$\sigma_{cl} = \frac{Et}{R\sqrt{3\left(1-\nu^2\right)}} \approx 0.605\frac{Et}{R} \tag{1.16}$$

However, early experiments on axially compressed isotropic cylinders have shown that their strengths fall far below this theoretical value and are very scattered (Harris *et al.*, 1957), as shown on Fig. 1.16 below. Though many factors contribute to the discrepancy between the ideal and actual buckling strengths, including the effect of pre-buckling deformations (e.g. Donnell, 1934; Yamaki, 1984) and local inelastic bending near boundary conditions (e.g. Rotter; 1983a; 1985b), by far the most important cause of this loss of strength was found to be due to geometric imperfections.

Imperfections are deviations from the perfect shell surface. Their effect on the buckling strength of axially compressed cylinders was first investigated by Koiter (1945), then subsequently by many others including Donnell and Wan (1950), Koiter 1963, Hutchinson (1965), Hutchinson and Koiter (1970), Cohen (1971), Hutchinson *et al*. (1971), Arbocz and Sechler (1974), Singer (1980, 1982) and Yamaki (1984). It was

found that increasing the amplitude of these deviations resulted in a disproportionately detrimental effect on the buckling strength of an axially compressed cylinder (Almroth, 1963; 1966; Yamaki 1984). A detailed discussion of the historic development of this topic may be found in Rotter *et al.* (1986) and, more recently, in Rotter (2004).

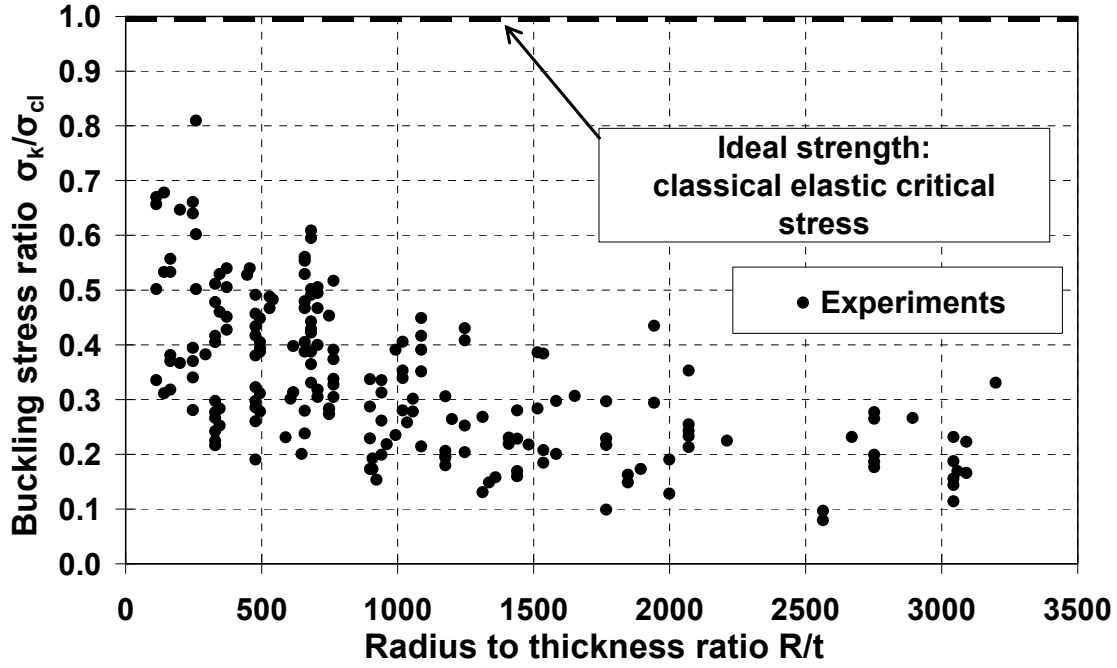

Fig. 1.16 – Experimental strength of isotropic axially compressed cylinders (after Harris *et al.*, 1957)

Imperfections are ubiquitous in real silos but it would be extremely difficult to quantify and to take account of every possible form. It is equally difficult to investigate the nonlinear behaviour of imperfect and more realistic shell structures without resorting to computational finite element analyses, which are discussed shortly. The most deleterious imperfection form should be therefore identified to ensure a conservative structural design, but this depends on every aspect of the system including the geometry, boundary conditions and loading. The exact form that the most deleterious imperfection should assume is thus open to serious debate. Furthermore, the imperfection that is most damaging at one particular amplitude may not necessarily be the most damaging at another (Song *et al.*, 2004), so a search for the most deleterious form is far from simple. An overview of common imperfection forms in shells is, however, central to any discussion about shell buckling.

Lastly, the effect of internal pressure has generally been found to be beneficial to the buckling strength of a silo. It has been shown that internal pressure may significantly reduce the effect of geometric imperfections (e.g. Lo *et al*., 1951; Harris *et al.*, 1957; Hutchinson, 1965; Weingarten *et al.*, 1965; Steinhardt and Schulz, 1971; Baker *et al.*, 1972; Saal *et al.*, 1979; Galambos, 1988; Rotter and Teng, 1989a; Trahair *et al.*, 1983; Li, 1994; Greiner and Guggenberger, 1998; Rotter, 2001a). However, very high internal pressure is likely to lead to yielding of the wall, reducing the buckling strength thus causing plastic buckling. The most common failure mode of this type is elephant's foot buckling (Rotter, 1985b; 1989; 1990; 2006) which forms at the base of the silo or at critical locations of changes of thickness or stiffness. The behaviour of local supports has also been investigated (e.g. Knödel & Ummenhofer, 1998; Guggenberger *et al.*, 2004; Doerich, 2007; 2008) which have been found to introduce localised compressive stresses near the supports which contribute to early yielding and buckling. The beneficial effect of low internal pressure and the deleterious effect of high internal pressure on the buckling load of shell structures have both been incorporated into the European Standard for shell structures, EN 1993-1-6 (2007).

1.3.3 Shell imperfection forms

Historically, eigenmode-affine imperfections were the first obvious choice for study following their importance as imperfection forms in columns, beams and plates. These were initially taken only as linear bifurcation modes (e.g. Koiter, 1945, 1963; Yamaki, 1984; EN 1993-1-6, 2007). In addition, nonlinear (incremental) buckling modes (e.g. Guggenberger *et al.*, 2004) and pre- and post-buckling deformations (e.g. Esslinger and Geier, 1972; Song *et al.*, 2004; Doerich, 2008) may also be critical for buckling. The application of these to example shell structures yields a vast array of different results, and it is not possible to come to a definitive conclusion about which one is the most detrimental. The effects of these idealised imperfection forms are thus highly dependent on the context and, additionally, few of them are in any way particularly realistic.

A wiser choice of imperfection form attempts to emulate realistic features found in existing shell structures, typically as a result of the manufacturing or construction process. One of the more successful of such 'realistic' imperfection forms is the axisymmetric weld imperfection of Rotter and Teng (1989a), also found in Teng and Rotter (1992). Their work recognised the idea of Hutchinson (1965) who established

that axisymmetric imperfections may be more detrimental to the buckling strength under axial compression than eigenmode-affine imperfections at the same amplitude. Indeed, surveys of civil engineering shells (Bornscheuer and Hafner, 1983; Bornscheuer *et al.*, 1984; Clarke, 1987; Clarke and Rotter, 1988; Rotter, 1988; Rotter *tl al.*, 1992; Ding *et al*., 1996; Knödel & Ummenhofer, 1996; Ummenhofer & Knödel, 1996; Teng *et al*., 2005) have shown that the imperfections found therein are predominantly axisymmetric and often directly attributable to the welding process. The axisymmetric weld imperfection form is thus an idealised simulation of the curving of sheet metal panels during the rolling process and their subsequent welding during construction. It has been found to be an almost universally detrimental imperfection form in a wide range of studies (Rotter and Zhang, 1990; Knödel *et al.*, 1994; 1995; Berry and Rotter, 1996; Ummenhofer, 1996; Berry *et al.*, 1997; 2000; Pircher *et al*., 2001; Song *et al.*, 2004; Hübner *et al.*, 2006; Rotter, 1996; 1997; 2008), and has also been reported to be a damaging imperfection under local axial compression (Cai *et al.*, 2002; Song *et al.*, 2004; Schmidt and Winterstetter, 2004a; 2004b).

Residual stresses or strains are another type of realistic imperfection, though they have not received a lot of attention apart from a handful of publications due to the difficulty in carrying out a rigorous treatment of these (Rotter, 1997). Hübner *et al.* (2006), Holst *et al.* (1996; 2000) and Holst and Rotter (2002), amongst others, investigated the effect of a dimpling of a shell subject to biaxial membrane shrinkage and swelling effects, and generally found that a shrinkage strain is detrimental to the buckling strength of a uniformly compressed silo. Darcourt *et al.* (2004), Josserand *et al.* (2007) and Jullien *et al.* (2008) performed complex heat transfer analyses and computer simulations to predict the residual stresses due to laser-beam welding of thin sheets of aluminium for aircraft construction, though they did not do a structural analysis. These are, however, highly specialised applications which are very difficult to generalise.

Additional realistic imperfection forms include local settlement (e.g. Greiner, 1980; Holst and Rotter, 2003; 2004), geometric misfits during construction (e.g. Holst *et al.*, 1999; Holst, 2008), dents (e.g. Rotter and Teng, 1989b), lap-joints (e.g. Esslinger, 1973; Essligner and Geier, 1977), out-of-round global deformations (e.g. Hübner *et al.*, 2007) and many others. The choice of imperfection form and the required imperfection amplitudes for design are specified for the first time in the EN 1993-1-6 (2007)

European Standard, where the amplitudes are related directly to the fabrication tolerance requirements of the silo structure (Rotter, 2004). Furthermore, it will be shown in this thesis a slender silo under eccentric discharge exhibits a very unusual imperfection-sensitivity behaviour, with many imperfection forms actually having a beneficial effect on its predicted buckling strength. A proposal will be made for a novel imperfection form that results in consistent buckling strength reductions under eccentric discharge.

1.3.4 Computational analysis

The analysis of structures has received an incomparable boost with the invention of the computer and the parallel development of the finite element method for structural analysis. A finite element formulation of a curved shell element with appropriate stress-strain relations, shape functions and nonlinear strain-displacement relations allows complex nonlinear problems to be solved, including those of stability and dynamics, for virtually any geometry and loading.

There is a very large volume of literature on the finite element method spanning almost three-quarters of a century, but some of the more relevant for structural analysis include Przemieniecki (1967), Zienkiewicz and Taylor (2006; 1st ed. 1967) and Cook *et al*. (2002; 1st ed. 1974). The finite element method has been implemented in several powerful commercial packages, including ABAQUS (2009), ANSYS (2009) and, NASA's original FEA solver from the 1960s that has been used ever since in several reincarnations, NASTRAN (2009).

The most trusted commercial package in the nonlinear and shell buckling community is ABAQUS, and all finite element analyses in this thesis were carried out with this program. The ABAQUS software offers various shell elements, ranging from 3 nodes to 9, and an efficient nonlinear solver. The two best elements for nonlinear shell analysis are the doubly-curved reduced-integration S8R5 and S9R5 rectangular elements. The former, having eight nodes, is usually more economic, but the lack of an interior node makes it more sensitive to element shape distortion (MacNeal, 1994; Song *et al.*, 2004). Since the author had access to a powerful machine, there was no reason not to use the best available S9R5 element in most FEA analyses. ABAQUS is very well suited to the nonlinear bifurcation analysis of shells with its implementation of the modified Riks algorithm (Riks, 1979), which allows the tracking of the nonlinear load-displacement

path and identification of negative eigenvalues in the tangent stiffness matrix with considerable accuracy.

1.3.5 Current structural design

1.3.5.1 The Eurocodes

The standards most relevant to the design of steel silos are the Eurocodes EN 1993-1-6 (2007) and EN 1993-4-1 (2007). Aside from both being the most current pan-European design standards, these documents offer numerous useful results for common load cases and geometries derived from shell theory. The EN 1993-1-6 (2007) Standard on the Strength and Stability of Steel Structures, however, is special in that it pioneers a state-of-the-art novel framework for both direct (by hand) and computer-aided design (with the implicit assumption of the finite element method).

Six distinct types of computational analysis, each with an increasing level of sophistication, are introduced depending on which ultimate limit state the design is being made for: plastic limit (LS1), cyclic plasticity (LS2), buckling (LS3) and fatigue (LS4). Each such type of analysis can, in principle, be used to address every one of the defined limit states, but each type of analysis produces a different result, so the criteria of failure in each limit state must be defined differently according to which analysis is used. The strength assessments are, however, effectively based only on three calculation processes: linear-elastic analysis (LA), linear bifurcation with plastic collapse (LBA and MNA), and complete geometrically and materially nonlinear analysis including explicit incorporation of geometric imperfections (GMNIA). Combined, these serve to calculate a series of buckling interaction parameters, based on the concept of the capacity curve of Rotter (2002; 2006; 2008), which characterise the buckling strength of the shell.

The most sophisticated numerical design procedure is that of the geometrically and materially non-linear analysis with explicit modelling of geometric imperfections (GMNIA). This requires the results of LBA and MNA above, and additionally the computation of the geometrically nonlinear elastic factors for the perfect (GNA) and imperfect shells (GNIA), and the geometrically nonlinear plastic limit load (GMNA). The GMNIA analysis thus allows the buckling strength of the structure to be found directly, but the result is highly dependent on the chosen form and amplitude of

imperfection (see previous discussion in Section 1.3.3). The different computational shell buckling calculations are summarised in full in Table 1.1.

Table 1.1 – Computational shell buckling calculations, after EN 1993-1-6 (2007)

Acronym	Description of Analysis	Geometry Law	Material Law	Geometric Imperfections	Objective of Analysis
LA	Linear Elastic	Linear	Linear	None	Reference stresses
LBA	Linear Bifurcation	Linear	Linear	None	First buckling eigenvalue & mode
MNA	Materially Nonlinear	Linear	Nonlinear	None	Reference plastic collapse load
GNA	Geometrically Nonlinear	Nonlinear	Linear	None	Lowest buckling load & mode
GMNA	Geometrically & Materially Nonlinear	Nonlinear	Nonlinear	None	Lowest buckling load & mode
GNIA	Geometrically Nonlinear with Imperfections	Nonlinear	Linear	Yes	Lowest buckling load & mode
GMNIA	Geometrically & Materially Nonlinear with Imperfections	Nonlinear	Nonlinear	Yes	Lowest buckling load & mode

1.3.5.2 Quality-based direct structural design

The European Standard EN 1993-1-6 defines three different Fabrication Tolerance Quality Classes ranging from 'Excellent' (best) to 'Normal' (worst). These influence the prescribed amplitudes of the imperfections in the silo and therefore the design buckling strength, but the onus is on the builder to meet the relevant construction tolerances specified by EN 1993-1-6 if it is to be permitted to employ the full design buckling strength of the silo during operation. Thus the three Quality Classes define corresponding Quality Parameters Q for meridional buckling which in turn influence the prescribed imperfection amplitudes for use in the hand design procedure through an 'elastic imperfection reduction factor' α_x. The Quality Classes and the Q parameter are summarised in Table 1.2.

The focus in this discussion is on the Quality Parameter for meridional (axial) buckling Q because buckling under axial compression is possibly the single most common and important design consideration. This is mainly due to the frictional tractions exerted by the granular solid, but also due to the much higher magnitudes of local axial compression which may arise from other causes including discrete supports (e.g Greiner and Guggenberger, 1998; Guggenberger *et al.*, 2004; Doerich, 2008), differential settlement (e.g. Holst and Rotter, 2003; 2004) and eccentric discharge (Rotter, 1986). However, Annex D of EN 1993-1-6 also defines corresponding elastic imperfection reduction factors for circumferential and shear buckling, α_θ and α_τ respectively, which should be used in design if required. These are not discussed further here.

The prescribed imperfection amplitude decreases as the construction quality increases, thus allowing one to be rewarded for good construction with a more economical structure. This is a superior treatment to the traditional uniformly lower bound approach which assigned the same low strength to all shells irrespective of quality, a procedure used in all structural design rules before EN 1993-1-6 which may be traced back to at least Robertson (1928) and Wilson and Newmark (1933). An interesting historical account may be found in Bornscheuer (1982) and Rotter (2004).

Table 1.2 – Recommended values for the meridional buckling quality parameter from EN 1993-1-6 (2007) Annex D

Fabrication Tolerance Quality Class	Description	Quality Parameter Q
Class A	Excellent	40
Class B	High	25
Class C	Normal	16

The Quality Parameter Q for meridional buckling is thus dependent on the Fabrication Tolerance Quality Class chosen by the designer (Table 1.2) and, together with the radius to thickness ratio of the silo wall, defines a characteristic imperfection amplitude for meridional buckling design by hand calculation, Δw_x. This amplitude is in turn incorporated into an empirical expression for the elastic imperfection reduction factor for meridional buckling α_x, shown in Eq. 1.17 below (source: EN 1993-1-6, Eqs D.14 & D.15):

$$\alpha_x = \frac{0.62}{1+1.91\left(\frac{\Delta w_k}{t}\right)^{1.44}} \text{ where } \frac{\Delta w_k}{t} = \frac{1}{Q}\sqrt{\frac{R}{t}} \tag{1.17}$$

The development of this expression is described in Rotter (1999b; 2004). It is illustrated in Fig. 1.17 as function of the characteristic imperfection amplitude Δw_x, which shows that even the buckling strength of a perfect shell under axial compression is allowed to be only 62% of the classical value σ_{cl} (Eq. 1.16). In conjunction with other buckling parameters and partial safety factors it serves to calculate the design buckling strength of the shell when designing by hand. It may be noted that the low value of 0.62 arises from matching Eq. 1.17 (Rotter, 1998) to the shell buckling prediction of ECCS EDR4 (1988), where the factor 0.83 appeared in the basic strength formula due to Pflueger (source not known), and an 'additional safety factor' of 0.75 was imposed on all axial compression buckling because of the unstable post-buckling behaviour of axially-compressed cylinders, thus giving 0.83 × 0.75 = 0.62. This is a slight anomaly that should be remedied in future modifications to the shell buckling standard.

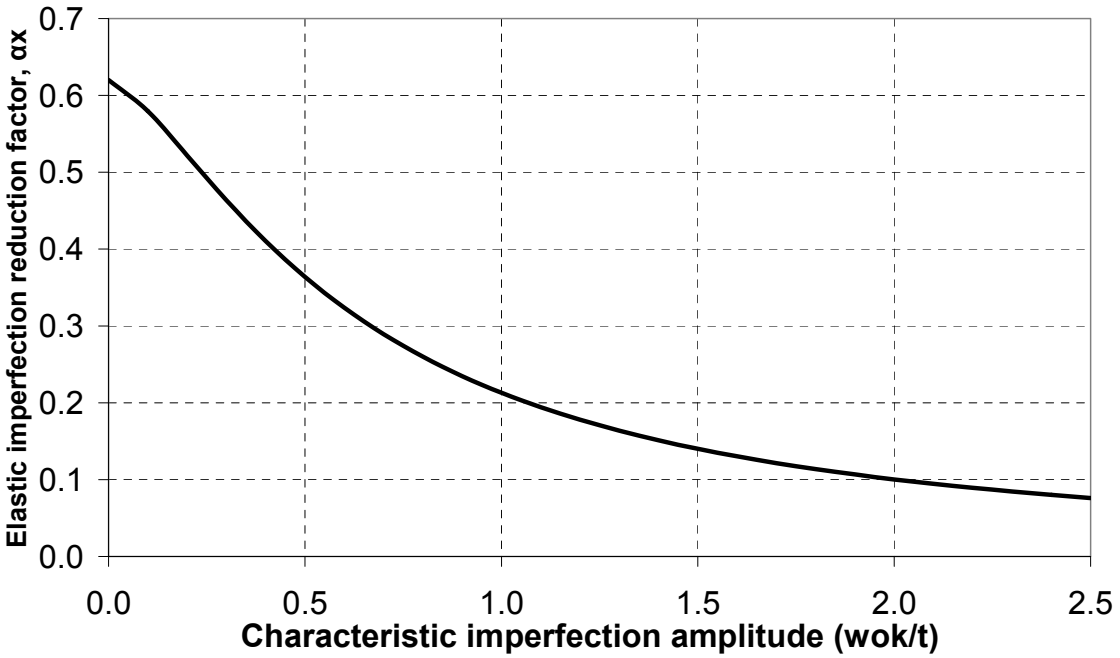

Fig. 1.17 – Reduction in elastic buckling strength with the characteristic imperfection amplitude (after EN 1993-1-6, 2007)

The EN 1993-4-1 (2007) standard that is specific to the design of silos (as opposed to EN 1993-1-6 which is the general standard for shells) prescribes a slightly modified

version of α_x in Eq. 1.17. Assigned the notation α_0, the equation includes a parameter ψ (Rotter, 1986) to assess the non-uniformity of the axial compression used when designing for high local axial compression:

$$\alpha_0 = \frac{0.62}{1+1.91\psi\left(\frac{\Delta w_0}{t}\right)^{1.44}} \text{ where } \frac{\Delta w_0}{t} = \frac{1}{Q}\sqrt{\frac{R}{t}} \tag{1.18}$$

The reason for placing ψ in the denominator of Eq. 1.18 is that the imperfection sensitivity of the buckling strength can be changed from the worst case of uniform compression when $\psi = 1$ (the default conservative recommendation in EN 1993-4-1), to no imperfection sensitivity at all when $\psi = 0$. This is because, under highly local axial compression, the elastic buckling resistance is unaffected by geometric imperfections, and the shell can attain the classical elastic critical stress locally before a buckle forms (Libai and Durban, 1973; 1977). The evaluation of the stress non-uniformity parameter ψ is described in detail in Chapter 9 in the specific context of a failure criterion for buckling under the highly-localised axial compression that arises under eccentric discharge (Rotter, 1986).

Closely related to the imperfection sensitivity is the incorporation of the effect of local internal pressure, and allows the elastic unpressurised factor α_x to be upgraded to a pressurised factor which takes account of the dual nature of internal pressure, α_{xp}. Low internal pressure is beneficial and leads to an elastic strength gain because of its stabilising effect that counters the detrimental geometric imperfections (see previous discussion in Section 1.3.2). This effect is implemented in Eq. D.41 of EN 1993-1-6 through an elastic stabilisation factor, α_{xpe} (Eq. 1.19). This equation was derived by Rotter (1997) from the analysis of a weld depression that is far removed from any boundary or change of thickness. It adjusts the rate of strength gain to the initial imperfection sensitivity of the shell resulting in more rapid strength rises in imperfect shells, especially with axisymmetric imperfections (Rotter, 2004).

$$\alpha_{xpe} = \alpha_x + \left(1-\alpha_x\right)\left[\frac{\overline{p}}{\overline{p}+0.3\alpha_x^{-0.5}}\right] \text{ where } \overline{p} = \frac{p_{local,fill}R}{\sigma_{cr}t} \tag{1.19}$$

By contrast, high internal pressure has a destabilising effect as it leads to a local plasticity and thus a reduction in strength that is *not* associated with the imperfections (Rotter, 1990; 1996; 2001a; 2006). This effect is implemented in Eq. D.42 of EN 1993-

1-6 through a plastic destabilisation factor, α_{xpp} (Eq. 1.20). The original equation may be found in Rotter (1990). The strength reduction is due to the axisymmetric plastic elephant's foot stability phenomenon, most severe at a boundary but also possible at major changes of plate thickness.

$$\alpha_{xpp} = \left[1 - \left(\frac{\bar{p}}{\lambda^2}\right)^2\right]\left[1 - \frac{1}{1.12 + s^{1.5}}\right]\left[\frac{s^2 + 1.21\lambda^2}{s(s+1)}\right] \tag{1.20}$$

where $\bar{p} = \frac{p_{local,disch} R}{\sigma_{cr} t}$, $s = \frac{R}{400t}$ and $\lambda^2 = \frac{\sigma_y}{\sigma_{cr}}$

Although the elastic stabilisation and plastic destabilisation phenomena are clearly very different, the final pressurised elastic imperfection factor in design according α_{xp} is simply taken as the smaller of α_{xpe} and α_{xpp}. This leads to a simplified relationship between the internal pressure and strength gain or reduction, demonstrated in Fig. 1.18 for a typical value of α_x of 0.21 ($\Delta w_k/t$ = 1.0). According to this relationship, internal pressure is greatly beneficial up to a certain point, but beyond this point it causes the shell to yield locally. Thus the behaviour changes from elastic bifurcation to plastic buckling.

The final value of α_{xp} (lowest of Eqs 1.19 and 1.20) is incorporated into a series of expressions which ultimately give the characteristic buckling resistance of the shell $\sigma_{x,Rk}$ as a function of its relative slenderness $\bar{\lambda}$, which itself is given by the square root of the ratio of the characteristic yield strength f_{yk} and the elastic critical buckling stress $\sigma_{x,Rcr}$ (given by the classical relation, Eq. 1.16). For shells where the behaviour is fully-elastic, the characteristic buckling resistance is given directly as $\sigma_{x,Rk} = \alpha_x \sigma_{x,Rcr}$ using Eq. 1.17, without considering either the beneficial or detrimental effect of internal pressure.

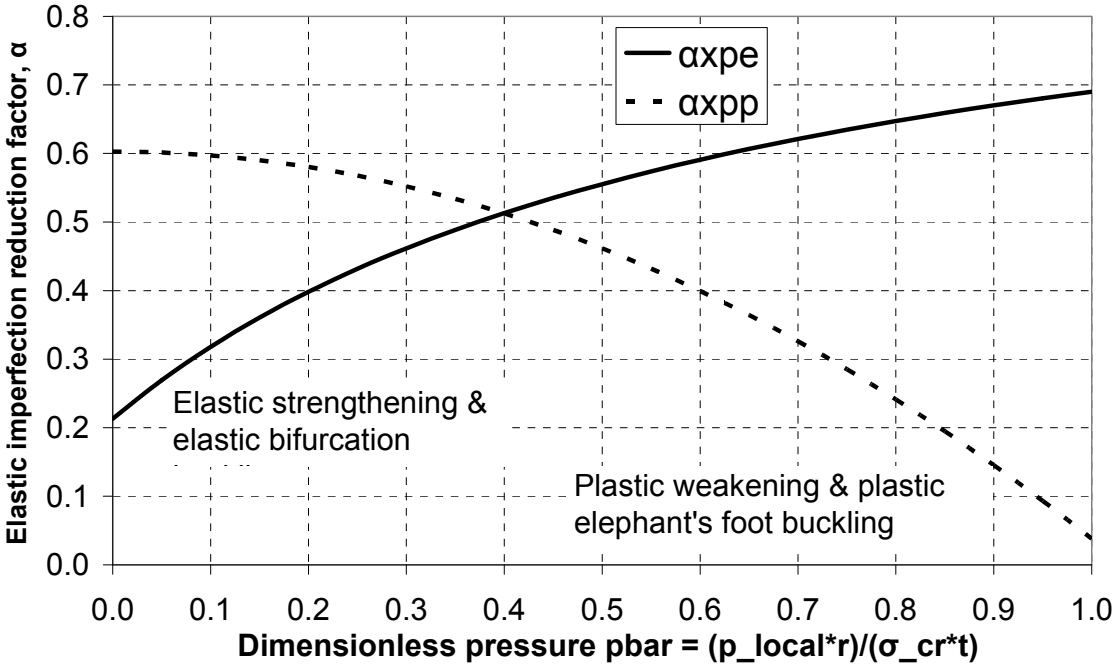

Fig. 1.18 – Effect of internal pressure on buckling strength of cylinders for a typical characteristic imperfection amplitude, after EN 1993-1-6 (2007) and Rotter (2001)

1.3.5.3 Quality-based computer-aided (GMNIA) structural design and tolerances

If a full GMNIA computational analysis is used as the basis for structural design, EN 1993-1-6 Section 8.7 prescribes a different set of imperfection amplitudes, founded on a different concept than the effective lower bound approach of the previous hand-based design procedure. The required imperfection amplitude for GMNIA-based design is related to a dimple parameter U_n which itself depends on the Fabrication Tolerance Quality Class. Thus the imperfection amplitude for the given imperfection form $\Delta w_{0,eq}$ should be taken as the larger of $\Delta w_{0,eq,1}$ and $\Delta w_{0,eq,2}$, given in Eqs 1.21 and 1.22.

$$\Delta w_{0,eq,1} = \ell_g U_{n1} \tag{1.21}$$

$$\Delta w_{0,eq,2} = n_i t U_{n2} \tag{1.22}$$

where ℓ_g is a dimple measurement gauge length for the relevant design condition (see below), t is the local shell wall thickness and n_i is a multiplier to achieve an appropriate tolerance level (EN 1993-1-6 recommends this to be 25, though it can be different in a National Annex) and U_{n1} and U_{n2} are two versions of the dimple imperfection amplitude parameter.

The gauge length ℓ_g refers to a physical measuring stick of a certain length which should be placed at different positions and in different directions *after* construction to verify

that the maximum permissible dimple tolerance $U_{0,max}$ has been met. The parameter $U_{0,max}$ is thus different from U_n which refers to imperfection amplitudes which are to be used *before* construction in a GMNIA-based design calculation, but it is also dependent on the Fabrication Tolerance Quality Class that the builder is required to achieve. The recommended values for $U_{0,max}$ and U_n are summarised in Table 1.3. Furthermore, EN 1993-1-6 notionally recommends the same value for both U_{n1} and U_{n2} (Eqs 1.21 and 1.22), though these may be different in a National Annex.

Table 1.3 – Recommended values for the dimple tolerance and imperfection amplitude parameters from EN 1993-1-6 (2007) Sections 8.4 and 8.7

Fabrication Tolerance Quality Class	Description	Dimple tolerance parameter $U_{0,max}$	Dimple imperfection amplitudes U_{n1} and U_{n2}
Class A	Excellent	0.006	0.010
Class B	High	0.010	0.016
Class C	Normal	0.016	0.025

The application of measurement gauges ℓ_g is illustrated in Fig. 1.19. Section 8.4 of EN 1993-1-6 defines three different gauge measurements, each based on a different buckling consideration (Rotter, 2004). The most important is the meridional gauge ℓ_{gx}, which is straight and has a length $4(Rt)^{½}$; it is supposed to test for the square eigenmode of the perfect shell under uniform axial compression (Koiter, 1945; Calladine, 1983) which has a critical wavelength in each direction of approximately $3.5(Rt)^{½}$. Next comes the much shorter gauge ℓ_{gw} for measurements across meridional and circumferential welds, equal to a length of $25t \leq 500$ mm; this gauge is applied in view of the possibility of local plastic failure due to deep local deviations. Finally, there is the long circumferential gauge $\ell_{g\theta}$ of length $2.3(\ell^2 Rt)^{¼} \leq R$ (where ℓ is the meridional length of the shell segment); this gauge tests for long-wave circumferential buckling. Thus, for the purposes of Eq. 1.21, the gauge length ℓ_g corresponds to the condition which is being designed for, i.e. if the design is for axial compression, $\ell_g = \ell_{gx} = 4(Rt)^{½}$. Note that any gauge used for measurement in the circumferential direction should have a radius of curvature R equal that of the *outer* surface of the silo (EN 1993-1-6 actually mentions the *middle* surface, but this is clearly a mistake since only outer and inner surfaces are practically reachable in a real silo).

The dimple tolerances were described in detail in this chapter because they are central to the imperfection requirement for GMNIA-based structural design and are used in the analyses presented in this thesis. For completeness, it should be noted that Section 8 of EN 1993-1-6 specifies other geometric tolerances which are known to have a large impact on the safety on the structure and that the builder is also required to meet, including out-of-roundness ($U_{r,max}$) and accidental eccentricity of shell joints ($U_{e,max}$). These are not pursued further here.

Finally, Section 8.7 of EN 1993-1-6 requires the shell analyst to find the worst imperfection form and the standard recognises that this may or may not occur at the prescribed imperfection amplitudes. The analyst is therefore required to run an additional GMNIA analysis at an imperfection amplitude 10% lower than $\Delta w_{0,eq}$. If the resulting load factor is higher at 90% of the amplitude than at 100% of the amplitude, an iterative procedure should be adopted to find the lowest GMNIA load factor and corresponding imperfection amplitude. This is a careful, though onerous, procedure.

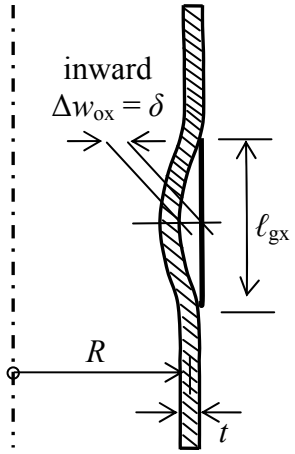

a) Measurement on a meridian

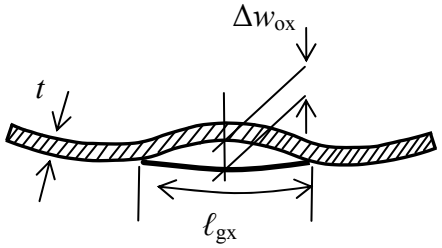

b) First measurement on a circumferential circle

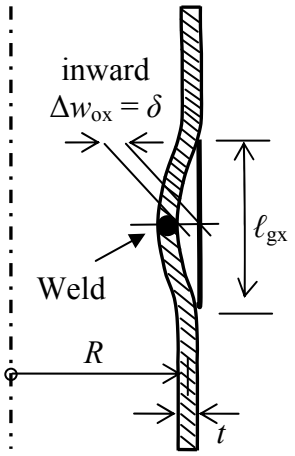

c) First measurement on a meridian across a weld

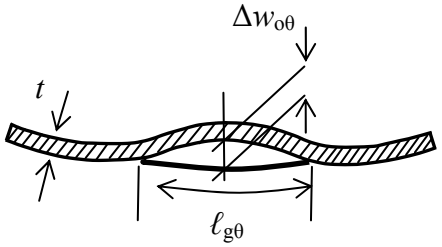

d) Second measurement on a circumferential circle

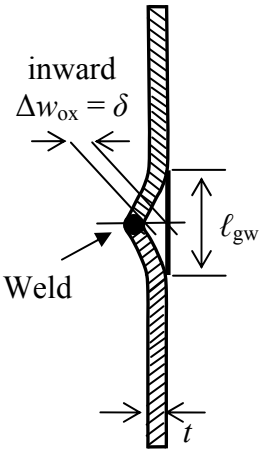

e) Second measurement across a weld with special gauge

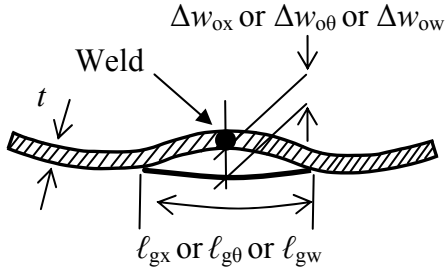

f) Measurements on circumferential circle across weld

Fig. 1.19 – Dimple imperfection measurements to satisfy the dimple tolerance requirement of EN 1993-1-6 (2007) Section 8.4

1.4 Conventions used in this thesis

The final section of this chapter briefly defines the conventions used in this thesis. Stresses are assumed to be positive when in tension, while positive bending moments are assumed to produce tension on the inner surface of the shell. The first vertical coordinate y is defined as upwards-positive, with its origin at the base of the silo (assuming no hopper). The second vertical coordinate z, used more extensively due to the nature of the equations governing the pressure in the granular solid, is defined as downwards-positive with the origin at the top of the silo wall. There is a plane of symmetry present in analyses of eccentric discharge, and the flow channel is assumed to be centred on this plane. The circumferential coordinate θ is equal to 0 and π adjacent to and opposite the outlet respectively on the symmetry plane. These conventions are illustrated in Fig. 1.20, and are valid throughout unless stated otherwise.

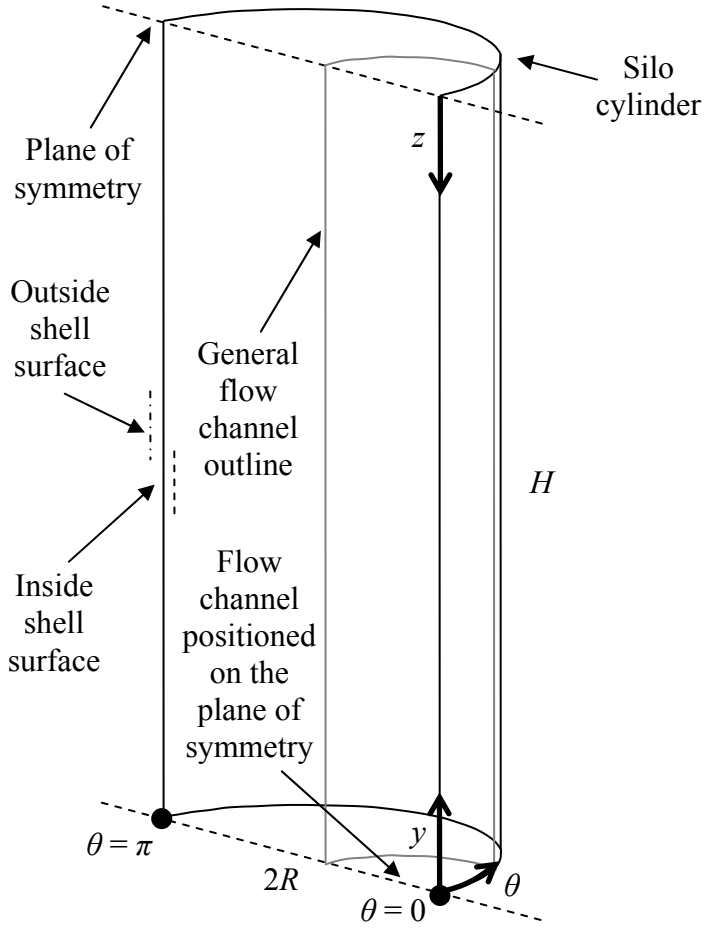

Fig. 1.20 – Definition of sign conventions used in this thesis

Chapter 2 – A preliminary study of failure modes in steel silos under EN 1991-4-defined concentric and eccentric discharge pressures

2.1 Introduction

The most serious loading condition for slender thin-walled metal silos has long been recognised to be the condition of discharge, with eccentric discharge causing more catastrophic failures than any other. Two key reasons for this high failure rate are the difficulties in characterising the pressure distribution caused by eccentric solids flow and in understanding the associated unsymmetrical stresses in the silo wall. Few studies have addressed either the linear elastic behaviour of such a silo or its buckling failure under eccentric discharge.

Design criteria for metallic silos are therefore dominated by their susceptibility to buckling failures. The condition of discharge from a silo causes an significant increase in normal wall pressure, and this is the condition for which most silos are designed. Furthermore, the unsymmetrical pressure regime occurring during eccentric discharge of the stored granular material frequently leads to catastrophic buckling failures, and slender metal silos are particularly susceptible to this failure mode. The commonest failure mode in a slender thin-walled steel silo under eccentric discharge is by serious damage on the side adjacent to the flowing solid often leading to catastrophic collapse (Fig. 1.1), but the mechanics of such failures have not been widely appreciated in the past.

In this initial study of the phenomenon, the eccentric discharge pressures are characterised using the new rules of the European Standard EN 1991-4 on Silos and Tanks. This novel description of unsymmetrical pressures permits a study of the structural behaviour leading to buckling during eccentric discharge, including the critical effects of geometric nonlinearity and imperfection sensitivity. The study is undertaken using geometrically and materially nonlinear computational analyses within the framework of the EN 1993-1-6 (2007) standard. The mechanics of the behaviour are found to be quite complicated. A silo which is safe under axisymmetric loading is found to be susceptible to catastrophic stability failure under eccentric discharge.

It will be shown that the failure mode is clearly by buckling under local axial compressive membrane stresses induced by unsymmetrical normal pressures exerted by the solid on the wall. This explanation follows that of Rotter (1986, 2001a, 2001b) but runs counter to those previously offered by Jenike (1967), Wood (1983), Roberts and Ooms (1983) and others. The buckling failure in the example structure occurs well before the material yields and is thus an elastic failure in which the strength of the material plays no role.

The low pressures where the flow channel is in contact with the silo wall were shown by Rotter (1986) to lead to dangerous stress patterns in the silo wall, which can easily become catastrophic for structural stability. Despite this risk, eccentric discharge may be necessary for the effective operation of the silo, or it may occur accidentally due to segregation or agglomeration of the contents, partial blockage of an outlet or a feeder malfunction (Rotter, 2001a).

2.2 Investigation of the effects of the EN 1991-4 eccentric discharge pressure distribution

The unsymmetrical pressures caused by eccentric discharge are investigated in this chapter using the new rules of the European Standard EN 1991-4 (2007) for highly eccentric discharge (usually where the outlet eccentricity is greater than 0.25D), based on a simplified version of the theory of Rotter (1986, 2001a, 2001b). This theory proposes a distribution for the pressures resulting from a parallel-sided circular flow channel forming against the wall, shown in
Fig. 2.1.

In the EN 1991-4 version, the solid exerts Janssen pressures outside the channel, elevated pressures at the edges and decreased pressures within the flow channel, thus radically simplifying what has been observed in experiments (e.g. Wood, 1983; Rotter, 1986; Chen 1996). The relationship between the pressure drop and increase is such that horizontal equilibrium is satisfied and the mean pressure is maintained at the Janssen filling value, though it does lead to a small global overturning moment on the silo. EN 1991-4 requires this distribution to be used in the design of silos where eccentric discharge is expected and if the silo is in Action Assessment Class 2 or 3.

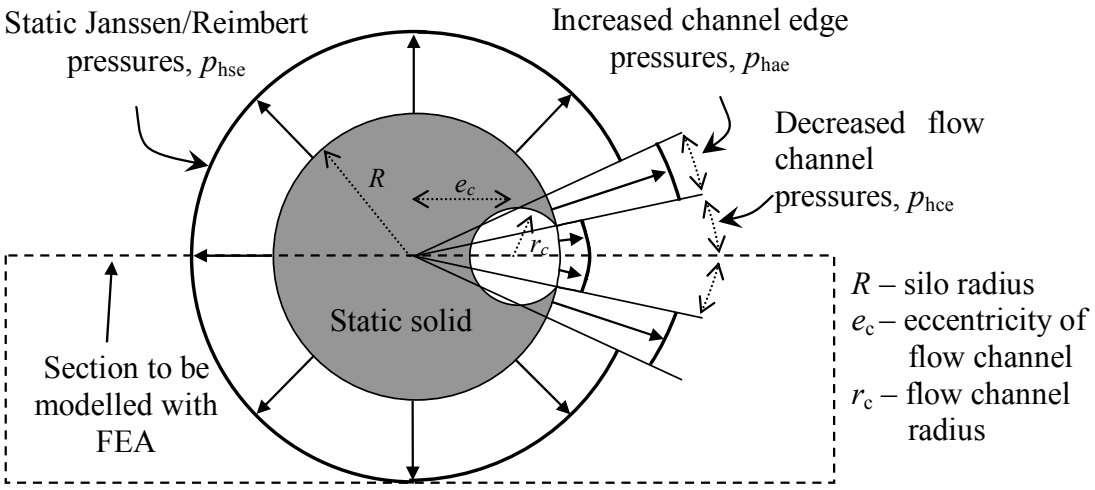

Fig. 2.1 – Circumferential cross-section of eccentric flow channel horizontal pressures, after EN 1991-4 (2007)

The horizontal static pressure, p_{hse}, at any depth far from the flow channel is taken as equal to the Janssen silo pressure:

$$p_{hse} = \gamma K z_0 (1 - e^{-z/z_0}) \text{ where } z_0 = \frac{A}{KU\mu} \tag{2.1}$$

The original derivation of the eccentric discharge pressure model (Rotter, 1986) employed a different distribution for the pressure in the stationary solid, based on considerations of static equilibrium and continuity on the static-flowing solid interface. In EN 1991-4, however, the above simplification was adopted.

The horizontal pressure within the flowing zone is treated as circumferentially constant and is given by:

$$p_{hce} = \gamma K z_{c0} (1 - e^{-z/z_{c0}}) \text{ where } z_{c0} = \frac{1}{K}\left(\frac{A_c}{U_{wc}\mu + U_{sc}\tan\phi_i}\right) \tag{2.2}$$

Here K is the upper characteristic value of the lateral pressure ratio, γ is the upper characteristic value of the unit solid weight, μ upper characteristic value of the wall friction coefficient, ϕ_i is the upper characteristic value of the internal friction angle of the granular solid, A is the cross-sectional area of the silo, A_c is the cross-sectional area of the channel, U is the full silo perimeter, U_{wc} is the perimeter between the silo wall and the channel, and U_{sc} is the perimeter between the static solid and the channel.

The pressure at the edges of the channel is increased by the same extent as the channel pressure drop over the same circumferential range:

$$p_{hae} = 2p_{hse} - p_{hce} \tag{2.3}$$

The associated frictional tractions at discharge, p_{wse}, p_{wce} and p_{wae}, are based on the assumption of fully-developed wall friction:

$$p_w = \mu p_h \tag{2.4}$$

The magnitude of the flow channel pressure additionally depends on the size of the channel, defined by its radius and eccentricity, r_c and e_c, respectively. EN 1991-4 recommends at least three different values of r_c to be tested to find the most destructive flow channel geometry. These values are suggested as equal to k_cR where k_c is 0.25, 0.40 or 0.60. The focus in this chapter is on the k_c value of 0.60, as it was provisionally expected to be the most deleterious. Detailed parametric studies of the effects of flow channel size, where the value of k_c is varied from 0.0 to 0.9 (a value of 1.0 corresponding to mass flow), may be found in Chapter 5.

2.3 Design of an example slender silo

The novel pressure distribution of

Fig. 2.1 for highly eccentric discharge appears for the first time in the European Standard EN 1991-4 (2007) and few existing silos would have so far been designed according to it. It is therefore important to explore the structural behaviour of a silo under eccentric discharge as defined by EN 1991-4 when it has not been specifically designed for it. To this end, a traditional design was produced for a simple example silo subjected to axisymmetric loads only (no patch loads), and its behaviour under both concentric and eccentric discharge conditions (i.e. axisymmetric and unsymmetrical loads) was investigated using the finite element method.

A simple cylindrical steel silo with a vertical wall and flat bottom was designed for symmetrical loads only, resulting from the storage of 680 tonnes (510m^3) of cement, as shown in Fig. 2.2. The structural design was performed according to the EN 1993-1-6 (2007) hand calculation procedure, described in Section 1.3.5 of the literature review. The properties for cement were taken from EN 1991-4 using the maximum friction case, since buckling resistance dominates in such a design. The friction properties of the D2 ‘smooth’ wall were adopted.

The cylinder wall height was 26 m and radius 2.5 m, giving an aspect ratio of 5.2 (classed as 'Slender'). The requirement for an unsymmetrical patch load was omitted to simplify the interpretation of the outcome of the calculations. Action Assessment Class 2 was assumed, based on the storage capacity. The beneficial effect of internal pressure was included when designing against buckling. The discharge factors for normal pressures and frictional tractions, C_h and C_w, were taken as 1.15 and 1.1 respectively. The partial safety factor for unfavourable structural actions and the resistance partial safety factor for stability, γ_F and γ_{M1}, were taken as 1.5 and 1.1 respectively (EN 1993-4-1, 2007), thus separating the characteristic values by a factor of 1.5 × 1.1 = 1.65. This value is important in the context of the outcome of later nonlinear computational calculations against which it may be assessed.

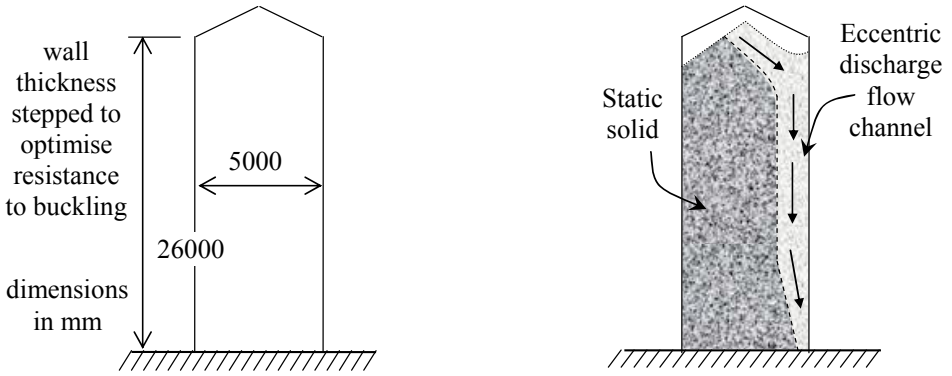

a) overall dimensions b) eccentric discharge flow channel

Fig. 2.2 – Illustration of geometry of the example design silo and eccentric flow channel

The buckling strength assessment according to EN 1993-1-6 requires that the expected quality of construction be considered at the design stage. A Fabrication Tolerance Quality Class of C (i.e. 'Normal') was therefore adopted, making the shell more imperfect and thus requiring a thicker wall. The material of the shell was assumed to be isotropic steel with an elastic modulus E = 200 GPa, a Poisson's ratio ν = 0.3 and a yield stress σ_y = 250 MPa.

To thoroughly investigate the structural consequences of the EN 1991-4 eccentric discharge distribution, two silo designs were produced: one with a uniform wall thickness (9 mm) for clarity of understanding and one with a stepwise varying wall thickness (changing from 3 mm at the top to 9 mm at the base) to follow normal engineering practice for silo design. This made the wall just thick enough at the base of

each strake and at the silo base. To ensure that the design was just critical at the base of each strake, the strakes were permitted to have any length and were not constrained by practical steel sheet widths. The beneficial effect of internal pressure was considered in design (α_{xpe} dominates, Eq. 1.19). The design axial membrane stress resultants are shown in Fig. 2.3, while Fig. 2.4 shows the corresponding design thicknesses as well as those required to withstand simple bursting failure.

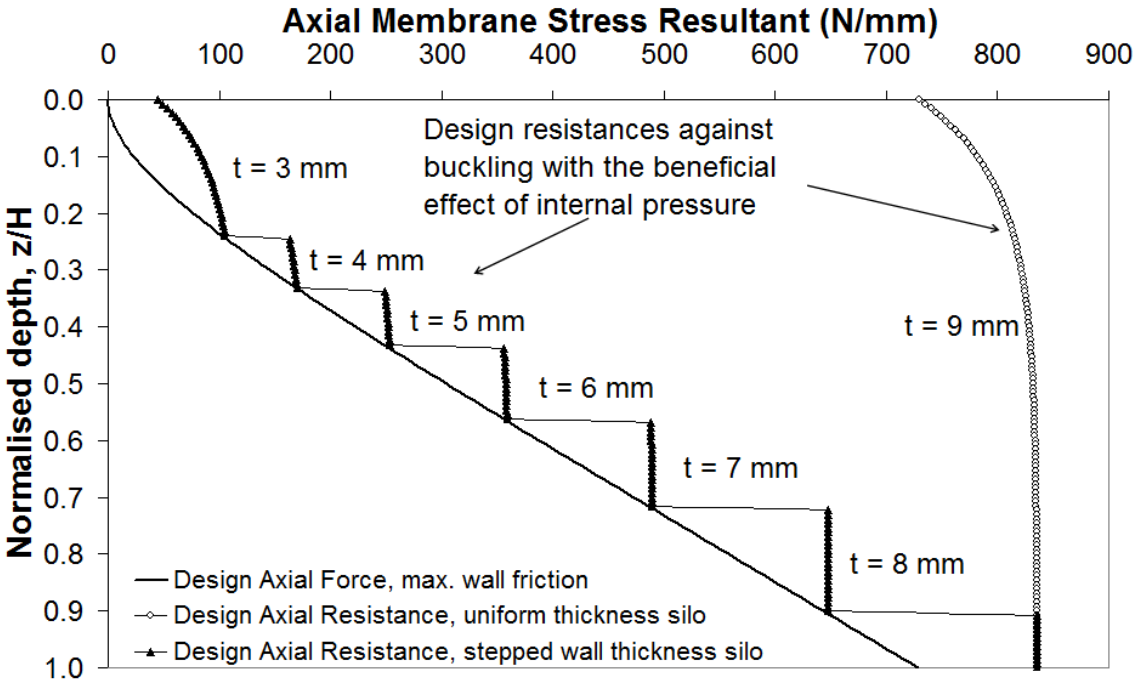

Fig. 2.3 – Axial distribution of the design axial membrane stress resultants

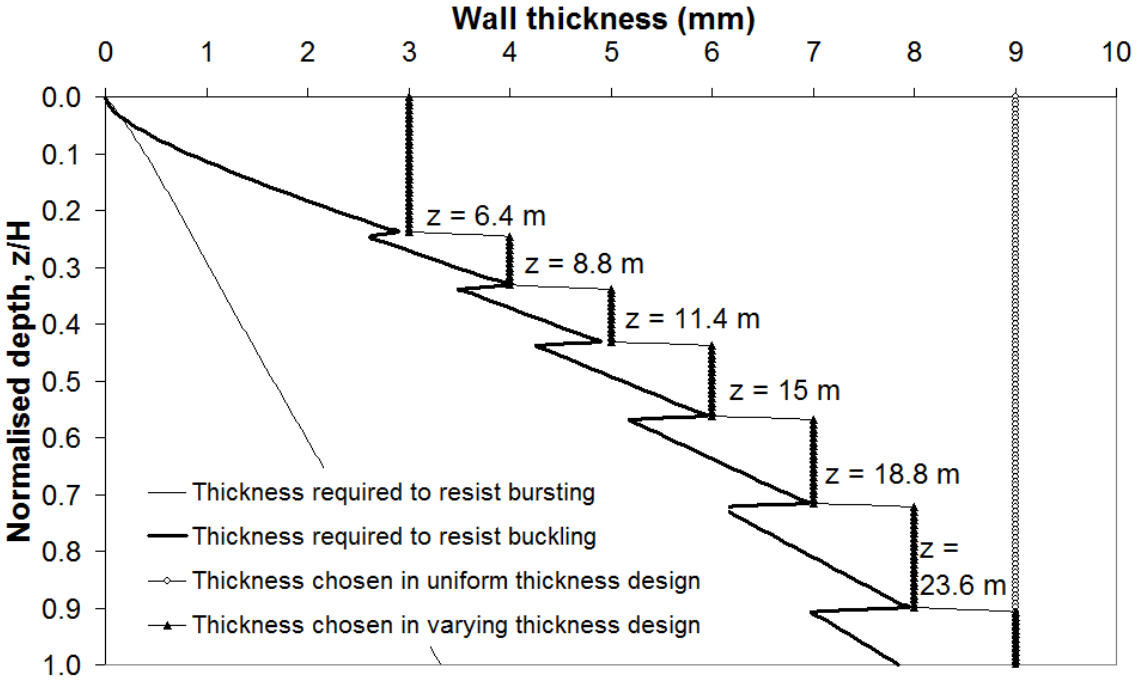

Fig. 2.4 – Axial distribution of design thicknesses to resist bursting and buckling

2.4 Numerical model

To investigate the behaviour of the design silo under different conditions, many different computational analyses were undertaken with different load cases. The two design silos were thus analysed using the commercial finite-element package ABAQUS (2009). This software is considered to be the most reliable for nonlinear stability analyses in the shell buckling research community. A pinned based was assumed, as well as a thin conical roof of inclination 15º to the horizontal to realistically restrict out of round displacements at the upper boundary. Such displacements would strongly affect the stress patterns in silos under unsymmetrical loads (Rotter, 1987b; Calladine 1983).

Using symmetry boundary conditions, only half of the silo was modelled with nine-node reduced-integration S9R5 elements when eccentric discharge was being investigated. For concentric discharge, only a quarter of the silo was modelled with appropriate symmetry and anti-symmetry boundary conditions. The conical roof, which had a high thickness of 9 mm to prevent it from participating in any buckling modes, was modelled with a sufficient number of four-node S4R5 elements. After careful verification, the mesh resolution was increased near changes of wall thickness, the base of the silo, weld depressions, flow channel and edge pressures and at locations of expected buckles. Typical model mesh details are shown in Fig. 2.5 for the perfect uniform thickness silo and the imperfect varying thickness silo. The geometrically nonlinear load-deflection path was followed using the modified Riks procedure (Riks, 1979). An ideal elastic-plastic material law with no hardening was assumed where applicable. This was thought to be sufficient in this study, as plasticity was expected to be highly localised. This exact same procedure for computational analyses was employed in every finite element study presented in this thesis.

The full suite of computational shell buckling calculations were performed according to EN 1993-1-6 (2007), summarised in Table 1.1: linear elastic analysis (LA), linear bifurcation analysis (LBA), materially nonlinear analysis (MNA), geometrically nonlinear analysis assuming a linear and nonlinear material law (GNA and GMNA) and imperfections (GNIA and GMNIA).

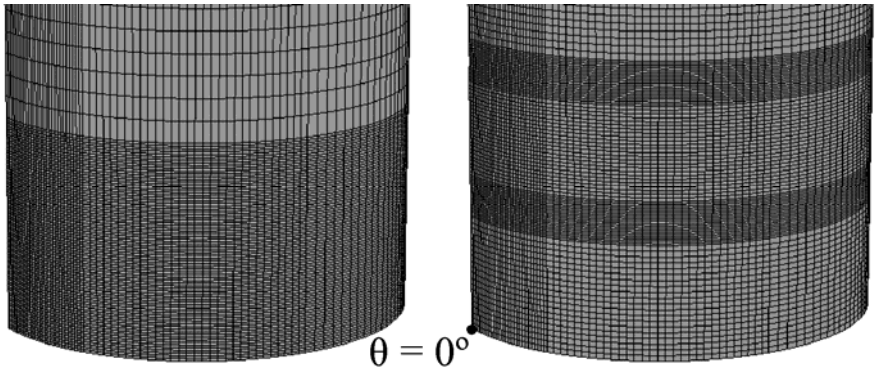

Fig. 2.5 – FEA mesh details – left) base of perfect uniform thickness silo; right) – base of imperfect varying thickness silo

Characteristic values of loads were adopted in all calculations so that the outcome of the calculation could be used to explore the remaining safety margin between the required and characteristic resistances. The stored solid was assumed to have no stiffness in both the static and flowing zones.

Axisymmetric imperfections representing modified Type A weld depressions as defined by Rotter and Teng (1989a), given in Eq. 2.5 below, were introduced at evenly-spaced intervals up the silo wall and at changes of wall thickness so that the silo had many local imperfections. This imperfection form was initially developed as a realistic simulation of the joints created during welding of metal sheets, and has been widely used in numerical studies of imperfection sensitivity in cylinders because it is one of the most damaging credible imperfection forms for a uniformly compressed cylinder (e.g. Teng & Rotter, 1992; Rotter and Zhang, 1990; Knödel *et al.*, 1995; Berry *et al.*, 1997; 2000; Rotter, 2004; Song *et al*., 2004).

The purpose of these GNIA and GMNIA analyses is to obtain a realistic estimate of the effects of this commonly found axisymmetric imperfection form (Ding *et al*., 1996; Pircher *et al.*, 2001; Teng *et al*., 2005) under the highly unsymmetrical eccentric discharge distribution, which has not been investigated before. This contrasts with the EN 1993-1-6 requirement that the analyst should seek out the most damaging imperfection form, as many of the most damaging forms are not very realistic in most conditions (e.g. pre-buckling deformations, post-buckling deformations or the linear bifurcation mode).

The adopted imperfection form (Eq. 2.5) includes an additional tiny non-symmetric perturbation to help identify the correct first bifurcation point in the load-deflection path (visible change of slope and/or first negative eigenvalue in the tangent stiffness matrix) by introducing a small asymmetry. This is especially important where the silo is analysed under axisymmetric loads where very many eigenmodes may be critical within 1% of the same load factor (Koiter, 1945; Rotter, 2004), and the numerical analysis may run into problems in detecting the lowest one (Riks *et al.*, 1996). The perturbation factor, k, is of the order of 10^{-2} and n is the integer circumferential mode number, usually a value between 10 and 30, both of which are arbitrarily chosen in order to achieve bifurcation. The outcome of all calculations, however, was found to be insensitive to the choice of either k or n.

$$\delta = \delta_0 e^{\frac{-\pi z}{\lambda}} (\cos\frac{\pi z}{\lambda} + \sin\frac{\pi z}{\lambda})(1 + k\cos n\theta) \qquad (2.5)$$

where $\lambda = \frac{\pi}{\left[3(1-\nu^2)\right]^{0.25}}\sqrt{Rt}$ is the linear meridional bending half-wavelength

The depression amplitude δ_0 was chosen to be identical, in each strake, to the value from the hand design process according to Equation D.15 of EN 1993-1-6 Annex D (Δw_k), for Fabrication Tolerance Quality Class C. This was done in preference to the special requirement of the same standard for GMNIA design as specified in Section 8.7.2 (i.e. larger of Equations 8.29 and 8.30, Δw_0). Both are summarised in Table 2.1. This choice was made to produce a design silo that corresponds to typical commercial practice and to retain scientific consistency between the design and the calculations for the purposes of this initial computational study of a difficult phenomenon. It will be shown later in this and other chapters of this thesis that the prescribed imperfection amplitude of Annex D is already too high to obtain appropriate buckling behaviour when the eccentric discharge pressure pattern is used with certain imperfection forms.

Table 2.1 – Summary of selected properties and dimensionless imperfection amplitude requirements according to EN 1993-1-6 Annex D and Section 8.7.2

Wall thickness (mm)	Down to a depth below the roof (m)	Ratio of adjacent plate thicknesses (i.e. $^4/_3$, $^5/_4$ etc.)	Local radius to thickness ratio (R/t)	Linear meridional bending half-wavelength (mm)	Dimensionless imperfection amplitude (δ_0/t)	
					Eq. D.15	Eq. 8.29
3	6.4	1.333	833.33	158.94	1.8042	2.8868
4	8.8	1.250	625.00	183.53	1.5625	2.5000
5	11.4	1.200	500.00	205.19	1.3975	2.2361
6	15.0	1.167	416.67	224.78	1.2758	2.0412
7	18.8	1.143	357.14	242.79	1.1811	1.8898
8	23.6	1.125	312.50	259.55	1.1049	1.7678
9	26.0	n/a	277.78	275.30	1.0417	1.6667

Where a cylindrical shell is subjected to non-symmetric pre-buckling components, the post-buckling deformations naturally contain components of both the pre-buckling and post-buckling modes (Esslinger and Geier, 1972; Rotter, 2004). The mode that characterises the bifurcation process is clearly only incremental, and is obtained by subtracting the pre-buckling deformation at bifurcation from the complete deformation just after bifurcation. This is termed the 'incremental buckling mode', and is adopted throughout the thesis when describing the 'buckling modes' in geometrically nonlinear analyses.

2.5 Results and discussion

2.5.1 Behaviour of the silo under axisymmetric discharge pressures

The silo was first analysed under axisymmetric loading at characteristic discharge pressures and frictional tractions obtained from the hand design calculations. The hand design process includes many conservative assumptions, so it is natural to expect that the design safety margin (= 1.65) will be exceeded when the silo is analysed using a GMNIA analysis with axisymmetric loading.

A summary of the load proportionality factors at failure achieved for the case of concentric discharge is given in Table 2.2. The buckling modes for these load factors are shown in Fig. 2.6 and Fig. 2.7, while the nonlinear load-axial displacement paths,

very typical for shells under axisymmetric loading (Yamaki, 1984), are presented in Fig. 2.8. In all cases, the axial displacement followed is at a node at the top of the silo above the centre of the eccentric flow channel.

Table 2.2 – Summary of load proportionality factors at failure for concentric discharge

	LBA	MNA	GNA	GMNA	GNIA	GMNIA
Uniform thickness	9.15	4.58	7.85	3.80	4.00	3.09
Varying thickness	7.65	4.54	7.31	3.85	3.41	2.83

For the uniform thickness silo under axisymmetric loading (Fig. 2.6), the critical buckling location is naturally always at the base of the silo since the axial compression increases monotonically from top to bottom (Fig. 2.3). The high values for the LBA and MNA load factors suggest the stability and plasticity will interact, which is confirmed by the large difference between the GNA and GMNA load factors. These load factors at failure relate to the plastic elephant foot's mode (Rotter, 1990; 2006).

The critical locations in the stepped wall thickness silo (Fig. 2.7) are at the base of each strake. In this case the critical locations are either at the bottom of the thinnest 3 mm or 8 mm strakes, though in general it is hard to predict with certainty where the critical zones will be. It is possible, however, that the base of the 8 mm strake may be critical because the ratio of adjacent plate thicknesses is lowest at this point (Table 2.2 and Teng and Rotter, 1989). The very base of the silo is not expected to be critical in the stepped wall thickness silo because the design axial resistance of the wall far exceeds what is required against buckling at this point (Fig. 2.3).

The MNA and GMNA load factors are very similar for both silos and this is reflected in the similarity of the type and location of the elephant's foot plastic buckling modes. This is because the critical location at the base of the 8 mm strake in the stepped wall thickness silo is little different from that at the base of the uniform thickness silo, given the close proximity of these two locations and the essentially constant Janssen pressure at great depth. Additionally, the load factor and buckling mode are very similar for the LBA and GNA analyses for both silos (with the load-deflection paths overlapping significantly, Fig. 2.8), which corresponds to the similarity of the buckling behaviour.

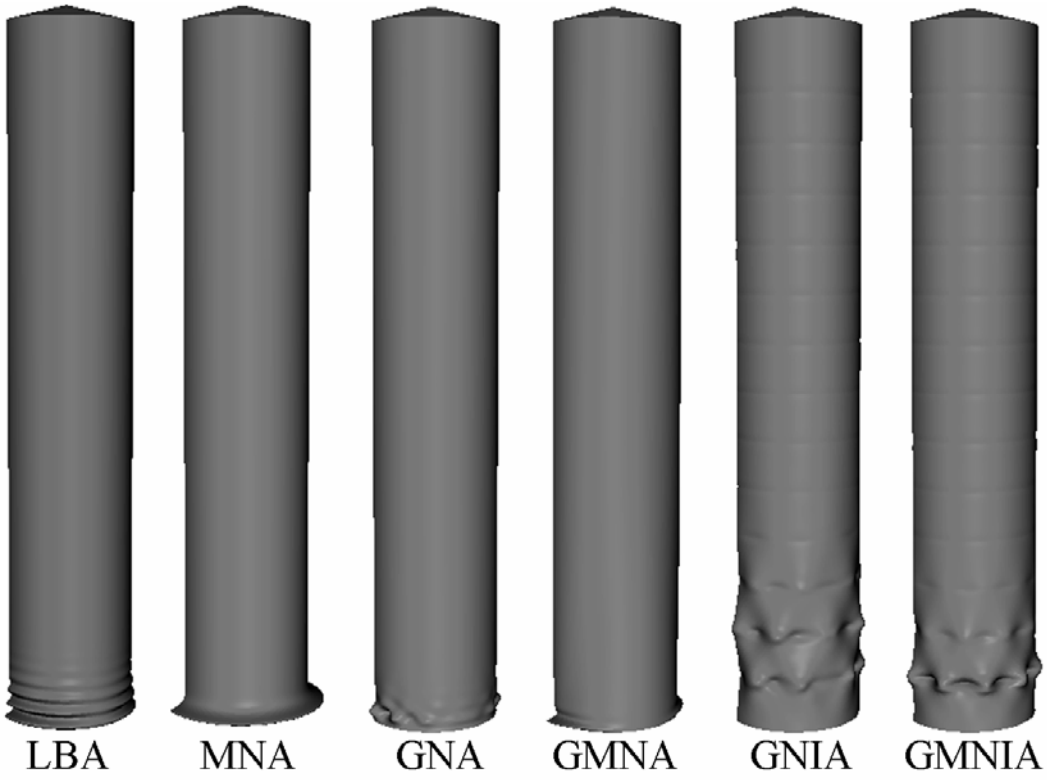

Fig. 2.6 – Failure modes for the uniform thickness silo under concentric discharge. The geometric scale factors are 200, 2, 100, 750, 100 and 200 respectively.

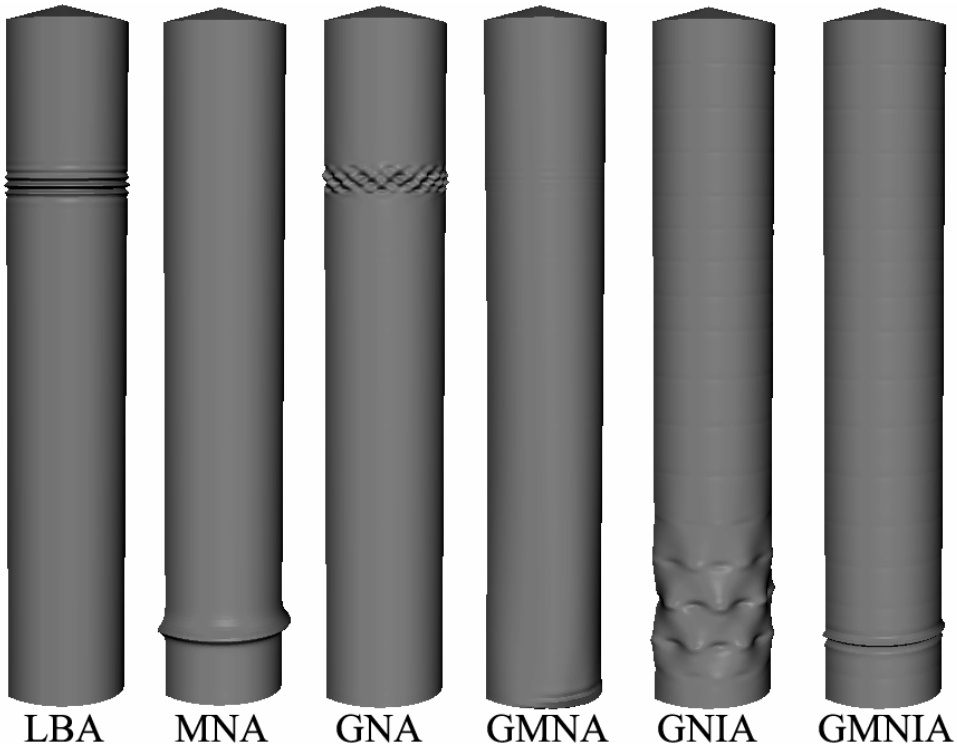

Fig. 2.7 – Failure modes for the stepped thickness silo under concentric discharge. The geometric scale factors are 100, 0.1, 700, 700, 30 and 200 respectively.

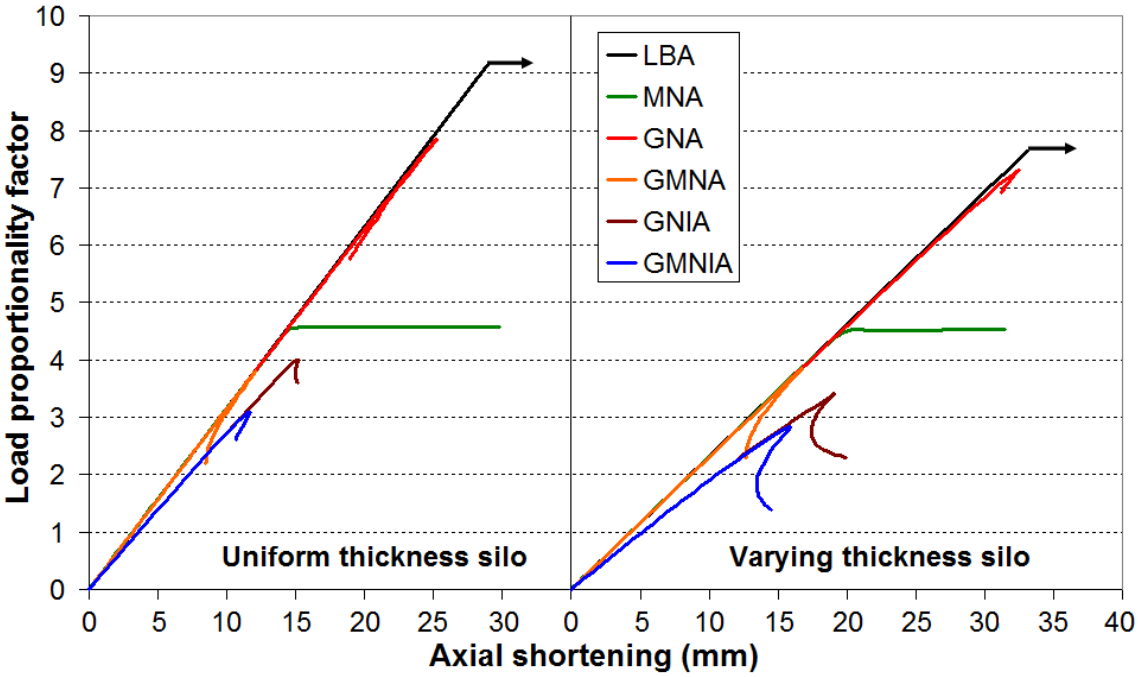

Fig. 2.8 – Nonlinear load-axial displacement paths under concentric discharge

The GNIA and GMNIA factors are quite close to each other for the two silos, suggesting that buckling occurs under predominantly elastic conditions leading to diamond buckling modes (Fig. 2.6 and Fig. 2.7) in all cases except GMNIA of the stepped thickness silo, which instead closely reflects the MNA plastic collapse mechanism for that silo. The introduction of axisymmetric weld depressions is clearly very detrimental to the silo strength under axisymmetric loads. As more sophisticated analyses are used, the load factor progressively falls: hence both geometric and material nonlinearity must be included in silo design. Ultimately, the silo with stepped wall thickness is slightly weaker than the uniform thickness silo because the wall thickness is piecewise optimised.

For the varying thickness silo, the final GMNIA load factor of 2.83 exceeds the hand calculation value of 1.65 by almost 72%. If it is accepted that the axisymmetric weld depression is close to the most damaging form (Rotter, 2004), then under symmetric loads it appears that the assumptions in the hand calculation design process are quite conservative, both for elastic stability and plastic collapse mechanisms. This is primarily because the EN 1993-1-6 elastic imperfection reduction factor for meridional buckling α_x was chosen as an empirical lower bound to a very wide scatter of experimental data on uniform thickness cylinders (Harris *et al.*, 1957; Rotter, 2004) and cannot be reproduced by calculations that use the same imperfection amplitude (Rotter,

1997). The calculation of the buckling strength is thus very conservative, which in turn leads to a very conservative design. Furthermore, the critical location in any stepped-wall silo lies in the thinner plate at a change of plate thickness. The thicker plate at this change provides considerable restraint against buckling, thus raising the buckling resistance (Rotter and Teng, 1989a). These factors combine to make the computed strength of the structure much greater than the hand design assessed value.

2.5.2 Behaviour of the silo under eccentric discharge

The main goal of this chapter is to explore the behaviour of the silo under eccentric discharge. Such conditions often precipitate silo failures and may occur accidentally when either a feeder malfunctions, an outlet intended for final cleanout is opened when the silo is full, a new discharge device is fitted without proper testing and other similar conditions (EN 1991-4, 2007). The pattern of pressures arising in this condition is quite realistically characterised in EN 1991-4 and the calculations presented here, believed to be the first of their kind to use this new pressure model, give a good insight into many silo disasters as well as other phenomena.

2.5.2.1 Behaviour of the uniform thickness silo

Under the set of unsymmetrical pressures associated with a flowing channel of stored solid (

Fig. 2.1), very high axial compressive membrane stresses develop around the midheight of the silo down the centre of the flow channel. By contrast, high axial tensile stresses develop at the edges of the channel throughout most of the silo height, becoming compressive at the base of the silo. At these key locations, the axial compressive membrane stresses are enormously greater than those for which the silo was designed (over 3700 N/mm at the base compared to a design value of 830 N/mm, see Fig. 2.3). Clearly, either of these two regions of high compressive stresses may become critical for buckling failures, depending on the design of the silo and the axial variation of plate thicknesses and internal pressure. This stress distribution, originally described by Rotter (1986, 2001b), is shown in Fig. 2.9 for the GMNA analysis at the instant before bifurcation, along with the LA analysis factored to the GMNA load factor for comparison.

In the uniform thickness silo, the compressive stresses at the edge of the flow channel at the bottom of the silo are by far the largest and are responsible for the localised modes

seen in Fig. 2.10. The silo wall is also vulnerable at midheight at the centre of the flow channel and buckling could occur here if the wall were thinner at this location. On the opposite side of the silo from the channel, the axial membrane stress resultant is largely unaffected by the flow channel pressures and corresponds to the axisymmetric loading case, not exceeding 830 N/mm.

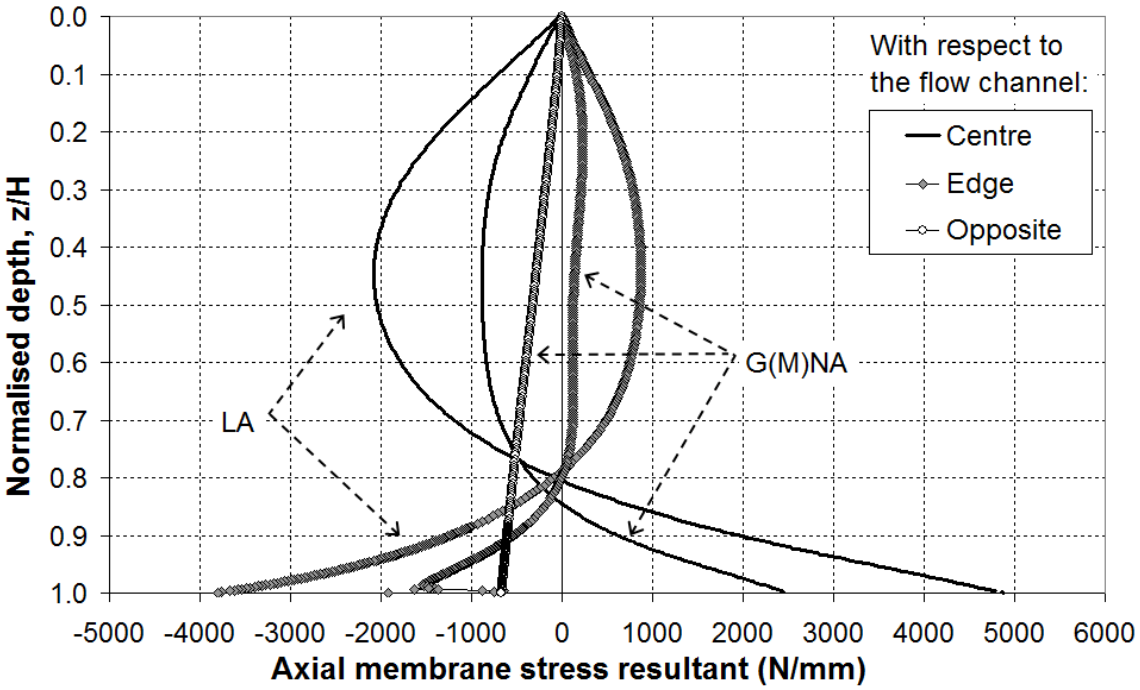

Fig. 2.9 – Axial membrane stress resultant distribution at the instant before bifurcation for the uniform thickness silo under eccentric discharge analysed with LA and GMNA at the same load factor

A summary of the load factors achieved for the uniform thickness silo under the unsymmetrical pressures caused by eccentric discharge with k_c = 0.60 is presented in Table 2.3. The incremental buckling modes are shown in Fig. 2.10 and the nonlinear load-axial deflection curves are shown in Fig. 2.11.

Table 2.3 – Summary of predicted load factors for the uniform thickness silo under eccentric discharge

	LBA	MNA	GNA	GMNA	GNIA	GMNIA
Computed load factor	1.47	1.40	4.32	1.31	3.35	1.34
% of concentric discharge value	16.07	30.57	55.03	34.47	83.75	43.37

All of the load factors in Table 2.3 are significantly below the concentric discharge values, especially when only small deformation laws are considered (LBA and MNA). This illustrates the damaging effect of unsymmetrical pressures on cylindrical shells, though the design in this case is still able to just about withstand them, the lowest load factor still being greater than unity. The GNA factor is, remarkably, almost triple the LBA factor, suggesting that finite deformations have a significant and positive impact on the strength. Indeed, the load-deflection curve of Fig. 2.11 shows the structure stiffening significantly as it deforms under the unsymmetrical loads. Since the applied pressures induce high circumferential bending, geometric nonlinearity results in a considerable change in the pre-buckling stress pattern. Accordingly, Fig. 2.9 shows that the LA stresses are significantly bigger (over 100% larger at midheight when scaled to the GMNA factor) than the GMNA stresses. As a result, the LBA predicts a much lower bifurcation load. This rather unexpected finding illustrates the need for further detailed investigation and will be returned to in subsequent chapters.

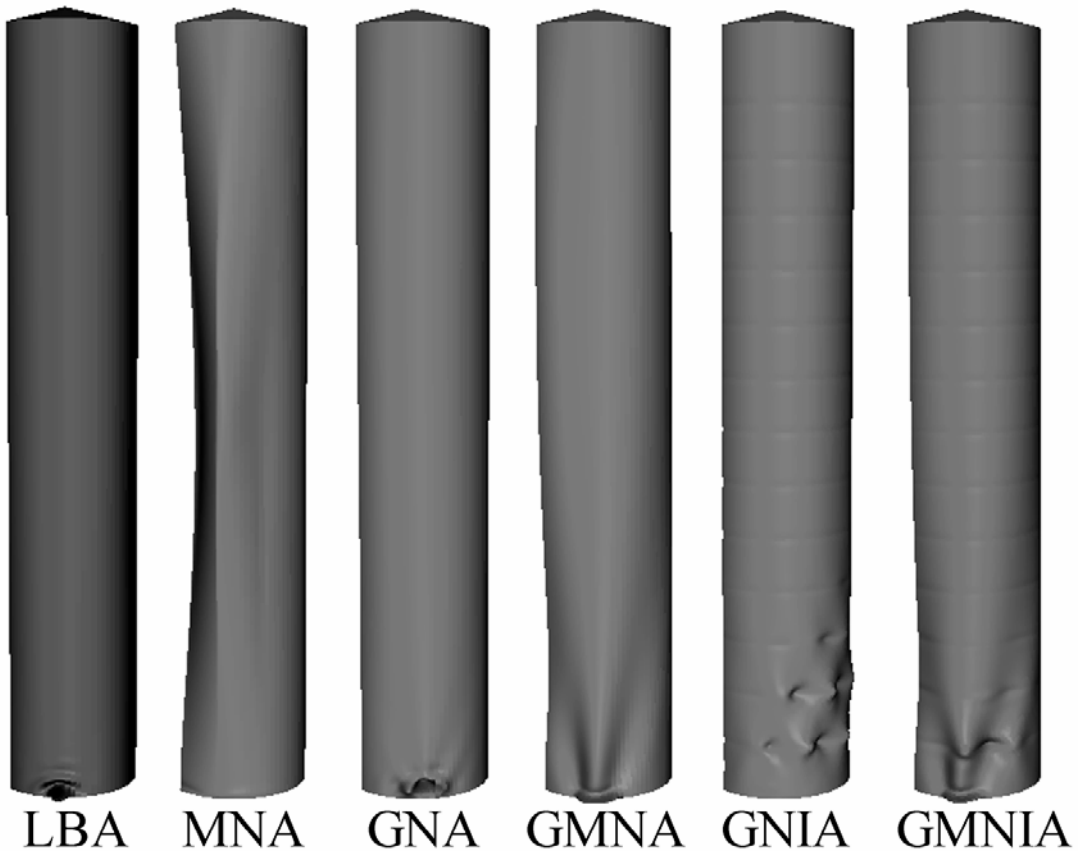

Fig. 2.10 – Failure modes for the uniform thickness silo under eccentric discharge. The geometric scale factors are 500, 0.1, 700, 700, 30 and 200 respectively.

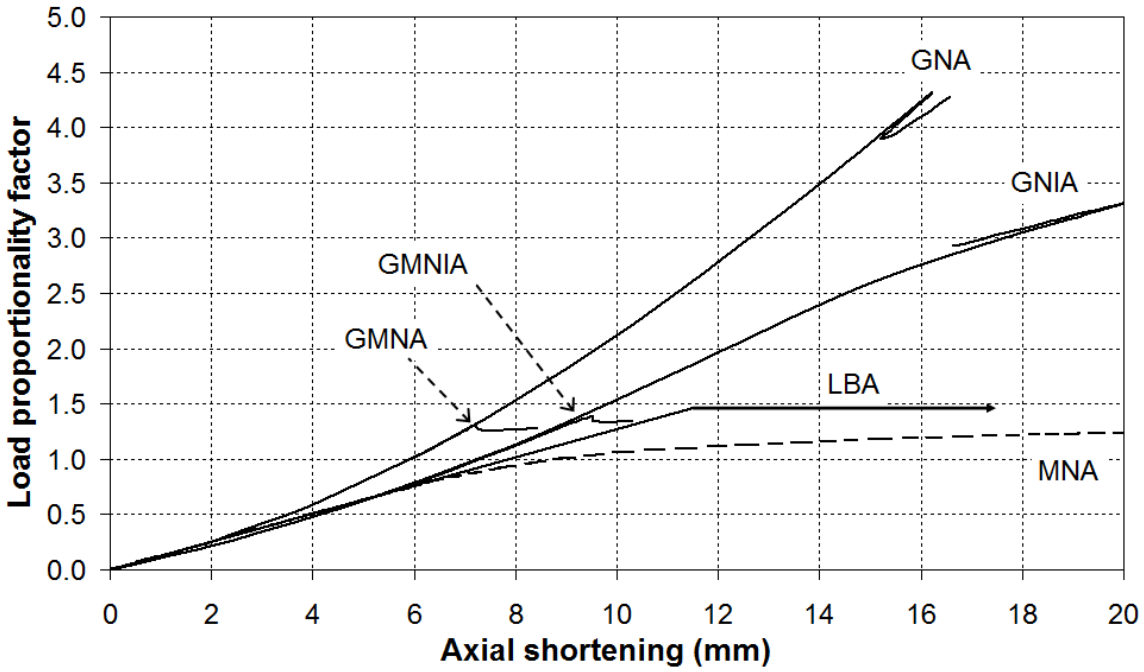

Fig. 2.11 – Nonlinear load-axial displacement paths for the uniform thickness silo under eccentric discharge

Material plasticity (GNA → GMNA) significantly reduces the silo strength and changes the buckle shape towards a quite distinct and local elephant's foot mode. The effect of plasticity seems to affect the load-deflection paths very suddenly (Fig. 2.11), but since the axial deformations are being followed at a node at the very top of the silo, they are somewhat insensitive to the progressive development of a local buckle at the silo base. The sharp bifurcation and load path reversal shown for all uniform wall thickness silos demonstrates unstable post-buckling behaviour (Yamaki, 1984). The plastic collapse MNA calculation relates to a circumferential bending mechanism, which was the misguided focus of several previous studies of eccentric discharge (Jenike, 1967; Wood 1983; Roberts and Ooms, 1983). The GMNIA result is very similar to the GMNA result because the critical mode lies near the base and is distant from any of the imposed local imperfections.

2.5.2.2 Behaviour of the varying thickness silo

The uniform thickness silo investigated in the preceding section yielded several interesting observations, some of which remain valid in this section. However, practical silos are always designed with different wall thicknesses at different location to minimise cost. The more realistic stepped wall design was therefore explored next.

For the varying thickness silo, a summary of the load factors achieved under eccentric discharge with k_c = 0.60 is given in Table 2.4. The incremental buckling modes are shown in Fig. 2.12. The axial membrane stress resultant distributions for the perfect shell just before bifurcation are shown in Fig. 2.13. The values in Table 2.4 marked with an asterisk (*) represent load factors at the first inflection point on the load-displacement curve (Fig. 2.14).

Table 2.4 – Summary of predicted load factors for the varying thickness silo under eccentric discharge

	LBA	MNA	GNA	GMNA	GNIA	GMNIA
Computed load factor	0.21	0.65	0.37	0.37	0.22*	0.20*
% of concentric discharge value	2.75	14.32	5.06	9.61	6.45	7.07

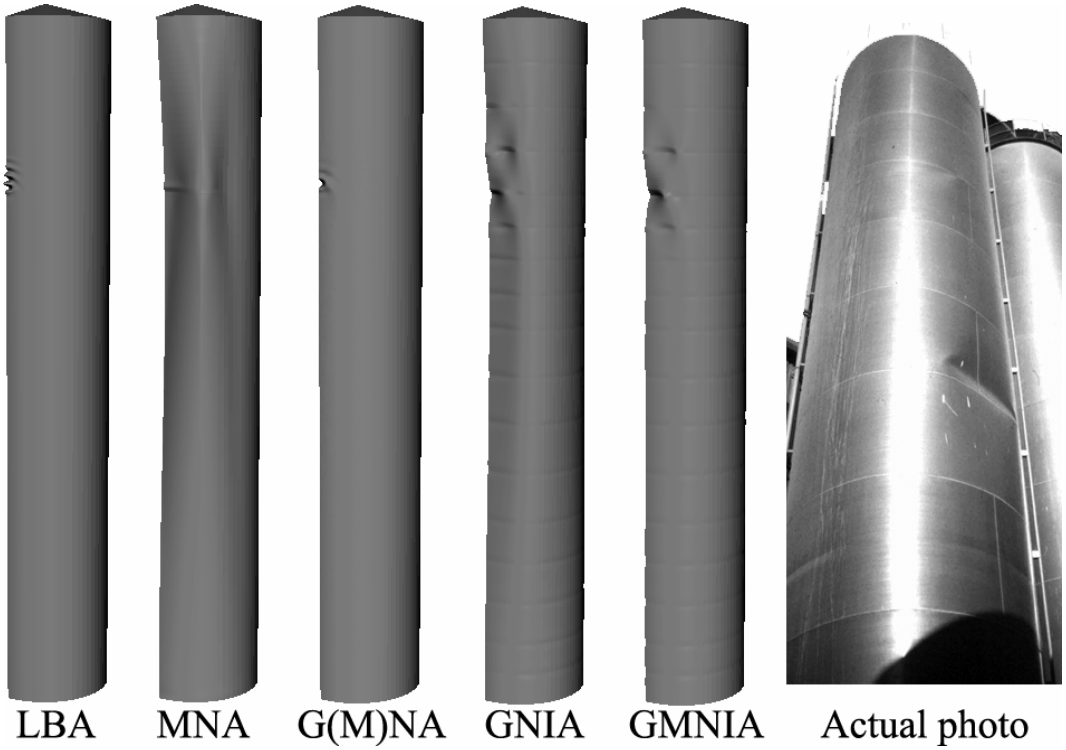

Fig. 2.12 – Failure modes for the varying thickness silo under eccentric discharge, and an actual example for comparison (courtesy of J.M. Rotter). The geometric scale factors are 200, 0.025, 10^5, 100 and 15 respectively.

The load factors in Table 2.4 are all significantly below unity and each is a small fraction of the corresponding value under concentric discharge. The silo with varying wall thickness, designed to EN 1991-4 to comfortably withstand axisymmetric loading, is now wholly inadequate under eccentric discharge. The buckling modes in Fig. 2.12 show that failure occurs exclusively at midheight in all analyses. This is a region of high axial compressive membrane stresses and the wall is thinner here. The thinner wall reduces the linear bifurcation stress and assumes a larger relative imperfection amplitude in design according to EN 1993-1-6. Consequently, these buckling stresses are lower than they were for the uniform thickness silo (Fig. 2.13). Thus, in changing from a uniform to a stepped wall, the critical buckling location moves from the edge of the flow channel at the base to the centre of the channel at midheight. The identical values of the load factors for the GNA and GMNA analyses, and the very close values of the GNIA and GMNIA analyses, show that the buckling is essentially elastic whether the silo is perfect or imperfect. This elastic midheight buckle relates well to known failures in service (Fig. 2.12). Eccentric discharge clearly leads to a very serious stability failure at very low stresses near the midheight of a stepped wall silo.

In the stepped wall silo, the GNA factor is 68% higher than the LBA factor. This surprising outcome is again caused by geometric nonlinearity which reduces the stresses in the critical zone, leading to a lower elastic bifurcation load. The GNA and GMNA load-deflection paths (Fig. 2.14) are a good example of unstable post-buckling behaviour. The paths descend very steeply before beginning to ascend again, suggesting a high imperfection sensitivity. The GNIA and GMNIA paths, however, show a clear point of inflection and indefinite geometric hardening with a progressive growth of the imperfection mode. With no negative eigenvalues reported at the change of slope, it is evident that the bifurcation point has been lost. A smooth transition from the pre- to post-buckling stages has occurred with stable post-buckling displacements developing strongly after this point, a phenomenon illustrated succinctly in Fig. 2.15.

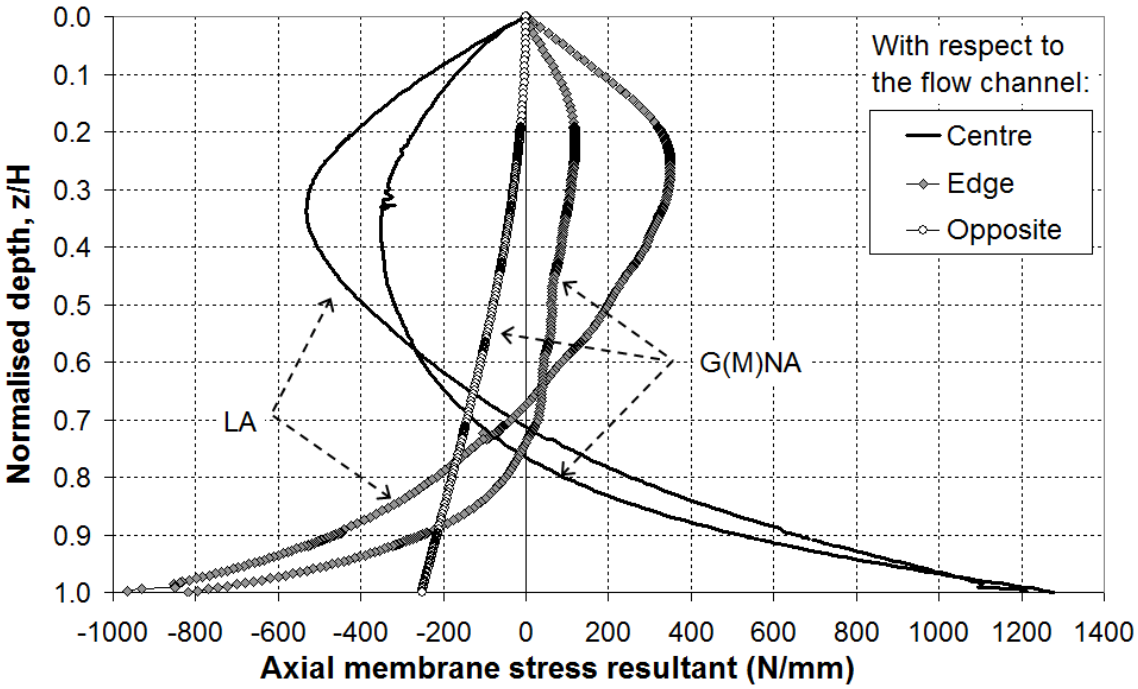

Fig. 2.13 – Axial membrane stress resultant distribution at the instant before bifurcation for the uniform thickness silo under eccentric discharge analysed with LA and GMNA at the same load factor.

This phenomenon often occurs when imperfection amplitudes are large resulting in a blurring of the buckling behaviour (Yamaki, 1984; Rotter, 2007b). It raises the key question of what criterion of failure should be used if the transition from pre- to post-buckling is smooth. It is illustrated further by the imperfection sensitivity curve in Fig. 2.15. As the imperfection amplitude is increased, the bifurcation point progressively disappears and turns into a point of inflection on the load-displacement path. This figure

also shows that a smaller imperfection amplitude would have resulted in a bifurcation point at a lower load factor of approximately 0.16 instead of the calculated inflection point at 0.22. Thus the imperfection sensitivity curve of Fig. 2.15 follows the style of Yamaki (1984), but it presents significant problems in terms of the re-drafting of EN 1993-1-6 (2007) because the analyst exploiting GMNIA calculations cannot be expected to generate such a laborious imperfection sensitivity curve to identify this complex condition when designing just one structure, whilst the standard currently specifies large amplitude imperfections in the expectation that this will lead to low strength evaluations. For unsymmetrical loads, this expectation is clearly shown to be at fault.

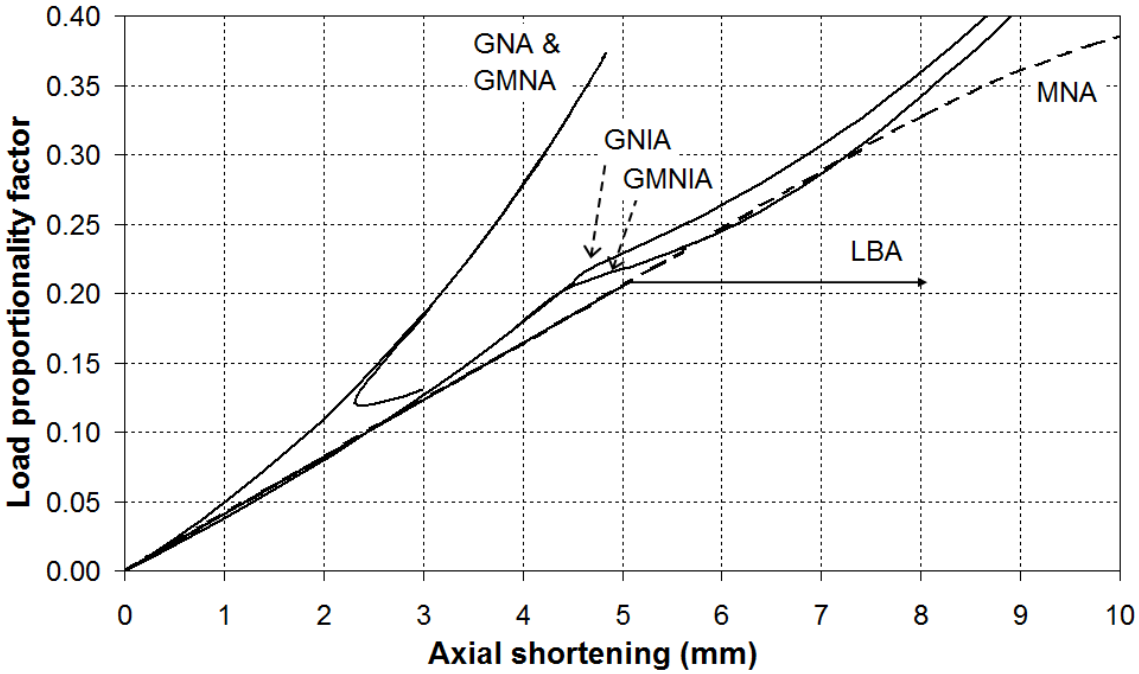

Fig. 2.14 – Nonlinear load-axial displacement paths for the varying thickness silo under eccentric discharge

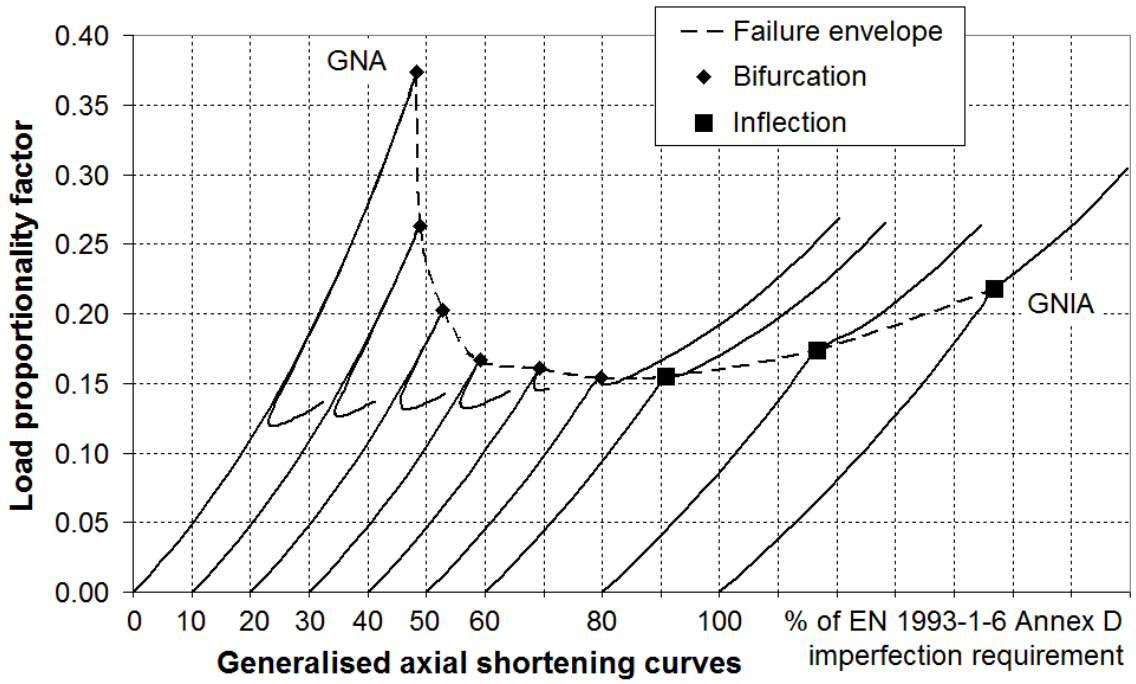

Fig. 2.15 – GNA → GNIA imperfection sensitivity curves

The plastic collapse MNA calculation relates to a circumferential bending mechanism, which was noted above to be the misguided focus of previous studies of eccentric discharge (e.g Jenike, 1967; Wood 1983). The corresponding load factor is very high and does not contribute to the behaviour at all.

2.6 Conclusions

The following conclusions may be drawn based on the results of this study:

A silo designed according to the new rules of EN 1991-4 and EN 1993-1-6 for the condition of concentric filling, storage and discharge of contents is found by non-linear finite element analysis to have a significant reserve of strength under the design loads (GMNIA load factor of 2.83) beyond the value indicated by the partial factors (safety factor of 1.65). This is due to the conservatism of the assumptions upon which the hand design procedure is founded. The design procedure is thus conservative both for stability and plastic collapse calculations under axisymmetric loading.

EN 1991-4 limits the range of silos which must be explicitly designed for eccentric discharge to those in which high eccentricities are anticipated. The example silo considered in this study, still a large structure (5×26 metres), would not have been designed for eccentric discharge. The low load factors obtained in this study indicate

that a silo that functions perfectly under normal symmetrical conditions may experience a catastrophic stability failure if an accidental eccentric pipe flow channel develops. This has often occurred in service.

Under the eccentric discharge pressures of EN 1991-4, the regions of highest compressive axial membrane stress are at the centre of the channel at midheight and at the edge of the channel at the base of the silo. These are both critical regions where this pressure model indicates that the silo may buckle.

At midheight, very high compressive axial membrane stresses develop in the thin wall and the buckling mode is elastic. The low internal pressure in the flow channel also reduces the strength gain that might have been expected due to internal pressure. This midheight buckling mode has often been observed in practice and is responsible for many failures.

At the base of the silo, the internal pressures are much higher, so the predicted buckling mode becomes plastic. There are two main reasons why this mode is not observed in practice: the narrower or absent flow channel in real structures and the elastic restraint provided by the stationary solid at this location.

The behaviour of a cylindrical silo under eccentric discharge pressures has been found to be rather complicated, with several counter-intuitive phenomena. A clear explanation for the enhanced strength caused by geometric nonlinearity when the shell curvature is reduced at the centre of the flow channel is still needed.

Geometric nonlinearity, which reduces buckling loads under axisymmetric conditions and is commonly thought to be highly detrimental, surprisingly gives additional strength under this unsymmetrical load. Geometric imperfections in the form of axisymmetric weld depressions were explored and were found to reduce the strength greatly under axisymmetric loads, but their effect under unsymmetrical loads is more complex. Calculations involving deeper imperfections require very careful interpretation.

At small imperfection amplitudes, dramatic bifurcation buckling was found to occur under eccentric discharge. But larger amplitudes may completely remove the bifurcation

point, turning it into a point of inflection on the smooth path from pre-buckling to post-buckling. This provokes the vital question for all computational analysts of imperfect shells: what criterion of failure should be used in structures with such a pattern of behaviour?

The lowest GMNIA buckling load factor may well occur at imperfection amplitudes much lower than those prescribed by EN 1993-1-6 and, although it is required by that standard, it is very onerous for the shell analyst to be required to seek out the lowest point on the imperfection sensitivity curve for every designed structure.

The provision of the EN 1993-1-6 standard for nonlinear computational analyses of imperfect shells may need to be re-drafted. It is clear that they were formulated by considering the experimental database, which is dominated by axisymmetric loading. When these provisions are applied to shells under non-symmetric loading that leads to complex behaviour, the interpretation of the calculations for design purposes may be quite difficult.

Chapter 3 – The structural consequences of different circumferential forms of the EN 1991-4 eccentric discharge pressure distribution

3.1 Introduction

The EN 1991-4 (2007) eccentric discharge pressure distribution incorporates zones of high pressures in the wall immediately adjacent to the flow channel, illustrated in Fig. 3.1. Though it is known that there should be a small rise in normal wall pressures at this location based on experimental observations, it is not known what circumferential form the distribution of these pressures should assume (Jenike, 1967; Wood, 1983; Rotter, 1986; Chrisp *et al.*, 1988; Chen, 1996).

The low pressures exerted by the flow channel on the silo wall already constitutes a severe structural action. The inclusion of regions of high wall pressures near the edge of the channel, especially in the circumferential form specified in the current European Standard, may unnecessarily further exacerbate an already damaging load condition. This question was introduced in the wider context of silo pressures in the literature review. An analytical study of the circumferential form based on elasticity theory is presented in Appendix B.

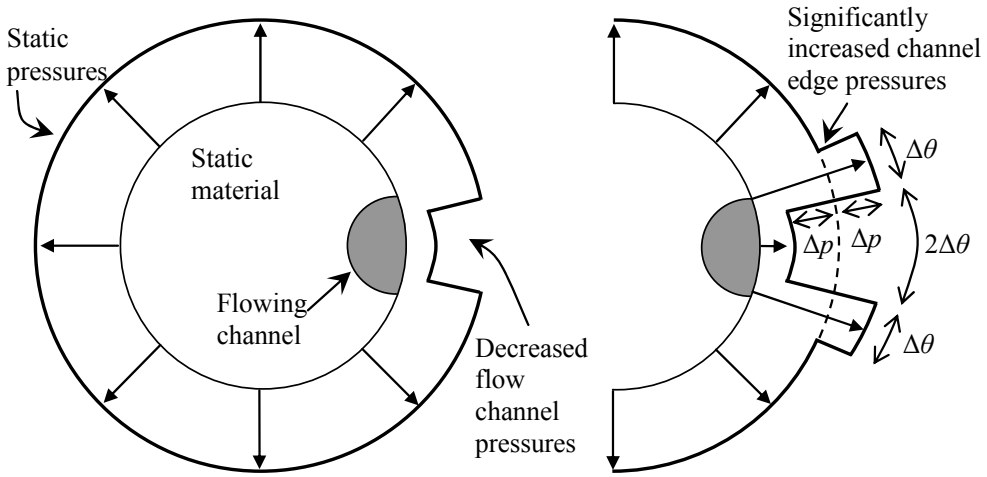

Fig. 3.1 – Limiting cases for the form of normal pressures against the wall of an eccentrically discharging silo

The circumferential form of the pressure increase at the edges of the flow channel specified in EN 1991-4 is rather simplistic and unrealistic, though it has the virtue of being conservative for the purposes of structural design. Unfortunately, there is insufficient research evidence at this stage to confidently propose a more realistic alternative that could be implemented easily in design. This chapter investigates the effect of removing these regions of high pressure altogether, to determine how large an influence this may have on the load proportionality factors and stresses within the silo, and whether any other important observations may be made. The two versions of the circumferential distribution of pressure shown in Fig. 3.1 may therefore be thought of as limiting cases, with the 'true' behaviour lying somewhere in between.

This study employs the derivation of Rotter (1986) for an eccentric flow channel with no high channel edge pressures, based on a formulation of the channel geometry originally conceived by Jenike (1967). The EN 1991-4 version is directly descended from Rotter's version which has a firmer basis in mechanics but cuts many corners for the sake of simplicity in design calculations. The merits of the two versions will be compared in this chapter. This study is therefore a natural stepping stone on the path from the current code-defined eccentric discharge model towards a potentially more powerful and realistic silo pressure theory, which will be presented in Chapter 7.

3.2 Design of example silos

The 'very slender cement' silo (CVS: H = 26, R = 2.5 m, H/D = 5.2) introduced in Chapter 2 was employed in this study. To cover a wider range of aspect ratios, a new stepped-wall thickness silo was designed according to EN 1993-1-6 (2007) in a manner identical to Silo CVS. Named the 'slender cement' (CS) silo, it was also designed to hold cement but has a lower aspect ratio (H = 18, R = 3 m, H/D = 3.0), though still well within the slender range. Silos CS and CVS are both linked by a common volume and are thus alternative designs to the same storage requirement.

A comparison of the axial distributions of the design axial membrane stress resultants and required shell thicknesses is shown in Fig. 3.2 and Fig. 3.3. For additional illustration, these figures also contain data for two silos used elsewhere in this thesis, 'slender wheat' (S) and 'very slender wheat' (VS). Sharing the same aspect ratios, Silos S and VS are respectively analogous to Silos CS and CVS but were designed to hold

wheat rather than cement. The two figures demonstrate the interesting feature that, due to the higher unit weight of cement (Table 3.1), Silos CS and CVS are under significantly higher compressive axial membrane stresses than Silos S and VS. Consequently, they require a much thicker wall throughout their height. A full summary of the custom silo designs performed especially for the different studies in this thesis is presented in Chapter 4. Granular solids properties, imperfection amplitudes and exact wall thickness distributions as required by EN 1991-4 and EN 1993-1-6 may also be found in that chapter.

Table 3.1 – Summary of characteristic values of granular solids properties from EN 1991-4 (2007) Annex E (friction properties for a D2 'smooth' wall)

Granular solid name	Upper unit weight, γ_u (kN/m^3)	Lower unit weight, γ_l (kN/m^3)	Angle of repose, ϕ_r (degrees)	Upper internal friction angle, ϕ_i (degrees)	Upper lateral pressure ratio, K	Upper wall friction coefficient (D2), μ_u	Lower wall friction coefficient (D2), μ_l
Wheat	9	7.5	34	33.6	0.60	0.44	0.33
Cement	16	13	36	36.6	0.65	0.49	0.43

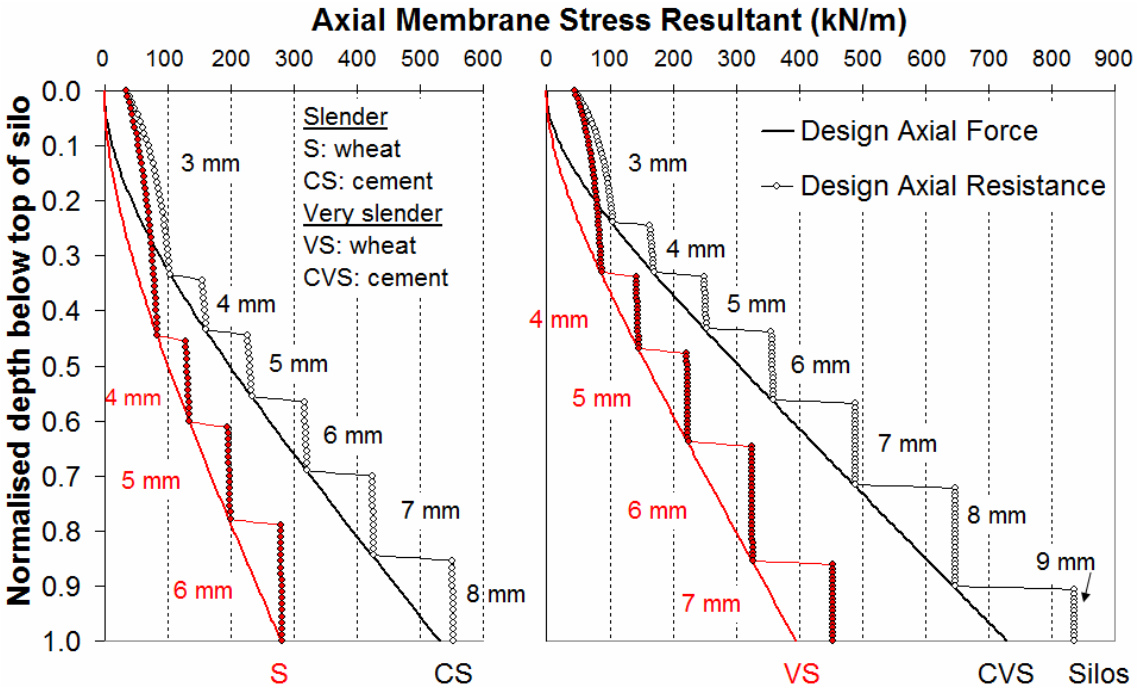

Fig. 3.2 – Comparison of the axial distribution of the design axial membrane stress resultants for Silos S, CS, VS and CVS

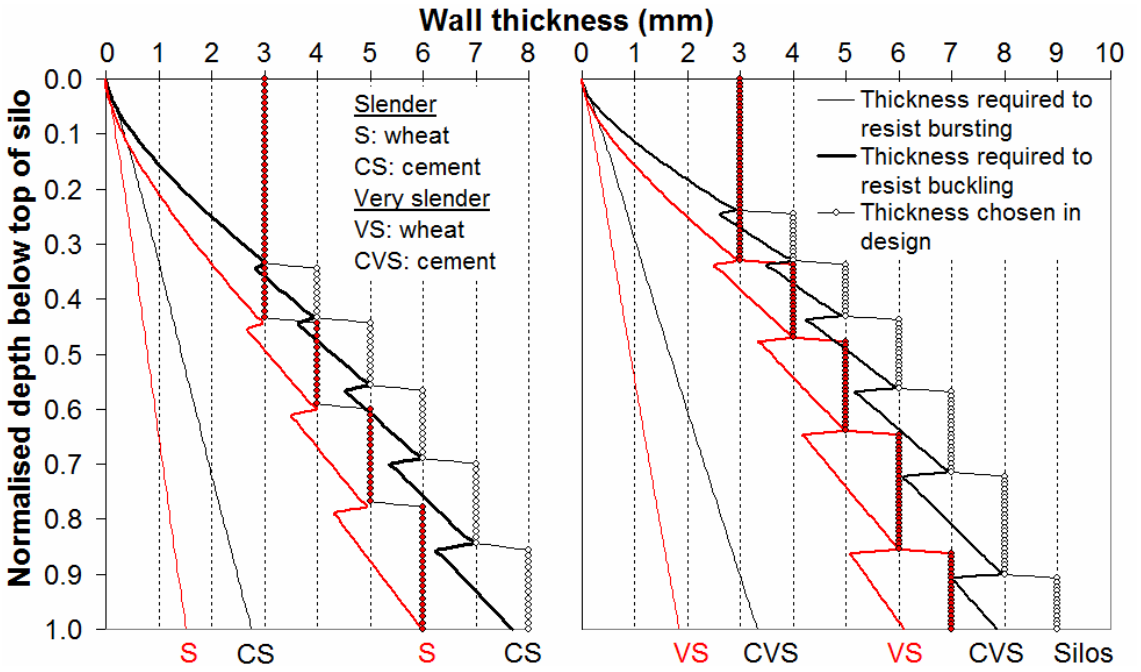

Fig. 3.3 – Comparison of the axial distribution of the design thicknesses for Silos S, CS, VS and CVS

3.3 Computational analyses

Silos CS and CVS were analysed using four of the standard EN 1993-1-6 (2007) types of computational analysis, namely LBA, MNA, GNA and GMNA. Material properties for mild steel were assumed as before (E = 200 GPa, ν = 0.3 and σ_y = 250 MPa). Both silos were first analysed under concentric discharge with EN 1991-4 pressures to obtain a set of reference load factors for this simplest of the present load cases. Next, the silos were analysed under the full eccentric discharge pressures of EN 1991-4 for the three recommended channel sizes, $k_c = r_c/R$ = 0.25, 0.40 and 0.60, with the regions of high channel edge pressures included. This again yielded a set of reference load factors for the eccentric discharge load case exactly as it is prescribed in the Standard.

The silos were then analysed once more using the EN 1991-4 pressures, but this time with no regions of high channel edge pressures. The static zone Janssen pressures were instead extended right up to the flow channel boundary, after which the reduced flow channel pressures were applied. Lastly, the silos were analysed under the set of equations for eccentric discharge without high pressure zones as devised by Rotter (1986), which prescribes static zone pressures from analysis of the channel interface and wall frictions.

3.4 Eccentric discharge pressure models

In his pressure model for a parallel-sided eccentrically-discharging flow channel, Rotter (1986) assumed that the flow channel would change its geometry to maximise the weight of each slice of material whilst minimising the frictional drag from the channel sides. This leads to the condition in Eq. 3.1 which must be solved numerically for the angles θ_c and ψ (it is reproduced here with a different notation). The geometry of the system is shown in Fig. 3.4.

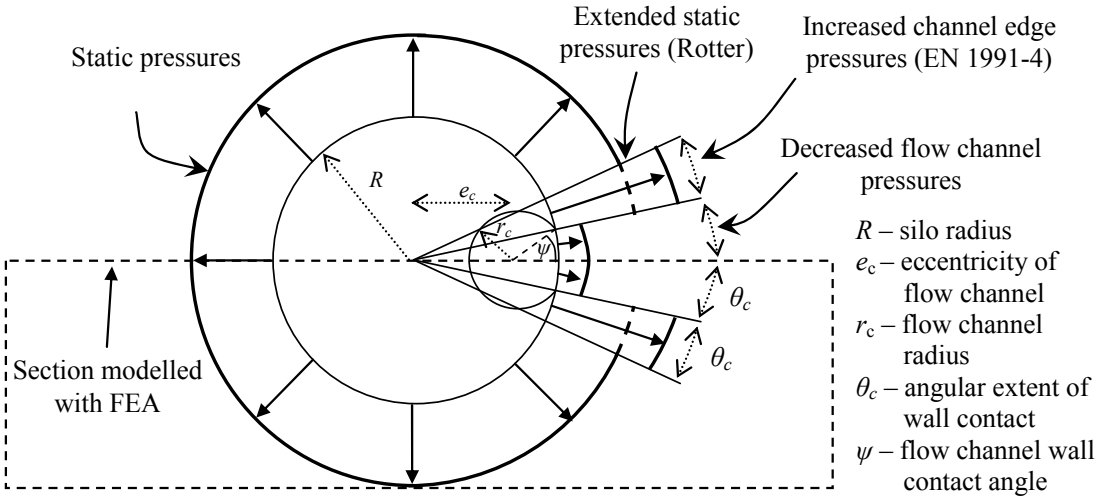

Fig. 3.4 – Notation and geometry of the eccentric flow channel wall pressures, after EN 1991-4 (2007)

$$\left[\left(\pi-\psi\right)k_c^2+\theta_c-k_c\sin\left(\psi-\theta_c\right)\right]\left(1-\frac{\cos\theta_c}{\cos\psi}\frac{\mu_{sc}K_{sc}}{\mu_w K_w}\right)$$
$$=\left[\theta_c+\left(\pi-\psi\right)k_c\frac{\mu_{sc}K_{sc}}{\mu_w K_w}\right]\left[1-\frac{\cos\left(\psi-\theta_c\right)\cos\theta_c}{\cos\psi}+k_c\left(\cos\left(\psi-\theta_c\right)-\frac{\cos\theta_c}{\cos\psi}\right)\right] \tag{3.1}$$

In the above equation, subscripts *w* and *sc* denote the lateral pressure ratios (K) and fully-developed wall friction coefficients (μ) of the solid against the wall and of the stationary solid against the flow channel respectively. The angles θ_c and ψ follow the simple sine rule relation:

$$\psi=\sin^{-1}\left(\frac{\sin\theta_c}{k_c}\right) \tag{3.2}$$

The eccentricity e_c is determined last:

$$e_c=R\cos\theta_c-r_c\cos\psi \tag{3.3}$$

The simpler EN 1991-4 model requires the calculation of the eccentricity first through the following equation (reproduced here in a different notation):

$$e_c = R\left\{\frac{\mu_w}{\mu_{sc}}\left(1-k_c\right)+\left(1-\frac{\mu_w}{\mu_{sc}}\right)\sqrt{1-k_c}\right\} \tag{3.4}$$

Equation 3.4 above is an empirical fit (Rotter, 2001a; 2001b) in terms of the parameters μ_w/μ_{sc} and $(1 - k_c)$ to the results of the original but more onerous Eq. 3.1. The angles θ_c and ψ are then found through Eq. 3.5 below and Eq. 3.2 above.

$$\theta_c = \cos^{-1}\left(\frac{R^2+e_c^2-r_c^2}{2Re_c}\right) \tag{3.5}$$

The choice of the notation presented here differs slightly from what is in both EN 1991-4 and Rotter's paper. Furthermore, both of these sources must make further assumptions about the values of frictional and lateral pressure ratio parameters. Since these assumptions are not based on the geometrical relations of Fig. 3.4, they are not strictly a part of the derivations.

In the EN 1991-4 Standard, the friction coefficient of the solid against the wall μ_w is taken as the lower characteristic μ value (thus emphasising the normal pressure component, rather than frictional traction), whilst the friction coefficient of the solid against itself along the static-flowing interface is taken as the tangent of the upper characteristic internal friction angle, $\tan\phi_1$. The lateral pressure ratio within the solid is different depending on its position with respect to the flow channel, but the Standard suggests a uniform value of K throughout, given by the upper characteristic value, such that K_w/K_{sc} gives unity and hence this ratio is present in Eq. 3.1 but absent in Eq. 3.4 (or in Rotter's reworking of the theory, 2001b).

Rotter (1986) made no assumptions about the friction coefficients, but drew from the theory of Rankine (1857) and Walker (1966), discussed in Section 1.2.3 of the literature review, to make assumptions about the lateral pressure ratio under these conditions. The solid against the wall in the flow channel was assumed to be at active failure while sliding and shearing against the wall so that K_w is given by Eq. 1.8. The stationary solid adjacent to the channel is assumed to be sliding and at active failure (Eq. 1.9) whilst on the other side of the interface the flowing solid is assumed to be sliding and at passive failure (inverse of Eq. 1.9). This is contrary to the single value of K_{sc} assumed in EN 1991-4 and in this study, and was revised in a later version (Rotter, 2001b). It is clear, however, that the appropriate value for each of these parameters remains uncertain at the present time. The above comparison is summarised in Table 3.2.

Table 3.2 – Comparison of the EN 1991-4 (2007) and original Rotter (1986) eccentric discharge pressure models

	EN 1991-4 (2007)	Rotter (1986)
Pressures in the static region, p_{hse}	Janssen pressures, Eq. 2.1	Special derivation, Eq. 1.15
Pressures in the flow channel, p_{hce}	Special derivation, Eq. 2.2	Eq. 1.13, giving same result as Eq. 2.2
Flow channel wall contact angle measured from silo centre, θ_c	Eq. 3.5, based on the eccentricity, e_c	Numerical solution to Eq. 3.1
Flow channel wall contact angle measured from channel centre, ψ	Eq. 3.2	Eq. 3.2
Eccentricity of the flow channel centre, e_c	Eq. 3.4, empirical fit to original Eq. 3.1	Eq. 3.3, geometrical relation to θ_c and ψ
Friction coefficient of the solid against the wall, μ_w	Lower characteristic value from Annex E	No assumption
Friction coefficient of the solid against itself, μ_{sc}	Tangent of the upper characteristic value of the internal friction angle from Annex E	No assumption
Lateral pressure ratio of the solid against the wall, K_w	Upper characteristic value from Annex E	Sliding, shearing and active failure Walker value, Eq. 1.8
Lateral pressure ratio of the solid against itself, K_{sc}	No distinction from K_w	Distinction between the two sides of the stationary-flowing interface (Eq. 1.9 and its inverse)

When the same set of material property values is used for both models (here it is the EN 1991-4 Annex E values for cement, summarised in Chapter 4), it is found that they both yield very similar values for the different flow channel geometry parameters, as one would expect. A comparison using material property values for cement is shown in Table 3.3.

Table 3.3 – Comparison of flow channel geometries for EN 1991-4 Annex E material property values for cement

	EN 1991-4 (2007)			Rotter (1986)		
$k_c = r_c / R$	0.25	0.40	0.60	0.25	0.40	0.60
θ_c (°)	9.53	16.19	26.92	8.52	15.10	26.59
ψ (°)	41.47	44.19	48.98	36.36	40.63	48.25
e_c / R	0.80	0.67	0.50	0.79	0.66	0.50
A_c / A_{tot} (%)	5.90	15.09	33.98	6.01	15.29	34.08

The three-dimensional surface plots in Fig. 3.5 to Fig. 3.7 show the global distributions of the normal wall pressures for Silo CS. The corresponding distributions for Silo CVS are similar. This allows the components of the pressures to be seen clearly, such as the block of high pressures at the edge of the flow channel in Fig. 3.5, or its absence in Fig. 3.6 and Fig. 3.7.

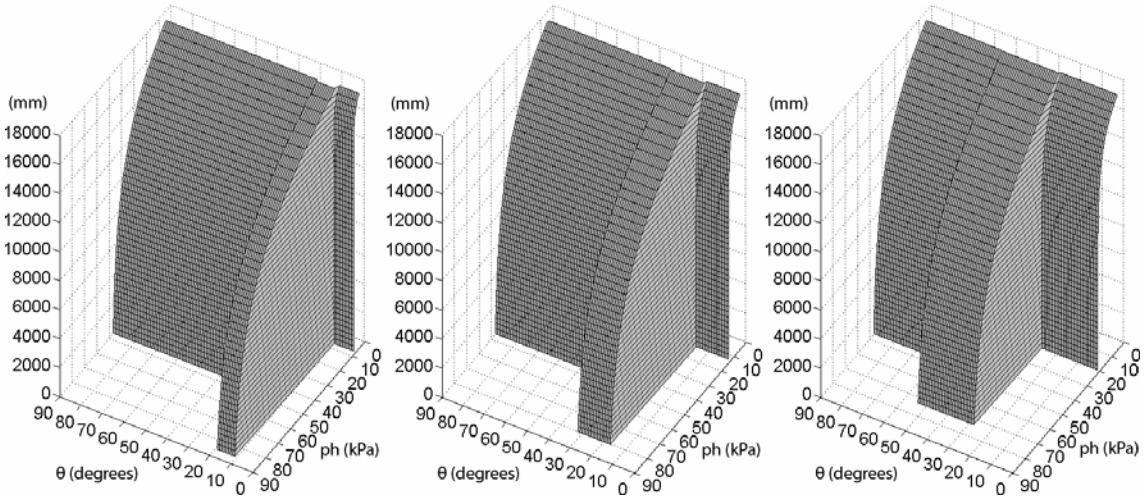

a) $k_c = 0.25$ b) $k_c = 0.40$ c) $k_c = 0.60$

Fig. 3.5 – 3D surface plots of EN 1991-4 eccentric discharge wall pressures in Silo CS with high pressures zones

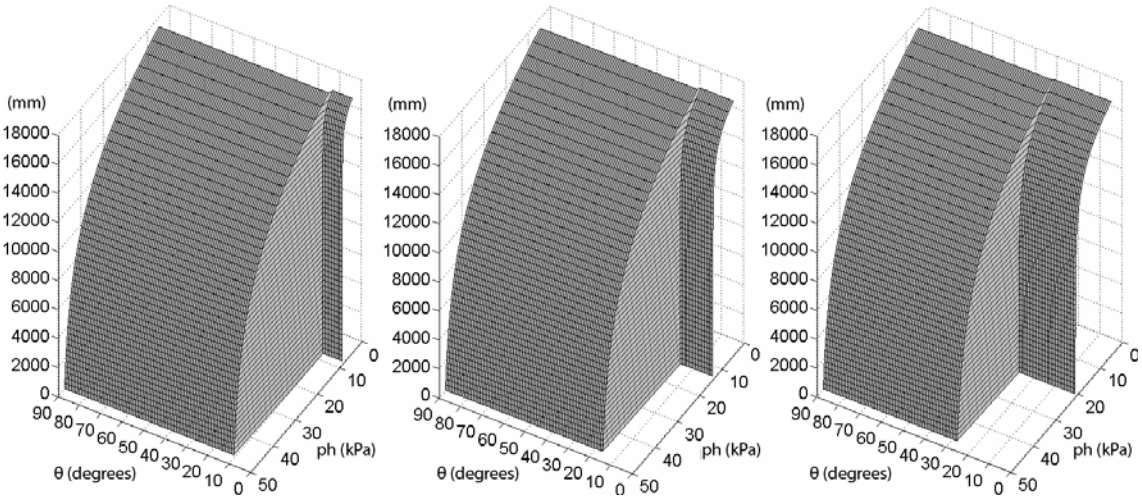

a) $k_c = 0.25$ b) $k_c = 0.40$ c) $k_c = 0.60$

Fig. 3.6 – 3D surface plots of EN 1991-4 eccentric discharge wall pressures in Silo CS without high pressures zones

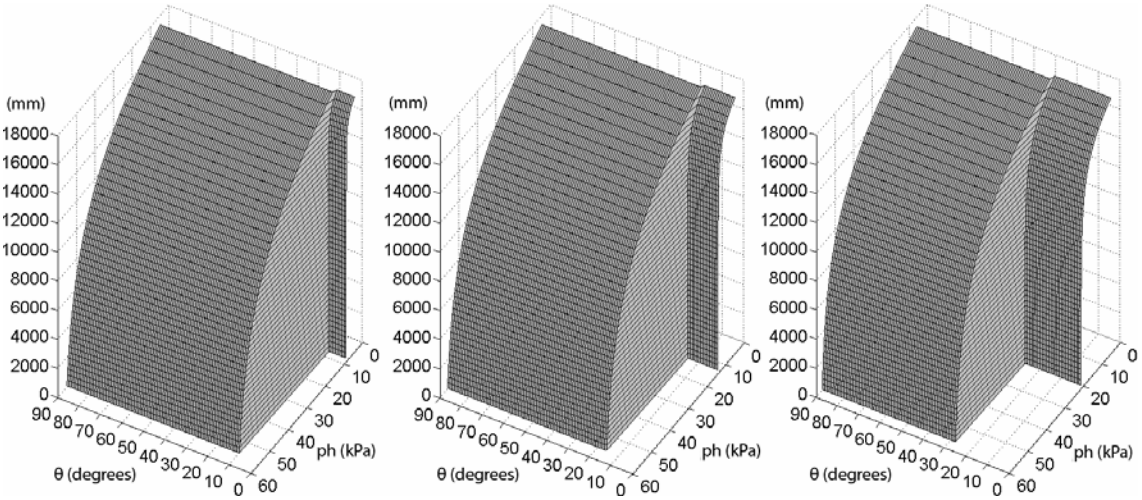

a) $k_c = 0.25$ b) $k_c = 0.40$ c) $k_c = 0.60$

Fig. 3.7 – 3D surface plots of Rotter eccentric discharge wall pressures in Silo CS without high pressures zones

The two sets of wall pressures in Fig. 3.6 and Fig. 3.7 are very similar, since the EN 1991-4 and Rotter distributions differ only in the equation for the pressures in the static solid. As the flow channel gets smaller ($k_c \rightarrow 0$), the Rotter static wall pressures tend to the Janssen value (see accompanying text to Eq. 1.15). The static solid pressures in the EN 1991-4 distribution are independent of k_c, and are given by the Janssen distribution throughout. This is illustrated more clearly for both silos in Fig. 3.8 below. For the largest flow channel size of $k_c = 0.60$, the Janssen equation may underestimate the wall pressures in the static solid by approximately 12%.

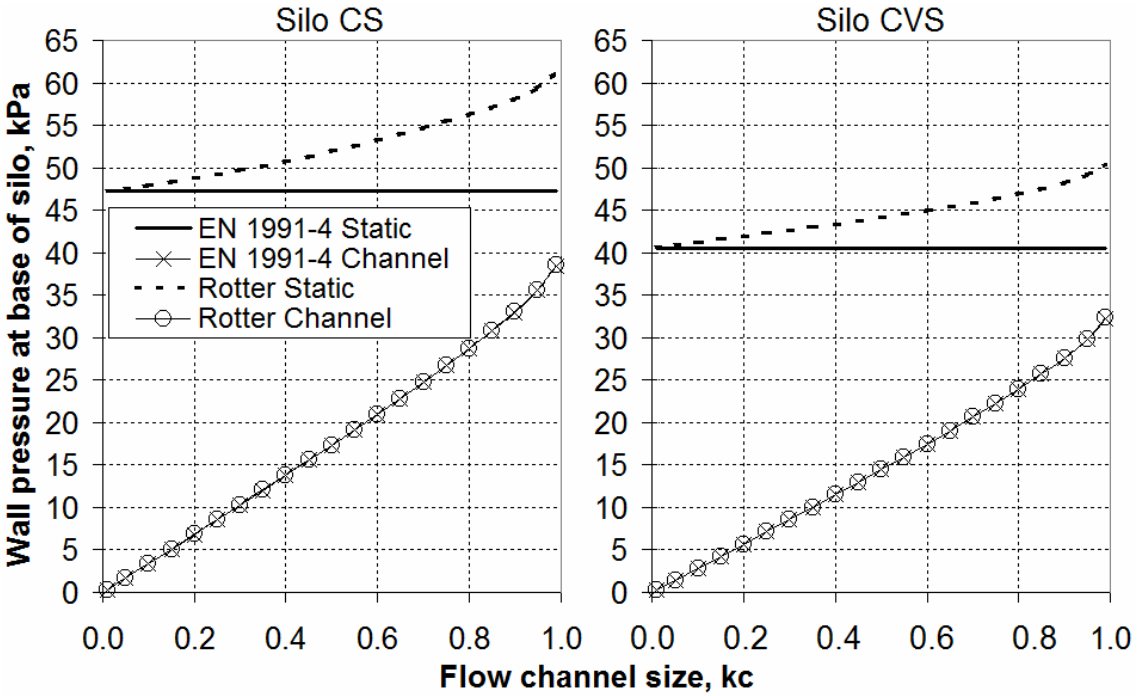

Fig. 3.8 – Variation of static solid and flow channel pressures with k_c according to the EN 1991-4 (2007) and Rotter (1986) models

3.5 Results and analysis of load proportionality factors

3.5.1 Overview

The load proportionality factors for the EN 1993-1-6 suite of computational analyses are listed in Table 3.4 and Table 3.5. The results are additionally shown on a bar chart in Fig. 3.9 in a form which allows a closer comparison of the three distributions for each analysis type and flow channel size.

Table 3.4 – Summary of load proportionality factors for Silo CS

	Concentric Janssen pressures	EN 1991-4 (2007) *with* regions of high pressures			EN 1991-4 (2007) *without* regions of high pressures			Rotter (1986) *without* regions of high pressures		
k_c	0.00	0.25	0.40	0.60	0.25	0.40	0.60	0.25	0.40	0.60
LBA	6.34	0.30	0.18	0.24	0.27	0.28	0.52	0.28	0.24	0.37
MNA	4.98	0.64	0.58	0.76	0.94	1.05	1.69	0.95	0.91	1.22
GNA	6.31	2.69	0.24	0.35	0.26	0.38	0.82	0.28	0.30	0.52
GMNA	3.93	2.35	0.24	0.35	0.26	0.38	0.82	0.28	0.30	0.52

Table 3.5 – Summary of load proportionality factors for Silo CVS

	Concentric Janssen pressures†	EN 1991-4 (2007) *with* regions of high pressures			EN 1991-4 (2007) *without* regions of high pressures			Rotter (1986) *without* regions of high pressures		
k_c	0.00	0.25	0.40	0.60	0.25	0.40	0.60	0.25	0.40	0.60
LBA	7.65	0.47	0.25	0.21	0.33	0.29	0.39	0.34	0.26	0.29
MNA	4.54	0.88	0.64	0.65	1.00	0.95	1.17	1.00	0.85	0.94
GNA	7.63	2.55	0.49	0.37	0.34	0.36	0.70	0.35	0.30	0.43
GMNA	3.85	2.55	0.49	0.37	0.34	0.36	0.70	0.35	0.30	0.43

The GMNA results for $k_c = 0.00$ correspond to a plastic elephant foot buckling mode at the base of the thinnest 3 mm strake in both silos, similar to those in Fig. 2.7. For $k_c \neq 0.00$, the LBA, GNA and GMNA load factors correspond to a localised elastic midheight buckle within the thinnest strake of both silos, while the MNA all correspond to a global circumferential plastic collapse mode. For both types of failure mode, the illustrations are similar to those shown in Fig. 2.12.

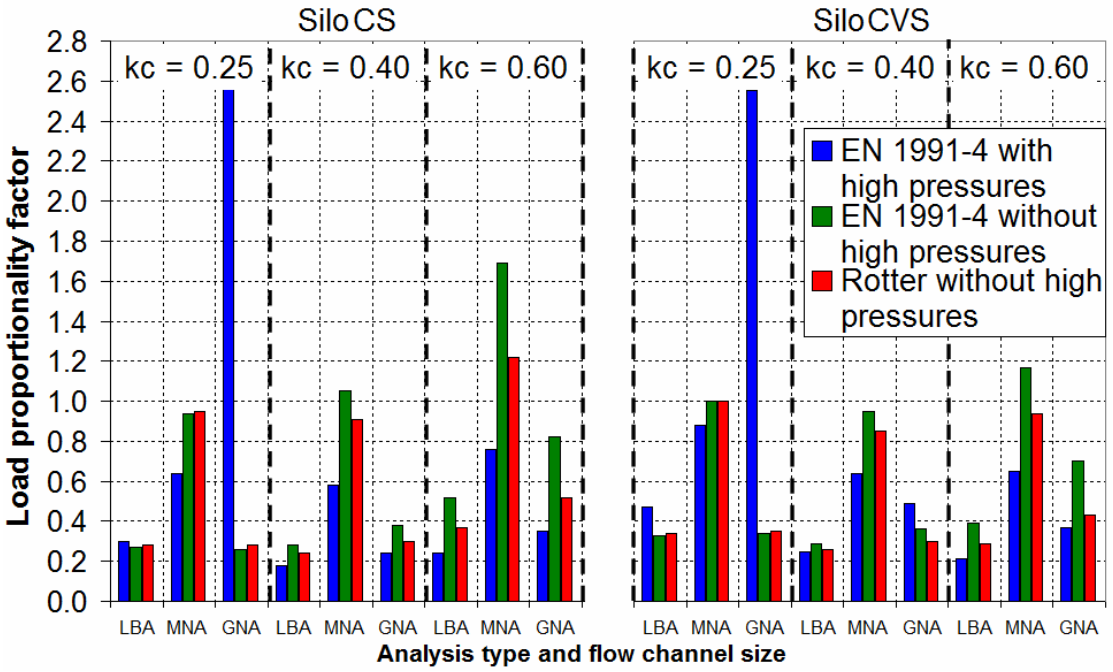

Fig. 3.9 – Bar chart of the LBA, MNA and GNA load proportionality factors

3.5.2 Comparison of load proportionality factors under eccentric discharge to the reference concentric discharge values

A simple comparison of the load factors for each silo under eccentric discharge to the load factors under concentric discharge suggests that there is little new to discuss beyond what was found in Chapter 2, since the load factors are clearly all much lower and significantly below unity. The removal of the high edge pressures, or the use of the more correct Rotter distribution, does little to change the underlying fact that this load condition is extremely serious to the stability of the silo and results in extremely low load factors.

The load factors due to the EN 1991-4 pressures for larger values of k_c (0.40 and 0.60) without high edge pressures are marginally higher than those with these pressures included, while the load factors due to Rotter's pressures lie somewhat between the two EN 1991-4 versions. Since the wall pressures in the static zone increase with channel size according to Rotter's model, they appear to have an increasingly deleterious effect on the load factor at larger values of k_c.

The buckling behaviour under eccentric discharge is completely elastic regardless of silo (CS or CVS), flow channel size or pressure distribution, shown by identical GNA and GMNA load factors. The single exception to this is $k_c = 0.25$ for Silo CS (but not Silo CVS) under full EN 1991-4 pressures. The load factors for GNA and GMNA at $k_c = 0.25$ under full EN 1991-4 pressures are significantly higher than at higher values of k_c, and an explanation for this phenomenon is suggested in the subsequent two chapters. For this same reason, all results for $k_c = 0.25$ are considered by the author to be unrepresentative of appropriate behaviour of a silo under eccentric discharge. The channel appears to be unrealistically small and the behaviour is in transition between the typical behaviour under concentric discharge and the typical behaviour under eccentric discharge.

3.5.3 Comparison of load proportionality factors under eccentric discharge to each other

A comparison of the load factors under eccentric discharge to each other for the more reliable values of k_c of 0.40 and 0.60 suggests a more meaningful picture. Table 3.6 shows the percentage changes in load factor for the corresponding k_c value as the

regions of high pressures are removed from the applied pressure distributions. Removing the high edge pressures from the EN 1991-4 distribution (i.e. Fig. 3.6) leads to strength increases of over 85% for the larger channel, a massive rise. Higher values of k_c result in larger values of θ_c and hence wider 'blocks' of high pressure (Fig. 3.5). When these are removed, larger strength gains are found.

An anomalous value appears for the more slender Silo CVS when the high edge pressures are removed from the EN 1991-4 distribution at k_c = 0.40. This results in a decrease in the GNA load factor, while one would clearly expect it to rise. It is currently not known why this occurs.

Table 3.6 – Percentage change in load factor for values of k_c of 0.4 and 0.6 for distributions *without* regions of high pressures

		EN 1991-4 change from EN 1991-4 *with* high pressures		Rotter change from EN 1991-4 *with* high pressures		Rotter change from EN 1991-4 *without* high pressures	
	k_c	0.40	0.60	0.40	0.60	0.40	0.60
CS Silo	LBA	+ 55.6%	+ 116.7%	+ 33.3%	+ 54.2%	– 14.3%	– 28.5%
	GNA	+ 58.3%	+ 134.29%	+ 25.0%	+ 48.6%	– 21.1%	– 36.6%
CVS Silo	LBA	+ 16.0%	+ 85.7%	+ 4.0%	+ 38.1%	– 10.4%	– 25.6%
	GNA	**– 26.5%**	+ 89.2%	**– 38.9%**	+ 16.2%	– 16.7%	– 38.6%

Rotter's distribution results in an increase in the wall pressures in the static region by approximately 7 and 12% for k_c = 0.40 and 0.60 respectively (Fig. 3.8), yet this is sufficient to cause an average reduction in the GNA load factor of almost 20 and 40% respectively. Thus although removing the regions of high pressure results in significant strength gains, increasing the static zone pressures with flow channel size results in noticeable strength losses for larger channels. The silo modelled under eccentric discharge therefore appears to be sensitive to minor increases in the static solid pressures. Finally, it is clear that it is the reduction in wall pressures at the centre of the flow channel, rather than the large rise in wall pressures at the edge of the flow channel, that is the damaging component under eccentric discharge.

3.6 Exploration of the mechanics of geometric nonlinearity

3.6.1 Stress distributions from finite element analyses

It is evident from this and other studies in this thesis that GNA load factors under eccentric discharge are consistently higher than LBA load factors. This finding is contrary to the traditional wisdom in shell structures (e.g. Yamaki, 1984; Teng and Rotter, 2004; many others), where, based on analytical buckling studies of shells under uniform membrane stress states, the exact opposite is the established norm.

The LBA and GNA load factors at $k_c = 0.25$ for the EN 1991-4 and Rotter distributions with no high edge pressures, shown in Table 3.4 and Table 3.5, have been quite fortuitously found to be equal to one another. This allows a direct comparison to be made of the stress distributions under eccentric discharge pressures for both geometrically linear and nonlinear analyses and leads to important observations about the mechanics involved. Most importantly, it allows the isolation of two opposing phenomena, both due to geometric nonlinearity, which are occurring simultaneously and seem to balance each other for these particular analyses: the deleterious effect of local wall flattening (the buckling strength of a curved panel is reduced as its R/t ratio increases; Rotter, 1985a) and the beneficial effect of a greater portion of the shell being mobilised to carry the stresses.

The axial distributions of the axial membrane stress resultants in the shell adjacent to the centre of the flow channel for Silos CS and CVS are shown in Fig. 3.10. Although the Rotter (1986) model predicts a modest 5% increase in static pressures, this appears to have a negligible effect on the stresses in the silo since the load factors for both the EN 1991-4 and Rotter models are nearly identical for both the LA and GNA analyses.

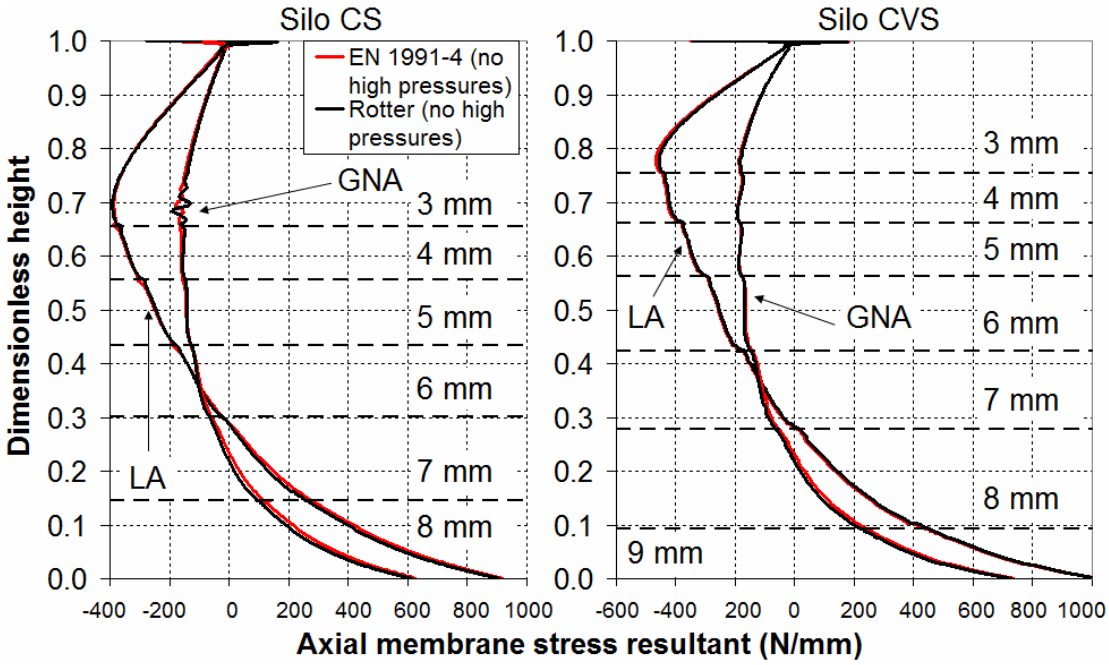

Fig. 3.10 – Vertical distribution of the axial membrane stress resultants at bifurcation through the centre of the flow channel for Silos CS and CVS at $k_c = 0.25$

The peak values of the axial membrane stresses in the two silos occur at the base of the thinnest 3 mm strake in each. The ratios of the peak compressive LA to GNA axial membrane stresses at bifurcation, and the percentage decrease from one to the other, are summarised in Table 3.7 below. On average, there is a 55% reduction due to geometric nonlinearity in the peak value of the axial compressive stress at buckling. Thus, the flattening of the silo wall clearly has a major destabilising effect.

Table 3.7 - Summary of beam analogy section properties ($k_c = 0.25$ data only)

	Silo CS EN 1991-4	Silo CS Rotter	Silo CVS EN 1991-4	Silo CVS Rotter	Average
Ratio of peak compressive $\sigma_{max\text{-}(LA)}$ / $\sigma_{max\text{-}(GNA)}$	2.16	2.04	2.37	2.44	**2.25**
% decrease	53.66	51.00	57.85	59.01	**55.38**

The circumferential distributions of the axial membrane stress resultants at bifurcation just above the respective 3 mm strake are shown in Fig. 3.11 for the two silos. It is evident that the change of geometry causes a greater circumferential portion of the shell to be mobilised in carrying the stresses, which leads to an overall reduction in their magnitudes. This observation is reinforced in later chapters, but the mechanics through

which this occurs are explored here in the novel context of a beam analogy. The stresses are again almost identical for both the EN 1991-4 and Rotter distributions.

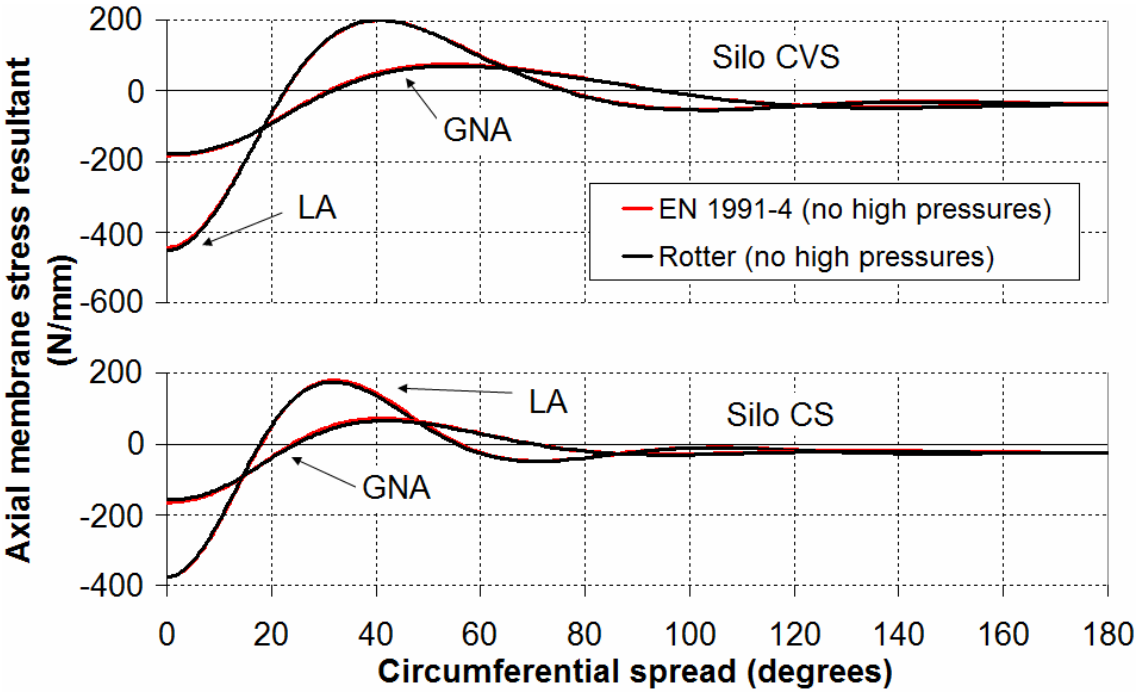

Fig. 3.11 – Circumferential distribution of the axial membrane stress resultants at bifurcation just above the base of the respective thinnest 3 mm strake for Silos CS and CVS at $k_c = 0.25$

3.6.2 Beam theory analogy

Appendix A contains a detailed investigation into the behaviour of a silo shell under eccentric discharge by analogy with a propped cantilever beam (Fig. 3.12). The properties of several complex and unusual shell-like beam sections are derived, and the effect of changes of shape on the section modulus Z (ratio of the second moment of area about the centroidal axis to the distance from the extreme fibre to the section centroid) are investigated. The section modulus is a measure of the strength of a beam in bending, on the assumption that plane sections remain plane and no distortion of the cross-section occurs. Geometries with higher section moduli will therefore experience lower stresses at the same value of the bending moment.

The extreme fibre stresses which develop in a propped cantilever under a uniformly distributed transverse load (Fig. 3.12) are analogous to the characteristic distribution of axial membrane stresses in the silo under eccentric discharge (compare Fig. 3.12, for example, with Fig. 2.9 or Fig. 2.13). The stresses in the top beam fibre, which are

tensile near the built-in support and become compressive towards the simple end support, correspond to the channel centre stresses. Conversely, bottom fibre stresses correspond to the channel edge stresses.

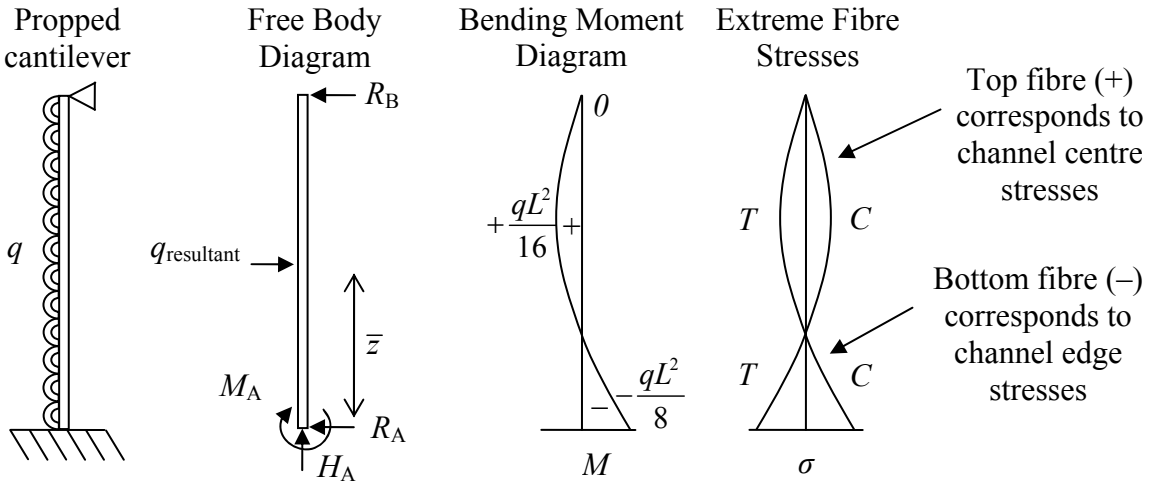

Fig. 3.12 – System diagrams for a uniform thickness propped cantilever with a uniformly distributed load

An example set of data for the circumferential distribution of axial membrane stresses is shown in the top half of Fig. 3.13. The curve oscillates around a reference value, which is the unperturbed axial membrane stress opposite the flow channel derived only from axisymmetric wall friction. Removing this reference value devides the distribution into compressive and tensile components akin to the stress distributions through the cross-section of a beam. The extreme fibres of the beam lie at $\theta = 0°$ (taken as the bottom fibre) and some value $\theta = \theta_c$, which must be calculated to make the integral of the compressive stresses equal to the integral of the tensile stresses. The elastic neutral axis of the beam passes through the point of zero stress at some value $\theta = \theta_{NA}$ which can be determined easily from the figure.

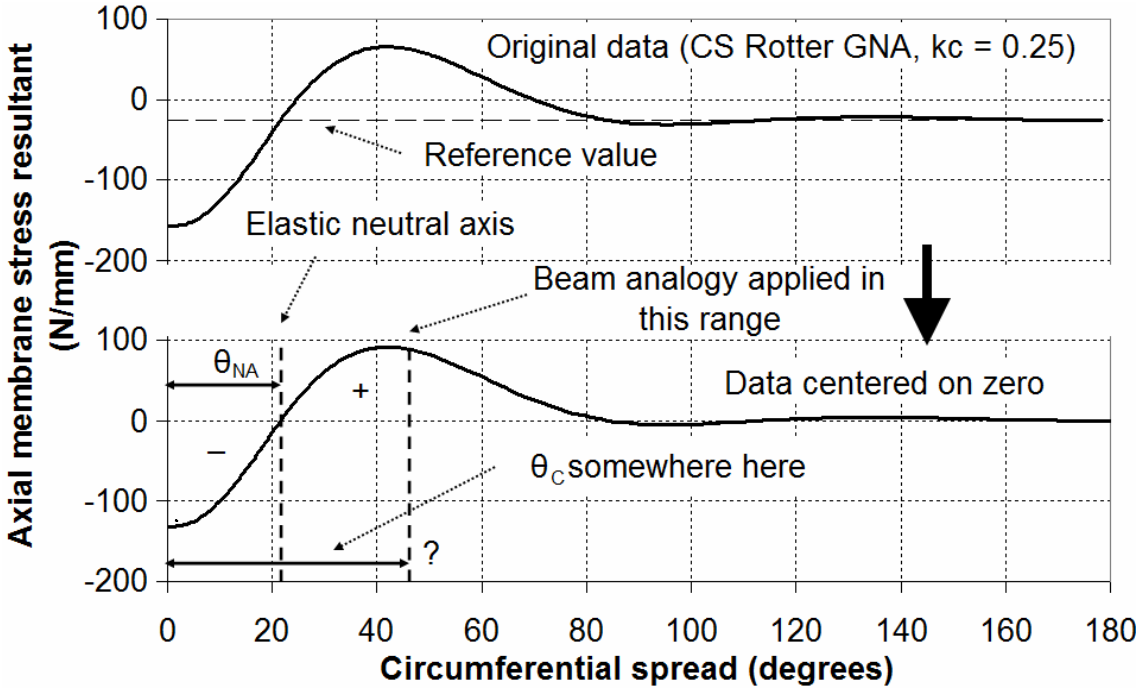

Fig. 3.13 – Application of a beam analogy to the shell

The simple beam geometry of a circular arc with finite thickness is now considered here, shown in Fig. 3.14. The maximum circumferential spread of the section is defined by the angle θ_c from the vertical axis. The angle to the neutral axis, θ_{NA}, is known from the stress distribution and θ_c is determined numerically from it through geometrical relations (Section A.3.1). The radius and thickness of the circular arc, R and t respectively, are taken as those of the silo at the strake where the shell stresses are being considered, in this case the 3 mm strake (recall that the Silos CS and CVS have radii 3000 and 2500 mm respectively).

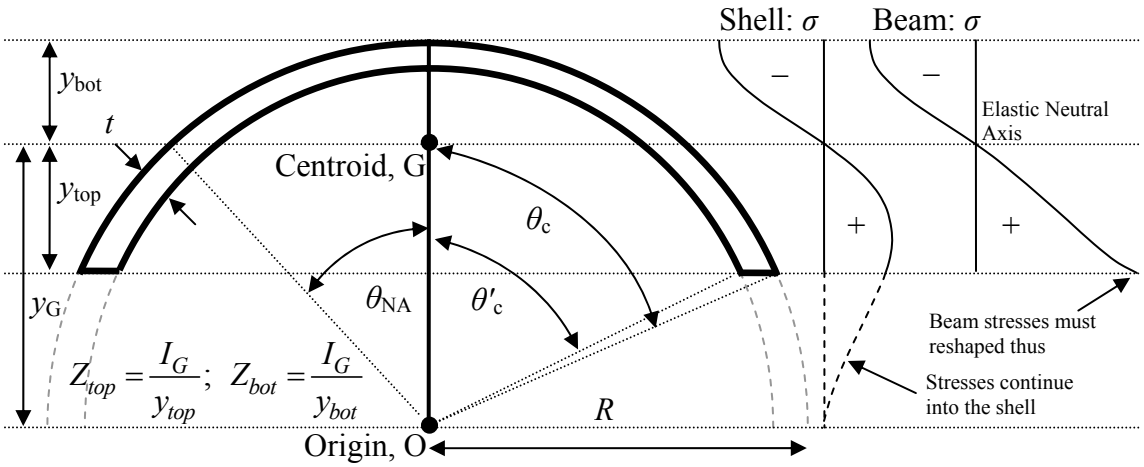

Fig. 3.14 – Circular arc beam geometry and cross-sectional stress distributions

Returning to Fig. 3.11 and applying the beam analogy to the comparison of the LA and GNA stresses, it is clear that the GNA data will have larger values of both θ_{NA} and therefore θ_c. This in turn implies that the location of the centroid will be lower in relation to the bottom fibre (making the distance y_{bot} greater) and the larger spread of the circular arc will yield a much greater second moment of area. The section modulus for the 'GNA beam' will therefore be significantly larger than for the 'LA beam', causing the peak stresses in the former to be lower and thus making it much stronger.

3.6.3 Comparison

The critical question is whether the rise in the section modulus is sufficiently large to support the huge decreases in the buckling strength (up to 55%) that have been found with the finite element analyses? The answer is yes. The results of this relatively simple yet insightful analysis, summarised in Table 3.8, show that the average rise in section modulus is by a factor of two, implying an average reduction in peak stresses of 50%. This is in remarkably close agreement to the reductions found previously in the nonlinear finite element analysis (Fig. 3.10 and Fig. 3.11).

Table 3.8 – Summary of beam analogy section properties (k_c = 0.25 data only)

Silo	Pressure distribution	Analysis Type	θ_{NA} (°)	θ_C (°)	y_G (mm)	Z_B (mm^3)	$Z_{B(GNA)}$ / $Z_{B(LA)}$†	% decrease
CS	EN 1991-4 (2007)	LA @ LBA	17.08	29.57	2867.63	486145.1	1.96	48.89
		GNA @ Bif.	21.33	37.03	2794.44	951212.3		
	Rotter (1986)	LA @ LBA	16.67	28.84	2873.96	451108.6	2.19	54.32
		GNA @ Bif.	21.60	37.50	2789.32	987542.0		
CVS	EN 1991-4 (2007)	LA @ LBA	21.11	36.62	2332.23	638449.2	1.92	47.92
		GNA @ Bif.	26.21	45.64	2242.89	1226002.0		
	Rotter (1986)	LA @ LBA	21.00	36.43	2333.90	628766.6	1.97	49.14
		GNA @ Bif.	26.29	45.77	2241.50	1236201.1		
† $Z_{B(GNA)} / Z_{B(LA)} \equiv \sigma_{max\text{-}(LA)} / \sigma_{max\text{-}(GNA)}$					Average	**2.01**	**50.09**	

The thin circular arc beam is therefore a valid analogy for the silo wall under local eccentric discharge pressures. With geometric nonlinearity, a greater portion of the shell acts like a beam section which leads to a favourable change in its section properties and consequently significantly lower stresses.

3.7 Conclusions

This chapter has presented a detailed comparison of the current EN 1991-4 eccentric discharge pressure model with its more complete precursor, the theory of Rotter (1986). The former is a stripped-down yet more conservative version of the latter, making it marginally simpler in its practical application but resulting in lower silo strength predictions. It has the advantage of conservatism, but possibly the disadvantage of too much of it.

The effect of removing the region of high normal pressures at the edge of the channel for the EN 1991-4 distribution results in slightly higher eccentric discharge load factors. By comparison with the concentric discharge values, these are still extremely low, and it may be concluded that removing the high local wall pressures has a rather small effect.

Comparing the eccentric discharge buckling predictions to each other, it was found that the removal of the high edge pressures in the EN 1991-4 distribution results in significant strength increases in the LBA and GNA load factors for k_c = 0.40 and 0.60. Using the Rotter distribution, strength increases were still found but were much lower. This is because, in the Rotter model, the stationary solid pressure increases with channel size unlike in the EN 1991-4 version where it is always given by the Janssen filling pressure.

An unexpected result of this analysis was that, for the pressure distributions with no high edge pressures, the LBA and GNA load factors for the smallest channel of k_c = 0.25 were the same. This allowed a direct comparison of the two sets of stresses which lead to an important insight into the mechanics of the geometrically nonlinear behaviour in the context of a propped cantilever beam theory analogy.

It was found that, with geometric nonlinearity, a greater circumferential portion of the shell acts as an arc-profile beam which consequently has a higher section modulus to the extreme fibre corresponding to the centre of the flow channel. The subsequent extreme fibre stress reductions are by a factor of approximately 2, and correspond remarkably closely to the finite element predictions.

Chapter 4 – The structural behaviour of silos of different aspect ratio under the EN 1991-4 concentric and eccentric discharge pressures

4.1 Introduction

In Chapter 2 of this thesis, the pressure distribution of the European Standard EN 1991-4 (2007) for a eccentric parallel-side pipe flow was introduced. Its effects on an example structure were explored in what is thought to be the first computational study of its kind, and many revealing observations were made. The model for eccentric discharge pressures in this new standard is a giant step forward in the prescriptive treatment of such a destructive phenomenon, yet the theory behind the pressure distribution has not figured prominently in the silo research literature since its original publication by Rotter (1986).

Given the short length of time that has currently passed since the publication of EN 1991-4, it is currently largely unknown what behaviour can be expected from the application of this new pressure distribution. The behaviour is likely to be highly dependent on the geometry of the silo, the size and position of the flow channel, the material properties of the granular solid and even the type analysis of computational analysis, since the presentation of the full suite of linear and nonlinear computational calculations in EN 1993-1-6 (2007) is an equally recent and state-of-the-art framework for shell analysis.

It is precisely this kind of parametric study that is presented here and in Chapter 5. The study in this chapter explores the effect of varying the silo aspect ratio (H/D), under both concentric and eccentric discharge, using the three different channel sizes specifically recommended by EN 1991-4. Special attention is additionally paid to the results of varying the aspect ratio under concentric discharge, as even this application of EN 1991-4, EN 1993-1-6 and EN 1993-4-1 (2007) is yet to be fully explored.

4.2 Background

The classification of silos in the European Standard on actions on silos and tanks, EN 1991-4, is made on the basis of their aspect ratio (ratio of the height to diameter, H/D). The aspect ratio greatly influences the flow pattern of the granular solid in the silo, with squat silos having significantly different flow regimes from slender ones (Hampe, 1987;

Rotter, 2001a). The effect of the aspect ratio on flow patterns is illustrated succinctly in EN 1991-4 (2007), reproduced here in Fig. 4.1. A varying aspect ratio in turn influences the pressure exerted by both the static and flowing solid on the silo wall, and the behaviour of the silo as a shell structure. The classification criteria according to the silo aspect ratio as defined by EN 1991-4 are given in Table 4.1 below.

Table 4.1 – Summary of slenderness categories according to EN 1991-4 (2007)

Aspect ratio range	Pressure law	Silo category
$H/D \geq 2.0$	Janssen	Slender
$1.0 < H/D < 2.0$	Modified Reimbert	Intermediate slender
$0.4 < H/D \leq 1.0$	Modified Reimbert	Squat
$H/D \leq 0.4$	Hydrostatic	Retaining silo, flat bottom

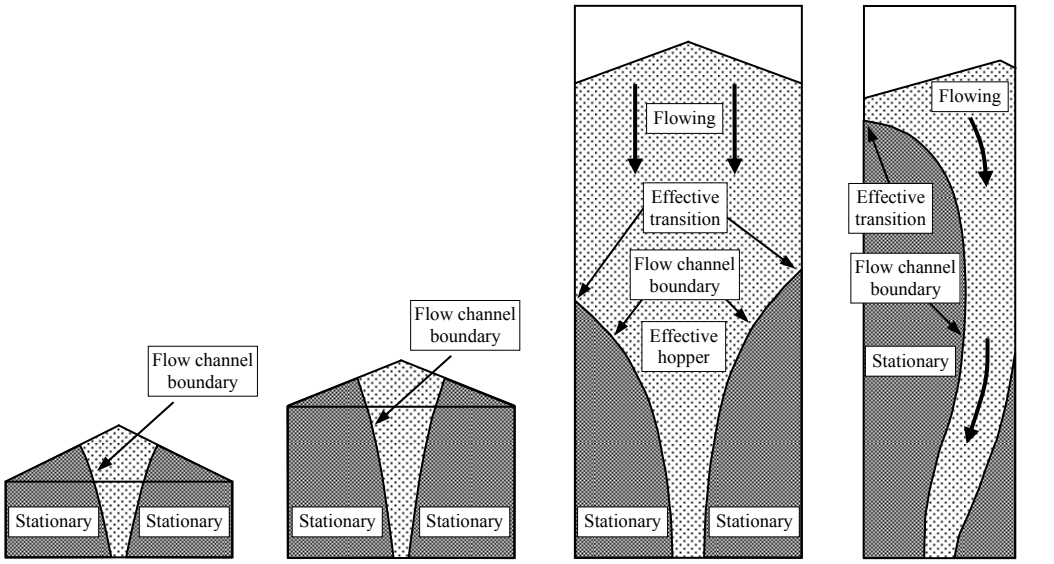

Fig. 4.1 – Aspect ratio effects in mixed and pipe flow patterns, after EN 1991-4 (2007)

The range of aspect ratios chosen in this study is such that the volume and capacity of each silo is approximately equal (whilst maintaining neat dimensions), so that each silo is by itself a plausible alternative design to the same storage requirements. Additionally, since the main objective is to investigate the structural behaviour caused by an eccentric channel of flowing solid, most aspect ratios were kept within a range where such a flow pattern is physically possible. Therefore, although eccentric pipe flow is known to occur in slender silos storing densely packed or slightly cohesive solids (Rotter, 2001a), it is

really no longer credible for squat silos which are more likely to exhibit internal or mixed flow pattern where the channel progressively spreads out from the outlet. The precise shape of flow patterns as a function of the aspect ratio, however, cannot yet be predicted with any certainty.

Where the EN 1991-4 eccentric pipe flow model is imposed on a silo of a lower aspect ratio, the structural behaviour will be shown to be rather different to that of a slender silo. Furthermore, unlike the predicted elastic midheight buckling mode for a slender silo which is known to have been observed in practice (Fig. 2.12), the predicted corresponding buckling modes for squatter silos, shown in this chapter, are not known to have been reported.

The EN 1991-4 pattern also assumes that the parallel-sided flow channel covers the entire height of the silo, which is unlikely to occur in reality because the channel must become smaller as it approaches the outlet and it usually spreads out somewhat near the surface (Rotter, 2001a). Nonetheless, the channel has been defined with parallel sides in EN 1991-4 in the interests of achieving a simple model for design calculations. Though the effects of this error are confined to a small part of the structure in slender silos, in squatter silos this error covers a significant part of the structure and results in quite unrealistic imposed pressure patterns leading to unreliable predictions in finite element studies.

4.3 The design silos

Five steel silos with different aspect ratios were designed for the purposes of the aspect ratio study. The designs were all made to support the symmetrical loads arising from the storage of 510 m^3 of wheat. Structural design was carried out according to EN 1993-1-6 and EN 1993-4-1 using the design pressures from EN 1991-4 under the maximum friction design case, in a manner identical to the design of Silo CVS in Chapter 2. No provision was made for eccentric discharge at the design stage, not even with unsymmetrical patch loads, and no hopper was included. The design of each silo accounted for the effect of internal pressure and this was found in all cases to be in the beneficial range. The design was therefore dominated by the elastic stabilisation factor α_{xpe} (Eq. 1.19).

The new eccentric discharge design rules in EN 1991-4 appear to have been implicitly envisaged with slender silos in mind, since this geometry of silo has suffered many failures due to eccentric discharge (Rotter, 1986; 2001a). However, for want of more accurate information, the standard requires that exactly the same procedure should be applied to intermediate slenderness and squat silos. The lowest aspect ratio considered in this chapter under eccentric discharge was 1.47, in the middle of the 'intermediate slender' category (Table 4.1), requiring a modified version of the Reimbert pressures to be applied. However, even this results in visibly different behaviour to the higher aspect ratio silos, which all used Janssen axisymmetric pressures. A squat silo, with an aspect ratio of 0.65, was also designed but analysed only under concentric discharge.

The results of the present study support the application of the EN 1991-4 eccentric discharge model to slender silos (or, in general, those assuming Janssen pressures in the static zone), but not to intermediate slender and or squat silos. More generally, the EN 1991-4 model has been found to lead to artificial results where modified Reimbert pressures are assumed in the static zone.

The geometries of the designed silos are summarised in Table 4.2. The material properties for cement and wheat were taken from EN 1991-4 Annex E for a Class D2 'Smooth' wall. These are listed in Table 4.3. The parameters of other example silos used elsewhere in the thesis are also listed for comparison.

Table 4.2 – Summary of the parameters of the seven design silos

Silo name (Acronym)	*H* (m)	*D* (m)	*H/D*	Material	Stored Volume (m^3)	Steel Volume (m^3)	Rating† capacity (t)	Loading† capacity (t)	Pressure law
Cement Very Slender (CVS)	26.0	5.0	5.20	Cement	510.5	2.35	676.5	832.6	Janssen
Very Slender (VS)	26.0	5.0	5.20	Wheat	510.5	1.91	390.3	468.4	Janssen
Cement Slender (CS)	18.0	6.0	3.00	Cement	508.9	1.73	674.4	830.1	Janssen
Slender (S)	18.0	6.0	3.00	Wheat	508.9	1.41	389.1	466.9	Janssen
Boundary (B)	14.0	6.8	2.06	Wheat	508.4	1.12	388.7	466.5	Janssen
Intermediate (I)	11.2	7.6	1.47	Wheat	508.1	0.89	388.4	466.1	Modified Reimbert
Squat (Q)	6.5	10.0	0.65	Wheat	510.5	0.32	390.3	468.4	Modified Reimbert

† the lower characteristic value of the unit weight (γ_l) is used for the rating capacity to determine the Action Assessment Class, whilst the respective upper characteristic value (γ_u) is used to calculate the actions (loads) on the silo wall (EN 1991-4, 2007: Annex E)

Table 4.3 – Summary of characteristic values of granular solids properties from EN 1991-4 (2007) Annex E (friction properties are for a D2 'smooth' wall)

Granular solid name	Upper unit weight, γ_u (kN/m^3)	Lower unit weight, γ_l (kN/m^3)	Angle of repose, ϕ_r (degrees)	Upper internal friction angle, ϕ_i (degrees)	Upper lateral pressure ratio, *K*	Upper wall friction coefficient (D2), μ_u	Lower wall friction coefficient (D2), μ_l
Wheat	9	7.5	34	33.6	0.60	0.44	0.33
Cement	16	13	36	36.6	0.65	0.49	0.43

The distribution of wall thicknesses for the silos containing wheat is given in Table 4.4. The required imperfection amplitudes according to EN 1993-1-6 Annex D (characteristic imperfection amplitude for direct design Δw_k) for a 'Normal' Fabrication Tolerance Quality Class are listed in Table 4.5. The imperfection requirements for GMNIA-based design, from Section 8.7.2 of EN 1993-1-6, were not used in the numerical analyses in the present chapter, but are included for comparison in Table 4.6

as they are used elsewhere. A scaled visualisation of the silos is given in Fig. 4.2. The EN 1993-1-6 design procedure is described in detail in Section 1.3.5 of the literature review.

Table 4.4 – Summary of design wall thicknesses

Wall thickness (mm)	Down to a depth below top of silo (m)						
	Silo CVS (H/D = 5.20)	Silo VS (H/D = 5.20)	Silo CS (H/D = 3.00)	Silo S (H/D = 3.00)	Silo B (H/D = 2.06)	Silo I (H/D = 1.47)	Silo Q (H/D = 0.65)
1	*n/a*	*n/a*	*n/a*	*n/a*	*n/a*	*n/a*	3.3
2	*n/a*	*n/a*	*n/a*	*n/a*	*n/a*	*n/a*	6.0
3	6.4	8.8	6.2	8.2	8.0	8.4	6.5
4	8.8	12.4	8.0	11.0	10.4	10.4	*n/a*
5	11.4	16.8	10.2	14.2	13.0	11.2	*n/a*
6	15.0	22.4	12.6	18.0	14.0	*n/a*	*n/a*
7	18.8	26.0	15.4	*n/a*	*n/a*	*n/a*	*n/a*
8	23.6	*n/a*	18.0	*n/a*	*n/a*	*n/a*	*n/a*
9	26.0	*n/a*	*n/a*	*n/a*	*n/a*	*n/a*	*n/a*

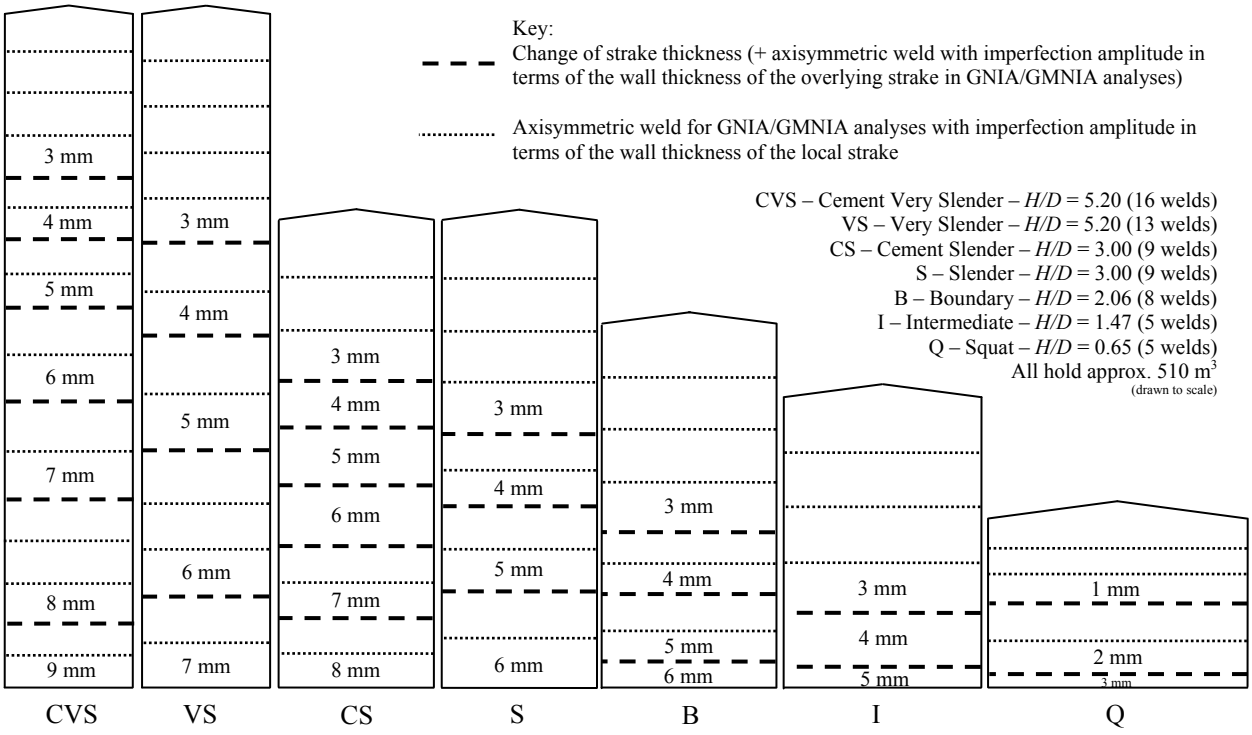

Fig. 4.2 – Schematics of the seven design silos, drawn to scale

In all cases, the silo is constructed from isotropic steel plate with an elastic modulus of 200 GPa, a Poisson's ratio of 0.3 and a yield stress of 250 MPa. A Fabrication Tolerance Quality Class of C ('Normal') was adopted, requiring a thicker wall and deeper imperfections.

The squat Silo Q is different in that it alone was designed with a wall thickness of 1 mm for over half of its height, which is at the very limit of what may be practicably possible to construct. Nonetheless, this is the theoretical thickness which satisfies the required design rules, and it was adopted for the purposes of this study. A silo of such squat proportions falls outside the range of aspect ratios in which an eccentric pipe flow channel of the type being studied here is likely to develop, and it was only investigated under the axisymmetric loads occurring during concentric discharge.

Table 4.5 – Summary of the imperfection amplitudes to be adopted in design, according to EN 1993-1-6 (2007) Annex D for direct design

Wall thickness (mm)	Units of wall local thickness						
	Silo CVS (H/D = 5.20)	Silo VS (H/D = 5.20)	Silo CS (H/D = 3.00)	Silo S (H/D = 3.00)	Silo B (H/D = 2.06)	Silo I (H/D = 1.47)	Silo Q (H/D = 0.65)
1	*n/a*	*n/a*	*n/a*	*n/a*	*n/a*	*n/a*	4.419
2	*n/a*	*n/a*	*n/a*	*n/a*	*n/a*	*n/a*	3.125
3	1.804	1.804	1.976	1.976	2.104	2.224	2.552
4	1.563	1.563	1.712	1.712	1.822	1.926	*n/a*
5	1.398	1.398	1.531	1.531	1.630	1.723	*n/a*
6	1.276	1.276	1.398	1.398	1.488	*n/a*	*n/a*
7	1.181	1.181	1.294	*n/a*	*n/a*	*n/a*	*n/a*
8	1.105	*n/a*	1.210	*n/a*	*n/a*	*n/a*	*n/a*
9	1.042	*n/a*	*n/a*	*n/a*	*n/a*	*n/a*	*n/a*

Table 4.6 – Summary of the imperfection amplitudes to be adopted in design, according to te EN 1993-1-6 Section 8.7.2 for GMNIA-based design

Wall thickness (mm)	Units of wall local thickness						
	Silo CVS (*H*/*D* = 5.20)	Silo VS (*H*/*D* = 5.20)	Silo CS (*H*/*D* = 3.00)	Silo S (*H*/*D* = 3.00)	Silo B (*H*/*D* = 2.06)	Silo I (*H*/*D* = 1.47)	Silo Q (*H*/*D* = 0.65)
1	*n/a*	*n/a*	*n/a*	*n/a*	*n/a*	*n/a*	7.071
2	*n/a*	*n/a*	*n/a*	*n/a*	*n/a*	*n/a*	5.000
3	2.887	2.889	3.162	3.162	3.367	3.559	4.083
4	2.500	2.500	2.739	2.739	2.912	3.082	*n/a*
5	2.236	2.236	2.450	2.450	2.608	2.757	*n/a*
6	2.041	2.041	2.236	2.236	2.381	*n/a*	*n/a*
7	1.890	1.890	2.070	*n/a*	*n/a*	*n/a*	*n/a*
8	1.768	*n/a*	1.937	*n/a*	*n/a*	*n/a*	*n/a*
9	1.667	*n/a*	*n/a*	*n/a*	*n/a*	*n/a*	*n/a*

The imperfection amplitudes defined in EN 1993-1-6 Section 8.7.2 for GMNIA analyses (Table 4.6) are always greater than the hand design values (Table 4.5). In both cases, the standard relates the imperfection amplitudes to tolerance requirements (Fabrication Tolerance Quality Class) to which the silos are expected to be constructed. A silo constructed to stricter tolerances is rewarded with lower imperfection amplitudes and hence, in theory, higher buckling loads. Section 1.3.5 of the literautre review presents the background to this in greater detail.

It will be shown in this chapter that, for the case of the axisymmetric weld depression (Type A from Rotter and Teng, 1989a) under eccentric discharge, neither of the imperfection amplitudes for direct or GMNIA-based design leads to a safe assessment of the silo strength. Though axisymmetric weld depressions are known to be very deleterious under axisymmetric conditions, especially under axial compression (studied by very many authors, including Rotter and Zhang, 1990; Teng and Rotter, 1992; Knödel *et al.*, 1995; 1996; Knödel & Ummenhofer, 1996; Ummenhofer & Knödel, 1996; Rotter, 1996), they cannot be relied upon to give conservative strength estimates with eccentric discharge since they result in significant strength gains due to the nature of the structural response. This is discussed later in this chapter. A different, yet still

practically credible, structural imperfection form was conceived for the condition of eccentric discharge and is presented in Chapter 6.

Two designs were produced for each silo, one with a uniform wall thickness and the other with a more practical stepwise varying wall thickness, though only the latter was investigated in the study presented in this chapter. For each silo, the walls are just thick enough at the base of each strake to meet the requirements of the standard with respect to buckling, regardless of practical steel sheet sizes. The changes of plate thickness consequently become the critical locations for buckling, under axisymmetric conditions at least. Plots of the axial distributions of the design axial membrane stress resultants and design resistances for each silo are presented in Fig. 4.3. The design required thicknesses to resist bursting and buckling, together with the chosen plate thicknesses, are shown in Fig. 4.4. The EN 1991-4 discharge factors for normal pressures and frictional tractions, C_h and C_w, were taken as 1.15 and 1.1 respectively and were applied to every silo design, including Silo Q for consistency (EN 1991-4 does not require discharge factors for squat silos).

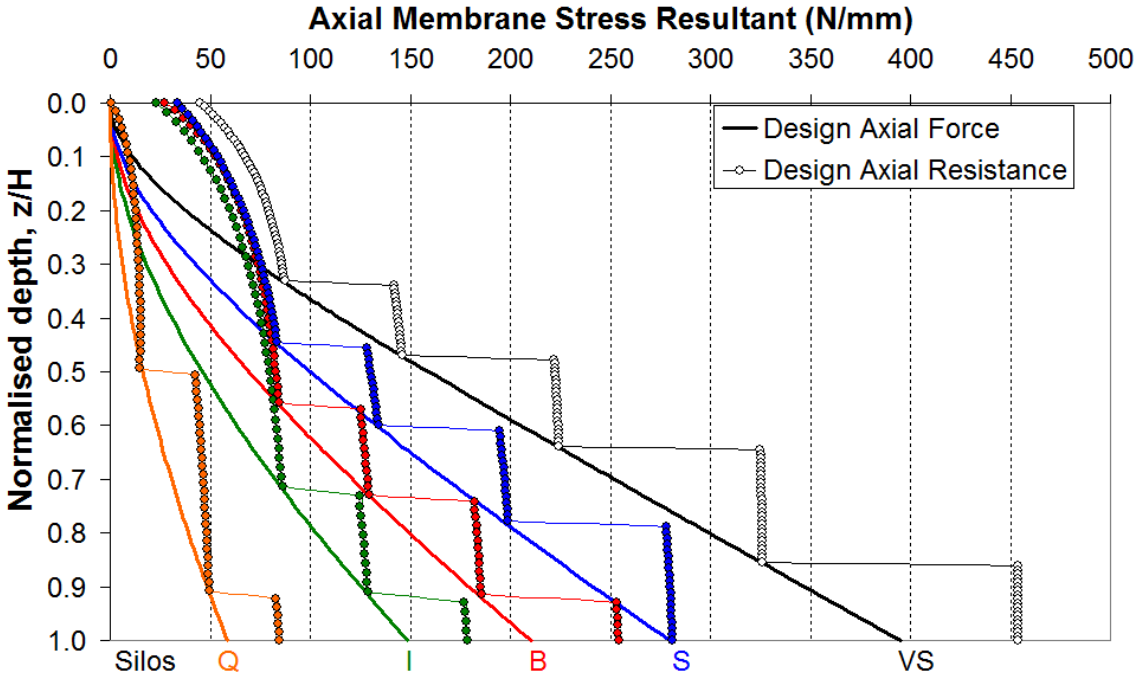

Fig. 4.3 – Axial distribution of the design axial membrane stress resultants for the five designed silos holding wheat

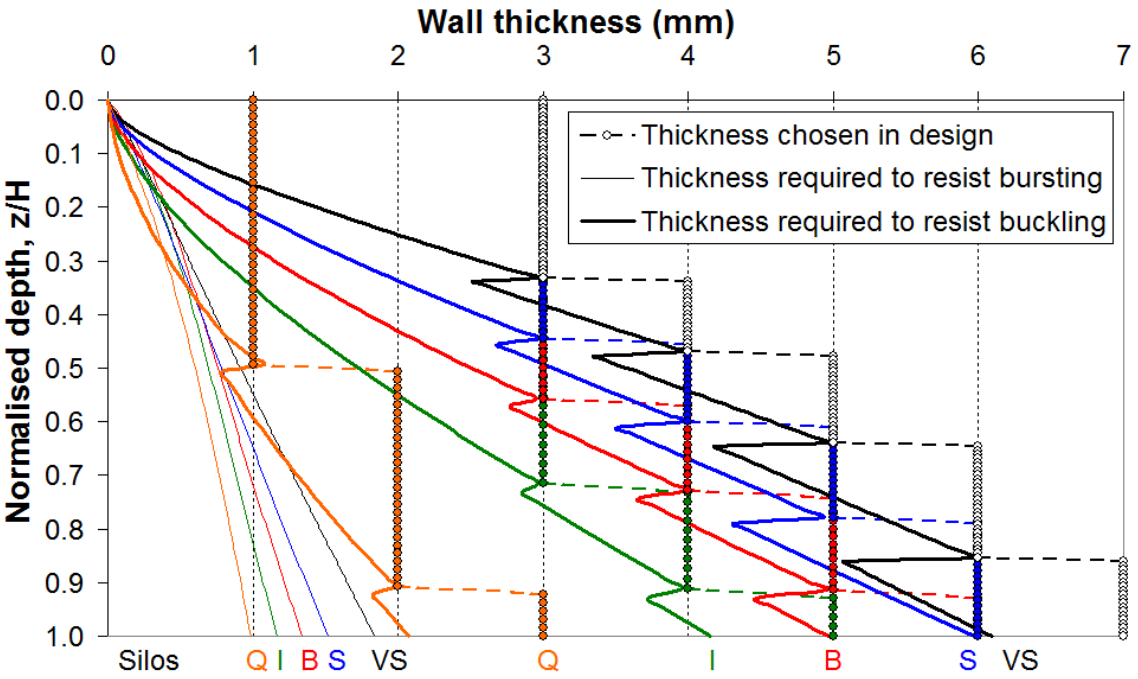

Fig. 4.4 – Axial distribution of required design thicknesses to resist bursting and buckling for the five designed silos holding wheat

The maximum axial membrane stress, occurring at the base of the silo, increases approximately linearly with the aspect ratio when the silos are linked by a common storage volume (Fig. 4.5a). The volume of steel required for each silo cylinder is shown as a function of the aspect ratio (Fig. 4.5b) also exhibits a roughly linear relationship.

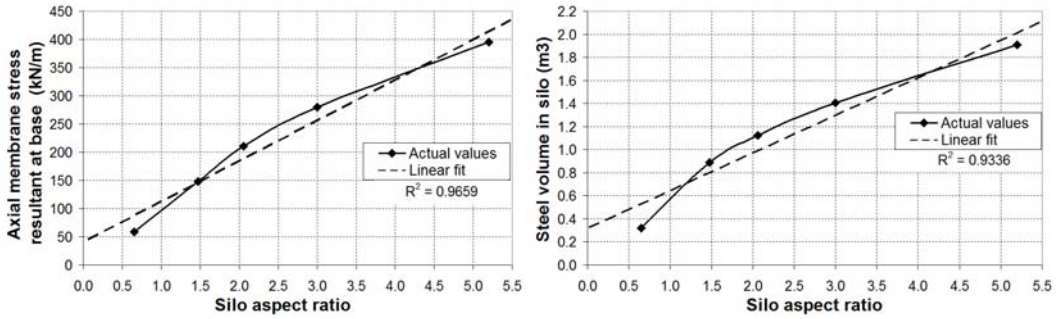

a) Max. axial membrane stress resultant at the base of the silo

b) Required steel volume

Fig. 4.5 – Variation of the key parameters of the design with the silo aspect ratio

It will be shown that roughly all the silos except for Silo Q have a significant reserve of strength beyond the overall partial safety factor for hand-design of 1.65 required by EN 1993-4-1 (2007) for concentric discharge. The computed GMNIA load factors are also very close to each other, suggesting that Silos VS, S, B and I are essentially equally

strong regardless of the different volumes of steel required. Since all of these are nonetheless valid designs for the same storage requirements, it would be up to a potential client to decide on the amount he would wish to spend on such a structure in terms of steel volume, taking into account other factors including the footprint required.

4.4 The EN 1991-4 eccentric discharge pressure regime

The European Standard EN 1991-4 on actions on silos and tanks requires that the eccentric discharge pressures are characterised by the following for silos in Action Assessment Classes 2 and 3 where loading and discharge eccentricities greater than 0.25D are expected to occur. The geometry of the model is reproduced in Fig. 4.6. The values of each of the geometric parameters, based on the geometry of the four relevant design silos (VS, S, I and B) and the properties of wheat as given in EN 1991-4, are summarised in Table 4.7. The Standard explicitly requires three flow channel sizes to be investigated, defined by the ratio of the flow channel radius to the silo radius, $k_c = r_c/R$. The sizes that are recommended are 0.25, 0.40 and 0.60, shown to scale on Fig. 4.7 for Silo S.

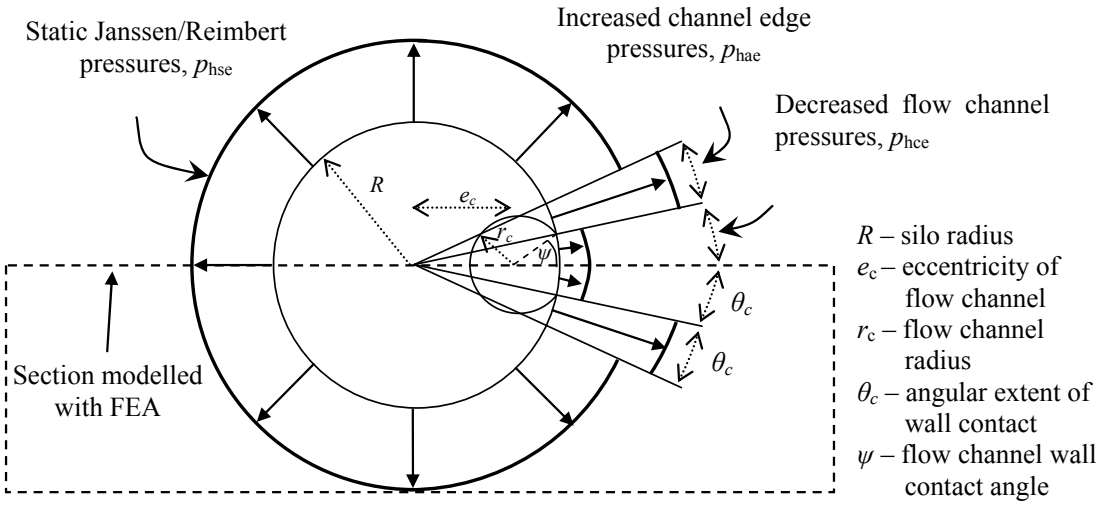

Fig. 4.6 – Notation and geometry of the eccentric flow channel wall pressures, after EN 1991-4 (2007)

Table 4.7 – Summary of flow channel properties for all silos holding wheat

$k_c = r_c / R$	0.25	0.40	0.60
θ_c (º)	10.28	17.40	28.73
ψ (º)	45.53	48.36	53.25
e_c / R	0.808	0.688	0.517
A_c / A_{tot} (%)	0.058	0.148	0.334

The flow channel contact angle θ_c (Eq. 4.1) and the area ratio A_c/A_{tot} (Eq. 4.3) are independent of the aspect ratio of the silo. The angle subtended at the flow channel centre by the last contact between the flowing solid and the wall ψ (Fig. 4.7 and Eq. 4.2) is depends on the eccentricity of the channel, which in turn is governed by the friction properties of the solid and the silo wall (Eq. 4.4). The angle ψ approaches 90º when the wall is very smooth (Rotter, 1986).

$$\theta_c = \cos^{-1}\left(\frac{R^2 + e_c^2 - r_c^2}{2Re_c}\right) \tag{4.1}$$

$$\psi = \sin^{-1}\left(\frac{R}{r_c}\sin\theta_c\right) \tag{4.2}$$

$$A_c = (\pi - \psi)r_c^2 + \theta_c R^2 - r_c R\sin(\psi - \theta_c) \tag{4.3}$$

$$e_c = R\left\{\frac{\mu_{lower}}{\tan\phi_{i,upper}}\left(1 - \frac{r_c}{R}\right) + \left(1 - \frac{\mu_{lower}}{\tan\phi_{i,upper}}\right)\sqrt{1 - \frac{r_c}{R}}\right\} \tag{4.4}$$

The origin of the above equations and a comparison between the EN 1991-4 eccentric discharge model and its more complete predecessor (Rotter, 1986) are described in Chapter 3.

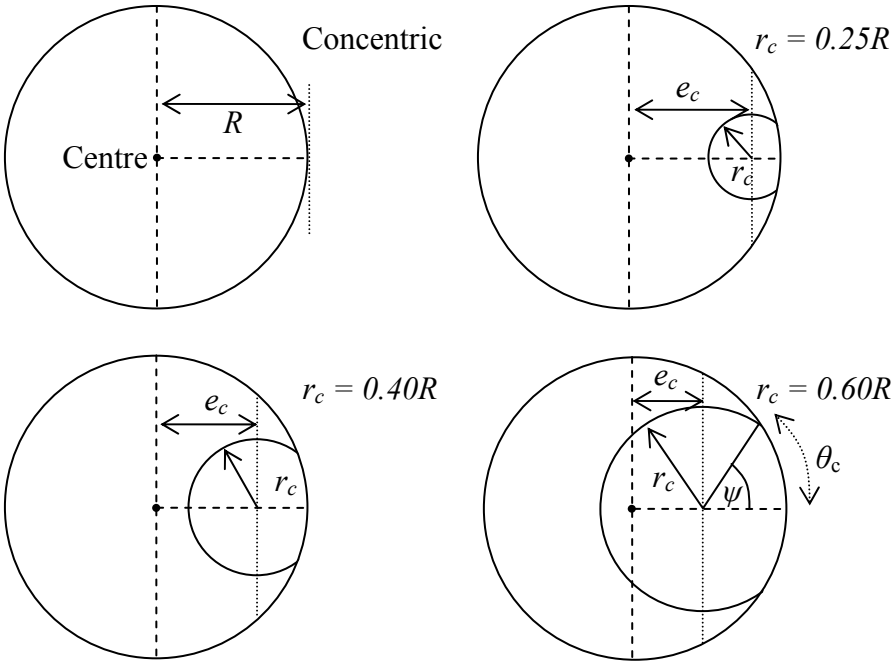

Fig. 4.7 – Comparison of the geometry of the four different discharge conditions that are required by EN 1991-4 to be applied to each design silo, drawn to scale for Silo S

4.5 The numerical model

The numerical procedure used to analyse the silos under the four discharge conditions was the same as that used in Chapter 2. The full suite of computational shell buckling calculations was performed according to EN 1993-1-6 (LA, LBA, MNA, GNA, GMNA, GNIA & GMNIA). Each calculation was performed on each silo at each discharge condition, resulting in a total of 102 different predictions. Many of the nonlinear analyses had to be repeated several times to achieve satisfactory convergence or behaviour. Nine-node reduced-integration S9R5 shell elements were used, with an average model employing between 20,000 and 40,000 elements.

4.6 Global overview of the results of the FEA study

A set of acronyms has been devised summarising the main characteristics of the possible linear bifurcation, incremental buckling or plastic collapse modes. These are presented in Table 4.8 and will be used throughout the rest of the thesis to describe the predicted failure mode in shorthand, since many of the same failure modes will appear repeatedly. The complete summary of load proportionality factors for each discharge condition for each silo, with accompanying failure mode acronyms, is presented in Tables 4.9 to 4.13.

Table 4.8 – Description of short-hand acronyms to describe failure mode types

Acronym	Description
Axi-EF	Axisymmetric plastic elephant's foot buckling or yielding.
Axi-DD	Diamond pattern of deformation around the entire circumference, limited to being within a close distance of a wall strake or other boundary.
Axi-EL	Fully or partially axisymmetric elastic buckle.
Glb-EF	Global deformations, but with the main component of plastic elephant's foot-type buckling or yielding.
Glb-DD	Global diamond buckling mode
Glb-PL	Global plastic circumferential bending mode (the MNA mode).
Loc-CH	The characteristic or 'classic' mode associated with an eccentrically flowing channel: a local (predominantly) elastic buckle in the centre of the flow channel, at approximately midheight.
Loc-EG	This is also associated with this form of eccentric discharge, but seen more in squatter or uniform wall thickness silos as it requires a different location to be critical. A localised elastic or plastic buckle at the edge of the flow channel near the base of the silo.
Loc-2	This is a rare buckling mode usually found for squatter silos which contains features of both critical locations under eccentric discharge. It may be either elastic or elastic-plastic.

When referring to a specific result, a notation style is used in this chapter. For example; VS00LBA refers to Silo VS with k_c = 0.00 (concentric flow) and the LBA result. Similarly, VS00 by itself refers to the suite of results for Silo VS with k_c = 0.00, while VSLBA refers to all LBA results for Silo VS for all channel sizes. Additionally, for the purposes of conciseness, the general term 'failure mode' will be taken to encompass all the possible failure modes, including the linear bifurcation LBA mode, the plastic collapse MNA mode and the nonlinear incremental buckling modes of GNA and others like it.

The elastic Loc-CH mode is highlighted in bold in Tables 4.9 to 4.13. It indicates the mode that has been widely observed in the field where eccentric discharge is the cause of buckling failures (e.g. Fig. 2.12). It is thus considered to be the *desirable* outcome of an analysis in the sense that the employed pressure pattern, combined with the

imperfection form (or lack thereof), is suitable at this aspect ratio and channel size to reproduce the typically observed behaviour associated with eccentric pipe flow. This may be seen to be generally case for slender silos, but it is much less common in squatter silos.

Failure modes other than Loc-CH are *also* successful numerical analyses, but conceptually they have not captured the behaviour seen in practice, and this lack of success is really due to the inadequacy of the pressure model for the given aspect ratio. For example, Fig. 4.8 shows two modes that were counted as Loc-CH (S25LBA and S60GNIA, elastic midheight buckles), but Fig. 4.9 shows two which were not. In Fig. 4.9, the failure mode for B25GMNIA is a localised, fully plastic buckle which actually occurs at the base of the thinnest 3 mm strake at the centre of the flow channel rather than at midheight: it was therefore counted as mode Glb-EF. The failure mode for I60GMNIA includes features of both critical locations under eccentric pipe flow (i.e. silo base near the edge of the channel, Fig. 2.10, and silo midheight across the channel, Fig. 2.12), and was counted as mode Loc-2.

The mode named Loc-2 is an interesting discovery, because it seems that both buckling locations associated with eccentric discharge have become critical at the same load factor. It may be the case that stable plastic deformations developed in one of the two critical locations, but an elastic bifurcation occurred in the other. This mode has only been observed in one analysis so far for the intermediate slender Silo I at the largest flow channel, $k_c = 0.60$.

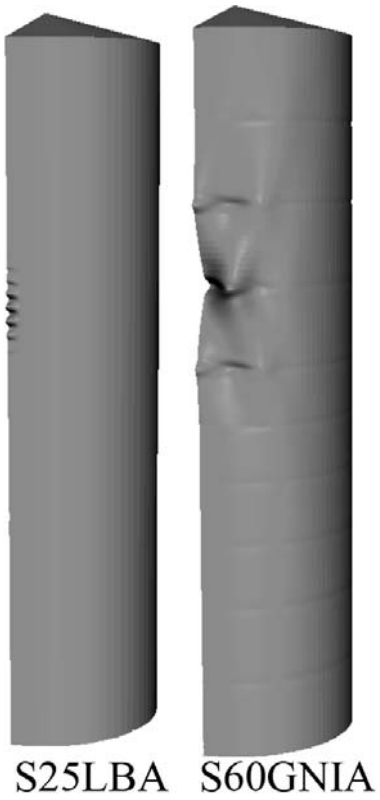

Fig. 4.8 – Examples of failure modes counted as Loc-CH

Fig. 4.9 – Examples of failure modes *not* counted as Loc-CH (left: Glb-EF and right: Loc-2)

Table 4.9 – Summary of predicted load factors and failure modes for Silo VS

	Silo VS load factors				Silo VS behaviour acronyms			
k_c	0.00	0.25	0.40	0.60	0.00	0.25	0.40	0.60
LBA	9.07	0.72	0.33	0.28	Axi-EL	**Loc-CH**	**Loc-CH**	**Loc-CH**
MNA	6.43	0.86	0.75	0.80	Axi-EF	Glb-PL	Glb-PL	Glb-PL
GNA	8.90	3.64	0.81	0.39	Axi-DD	**Loc-CH**	**Loc-CH**	**Loc-CH**
GMNA	5.11	2.82	0.81	0.39	Glb-EF	**Loc-CH**	**Loc-CH**	**Loc-CH**
GNIA	4.40	3.91	3.76	0.24*	Glb-DD	Glb-DD	Glb-DD	**Loc-CH**
GMNIA	3.77	3.57	2.85	0.22*	Glb-DD	Glb-DD	Glb-DD	**Loc-CH**

Table 4.10 – Summary of predicted load factors and failure modes for Silo S

	Silo S load factors				Silo S behaviour acronyms			
k_c	0.00	0.25	0.40	0.60	0.00	0.25	0.40	0.60
LBA	7.85	0.46	0.25	0.42	Axi-EL	**Loc-CH**	**Loc-CH**	**Loc-CH**
MNA	6.89	0.83	0.74	1.13	Axi-EF	Glb-PL	Glb-PL	Glb-PL
GNA	7.77	4.11	0.37	0.66	Axi-DD	**Loc-CH**	**Loc-CH**	**Loc-CH**
GMNA	4.91	3.37	0.37	0.66	Axi-EF	**Loc-CH**	**Loc-CH**	**Loc-CH**
GNIA	5.62	5.01	4.28	0.29*	Glb-DD	Glb-DD	**Loc-CH**	**Loc-CH**
GMNIA	3.99	3.52	2.28	0.29*	Glb-EF	Glb-DD	Glb-EF	**Loc-CH**

Table 4.11 – Summary of predicted load factors and failure modes for Silo B

	Silo B load factors				Silo B behaviour acronyms			
k_c	0.00	0.25	0.40	0.60	0.00	0.25	0.40	0.60
LBA	6.97	0.34	0.28	0.77	Axi-EL	**Loc-CH**	**Loc-CH**	Loc-EG
MNA	6.64	0.74	0.87	1.63	Axi-EF	Glb-PL	Glb-PL	Glb-PL
GNA	6.93	0.67	0.38	1.25	Axi-EL	**Loc-CH**	**Loc-CH**	**Loc-CH**
GMNA	5.55	0.67	0.38	1.25	Axi-EF	**Loc-CH**	**Loc-CH**	**Loc-CH**
GNIA	4.55	4.39	3.85	0.57	Glb-DD	Glb-DD	**Loc-CH**	**Loc-CH**
GMNIA	3.75	3.46	1.56	0.57	Glb-EF	Glb-EF	Glb-EF	**Loc-CH**

Table 4.12 – Summary of predicted load factors and failure modes for Silo I

	Silo I load factors				Silo I behaviour acronyms			
k_c	0.00	0.25	0.40	0.60	0.00	0.25	0.40	0.60
LBA	5.55	0.32	0.40	0.80	Axi-EL	**Loc-CH**	**Loc-CH**	Loc-EG
MNA	5.65	0.85	1.16	2.05	Axi-EF	Glb-PL	Glb-PL	Glb-PL
GNA	5.55	0.63	0.70	1.92*	Axi-EL	**Loc-CH**	**Loc-CH**	Loc-EG
GMNA	4.70	0.63	0.70	1.58	Axi-EF	**Loc-CH**	**Loc-CH**	Loc-EG
GNIA	4.57	4.37	2.06*	1.56	Axi-DD	Loc-EG	Loc-EG	**Loc-CH**
GMNIA	3.09	2.77	1.22*	1.34	Axi-EF	Glb-EF	Loc-EG	Loc-2

Table 4.13 – Summary of predicted load factors and failure modes for Silo Q

	Silo Q load factors	Silo Q behaviour acronyms
k_c	0.00	0.00
LBA	1.79	Axi-EL
MNA	2.48	Axi-EF
GNA	1.76	Axi-EL
GMNA	1.60	Axi-EF
GNIA	1.58	Axi-EL
GMNIA	1.28	Axi-EF

The load factors marked with an asterisk (*) indicate a kink in the load-axial displacement curve, followed by geometric hardening. No negative eigenvalues are reported and there is no reversal of the load path. This occurs when a high value of the imperfection amplitude eliminates the bifurcation point (Yamaki, 1984). An example of such behaviour is given in Fig. 4.10 below for the VS60 suite. A similar example may be found for Silo CVS in Fig. 2.14. In all figures showing load-axial displacement curves, the node whose axial displacement is being followed is located at the top of the silo at the centre of the flow channel. If there is no flow channel, as is naturally the case for concentric discharge, the exact position of the node at the top of the silo is not important.

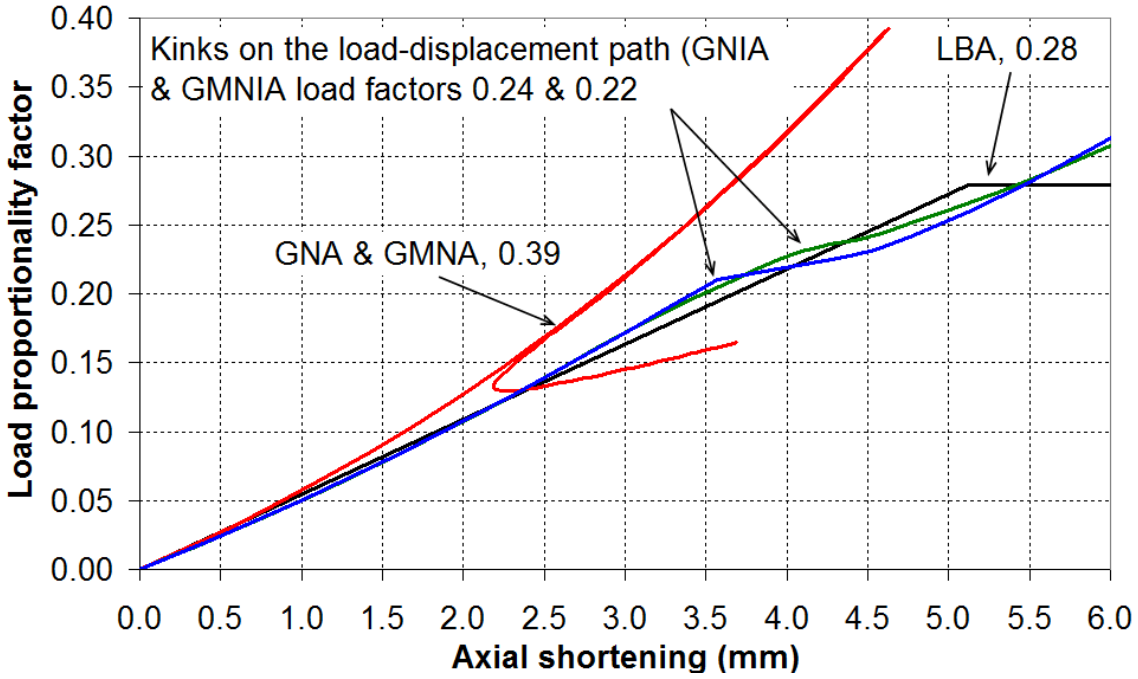

Fig. 4.10 – Load-axial deflection curves for the VS60 suite of analyses, also typical of other slender silos under eccentric discharge

4.7 Detailed analysis – Axisymmetric concentric discharge

In the analyses of Silos VS, S, B and I under concentric discharge, the lowest GMNIA load factors were all found to be consistently above 3, which is approximately double the EN 1993-4-1 partial safety factor for hand design of 1.65. This was first noticed and justified in the preliminary investigation of Chapter 2, but here it is consistent over a wider range of aspect ratios for both elastic stability and plastic collapse failure modes, thus generally reinforcing the conservatism of the hand design process for axisymmetric loads.

Silo Q is an exception due to its very thin wall over much of its height. Even so, the final GMNIA value of 1.28 falls troublingly below the strength assessment of 1.65 guaranteed by EN 1993-1-6 and EN 1993-4-1 (which is however achieved up to and including the GMNA analysis). Silo Q is anomalous since it is actually very small for its aspect ratio with a volume of only 510 m^3, imposed on it by the desire to have all design silos linked by the same capacity (Table 4.2). Silos are usually designed to be squat when they are required to be very large (Rotter, 2001a), and as such would have wall thickness values far above 1 mm. Thus the reduction of the GMNIA load factor below the 1.65 partial safety factor may be explained by the fact that the relative change in wall thickness from 1 to 2 mm is a massive 100%, making the base of the 1 mm

strake act like a base boundary condition (critical for elephant's foot modes), exacerbated by the presence of a deep weld imperfection (amplitude of 4.419*t*, Table 4.5).

In all of the present analyses of concentric discharge, the LBA and GNA predictions are very close, suggesting the silo behaviour has a high degree of geometric linearity. As the aspect ratio decreases, the MNA and LBA/GNA load factors become closer to each other, eventually intersecting at around H/D = 1.5 (Fig. 4.11). The computational analyses thus exclusively predict bursting modes at lower aspect ratios, which is to be expected according to EN 1993-1-6 and EN 1993-4-1 because axial forces become smaller and wall pressures become higher at lower aspect ratios.

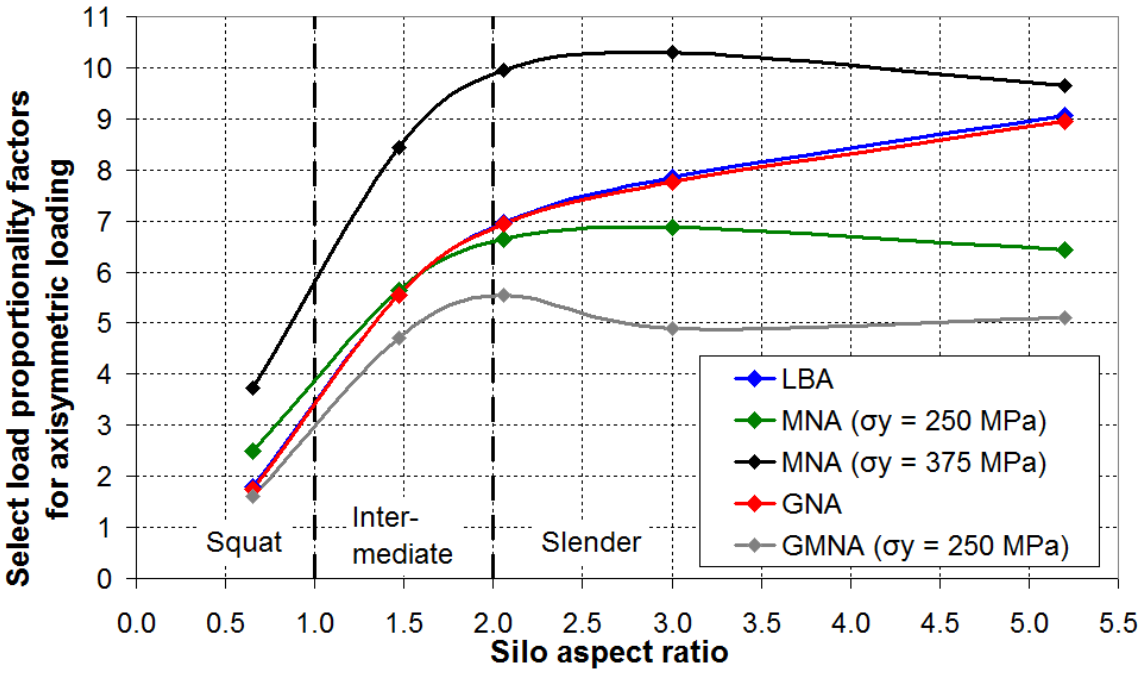

Fig. 4.11 – Plot of the LBA, MNA, GNA and GMNA load factors for concentric discharge as a function of the silo aspect ratio

It is important for the shell analyst to ascertain whether the failure mode will indeed be elastic or plastic, as this will influence the decision on whether to spend money on a higher steel grade with a higher yield stress. It can be seen on Fig. 4.11 that slender silos under concentric discharge will exhibit plastic buckles as the MNA curve for σ_y = 250 MPa is usually the lowest. It may therefore be worthwhile investing in a stronger grade of steel, which would place the MNA curve (σ_y = 375) above those of LBA or GNA.

However, for aspect ratios below H/D = 1.5, the LBA and GNA curves are the lowest, and increasing the steel grade to σ_y = 375 MPa may serve no purpose.

The bar charts in Fig. 4.12 show the load factors normalised by the LBA value, and show a gradual reduction in strength with the inclusion of material plasticity and imperfections. These reductions are clearly greatest for the slender silos.

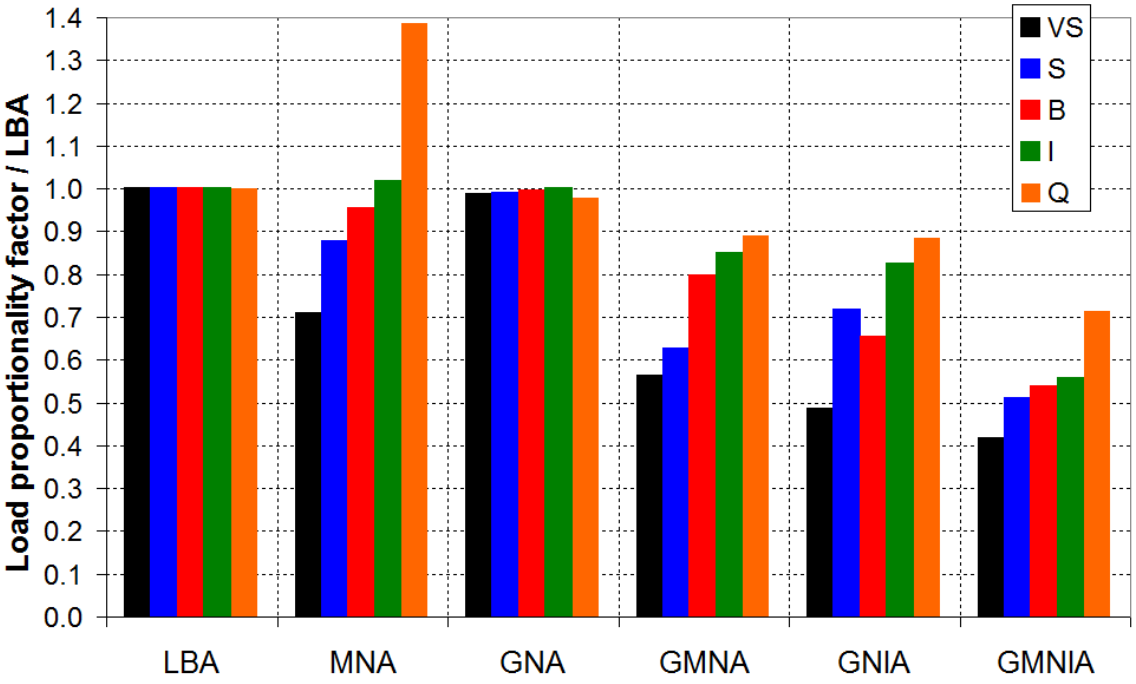

Fig. 4.12 – Bar chart of the concentric discharge load factors normalised with the respective LBA factor

The buckling modes for concentric loading for the intermediate and very slender Silos I and VS, close to either extreme of the aspect ratio range, are shown in Fig. 4.13 and Fig. 4.14 respectively. As mentioned previously, the squatter silo exhibits a consistent axisymmetric elephant's foot type mode at the same location if the analysis includes material plasticity, and a similarly-shaped bursting mode if the analysis is elastic. This reflects the fact that the LBA, MNA and GNA load factors are essentially the same for Silo I (Table 4.12). The most likely critical location for squatter silos under concentric discharge therefore appears to be the base of the thinnest strake due to the largest ratio of adjacent wall strake thicknesses, and the very squat Silo Q exhibits a very similar behaviour.

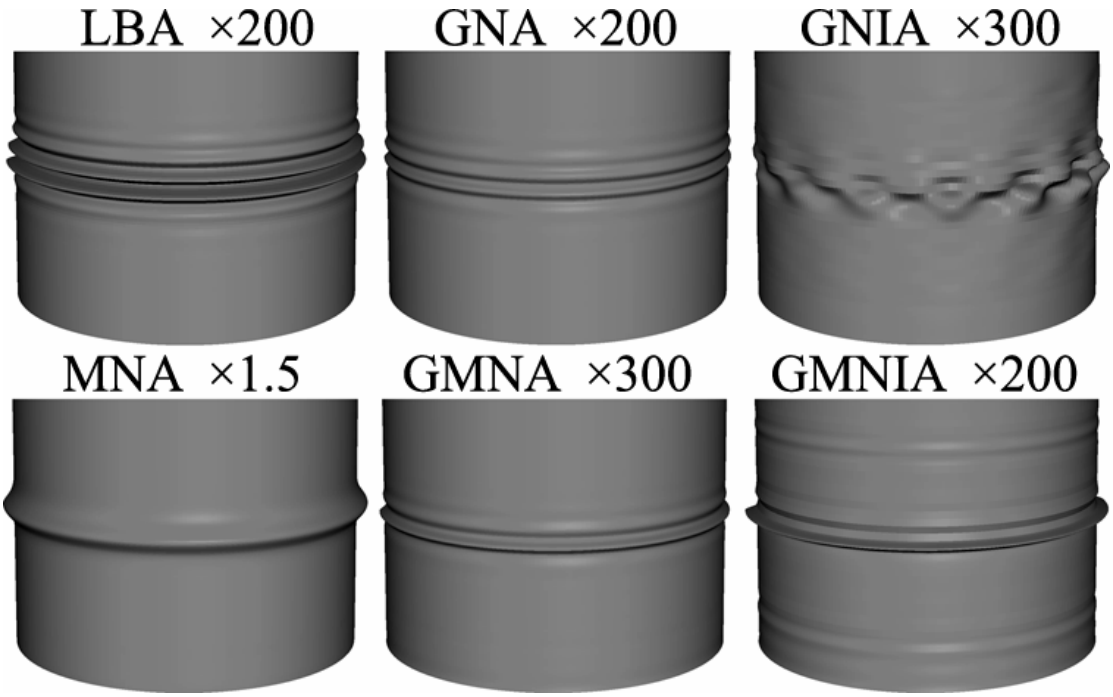

Fig. 4.13 – Failure modes for the I00 suite of analyses

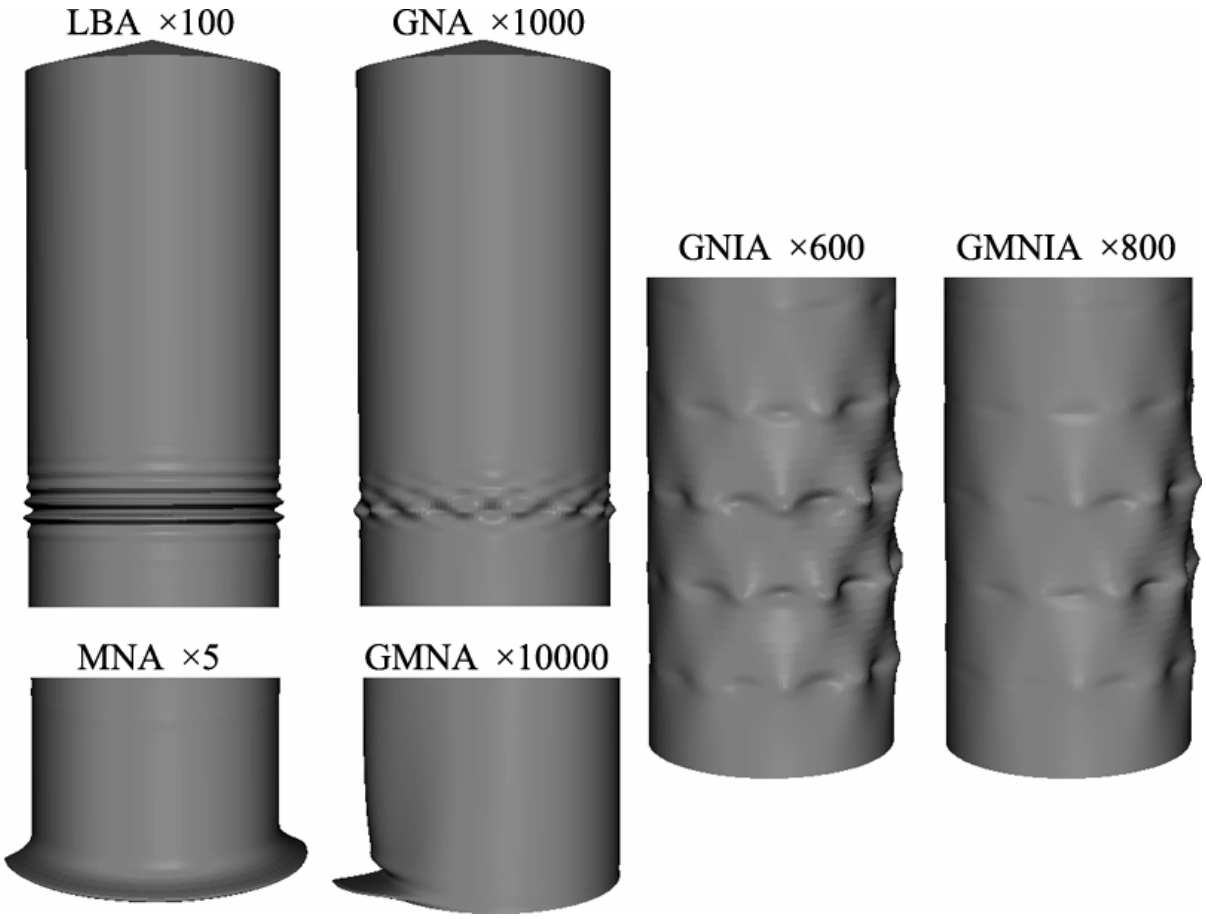

Fig. 4.14 – Failure modes for the VS00 suite of analyses

Silo VS exhibits similar behaviour under concentric discharge to that of Silo CVS presented in Chapter 2 (compare Fig. 4.14 and Fig. 2.7). The load factors for the LBA and GNA, the MNA and GMNA and the GNIA and GMNIA analyses for these two silos are very similar, and each of these pairs of analyses also have very similar bifurcation modes. The critical locations are the base of the silo for the plastic analyses and the bottom of the 3 mm strake for the elastic analyses, both for the perfect structure. The imperfect versions of Silos VS and CVS buckle in an elastic global diamond mode Glb-DD. Silo S was found to exhibit very similar behaviour.

The load-axial deflection curves for VS00 are shown in Fig. 4.15. These curves are quite typical of shells under axisymmetric loads exhibiting high imperfection sensitivity (Yamaki, 1984). The load-deflection curves are very similar for all five silos under concentric discharge, and the same general observations may be made. The axisymmetric weld imperfection consistently leads to a loss of axial stiffness and a significantly reduced buckling strength.

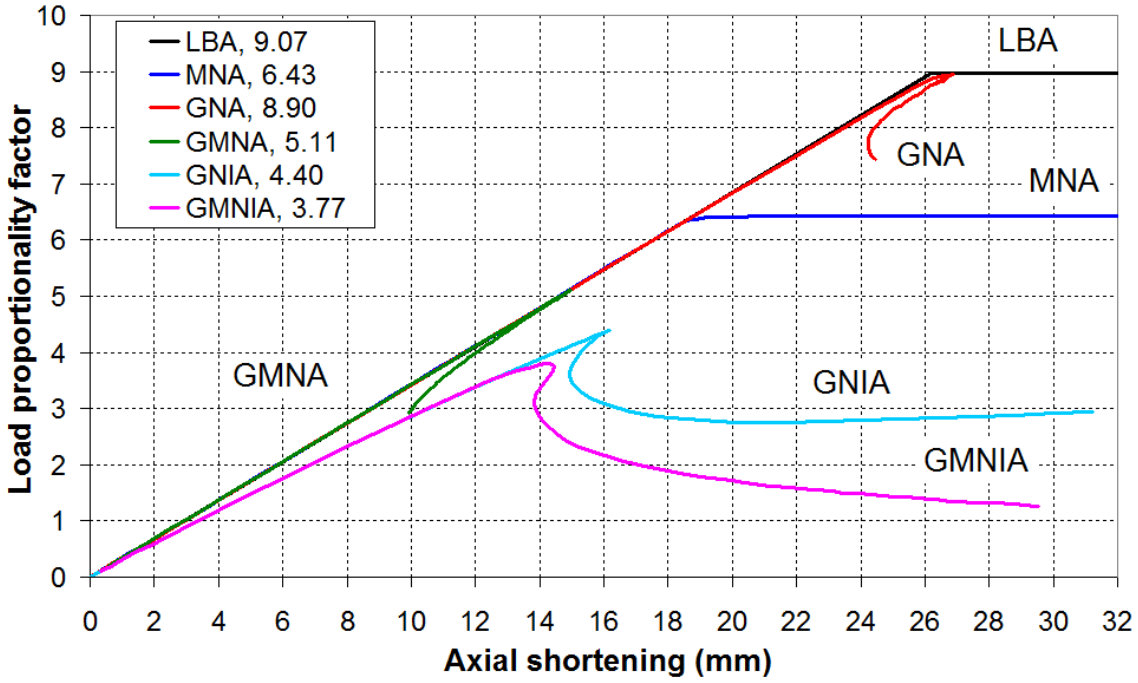

Fig. 4.15 – Load-axial deflection curves for the VS00 suite of analyses, typical of shells under axisymmetric loads

A schematic showing the complete set of buckling mode locations for each silo under concentric loads is shown in Fig. 4.16. It is difficult to predict exactly which one of the changes of thickness in any given silo will be most critical in any given computational

analysis. However, since the silos were designed according to the EN 1993-1-6 and EN 1993-4-1 hand design procedure to make each strake equally critical, the scattered set of failure modes is entirely to be expected and supports the hand design rules as giving a relatively uniform safety factor throughout. The failure modes identified here are, of course, simply those that occur at the lowest load factor, and no indication is available of their proximity to failure at another location. Consequently, it is not possible to read too much into the calculated failure locations.

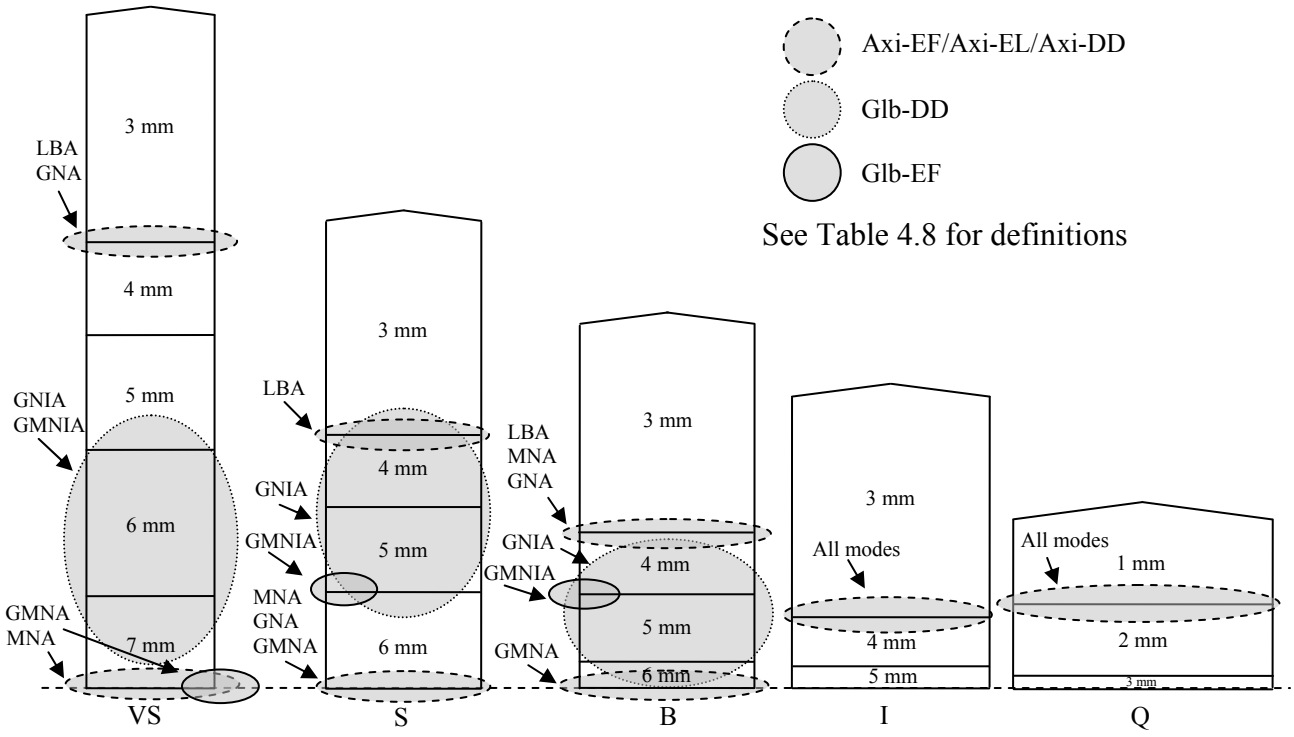

Fig. 4.16 – Schematics of failure mode locations for concentric discharge (to scale)

4.8 Detailed analysis – Unsymmetrical eccentric discharge

4.8.1 Overview

The results of the eccentric discharge computations are very complex and by way of introduction, Fig. 4.17 shows the variation with aspect ratio of the number of modes Loc-CH and Loc-EG obtained per suite of EN 1993-1-6 computations. These two modes refer to failure in the two critical regions of the silo which exhibit the highest compressive stresses under this pressure pattern of eccentric discharge. In Chapter 2, it was shown that the critical regions are the centre of the channel at approximately midheight (Loc-CH, Fig. 2.12), and the edge of the channel at the base of the silo (Loc-EG, Fig. 2.10).

It was found that out of a total of 18 computations for each silo that used eccentric discharge, on average 11 reproduced mode Loc-CH when the silo was still slender. For those that did not, this was caused for reasons other than the features of the pressure model (e.g. it was an MNA mode which captured the circumferential bending plastic collapse mechanism, or the chosen form of geometric imperfection was found to have a beneficial effect). Mode Loc-EG was not found in any analysis of a slender silo. Conversely, when the silo was of intermediate slenderness, much squatter and using modified Reimbert pressures in the static zone, the number of modes Loc-EG rose immediately, replacing most of the modes Loc-CH. Thus the elastic midheight buckle, which is the failure mode most strongly associated in field observations with this discharge condition, was only found in slender silos. The distribution of EN 1991-4 in its current form should perhaps be limited to these.

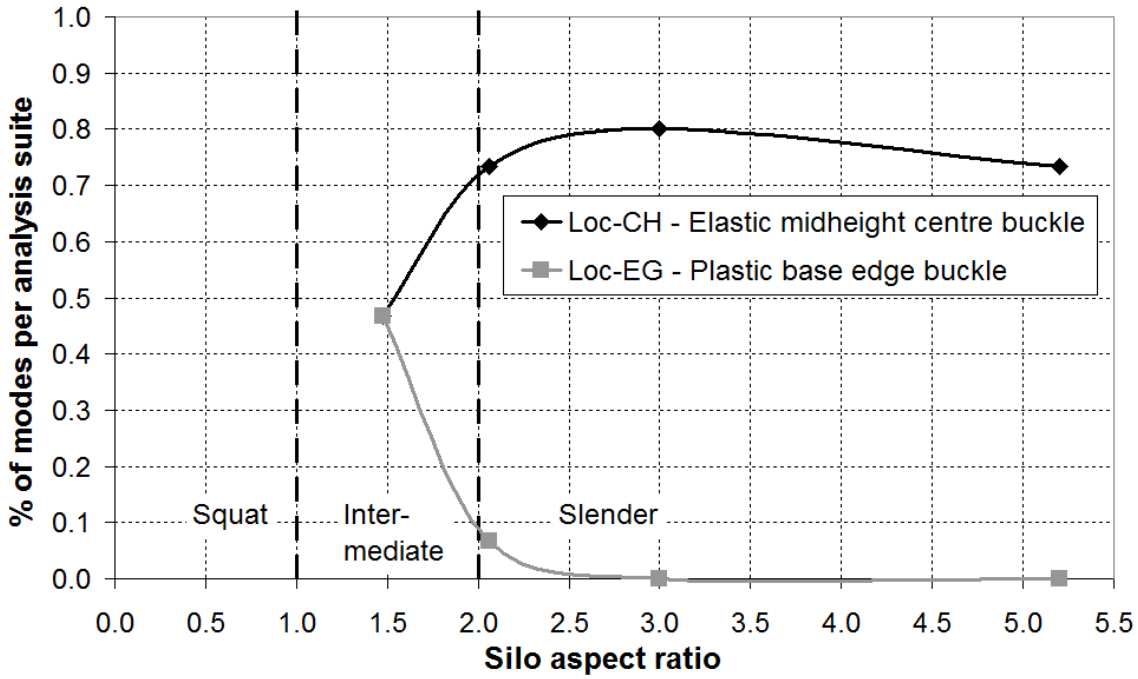

Fig. 4.17 – Plot of the number of predicted modes Loc-CH and Loc-EG per suite of eccentric discharge computations as a function of the aspect ratio

Buckling at the base of the silo near the edge of the channel (mode Loc-EG) has not been observed in silos in service. In reality, the granular solid at the base of the silo offers significant stiffness that enhances the buckling strength (Rotter and Zhong, 1990). Furthermore, mode Loc-EG is always plastic if the analysis included plasticity, and it is very probable that it is caused by the high edge pressures the form of which is anyway thought to be questionable and exaggerated, as discussed in Section 1.2.8 of the

literature review. Additionally, a parallel-sided flow channel, like that assumed in the EN 1991-4 model, requires sufficient height to develop, which is simply not available in squatter silos (Rotter, 2001a). The results of the analyses of intermediate slender and squat aspect ratio silos ($H/D \leq 2$) that were found to predict mode Loc-EG are therefore thought to be artificial and not to be trusted.

The load factors for the eccentric discharge computations are presented as bar charts in Fig. 4.18 to Fig. 4.20 for the three different flow channel sizes, normalised by the LBA factor. It is clearly visible that the traditional hierarchy of LBA > GNA > GMNA > GNIA > GMNIA is consistently violated. Geometric nonlinearity increases the strength of the structure to many times the LBA value. Additionally, axisymmetric weld imperfections lead to massive increases in strength, up to almost 17 times the LBA value for the smaller channels with k_c of 0.25 and 0.40. This is very unusual and unexpected.

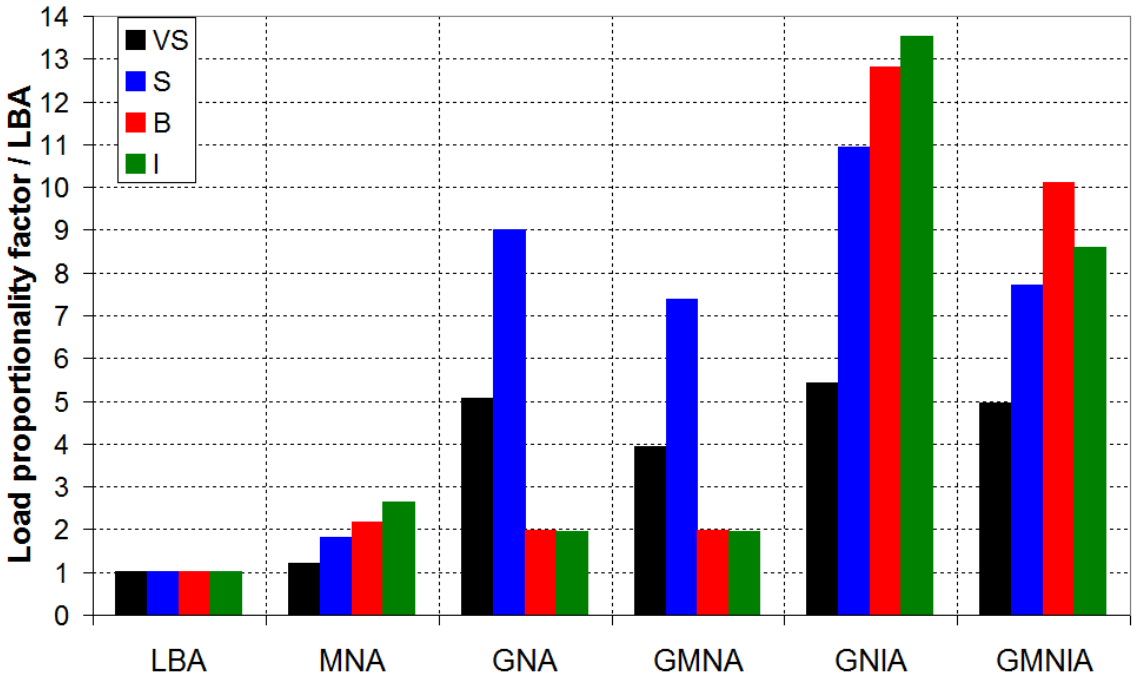

Fig. 4.18 – Bar chart of the load factors for eccentric discharge with $k_c = 0.25$ normalised by the LBA factor

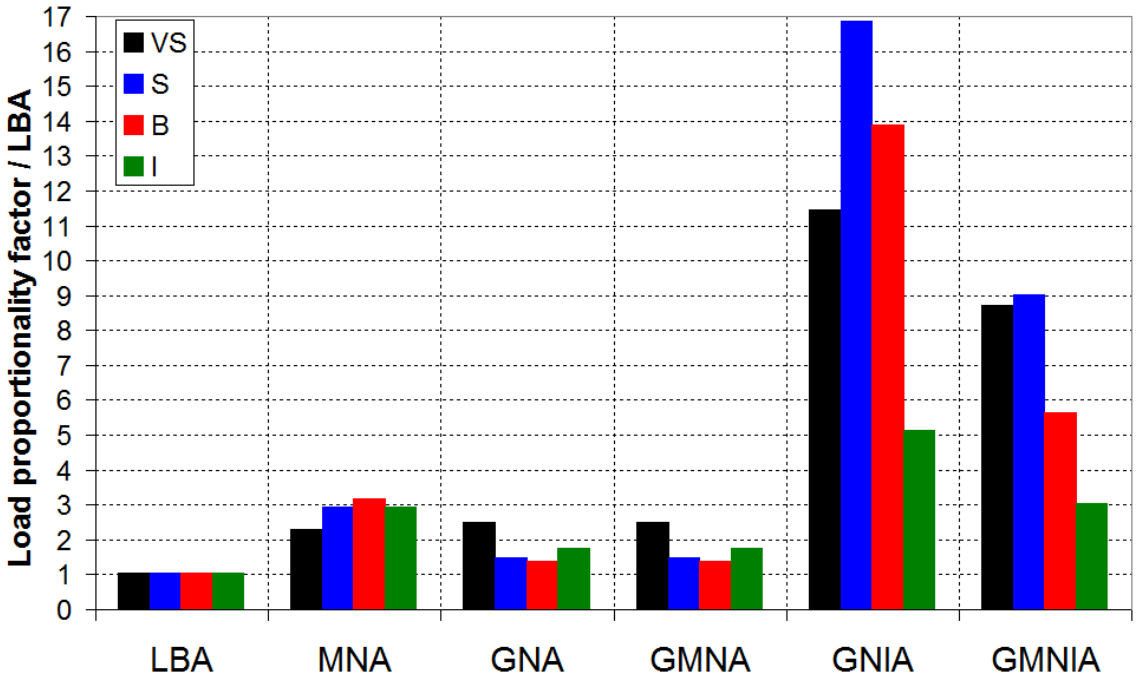

Fig. 4.19 – Bar chart of the load factors for eccentric discharge with $k_c = 0.40$ normalised by the LBA factor

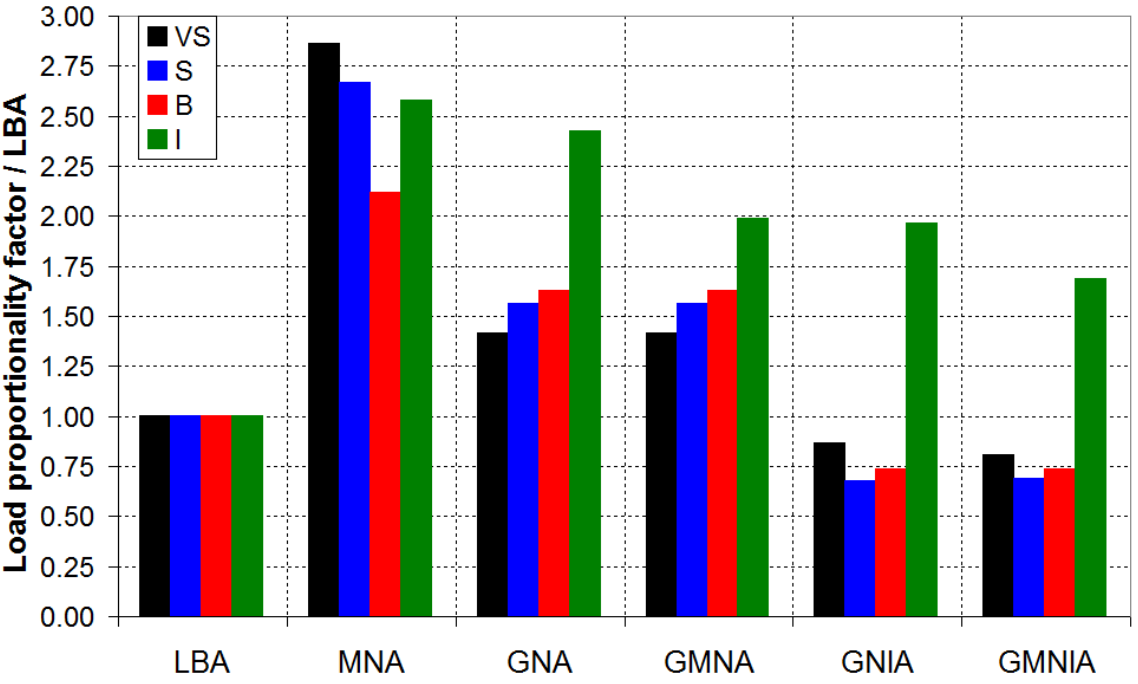

Fig. 4.20 – Bar chart of the load factors for eccentric discharge with $k_c = 0.60$ normalised by the LBA factor

4.8.2 The effect of geometric nonlinearity

Geometric nonlinearity has been found to have a consistently beneficial effect on the silo as it deforms under the highly non-symmetric pressures arising from eccentric discharge. This is illustrated by considering the predictions for Silo S, set out below.

4.8.2.1 The reference case, $k_c = 0.00$

Contour plots of compressive axial stresses only (hereafter referred to simply as the axial 'stress field' for the LA and GNA analyses of the S00 suite are presented in Fig. 4.21. The colourless grey regions in this figure and others like it represent areas under tension. The GNA values are shown at the LBA load factor. The LBA and GNA factors are actually very similar, the latter slightly lower, and have rather similar stress fields and bifurcation modes. These images provide a reference axisymmetric case which serves as a comparison with the eccentric discharge results.

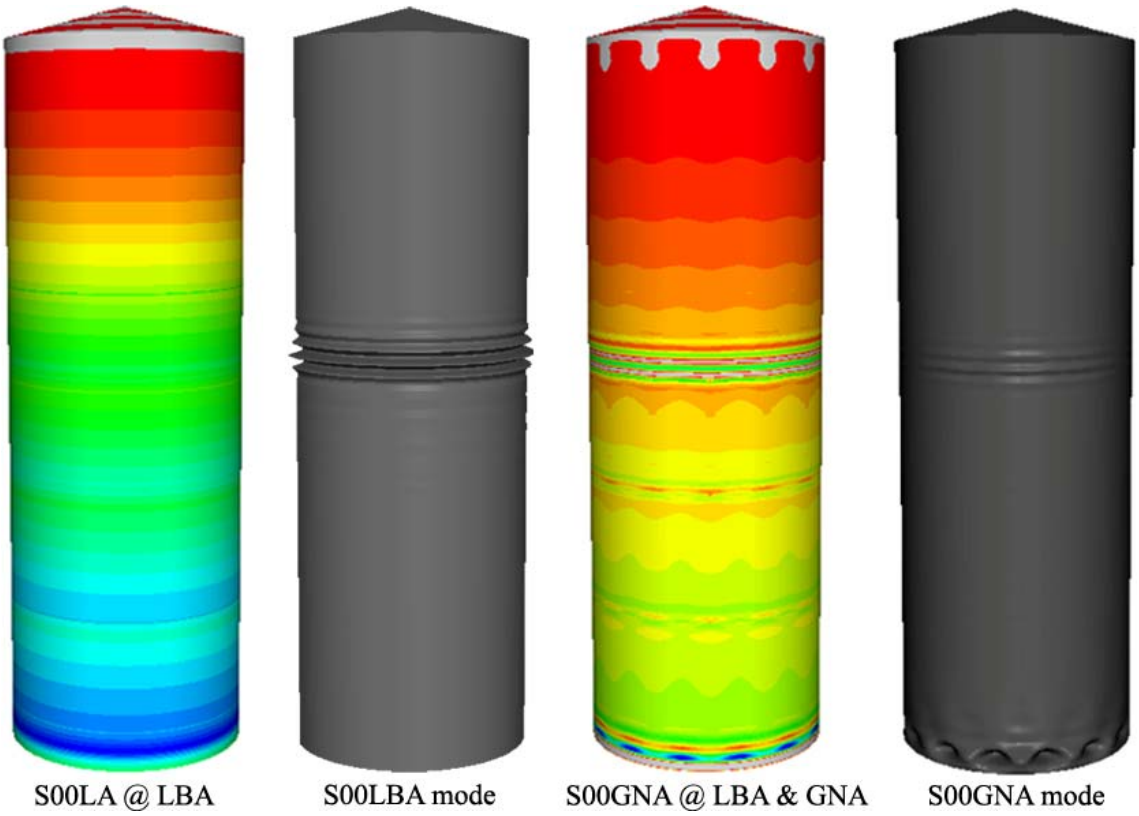

Fig. 4.21 – Axial stress fields and buckling modes of LBA and GNA for S00

4.8.2.2 The smallest channel, $k_c = 0.25$

If the smallest flow channel, $k_c = 0.25$, is now imposed on the silo, a different behaviour emerges. Recall that the S25LBA, S00GNA and S25GNA load factors are 0.46, 7.77

and 4.11 respectively, and that there is a huge increase in strength for S25 from LBA to GNA, far more than for S40 or S60. If S25GNA were to give a similar result to S25LBA, then its stress field at bifurcation should be similar to the LA stress field at the LBA factor. This is very far from the case, as shown in Fig. 4.22.

The stress field at bifurcation outside the flow channel of S25GNA bears a significantly closer resemblance to the stress field at bifurcation of S00GNA (Fig. 4.21). There is a visible disturbance in the stress field adjacent to the flow channel. At the LBA load factor, however, the GNA stress field bears little resemblance to that of S25LBA. This shows that the geometrically nonlinear behaviour of S25 is still essentially very similar that of S00, i.e. it is dominated by the axisymmetric load component.

The flow channel for $k_c = 0.25$ appears to have a large enough effect to reduce the GNA load factor from 7.77 to 4.11, but not to modify the fundamental behaviour and displace the buckling mode elsewhere. In a sense, the small flow channel of S25 acts more like an imperfection to S00 than as a separate load case. The incremental buckling mode predicted by the S25GNA analysis is furthermore very small, requiring a magnification of 50,000 to be seen clearly. For consistency it was judged to be mode Loc-CH, since it is predominantly elastic and lies within the flow channel.

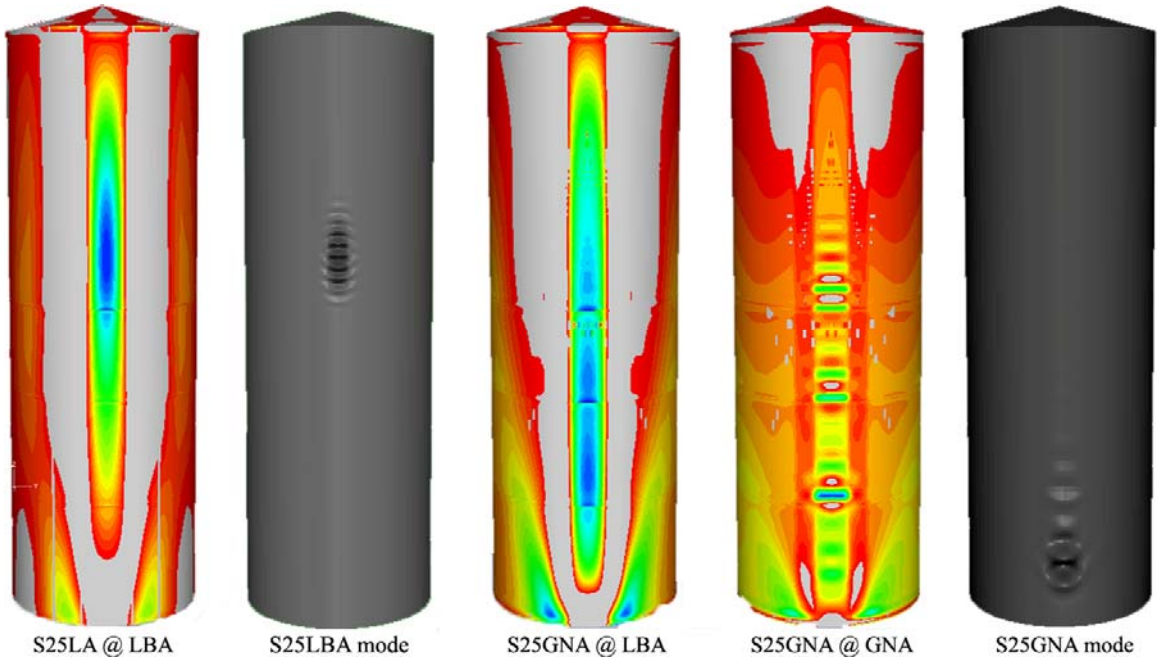

Fig. 4.22 – Axial stress fields and buckling modes of LBA and GNA for S25

Although the S25GNA buckling mode was assessed to be Loc-CH, it is a rather odd mode because it occurs quite near the bottom rather than at midheight where it would usually be expected. The reason for this is illustrated in Fig. 4.23, which shows the vertical distribution of axial membrane stress resultants through the centre of the flow channel for the SLA and SGNA analyses at the LBA load factor. While the LA analyses consistently show a peak compressive stress at approximately midheight, regardless of flow channel size, the GNA analyses show a progressive growth and upward movement of the peak value, which only really establishes itself in channel sizes bigger than k_c = 0.40. For k_c = 0.25, the peak is neither apparent nor significant, and it is clear that a buckle could form in several alternative places at the centre of the flow channel. Here a slight peak can be seen near a depth of z/H = 0.77, corresponding to the location of the buckle on Fig. 4.22.

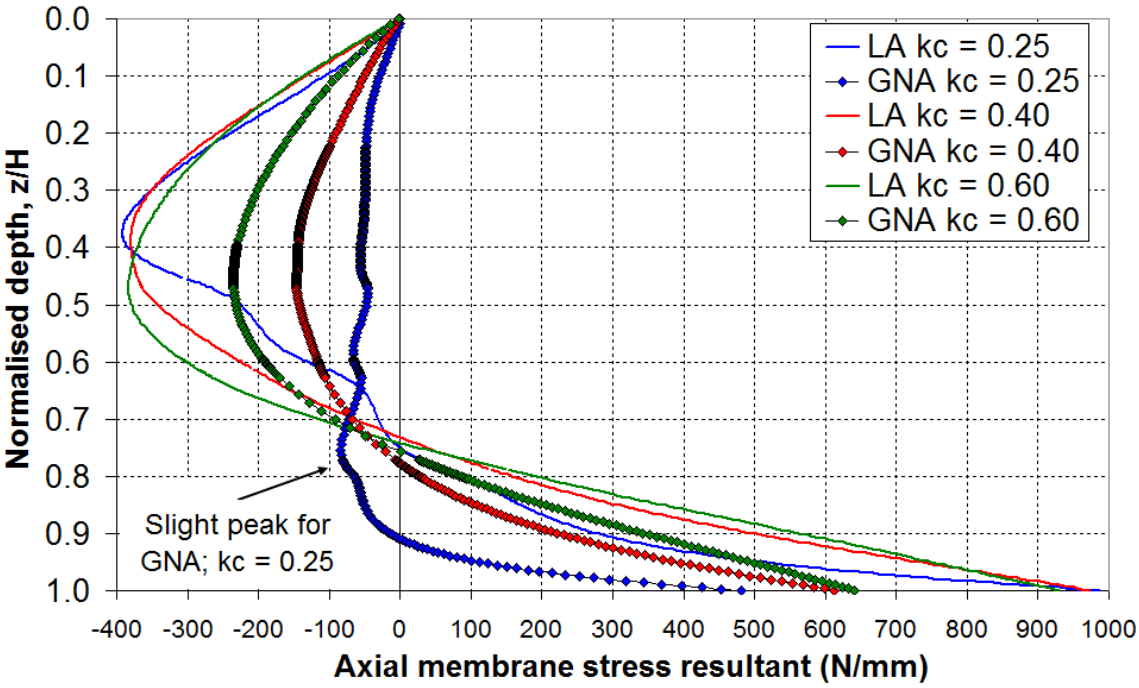

Fig. 4.23 – Axial membrane stress distribution through the centre of the flow channel for the SLA and SGNA analyses at the LBA load factor

4.8.2.3 The larger channels, k_c = 0.40 and 0.60

Axial stress fields for the larger flow channels with k_c = 0.40 and 0.60 are shown in Fig. 4.24 and Fig. 4.25. These are closer to the outcome of earlier analyses, with the stress field of the GNA at bifurcation beginning to resemble that of the LA at bifurcation. This is also reflected in the much closer proximity of the load factors (recall that the S40LBA, S40GNA, S60LBA and S60GNA load factors are 0.25, 0.37, 0.42 and 0.66

respectively) and in the size, position and shape of the buckles than for k_c = 0.25. At k_c = 0.60, the LBA and GNA analyses predict very similar buckles and stress fields. The GNA load factor is still some 60% higher than the LBA, but this is due to the overall stiffening effect of geometric nonlinearity. The bifurcation modes are now 'true' Loc-CH.

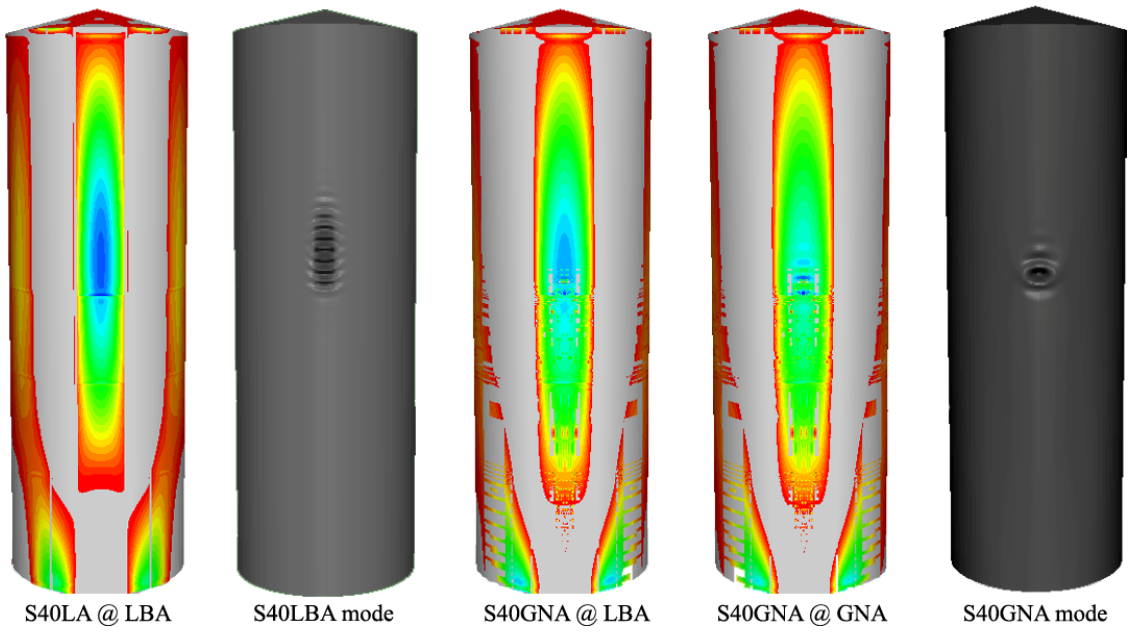

Fig. 4.24 – Axial stress fields and buckling modes of LBA and GNA for S40

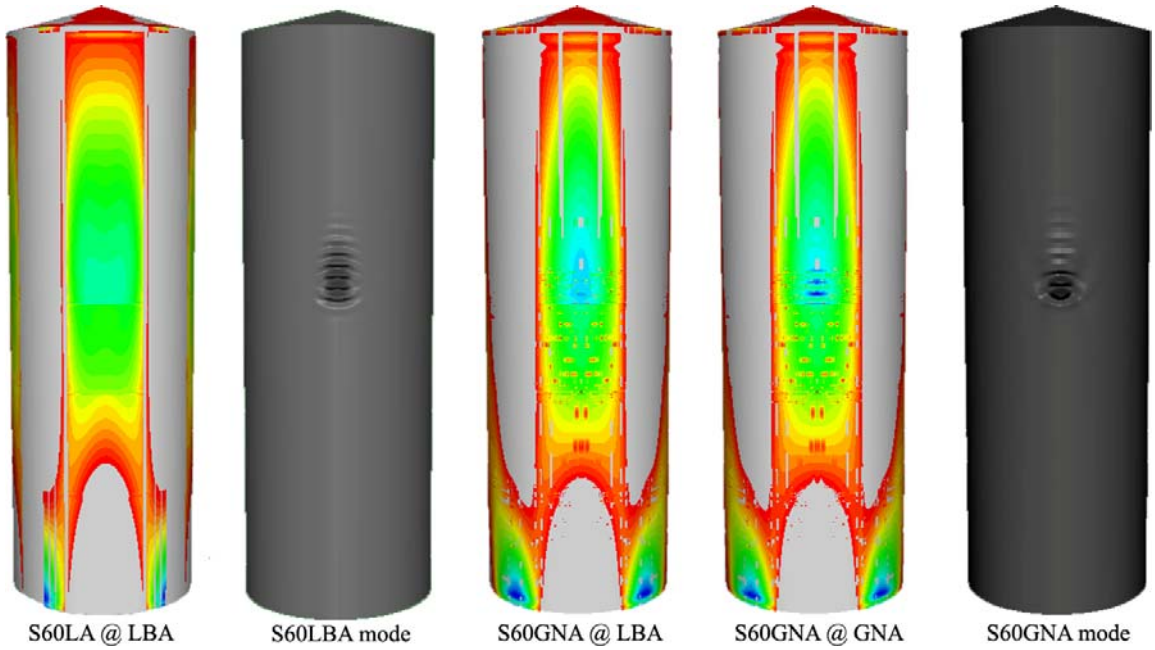

Fig. 4.25 – Axial stress fields and buckling modes of LBA and GNA for S60

One could therefore conclude that small flow channels do not cause buckles at midheight at the centre of the channel, but that larger flow channels do. It may, however, be wrong to conclude outright that a small flow channel has no significant effect on the silo. Given the uncertainty in the pressure model and the complex behaviour of the shell under such unsymmetrical loading, the opposite may prove true for some aspect ratio or granular solid that has *not* been explored here.

The rather arbitrary EN 1991-4 recommendation that $k_c = 0.25$ be tested is considered by the author to be not only unnecessary, but also potentially misleading. A wiser set of flow channel sizes may instead be $k_c = 0.40$, 0.55 and 0.70, to ensure that only mid-sized channels are tested. Although only Silo S was shown here in detail, the behaviour shown by the other silos is very similar and these observations may be applied to them. The effect of geometric nonlinearity is investigated in more detail in Chapter 5 where the full range of possible flow channel sizes is studied, $0.00 \leq k_c \leq 0.90$.

4.8.3 The effect of plasticity

The MNA predictions, normalised by both the LBA and GNA, are shown in Fig. 4.26. For the case for concentric discharge, in which the silo is under a state of quasi-uniform axial compression and internal pressure, plasticity is global and has been found to interact closely with the buckling mode (i.e. elastic-plastic buckling dominates). However, when the silo is subjected to eccentric discharge, the stress state can be highly localised in places and elastic buckling is the most likely outcome. For squatter silos, however, both buckling and plastic collapse may occur simultaneously at different locations. The analysis of squat silos under eccentric discharge requires further study, both in terms of structural consequences and in the conception of an appropriate pressure model.

For slender silos under eccentric discharge, the MNA load factors generally exceed the LBA and GNA factors by over 100%, confirming that the behaviour will probably be predominantly elastic. This is not the case for GNA at $k_c = 0.25$ for the two most slender silos, but under these conditions another phenomenon dominates, as explained in the previous section.

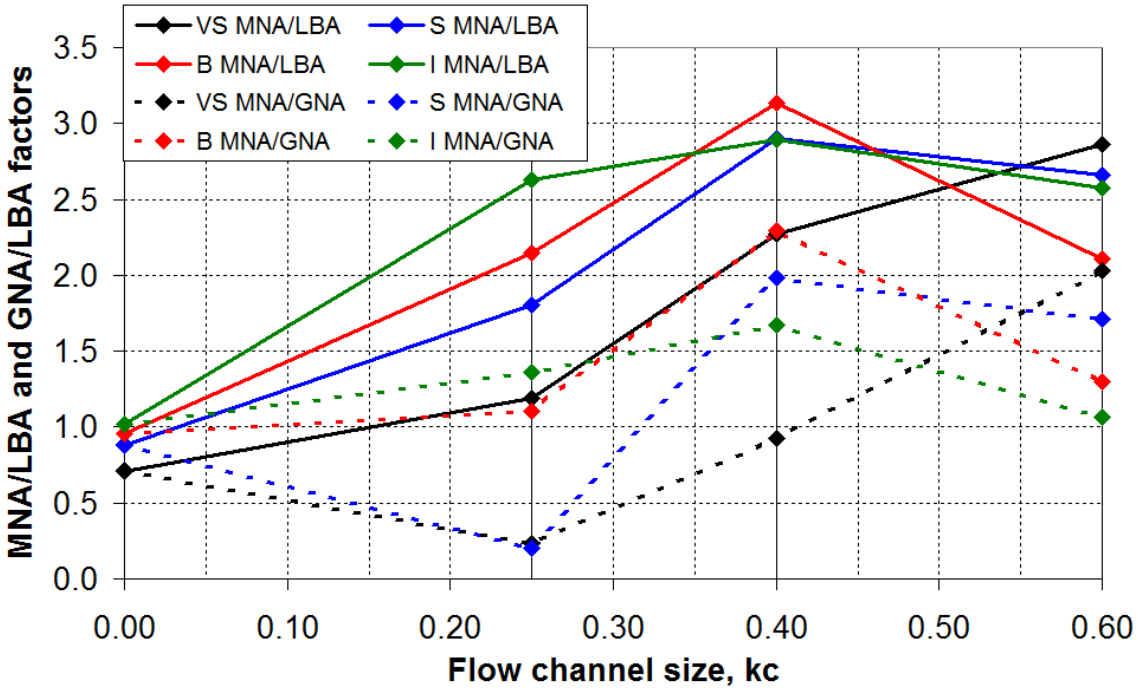

Fig. 4.26 – Comparison of MNA/LBA and MNA/GNA for all four silos

The effect of material plasticity therefore appears to be very limited in the eccentric discharge predictions. The buckling phenomenon is generally elastic and occurs at very low local stresses. High stresses may occur in the buckled regions that may then yield locally, if analysed with a GMNA analysis, which will slightly reduce the predicted buckling strength. Similarly, regions immediately adjacent to the axisymmetric weld depressions are usually subject to very high local stresses, leading to plasticity in GMNIA analyses. The effect is always weakening.

4.8.4 The effect of axisymmetric weld imperfections

The effect of axisymmetric weld imperfections on the elastic nonlinear analyses (GNIA) is discussed next. Previously, it was found that the S25GNA analysis produced a similar buckling behaviour to S00GNA, with the small k_c = 0.25 flow channel acting as a kind of 'perturbation' to the concentric discharge condition. This effect becomes even more pronounced when the axisymmetric weld imperfection is introduced, as shown in Fig. 4.27. Previously it was shown that a larger channel size (k_c = 0.40) was needed to produce mode Loc-CH in a GNA analysis. With the addition of weld depressions, the same mode Loc-CH is only produced when the flow channel is significantly larger (k_c = 0.60).

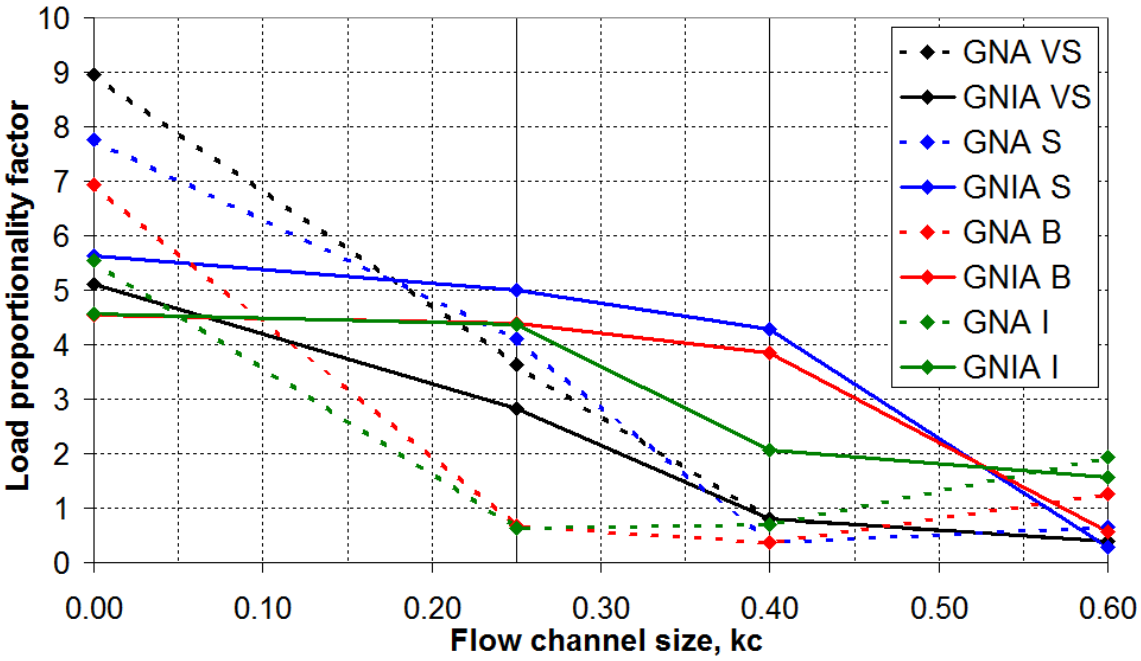

Fig. 4.27 – Comparison of GNA and GNIA load factors

The eccentric discharge pressure distribution (Fig. 4.6) results in significant inward circumferential bending of the wall due to the large difference in pressures between the edge region and the channel region. The weld depression, so deleterious under concentric discharge, has the curious property that it increases the second moment of area of the shell in circumferential bending, enhanced by an inward displacement of the effective section centroid (Fig. 4.28). This is curious in the sense that, according to the conceptual basis of EN 1993-1-6, an imperfection is intended to have a detrimental effect on the structure.

The increased second moment of area for circumferential bending makes the shell much more resistant to the inward bending action in the flow channel region. When combined with the stiffening effect of geometric nonlinearity, the shell resists these eccentric discharge pressures very well. This causes the elastic midheight buckles to be predicted only when the silo is subjected to the largest flow channel of $k_c = 0.60$ (Fig. 4.29). The evaluation of the value of k_c at which the effect of the axisymmetric weld depression changes from being beneficial to detrimental is not yet fully understood. Gillie and Holst (2003) report a similar outcome where the axisymmetric weld depression was found to be beneficial to the buckling strength of silos supported on discrete, eccentric brackets.

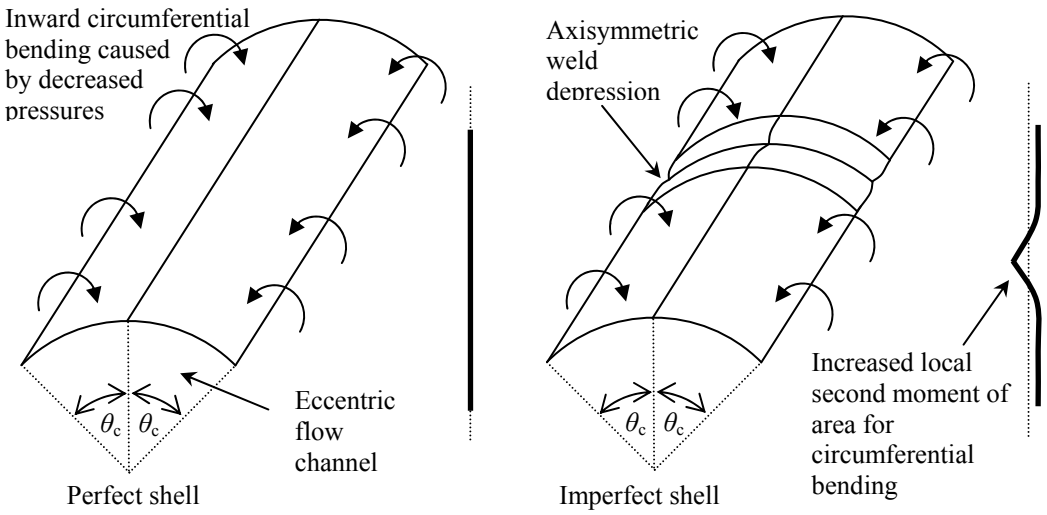

Fig. 4.28 – Comparison of the behaviour of perfect and imperfect shells with axisymmetric weld imperfections

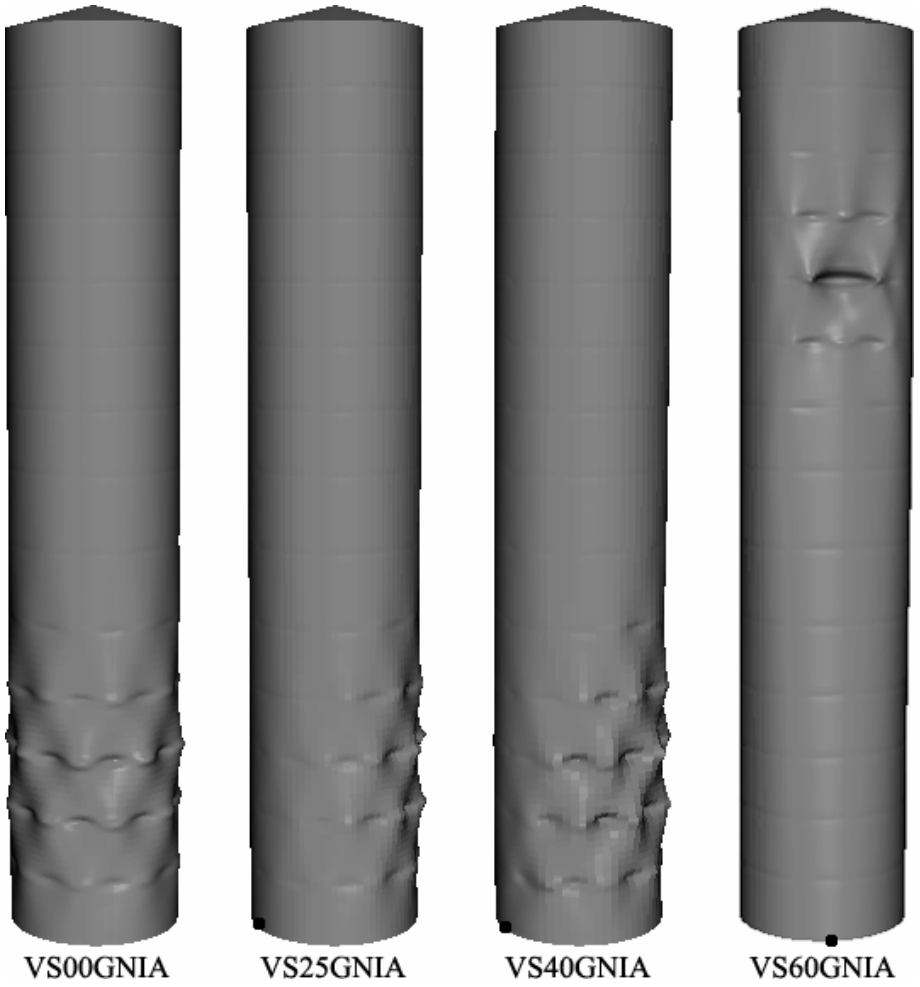

Fig. 4.29 – Buckling modes for VSGNIA (black dots represent the centre of the flow channel): geometric scale factors are ×100, ×100, ×50 and ×50 respectively

Clearly, more research is required to determine a realistic, yet still deleterious, imperfection mode for the silo under the EN 1991-4 eccentric discharge pressures. This issue is explored in Chapter 6.

4.9 Conclusions

In this chapter, five example silos designed according to the EN 1993-1-6 and EN 1993-4-1 hand design procedure under the EN 1994-1 concentric discharge loads have been studied. These spanned a wide range of aspect ratios: $0.65 \leq H/D \leq 5.2$. The failure modes of these silos under concentric discharge have been explored in detail. Additionally, four of these silos, within the range $1.45 \leq H/D \leq 5.2$, were investigated under the EN 1994-1 eccentric discharge pressures.

For four of the design silos analysed by a computational GMNIA analysis, the EN 1993-1-6 and EN 1993-4-1 hand design procedure was shown to deliver significant reserves of strength, by a factor of approximately 2, beyond the inherent 1.65 partial safety factor. The reasons for this were presented in Chapter 2.

The exception to this conservatism is the squattest silo of the group, with $H/D = 0.65$, whose GMNIA load factor was predicted to be 1.28 (22% below the 1.65 partial safety factor of EN 1993-1-6 and EN 1993-4-1). Though designed strictly according to the EN 1993-1-6 procedure, this silo has a very thin 1 mm wall over half of its height. In reality, a silo with such a relatively small volume would not normally be designed as squat, and if it were, it would have been built with a more practical and thicker wall, possibly a minimum of 3 mm, which would have raised its buckling strength significantly.

The predictions in this study suggest that the critical locations for buckling under concentric discharge are at the base of the silo and, commonly, the base of the thinnest strake. The buckling mode for these locations appears to be by elephant's foot. With the inclusion of axisymmetric weld imperfections and geometric nonlinearity, a global diamond buckling pattern may develop instead for more slender silos.

Under the eccentric discharge pressures of EN 1994-1, two critical locations for buckling failure have been identified. The first is in the silo wall within the centre of the flow channel at approximately silo midheight, originally described by Rotter (1986),

where the buckling is always elastic. The second is in the silo wall within the edge of the flow channel at the base of the silo, where the buckle may be plastic.

The critical location at midheight matches observations of buckling failures of silos in service under eccentric discharge. It is reproduced in FEA analyses for slender silos designed to Janssen pressures. In squatter silos designed to modified Reimbert pressures, the base critical location may dominate instead.

Computational analyses which predict the buckling mode at the edge of the channel at the base of the silo are thought to be artificial, since no such buckling modes have ever been observed in silos in service. Such modes have only been predicted for intermediate slender and squat silos. It is thought that, in reality, the stiffness of the solid at the base of the silo offers significant resistance against buckling at this location. An eccentric pipe flow channel is also highly unlikely to form all the way up the wall in squatter silos as it requires sufficient height to spread radially outwards from the outlet. Additionally, a flow channel would not exert such massive high pressures at the edge of its contact spread with the wall as the EN 1991-4 provisions would suggest. These regions of high pressure certainly contribute to the early formation of the elastic-plastic base edge buckling mode in a computational analysis.

The buckling strength of a silo under the EN 1994-1 eccentric discharge pressures is higher when analysed with a geometrically nonlinear FEA analysis (i.e. GNA) than with a linear analysis (i.e. LBA). The flow channel is additionally required to be quite large ($k_c \geq 0.40$) in order to significantly alter the buckling behaviour from that under symmetric loads. Small channels appear to act almost like ‘imperfections’ in the shell, which still largely behaves as if under axisymmetric loading.

For smaller channels ($k_c \leq 0.40$), axisymmetric weld imperfections lead to further strength gains. This imperfection form, so deleterious under axisymmetric loading, increases the circumferential bending stiffness of the shell. It is evident that significant weld depressions enhance the strength of silos under eccentric discharge if the flow channel is relatively small. Only very large flow channels still cause buckling across the flow channel at midheight when weld depressions are present. If the higher imperfection amplitudes of EN 1993-1-6 for GMNIA-based design had been adopted in the present

computational analyses, it is very likely that the strengthening effect would have increased further. These findings indicate that different imperfection forms are needed when studying eccentric discharge, and that the underlying assumption of EN 1993-1-6, that deeper imperfections cause lower buckling loads, is seriously in error for this load condition.

Chapter 5 – The structural behaviour of silos subject to different flow channel sizes under the EN 1991-4 eccentric discharge pressures

5.1 Introduction

5.1.1 Details of the flow channel size study

This chapter presents a detailed parametric study into the structural effects of changes in the size of an eccentric pipe flow channel according to the EN 1991-4 (2007) model. The flow channel size in this pressure model is defined in terms of the ratio of the flow channel radius to the silo radius, r_c/R, denoted by the symbol k_c.

A comprehensive suite of FEA calculations was performed on the very slender cement Silo CVS (H/D = 5.2, designed for the storage of cement, Table 4.2) subjected to the EN 1991-4 eccentric discharge pressures within the EN 1993-1-6 (2007) and EN 1993-4-1 (2007) framework. The channel size, defined in terms of the k_c value in EN 1991-4, was varied from 0.00 to 0.90 in intervals of 0.10. The value of k_c = 0.00 corresponds to concentric discharge. The channel properties according to the EN 1991-4 model are summarised in Table 5.1. The angles θ_c and ψ defined in Fig. 5.1.

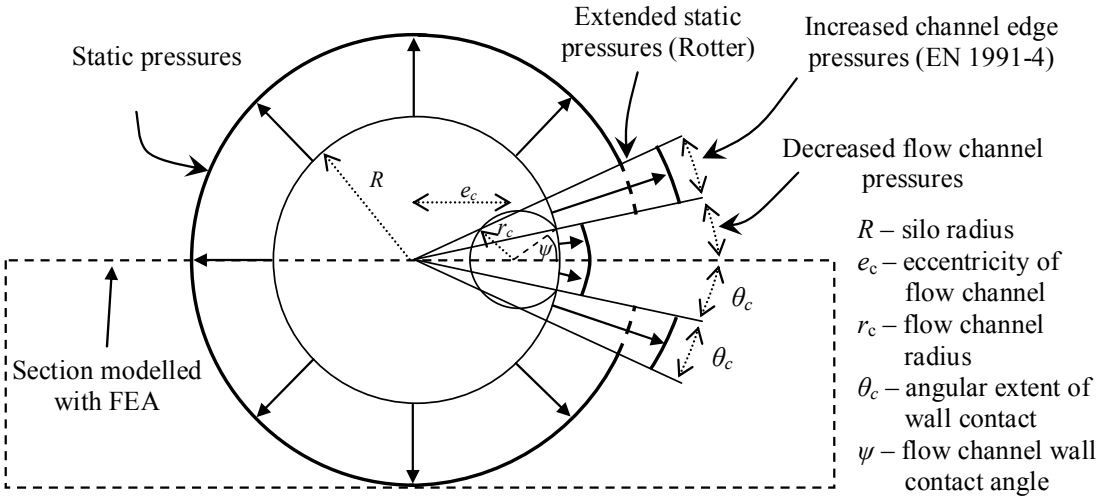

Fig. 5.1 – Notation and geometry of the eccentric flow channel wall pressure distribution, after EN 1991-4 (2007)

Table 5.1 – Summary of eccentric flow channel properties (values in bold are those recommended by EN 1991-4)

k_c	**0.00**	0.10	0.20	**0.25**	0.30	**0.40**	0.50	**0.60**	0.70	0.80	0.90
r_c (m)	0.00	0.25	0.50	0.63	0.75	1.00	1.25	1.50	1.75	2.00	2.25
e_c (m)	0.00	2.30	2.10	2.00	1.89	1.68	1.47	1.25	1.01	0.76	0.48
θ_c (°)	0.00	3.62	7.49	9.53	11.65	16.19	21.22	26.92	33.61	41.93	53.65
ψ (°)	0.00	39.20	40.67	41.47	42.31	44.19	46.37	48.98	52.25	56.65	63.49
$2\theta_c/\pi$ (%)	0.00	4.03	8.32	10.59	12.95	17.99	23.58	29.91	37.34	46.59	59.61
A_c/A_{tot} (%)	0.00	0.94	3.77	7.12	8.56	15.09	23.58	33.98	46.32	60.69	77.34

5.1.2 Investigation of the variation of pressure components with channel size

The value of the relative flow channel size k_c is directly related to the channel wall contact angle θ_c (Eq. 3.5), and the combined region of decreased and increased pressures associated with the flow channel and its adjacent effects covers a total spread of $4\theta_c$ on the silo wall. The relationship between $2\theta_c/\pi$ (the fraction of the silo perimeter that is directly adjacent to the pressure changes) and k_c is shown in Fig. 5.2a. The variation of the ratio of the normal wall pressure in the flow channel to the stationary solid p_{hc0}/p_{h0} is shown in Fig. 5.2b. The difference between the normal wall pressure in the static and flowing solid, expressed as a percentage of the normal wall pressure in the stationary solid $100\times(p_{h0} - p_{hc0})/p_{h0}$, is shown in Fig. 5.2c. In all cases, the variation is with the relative size of the flow channel k_c and the values are taken at great depth where they are independent of the height and can be compared directly.

The relationship between $2\theta_c/\pi$ and k_c is close to linear until $k_c = 0.7$, after which the perimeter spread rises rapidly for only small increases in k_c. The channel pressures at great depth p_{hc0} increase very linearly with channel size over almost the entire range of k_c. However, it is evident that the EN 1991-4 model predicts huge drops in wall pressures, $(p_{h0} - p_{hc0})/p_{h0}$, for very small channels that are in contact with only small portions of the silo wall. This is by itself not unrealistic, but the EN 1991-4 model also predicts a rise in wall pressures at the edges of the channel equal to the fall at its centre, and the combined effect leads to very severe loading on the shell for smaller channels. Conversely, wall pressures in ever larger flow channels approach the stationary solid value, i.e. as $\theta_c \rightarrow ½\pi$, $p_{hc0} \rightarrow p_{h0}$ and $(p_{h0} - p_{hc0})/p_{h0} \rightarrow 0$.

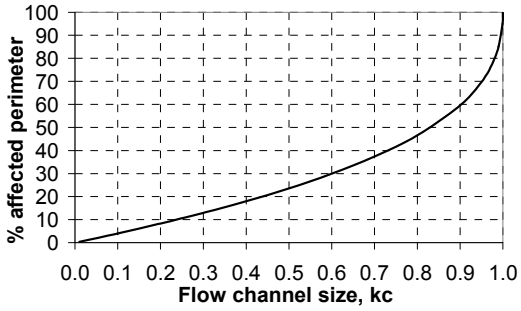

a) Variation of the % affected perimeter, $2\theta_c/\pi$

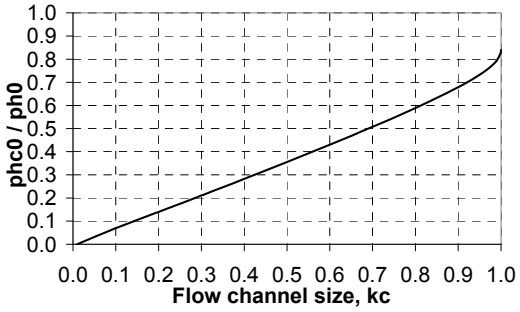

b) Variation of the ratio of channel to stationary solid wall pressures at great depth

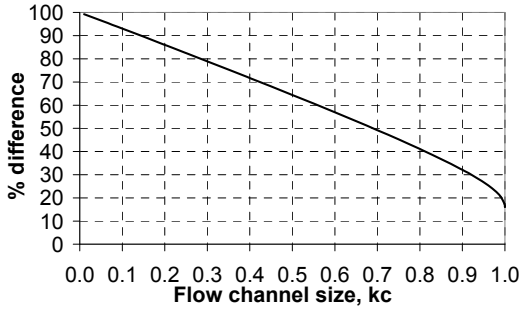

c) Variation of the % difference in wall pressures in both solid components to those in the stationary solid, $100\times(p_{h0} - p_{hc0})/p_{h0}$

Fig. 5.2 – Variation of select entities with relative channel size k_c

Very small channels with $k_c \leq 0.20$ may arise in the form of a rathole, which is common for funnel flow silos containing cohesive solids (Rotter, 2001a). In this case the solid would have discharged from the flow channel only, leaving an empty hole with zero wall pressures running all the way up the silo from the outlet. Such a small channel is demonstrated on the left half of Fig. 5.3 for $k_c = 0.10$. The EN 1991-4 model predicts that such a channel forms almost internally with a very small contact angle with the wall, near-zero pressure at the centre of the contact and a sudden massive rise in pressure at the edge of the channel to almost twice the adjacent stationary solid pressure. Conversely, a huge flow channel with $k_c > 0.70$ sees oddly thin regions of static solid exerting quite high normal pressures on the silo wall, over the entire height of the silo. The geometry for $k_c = 0.90$ is shown on the right half of Fig. 5.3. The EN 1991-4 eccentric discharge pressure model is therefore conceptually uncertain for both very small and very large values of the relative flow channel size k_c.

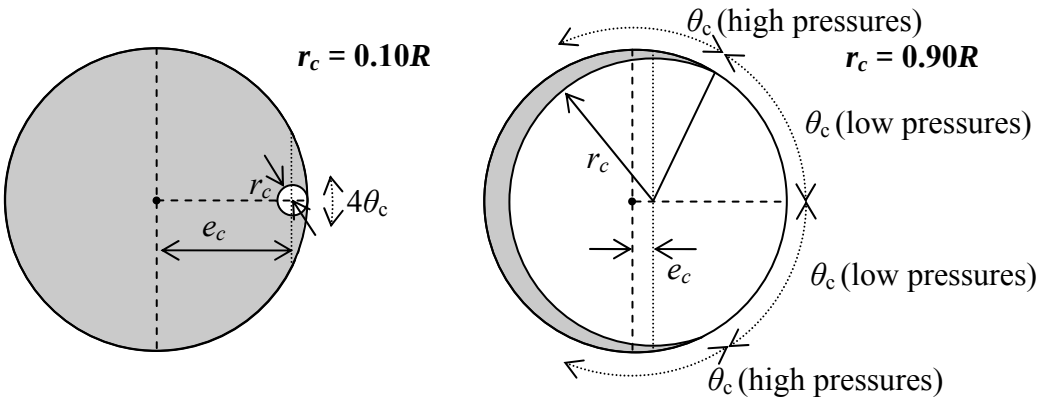

Fig. 5.3 – Very small and large flow channel according to EN 1991-4 (2007), to scale

Clearly, for these extremes, the results of a flow channel size study using the EN 1991-4 eccentric discharge model should be treated with care. However, it should be added that, since only k_c = 0.25, 0.40 and 0.60 are notionally recommended by EN 1991-4, the design procedure should be shielded from these extreme values (unless different values are recommended in a National Annex).

5.1.3 Investigation of eigenmode-affine imperfections

According to EN 1993-1-6 (2007), an analyst undertaking a full GMNIA analysis for the purposes of design is required to find the most deleterious imperfection form (within reason). Traditionally, this has been taken to the first buckling eigenmode of the perfect shell (Koiter, 1945; 1963; Deml and Wunderlich, 1997; Teng and Song, 2001; Rotter, 2004). If he/she can justify it, the analyst is free to choose an imperfection form other than the traditional eigenmode-affine pattern, including those which have a practical basis such as the axisymmetric weld depression of Rotter and Teng (1989a) investigated in Chapter 4. However, it was established in that chapter that the axisymmetric weld imperfection is not a suitably deleterious imperfection form under eccentric discharge, due to the beneficial effects of such an indentation when the silo wall is subject to circumferential bending.

Consequently, this chapter additionally examined whether a return to the more 'traditional' eigenmode-affine imperfection form (i.e. the reference imperfection form according to EN 1993-1-6) would result in a more successful outcome. Thus the imperfection forms which were investigated include the first LBA mode (as calculated, going 'outwards'), the reversed first LBA mode (in the form actually required by EN 1993-1-6, with shape deviations unfavourably oriented towards the centre of the shell

curvature) and the GNA deformed shape at the instant before bifurcation (Esslinger and Geier, 1972).

5.2 Global axial stress fields and buckling modes of the perfect shell

The results of the parametric flow channel size study are introduced here with the help of compression-only axial stress fields, first discussed in Chapter 4. The stress fields for the LA and GNA analyses at bifurcation are shown in Fig. 5.4 and Fig. 5.5 respectively. Shades of plain grey represent regions of the shell under tensile stress, which are of little interest when studying buckling.

It appears to be the case that, with geometric nonlinearity, a very small flow channel acts more like a perturbation to the axisymmetric pressures of concentric discharge rather than as a separate load case, and the stress field resembling the characteristic strip pattern of eccentric discharge does not begin to develop before the relative flow channel size k_c reaches 0.30. This strip-like pattern of stresses is, in addition, fully elastic because the predicted GNA and GMNA load factors are identical for channels with $k_c \geq 0.25$. For the LA analysis, however, this characteristic pattern is seen to develop for even smaller channels, and is present already at $k_c = 0.10$.

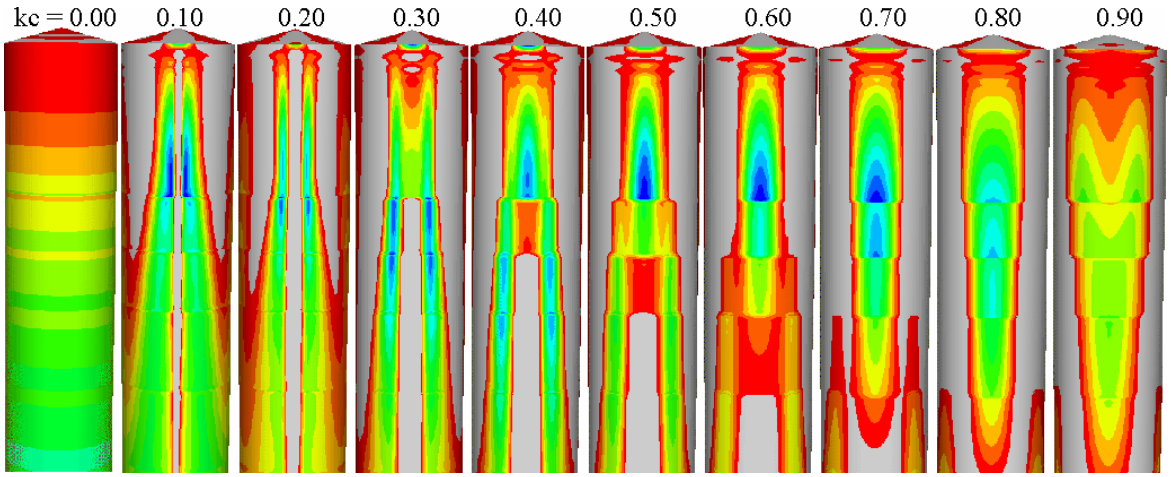

Fig. 5.4 – LA axial compressive stress fields for k_c from 0.00 to 0.90

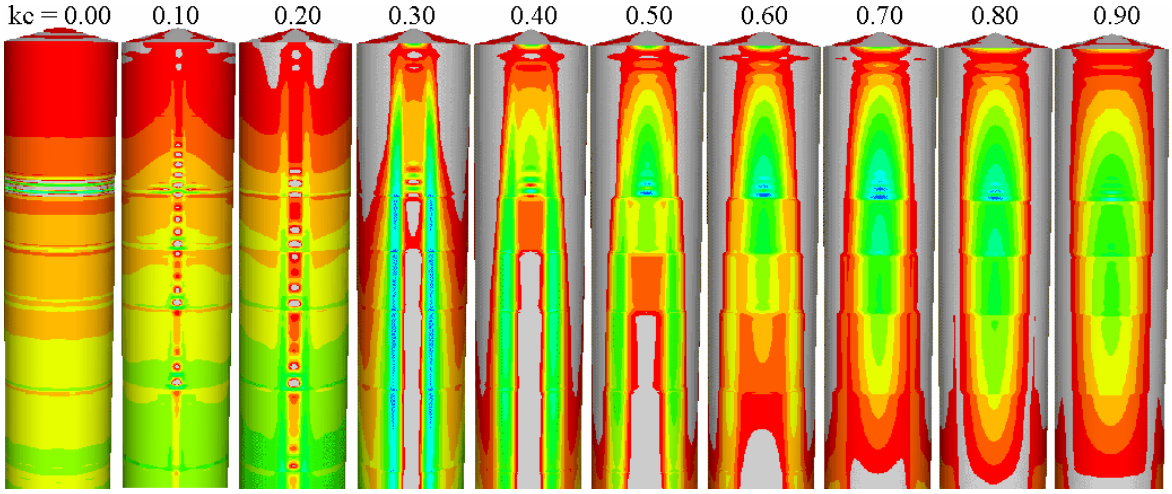

Fig. 5.5 – GNA axial compressive stress fields at bifurcation for k_c from 0.00 to 0.90

The LBA linear bifurcation modes and the GNA incremental bifurcation modes are shown in Fig. 5.6 and Fig. 5.7 respectively. The GNA incremental mode for $k_c = 0.10$ is found to develop on the side opposite the flow channel, and is therefore *not* considered as a characteristic elastic midheight mode Loc-CH that forms adjacent to the flow channel (Table 4.8). However, buckling modes at all other values of $k_c \neq 0.00$ *are* Loc-CH for both LBA and GNA analyses (except at $k_c = 0.00$, where the buckling mode is in both cases Axi-EL).

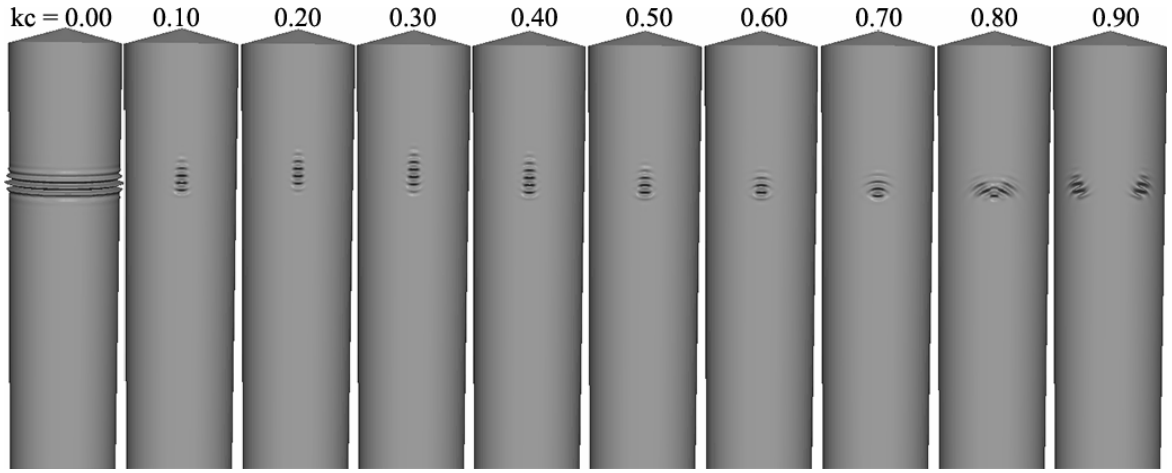

Fig. 5.6 – LBA linear bifurcation modes with relative channel size k_c (all ×200)

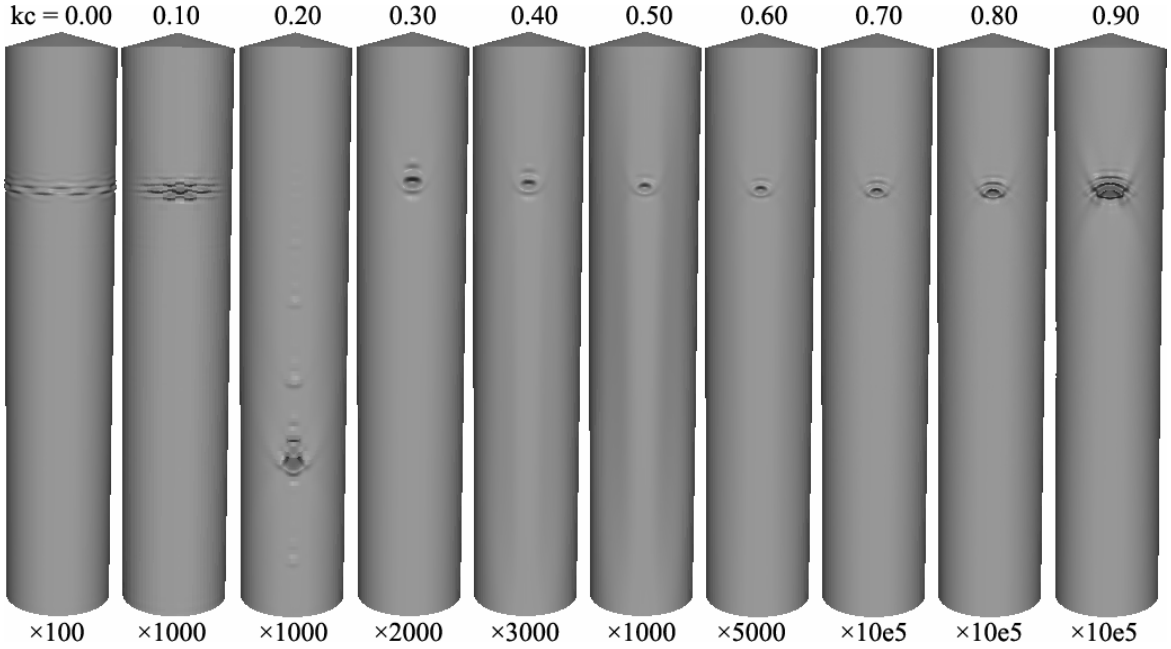

Fig. 5.7 – GNA incremental buckling modes with relative channel size k_c

The flow channel range $0.00 < k_c < 0.20$ thus appears to be more of a 'transition' range, in which the GNA buckling behaviour gradually shifts from characteristic concentric to eccentric discharge behaviour. As expected based on Fig. 5.4, the LBA exhibits the characteristic midheight buckle already at $k_c = 0.10$. Once the 'characteristic' strip-like pattern of stresses under eccentric discharge has established itself ($k_c \geq 0.10$ for LBA or $k_c \geq 0.30$ for GNA), the LBA and GNA buckles become very similar in shape, size and location, athough GNA buckles are 'smoother' and do not exhibit so many tightly-spaced indentations like the LBA eigenmode. All buckles in Fig. 5.6 and Fig. 5.7 were found to occur at the base of the thinnest 3 mm strake with the exception of $k_c = 0.20$ for the GNA analysis, the reason for which is given below. Thus the base of the thinnest strake is clearly the critical location in this silo.

For flow channels with $k_c \geq 0.70$, the region of axial compressive membrane stresses in the vicinity of the midheight buckle spreads steadily wider both axially circumferentially as the flow channel grows, resulting in an increase in the size of the buckle. The LBA and GNA buckles for $k_c = 0.80$ and 0.90, especially, look quite odd. Such shapes of buckling modes have so far not yet been encountered in the studies on eccentric discharge undertaken for this thesis, though they clearly seem to be possible where large circumferential spreads of compressive axial membrane stresses are present.

5.3 Local stress distributions in the perfect shell

5.3.1 Axial distribution of axial membrane stress resultants

In order to understand more fully the patterns of stresses which develop in the silo wall under the EN 1991-4 eccentric discharge pressures at various channel sizes, it is necessary to look at stress distributions at specific locations. The vertical distributions of the axial membrane stress resultants in the silo wall at the centre of the flow channel for the LA analyses factored by the LBA values (henceforth termed LA @ LBA) and the GNA analyses at the instant before bifurcation (henceforth termed GNA @ bifurcation) are shown in Fig. 5.8 and Fig. 5.9 below.

Considering the LA @ LBA stresses (Fig. 5.8), a compressive peak in axial membrane stresses at the base of the 3 mm strake (at approximately $z/H = 0.25$) at the centre of the flow channel is established already at a relative channel size of $k_c = 0.10$, as are tensile membrane stresses at the base of the silo. Thus, for $k_c = 0.10$, the stress state already resembles the characteristic stress distribution for eccentric pipe flow (Rotter, 1986; Fig. 2.9 and Fig. 2.13). The compressive peak remains near $z/H = 0.25$ until $k_c = 0.60$, and for larger channels the peak descends to approximately $z/H = 0.40$. The critical buckling location in the silo wall, however, remains unchanged because the buckling resistance is lowest in the thinner part of the wall.

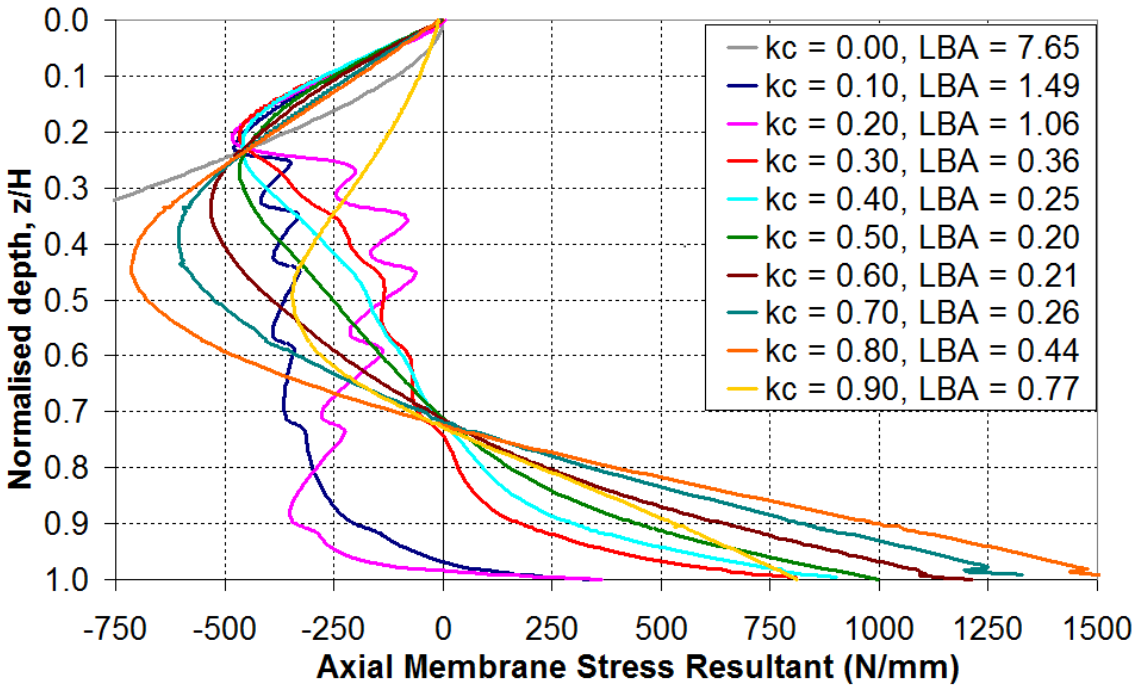

Fig. 5.8 – LA @ LBA axial membrane stress resultants at the channel centre

In the GNA analyses (Fig. 5.9), a gradual transition from compressive to tensile axial membrane stress resultants at the base can be seen clearly. The change from compressive to tensile seems to occur rather suddenly, somewhere in the range $0.20 \leq k_c \leq 0.30$ (between the pink and red curves). The distributions for $k_c = 0.00$, 0.10 and 0.20 share similar features, as expected since the behaviour is still similar to that for concentric discharge, with each subsequent curve being a 'corruption' of the former due to the effect of an increasingly large flow channel.

The curves for $k_c \leq 0.30$ do not exhibit well-defined peaks, but rather several smaller ones down the entire height, usually adjacent to a change of wall thickness. Any one of these may become critical depending on the local buckling resistance, as was the case in the previous chapter (Fig. 4.23). This explains the rather curious GNA buckling mode for $k_c = 0.20$ shown in Fig. 5.7 where the buckle was located at $z/H = 0.70$ rather than 0.25 (the base of the 3 mm strake). Indeed, for GNA analyses a clear midheight peak in the compressive membrane stress resultants does not really develop until the channel size exceeds $k_c = 0.50$.

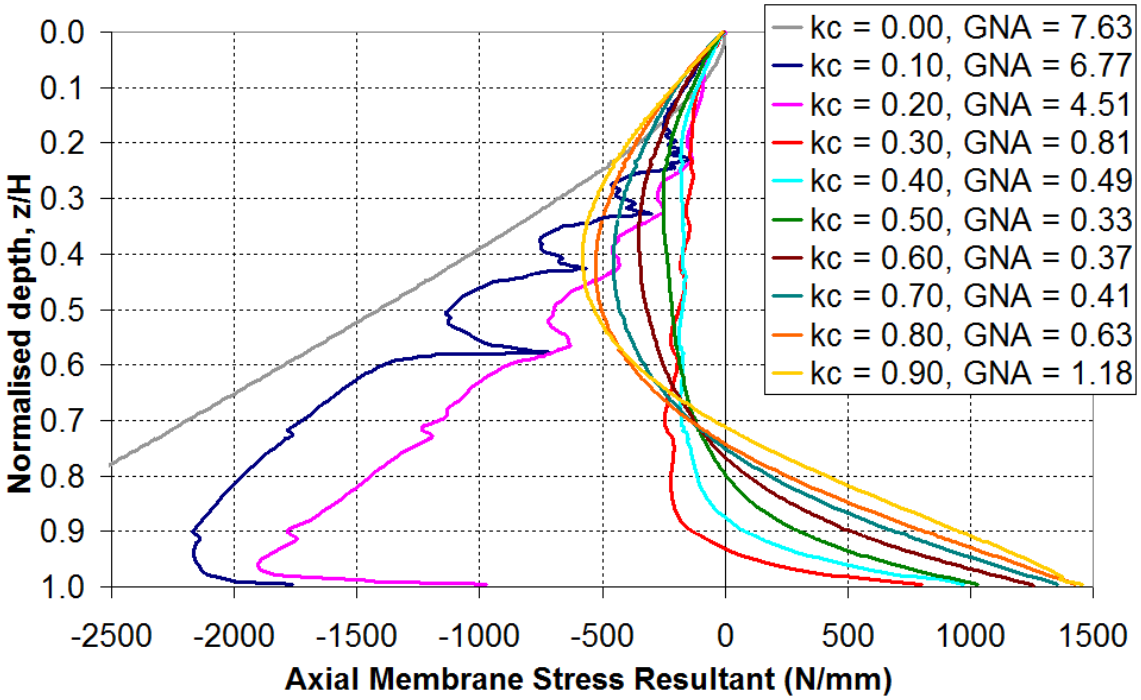

Fig. 5.9 – GNA @ bifurcation axial membrane stress resultants at the channel centre

5.3.2 Circumferential distribution of axial membrane stress resultants

The circumferential distributions of the axial membrane stress resultants, starting at the centre of the flow channel at the base of the 3 mm strake for both LA @ LBA and GNA @ bifurcation suites of analyses, are shown in Fig. 5.10 and Fig. 5.11. This critical axial location is common to every computational result, and is close to the location of every elastic midheight buckle predicted so far in this chapter. It is therefore an important place at which to compare stresses.

The general features of the circumferential distribution for both LA and GNA analyses include a region of high compressive membrane stresses in the wall directly adjacent to the channel centre, followed by a steep rise to a region of high tensile membrane stresses in the wall near the edge of the channel. This in turn gradually decays into the axisymmetric value present in the wall opposite the channel. This pattern is consistent for all analyses where the characteristic stress pattern has developed under eccentric pipe flow.

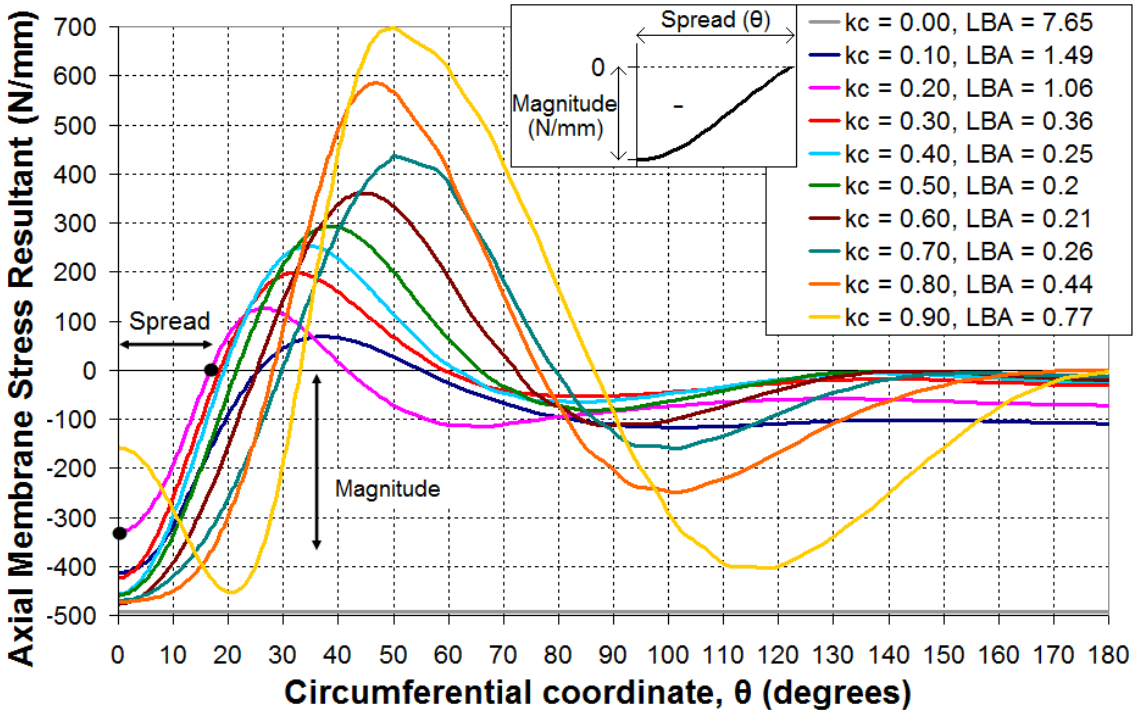

Fig. 5.10 – LA @ LBA axial membrane stress resultants @ base of 3 mm strake

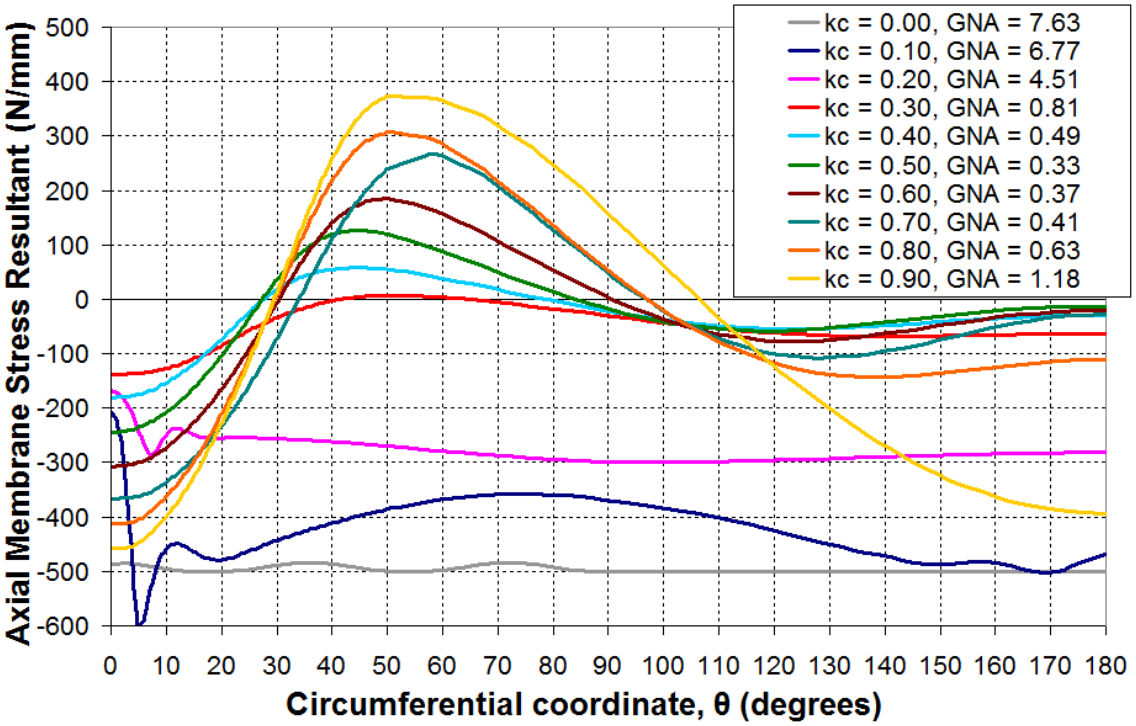

Fig. 5.11 – GNA @ bifurcation axial membrane stress resultants @ base of 3 mm strake

The gradual transition of axial membrane stress resultant patterns from the characteristic concentric discharge (single axisymmetric value) to the characteristic eccentric discharge pattern is best illustrated by the GNA curves for $0.00 \leq k_c \leq 0.30$ on Fig. 5.11 (as in Fig. 5.9). Note that the $k_c = 0.00$ curve for GNA is not perfectly constant because a small perturbation had been introduced into the finite element mesh in order to ensure bifurcation at the correct load factor, which in turn resulted in a slight perturbation in the otherwise axisymmetric stress pattern. For the smallest channels of $k_c = 0.10$ and 0.20, the pattern is still close to constant around the circumference, though clearly affected by the flow channel, most noticeably near $\theta = 0^o$ where there is a local increase in compression. The unperturbed axisymmetric membrane stress resultant opposite the channel at $\theta = 180^o$ naturally does not remain constant with k_c, but decreases with the GNA load factor for larger channels. Eventually the channel becomes large enough ($k_c \geq 0.30$) to induce tensile axial membrane stresses near the edge of the flow channel.

5.4 Load proportionality factors for the perfect shell

The computed load proportionality factors for the flow channel size study of the perfect shell (LBA, MNA, GNA and GMNA) are summarised in Table 5.2 and shown in Fig. 5.12 and Fig. 5.13 as a function of k_c.

Table 5.2 – Load proportionality factors for the perfect shell (values in bold represent a predicted mode Loc-CH)

k_c	0.00	0.10	0.20	0.25	0.30	0.40	0.50	0.60	0.70	0.80	0.90
LBA	7.65	**1.49**	**1.06**	**0.47**	**0.36**	**0.25**	**0.20**	**0.21**	**0.26**	**0.44**	**0.77**
MNA	4.54	2.51	1.14	0.88	0.77	0.64	0.60	0.65	0.75	0.94	1.52
GNA	7.63	6.77	4.51	**2.55**	**0.81**	**0.49**	**0.33**	**0.37**	**0.41**	**0.63**	**1.18**
GMNA	3.85	3.71	3.60	**2.55**	**0.81**	**0.49**	**0.33**	**0.37**	**0.41**	**0.63**	**1.18**
GNA/LBA	0.997	4.54	4.25	5.43	2.25	1.96	1.65	1.76	1.58	1.43	1.53
GNA/GMNA	1.98	1.82	1.25	1.00	1.00	1.00	1.00	1.00	1.00	1.00	1.00

In Section 5.2, it was reported that the LBA and GNA analyses predicted the characteristic mode Loc-CH for flow channels starting at $k_c \geq 0.10$ and $k_c \geq 0.25$ respectively. It can be seen now that in each case mode Loc-CH is accompanied by a severe drop in the computed load factor from the reference concentric discharge value. The LBA load factor, for example, has plummeted from 7.64 to 1.49 (an 80% reduction) as a result of a flow channel whose pressure components cover barely 4% of the silo wall (Table 5.1).

Flow channels with $k_c \geq 0.25$ produce an entirely elastic structural response, and geometric nonlinearity results in an average rise of 75% in the predicted load factor from LBA to GNA in the range of flow channels with $0.30 \leq k_c \leq 0.90$. The MNA analyses represent the circumferential plastic collapse modes which do not participate in the silo behaviour anymore after mode Loc-CH is established for $k_c \geq 0.30$, and the predicted MNA load factors are consistently higher than both LBA and GNA in this range. However, in the transitional range of flow channels, defined for the GNA/GMNA analyses as $0.00 \leq k_c \leq 0.25$, plasticity still affects the predicted buckling strength.

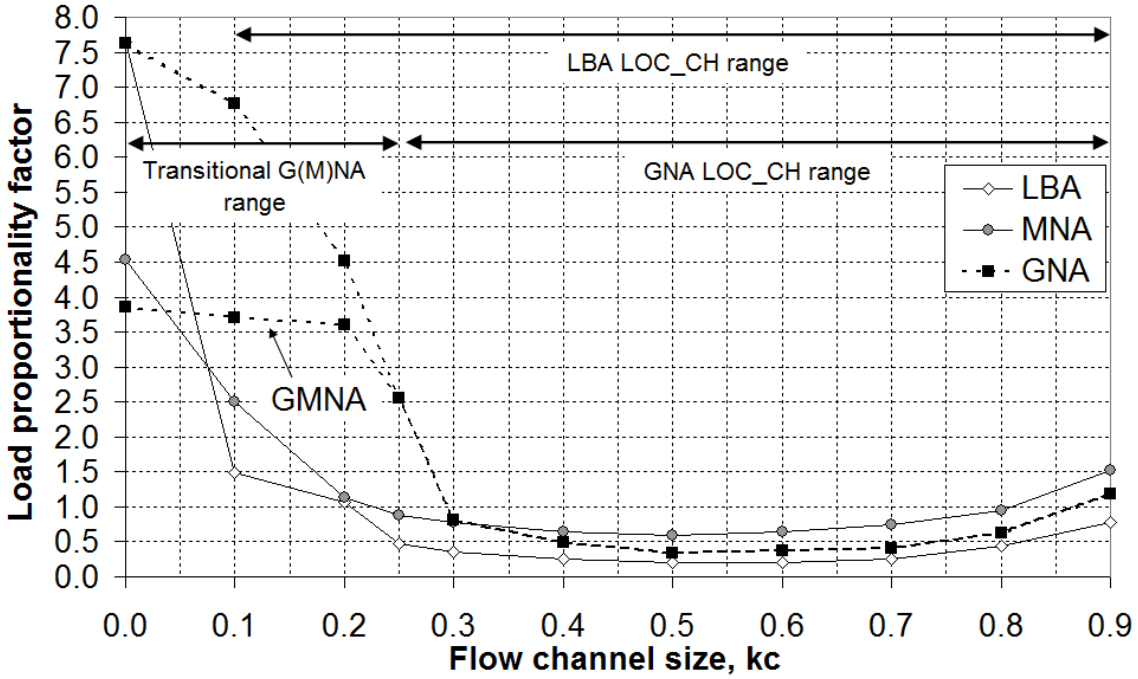

Fig. 5.12 – Variation of the load proportionality factor for the perfect shell with relative flow channel size k_c; global view

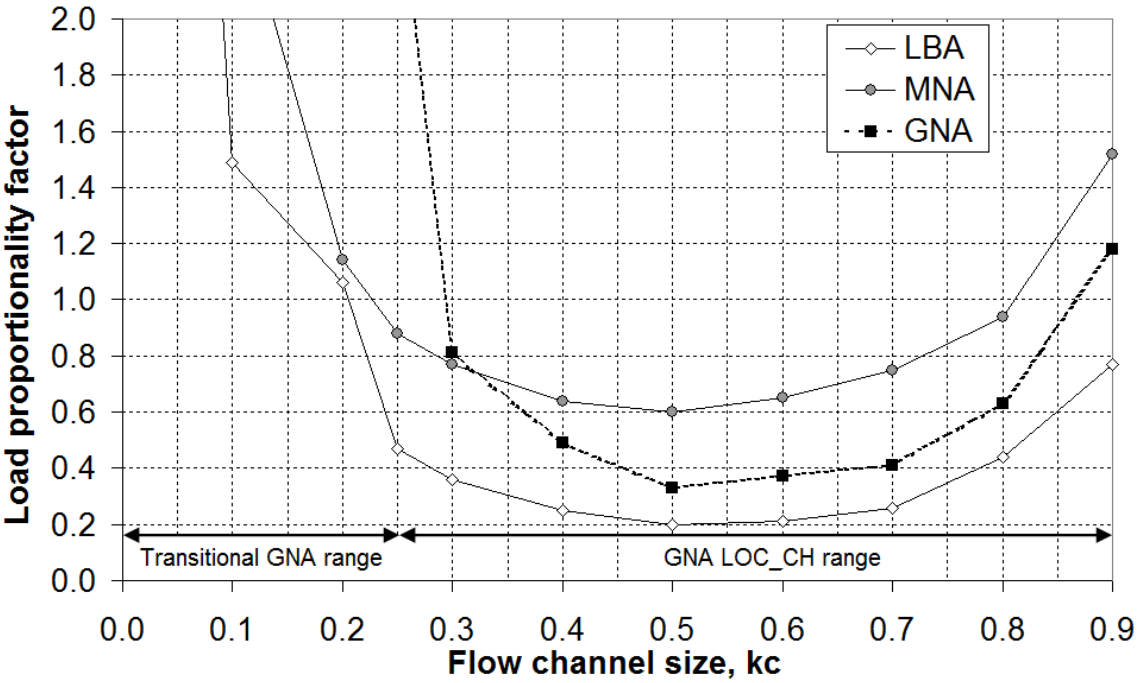

Fig. 5.13 – Variation of the load proportionality factor for the perfect shell with relative flow channel size k_c; close-up of the region with lower load factors

Taking into account the uncertainties about the EN 1991-4 eccentric discharge model near the two extremes of the flow channel size range, supported by the FEA evidence in this study, it might be wise to impose a range on the values of k_c which should be taken

into consideration in design and to revise the default values currently recommended in EN 1991-4 (k_c = 0.25, 0.40 and 0.60).

The EN 1991-4 Standard has for the first time attempted to make eccentric pipe flow a condition which may be reliably designed for. But if it is indeed eccentric pipe flow that is the design aim, then it should be ensured that the corresponding characteristic silo behaviour, as predicted by FEA analyses, has also developed. This means that there should be high compressive axial membrane stresses at the centre of the channel which become tensile near the base, and high compressive axial membrane stresses at the edge of the channel near the base. The corresponding buckling mode should then be either Loc-CH (for stepped wall thickness silos) or Loc-EG (for uniform wall thickness silos or those with high buckling resistance in the upper part). Though it is by no means implied here that these are the *only* possible silo responses under eccentric pipe flow, it is apparent in this thesis so far that these buckling modes are ubiquitous for this loading condition and closely associated with very low predicted load factors. Thus, if these buckling modes are obtained from a FEA analysis, one can be confident that one is at or near the bottom of the load factor vs. channel size curve (e.g. Fig. 5.12). The predicted structural response due to smaller channels may also be considered as genuine, but it places the load factor in the transitional range which is nowhere near the base of the curve, especially for the more realistic GNA analyses. Given the difficulty inherent in accurately predicting flow channel sizes, prescribing mid-sized channels or larger may help to obtain a conservative design for this dangerous load case by ensuring that only the lowest load factors are considered.

Consequently, it is recommended that the LBA range should be limited to $0.20 \leq k_c \leq 0.70$. The GNA range should be limited instead to $0.40 \leq k_c \leq 0.70$, since the characteristic eccentric discharge pattern requires a larger channel to develop when geometric nonlinearity is included. Each of these may then be referred to as a ‘central range’. If three suitable values of k_c are specifically required, they may be taken as 0.40, 0.55 and 0.70.

5.5 The beneficial effect of geometric nonlinearity based on the EN 1991-4 flow channel size study

The features of greatest interest in this structural analysis are the extent to which the compressive membrane stresses, which are responsible for buckling, are spread around the circumference, how large they become and the differences between their predictions by LA or GNA analyses. Considering once again the distributions of Fig. 5.10 and Fig. 5.11, it may be identified that the compressive region of axial membrane stress resultants directly adjacent to the flow channel centre has a maximum value (a 'magnitude') and a maximum circumferential extent (a 'spread') before the values become tensile. These parameters are extracted from the LA and GNA analyses and shown in Fig. 5.14 as a function of k_c in the central range.

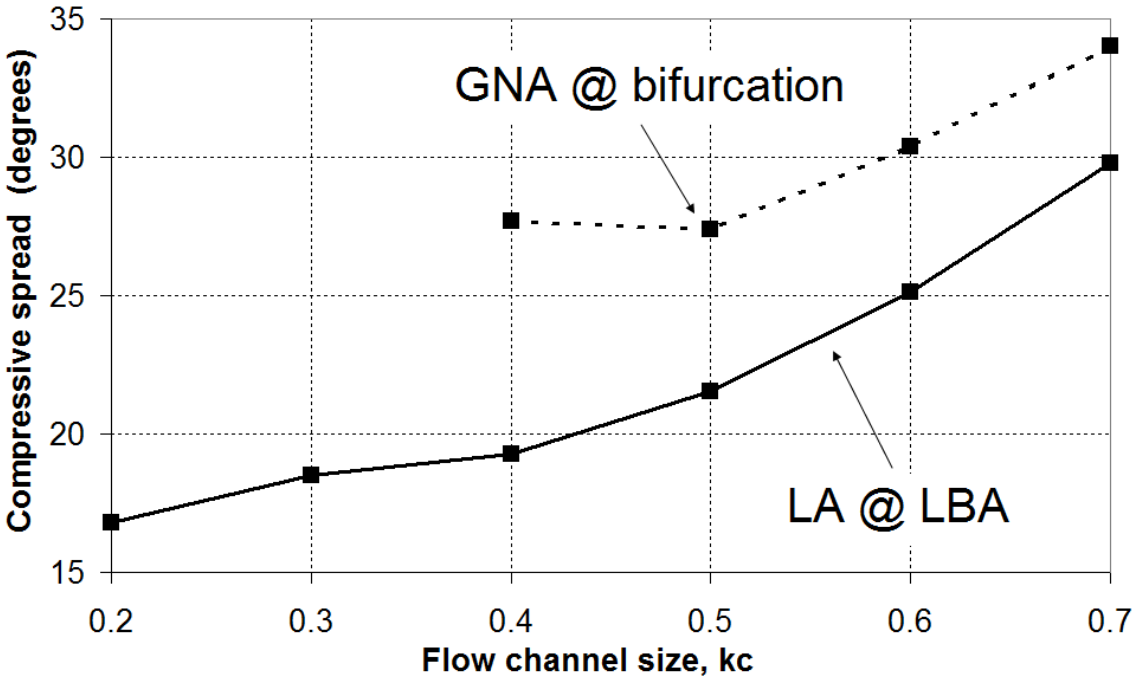

a) Variation of the compressive spread with relative flow channel size k_c

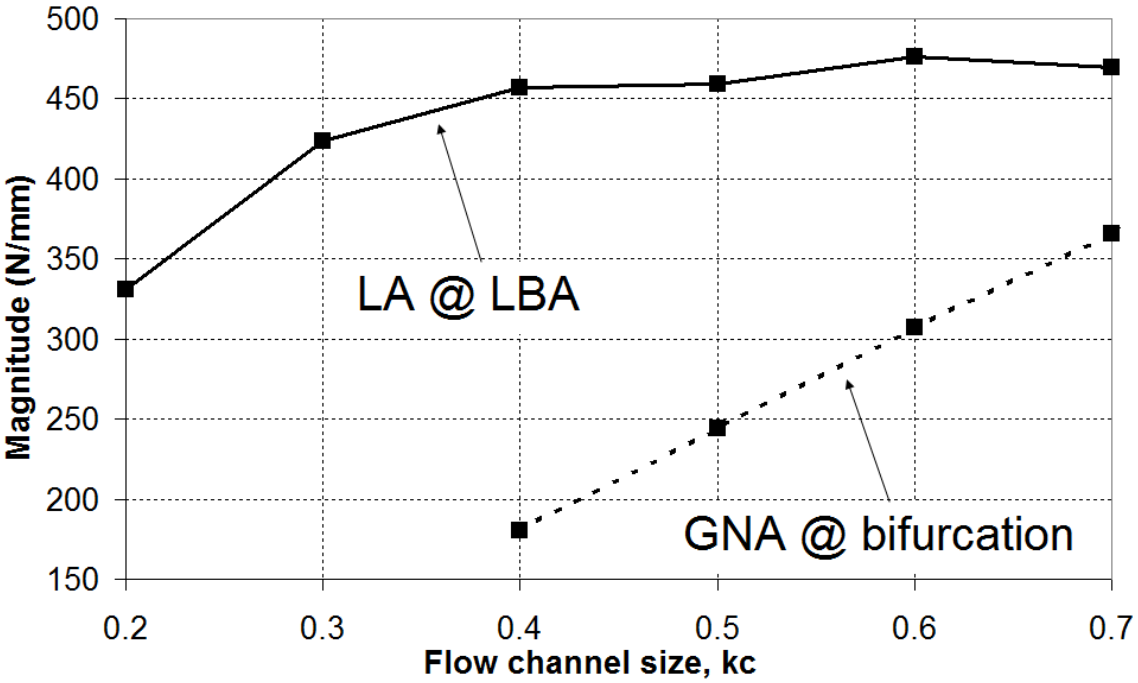

b) Variation of the peak compressive magnitude with relative flow channel size k_c

Fig. 5.14 – Variation of two measures of the central compressive region of axial membrane stresses at the base of the 3 mm strake with relative channel size k_c in the central range

The general pattern apparent in Fig. 5.14 is that the spread of the compressive region increases steadily with the flow channel size while at the same time decreasing in peak magnitude. The compressive stresses therefore become lower, but more spread out, as the flow channel increases. The compressive stresses from a GNA analysis, however, cover a significantly larger spread of the silo wall whilst at the same time attaining a lower maximum value than those from a LA analysis.

Geometric nonlinearity therefore reveals that the portion of the shell mobilised to resist the effects of the eccentric pipe flow channel is actually greater than that predicted by the linear assumption. This in turn results in lower overall magnitudes of compressive stresses, and consequently higher buckling loads. The beneficial effect of the change of geometry is substantial, and in the central k_c range it may lead to an increase in load factor by as much as 75%. This phenomenon has been documented previously in Chapter 3 and is shown here to be consistent across the entire range of flow channel sizes.

5.6 The effect of eigenmode-affine imperfections under eccentric discharge

The results of a suite of elastic computational analyses for the imperfect shell (GNIA) are summarised in Table 5.3 and plotted in Fig. 5.15 as a function of the relative flow channel size k_c.

Table 5.3 – Load proportionality factors for the imperfect shell

k_c	0.00	0.10	0.20	0.25	0.30	0.40	0.50	0.60	0.70	0.80	0.90
GNA	7.63	6.77	4.51	2.55	0.81	0.49	0.33	0.37	0.41	0.63	1.18
GNIA#1 †	3.32	6.03	4.51	3.44	2.37	2.66	0.20	1.58	0.16	0.26	0.69
GNIA#2 ‡	3.40	6.15	4.58	3.43	2.04	2.55	1.31	1.59	0.17	0.25	0.66
GNIA#3 *	5.21	4.33	5.93	6.98	3.03	3.43	0.80	0.49	0.41	0.59	0.94

† - calculated 1st LBA mode (‘outward’)

‡ - reversed 1st LBA mode (‘inward’ - as required by EN 1993-1-6)

* - deformed GNA shape just before bifurcation

The LBA eigenmodes are always scaled to deliver a peak value of unity. The amplitude of the LBA imperfections was therefore chosen as the EN 1993-1-6 Annex D value for direct design (Table 4.5) corresponding the strake in which the peak occurs in the LBA mode. In this study this peak always lay within the thinnest 3 mm strake.

In the case of GNA buckling modes, the procedure was similar but the maximum absolute radial displacement from a GNA analysis at the increment just before bifurcation was first factored to unity, before being factored again to the required EN 1993-1-6 Annex D direct design value corresponding to the imperfection amplitude of the strake in which it occurred. In GNA analyses, the maximum radial displacement did *not* always occur at the base of the 3 mm strake.

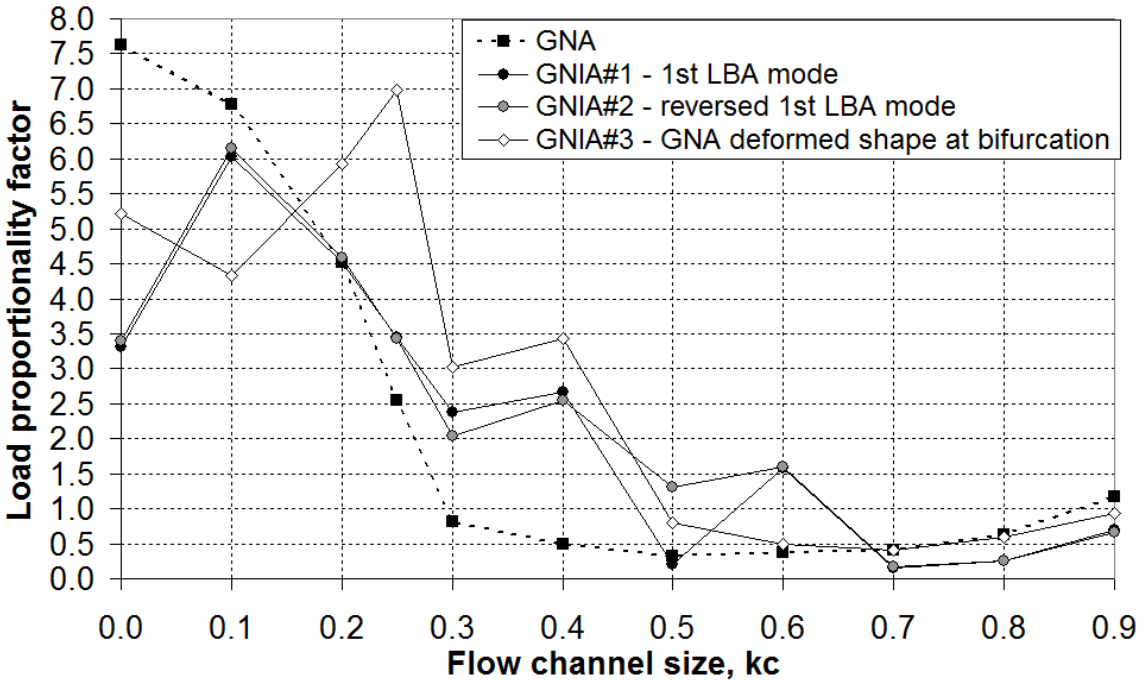

Fig. 5.15 – Variation of the load proportionality factor for the imperfect shell with flow channel size

The first LBA buckling eigenmodes are shown in Fig. 5.6 and it is evident that their shape depends directly on the value of k_c. The deformed GNA shapes at bifurcation are similarly dependent on the channel size. Eigenmode-affine imperfections are always dependent on the geometry and the load case in a way that makes them impossible to predict in advance, unlike imperfections based directly on structural forms which may be expressed by a neat equation (such as the previously-used axisymmetric weld of Rotter and Teng, 1989a).

It is evident in Fig. 5.15 that the effect of an eigenmode-affine imperfection on the silo strength is variable and may result in either an increase or a decrease in strength in what appears to be a random manner. However, in the range of k_c values of $0.20 \leq k_c \leq 0.70$, the effect of the all three of these imperfection forms seems to be consistently beneficial.

All LBA buckling modes consist of a series of tightly-spaced alternating inward and outward indentations in the silo wall adjacent to the centre of the flow channel at the bottom of the thinnest strake. The GNA pre-buckling deformations similarly include significant indentations due to axial bending at the change of plate thickness that are amplified by the high axial compression at this location (Brush and Almroth, 1976;

Rotter, 1989), which are taken as a part of the imperfection form used in the GNIA analysis. It appears that this type of imperfection results in a beneficial stiffening effect against the circumferential bending that occurs in the shell adjacent to the flow channel as a result of the pressure drop (Fig. 5.16), in a manner almost identical to the axisymmetric weld imperfection (Fig. 4.28). This phenomenon is explained in detail in Section 6.4.

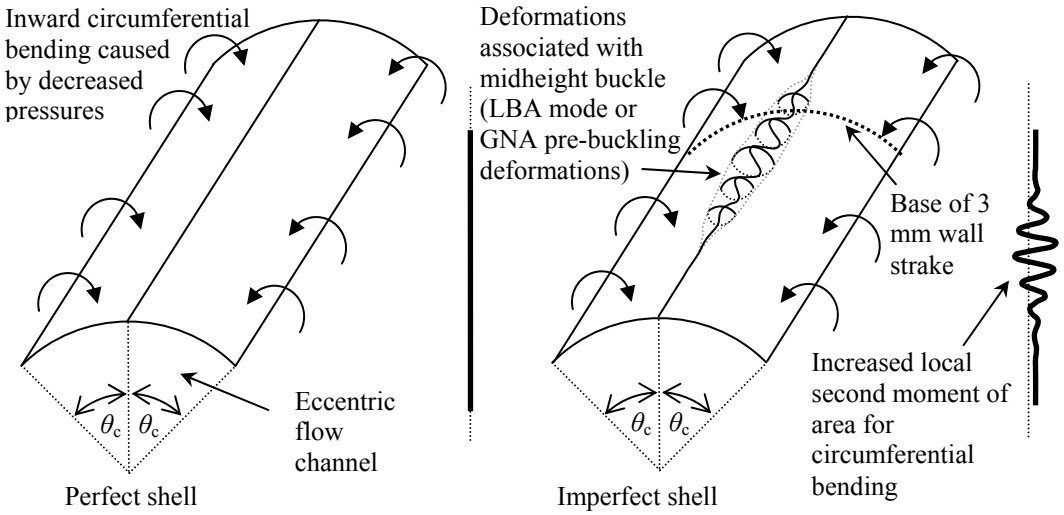

Fig. 5.16 – Comparison of the behaviour of perfect and imperfect shells with eigenmode-affine imperfections

Thus the imperfection forms investigated so far have all had the unfortunate characteristic that they produce a specific geometric configuration at the very location where it becomes favourable. Given that the elastic midheight buckle is a ubiquitous computational prediction for slender silos under eccentric pipe flow, this characteristic will be a part of every LBA mode and GNA shape and there is no way to avoid this. Eigenmode-affine imperfection forms therefore cannot be relied upon to give strength decreases for the silo under eccentric discharge.

An analysis of the GNA deformed radial shape at bifurcation, in the context of a beam theory analogy, is presented in Appendix A. The closer study of the GNA deformed shape allowed the extraction of a set of detrimental geometric components from which a suitable imperfection form was able to be constructed. A parametric study of a novel imperfection form that has been found to result in consistent decreases in buckling strength of the silo under eccentric discharge is presented in detail in Chapter 6.

5.7 Conclusions

In this chapter, the structural effects of the variation of the size of an eccentric pipe flow channel according to the EN 1991-4 eccentric discharge pressure model were investigated in greater depth. The smallest channel was taken as $k_c = 0.10$ and the largest one as $k_c = 0.90$, thus covering most of the practical range of flow channel sizes. The example silo used had been previously designed for concentric discharge pressures according to EN 1991-4 and EN 1993-1-6.

The author recommends that the range of values for k_c should be limited to $0.20 \leq k_c \leq 0.70$ for geometrically linear analyses, and to $0.40 \leq k_c \leq 0.70$ for geometrically nonlinear analyses. Three suitable values of k_c may be taken as 0.40, 0.55 and 0.70.

It has been revealed that, when geometric nonlinearity is included, a greater circumferential portion of the silo wall is mobilised to carry a greater portion of the compressive stresses which develop in the channel centre during eccentric discharge. This in turn reduces their magnitude at the centre, and leads to significant gains in buckling strengths. A geometrically linear analysis does not capture this phenomenon, resulting in higher stresses and lower predicted buckling strengths.

This study also investigated the effect of eigenmode-affine imperfections in the form of variants of the first LBA mode and the GNA deformed shape just before bifurcation. It has been found that these imperfections are of a unique form under eccentric discharge that provides effective stiffening against circumferential bending in a manner similar to the axisymmetric weld imperfection, and hence have a beneficial effect on the structure.

Chapter 6 – Exploration of geometric imperfection forms in buckling failures arising from the EN 1991-4 eccentric discharge model

6.1 Introduction

It was established in Chapter 4 that the axisymmetric weld depression of Rotter and Teng (1989a), widely used in many other studies (e.g. Rotter and Zhang, 1990; Knödel *et al.*, 1995; 1996; Knödel & Ummenhofer, 1996; Ummenhofer & Knödel, 1996; Song *et al.*, 2004; Hübner *et al.*, 2006; Rotter, 2008), is not an appropriately damaging imperfection form for silos under eccentric discharge. This was due to the beneficial properties of the weld depression under this particular form of loading, as it was found to increase the circumferential bending stiffness of the shell and thus result in higher predicted buckling strengths. In Chapter 5, the non-symmetric eigenmode-affine imperfection forms under eccentric discharge were investigated as an alternative, but the results proved equally unsatisfactory, for many of the same reasons. In Chapter 3, however, it was shown that flattening of the silo wall adjacent to the flow channel causes a reduction in strength in geometrically nonlinear analyses. It was thus realised that the flattened wall feature may be exploited as the foundation of a reliable imperfection form under eccentric discharge.

6.2 Imperfection amplitudes and tolerances in EN 1993-1-6

For computational analyses, Section 8 of EN 1993-1-6 (2007) requires a number of geometric tolerance limits to be observed for the buckling limit state (LS3). These tolerances relate to the maximum allowable extents of various possible geometric deficiencies which may be present in the silo upon construction, and the onus is on the builders to meet these in accordance with the standard. Such tolerances specifically control for out-of-roundness, accidental eccentricity/offset of joints and dimples (axial, circumferential and across welds). The maximum allowable tolerance is related directly to the assumed Fabrication Tolerance Quality Class of the silo which, as stated previously, allows the designer to use lower imperfection amplitudes and thus rewards those involved with a higher permissible silo strength if stricter tolerances are met in construction. The Classes range from ‘Excellent’ (best) to ‘Normal’ (worst), and all silos in this thesis were designed to the ‘Normal’ class, requiring higher imperfection

amplitudes and thicker walls, but allowing laxer tolerances. Tolerances were discussed in Section 1.3.5 of the literature review.

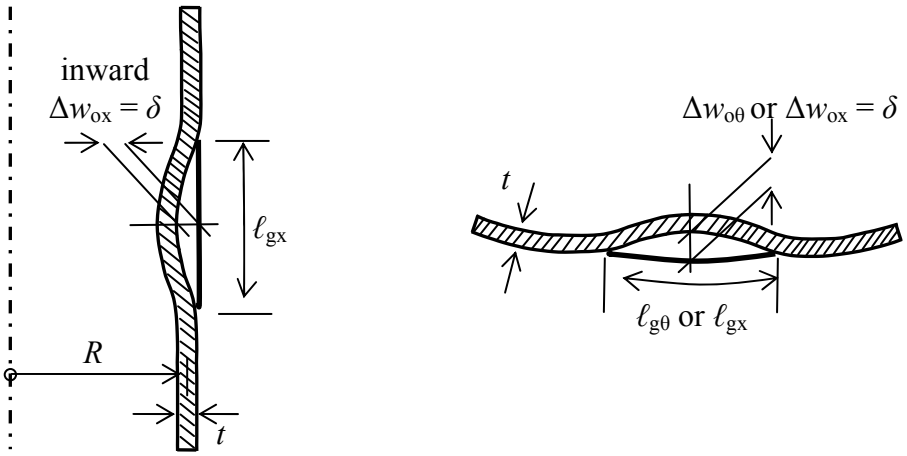

a) Measurement on a meridian

b) First and second measurements on a circumferential circle

Fig. 6.1 − Select dimple tolerance measures from EN 1993-1-6 (2007)

The rules of Section 8 of EN 1993-1-6 (2007) are considered so important in the context of the present study that the relevant ones are reproduced here verbatim. Clause 8.7.2(18) states that:

"The amplitude of the adopted equivalent geometric imperfection form should be taken as dependent on the fabrication tolerance quality class. The maximum deviation of the geometry of the equivalent imperfection from the perfect shape $\Delta w_{0,eq}$ should be the larger of $\Delta w_{0,eq,1}$ and $\Delta w_{0,eq,2}$ where:

$\Delta w_{0,eq,1} = \ell_g U_{n1}$ and $\Delta w_{0,eq,2} = n_i t U_{n2}$"

For all the design silos presented in Chapter 4, it was found that that $\Delta w_{0,eq,1}$ always gave the largest imperfection amplitude. Hence it was considered necessary to analyse the rules for this equation only, in which ℓ_g is the relevant gauge length according to Clause 8.4.4(2) and U_{n1} is the dimple imperfection amplitude parameter for the relevant fabrication tolerance quality class.

Further to the present discussion, Clause 8.4.4(2) states that:

"The depth Δw_0 of initial dimples in the shell wall should be measured using gauges of length ℓ_g which should be taken as follows:

a) Wherever meridional compressive stresses are present, including across welds, measurements should be made in both the meridional and circumferential directions, using a gauge of length ℓ_{gx} given by $4(Rt)^{½}$;
b) Where circumferential compressive stresses or shear stresses occur, circumferential direction measurements should be made using the gauge of length $\ell_{g\theta}$ given by $2.3(\ell^2 Rt)^{¼}$ but $\ell_{g\theta} \leq R$ where ℓ is the meridional length the shell segment... ”

There is a further part c) on gauge measurements across welds, but this was not considered important in the present study. The meridional length of the shell segment ℓ may be taken as the distance between ring stiffeners (if present), or the length between a boundary and a change of plate thickness The tolerance measurements for meridional and circumferential dimples are shown in Fig. 6.1. It has been shown that local axial compression is the critical buckling condition in a thin-walled silo under eccentric discharge, so part a) of Clause 8.4.4(2) above would strictly apply.

In Chapter 4 of this thesis, the designs of seven silos were introduced together with the prescribed imperfection amplitudes for every wall strake (Table 4.6). For example, the EN 1993-1-6 GMNIA imperfection amplitude according to Clause 8.7.2(18) for the 3 mm strake of Silo CS was $3.162t$, based on a meridional gauge of length $\ell_{gx} = 4(Rt)^{½} =$ 379.5 mm. The meridional gauge was used in accordance with part a) of Clause 8.4.4(2) above because the silos were originally designed for concentric discharge and only meridional compressive stresses were expected. If it were necessary to consider compressive circumferential stresses too, the circumferential gauge length would be $\ell_{g\theta} = 2.3(\ell^2 Rt)^{¼} = 1763.9$ mm and the corresponding imperfection amplitude for the 3 mm strake would be a much higher value of $14.935t$, but extending over a much larger surface of the shell. The tolerance-based imperfection amplitudes according to Section 8 of EN 1993-1-6 for the thinnest strakes of Silos CS and CVS are summarised in Table 6.1.

It has been discussed extensively so far in this thesis that eccentric discharge results in critical meridional compression at the centre of the flow channel, so a strict reading of the rules of EN 1993-1-6 leads to a value of $3.162t$ for the imperfection amplitude. However, there is also extensive circumferential bending at the centre of the flow channel which results in circumferential dimple-like deformations which, it will be

shown in this chapter, are a necessary basis for a consistently deleterious imperfection form under eccentric discharge. It is therefore unclear whether the standard should use Clause 8.7.2(18), which defines the GMNIA imperfection amplitude, to couple with the limitations of Clause 8.4.4(2), which was written in the context of uniform stress states. Perhaps long-wave imperfection forms of the type that will be presented here should be an additional requirement where the axial compression is *localised*. However, given the rules as they stand, this study is chiefly conducted in the context of the strict EN 1993-1-6 rules, but with one eye on the possibility that the rule should be amended to require control of long circumferential wavelength imperfections under all stress conditions.

Table 6.1 − Translations of selected tolerances into GMNIA imperfection amplitudes according to EN 1993-1-6 (2007) Section 8

Fabrication tolerance quality class	Description	Dimple imperfection amplitude parameter U_{n1}	Equivalent imperfection amplitude δ/t			
			Meridional dimple $\Delta w_{ox}/t$		Circumferential dimple $\Delta w_{o\theta}/t$	
			Silo CS†	Silo CVS‡	Silo CS†	Silo CVS‡
A	Excellent	0.010	1.265	1.155	5.880	5.708
B	High	0.016	2.024	1.878	9.408	9.132
C	**Normal**	**0.025**	**3.162**	**2.887**	**14.700**	**14.269**

† assuming Silo CS data and the top strake (ℓ = 6.2 m, R = 3 m, t = 3 mm) with $\ell_{gx} = 4(Rt)^{1/2}$ = 379.5 mm and $\ell_{g\theta} = 2.3(\ell^2 Rt)^{1/4}$ = 1763.9 mm

‡ assuming Silo CVS data and the top strake (ℓ = 6.4 m, R = 2.5 m, t = 3 mm) with $\ell_{gx} = 4(Rt)^{1/2}$ = 346.4 mm and $\ell_{g\theta} = 2.3(\ell^2 Rt)^{1/4}$ = 1712.3 mm

6.3 Characteristic features of the deformed radial shape of the silo

A typical pre-buckling deformed shape of a slender silo under the EN 1991-4 (2007) eccentric discharge model is shown in Fig. 6.2. The silo wall undergoes extensive inward deformation due to the low pressure in the flow channel which results in flattening of the silo wall, and extensive outward deformation due to the rise in normal pressure at the edge of the flow channel. The representative circumferential and meridional distributions of the deformed radial shape of a slender silo before buckling

under eccentric discharge are shown in Fig. 6.3 and Fig. 6.4 respectively. The deformed shape at the level through the critical buckling region (Fig. 6.3) is usually near midheight in uniform wall thickness silos or near the base of the thinnest wall strake in stepped wall thickness silos.

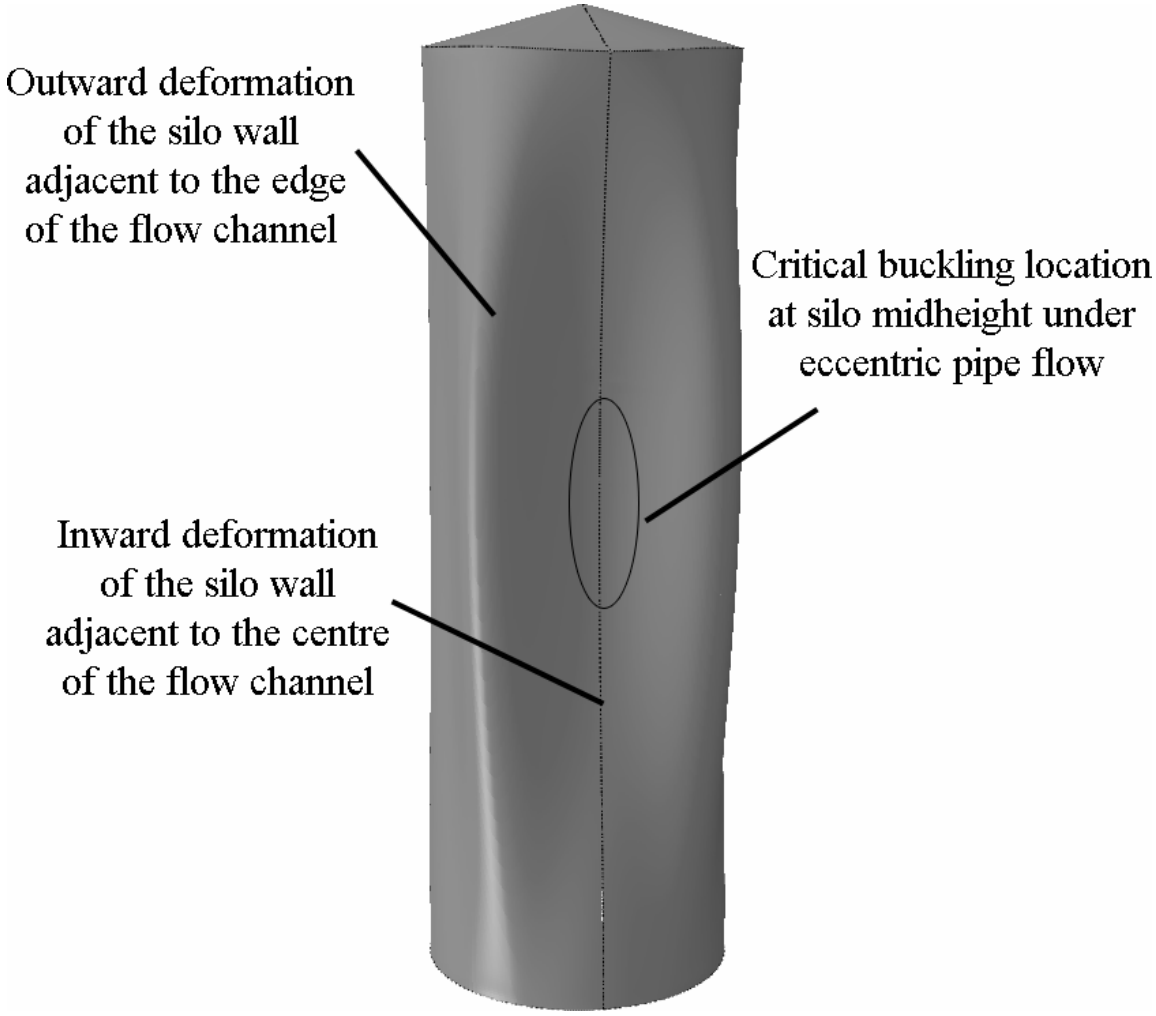

Fig. 6.2 – Typical global deformed shape of a slender silo under eccentric pipe flow

Three main radial deformation features at these locations may be identified on Fig. 6.3. There is a large primary inward deformation feature adjacent to the low wall pressure in the flow channel; a smaller primary outward deformation feature adjacent to the steep rise in wall pressure at the edge of the flow channel; and a much smaller secondary inward deformation feature further around the shell circumference. The eccentric discharge model of Rotter (1986), which does not feature regions of high pressure near the edge of the flow channel unlike EN 1991-4 (2007) (e.g. Fig. 3.1), results in a very similar deformed shape on which the same radial features may be identified.

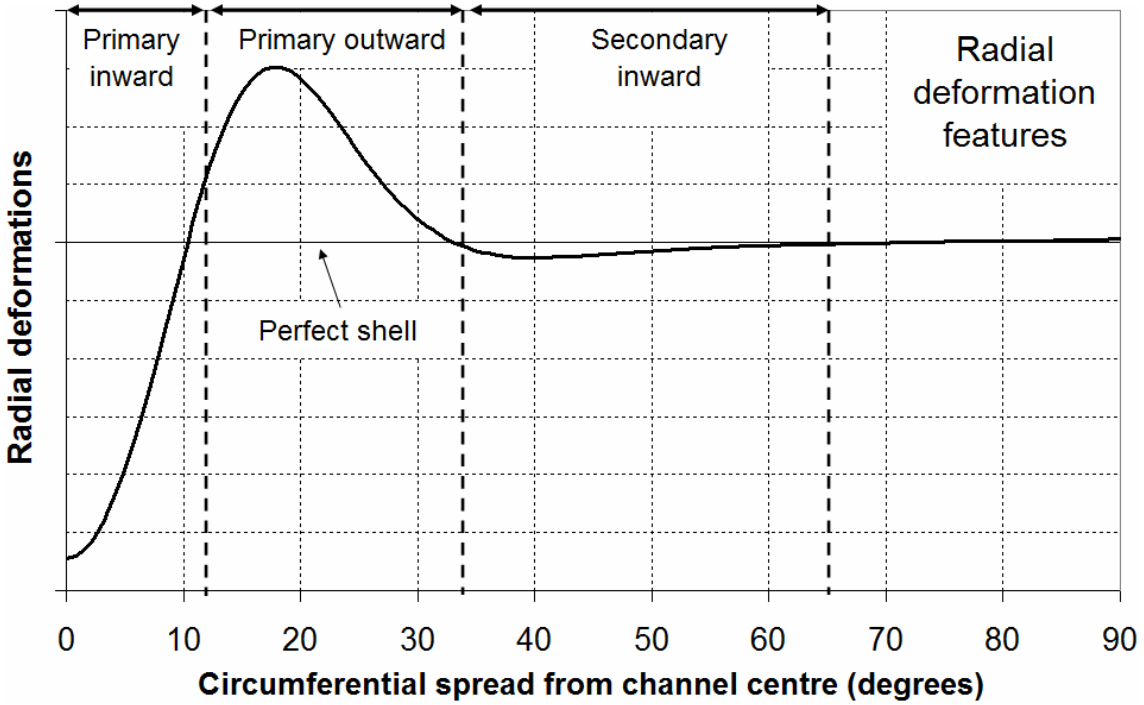

Fig. 6.3 – Circumferential distribution of typical radial deformations near midheight of a slender silo under eccentric pipe flow

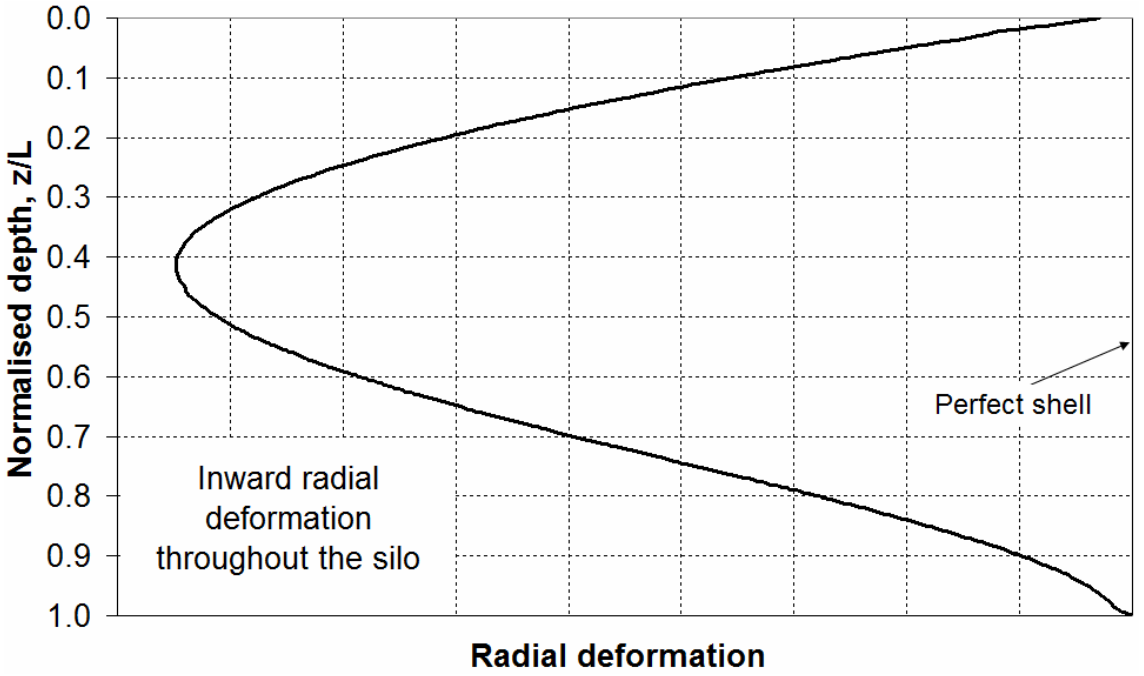

Fig. 6.4 – Meridional distribution of typical radial deformations of a slender silo under eccentric pipe flow

It is known that the buckling strength of a curved panel is reduced as the panel becomes flattened and its radius to thickness ratio R/t increases (Rotter, 1985a), and it was noted in Chapter 3 that this nonlinear phenomenon does indeed have a deleterious effect on

the buckling strength of the silo under eccentric discharge. Thus, a geometric imperfection form which reproduces this feature is likely to be successful in causing consistent decreases in the predicted buckling strength where other imperfection forms have failed to do so. The reader is reminded that the axisymmetric weld and eigenmode-affine imperfection forms studied in Chapters 4 and 5 were found to be unsuitable for this purpose.

6.4 Introduction to the global imperfection forms used in this study

In the voluminous literature on buckling of imperfect shells, the form of an imperfection has traditionally been defined in terms of a local perturbation that is superimposed on the perfect shell (e.g. Koiter, 1945; 1963; Yamaki, 1984; Rotter and Teng, 1989a). Thus the circumferential and meridional distributions of the imperfection are usually defined through some relation in the form $\delta = f(\theta, y)$, which is then applied to the perfect shell to generate the local geometry of the imperfect shell.

In a break from this tradition, the imperfection forms presented in this chapter define the total geometry of the entire imperfect shell directly, though still relating the deviation from the perfect shell to a reference imperfection amplitude at some point in the structure δ_0. Considering the deformed shape in Fig. 6.3 and the complexity involved in defining a successful imperfection form for a global load condition like eccentric discharge, it was felt that a new description is necessary in order to ensure full control over the exact shape of the entire imperfect shell. Thus in all analyses of the imperfect shell presented in this chapter, the global radial coordinate of the imperfect silo wall r is defined by:

$$r(\theta, y) = R - \delta(\theta, y) \text{ such that } \delta(\theta, y) = u(\theta)\, w(y) \qquad (6.1)$$

where $u(\theta)$ and $w(y)$ are, respectively, the independent circumferential and meridional distributions of the radial form of the imperfection. The range is, naturally, $0 \le \theta \le 2\pi$ and $0 \le y \le H$, where H is the height of the silo.

Various different forms for the circumferential component $u(\theta)$ were investigated in this imperfection study, which will be presented shortly. However, the meridional component of the imperfection $w(y)$ was in all cases assigned a two-part sinusoidal variation comprised of two sine quarter-waves whose junction (and therefore peak

amplitude) occurs at some height y_0, illustrated in Fig. 6.5. The form of the meridional component is thus given by:

$$w(y)=\begin{cases}\sin\left(\dfrac{y}{2y_0}\pi\right) & \text{for } 0\le y\le y_0\\ \sin\left(\dfrac{(H-y)}{2(H-y_0)}\pi\right) & \text{for } y_0\le y\le H\end{cases} \tag{6.2}$$

The meridional form of the imperfection is similar to the observed meridional distribution of the radial deformation at the centre of the channel (Fig. 6.4). The composite function in Eq. 6.2 obeys continuity of displacement and slope at y_0, but not of curvature. It was thought that this would be satisfactory for the purposes of an imperfection form, since y_0 usually occurs near midheight (see below) and the error in the curvature is thus expected to be small.

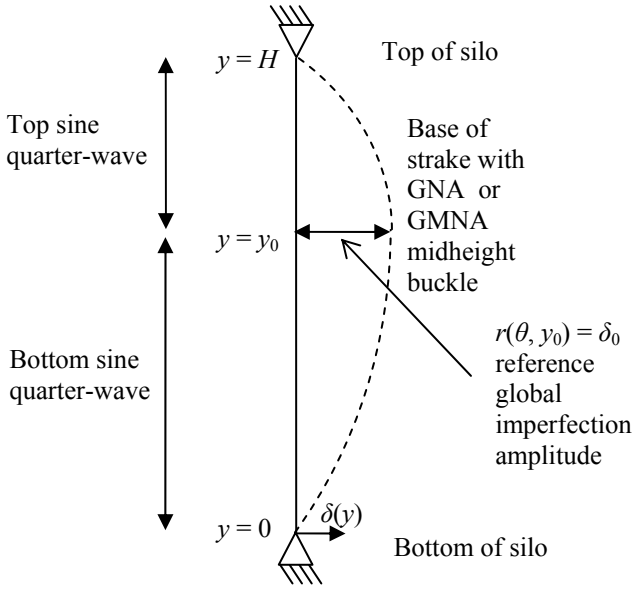

Fig. 6.5 − Meridional form $w(y)$ of the imperfect shell

In Chapter 5 it was found that the characteristic buckling mode of a stepwise variable thickness silo, under the pressures predicted by the EN 1991-4 eccentric discharge model, occurs across the channel near midheight (mode Loc-CH, Table 4.8). The buckle is predominantly elastic, and is caused by greatly increased axial compressive membrane stresses at this location. In order to maximise the effectiveness of the imperfection forms presented in this chapter, it is supposed that the base of the strake in which the elastic midheight buckle is predicted to occur in a GNA or GMNA analysis

should be identified, and that this location defines y_0. Thus $w(y)$ may be adjusted so that the highest flattening of the shell occurs close to the location where it is likely to be most detrimental, notably at the base of the critical strake. If a uniform wall silo is being analysed instead, y_0 is here proposed as the midheight position unless there is reason to do otherwise. In Silos CS and CVS, for example, y_0 is given by $0.66H$ and $0.76H$ respectively.

There have been many proposals to use the deformed shape from a GNA analyis as an appropriate imperfection (Esslinger and Geier, 1972; Yamaki, 1984; Guggenberger *et al.*, 2004; Rotter, 2004), and this would have been a natural choice for an imperfection mode in this study. It is thus important to explain why the deformed shape from a GNA analysis cannot be used directly as an imperfection form for the present load case, considering that the imperfection forms that are presented in this chapter clearly drew on the features of the GNA deformed shape. The most important reason for this is that previous studies were all concerned with shells of uniform wall thickness, so they all lost the critical feature that arises in a stepped wall shell as a result of the discontinuities at changes of plate thickness.

Eigenmode-affine imperfection forms under eccentric discharge were explored in Section 5.6, where it was found that the GNA pre-buckling deformations near the location of the future buckle may be quite significant and that they form a part of the GNA deformed shape both before and after bifurcation. These deformations include a significant component that arises from the geometric discontinuity at the change of plate thickness at the base of the 3 mm strake. Here, local indentations due to the axial bending induced induced by the discontinuity are amplified at the centre of the channel by the axial compressive membrane stresses caused by eccentric discharge (e.g Fig. 2.9) as they approach the elastic critical stress (Brush and Almroth, 1976; Rotter, 1989). The result is that approximately axisymmetric waves develop above the change of plate thickness as the buckling condition is approached (Fig. 6.6, similar to Fig. 5.16). These wide axially-short waves in the deformed shape lead to a significant increase in the incremental value of the circumferential bending stiffness of the shell, leading to an increase in its resistance to buckling.

Thus when such a deformed shape is used as an imperfection form, these local waves are also introduced near the critical location and increase the circumferential bending stiffness of the shell in a manner similar to the axisymmetric weld. This has a beneficial effect on the buckling strength of the silo. The GNA deformed shape therefore cannot be used directly as an imperfection form under eccentric discharge, though its general overall geometric features can be. In what follows, these overall geometric features are isolated and approximately represented, thus leaving out the local effects associated with plate thickness change discontinuities. The necessity of taking this action also has significant implications for the more general specification of appropriate imperfection forms in cylinders with stepwise variable walls.

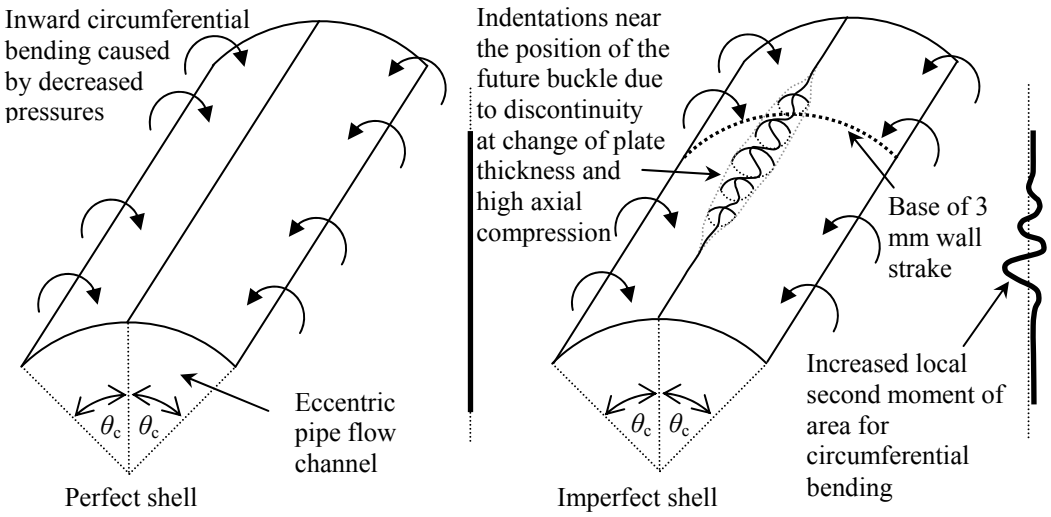

Fig. 6.6 – Comparison of the behaviour of perfect and imperfect shells with an imperfection form of the GNA deformed shape before, before and after buckling

6.5 Investigation of an imperfection form with local circular flattening

6.5.1 Definition of the shape of the imperfect shell

A relatively simple geometric form of local wall flattening was investigated first. An arc of the original circular wall adjacent to the flow channel was replaced with an arc of a circle with a larger radius of curvature, thereby making the wall locally flatter up to a local maximum imperfection amplitude of δ_0 at a height of y_0. This effectively omits both the secondary inward and primary outward radial features seen in Fig. 6.3, and includes only the primary central radial inward feature. The radial geometry of this imperfection form is shown in Fig. 6.7. A similar imperfection form has been used

previously in studies of the buckling of spherical caps under external pressure (e.g. Blachut *et al.*, 1990; Blachut and Galletly, 1987; 1990).

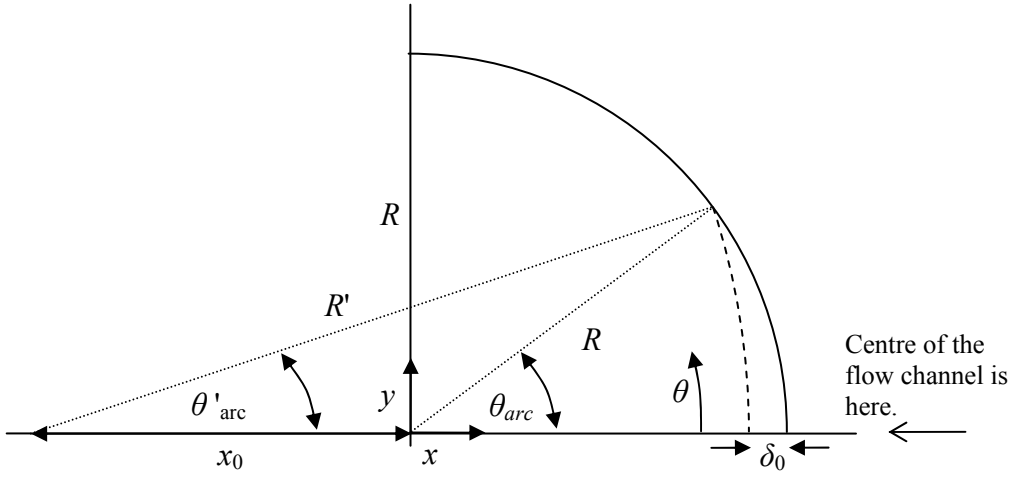

Fig. 6.7 − Geometry of local circular flattening imperfection form at height y_0

The limiting value of θ_{arc} is independent of y and may be chosen by the user as, for example, some multiple of the flow channel wall contact angle, θ_c (e.g. Fig. 5.1). The parameters x_0, R' and θ'_{arc} may be solved for numerically using the following compatibility relations:

$$R\sin\theta_{arc} = R'\sin\theta'_{arc} \tag{6.3}$$

$$x_0 + R\cos\theta_{arc} = R'\cos\theta'_{arc} \tag{6.4}$$

$$\delta_0 = x_0 + R - R' \tag{6.5}$$

Alternatively, an algebraic solution is also possible, though messy:

$$x_0 = \frac{b}{2a},\ R' = \frac{c}{2a} \text{ and } \theta'_c = \tan^{-1}\left(\frac{d}{f}\right) \tag{6.6}$$

where

$$a = \left(\delta_0 + R\cos\theta_{arc} - R\right),\ b = \delta_0\left(\delta_0 - 2R\right),\ c = 2\cos\theta_{arc}\left(R^2 - \delta_0 R\right) - 2R^2 + 2\delta_0 R - \delta_0^2$$

$$d = 2R\sin\theta_{arc}\left(\delta_0 + R\left(\cos\theta_{arc} - 1\right)\right),\ f = \delta_0^2 - 2\delta_0 R + 2R\cos\theta_{arc}\left(\delta_0 - R\left(1 - \cos\theta_{arc}\right)\right)$$

The arc of the flattened circle is assumed to retain the same sense of curvature, thus the following condition should additionally be satisfied:

$$\delta_0 < R\left(1 - \cos\theta_{arc}\right) \tag{6.7}$$

The coordinates of the circle with the larger radius of curvature are given by:

$$x(\theta) = (R - \delta_0)\cos\left(\theta \cdot \frac{\theta'_{arc}}{\theta_{arc}}\right) - x_0 \text{ and } y(\theta) = R\sin\left(\theta \frac{\theta'_{arc}}{\theta_{arc}}\right) \tag{6.8}$$

Thus the circumferential component of the radial form of the imperfection is given by:

$$u(\theta) = \begin{cases} R - \sqrt{x(\theta)^2 + y(\theta)^2} & \text{for } -\theta_{arc} \le \theta \le \theta_{arc} \\ 0 & \text{elsewhere} \end{cases} \tag{6.9}$$

The complete imperfect shell is thus generated by $r(\theta, y) = R - u(\theta)w(y)$ where $u(\theta)$ and $w(y)$ are given by Eqs 6.9 and 6.2 respectively. It is important to note that the flattened arc length $R' \times \theta'_{arc}$ is considerably smaller than the undeformed arc length $R \times \theta_{arc}$. Thus this imperfection form results in a shorter silo circumference, an undesirable feature which may have an unforeseen influence on the behaviour.

6.5.2 Parametric finite element study

The stepped wall thickness Silo CS (H/D = 3.0) was analysed under the eccentric discharge pressures of the Rotter (1986) model using the medium-sized flow channel ($k_c = r_c/R$ = 0.40). This model does not feature regions of high wall pressure at the edge of the flow channel and yields very similar behaviour to the EN 1991-4 eccentric discharge model, as discussed in Chapter 3. A number of GNIA analyses were carried out using a set of imperfection amplitudes in the range $0 \le \delta_0 \le 5t$, including the imperfection amplitude of the EN 1993-1-6 (2007) Section 8.7 GMNIA requirement of $3.162t$ (Table 6.1).

The spread of the flattened arc θ_{arc} was taken as several different multiples of the flow channel wall contact angle θ_c (in this case θ_c = 15.1°, Table 3.3). The values of θ_{arc} were thus chosen to be θ_c, $2\theta_c$, $4\theta_c$ and ½π. The resulting imperfection sensitivity curves, normalised by the GNA load factor (an already very low value of 0.30, Table 3.4), are shown in Fig. 6.8.

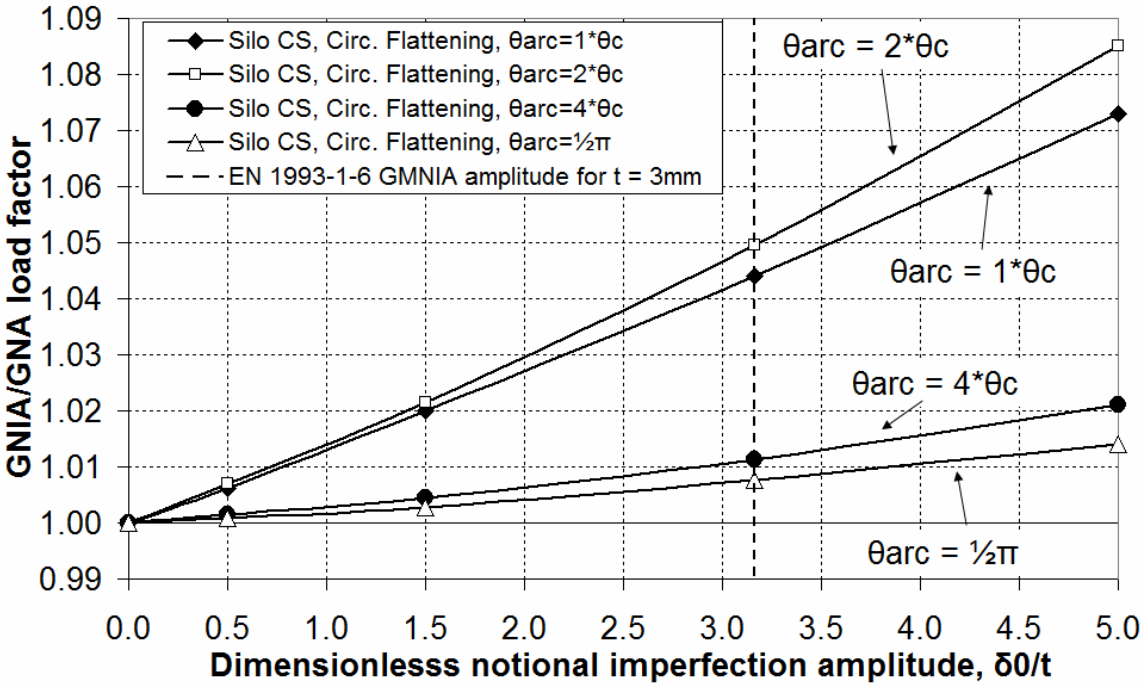

Fig. 6.8 − GNIA imperfection sensitivity curves for the local circular flattening imperfection using Rotter eccentric discharge pressures with k_c = 0.40 on Silo CS

Clearly, simply replacing an arc of the original shell with an arc of a shell of a larger radius of curvature adjacent to the flow channel does *not* serve the function of a strength-reducing imperfection under eccentric discharge. The localised flattened arc appears to have a similar strengthening effect as the axisymmetric weld and eigenmode-affine imperfection forms (Chapters 4 and 5), though it is not clear exactly why this is. This effect becomes significantly reduced as the spread of the arc increases, but does not disappear. The local flattened circular arc is therefore not a suitable imperfection form under eccentric discharge.

6.6 A novel superelliptical imperfection form

6.6.1 Lamé curves: the superellipse

It was found that the circumferential distribution of the radial deformation at midheight of the silo, close to the critical region for buckling under eccentric discharge (Fig. 6.3), can be expressed algebraically very closely by the generalised equation of the Lamé curve (Lamé, 1818; Gridgeman, 1970), otherwise known as the ‘superellipse’. The justification for this is presented in the following section, after a brief introduction to superelliptical shapes.

The general equation of the superellipse in Cartesian coordinates is defined by:

$$\left|\frac{x}{a}\right|^q + \left|\frac{y}{b}\right|^p = 1 \tag{6.10}$$

This may also be expressed parametrically in terms of t as:

$$x(t) = a\cos^{\frac{2}{q}} t \text{ and } y(t) = b\sin^{\frac{2}{p}} t \text{ such that } r(t) = \sqrt{x(t)^2 + y(t)^2} \tag{6.11}$$

where a, b, p and q are positive numbers, and $r(t)$ is the polar form of the radial coordinate.

The formula in Eq. 6.11 defines a closed curve in the range $-a \leq x \leq +a$ and $-b \leq y \leq +b$, where the parameters a and b are known as the 'semi-diameters'. The parameters p and q are the inverse powers of the *sin* and *cos* terms respectively, henceforth referred to simply as the 'powers'. Example curves for the special case of $a = b$, symmetrical about both Cartesian axes, are shown in Fig. 6.9a for $p, q \in \{1, 2, 3, 4\}$ and in Fig. 6.9b for slightly more unusual shapes with $p, q \in \{¼, 1, 5, 10\}$.

Assuming $a = b$, the powers $(p, q) = (1, 1)$ generate a diamond shape with straight sides while $(p, q) = (2, 2)$ generate a perfect circle. Values of either p or q less than unity cause the shape to appear squashed, with $(p, q) = (⅔, ⅔)$ resulting in a shape known as an 'astroid'. Curves with (p, q) both less than 2 are known as 'hypoellipses', while those with (p, q) both greater than 2 they are known as 'hyperellipses'. As both p and q increase, the resulting shape tends to one *resembling* a square with rounded corners, a so-called 'squircle'.

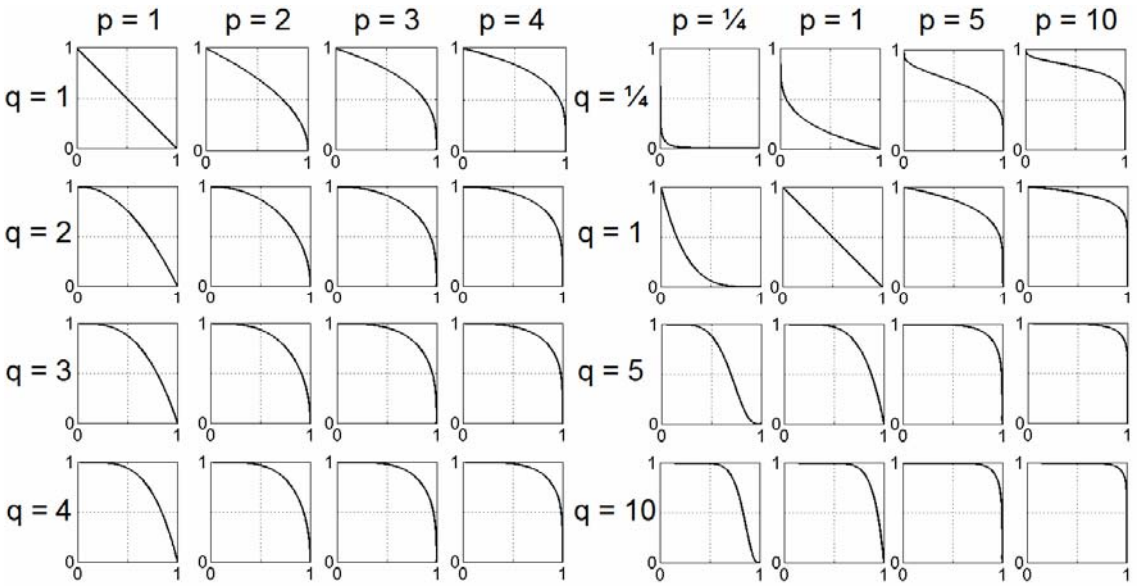

a) Common shapes b) More unusual shapes

Fig. 6.9 – General superellipse shapes as a function of the powers p and q

Clearly, a myriad of different geometries may be expressed with the superelliptical formula. A fascinating account of superelliptical forms seen in nature, including an even more general form of Eq. 6.11 known as the 'superformula', can be found in the botanical study of Gielis (2003).

6.6.2 The superellipse as an imperfection form under eccentric discharge

The radial deformation data of Silo CS (H/D = 3, Table 4.2), analysed under Rotter's (1986) eccentric discharge pressures with $k_c = r_c/R$ = 0.25, is shown in Fig. 6.10 normalised by the undeformed silo radius R. The data was extracted from an LA analysis at the LBA load factor and a GNA analysis at the instant before bifurcation, in both cases at the base of the thinnest 3 mm strake (thus $y_0 = 0.66H$). This location is close to midheight and to the critical region for elastic buckling under eccentric discharge. The three main features of the radial deformation identified on Fig. 6.3 are also shown in Fig. 6.10.

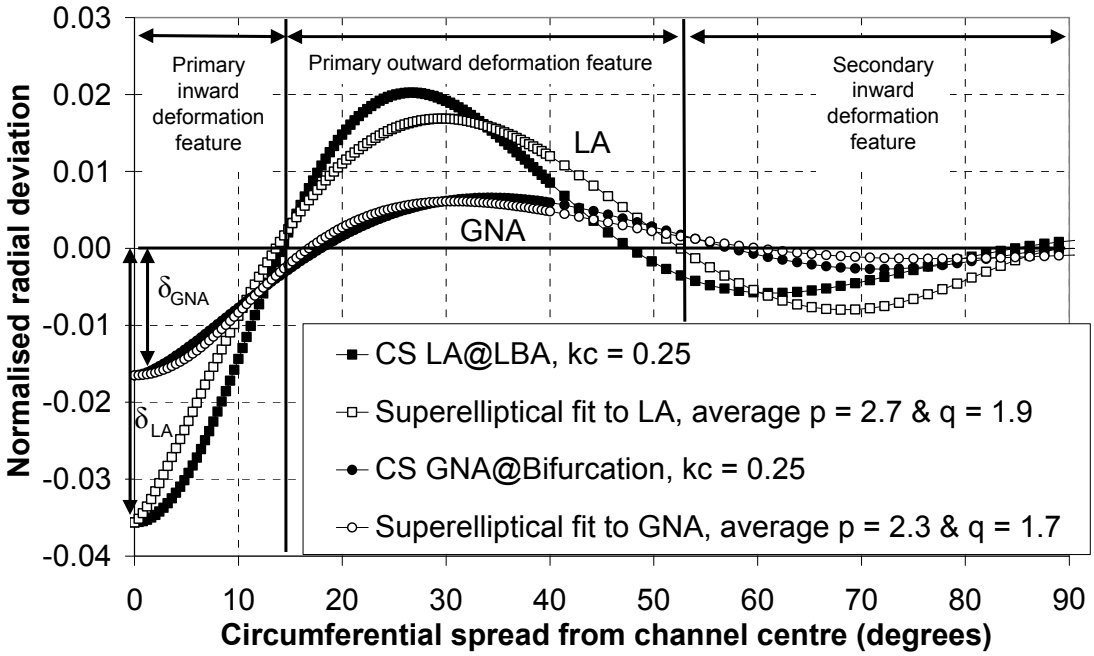

Fig. 6.10 – Normalised radial deviation at the base of the thinnest respective strake for the $k_c = 0.25$ flow channel in Silo CS with superelliptical fit

It was decided that the parametric form of the superellipse should be chosen in such a way as to be able to reproduce all three of the features of the radial deformation identified above. A possible form may therefore be given by:

$$x_s(\theta) = (R - \delta_0)\cos^{\frac{2}{q}}\theta \tag{6.12}$$

$$y_s(\theta) = R\sin^{\frac{2}{p}}\theta \tag{6.13}$$

The polar equation of the imperfect geometry is thus given by:

$$r_s(\theta) = \sqrt{x_s(\theta)^2 + y_s(\theta)^2} \tag{6.14}$$

where x_s and y_s are the Cartesian coordinates of the imperfect shell, R is the original perfect radius of the silo, δ_0 is the peak inward radial deviation adjacent to the centre of the flow channel at $\theta = 0$ (the characteristic imperfection amplitude), and p and q are the parameters controlling the shape of the *sin* and *cos* components respectively. It was assumed here that the centre of the flow channel is positioned on the x-axis. The radial component of the imperfection at constant y is thus given by:

$$u_s(\theta) = \begin{cases} R - r_s(\theta) & \text{for } -\dfrac{\pi}{2} \le \theta \le \dfrac{\pi}{2} \\ 0 & \text{elsewhere} \end{cases} \tag{6.15}$$

The imperfect shell is thus generated by

$$r(\theta, y) = R - u_s(\theta) w(y) \tag{6.16}$$

where $u_s(\theta)$ and $w(y)$ are given by Eqs 6.15 and 6.2 respectively.

A least-squares geometric fit of Eq. 6.14 to the radial data in Fig. 6.10 was performed to determine the values of p and q most representative of the deformed shape of Silo CS at buckling: these were found to be 2.9 and 1.7 for the LA data and 2.3 and 1.9 for the GNA data respectively. Therefore, roughly speaking, the shape of the inward deformation is controlled by a decreasing q power, and the shape of the outward deformation is controlled by an increasing p power. The LA analysis predicts higher magnitudes of the radial deformation than the GNA analysis, consistent with the respective predictions of the two analyses types on the magnitudes of the axial membrane stresses (Chapter 3). A full account of the geometric fitting procedure may be found in Appendix A.

6.6.3 Simple finite element study to probe the feasibility of the superelliptical imperfection form

A generalised version of the deformed shape shown in Fig. 6.3 and Fig. 6.10 could clearly form the basis of an imperfection form under eccentric pipe flow. As a first step, a preliminary set of finite element analyses was undertaken to probe the feasibility of doing a more detailed parametric study involving more elaborate and strictly-defined forms of the superellipse to model flattening as an imperfection form for this load condition.

The stepped wall Silo CVS was thus analysed under the EN 1991-4 eccentric discharge pressures with channel sizes in the range $0.00 \leq k_c = r_c/R \leq 0.90$. This was the same silo design as that used in the EN 1991-4 flow channel size study of Chapter 5, for the same range of flow channels. No specific imperfection amplitude δ_0 was defined in this preliminary analysis, as at this very early stage in this study the purpose was only to investigate whether a flattened shape adjacent to the flow channel, modelled by the superellipse, could produce a deleterious imperfection form over the full range of flow channel sizes. Further studies naturally included this important feature.

The geometry of the imperfect shell was thus modelled by Eq. 6.16 assuming $\delta_0 = 0$ for Eq. 6.12, which generates the primary outward and secondary inward radial features only (Fig. 6.10). The two sets of powers (p, q) of (2.9, 1.7) and (2.3, 1.9) reported above for the respective LA and GNA analyses of Silo CS were used to model the extent of the flattening, as no better guess could be made at the time of the study. The base of the thinnest strake of Silo CVS occurs at $y_0 = 0.75H$. The imperfect radial shapes at y_0 are shown in Fig. 6.11.

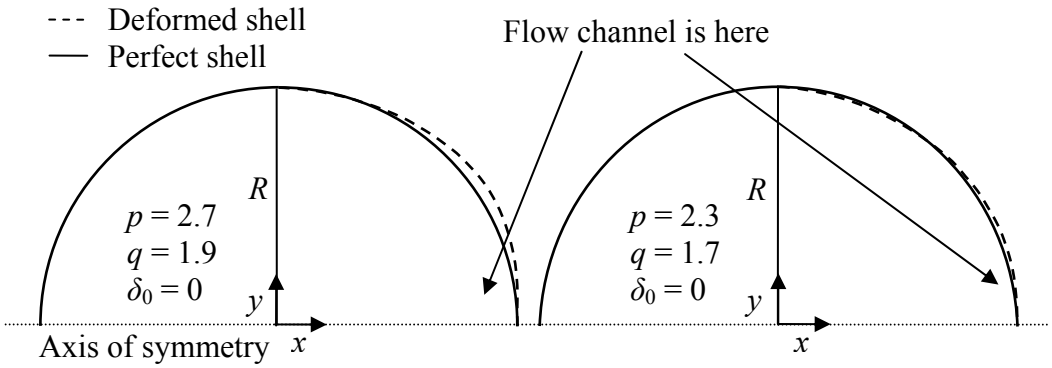

a) LA characteristic shape b) GNA characteristic shape

Fig. 6.11 – Flattened silo wall shapes for two sets of powers p and q at height y_0

The predicted GNIA load factors at buckling are summarised in Fig. 6.12, normalised by the respective GNA load factor for each value of k_c (Table 5.2). These figures show that this type of flattened shape may generally result in consistent reductions in predicted GNIA load factors from the GNA load factor over a wide range of flow channel sizes. The reduction in buckling strength may be as large as 35% for mid-sized values of k_c. There does, however, appear to be a rise in the predicted buckling strength for small channels ($0.2 \leq k_c \leq 0.4$) if the powers p and q representing the LA shape are used to model the superelliptical flattening, which produce larger deviation amplitudes than the powers representing the GNA shape. However, further investigations showed that this is the exception rather than the rule. These are presented shortly.

Additionally, a set of values of p and q originally derived for a deformed shape of Silo CS which included the central inward radial feature (Fig. 6.10) appear to be as effective in causing decreased buckling strengths in the significantly more slender Silo CVS which did not include this radial feature (Fig. 6.11). This suggests that an imperfection form modelled with the superellipse may have a high degree of robustness, and may be

valid over a wide range of imperfection amplitudes, different combinations of radial features and silo geometries.

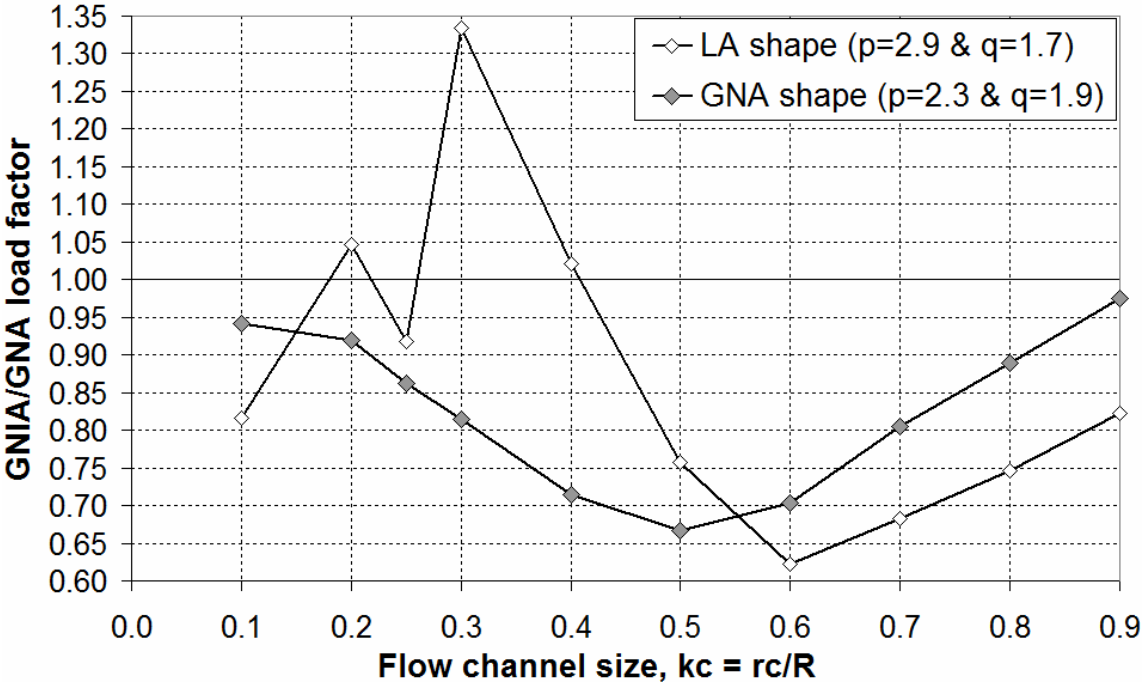

Fig. 6.12 − Variation of the GNIA load factor with flow channel size using the EN 1991-4 eccentric discharge pressures on Silo CVS

6.6.4 Preliminary conclusions

The initial investigation described in the preceding section suggested that the flattened superellipse is potentially a viable imperfection form to cause buckling strength reductions under eccentric discharge. It was thus decided that a more comprehensive investigation of this type of imperfection form would be worthwhile, and two different forms are explored in the following sections, inspired by the features of the deformed radial shapes identified in Fig. 6.3 and Fig. 6.10. It is thought that the imperfection forms presented in what follows have never been investigated before and because there is no precedent, it was therefore not known which combination of the radial features may produce significant structural effects and which would be the most deleterious circumferential form of the superelliptical imperfection.

6.7 First proposed form of the imperfection − Superelliptical flattening with central inward deviation

6.7.1 Circumferential geometry of the first imperfection form

The first proposed shape of the superelliptical imperfection form incorporates all three radial features identified in Fig. 6.10. The shell is allowed to deviate inwards adjacent to the flow channel at $\theta = 0$ up to a notional imperfection amplitude of δ_0 at the desired level of largest flattening y_0. The shell then deviates outwards to a peak amplitude of $n_a\delta_0$ at some coordinate $\theta = \theta_a$, and the inwards again to an amplitude of $n_b\delta_0$ at some coordinate $\theta = \theta_b$. Thus the amplitudes of the non-central peak deviations were assumed to be related to the central inward deviation by two parameters n_a and n_b which may be varied to control the flattened shape and to find the most deleterious configuration for the imperfection shape. The parameters n_a and n_b should be limited to being greater than zero, as otherwise the shape becomes inverted and fundamentally different. The geometry of the first superelliptical flattening imperfection form is shown in Fig. 6.13.

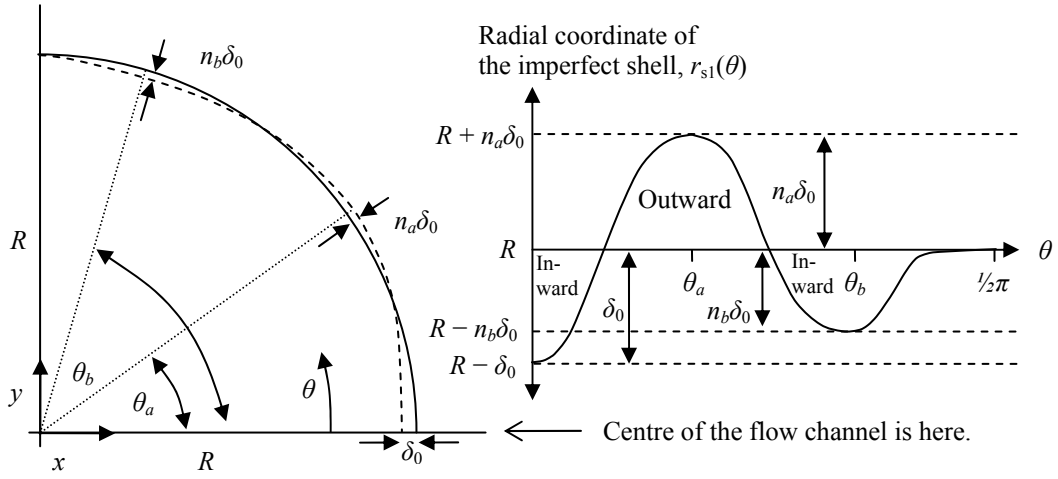

Fig. 6.13 − Geometry of the first superelliptical imperfection form at height y_0

It is important to clarify that δ_0 is a notional or reference imperfection amplitude for the whole silo. However, δ_0 need not define the *maximum* deviation of the imperfect shell as this depends on the choice of the parameters n_a and n_b which produce a deviation $n_a\delta_0$ and $n_b\delta_0$ at some coordinates (θ_a, y_0) and (θ_b, y_0) respectively, either of which may be greater than δ_0 if n_a or n_b are chosen to be greater than unity. Indeed, such values were used in the finite element analyses of this imperfection form presented later in this chapter to investigate the effect of different flattened shapes on the buckling strength of the silo. This choice was made to maintain consistency and full freedom in defining

different flattened shapes for the imperfect shell, but in a potential design situation the restriction may be made so that $0 \le n_a, n_b \le 1$ to ensure that δ_0 defines the maximum imperfection amplitude *anywhere* on the silo.

The Cartesian coordinates of the superelliptical flattening are given by:

$$x_{s1}(\theta) = (R - \delta_0)\cos^{\frac{2}{q}}\theta \text{ and } y_{s1}(\theta) = R\sin^{\frac{2}{p}}\theta \tag{6.17}$$

The polar forms of the radius and slope of the imperfect shell are:

$$r_{s1}(\theta) = \sqrt{x_{s1}(\theta)^2 + y_{s1}(\theta)^2} = \left((R-\delta_0)^2 \cos^{\frac{4}{q}}\theta + R^2 \sin^{\frac{4}{p}}\theta \right)^{\frac{1}{2}} \text{ and} \tag{6.18}$$

$$\frac{dr_{s1}}{d\theta}(\theta) = 2\left((R-\delta_0)^2 \cos^{\frac{4}{q}}\theta + R^2 \sin^{\frac{4}{p}}\theta \right)^{-\frac{1}{2}} \times \ldots \left[\frac{R^2}{p}\cot\theta \sin^{\frac{4}{p}}\theta - \frac{(R-\delta_0)^2}{q}\tan\theta\cos^{\frac{4}{q}}\theta \right] \tag{6.19}$$

Thus the circumferential component of the radial coordinate of the imperfect shell is given by:

$$u_{s1}(\theta) = \begin{cases} R - r_{s1}(\theta) & \text{for } -\frac{\pi}{2} \le \theta \le \frac{\pi}{2} \\ 0 & \text{elsewhere} \end{cases} \tag{6.20}$$

and the full imperfect geometry of the silo is generated by:

$$r(\theta, y) = R - u_{s1}(\theta) w(y) \tag{6.21}$$

where $u_{s1}(\theta)$ and $w(y)$ are given by Eqs 6.20 and 6.2 respectively.

The parameters p, q, θ_a and θ_b must be solved for numerically from the following four boundary conditions:

$$r_{s1}(\theta_a) = R + n_a\delta$$
$$r_{s1}(\theta_b) = R - n_b\delta$$
$$\frac{dr_{s1}}{d\theta}(\theta_a) = \frac{dr_{s1}}{d\theta}(\theta_b) = 0$$

Note that if $\delta_0 = 0$, $p = q = 2$ and Eq. 6.21 generates a perfect shell. A flattened shape with the features similar to those in Fig. 6.10 is obtained when $p > 2$, $q < 2$ and $\delta_0 > 0$.

The variation of the powers p and q and of the angles θ_a and θ_b with the dimensionless imperfection amplitude δ_0/t for a shell with $R/t = 1000$ is shown in Fig. 6.14 and Fig. 6.15 respectively for different combinations of the parameters n_a and n_b equal to 1 and 0.1. These were chosen simply to show approximately what happens when either parameter is made very small compared to the other, and when they are the same.

It appears that the larger the value for either n_a or n_b, the greater the change in both p and q from their reference value of 2. The variation of the angles θ_a and θ_b with δ_0/t appears to be very minor and is shown for the purposes of clarification and explanation only, as they are not needed to generate the imperfect shell form. The lowest value of δ_0/t used in Fig. 6.15 was 0.0001 as θ_a and θ_b have no meaning for a perfect shell. The relationship between the parameters p and q and the imperfection amplitude δ_0/t is approximately linear in all cases, which is very useful as it may allow a simple empirical fit to be devised which may be easily implemented in design as opposed to the above numerical procedure.

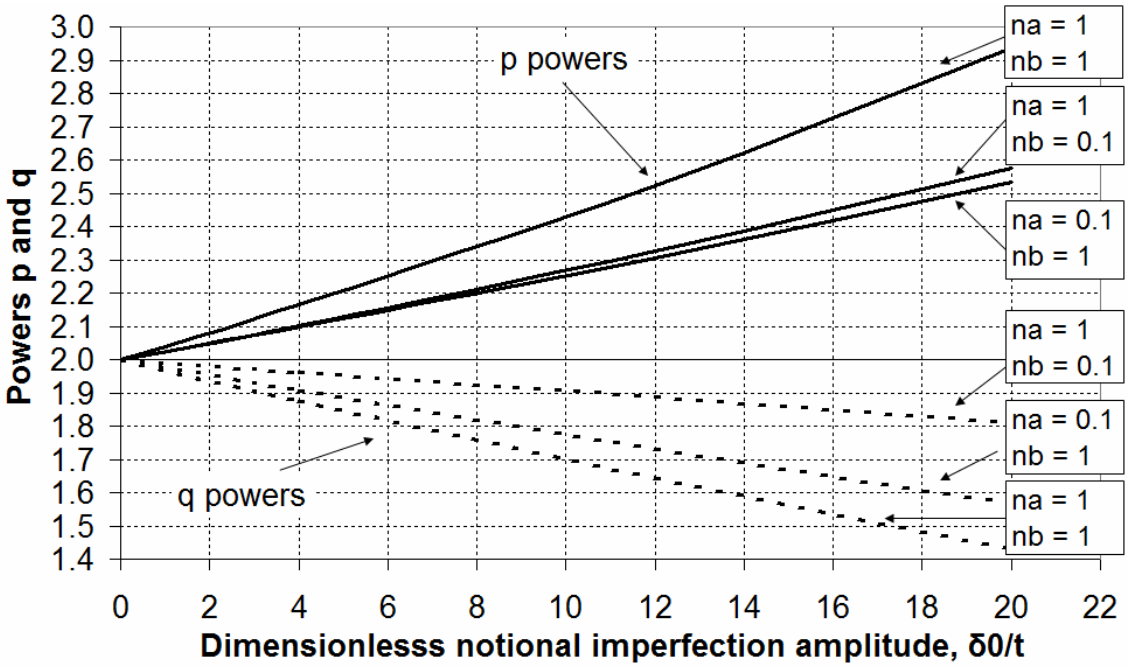

Fig. 6.14 − Typical variation of the powers p and q with δ_0/t for the first superelliptical imperfection form ($R/t = 1000$)

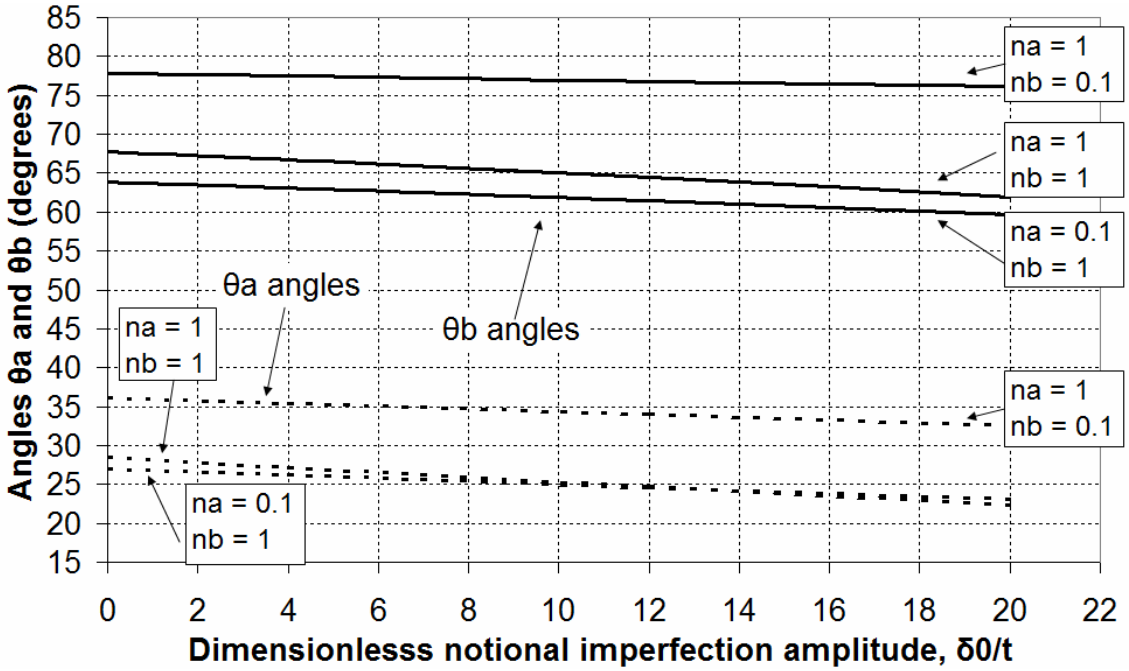

Fig. 6.15 − Typical variation of the angles θ_a and θ_b q with δ_0/t (lowest value 0.0001) for the first superelliptical imperfection form (R/t = 1000)

An important additional consideration is the change in the arc length of the shell under this imperfection form. During construction, the one aspect which builders usually cannot get wrong is the total circumference, because even if the strakes are welded badly, the sum of their lengths is always fixed. Thus it is necessary to compare the arc lengths of the imperfect and perfect shells. The arc length of the imperfect shell may be obtained by integrating the following equation:

$$s_{s1} = \int_0^{\frac{\pi}{2}} \sqrt{\left(\frac{dx_{s1}}{d\theta}\right)^2 + \left(\frac{dy_{s1}}{d\theta}\right)^2}\, d\theta \qquad (6.22)$$

The powers p and q are applied to trigonometric terms in the equations for x_{s1} and y_{s1} (Eqs. 6.17 and 6.18), hence it was only possible to integrate Eq. 6.22 numerically. The arc length of the imperfect shell was then normalised by the perfect circumference ($\frac{1}{2}\pi R$), and the result is shown in Fig. 6.16 as a function of δ_0/t for the same values of n_a and n_b as above. This figure shows that the error in the circumference is of the order of 1-2% in this range. Over the course of the analyses presented in this chapter that used this imperfection form, it was found that the error in the circumference did not go beyond 5%.

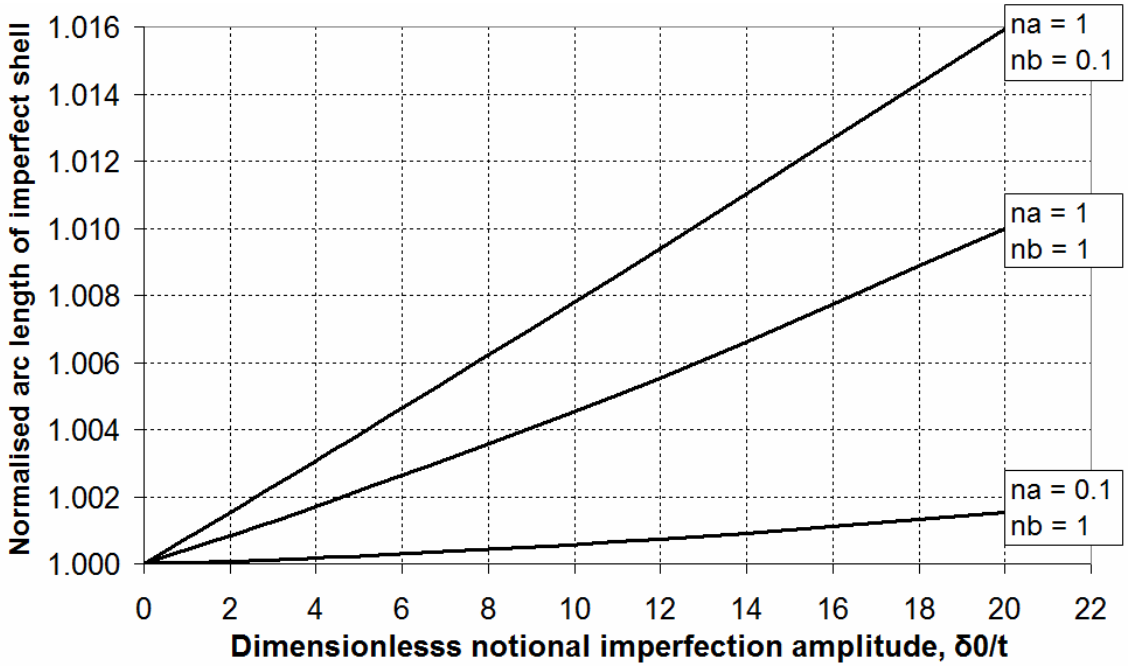

Fig. 6.16 − Typical variation of the normalised arc length of the imperfect shell with δ_0/t for the first superelliptical imperfection form (R/t = 1000)

6.7.2 Initial GNIA parametric study of the first superelliptical imperfection form on a slender silo with the Rotter 1986 eccentric discharge pressure model

A set of geometrically nonlinear analyses (GNIA) were carried out on Silo CS with the first superelliptical imperfection form modelled according to the equations of the preceding section. The Rotter (1986) eccentric discharge pressure distribution, which does not include regions of high wall pressure adjacent to the flow channel, was used in this first set of analyses. This pressure pattern was chosen because it was considered to be a more realistic and less severe distribution than that of EN 1991-4 (2007), and was thus a good place to start.

Notional imperfection amplitudes in the range $0 \leq \delta_0 \leq 15t$ were investigated for a medium-sized flow channel, $k_c = r_c/R = 0.40$. Many combinations of the n_a and n_b parameters are clearly possible, though only four different sets were considered here. The values of these parameters were generally taken to be greater than unity, thus exaggerating the flattened shape to allow a wider range of general trends to be observed. The combinations include (n_a, n_b) = (1, 1) where all deviation features are equal, (2, 1) where the frontal flattening is more pronounced, (2, ¼) where the secondary inward deviation away from the centre of the channel is made very small and (4, 1) where the frontal flattening is made even more pronounced. The imperfection sensitivity curves

for k_c = 0.40, normalised with by GNA load factor (0.30, Table 3.5.1), are shown in Fig. 6.17.

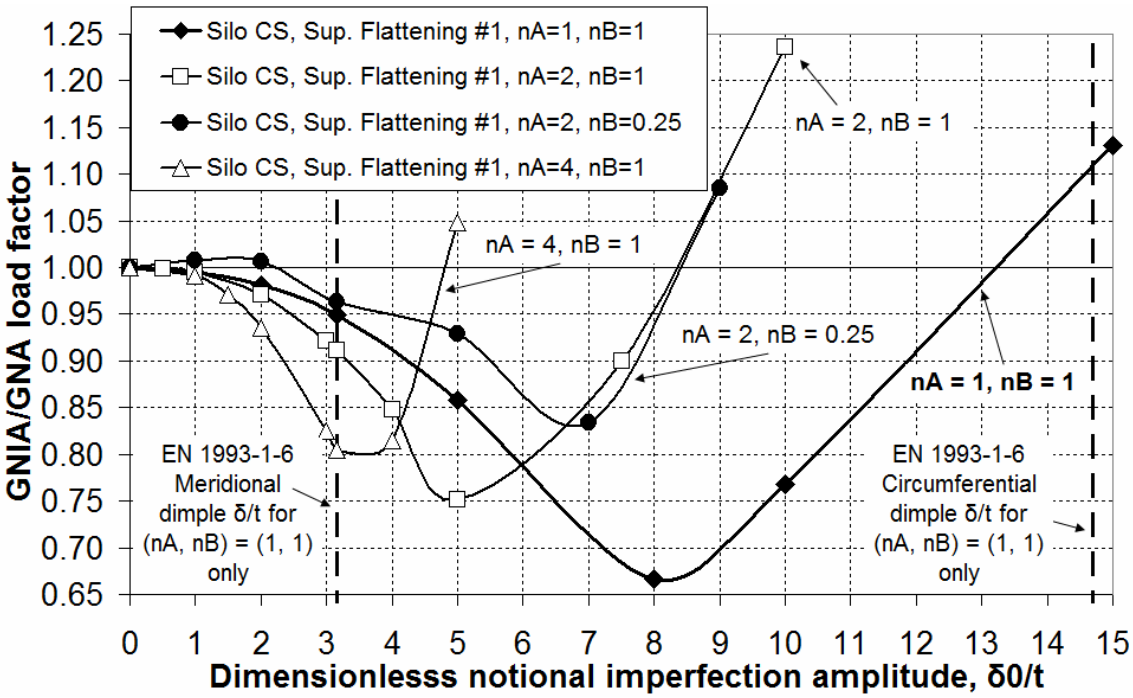

Fig. 6.17 − GNIA imperfection sensitivity curves for the first superelliptical imperfection form with k_c = 0.40 and Rotter eccentric discharge pressures on Silo CS

The trend for the un-exaggerated shape with (n_a, n_b) = (1, 1) suggests that the first superelliptical imperfection form is indeed detrimental to the buckling strength of the shell at small and medium imperfection amplitudes, including in the vicinity of the EN 1993-1-6 Section 8.7 value of 3.162t for meridional compression, but *not* near the amplitude of 14.7t for circumferential compression (Table 6.1). Indeed, at amplitudes greater than δ_0 = 8t it appears that the trend reverses sharply and the imperfection instead produces a beneficial effect. It is currently not clear why this reversal occurs, or why it is so sudden.

At small notional imperfection amplitudes, an increasingly deleterious effect is obtained when the frontal flattening is made more pronounced by increasing the primary outward radial feature with a larger value of n_a. For example, at δ_0 = 3.162t the set of values of (n_a, n_b) = (1, 1) results in a 5% decrease from the GNA load factor. Increasing n_a to 4 results in a drop of almost 20%. However, though higher values of n_a give larger strength decreases at smaller amplitudes, they also result in significantly more rapid

strength gains when these amplitudes become slightly larger. Indeed, the GNIA load factor for (n_a, n_b) = (4, 1) at $\delta_0 > 5t$ goes straight off the scale of the figure, but it should be remembered that, for this higher range of notional amplitudes, $n_a = 4$ produces a large deviation of $n_a\delta_0 > 20t$ at some coordinate (θ_a, y_0) on the imperfect shell (Fig. 6.13). At the same time, the secondary inward radial feature should not be neglected and n_b should not be taken as lower than unity, since (n_a, n_b) = (2, ¼) produces smaller strength reductions at low amplitudes than (2, 1).

6.7.3 Additional GNIA parametric study of the first superelliptical imperfection with on a slender silo with the EN 1991-4 eccentric discharge pressure model

It was shown above that superelliptical flattening adjacent to the flow channel may be a suitable imperfection form for the Rotter (1986) eccentric discharge pressure distribution, which omits high wall pressure regions adjacent to the edge of the channel. The next exploration attempted to verify that it would also be suitable when used with the original EN 1991-4 pressure model with all three recommended flow channel sizes of $k_c = r_c/R = 0.25$, 0.40 and 0.60.

A suite of GNIA analyses was carried out on Silo CS using the first superelliptical imperfection form with the set of parameters n_a and n_b that was found previously to result in a more severe effect on the buckling behaviour, (4, 1). The range of notional imperfection amplitudes was limited to $0 \leq \delta_0 \leq 5t$, though at the top value of this range, $n_a\delta_0$ produces an actual deviation of $20t$ at some coordinate (θ_a, y_0). The resulting imperfection sensitivity curves, normalised by the respective GNA load factors, are shown in Fig. 6.18. The GNA load factors are 2.35, 0.24 and 0.35 for $k_c = 0.25$, 0.40 and 0.60 respectively (Table 3.4).

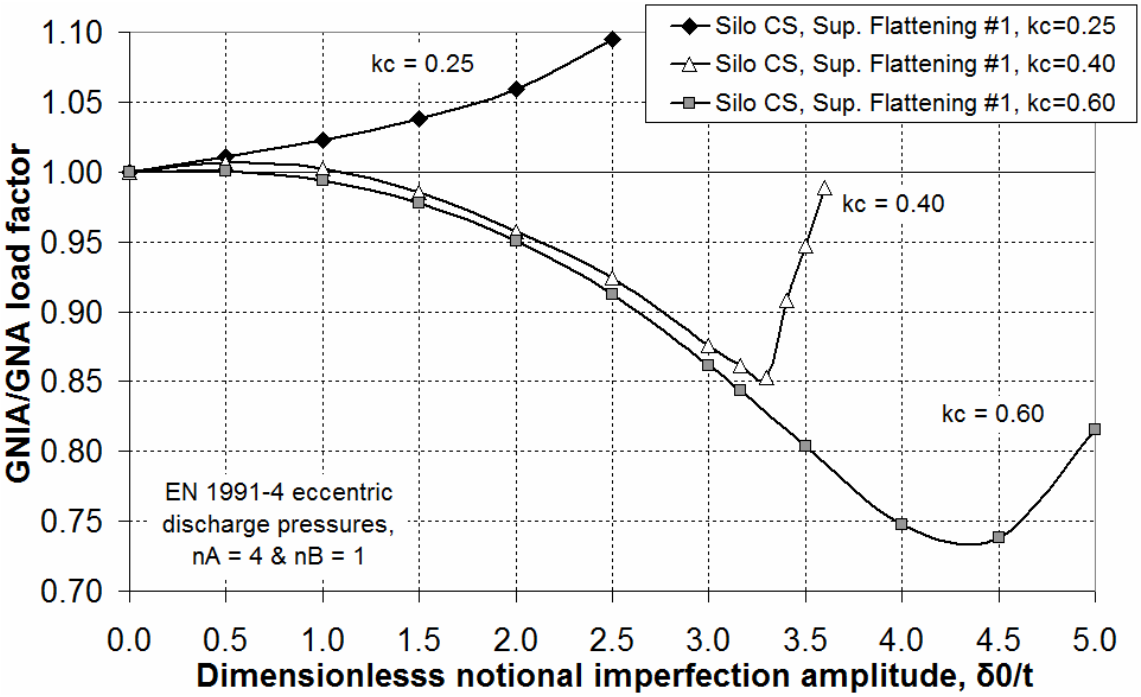

Fig. 6.18 − GNIA imperfection sensitivity curves for the first superelliptical imperfection form with (n_a, n_b) = (4, 1) and EN 1991-4 eccentric discharge pressures on Silo CS

These imperfection sensitivity curves suggest that the superelliptical imperfection form is similarly deleterious when there are regions of high wall pressure adjacent to the edge of the flow channel included in the GNIA analysis. However, for the smallest channel with k_c = 0.25, the imperfection is predicted to become beneficial at all notional imperfection amplitudes. Indeed, beyond 2.5t, the curve goes off the scale to a normalised load factor in excess of 2, indicating a gain in buckling strength of over 100%.

As described in Chapters 4 and 5, the geometrically nonlinear behaviour of the silo at small values of k_c under the full EN 1991-4 pressures is rather different from the expected buckling behaviour under eccentric discharge. The flow channel of k_c = 0.25 is very small and the midheight compressive axial membrane stresses, which are responsible for the elastic midheight buckle at the centre of the flow channel, have not yet fully developed in flow channels smaller than k_c = 0.40 (e.g. Fig. 4.23, Fig. 5.8 and Fig. 5.9). The corresponding behaviour for k_c = 0.25 in Fig. 6.18 thus appears to be highly anomalous.

For k_c = 0.40 and 0.60, the imperfection form is predicted to be progressively more deleterious up to values of δ_0 of approximately 3.2t and 4.4t. Beyond these notional amplitudes there is a sudden and steep rise in buckling strength, similar to Fig. 6.17 for the Rotter (1986) distribution. This rise in strength is found to occur later for the larger flow channel, and does not seem to be so steep.

6.8 Second form of the imperfection − Superelliptical flattening with no central inward deviation

6.8.1 Circumferential geometry of the second imperfection form

The second proposed shape of the superelliptical imperfection form incorporates only the primary outward and secondary inward radial features of Fig. 6.10, relating them to a notional imperfection amplitude δ_0 that occurs at $\theta = \theta_a$ (i.e. not central) at the desired level of largest flattening y_0. For $\theta = 0$ at the centre of the flow channel, it is assumed in this imperfection form that the shell has remained stationary and there is no inward central feature. Thus the flattened shape of the silo wall is produced only by an outward deviation of the shell near the edge of the flow channel to an amplitude δ_0 at some coordinate $\theta = \theta_a$, and an inward deviation of the shell away from the channel to an amplitude of $m\delta_0$ at some coordinate $\theta = \theta_b$. The amplitude of the inward feature was assumed to be related to the amplitude of the outward feature by a parameter $m > 0$, which may be varied to control the extent of the flattening. The geometry of the second superelliptical flattening imperfection form is shown in Fig. 6.19.

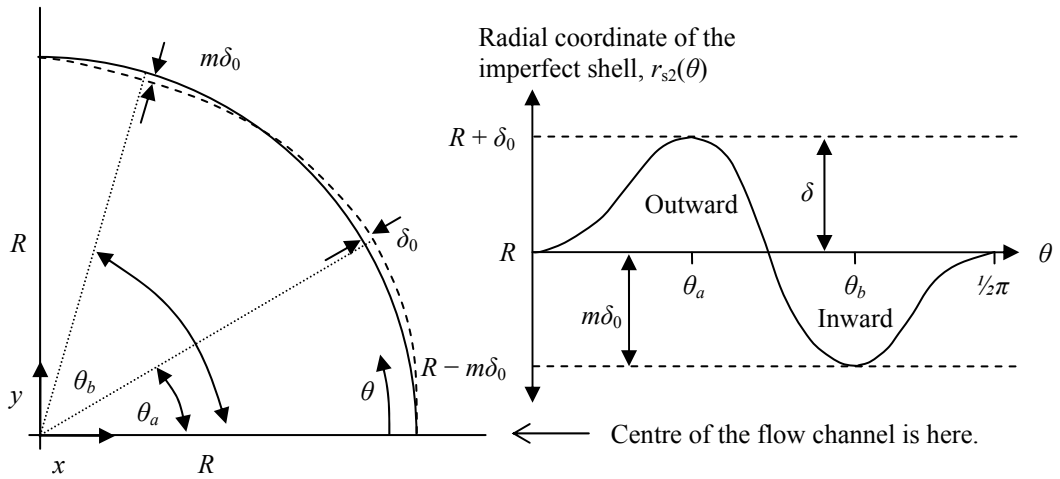

Fig. 6.19 − Geometry of the second superelliptical imperfection form at a height of y_0

The notional or reference imperfection amplitude δ_0 was assigned the same meaning for second superelliptical imperfection form as it was for the first form in Fig. 6.13. Depending on what value has been chosen for m, there may be a deviation of $m\delta_0$ at some coordinate (θ_b, y_0) that is greater than δ_0. This choice was again made for consistency and freedom in investigating different flattened shapes of the imperfect shell, but in design the restriction may be made so that $0 \leq m \leq 1$ to ensure that δ_0 is indeed the maximum imperfection amplitude on the whole silo.

The Cartesian coordinates of the superelliptical flattening are given by:

$$x_{s2} = R\cos^{\frac{2}{q}}\theta \text{ and } y_{s2} = R\sin^{\frac{2}{p}}\theta \tag{6.23}$$

The polar forms of the radius and slope of the imperfect shell are:

$$r_{s2}(\theta) = \sqrt{x_{s2}(\theta)^2 + y_{s2}(\theta)^2} = R\left(\cos^{\frac{4}{q}}\theta + \sin^{\frac{4}{p}}\theta\right)^{\frac{1}{2}} \text{ and} \tag{6.24}$$

$$\frac{dr_{s2}}{d\theta}(\theta) = 2R\left(\cos^{\frac{4}{q}}\theta + \sin^{\frac{4}{p}}\theta\right)^{-\frac{1}{2}}\left[\frac{1}{p}\cot\theta\sin^{\frac{4}{p}}\theta - \frac{1}{q}\tan\theta\cos^{\frac{4}{q}}\theta\right] \tag{6.25}$$

Thus the circumferential component of the radial coordinate of the imperfect shell is given by:

$$u_{s2}(\theta) = \begin{cases} R - r_{s2}(\theta) & \text{for } -\dfrac{\pi}{2} \leq \theta \leq \dfrac{\pi}{2} \\ 0 & \text{elsewhere} \end{cases} \tag{6.26}$$

and the full imperfect geometry of the silo is generated by:

$$r(\theta, y) = R - u_{s2}(\theta)w(y) \tag{6.27}$$

where $u_{s2}(\theta)$ and $w(y)$ are given by Eqs 6.27 and 6.2 respectively.

The parameters p, q, θ_a and θ_b must similarly be solved for numerically from the following four boundary conditions:

$$r_{s2}(\theta_a) = R + \delta$$
$$r_{s2}(\theta_b) = R - m\delta$$
$$\frac{dr_{s2}}{d\theta}(\theta_a) = \frac{dr_{s2}}{d\theta}(\theta_b) = 0$$

The arc length of the imperfect shell may be found by integrating the following equation numerically:

$$s_{s2} = \int_0^{\frac{\pi}{2}} \sqrt{\left(\frac{dx_{s2}}{d\theta}\right)^2 + \left(\frac{dy_{s2}}{d\theta}\right)^2}\, d\theta \tag{6.28}$$

If $\delta_0 = 0$, $p = q = 2$ and Eq. 6.24 generates a perfect shell, similar to Eq. 6.18. A flattened shape with the features similar to those in Fig. 6.10 is again obtained when $p > 2$, $q < 2$ and $\delta_0 > 0$. The variations of the powers p and q, angles θ_a and θ_b and the normalised arc length of the imperfect shell with m and the notional imperfection amplitude δ_0/t are presented in Fig. 6.20 to Fig. 6.22. These show very similar approximately linear relationships with δ_0/t as the corresponding figures for the first superelliptical flattening imperfection, Fig. 6.14 to Fig. 6.16. The error in the arc length (after numerical integration of Eq. 6.28) increases with both m and δ_0/t, but appears to be smaller than for the first imperfection form (Fig. 6.16), usually of the order of 1% or less.

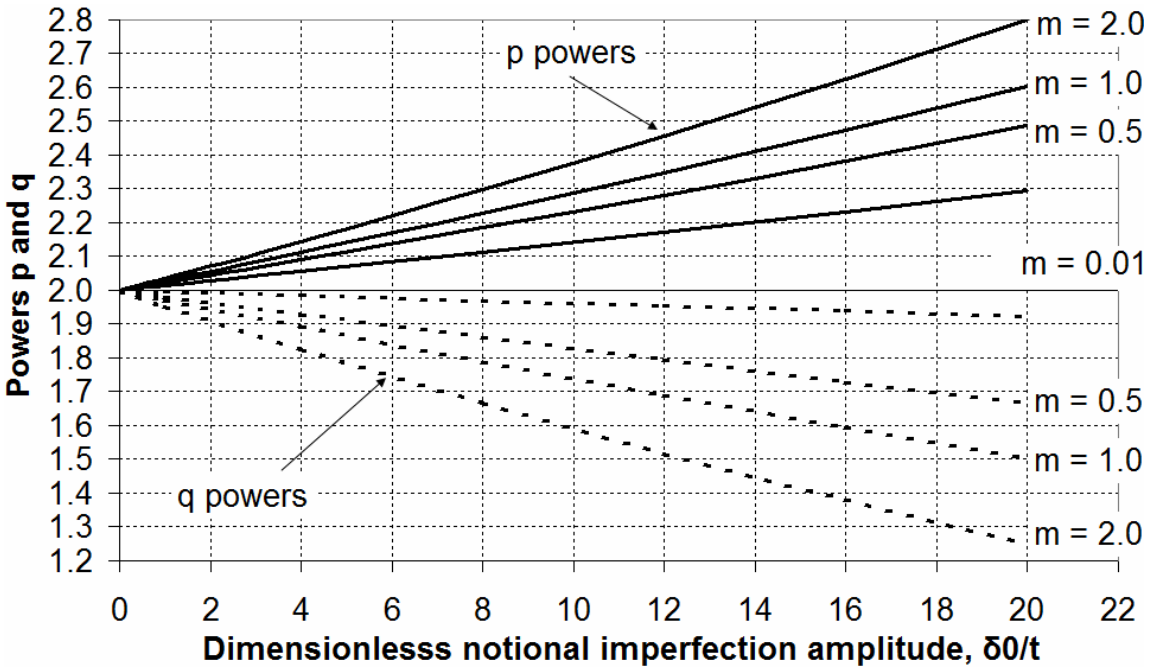

Fig. 6.20 − Typical variation of the powers p and q with δ_0/t for the second superelliptical flattening imperfection form ($R/t = 1000$)

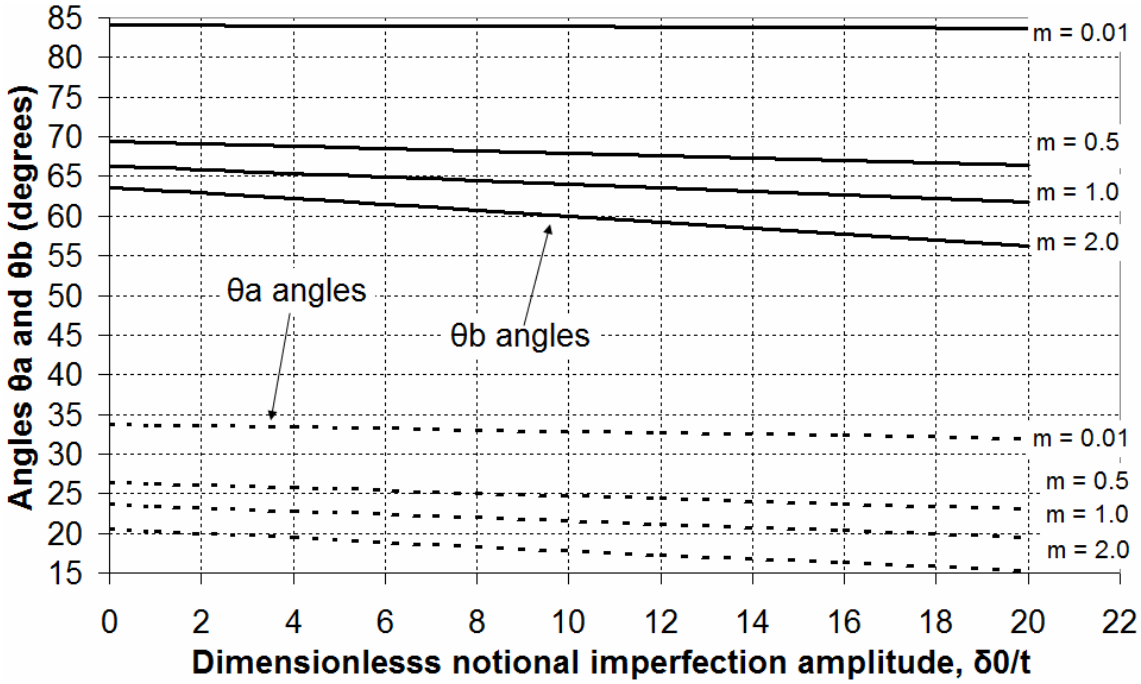

Fig. 6.21 − Typical variation of the angles θ_a and θ_b q with δ_0/t (lowest value 0.0001) for the second superelliptical flattening imperfection form (R/t = 1000)

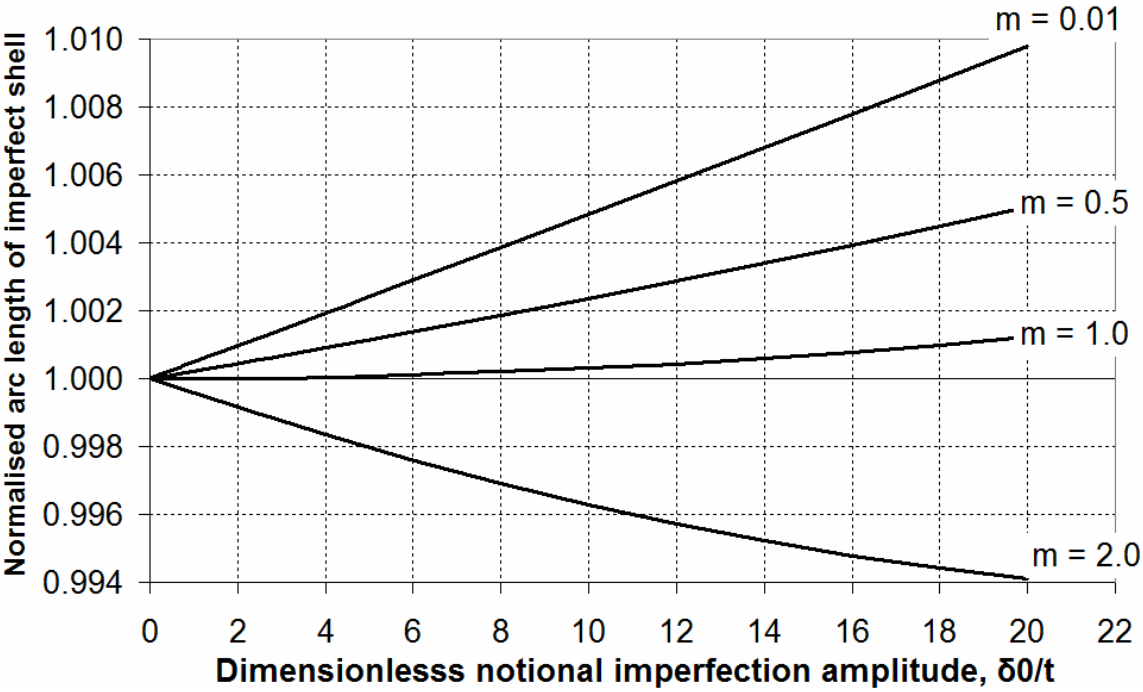

Fig. 6.22 − Typical variation of the normalised arc length of the imperfect shell with δ_0/t for the second superelliptical flattening imperfection form (R/t = 1000)

6.8.2 Initial GNIA parametric study of the second superelliptical imperfection form on a slender silo with the Rotter 1986 eccentric discharge pressure model

The effect of the second superelliptical imperfection form on the buckling strength of Silo CS was analysed through a series of GNIA analyses using the Rotter (1986) eccentric discharge pressure model, in a manner similar to the previous analyses of the first superelliptical imperfection form.

According to Fig. 6.19, the parameter m controls the extent of the secondary inward radial feature far away from the flow channel. To investigate what effect this feature may have on the GNIA load factor, the values of m were chosen to be 0.5, 1 and 2. The GNIA analyses were performed in the range of notional imperfection amplitudes of $0 \leq \delta_0 \leq 20t$ using, for consistency, the three recommended flow channel sizes in EN 1991-4; $k_c = 0.25$ (up to $\delta_0 = 10t$ only), 0.40 and 0.60. The amplitude of $20t$ is a very high one when compared with the EN 1993-1-6 Section 8.7 imperfection amplitude for both meridional and circumferential compression of $3.162t$ and $14.7t$ respectively (Table 6.1), but such high amplitudes were found to be necessary to obtain non-negligible strength reductions when analysing long-wave circumferential imperfection forms such as those considered here.

The imperfection sensitivity curves, normalised by the respective GNA load factor for each of the flow channels (GNA = 0.28, 0.30 and 0.52 for k_c = 0.25, 0.40 and 0.60 respectively, Table 3.4) are shown in Fig. 6.23 to Fig. 6.25.

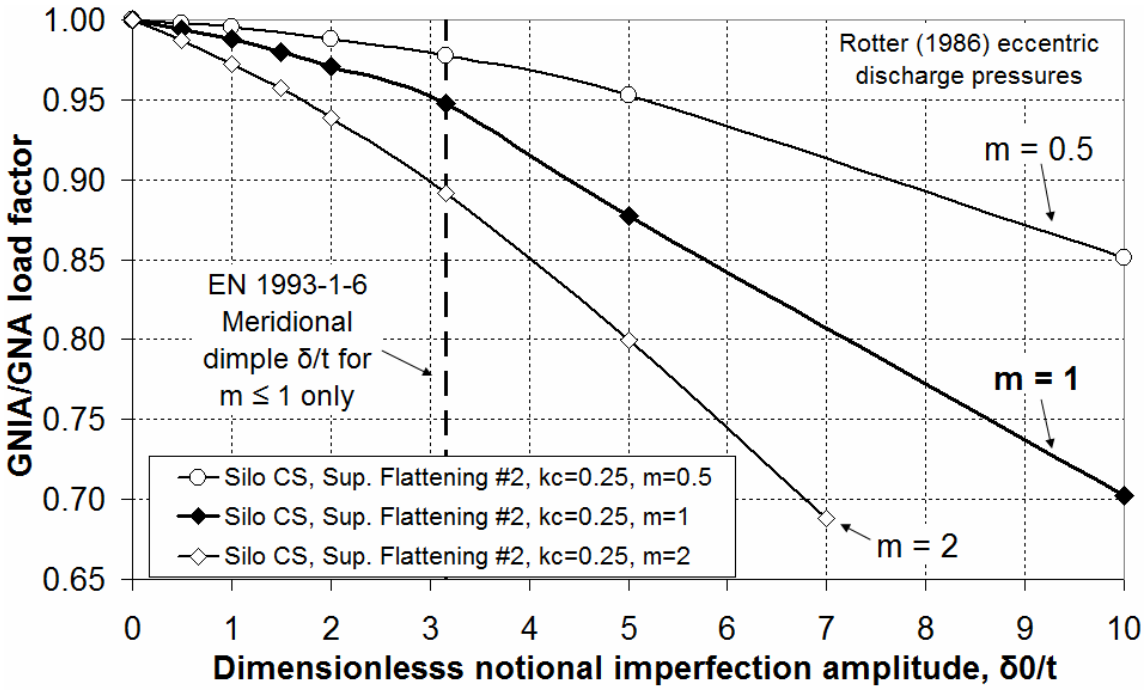

Fig. 6.23 − GNIA imperfection sensitivity curves for the second superelliptical imperfection form with k_c = 0.25 and Rotter eccentric discharge pressures on Silo CS

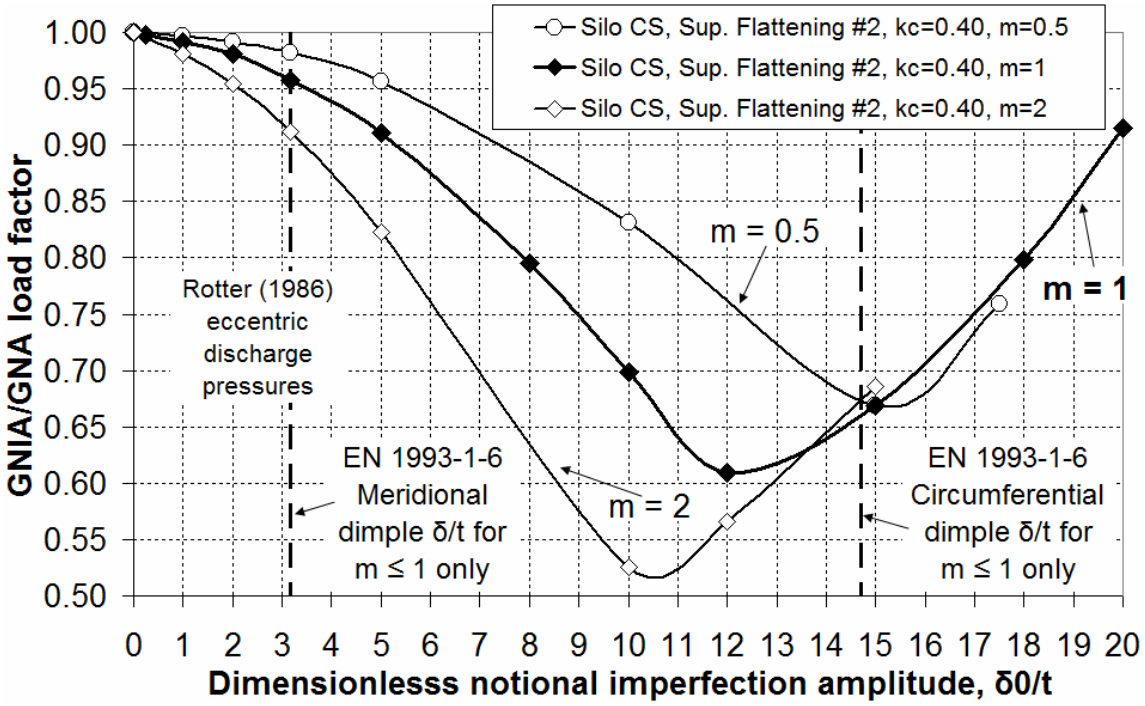

Fig. 6.24 − GNIA imperfection sensitivity curves for the second superelliptical imperfection form with k_c = 0.40 and Rotter eccentric discharge pressures on Silo CS

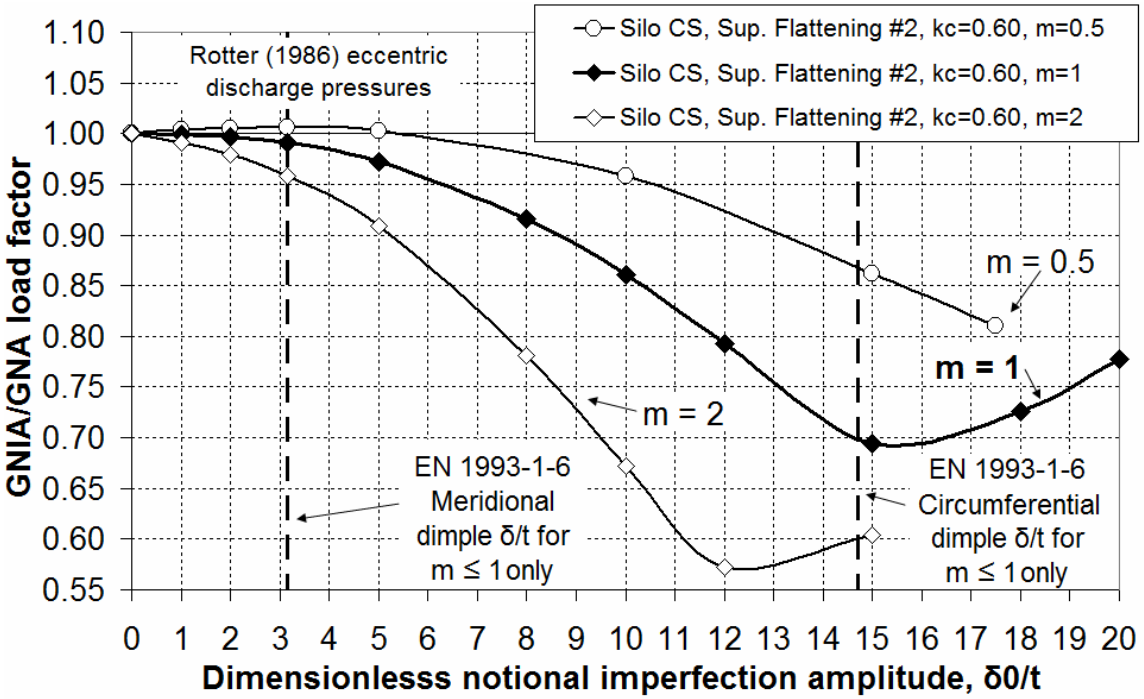

Fig. 6.25 − GNIA imperfection sensitivity curves for the second superelliptical imperfection form with $k_c = 0.60$ and Rotter eccentric discharge pressures on Silo CS

The trend for $m = 1$ from these graphs is very similar to that of $(n_a, n_b) = (1, 1)$ for the first superelliptical imperfection form in Fig. 6.17. The second superelliptical imperfection form results in consistent decreases in the predicted buckling strength for both small and medium imperfection amplitudes over a wide range of flow channel sizes. At larger imperfection amplitudes of $\delta_0 > 15$, comparable with the EN 1993-1-6 Section 8.7 amplitude of $14.7t$ for circumferential compression (Table 6.1), there is a reversal of the trend and the GNIA factor begins to rise.

The predicted decreases in strength for $m = 1$ are smaller than those for $(n_a, n_b) = (1, 1)$. For example, at an amplitude of $5t$, the normalised GNIA load factors for $k_c = 0.40$ for the first and second superelliptical imperfection forms with m, n_a and n_b equal to unity are 0.86 and 0.92 respectively. Additionally, where the GNIA factor begins to rise rather steeply at $8t$ for the first form, the rise occurs only after $12t$ for the second form and significantly less steeply. Thus the form of the superelliptical imperfection with no primary inward radial feature near the centre of the channel (Fig. 6.10 and Fig. 6.19) appears to have a significantly milder affect on buckling strength than a form which includes this radial feature.

The secondary inward radial feature should not be made smaller than the primary outward radial feature (Fig. 6.19), i.e. the value of m should not be set to smaller than unity, as doing this results in a less deleterious imperfection form (Fig. 6.25). For a more serious imperfection which results in lower predicted buckling strengths at low and mid-sized imperfection amplitude, though at a cost of causing a rise in the load factor at a lower value of δ_0, m should be greater than unity.

6.8.3 Additional GNIA parametric study of the second superelliptical imperfection form on a slender silo with the EN 1991-4 eccentric discharge pressure model

The second superelliptical imperfection form was subsequently investigated in a set of GNIA analyses under the full EN 1991-4 eccentric discharge pressure model with the three recommended flow channel sizes of k_c = 0.25, 0.40 and 0.60. This was done in order to verify the suitability of the imperfection for use with the original eccentric discharge model, similar to the study performed previously on the first superelliptical imperfection form (Fig. 6.18).

The more serious of the imperfection forms identified in the previous section (m = 2) was analysed in the range of notional imperfection amplitudes of $0 \leq \delta_0 \leq 5t$. Thus the secondary inward feature was assigned an actual deviation of $2\delta_0$ at some coordinate (θ_b, y_0), up to a maximum of $10t$, though still below the EN 1993-1-6 Section 8.7 amplitude of $14.7t$ for circumferential compression (Table 6.1).

The imperfection sensitivity curves, normalised by the respective GNA load factor, are shown in Fig. 6.26. These curves suggest that the second superelliptical form is also similarly deleterious under the more serious EN 1991-4 eccentric discharge model. However, it also appears to be significantly more reliable when compared with the first superelliptical form in Fig. 6.18, as it does not produce any beneficial effect for the smallest flow channel of k_c = 0.25, nor is there any apparent recovery in the buckling strength within the same range of δ_0. On the basis of this, the second variant of the superelliptical imperfection form, with no inward radial feature near the centre of the flow channel, is here considered to be the imperfection form in which most confidence can be placed for the analysis of silos under eccentric discharge. A value $m \geq 1$ should be used with this imperfection form, to increase its effectiveness.

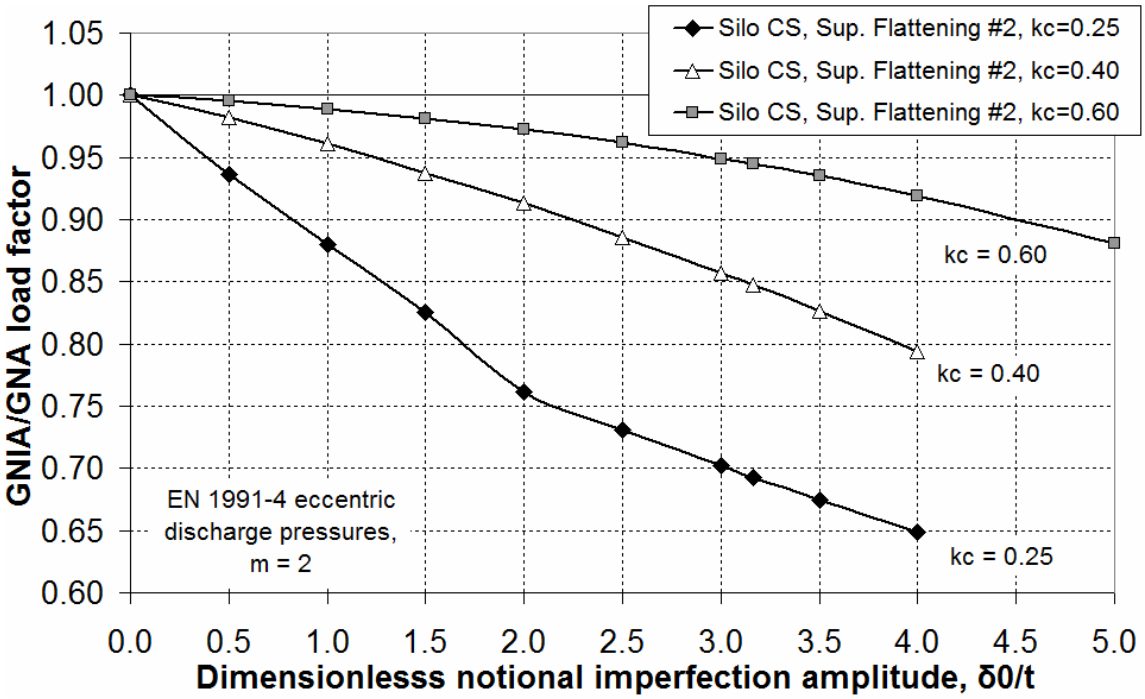

Fig. 6.26 − GNIA imperfection sensitivity curves for the first superelliptical imperfection form with m = 2 and EN 1991-4 eccentric discharge pressures on Silo CS

6.8.4 Final GNIA study of the second superelliptical imperfection form on a very slender silo with the EN 1991-4 eccentric discharge pressure model

Since the second superelliptical imperfection form with m = 2 was found to be a good choice for a deleterious imperfection form under eccentric discharge, an additional verification was undertaken to determine whether this was also the case for a silo of a larger aspect ratio. Silo CVS (H/D = 5.2) was thus analysed with the full EN 1991-4 eccentric discharge pressures for k_c = 0.25, 0.40 and 0.60 in the range of $0 \leq \delta_0 \leq 4t$. The imperfection sensitivity curves are shown in Fig. 6.27, normalised with the GNA load factor for the three channel sizes (which are 2.55, 0.49 and 0.37 for the three channel sizes respectively, Table 3.4).

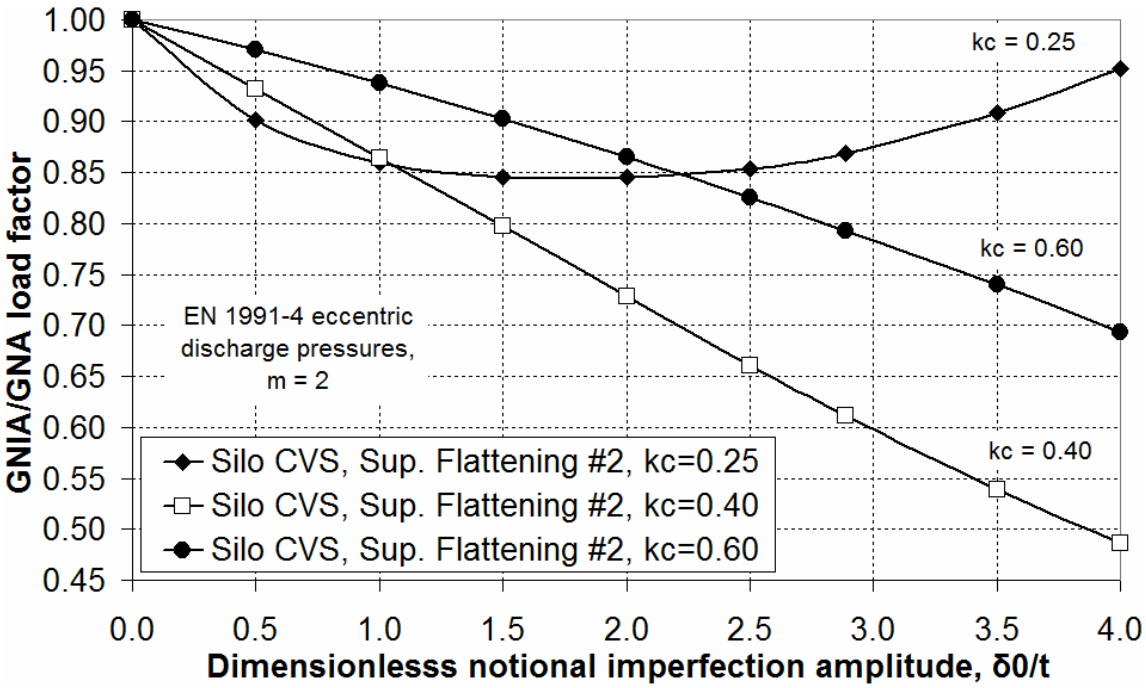

Fig. 6.27 − GNIA imperfection sensitivity curves for the first superelliptical imperfection form (m = 2) and EN 1991-4 eccentric discharge pressures on Silo CVS

The results shown in Fig. 6.27 confirm that the second superelliptical imperfection form with k = 2 does indeed cause significant strength losses in a silo with a higher aspect ratio. For the larger flow channels at, say, $\delta_0 = 2t$, k_c = 0.40 and 0.60, the reduction in GNA load factor is almost 27% and 13% respectively. It may be the case that this imperfection form is more deleterious in more slender silos, since Silo CS (H/D = 3.0) did not exhibit such large strength reductions for m = 2, which were instead 8% and 2% at $\delta_0 = 2t$ for k_c = 0.40 and 0.60 respectively (Fig. 6.26).

The curve for the small channel with k_c = 0.25 is again slightly anomalous when compared to the others as it predicts an almost parabolic relationship for the GNIA load factor with δ_0. The reasons for this are likely to be similar to those given in the previous section relating to the channel being too small to produce the characteristic eccentric discharge behaviour. Despite this, the second superelliptical imperfection form may still be considered damaging for k_c = 0.25 because although the curve in Fig. 6.27 is seen to rise for $\delta_0 > 2t$, above the EN 1993-1-6 Section 8.7 design amplitude for meridional compression of $2.887t$ which would be used here in a strict interpretation of the standard, EN 1993-1-6 has a special provision in Clause 8.7.2(20) applicable to this very case. The analyst is thus required to verify that the load factor at a 10% smaller imperfection amplitude is not lower than the load factor at the full design amplitude. If

this is found to be the case, the analyst must adopt an iterative procedure to locate the base of the imperfection sensitivity curve, and would have done so here, though unfortunately this is a very onerous process.

6.9 Conclusions

In this chapter, proposals have been put forward for a consistently deleterious imperfection form for GNIA and GMNIA analyses under the EN 1991-4 eccentric discharge pressure distribution. The imperfection form consists of flattening of the silo wall adjacent to the flow channel, maximised at the base of the strake where buckling was predicted in a corresponding GNA or GMNA analysis. Each circumferential section of the imperfect shell geometry was expressed by the equation of a superellipse, the specific shape of which is a combination of inward and outward radial deviation features that have been extracted from deformed shapes predicted by finite element analysis under Rotter (1986) and EN 1991-4 eccentric discharge pressures. It is expected that this imperfection form will only be relevant under pressure patterns that are similar to those for eccentric pipe flow. The GNA deformed shape could not be used as an imperfection form directly due to amplified indentations occuring at the change of thickness near the critical buckling region, which were found to beneficial to the buckling resistance of the shell.

Of the different shapes conceived for the imperfection form, the best form was decided on based on its performance in GNIA analyses. The most suitable superelliptical form assumes no departure from the ideal shape at the channel centre, an outward radial deviation near the channel edge and an inward radial deviation at larger circumferential coordinates. The imperfection form extends to 90° on either side of the centre of channel, beyond which the shell is assumed to be perfect.

The inward radial component of the imperfection form, located away from the edge of the flow channel, should be emphasised as this was found to lead to lower predicted load factors. Curiously, emphasising the outward radial component, which is immediately adjacent to the flow channel and is an integral part the flattened portion, does not actually produce the desired weakening effect. It is therefore recommended that the amplitude of the inward radial component should be at least twice the outward radial component.

The shell geometries considered in this imperfection form are very complex, and it is currently not fully understood what the relationship is between the combinations of these radial features and the distributions of axial compressive membrane stresses responsible for the reductions in buckling strength. Now that the superellipse has been established as a possible imperfection form under eccentric discharge, further research is needed to investigate the behaviour in greater detail.

The nature of the imperfection form proposed in this chapter is global, and it can be compared to an out-of-roundness or circumferential dimple tolerance. The amplitudes of the imperfection should therefore probably be defined in terms of the circumferential tolerance gauge, rather than the much shorter meridional gauge. This is currently only necessary where compressive circumferential stresses are explicitly being designed for, which would not be the case for either concentric or eccentric discharge. Consequently, it would require an amendment to the EN 1993-1-6 standard to make the design for compressive circumferential stresses mandatory. This may be necessary for long-wave circumferential imperfections such as those investigated in this chapter.

The analyses presented in this chapter show that very large imperfection amplitudes are generally necessary to produce any significant decreases in the buckling strength under eccentric discharge, and that the imperfection form must be of a global nature in order to be effective. The silo under eccentric discharge may therefore be considered to have a very low imperfection sensitivity.

On a final note, it should be added that eccentric discharge is by itself an extremely damaging phenomenon, resulting in predicted load factors that are only a fraction of those under concentric discharge. It may therefore be suggested that computational analyses of eccentric discharge could be limited to analyses of the perfect shell (GMNA). The decreases in buckling strength due to the superelliptical imperfection forms presented in this chapter are negligibly small in comparison with the buckling strength decreases already caused by eccentric discharge itself.

Chapter 7 – A mixed flow theory for the pressure distribution in silos during concentric and eccentric discharge

7.1 Introduction

In the preceding chapters, the pressure models for eccentric discharge relating to a parallel-sided truncated circular flow channel adjacent to the cylindrical silo wall have been studied. The formulation of this model was pioneered by Rotter (1986) and was recently incorporated into the European Standard, EN 1991-4 (2007). In itself, this already represents a major advance in this field, and has been shown to yield a wealth of information on the predicted behaviour of silos under the eccentric discharge phenomenon and, by extension, on the general behaviour of thin-walled shells under unsymmetrical non-uniform strip loads. Yet these models are unable to incorporate varying geometries or cross-sections, both for the flow channel itself and for the container in which the channel forms. Clearly, this poses severe limitations on the range of geometries and behaviours which may be investigated, as real flow channels may expand considerably from the outlet to cover the entire silo cross-section (Rotter, 2001a).

A novel mixed flow pressure theory is presented and expanded on here and in the remaining chapters of this thesis. It was first developed in the relatively unknown undergraduate thesis of Berry (1988) and presented in a conference by Rotter *et al.* (1990), but has not been published further since. It is based on the original application of vertical slice equilibrium to hoppers with inclined straight sides (Dąbrowski, 1957; Walker, 1966), generalised to varying channel slopes and truncated circular cross-sections. The strength of the theory lies in the fact that it acknowledges from the outset that the resulting differential equations must be solved numerically. Consequently, it becomes unnecessary to make many of the habitual crude simplifications in order to force the equation to have an analytical solution, making the theory much more powerful.

The theory presented here is applicable to flow channels of virtually any geometry and eccentricity. Additionally, though it is assumed here that the containing structure has a circular cross-section at any given level, the structure itself need not strictly be

cylindrical, though clearly cylindrical silos are the most common and will thus be the only ones considered here. It is possible to extend the theory to flow channels in conical containers (hoppers) and containers with other geometries. Additionally, the theory is not limited to a single channel, and it is possible to derive a more general model for multiple channels, which may or may not interact with each other, in a similar manner.

7.2 Presentation of a new eccentric discharge vertical pressure theory

7.2.1 Background

A detailed introduction to flow patterns in silos may be found in Rotter (2001a) and Section 1.2.7 of the literature review. Based on the idealised patterns on Fig. 1.10 and Fig. 1.11, one may generalise the vertical profile of the flow channel geometry to follow a parabolic-like radial distribution, expressed by a power law in the general form $r(y) = my^{(1/n)}$ where m and n are constants and y is the vertical coordinate, centred at some radial eccentricity e_c. This is demonstrated in Fig. 7.1 for four different flow patterns, with both shallow and steep sides.

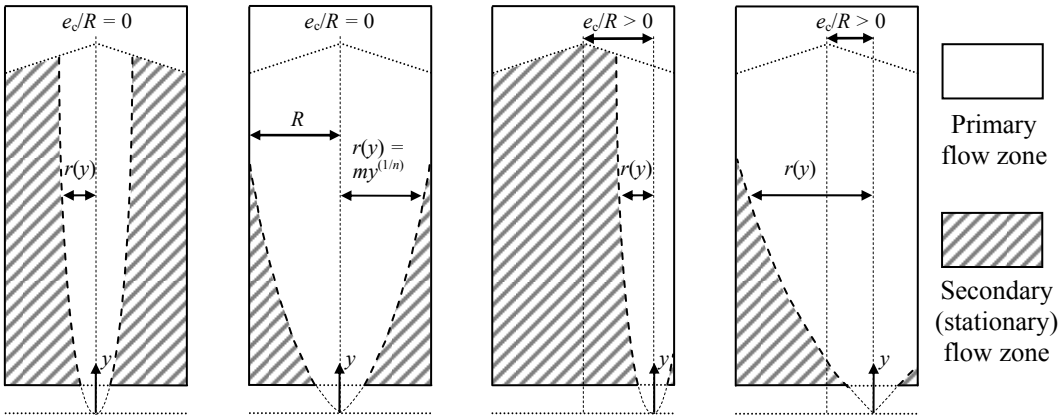

Fig. 7.1 – Modelling of idealised flow patterns

Early experimental evidence at the University of Sydney (Fleming, 1985; Fitz-Henry, 1986), related work (Berry, 1988; Rotter *et al.*, 1990) and more recent experimental studies at Edinburgh (Watson, 2010; Zhong *et al.*, 2010) suggest that the power law generalisation of the vertical profile is a valid approach to modelling flow channel geometries. For the form suggested above, $n = 1$ generates a conical channel form, $n = 2$

generates a parabolic form while as $n \rightarrow \infty$ the channel sides become progressively vertical and straight.

Parabolic profile forms were used by Berry (1988) in the first investigations of the new pressure theory. Furthermore, it has been observed in the above literature and in other studies (e.g. Kvapil, 1959; Deutsch and Clyde, 1967; Kroll, 1975; Leczner, 1963; Hampe, 1987; Sielamowicz and Kowalewski, 2007), that an ellipsoidal/parabolic form with $n \approx 2$ is a very close approximation of a typical flow channel profile, since measured flow channels tend to expand away from the outlet to produce a wider profile (Fig. 7.2). Profiles with $n < 1$ are rarely seen (e.g. Martens, 1988) and it is not certain whether these descriptions are truly genuine given the difficulties inherent in measuring flow channel profiles. Clearly, such a general model allows a high degree of control over the shape and position of the channel, and opens up new possibilities for analysis.

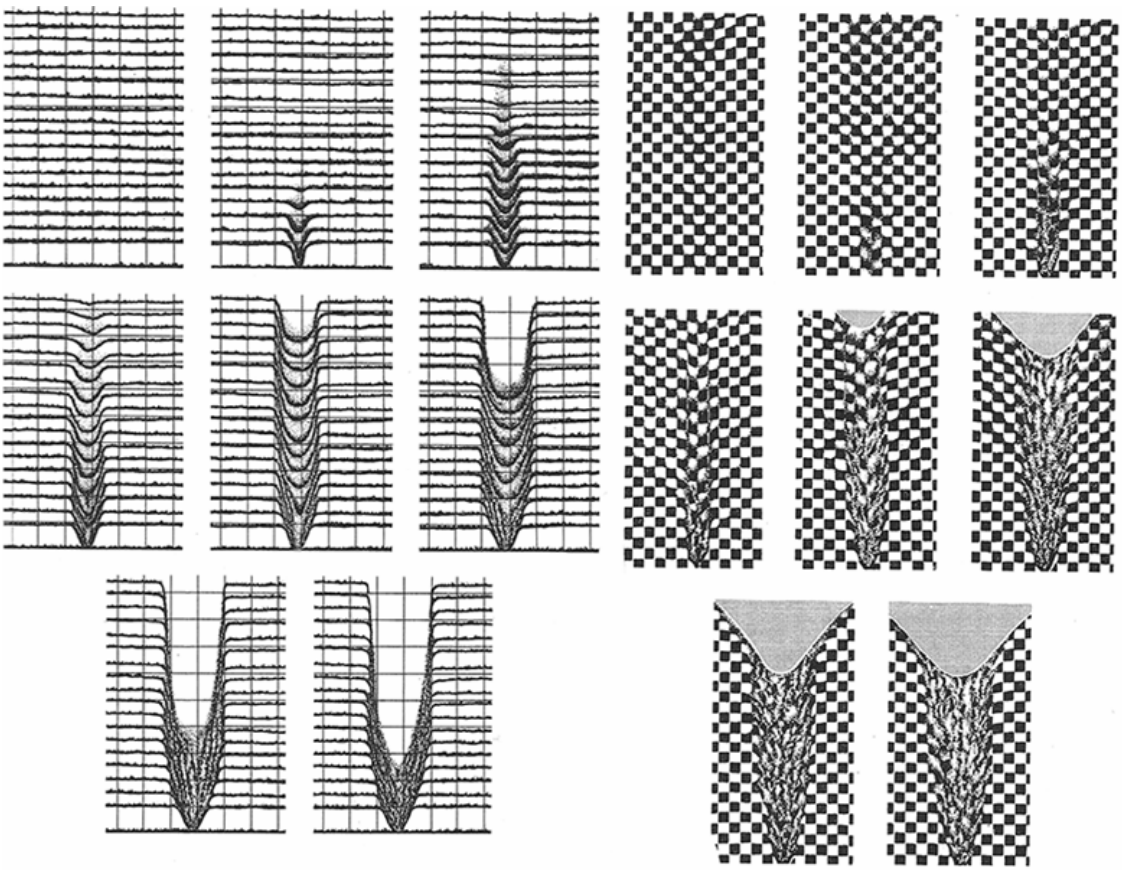

Fig. 7.2 – Schematics of two observed sets of phases of flow channel development in square cross-section silos showing parabolic-like channel profiles, from Kvapil (1959) and Hampe (1987)

7.2.2 Generalised flow channel geometry

The mixed flow pressure theory is introduced here with a description and definition of the full geometry of both the silo and the profile of the flow channel. The flow channel geometry is idealised in terms of three possible flow regions, presented in Fig. 7.3, for four distinct or 'fundamental' types of flow (Fig. 7.3 is a 3D version of Fig. 7.1): concentric pipe flow (ConP), concentric mixed flow (ConM), eccentric parallel or taper pipe flow (EccP) and eccentric mixed flow (EccM). It is assumed in this theory that both top the surface of the solid and the base of the silo are perfectly flat, and both the silo and the outlet cross-sections are circular. If the filling surface is not flat in the application, an equivalent surface should be assumed as is currently done for Janssen analyses. A plane of axial symmetry is present through the coordinates $\theta = 0°$ and 180°.

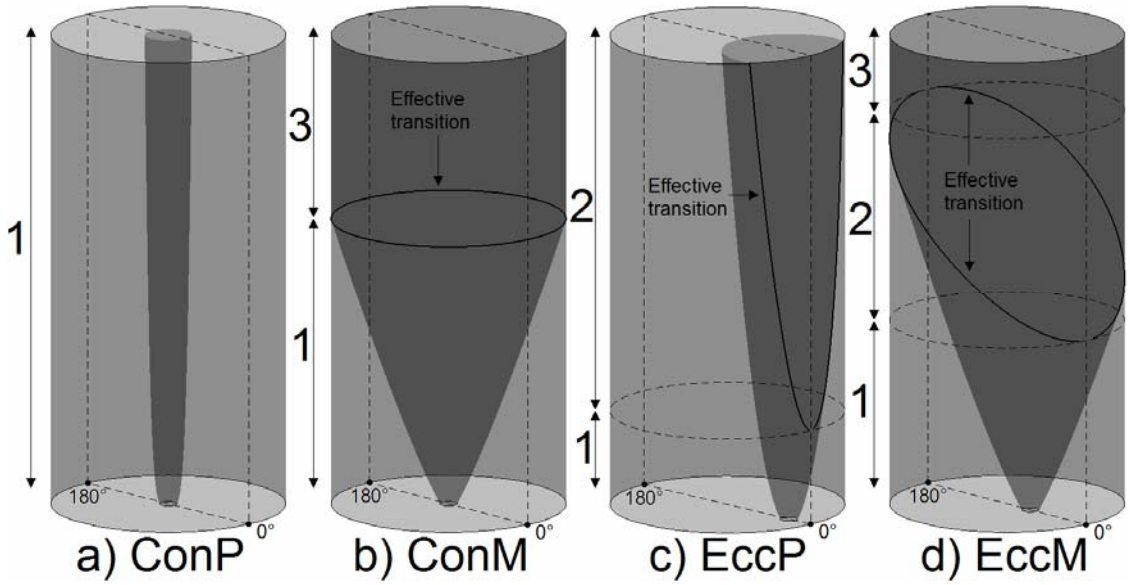

Fig. 7.3 – Idealised flow patterns and their relation to proposed flow regions

Three possible flow regions are defined as follows, assuming all three are present for a particular flow pattern (e.g. EccM on Fig. 7.3). Moving away from the outlet, there is a vertical portion of the silo in which the flow channel is assumed to be fully internal and has a fully circular cross-section; this is named the 'Hopper Region' or Region 1, as the internal flow channel may be thought of as an 'internal' hopper. As the channel widens moving further up the silo, it eventually intersects the wall at $\theta = 0°$ where a new region is assumed to begin. The new region is named the 'Transition Region' or Region 2, and the flow channel has a truncated circular cross-section with a partial circumferential contact with the silo wall. In Region 2, the axial position of the effective transition varies around the circumference. Moving further up the silo, the far side of the channel

eventually also intersects the wall at $\theta = 180°$, at which point the channel now extends across the entire silo cross-section and there is no longer any stationary solid present; this is named the 'Cylindrical Region' or Region 3. The silo is under mass flow in this region.

Naturally, if the flow is concentric (e.g. ConM on Fig. 7.3), the channel-wall intersect and therefore the entire effective transition is located at the same level around the full circumference, and there is no Region 2. Alternatively, if the channel is very steep, i.e. a rathole or pipe flow, Region 1 may exist over the entire silo height if the flow is concentric (e.g. ConP) or, if eccentric, may eventually come into contact with a narrow strip of the wall (e.g. EccP) entering into Region 2. If maximum eccentricity is assumed instead, the flow enters straight into Region 2 directly above the outlet.

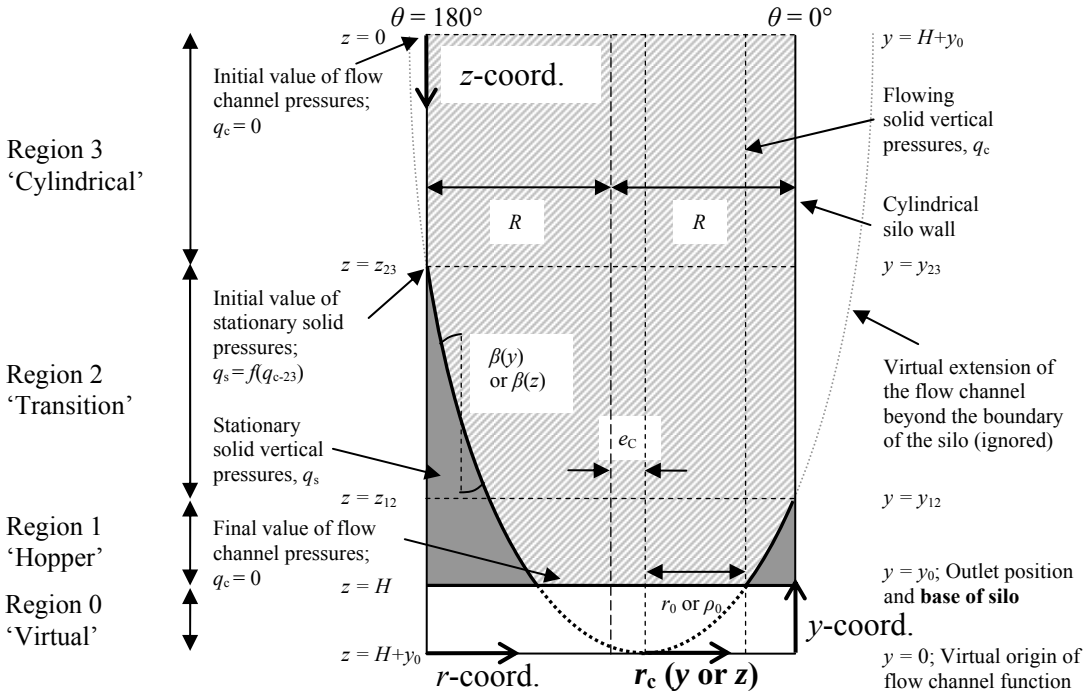

Fig. 7.4 – Silo region and coordinate system definition

A slice through the plane of symmetry identified on Fig. 7.3 is shown in Fig. 7.4. This figure is annotated with an algebraic definition of the assumed geometry and coordinate systems. The global and local positions of the channel sides, r and r_c, are defined in terms of the vertical coordinate which itself may be defined as starting from the base of the silo, y, or the top, z (Eqs 7.1 and 7.2, following the conventions introduced in Fig. 1.20). The slope of the flow channel to the vertical is given by β (Eq. 7.3). The vertical

pressures in the flow channel and the stationary solid are assigned the notation q_c and q_s respectively.

The required input parameters are the silo height and radius, H and R respectively, the outlet eccentricity e_c, the steepness of the flow channel profile n and the circular outlet radius r_0. All other geometric parameters are calculated from these. Additionally, the granular solid properties which are required include the fully-developed wall and internal friction coefficients, μ_w and $\mu_i = \tan\phi_i$, the wall pressure ratio K and the unit weight γ. In terms of the EN 1991-4 (2007) terminology, these should be the upper characteristic granular solid properties.

To ensure that the outlet radius has a non-zero value r_0, the y coordinate system was arranged so as to place the origin $y = 0$ of the flow channel curve (the 'virtual origin') at some distance y_0 below the base of the silo. The outlet is thus located at $y = y_0$, and the region between the virtual origin and the outlet is named the 'Virtual Region' or Region 0. It is not included in any calculations, as it is assumed that the integration terminates at the outlet. The location of the virtual origin is dependent on the assumed granular solid properties of the flow channel, the channel steepness n and the desired outlet radius r_0. Its derivation is presented shortly. The z coordinate system is arranged so that the (flat) surface of the solid is at the coordinate $z = 0$, the outlet at $z = H$ and the virtual origin at $z = H + y_0$. This is annotated on Fig. 7.4.

The local radial coordinate r_c of the flow channel profile is given by:

$$r_c(y) = m(y)^{\frac{1}{n}} \text{ or } r_c(z) = m(y_0 + H - z)^{\frac{1}{n}} \tag{7.1}$$

The global radial coordinate r through the symmetry plane, defined as being zero at $\theta = 180°$ on the wall opposite the outlet (though this is not so important), is thus given by:

$$r(y) = R + e_c \pm r_c(y) \text{ or } r(z) = R + e_c \pm r_c(z) \tag{7.2}$$

The slope of the flow channel is given by:

$$\beta(y) = \tan^{-1}\left[\frac{m}{n}(y)^{\frac{1-n}{n}}\right] \text{ or } \beta(z) = \tan^{-1}\left[\frac{m}{n}(y_0 + H - z)^{\frac{1-n}{n}}\right] \tag{7.3}$$

The parameter m represents the 'expansivity' of the flow channel and is dependent on the location of the outlet above the virtual origin y_0 and on the outlet radius r_0. It is given by:

$$m = r_0 \left(y_0 \right)^{-\frac{1}{n}} \tag{7.4}$$

The axial location of the boundary between Regions 1 and 2 is given by:

$$y_{12} = \left(\frac{R - e_c}{m} \right) - y_0 \text{ or } z_{12} = H + y_0 - \left(\frac{R - e_c}{m} \right) \tag{7.5}$$

Additionally, the axial location of the boundary between Regions 2 and 3 is given by:

$$y_{23} = \left(\frac{R + e_c}{m} \right) - y_0 \text{ or } z_{23} = H + y_0 - \left(\frac{R + e_c}{m} \right) \tag{7.6}$$

If the flow is concentric, then Region 2 does not exist and Eqs 7.2.5 and 7.2.6 naturally give the same result. The coordinate ranges for the flow regions are summarised in Table 7.1.

Table 7.1 – Summary of region definitions and description

Region	↑ +ive, y range	↓ +ive, z range	Description
0	$0 \le y \le y_0$	$H \le z \le H+y_0$	Ignored region below channel outlet
1	$y_0 \le y \le y_{12}$	$z_{12} \le z \le H$	Fully-internal flow channel
2	$y_{12} \le y \le y_{23}$	$z_{23} \le z \le z_{12}$	Partially-internal flow channel
3	$y_{23} \le y \le H+y_0$	$0 \le z \le z_{23}$	Axisymmetric mass flow

7.2.3 Assumptions regarding material properties

It is assumed that, for vertical solid-wall interfaces, the mean pressure normal to the wall is related to the mean vertical pressure in the granular solid through a *constant* lateral pressure ratio, K. This ratio may be different depending on whether the solid is stationary (K_{sw}) or flowing (K_{cw}). The ratio of the mean horizontal and vertical pressures within the flow channel itself was assigned the term K_c. These values are left open here and will be decided on during implementation, but it is important to note at this point that this is a very basic assumption for the lateral pressure ratio.

All vertical solid-wall interfaces are assumed to carry the same constant wall friction coefficient, μ_w, which relates the frictional traction on the wall to the normal pressure on that interface. The wall friction is assumed to be fully-developed in all cases.

For inclined stationary-flowing solid interfaces, it is assumed that mean pressure normal to the interface is related to the mean vertical pressure in the flowing solid through a normal pressure ratio akin to that for hoppers, F. It will be shown shortly that the value

of F is dependent on the local slope of the flow channel profile, β, and is obtained by considerations of local equilibrium.

All inclined stationary-flowing solid interfaces are assumed to carry the same internal friction coefficient, μ_i, which relates the frictional traction on the interface to the normal pressure on that interface. The internal friction coefficient is obtained from the internal friction angle of the granular solid through the usual relation $\mu_i = \tan \phi_i$.

It was assumed in this study that there is no radial variation in pressures within either the stationary or flowing solid, regardless of position. This aspect will be explored in Appendix B with an elasticity theory solution.

7.2.4 Derivation of geometry components per flow region

Due to the nature of the calculations involved in this theory, it is significantly easier to integrate the differential equations if they are written in terms of the downwards positive z coordinate system. Additionally, each of the three flow regions defined in the preceding section requires different expressions for the area, perimeter and angular components. The flow channel is fully-circular and therefore very simple to define for Regions 1 and 3, but it is only partially internal in Region 2, for which a more complex truncated circular cross-section is defined in Fig. 7.5. The full set of geometric components are summarised in Table 7.2.

The cross-section through Region 2 has the following geometric properties:

$$A_c = (\pi - \psi) r_c^2 + \theta_c R^2 - e_c R \sin\theta_c \tag{7.7}$$

$$A_s = \pi R^2 - A_c \tag{7.8}$$

$$\theta_c = \cos^{-1}\left(\frac{R^2 + e_c^2 - r_c^2}{2 e_c R}\right) \tag{7.9}$$

$$\psi = \sin^{-1}\left(\frac{R}{r_c}\sin\theta_c\right) \tag{7.10}$$

where r_c, ψ, θ_c (and therefore A_c and A_s) are functions of z. It is clear that the sine rule was used to derive ψ from θ_c, and care must be taken to ensure that the angle ψ falls into the correct quartile. A transformation $\psi \rightarrow \pi - \psi$ may be necessary.

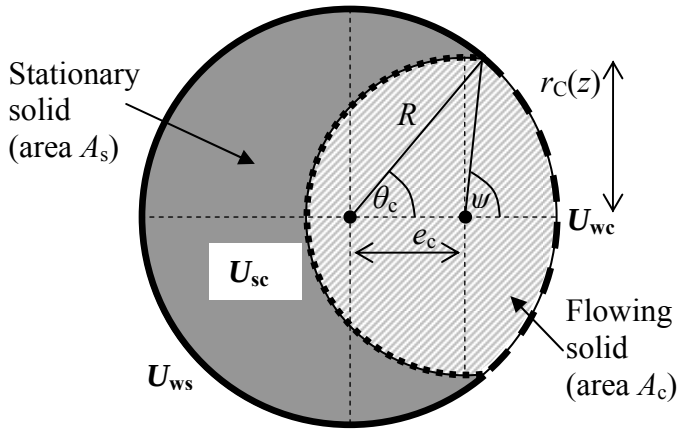

Fig. 7.5 – Channel geometry definition for Region 2

Table 7.2 – Region-dependent area and perimeter components

	Description	Region 1	Region 2	Region 3
U_{wc}	Perimeter between silo wall and flow channel	0	$2\theta_c R$	$2\pi R$
U_{ws}	Perimeter between silo wall and stationary solid	$2\pi R$	$2(\pi - \theta_c)R$	0
U_{sc}	Perimeter between stationary solid and flow channel	$2\pi r_c$	$2(\pi - \psi)R$	0
A_c	Cross-sectional area of flow channel	πr_c^2	Eq. 7.7	πR^2
A_s	Cross-sectional area of stationary solid	always $\pi R^2 - A_c$		
θ_c	Flow channel wall contact angle w.r.t silo centre	0	Eq. 7.9	2π
ψ	Flow channel wall contact angle w.r.t channel centre	0	Eq. 7.10	2π

7.2.5 Derivation of ordinary differential equations governing the solid pressures per flow region

7.2.5.1 Overview

The derivations of the ordinary differential equations governing the flow channel and stationary solid pressures are presented in the follows sections. Vertical equilibrium of a slice of granular material (assumed to be a continuum) with infinitesimally small thickness dz is resolved through each of the three different flow regions defined in Fig. 7.4. Regardless of the form of the flow channel profile, a straight slope is assumed between the two meridional boundaries of any elemental slice $z_{top} = z$ and $z_{bot} = z + dz$. The slope of each slice $\beta(z_m)$ is given by Eq. 7.3 where z_m is the z coordinate at the middle of the slice, such that $z_m = ½(z_{top} + z_{bot})$.

7.2.5.2 Region 1 - Vertical equilibrium through a slice of the silo cross-section

The slice equilibrium analysis for the fully-internal channel (Region 1) is summarised in Fig. 7.6.

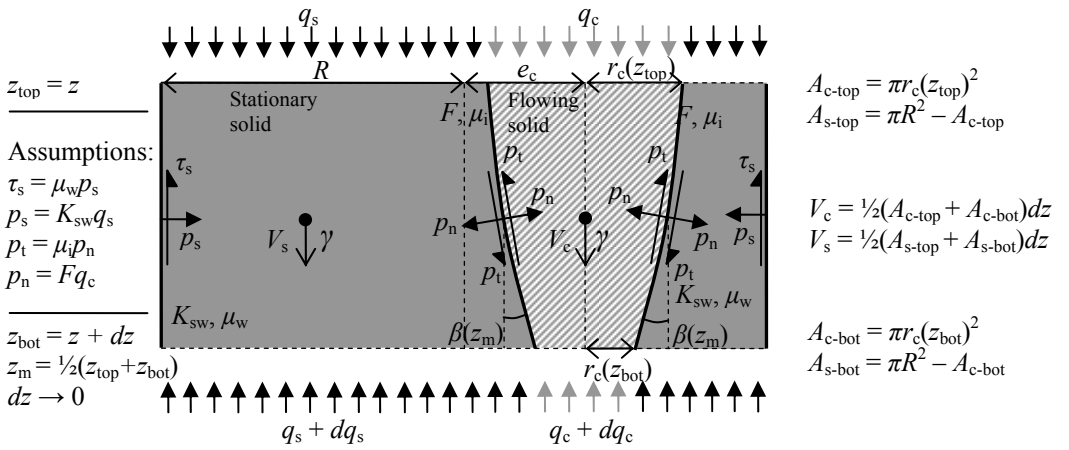

Fig. 7.6 – Elemental slice equilibrium and assumptions of Region 1

Resolving the vertical equilibrium of the flow channel component results in:

$$\sum\downarrow: \quad q_c A_{c-top} + \gamma V_c$$

$$\sum\uparrow: \quad \left(q_c + dq_c\right) A_{c-bot} + q_c \left(\sin\beta + \mu_i \cos\beta\right) F U_{sc} \frac{dz}{\cos\beta}$$

Equating these and incorporating the accompanying assumptions leads to the following differential equation governing the vertical pressure in the flow channel in Region 1:

$$dq_c = q_c \left(\frac{A_{c-top} - A_{c-bot}}{A_{c-bot}} \right) + \gamma \left(\frac{A_{c-top} + A_{c-bot}}{2A_{c-bot}} \right) dz - q_c \left(\tan\beta + \mu_i\right) F \frac{U_{sc} dz}{A_{c-bot}} \tag{7.11}$$

Resolving the vertical equilibrium of the stationary solid component yields:

$$\sum\downarrow: \quad q_s A_{s-top} + \gamma V_s + q_c \left(\sin\beta + \mu_i \cos\beta\right) F U_{sc} \frac{dz}{\cos\beta}$$

$$\sum\uparrow: \quad \left(q_s + dq_s\right) A_{s-bot} + q_s \mu_w K_{sw} U_{ws} dz$$

The corresponding differential equation governing the vertical pressure in the stationary solid in Region 1 is thus obtained in a similar manner:

$$\begin{aligned} dq_s = {} & q_s \left(\frac{A_{s-top} - A_{s-bot}}{A_{s-bot}} \right) + \gamma \left(\frac{A_{s-top} + A_{s-bot}}{2A_{s-bot}} \right) dz \ldots \\ & - q_s \mu_w K_{sw} \frac{U_{ws} dz}{A_{s-bot}} + q_c \left(\tan\beta + \mu_i\right) F \frac{U_{sc} dz}{A_{s-bot}} \end{aligned} \tag{7.12}$$

7.2.5.3 Region 1 - Local equilibrium at the interface of the flowing and static solid

Local equilibrium of a triangular element of the flow channel at the interface to the stationary solid is shown in Fig. 7.7.

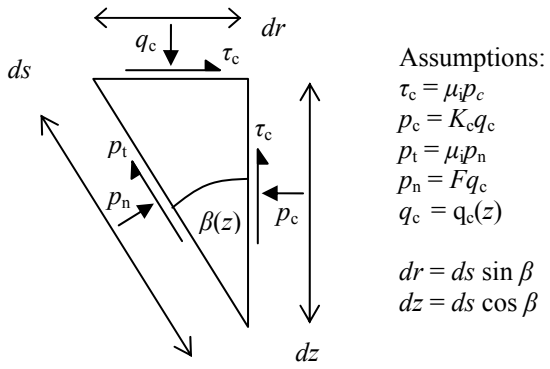

Fig. 7.7 – Local equilibrium within the flowing solid at the stationary solid interface in Region 1 with relevant assumptions

Resolving the vertical equilibrium leads to the following equations:

$\sum\downarrow: \; q_c dr$ and $\sum\uparrow: \; \tau_c dz + p_n ds \sin\beta + p_t ds \cos\beta$

Resolving the horizontal equilibrium leads to these equations:

$\sum\rightarrow: \; \tau_c dr + p_n ds \cos\beta$ and $\sum\leftarrow: \; p_c dz + p_t ds \sin\beta$

Equating, incorporating the accompanying assumptions and rearranging leads to the following condition for the normal wall pressure ratio within the internal hopper:

$$F = \frac{\tan^2\beta - K_c}{\tan^2\beta + 2\mu_i \tan\beta - 1} \tag{7.13}$$

Thus the normal wall pressure ratio is a function of the local flow channel slope, the internal friction angle and the lateral pressure ratio of the solid.

7.2.5.4 Region 2 - Vertical equilibrium through a slice of the silo cross-section

The slice equilibrium analysis for the partially-internal channel (Region 2) is summarised in Fig. 7.8.

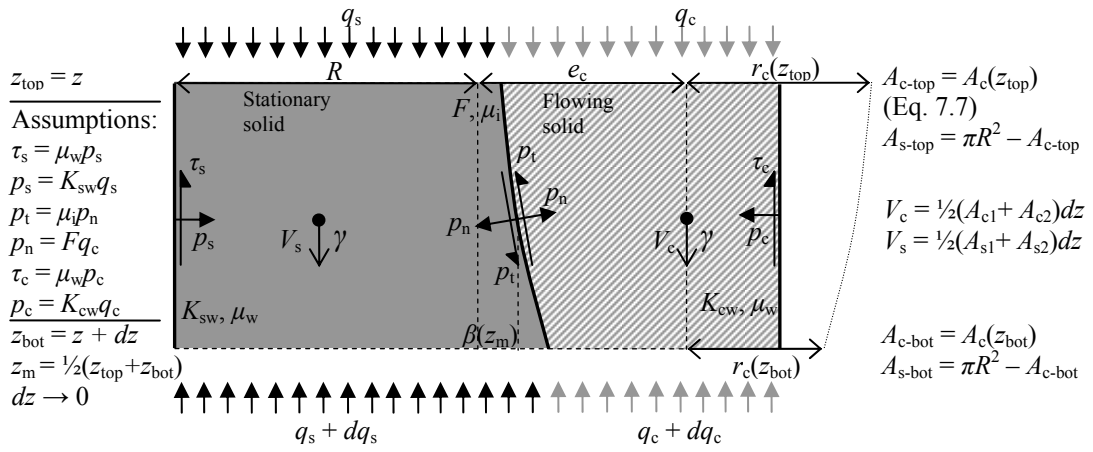

Fig. 7.8 – Elemental slice equilibrium and assumptions of Region 2

Resolving the vertical equilibrium of the flow channel component results in:

$$\sum\downarrow: \quad q_c A_{c-top} + \gamma V_c$$

$$\sum\uparrow: \quad \left(q_c + dq_c\right) A_{c-bot} + q_c \mu_w K_{cw} U_{wc} dz + q_c \left(\sin\beta + \mu_i \cos\beta\right) F U_{sc} \frac{dz}{\cos\beta}$$

Equating and incorporating the accompanying assumptions leads to the ordinary differential equation governing the vertical flow channel pressure in Region 2:

$$\begin{aligned} dq_c = q_c \left(\frac{A_{c-top} - A_{c-bot}}{A_{c-bot}}\right) + \gamma \left(\frac{A_{c-top} + A_{c-bot}}{2A_{c-bot}}\right) dz \ldots \\ - q_c \mu_w K_{cw} \frac{U_{wc} dz}{A_{c-bot}} - q_c \left(\tan\beta + \mu_i\right) F \frac{U_{sc} dz}{A_{c-bot}} \end{aligned} \tag{7.14}$$

The equation for dq_s is the same as for Region 1 (Eq. 7.12) though the expressions for the geometric components will be different (Table 7.2).

7.2.5.5 Region 3 - Vertical equilibrium through a slice of the silo cross-section

The slice equilibrium analysis for the channel covering the full silo cross-section (Region 3) is summarised in Fig. 7.9. Note that this is effectively the Janssen derivation.

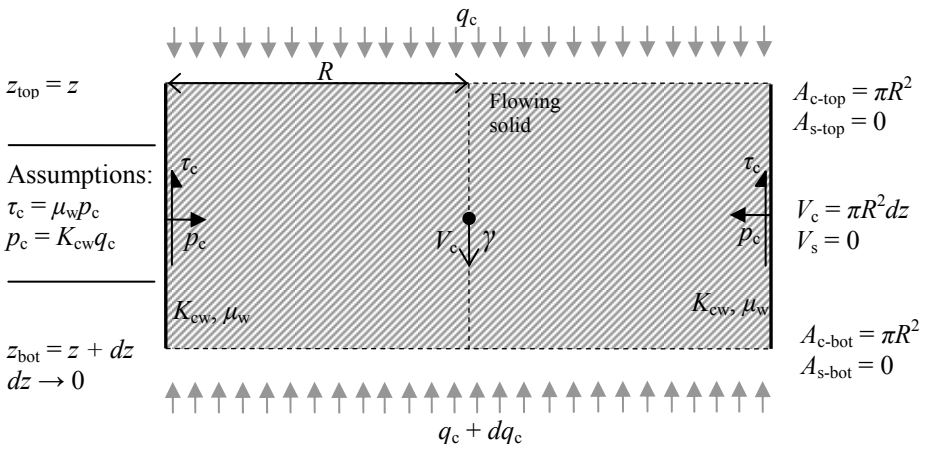

Fig. 7.9 – Elemental slice equilibrium and assumptions of Region 3

Resolving the vertical equilibrium of the flow channel component results in:

$$\sum\downarrow: \; q_c A_{c-top} + \gamma V_c$$

$$\sum\uparrow: \; \left(q_c + dq_c\right) A_{c-bot} + q_c \mu_w K_{cw} U_{wc} dz$$

Equating and incorporating the accompanying assumptions leads to the ordinary differential equation governing the vertical flow channel pressure in Region 3:

$$dq_c = q_c \left(\frac{A_{c-top} - A_{c-bot}}{A_{c-bot}} \right) + \gamma \left(\frac{A_{c-top} + A_{c-bot}}{2 A_{c-bot}} \right) dz - q_c \mu_w K_{cw} \frac{U_{wc} dz}{A_{c-bot}}$$

This is a reduced version of Eq. 7.12 without the term describing the shear at the interface between the stationary and flowing solids. With the proper substitutions for the area and perimeter terms, this equation may be solved analytically to give the Janssen equation. As the vertical pressure in the stationary solid is not defined for Region 3, there is corresponding equation for dq_s.

7.2.6 Specification of boundary conditions

7.2.6.1 BC1 - top surface condition

The vertical pressure within the flow channel and stationary solid (if present) are assumed to be zero at the top surface, which is also assumed to be flat. Hence: $q_c(0) = q_s(0) = 0$.

7.2.6.2 BC2 - intersection condition

Where the stationary solid does not reach the surface, its starting value of vertical pressure, $q_{s\text{-}23}$, is a function of the local vertical pressure in the flow channel $q_{c\text{-}23}$ based on local equilibrium of a triangular element of stationary solid at the boundary between

Regions 2 and 3 (Fig. 7.10). For the special case of concentric discharge, Region 2 is not present and this will instead be the boundary between Regions 1 and 3.

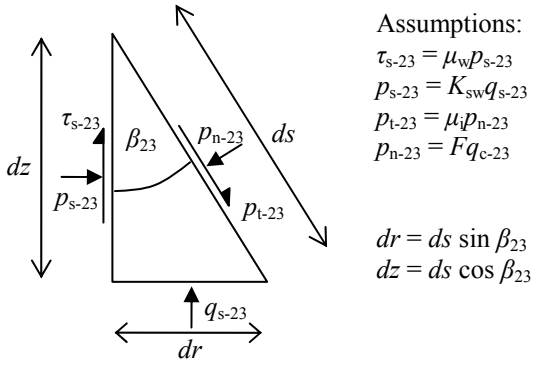

Fig. 7.10 – Local equilibrium within the stationary solid at effective transition: the boundary of Regions 1 and 2 or Regions 1 and 3

Resolving the vertical equilibrium of the triangular element leads to:

$\sum \downarrow: \; q_{s-23} dr + \tau_{s-23} dz$ and $\sum \uparrow: \; p_{n-23} ds \sin \beta_{23} + p_{t-23} ds \cos \beta_{23}$

Therefore:

$$q_{s-23} = q_{c-23} F_{23} \frac{\left(\tan \beta_{23} + \mu_i\right)}{\left(\tan \beta_{23} + \mu_w K_{sw}\right)} \tag{7.15}$$

where z_{23} is the z coordinate of the boundary between Regions 2 and 3, β_{23} is the channel slope at this boundary and $F_{23} = F(\beta_{23})$ is the normal pressure ratio for the internal hopper at this boundary. The equation for $F(\beta)$ is presented in Eq. 7.13. If there is no Region 2 in the flow pattern, the values for $q_{c\text{-}13}$, z_{13}, β_{13} and F_{13} are used instead to give $q_{s\text{-}13}$.

7.2.6.3 BC3 - outlet condition

It is assumed that the granular solid is in free fall at the base outlet, and it must be ensured that the vertical pressure in the flow channel falls to zero at this location. Returning to the internal hopper normal wall pressure ratio, Eq. 7.13, it is clear that this equation has the potential to lead to a singularity and consequently to a value of zero vertical pressure in the flow channel. Setting the denominator of this equation equal to zero, solving the resulting quadratic equation and taking only the positive root results in the following condition for the critical value of the flow channel slope, β_0.

$\tan \beta_0 = \sqrt{\tan^2 \phi_i + 1} - \tan \phi_i$ where $\mu_i = \tan \phi_i$

The value may be written in a different form: $\beta_0 = \frac{\pi}{4} - \frac{\phi_i}{2}$ (7.16)

The critical flow channel slope is dependent only on the angle of internal friction. The height above the flow channel origin at which this value is reached can be derived from Eqs 7.3 and 7.4:

$$y_0 = \frac{r_0}{n \tan \beta_0} \tag{7.17}$$

At this location, the vertical pressure in the flow channel must fall to zero and this must therefore be the location of the outlet. The outlet radius r_0 has been incorporated into Eq. 7.17 so that the flow channel radius at $y = y_0$ or $z = H$ is ensured to be r_0. It was mentioned previously that the z coordinate system was defined in relation to the virtual origin so that $z = 0$ is at the top of the silo and $z = H$ is at the outlet (Fig. 1.20 and Fig. 7.4).

7.2.6.4 BC4 - steepness condition

A direct consequence of BC 3 above, the entire flow channel assumes the critical slope angle of β_0 if the channel is conical ($n = 1$), and the wall pressure ratio of the internal hopper becomes infinite everywhere. This is evident from Eqs 7.2 and 7.17:

$$\beta = \tan^{-1} \frac{1}{m} = \tan^{-1} \frac{\rho_0}{\xi_0} = \beta_0$$

The power of the flow channel profile n therefore cannot be less than or equal to unity: $n > 1$. Though this is a minor limitation of this theory, in practice it is not known whether a channel can genuinely assume a profile with $n < 1$.

7.2.6.5 Constraint on the maximum eccentricity

The following is not considered as a boundary condition *per se*, but should nonetheless be satisfied when defining the initial geometry if a fully-circular outlet is desired. In this case, the eccentricity e_c cannot be such that the outlet circle itself becomes truncated, thus the maximum permissible eccentricity must be one outlet radius short of the silo radius. In algebraic terms: $e_c \leq R - r_0$. It should be added that, when $e_c = R - r_0$, there is no Region 1 flow.

7.2.7 Obvious limitations of this theory

The system has only one degree of freedom and consequently one of the most significant limitations of this new theory is the fact that it only considers vertical

equilibrium to calculate the vertical pressures in the flow channel and the stationary solid. These are then assumed to be constant throughout the given component at any one vertical coordinate. This implies, for example, that a narrow strip of stationary solid will have the same vertical pressure, and therefore will exert the same normal pressure on the wall, as a large concentration of stationary solid at the same level. Additionally, if the channel is fully internal, the pressures everywhere will be exactly the same regardless of whether the channel is fully concentric or almost touching the wall.

It is not possible to address this limitation without going deeply into the radial and circumferential equilibrium considerations of what is a very complex curved planar body. Such an analysis, using elasticity theory, is presented in Appendix B for completeness. It requires the use of bipolar coordinates and stress functions (complex-number potentials), and is extremely unwieldy in its application. Instead of broadening the range of possible uses that this new pressure theory would have, incorporating an additional layer of such complexity would instead most likely limit its appeal.

7.3 Initial analytical investigation: Numerical procedure and assumed material properties

The ramaining sections of this chapter explore some of the vast range of possible solutions to the differential equations derived above governing the vertical pressure in the stationary and flowing solids. The changes in the vertical solid pressure dq_s and dq_c are effectively controlled by just two equations throughout the entire silo (Eqs 7.12 and 7.14), with region-specific expressions for the area and perimeter components (Table 7.2).

The solutions to these differential equations have no discontinuities and hence do not require very small step sizes for adequate accuracy. Since computing power is inexpensive, a simple Euler integration scheme was assumed, with a relatively modest step size dz of $10^{-4}R$:

$$q(z+dz) = q(z) + dq(z) \tag{7.18}$$

The results in this section are presented both in terms of the vertical pressure in the flow channel and stationary solid, and in terms of the pressure acting normal to the silo wall. To this end, the lateral pressure ratio which includes both plastic and shearing failure of the granular solid was assumed in all calculations (AS 3774, 1996), given by:

$$K_{sw} = K_{cw} = \frac{1+\sin^2\phi_i - 2\sqrt{\sin^2\phi_i - \mu_w^2\cos^2\phi_i}}{4\mu_w^2 + \cos^2\phi_i} \tag{7.19}$$

Within the flow channel the solid is essentially shearing on itself, corresponding to a silo with ideally rough walls such that $\mu_w = \tan\phi_i$. In this case, the above simplifies to:

$$K_c = \frac{1-\sin^2\phi_i}{1+\sin^2\phi_i} \tag{7.20}$$

A discussion of the origin of the lateral pressure ratio may be found in the literature review, Section 1.2.3.

The following set of generic material properties was adopted for the purposes of these initial investigations: $\gamma = 9$ kN/m^3, $\mu_w = 0.44$ and $\phi_i = 33.6°$. Though these are clearly the upper characteristic values for wheat from Annex E of EN 1991-4 (2007), they are in fact reasonably representative of a wider range of solids. Over 70% of the materials listed in Annex E have solid properties within one standard deviation of the overall mean of that property. The above values may therefore be considered representative of at least wheat, sugarbeet pellets, sugar, sand, potatoes, maize, limestone, hydrated lime, coke, coal, powdered coal, cement and alumina. The material properties were kept constant throughout the analyses presented here, so that the effects of changes in flow channel geometry may be isolated and studied with clarity.

It should be noted that the relationship between channel geometry and material properties is currently unknown. It seems likely that the internal angle of friction ϕ_i may play an important role, since it appears in the equation for the critical channel angle β_0 (Eq. 7.15). Additionally, though a higher unit weight and a smoother wall may increase the magnitudes of the vertical solid pressures significantly, the actual axial distribution of these will not change significantly, especially when normalised by the local Janssen value. Furthermore, one may conclude from the initial study of this theory by Berry (1988) that variations in material properties have a minimal effect on the forms of the pressure distributions when compared to variations in the flow channel geometry, which have a radical effect.

7.4 Parametric studies of concentric flow patterns in a slender silo

7.4.1 Fully-internal concentric flow - variation of the outlet size

A slender silo with $H/D = 5.2$ was investigated first under fully-internal concentric flow (ConP, Fig. 1.1). The power of the channel shape was set constant at $n = 2$, while the outlet size was varied from a value of $r_0/R = 4\times10^{-4}$ (which generates a very steep, narrow channel) to 8×10^{-2} (which generates a wider, shallower channel that covers just about the whole silo cross-sectional area), which constitutes a representative range. The flow channel profiles corresponding to these two outlet sizes are shown in Fig. 7.11, and the full suite is shown in three-dimensions in Fig. 7.12. It is clear that the entire range of channels is in Region 1 flow only and there is no effective transition anywhere on the silo wall.

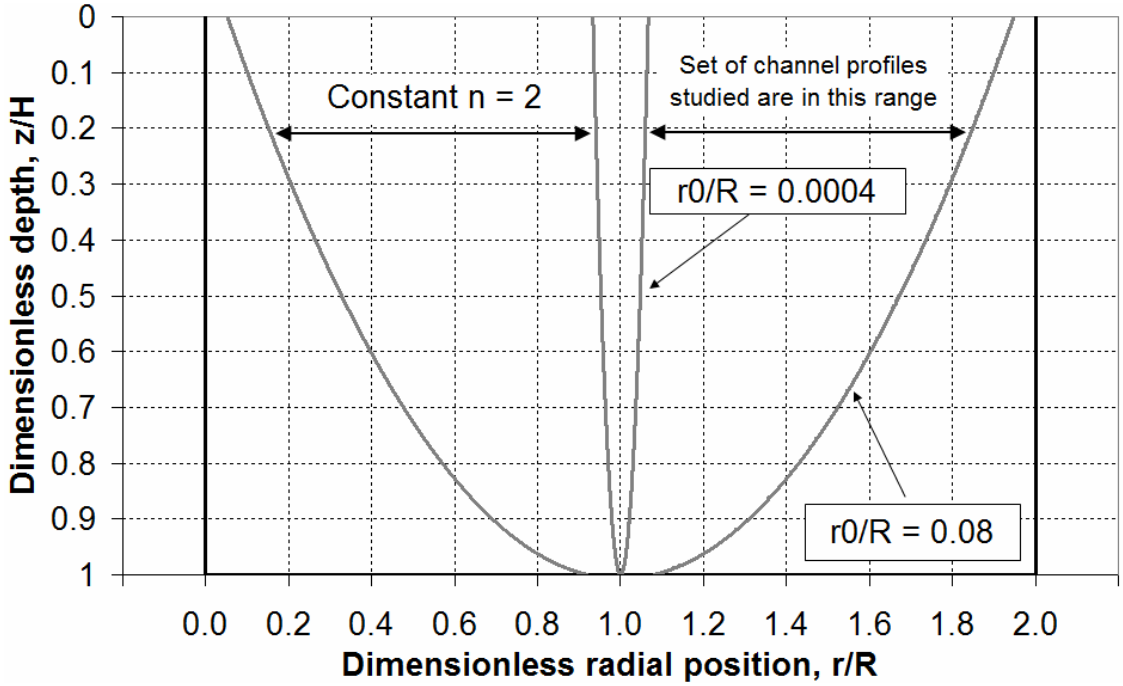

Fig. 7.11 – Profile outlines of the narrowest and widest investigated fully-internal concentric channel, with constant power $n = 2$

It can be seen in Fig. 7.11 that the actual steepness of the channel profile according to the mixed flow theory depends not only on the power of the distribution n but also on the outlet size r_0, since both of these parameters control the location of the virtual origin y_0. If it is desired that only the power n controls the channel steepness then the outlet size must be kept constant throughout.

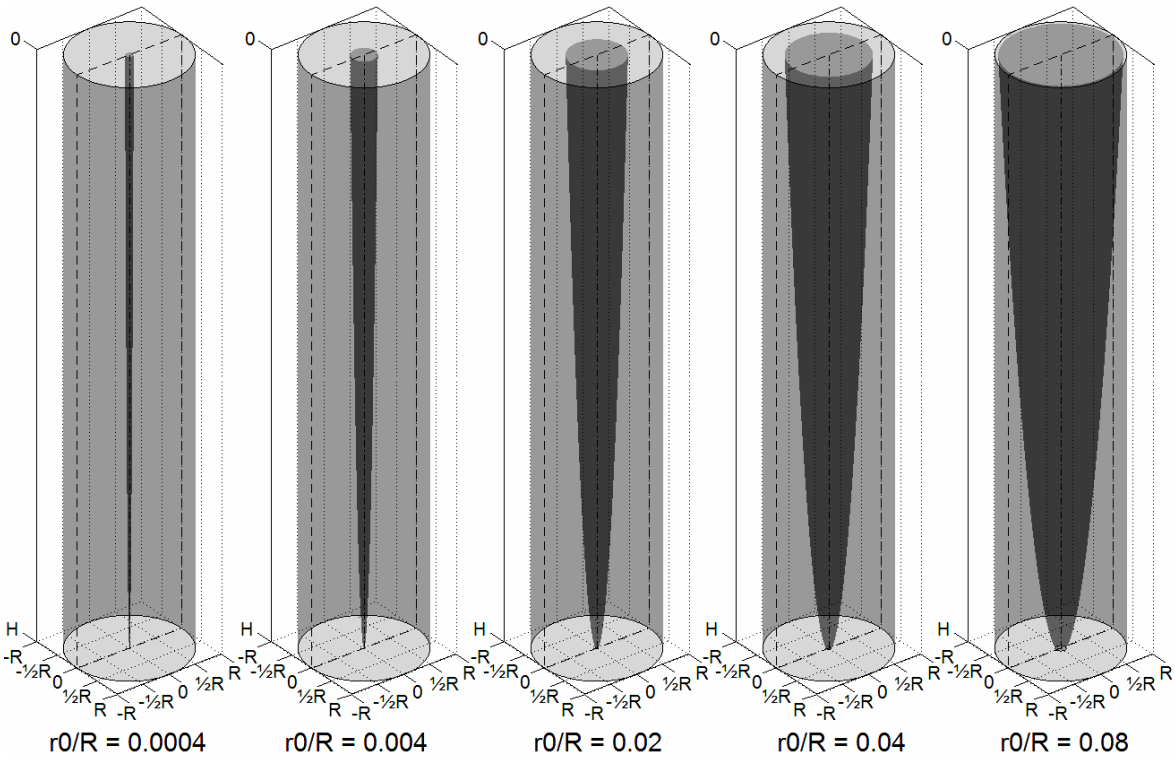

Fig. 7.12 – Three-dimensional channel and silo surfaces for the fully-internal suite of concentric channels, with constant power $n = 2$

The vertical pressures in both the flow channel and stationary solid are shown in Fig. 7.13 as a function of the outlet size. Clearly, the narrowest channel has a negligible influence on the pressure in the stationary solid, which effectively remains at the Janssen value (the green curve for $r_0/R = 4\times10^{-4}$ for the stationary solid pressure is not even visible). As the channel spreads out to cover a wider portion of the cross-sectional area of the silo, the vertical pressures in both the flow channel and stationary solid increase accordingly. However, in the part of the stationary solid below $z/H \approx 0.65$, a decrease in pressure is found instead. At the base of the silo, the vertical pressure for the widest channel $r_0/R = 0.08$ is predicted to have fallen to 88% of the base Janssen value, most likely as a result of the low flow channel pressure near the outlet. The Janssen equation by itself cannot predict this fall in vertical pressure near the base. Decreases in lateral pressure near the base of the silo under concentric discharge have been reported in the studies on square silos of Klopsch (1972), Gopalakrishnan (1978) and Kamiński and Zubrzycki (1981), and are of a similar order of magnitude. The results of the latter are demonstrated in Fig. 7.14 (based on the interpretation of Hampe, 1987) and show the pressure decrease quite clearly, in both model and full-scale silos.

The reported results mentioned above, like very many others in this field, should be treated with caution as it is difficult to ascertain exactly what it was that these authors measured and how they processed the corresponding results. It was mentioned in Section 1.2.6 of the literature review that experimenters usually confined their measurement to a single circumferential pressure cell and tended to report only on the measured peak pressure at that single point (Rotter, 2007a). As a consequence, confidently relating the predictions of the mixed flow pressure theory to 'measured' results is a difficult and risky process.

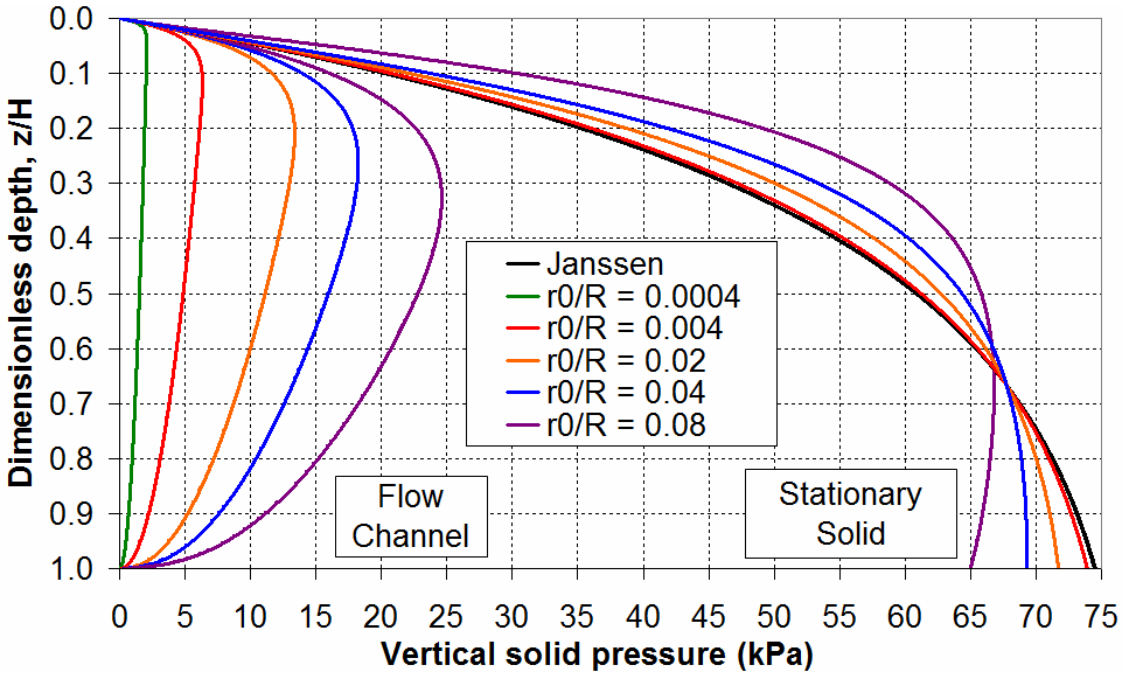

Fig. 7.13 – Vertical pressure in the flow channel and stationary solid under a widening internal concentric channel

Although the effect of internal pipe flow on the wall pressures is seen to be relatively minor, the actual shape of the axial distribution of the flow channel pressures (Fig. 7.13) is significant. It was previous explained that the precursor pressure models of eccentric discharge (Rotter, 1986; EN 1991-4, 2007) assumed parallel sides for the flow channel. The vertical pressure in the flow channel was therefore predicted to start at zero at the solid surface and tend to an asymptotic value with depth as there was no boundary condition of zero vertical stress at the base outlet. This is clearly not the case when the outlet boundary is incorporated (BC3), and the current mixed flow pressure theory instead predicts an expansion of the channel moving up from the outlet and consequently a rise in channel pressures with height. A few more detailed experimental

studies have reported that this may well be the case in reality (e.g. Ravenet 1976; Ooi *et al.*, 2005).

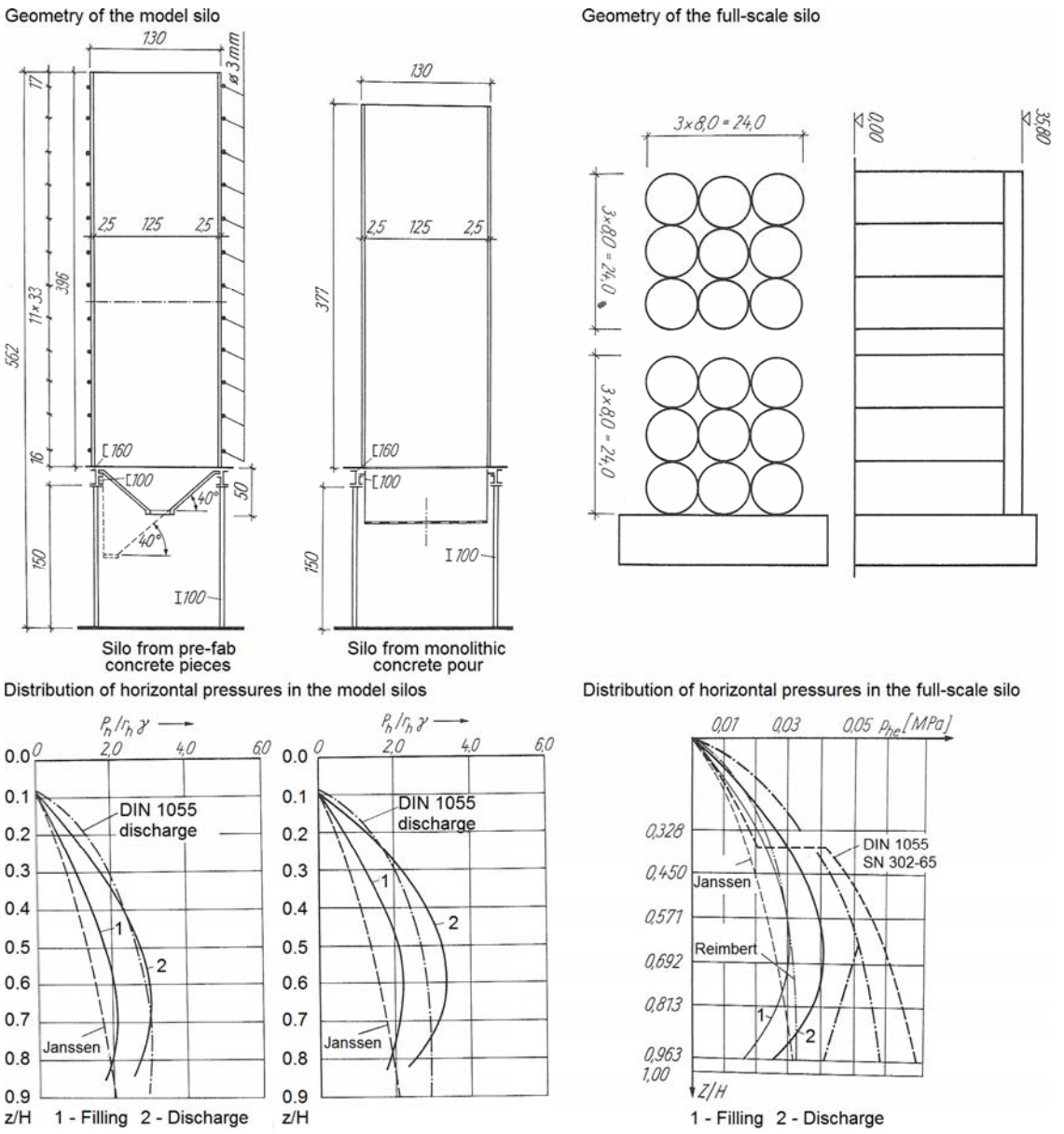

Fig. 7.14 – Reported results of an experimental study by Kamiński and Zubrzycki (1981), processed by Hampe (1987), showing the normal pressure distribution under concentric discharge and decreased pressures above the outlet

Solids which pack very loosely upon filling generally tend to form very wide channels during discharge, while densely-packed or slightly cohesive solids tend to form steeper flow channels (Rotter, 2001a; Zhong *et al.*, 2001). In funnel flow silos storing cohesive solids, steep channels may discharge completely while the adjacent solid remains stationary, a condition which arrests the flow entirely and is known as a ‘rathole’. This

would lead to a state of zero vertical stress in the now non-existent flowing solid, and it is likely that the surrounding stationary solid would retain the shape of a Janssen distribution for a silo of a smaller equivalent cross-sectional area (compare with Fig. 7.13).

A different outlook on the predicted effects of a widening internal flow channel is obtained when the normal wall pressure is made dimensionless by the local Janssen value, shown in Fig. 7.15. As the channel expands, a bulge is seen to develop near the top of the silo, increasing the normal wall pressure by over 50% for the largest channel. By contrast, the decrease at the base may be by as much as 15%. Note that this figure is based on the assumption of a constant value of K, which is unlikely to be the case in practice (e.g. Reimbert, 1961; Blight, 2006).

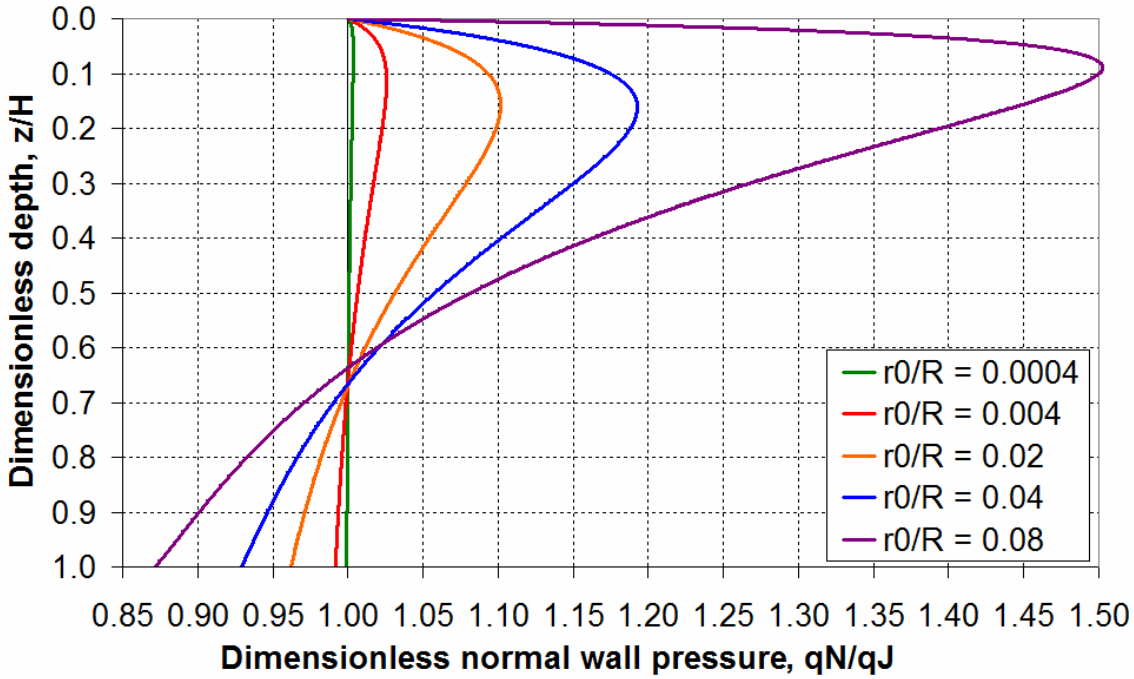

Fig. 7.15 – Dimensionless normal wall pressure under an internal concentric channel

The mixed flow pressure theory suggests that the predicted increases in normal pressures due to larger internal channels, though not likely to be very deleterious to the strength of the silo, may contribute to early yielding in upper parts of the silo wall due to the destabilising effect of high internal pressure (Eq. 1.20), thus exacerbating a potential elephant's foot failure mode at the base of a weaker strake (Rotter, 2006). This may be problematic since the wall is usually thinner in the upper region of a silo, having been designed for lower local Janssen pressures.

7.4.2 Mixed concentric flow - further variation of the outlet size

This second study investigated the effect of mixed concentric flow (ConM, Fig. 7.1) on the same slender silo, H/D = 5.2, as in the previous section. The power of the channel shape was set constant at n = 1.2, which generates significantly shallower profiles than n = 2. The outlet size was varied from $r_0/R = 4\times10^{-5}$ (which generates a fully-internal channel, but one covering almost the entire silo cross-section) to 0.2 (where the silo is almost completely under mass flow). The profiles of these two channels are shown in Fig. 7.16, and the full suite is shown in three-dimensions in Fig. 7.17. The flow patterns thus pass from Region 1 to 3 at the axisymmetric effective transition, which is seen to gradually descend down the height of the silo as the outlet becomes larger. There is no Region 2 flow.

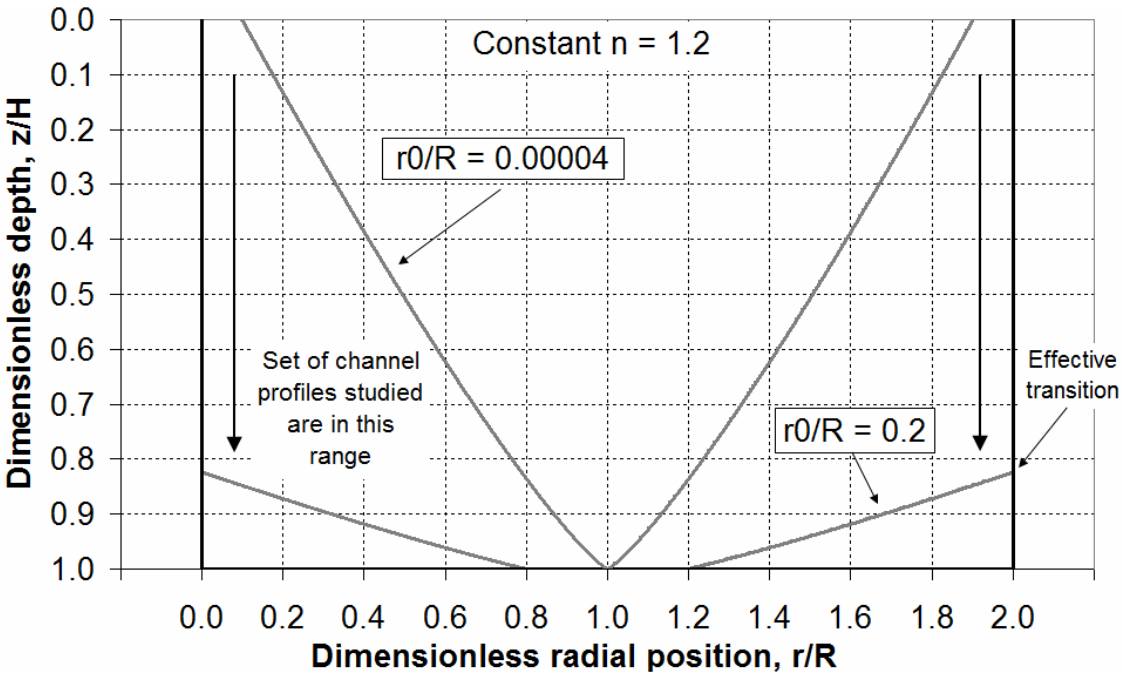

Fig. 7.16 – Profile outlines of the narrowest and widest investigated mixed flow concentric channel, with constant power n = 1.2

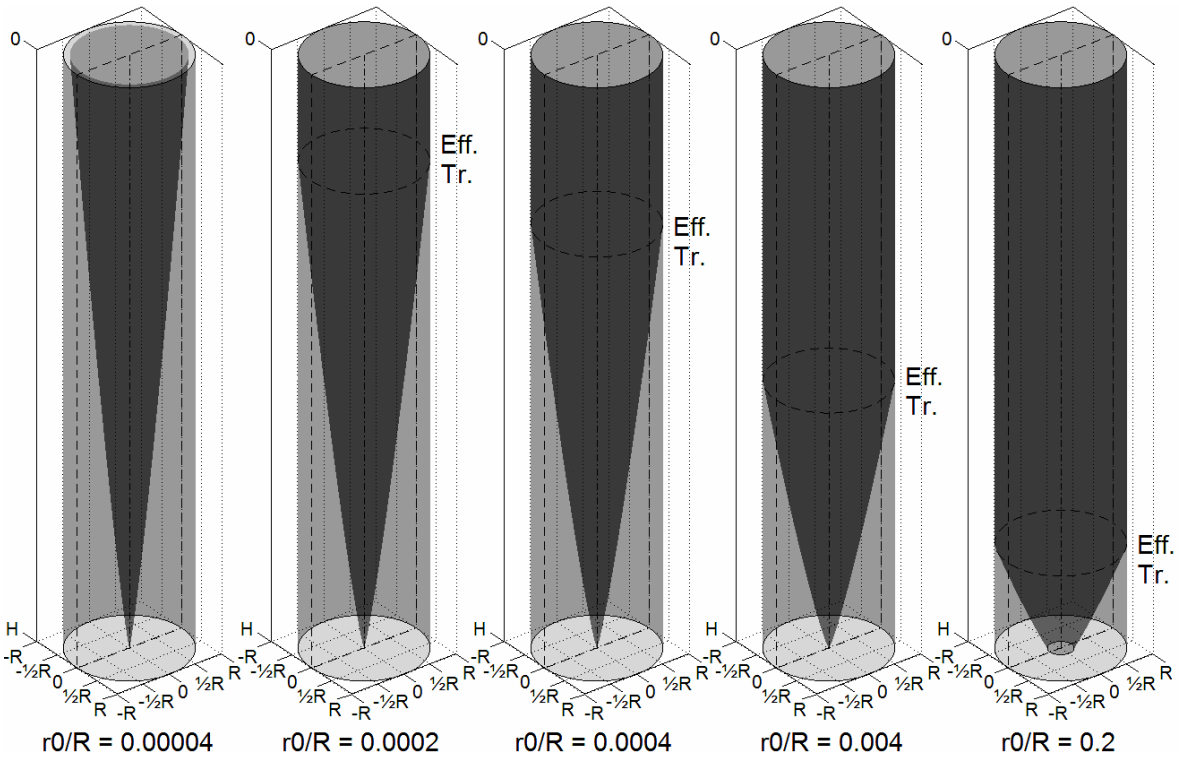

Fig. 7.17 – Three-dimensional channel and silo surfaces for the mixed flow suite of concentric channels, with constant power n = 1.2 (Note: Eff. Tr. = Effective Transition)

The vertical pressure in the flow channel and stationary solid is shown in Fig. 7.18 and Fig. 7.19 respectively as a function of the outlet size. The mixed flow regime starts at $r_0/R = 2\times10^{-4}$, and the solid adjacent to the wall at the position of the effective transition (the boundary of Regions 1 and 3) exhibits a sharp jump in vertical pressure. The phenomenon of the rise in normal wall pressure at the effective transition is illustrated further on the plot of normal wall pressure made dimensionless by the local Janssen value, Fig. 7.20. The pressure increases are up to at least 1.8 times the Janssen 'filling' value. For a slender silo with H/D = 5.2 under symmetrical discharge loads, the EN 1991-4 (2007) Standard prescribes a discharge factor for normal pressures of C_h = 1.15 + 1.5 (1 + 0.4 × e_c/D)C_{op} = 1.9 (where C_{op} is the patch load reference factor from Annex E, equal to 0.5 for wheat and many other granular materials) for Action Assessment Class 1 or C_h = 1.15 for (the less serious) Action Assessment Classes 2 or 3. The present predictions therefore suggest a remarkably close correlation with the Action Assessment Class 1 discharge factor for slender silos.

It should be noted that, for intermediate slender silos (1.0 < H/D < 2.0), C_h is a function of both the filling/outlet eccentricity and the aspect ratio but does not come anywhere

close to 1.8 unless quite large eccentricities are accounted for in the calculation. For squat silos ($H/D \leq 1.0$), a value of unity is prescribed for C_h, presumably because it is considered unlikely that significant mixed flows develop in silos of such low aspect ratios if to consider the example EN 1991-4 flow patterns (Fig. 4.1). In addition to corresponding well to the EN 1991-4 discharge factor for slender silos, the location and order of magnitude of the pressure spikes correspond well to those observed elsewhere (e.g. Nielsen and Kristiansen, 1980; Gale *et al.*, 1986; Rotter, 1999a).

The abrupt increase in wall pressures is achieved in the mixed flow pressure theory without tweaking the lateral pressure ratio in any way. Indeed, the value of the lateral pressure ratio was assumed constant throughout the silo, the simplest of assumptions. This is contrary to earlier attempts to explain the observed increases in normal wall pressures during discharge through sudden and unjustified rises in the lateral pressure ratio, most notably the 'switch' theory of Nanninga (1956), Walker (1966), Walter (1973), Jenike *et al.* (1973) and others who postulated a sudden switch from an active to a passive lateral pressure ratio which would result in a jump in normal pressure up to 10 times the filling value. However, it is recognised that the lateral pressure ratio need not be constant everywhere in the silo, and further experimental research is needed to calibrate this parameter for different flow patterns.

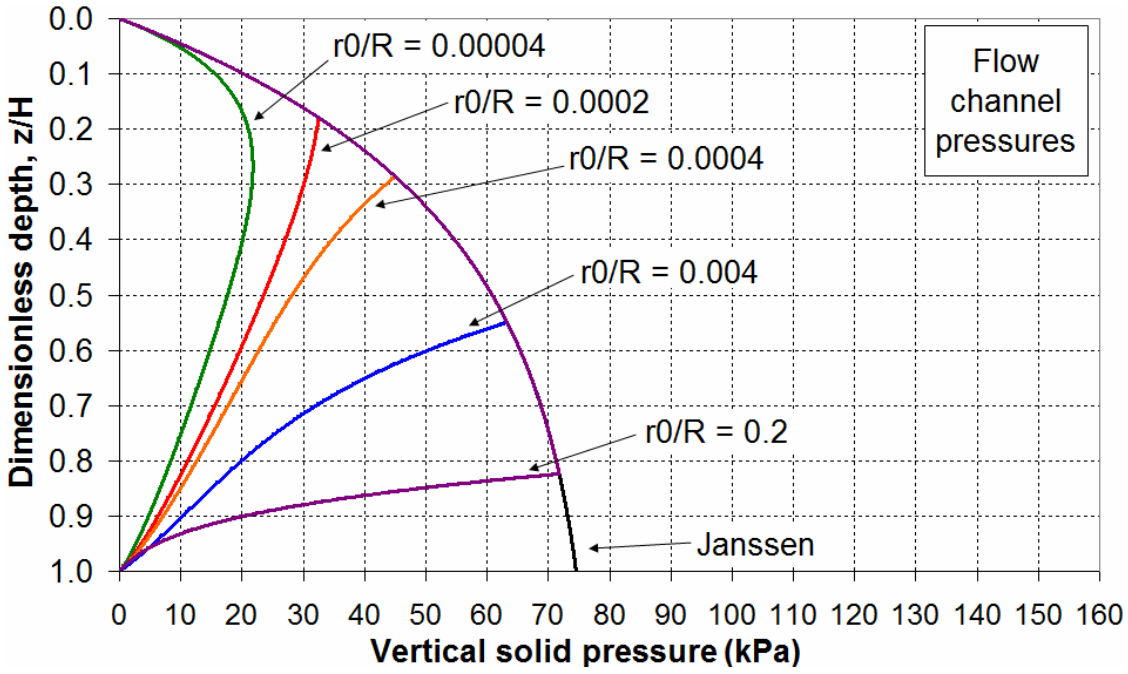

Fig. 7.18 – Vertical pressure in the flow channel under a widening concentric mixed flow regime

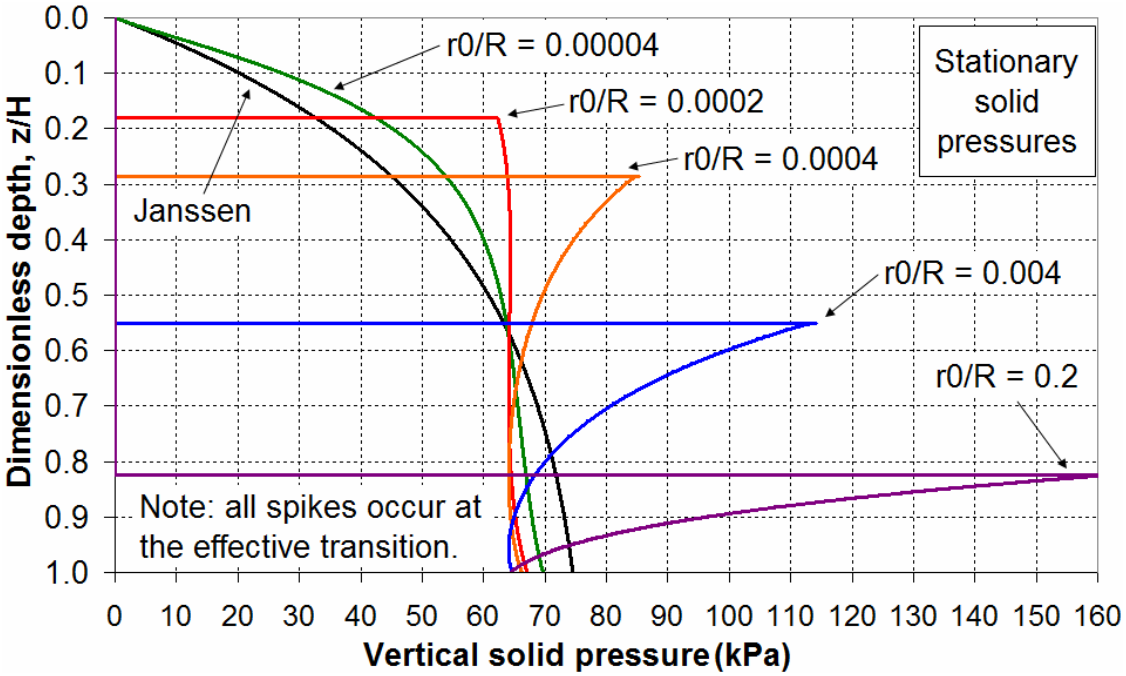

Fig. 7.19 – Vertical pressure in the stationary solid under a widening concentric mixed flow regime

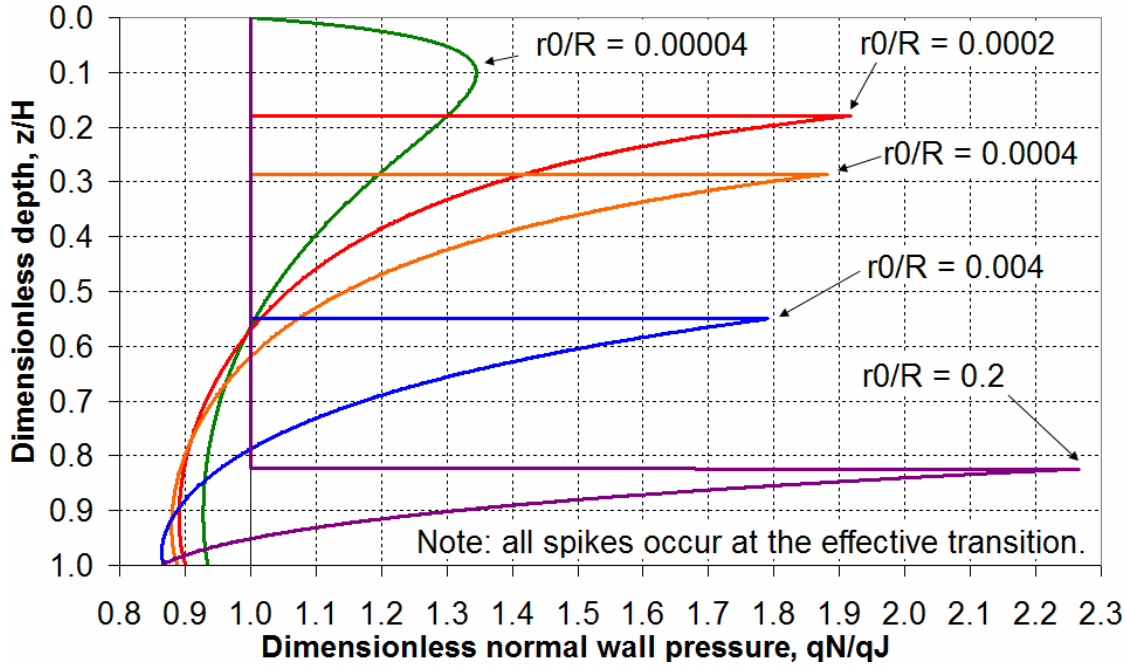

Fig. 7.20 – Dimensionless normal wall pressure under a widening concentric mixed flow regime

The starting value of vertical pressure in the stationary solid is significantly higher than the value of the local vertical pressure in the flow channel, a direct consequence of the local equilibrium implemented in BC2 at the effective transition (Fig. 7.10). It may be considered that the effective transition, which occurs at the boundary of the mass flow

and internal flow channel regions, is analogous to the transition between a silo and a hopper. The spike in normal wall pressure at the effective transition predicted by the mixed flow theory thus corresponds directly to similar abrupt rises in normal pressures at the silo-hopper transition, which have been predicted by application of the Janssen and Dąbrowski/Walker solid pressure theories (e.g. Hampe, 1987; Rotter, 2001a; 2007a) and widely observed experimentally (e.g. Motzkus, 1974; Nothdurft, 1976; Moriyama and Jotaki, 1980).

This analogy is illustrated in Fig. 7.21 and Fig. 7.22 which show, respectively, the distributions of normal wall pressure for the current suite of channel sizes and a set of curves showing the measured normal wall pressure on a square cross-section silo with hoppers of varying steepness under concentric discharge, adapted from Nothdurft (1976). A comparison of these two figures shows that the features of the predicted normal wall pressure distribution are reproduced qualitatively by experiment: the Janssen-like distribution above the effective transition, the spike in wall pressure at the transition and the subsequent steep reduction in wall pressure below the transition.

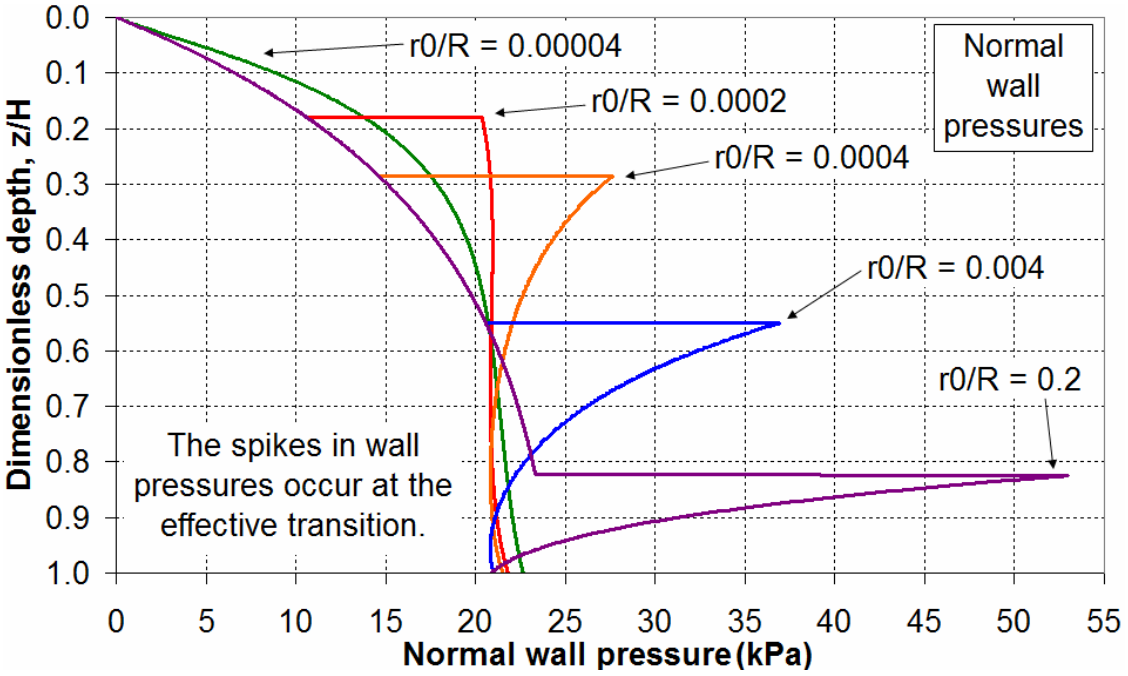

Fig. 7.21 – Normal wall pressures under a widening concentric mixed flow regime

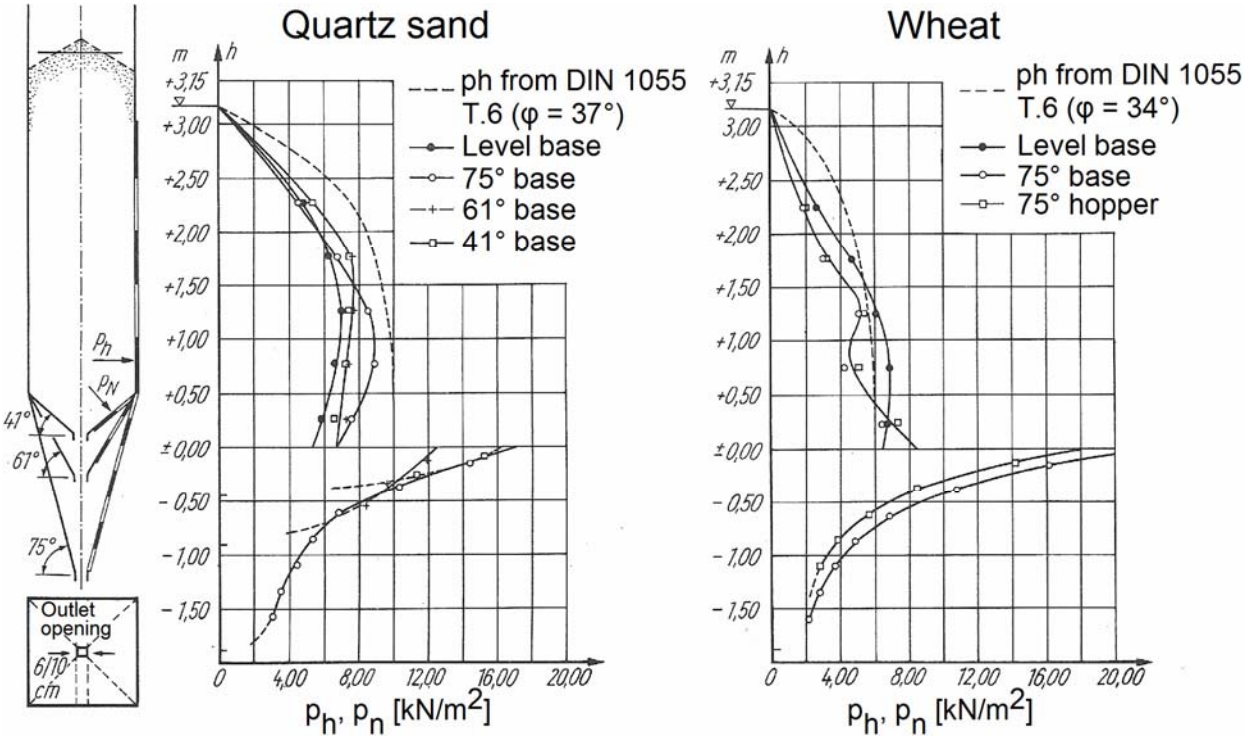

Fig. 7.22 – Normal wall pressures in a square cross-section silo with hoppers of varying steepness under concentric discharge of quartz sand and wheat, from Nothdurft (1976) and Hampe (1987)

7.5 Parametric studies of eccentric flow patterns in a slender silo

7.5.1 Variation of the flow channel eccentricity

This study investigated the effect of varying the eccentricity of a steep channel with a constant power $n = 2$ and outlet size $r_0/R = 0.08$ on a slender silo with $H/D = 5.2$. The dimensionless eccentricity e_c/R was varied between 0.00 (concentric internal pipe flow - ConP, Fig. 7.1) and 0.92 (eccentric pipe flow at maximum permissible eccentricity - EccP, Fig. 7.1). The outlines of the full set of channels are shown in Fig. 7.23 and in three dimensions in Fig. 7.24.

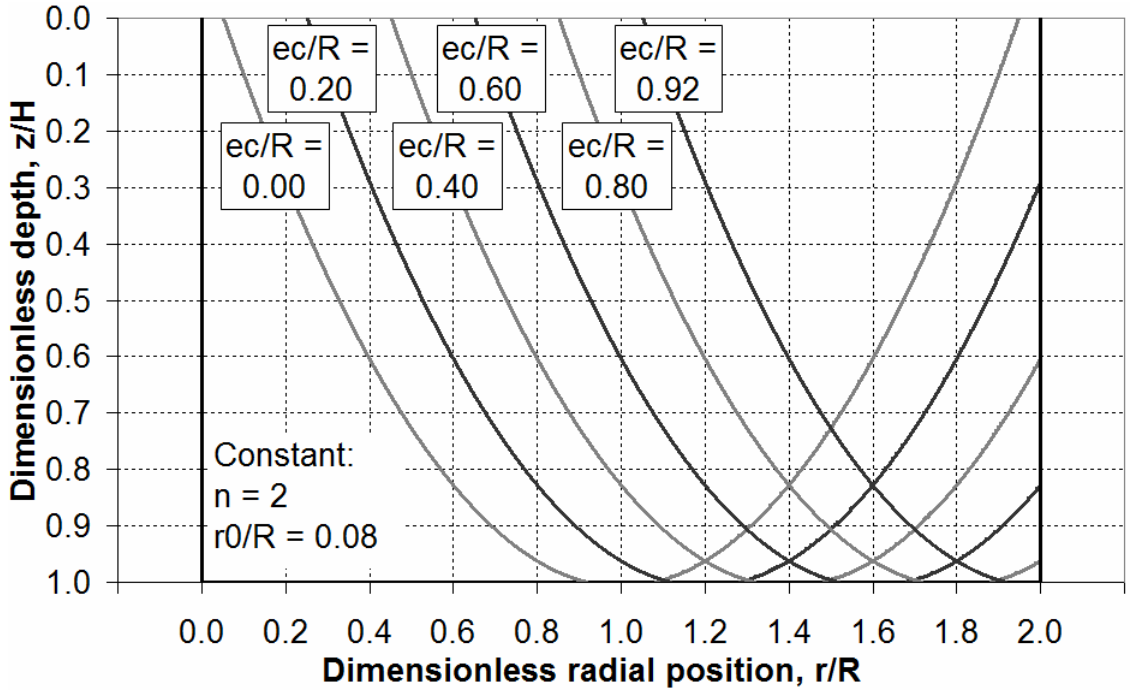

Fig. 7.23 – Profile outlines of channels under increasing outlet eccentricity, with constant power $n = 2$ and outlet size $r_0/R = 0.08$

The fully-internal concentric channel is in Region 1 flow throughout. As the eccentricity increases and the flow channel makes contact with the wall between $e_c/R = 0.00$ and 0.20, the flow regime passes from Region 1 to 2 at the lowest point of the circumferentially-varying effective transition. There is no abrupt rise within stationary solid pressure at this boundary as the *lowest* point of the effective transition does not invoke the implementation of BC2 (Region 3 flow is not present), but it will be shown that there is nonetheless an abrupt rise in the normal wall pressure. For the largest outlet eccentricity, $e_c/R = 0.92$, the channel is in Region 2 flow throughout. As there is no Region 3 flow present in any of the flow patterns, the effective transition does not extend around the whole circumference (hence BC2 is actually not implemented anywhere).

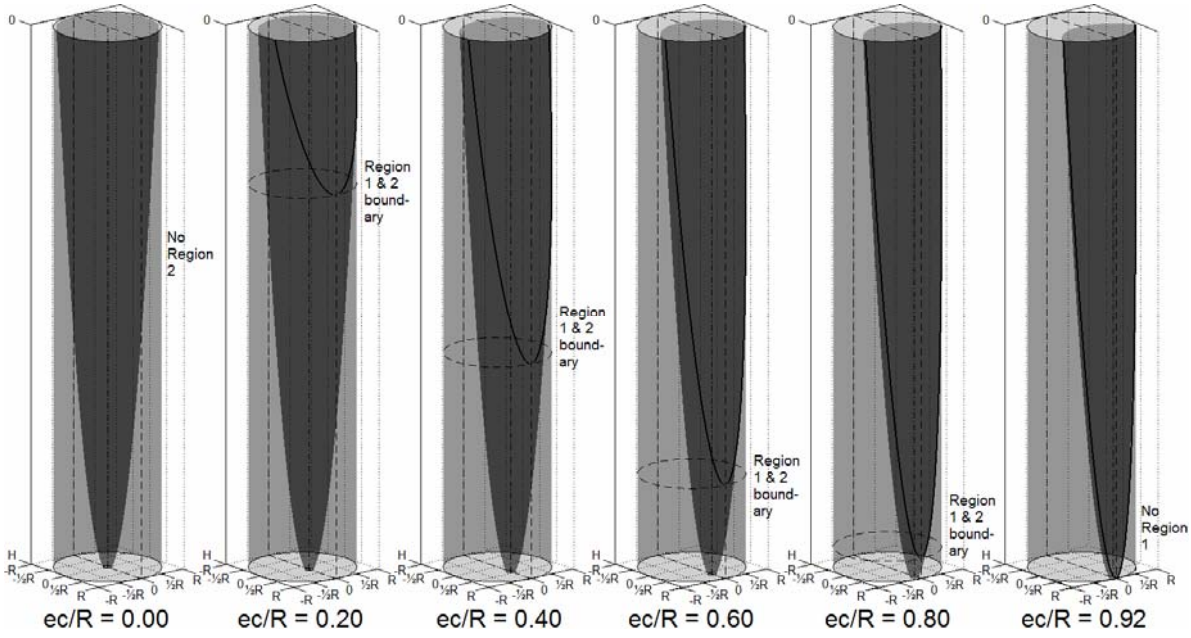

Fig. 7.24 – Three-dimensional channel and silo surfaces for the pipe-flow suite of eccentric channels, with constant power $n = 2$ and outlet size $r_0/R = 0.08$

The distributions of the vertical pressure in the flow channel as a function of the outlet eccentricity are shown in Fig. 7.25. The vertical pressure in the flow channel is predicted to be significantly lower than the Janssen value, and there does not appear to be any clear relation between the pattern or magnitudes of the channel pressure and the outlet eccentricity. Indeed, the variation of the peak vertical flow channel pressure appears to be no more than 6 kPa (or approximately 10% of the local Janssen value) across the entire range of eccentricities investigated here, with the peak occurring near $z/H = 0.3$. It may be concluded that, for this example, the vertical pressure in the flow channel appears largely insensitive to the outlet eccentricity once an eccentric pipe flow pattern has formed. The flow channel pressure may be seen to grow progressively with height moving away from the outlet, as reported elsewhere (e.g. Ravenet 1976; Ooi *et al.*, 2005). A further comment is that the highest vertical pressure does not occur in the flow channel of largest eccentricity, but rather at $e_c/R = 0.40$. A similar observation has been reported elsewhere, including Pieper (1969) and Gale *et al*. (1986). However, this is unlikely to be of structural consequence, since a lower channel pressure is far more likely to be detrimental to the silo in the case of eccentric pipe flow (Rotter, 2004a).

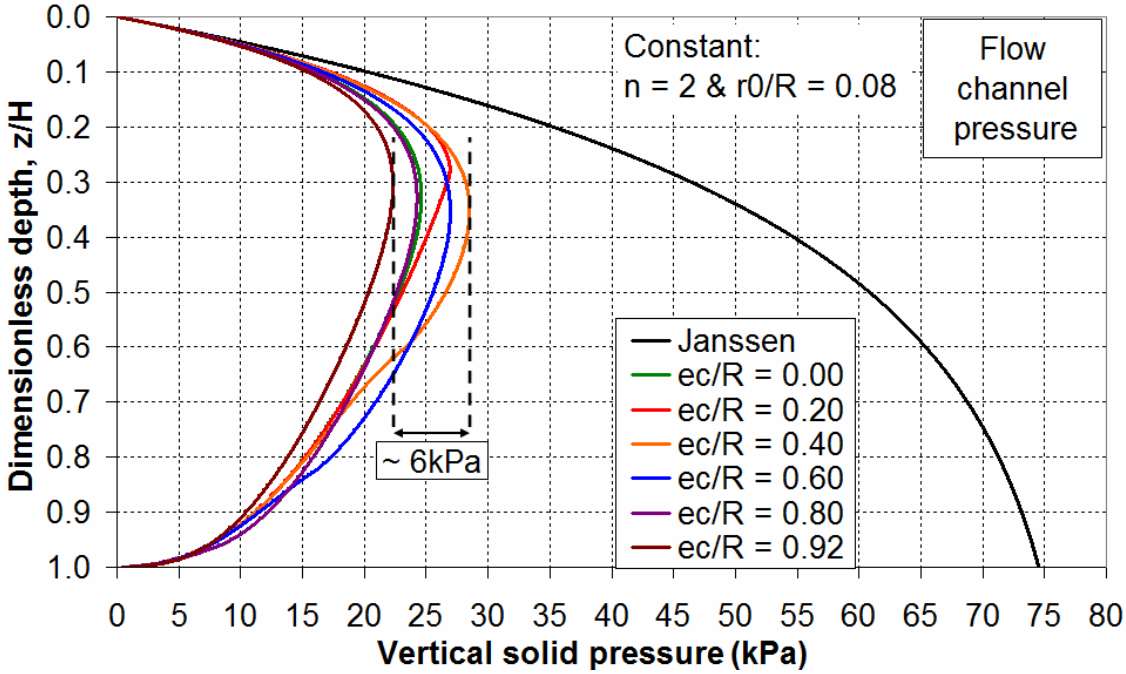

Fig. 7.25 – Vertical pressure in the flow channel under increasing outlet eccentricity

The vertical pressure in the stationary solid is shown in Fig. 7.26 as a function of the eccentricity, and exhibits a similar pattern to Fig. 7.13 which shows a progressive bulge developing near midheight and a decrease in pressure near the base. The stationary solid reaches the top surface in all flow patterns investigated here, hence there is no Region 3 flow present and the distributions of vertical pressure in the stationary solid are free from any abrupt rises unlike, for example, Fig. 7.19. However, this is not the case for the distributions of normal wall pressure on the side of the outlet, shown in Fig. 7.27.

The normal wall pressure on the side of the outlet (θ = 0°), normalised by the local Janssen value, is shown in Fig. 7.27. As the outlet eccentricity increases, the base of the effective transition between the flow channel and stationary solid (boundary between Region 1 and 2 flow) begins to touch the wall at a progressively lower depth. There is an abrupt jump in normal wall pressure at every such location due to the changeover from flowing to stationary solid, the magnitude of which increases with depth. However, though the effect is sudden, the normal wall pressure after the jump is in this case predicted to be not that much greater than the local Janssen pressure, being at most up to 1.35 times the Janssen value for e_c/R = 0.20, and decreasing with outlet eccentricity.

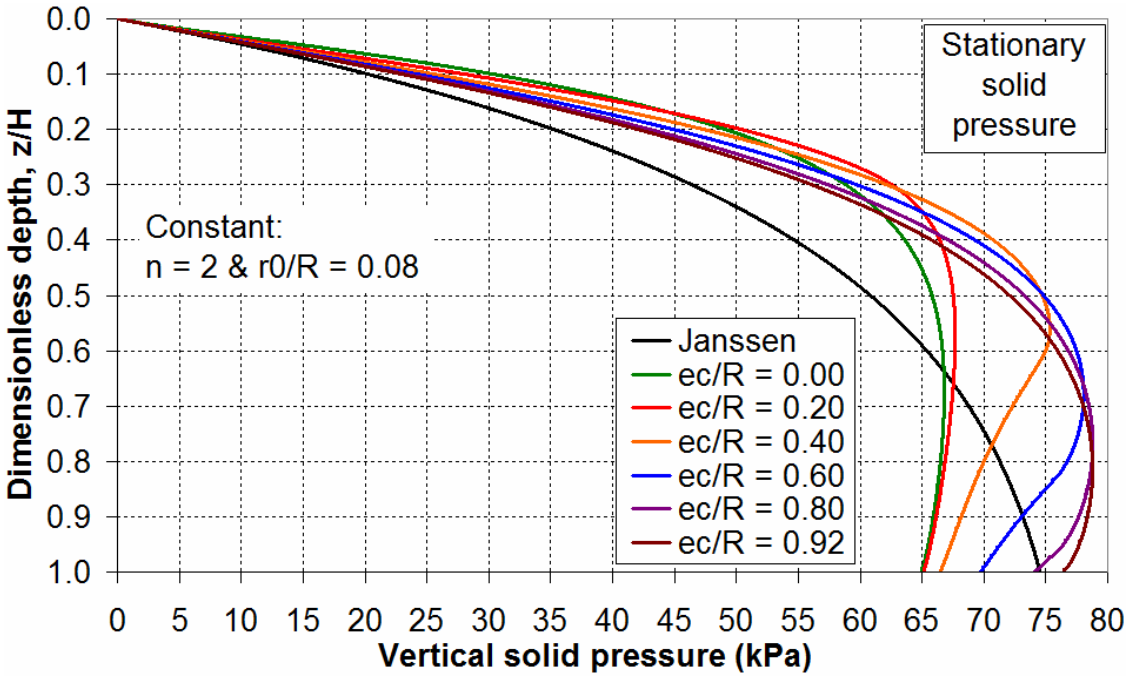

Fig. 7.26 – Vertical pressure in the stationary solid under increasing outlet eccentricity

The distributions of the normal wall pressure opposite the outlet ($\theta = 180°$ - where there is no discontinuity), are shown in Fig. 7.28 normalised by the local Janssen value. These patterns are highly similar to those of the normalised stationary solid pressures under progressively widening internal pipe flow presented in Fig. 7.14. There is a bulge in pressure in the upper part of the silo accompanied by a drop in pressure at the base, the magnitudes of which are comparable in both figures. This is due to the fact that the cross-sectional area of the eccentric pipe flow channel decreases with eccentricity, producing a similar effect on the stationary solid pressures as a progressively narrower internal pipe flow channel.

Based only on the above observation, one may expect that highly-eccentric flow patterns would be less damaging to the silo. However, as discussed in previous chapters, it is not the rise in normal pressure within the static solid that is so destructive for thin-walled metal silos under eccentric pipe flow, but rather a drop in normal wall pressure within the flowing solid. Unsymmetrical regions of low pressure lead to high local compressive axial membrane stresses which precipitate early and catastrophic failure through buckling (Rotter, 1986; Rotter *et al.*, 2006). It is therefore expected that, for $e_c/R \geq 0.40$, a silo subjected to such wall pressures may begin to exhibit the distinctive behaviour of the elastic midheight buckle, with localised strips of interchanging

compressive and tensile axial membrane stresses adjacent to the wall channel that was the focus of Chapters 2 to 5 (e.g. Fig. 2.9 and Fig. 2.13).

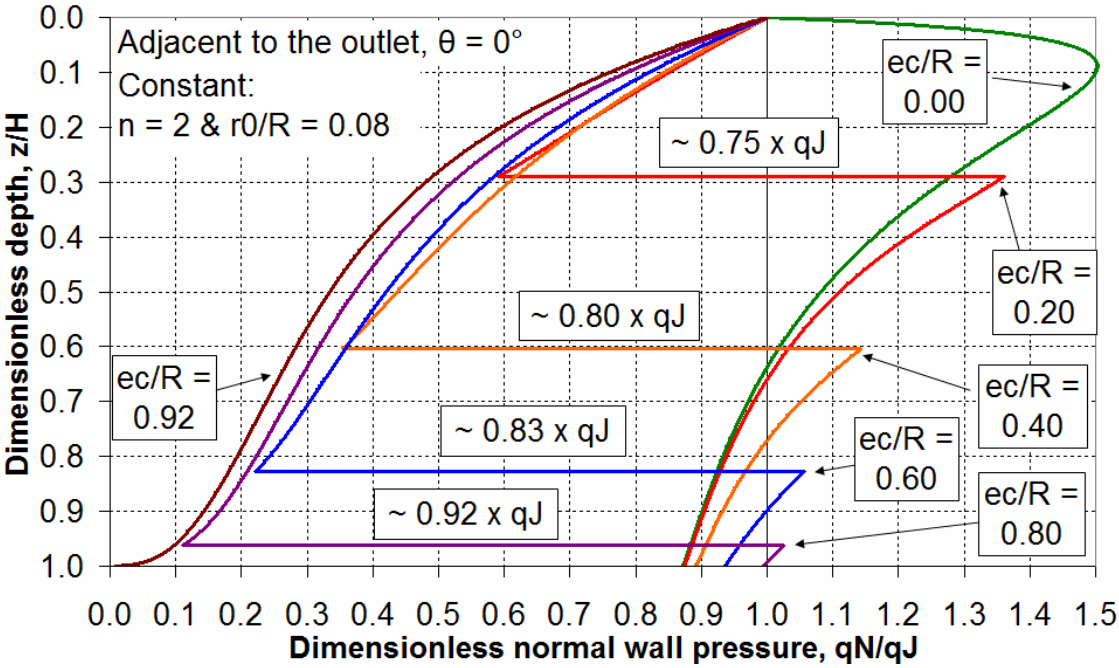

Fig. 7.27 – Dimensionless normal wall pressure at the coordinate adjacent to the outlet, $\theta = 0°$, under increasing outlet eccentricity

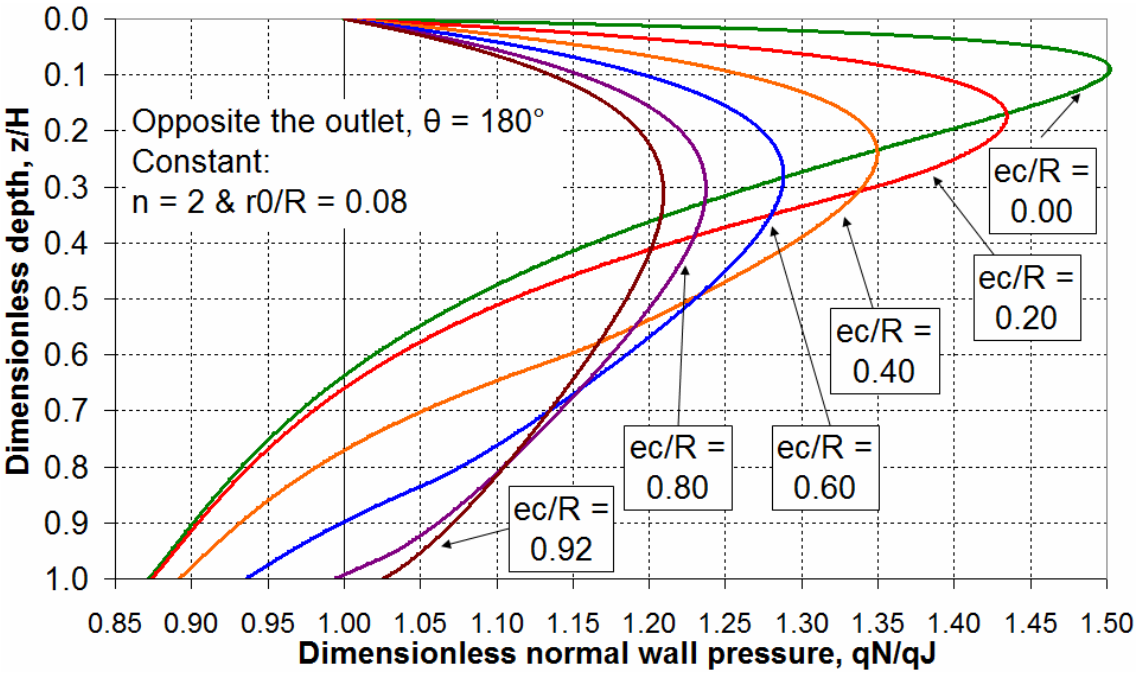

Fig. 7.28 – Dimensionless normal wall pressure at the coordinate opposite the outlet, $\theta = 180°$, under increasing outlet eccentricity

A set of three-dimensional surface plots of the silo normal wall pressure within a 90° circumferential spread of the outlet is presented in Fig. 7.29. These allow an appreciation of the global state of the pressures which are exerted on the silo by these flow patterns and show clearly the sudden drop in wall pressures at the effective transition between the flow channel and stationary solid.

It is very difficult to compare the present predictions for eccentric flows with experimental results. The primary reason for this is that it is currently very difficult to measure even approximately how a solid flows inside a model or full-scale silo, and to identify features such as the flow pattern profile or global position of the effective transition *and* at the same time take pressure measurements, without being able to physically see through the granular solid, despite techniques developed which attempt to overcome this severe limitation (e.g. Chen, 1996). Furthermore, much of the voluminous literature on discharge cannot be compared to reliably due to the vast differences in measuring and recording techniques used. Most notably, it was discussed in Section 1.2.8 of the literature review that most experimentalists either considered a single point on every circumference, or reported the highest measured value regardless of position or duration (Rotter, 2004a). A new experimental programme designed to verify specific aspects of this theory is therefore highly recommended.

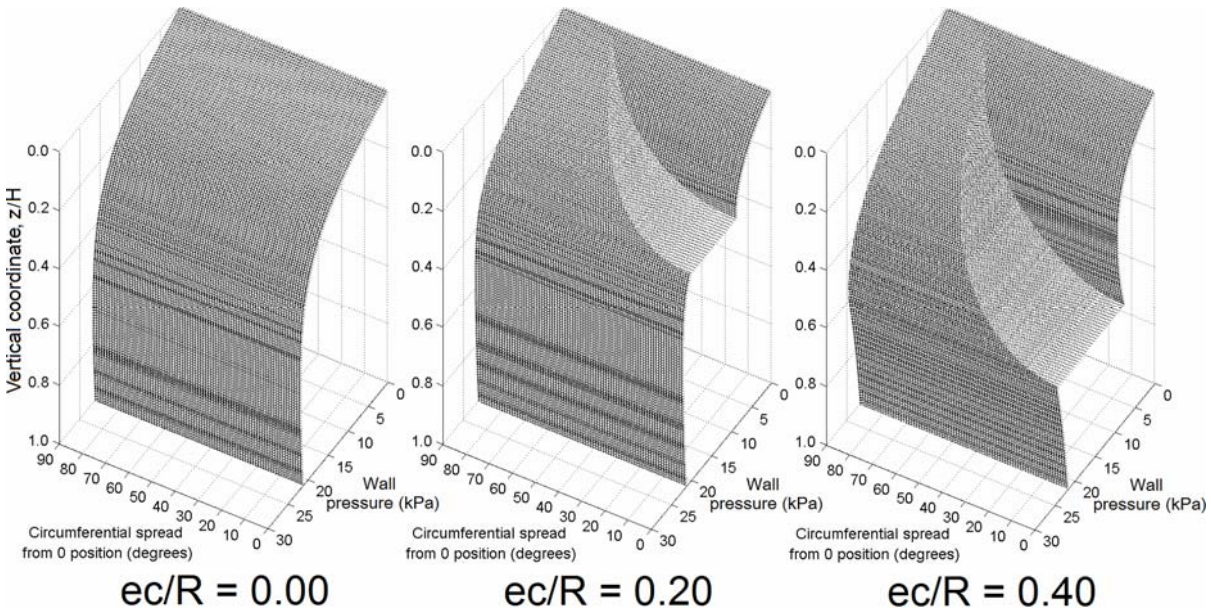

a) Outlet eccentricity range $0.00 \leq e_c/R \leq 0.40$

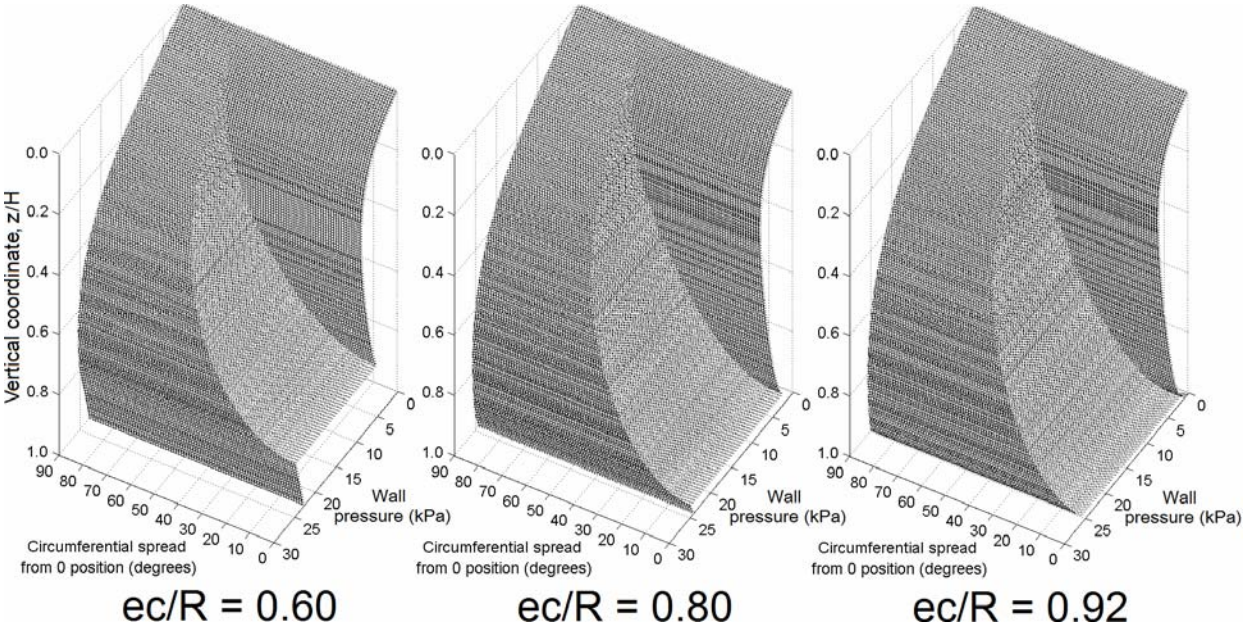

b) Outlet eccentricity range $0.60 \leq e_c/R \leq 0.92$

Fig. 7.29 – Three dimensional surface plots of normal wall pressure under increasing outlet eccentricity

7.5.2 Variation of the flow channel steepness

The final parametric study presented here investigated the effect of varying the power of the channel profile n on a flow channel with a constant outlet size and maximum eccentricity of $r_0/R = 0.08$ and $e_c/R = 0.92$ respectively. The power was varied from $n = 1.2$ (eccentric mixed flow pattern - EccM, Fig. 7.1), to $n = 100$ (eccentric pipe flow, with near vertical sides - EccP, Fig. 7.1). The outlines of the flow channel profiles are presented in Fig. 7.30 and in three dimensions in Fig. 7.31.

There is no Region 1 flow in any of the flow patterns investigated here since they are all located at maximum eccentricity and thus the channel cannot fully internal anywhere according to the current model. For $n = 1.2$, the effective transition starts at the base of the silo adjacent to the outlet and extends around the entire circumference. The highest point of the effective transition occurs at the boundary of Region 2 and 3 flow. This is also the point at which the BC2 boundary condition is invoked (Fig. 7.1), and consequently the location of an abrupt rise in the stationary solid and normal wall pressures.

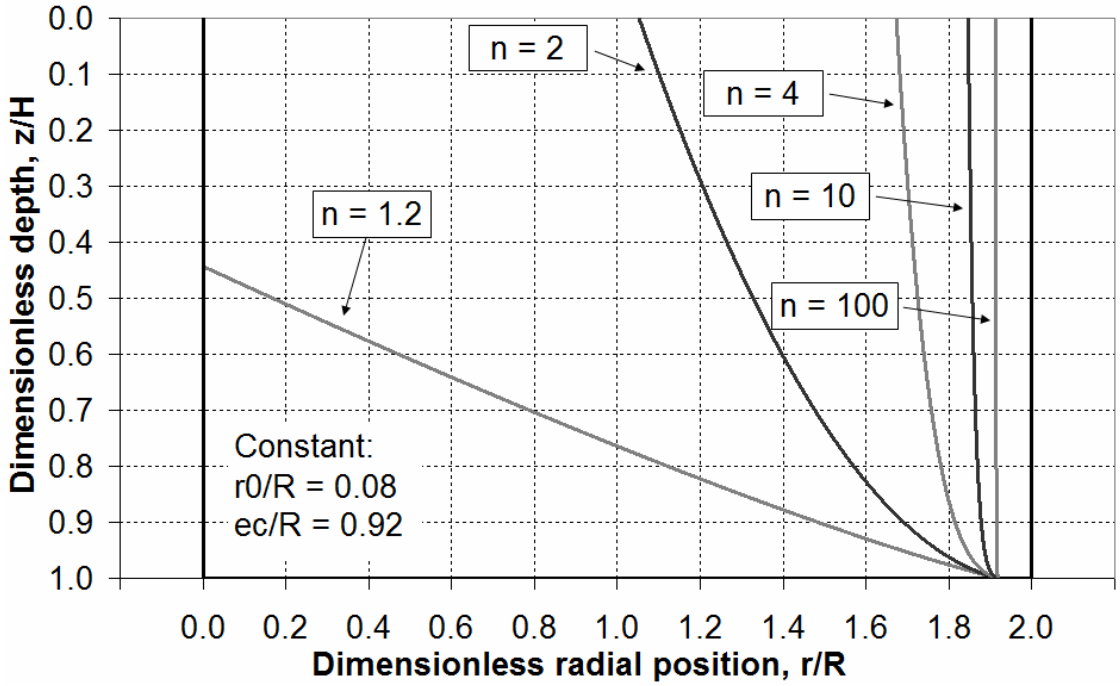

Fig. 7.30 – Profile outlines of channels under increasing steepness, with constant outlet size $r_0/R = 0.08$ and eccentricity $e_c/R = 0.92$

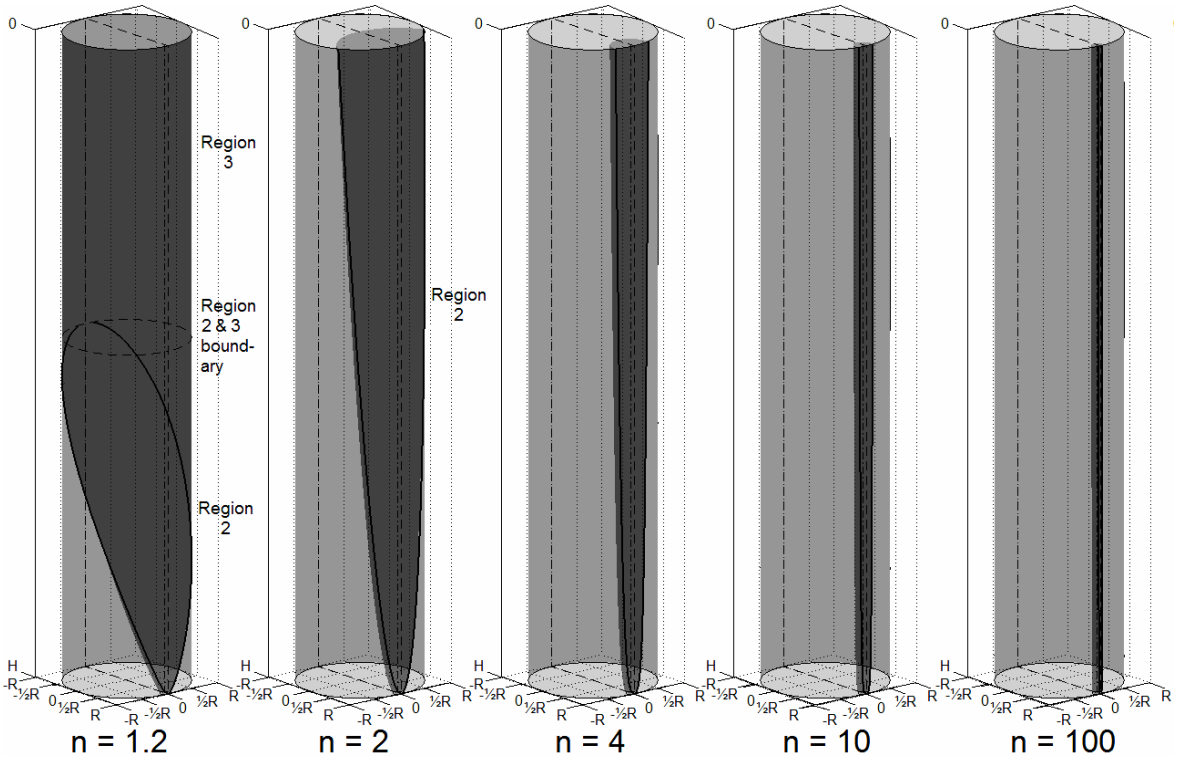

Fig. 7.31 – Three-dimensional geometry for the suite of eccentric channels of varying steepness, with constant outlet size $r_0/R = 0.08$ and eccentricity $e_c/R = 0.92$

The vertical pressure in the flow channel and stationary solid is shown in Fig. 7.32 and Fig. 7.33 respectively. As the outlet size is kept constant throughout, the steepness of

the channel profile is controlled solely by the power n. For values of $n > 2$, the flow channel quickly becomes very small due to the very steep sides and, consequently, the vertical pressure in the flow channel and its effect on the adjacent stationary solid quickly become very low. The distribution of vertical pressure in the stationary solid, Fig. 7.33, shows an abrupt change in form from $n = 1.2$ to $n = 2$ as the flow pattern progresses from eccentric mixed to eccentric pipe flow (EccM to EccP, Fig. 7.1).

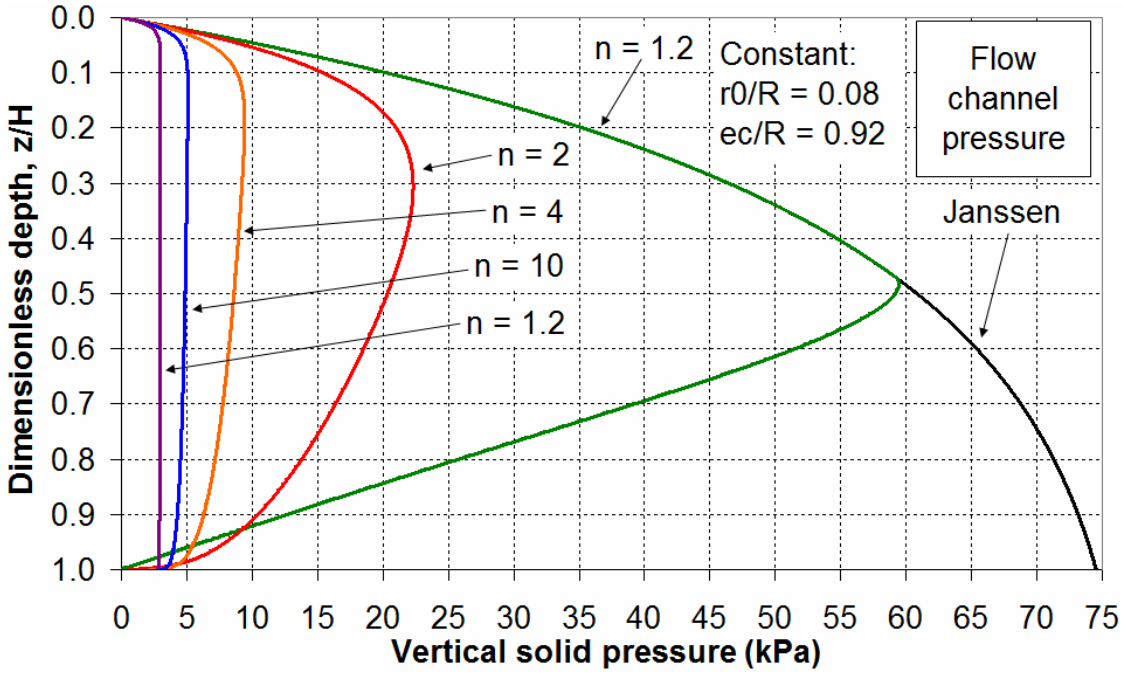

Fig. 7.32 – Vertical pressure in the flow channel under increasing channel steepness

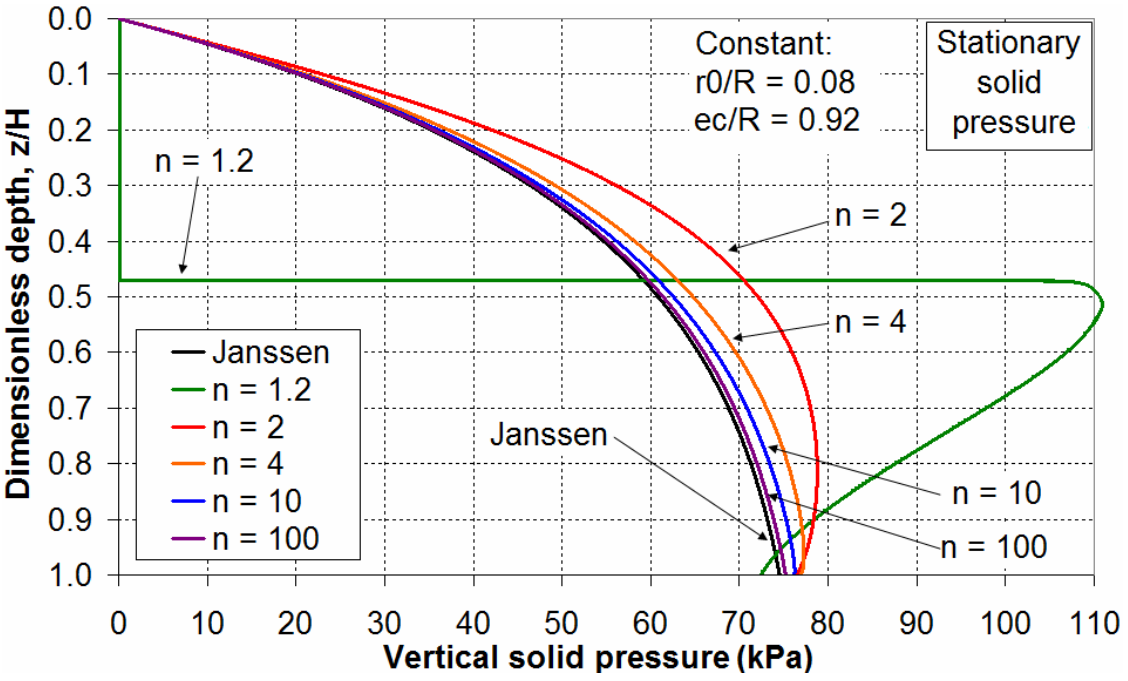

Fig. 7.33 – Vertical pressure in the stationary solid under increasing channel steepness

The dimensionless normal wall pressure acting on the wall adjacent and opposite to the outlet is shown in Fig. 7.34 and Fig. 7.35 respectively as a function of the channel steepness n. Similarly, a set of global distributions of normal wall pressure acting on the silo wall is shown in Fig. 7.36. At the boundary of Region 2 and 3 flow for the $n = 1.2$ mixed flow channel, there is a rise in normal wall pressure to over 1.8 times the Janssen value, which is present around the entire circumference, comparable with previous observations for concentric mixed flow (Fig. 7.20). Conversely, for channels with $n \geq 2$, it can be seen that there is instead a local drop in normal wall pressure on the side of the outlet, covering a progressively narrower portion of the wall as the channel sides become steeper. At the same time as the flow channel becomes ever narrower, the stationary solid pressure gradually approaches the Janssen value.

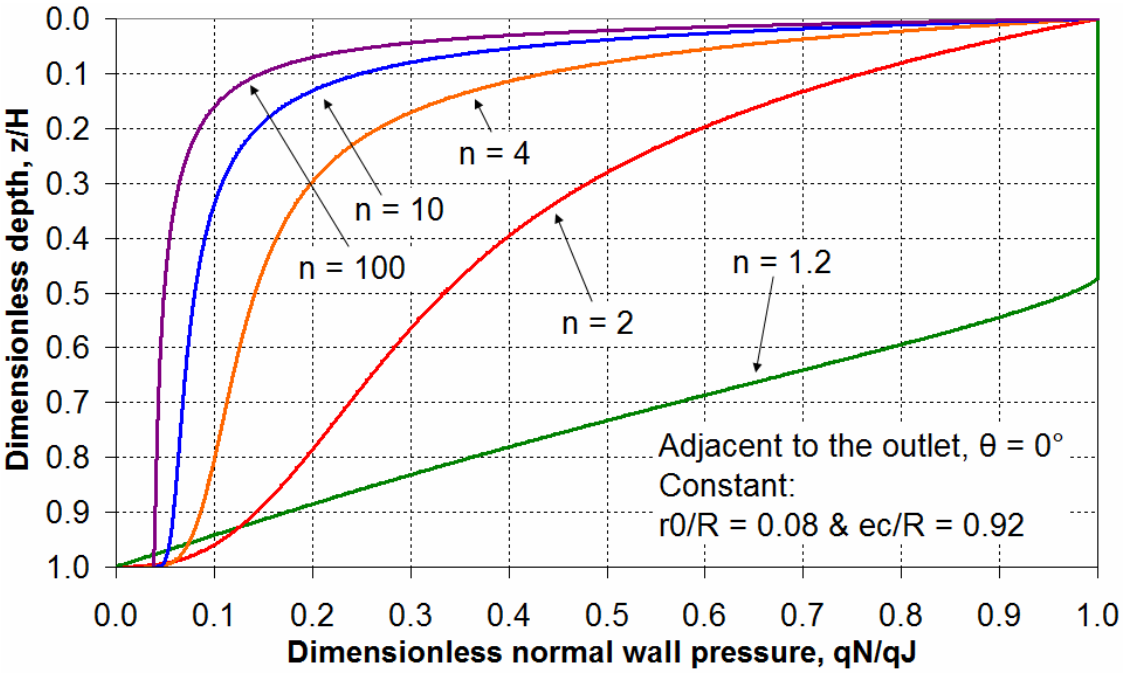

Fig. 7.34 – Dimensionless normal wall pressure at the coordinate adjacent to the outlet, $\theta = 0°$, under increasing outlet eccentricity

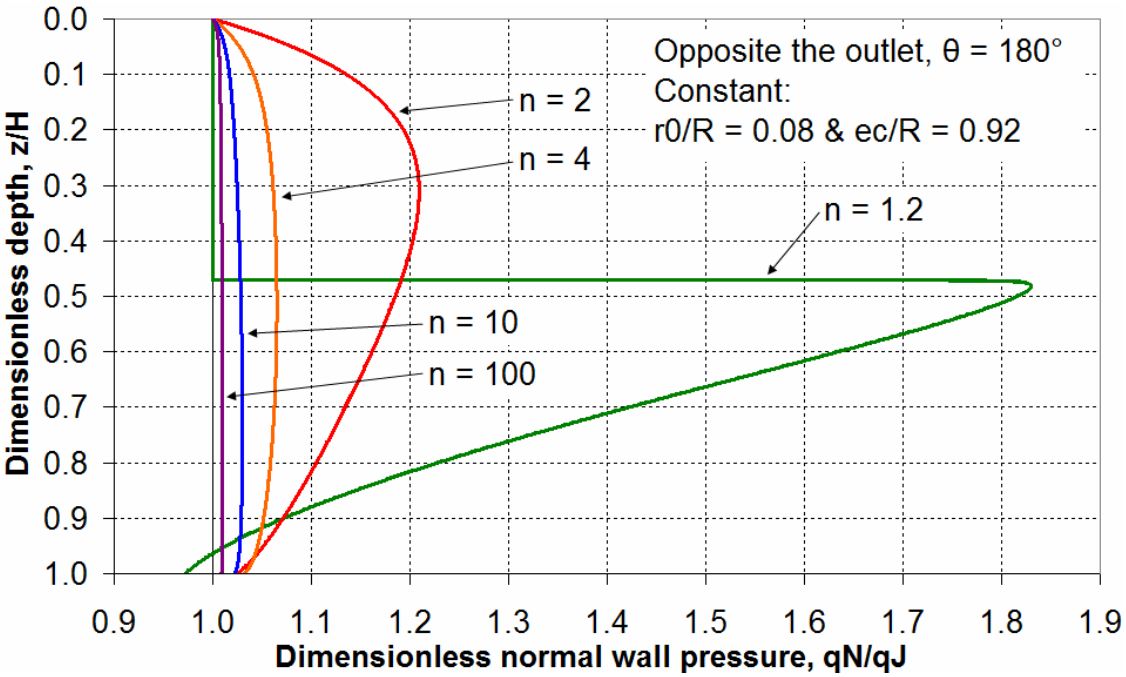

Fig. 7.35 – Dimensionless normal wall pressure at the coordinate opposite the outlet, θ = 180°, under increasing outlet eccentricity

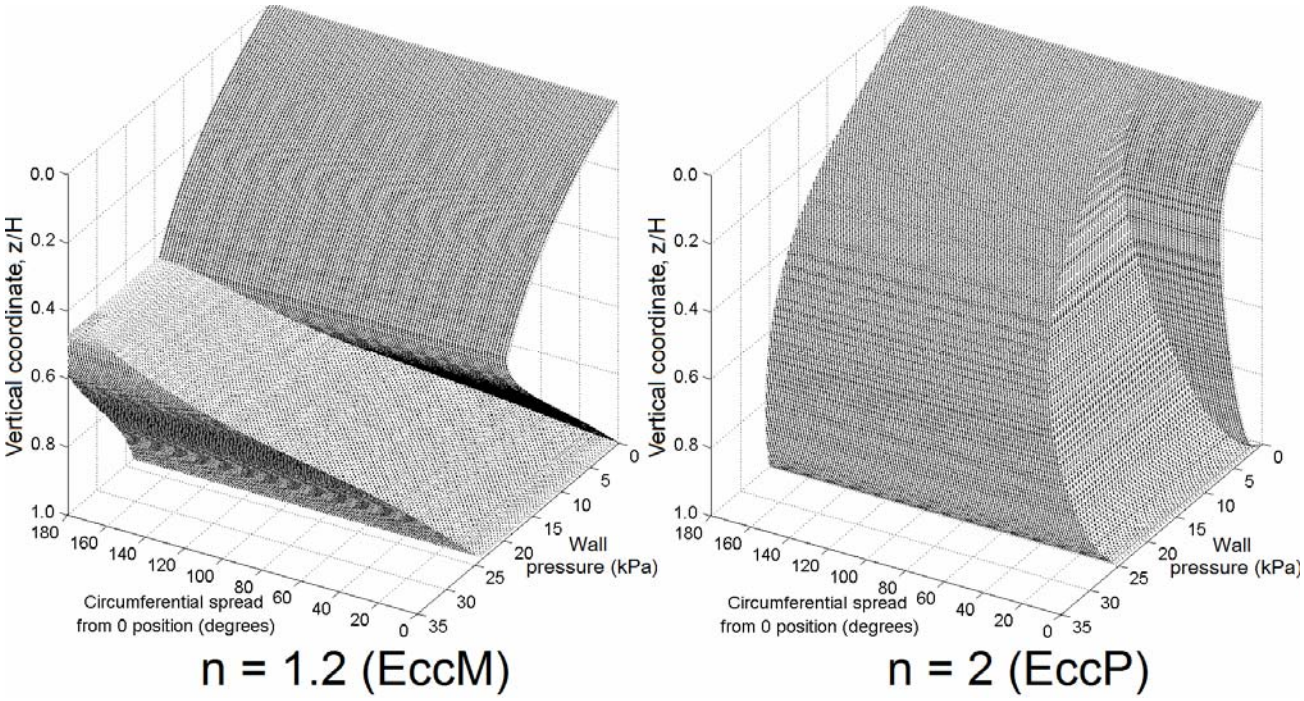

a) Channel steepness range $1.2 \leq n \leq 2$

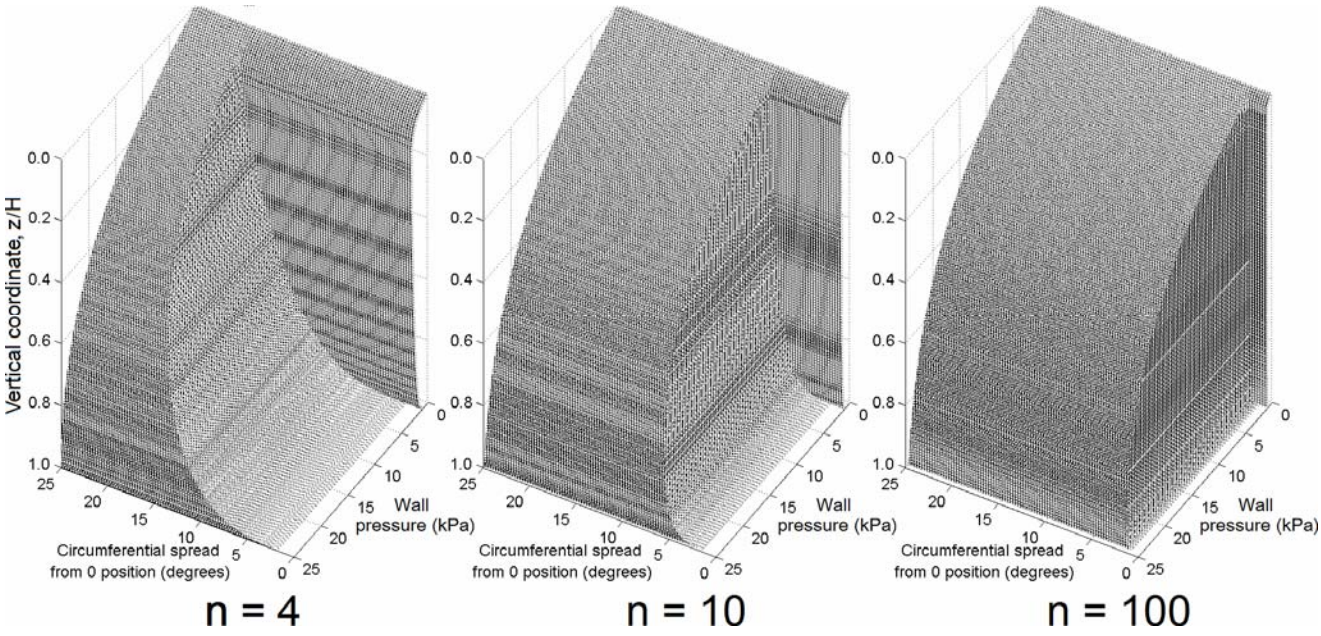

b) Channel steepness range $4 \leq n \leq 100$

Fig. 7.36 – Three dimensional surface plots of normal wall pressure under increasing channel steepness

Thus a simple variation of the power of the flow channel shape at constant eccentricity and outlet size leads to a fundamentally different flow regime and associated set of wall pressures. It is expected that the structural response would show significant differences between the pressures due to a flow channel with $n = 1.2$ (eccentric mixed flow) and one with $n \geq 2$ (eccentric pipe flow). Additionally, although there is a global rise in normal wall pressure around the entire circumference for eccentric mixed flow and only a localised decrease in normal wall pressure for eccentric pipe flow, it is expected that the latter will have by far the more severe structural consequences. The different possibilities of this model and their structural effects will be investigated with a series of computational analyses in Chapters 8 to 10.

7.6 Approximate comparison of the mixed flow pressure theory with the Rotter (1986) eccentric discharge model

It is relatively straightforward to compare the predictions of the current theory with the original work of Rotter (1986), from which the predictions of the EN 1991-4 (2007) eccentric discharge pressure model are directly descended. Such a comparison between the two previous models had already been made in Chapter 3. Rotter's model defines a truncated circular parallel-sided flow channel throughout the whole silo, which

effectively limits a comparison with the mixed flow theory presented in this chapter to eccentric pipe flow (EccP - Fig. 7.1) in Region 2 only.

Rotter's assumption of a truncated circular flow channel geometry and parallel sides additionally implies a truncated circular outlet at the base. However, it was stated in this chapter that to ensure a fully-circular outlet in the implementation of the mixed flow theory, the eccentricity of the outlet should obey the restriction $e_c \leq R - r_0$ where r_0 is the outlet radius. This restriction was adhered to in the parametric studies presented so far, but for the purposes of the current comparison it may be waived.

For the mixed flow theory, the outlet radius r_0 corresponds directly to the flow channel radius r_c from the Rotter and EN 1991-4 models. A steepness value of $n = 500$ may be considered sufficient to ensure near-parallel sides, and the value of the outlet eccentricity e_c is equivalent in all three models. However, the Rotter and EN 1991-4 models calculate e_c based on r_c, while in the mixed flow theory these parameters are defined separately.

Adopting a sample set of flow channel geometries for Silo CS ($H/D = 3$, Table 4.2), a comparison was made between the two eccentric discharge theories using $r_c = r_0 = 0.25R$, $0.40R$ and $0.60R$ (corresponding to outlet eccentricities $e_c = 0.79R$, $0.66R$ and $0.50R$, Table 3.3) and material properties for cement: $\gamma = 16$ kN/m^3, $\mu_w = 0.48$ and $\phi_i = 36.6°$. No discharge factors C_h or C_w were applied.

When comparing the mixed flow and Rotter (1986) pressure theories, it was considered more advantageous to return to the original differential equations governing the different models, reproduced here with consistent notation. The vertical pressure in the flow channel is thus given by Rotter (1986) as:

$$dq_c = \gamma dz - q_c \mu_w K_{cw} \frac{U_{wc} dz}{A_c} - q_c \mu_i K_c \frac{U_{sc} dz}{A_c} \tag{7.21}$$

and by the mixed flow theory as:

$$\begin{aligned} dq_c = {} & q_c \left(\frac{A_{c-top} - A_{c-bot}}{A_{c-bot}} \right) + \gamma \left(\frac{A_{c-top} + A_{c-bot}}{2A_{c-bot}} \right) dz \ldots \\ & - q_c \mu_w K_{cw} \frac{U_{wc} dz}{A_{c-bot}} - q_c \left(\tan\beta + \mu_i \right) F \frac{U_{sc} dz}{A_{c-bot}} \end{aligned} \tag{7.14}$$

It can be seen that, with the assumption of parallel sides, $n \to \infty$ hence $\beta \to 0$, $\tan(\beta) \to 0$, $A_{\text{c-top}} \to A_{\text{c-bot}}$ and $F(\beta \to 0) = \dfrac{\tan^2\beta - K_c}{\tan^2\beta + 2\mu_i \tan\beta - 1} \to \dfrac{-K_c}{-1} = K_c$ (using Eq. 7.13). Consequently, Eq. 7.14 simplifies directly to Eq. 7.21.

In the same manner, the vertical pressure in the stationary solid is given by Rotter (1986) as:

$$dq_s = \gamma dz - q_s \mu_w K_{sw} \frac{U_{ws} dz}{A_s} + q_c \mu_i K_c \frac{U_{sc} dz}{A_s} \tag{7.22}$$

and by the mixed flow theory as:

$$\begin{aligned} dq_s = {} & q_s \left(\frac{A_{s-top} - A_{s-bot}}{A_{s-bot}} \right) + \gamma \left(\frac{A_{s-top} + A_{s-bot}}{2A_{s-bot}} \right) dz \ldots \\ & - q_s \mu_w K_{sw} \frac{U_{ws} dz}{A_{s-bot}} + q_c \left(\tan\beta + \mu_i \right) F \frac{U_{sc} dz}{A_{s-bot}} \end{aligned} \tag{7.12}$$

It can be seen that as $n \to \infty$, Eq. 7.12 also simplifies to Eq. 7.22.

Assuming an Euler integration regime for both sets of equations, $dq(z+dz) = q(z) + dq(z)$, the vertical pressures in the flow channel and stationary solid were calculated and are presented in Fig. 7.37 for the three example channel sizes. It should come as no surprise that the two theories give an almost identical result under the conditions in which they are directly comparable, reproducing in both cases the result of increased vertical pressure in the flow channel and stationary solid with increased channel size.

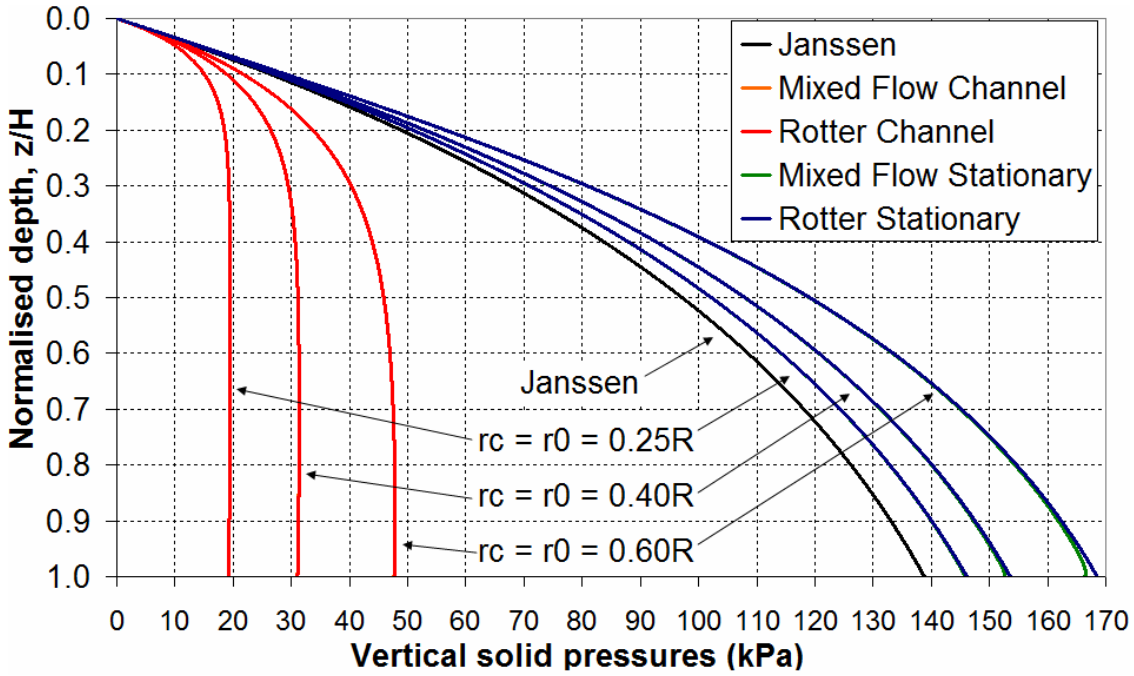

Fig. 7.37 – Comparison of the results of the Rotter (1986) and mixed flow pressure theories for three flow channel sizes, $r_c = r_0 = 0.25R$, $0.40R$ and $0.60R$

A final important point about this comparison, which can be seen in Fig. 7.37, is that if parallel sides are assumed, the outlet and steepness boundary conditions BC3 and BC4 become obsolete.

7.7 Conclusions

A mixed flow pressure theory based on a robust application of vertical slice equilibrium to channels with non-straight sides has been presented in this chapter. The theory is capable of predicting the wall pressure distributions for flow patterns of a very wide range of geometries and eccentricities with reasonable credibility. The profile of the channel follows a power-law distribution, which may be adapted to generate flow channels of varying steepness, width and outlet size. When the limiting case of near-parallel channel sides is considered, it is possible to reproduce earlier predictions from simpler theories. The theory thus grants freedom to investigate different flow channels like never before.

A series of non-structural parametric studies have been presented to explore the pressure distributions predicted by the mixed flow theory. These studies included both concentric and eccentric flow covering many possible patterns of pipe and mixed flow. The

pressures are in all cases highly dependent on changes in the flow channel geometry, disproportionately more so than on variations in material properties.

At every interface between the flow channel and stationary solid adjacent to the silo wall, the mixed flow theory predicts an abrupt rise in wall pressures. This rise is usually up to approximately 1.8 times the local Janssen pressure value, which corresponds well to more recent theoretical predictions and experimental observations, and is achieved solely through considerations of vertical equilibrium. It was not necessary to make any changes to the lateral pressure ratio which followed the simplest possible assumption, and consequently the current results do not support the 'switch' theory.

However, though there is some experimental evidence to support the flow patterns and predicted pressure distributions at least qualitatively, i.e. confirming the general predicted features such as decreased flow channel pressures and pressure jumps at the effective transition, more experimental confirmation is needed to obtain closer correlations and to calibrate and refine the new theory.

Chapter 8 – A preliminary study of the structural consequences of mixed flow pressure patterns

8.1 Introduction

The derivation of a new and potentially powerful discharge pressure theory was presented in full in the preceding chapter. The remainder of this thesis is dedicated to exploring aspects of the structural consequences of the pressure distributions predicted by this theory within the computational analysis framework of EN 1993-1-6 (2007). It is thought that such a numerical study has never been undertaken before, and the results presented here are the first of their kind.

The mixed flow pressure theory introduced in Chapter 7 is capable of describing a very wide range of different pressure patterns depending on the assumed flow channel geometry, the eccentricity of the channel, the size of the outlet and the aspect ratio of the silo structure. It is therefore not viable to attempt to explore all of these features in only a few studies. Instead, this first set of introductory analyses was conducted to investigate aspects of the structural consequences of four distinct flow patterns (first introduced in Fig. 7.1), using the resulting wall pressures predicted by the mixed flow theory. These patterns include concentric pipe flow (ConP), concentric mixed flow (ConM), eccentric (taper) pipe flow (EccP) and eccentric mixed flow (EccM), all based on idealised patterns commonly referenced in literature (e.g. Rotter, 2001a; EN 1991-4, 2007). The predicted wall pressures arising from the chosen flow patterns were applied to the stepped wall thickness Silo B (H = 14 m, R = 3.4 m, H/D = 2.06; Table 4.2) in a series of finite element analyses.

8.2 A preliminary investigation of the mixed flow pressure theory

8.2.1 Overview

The geometries of the four flow patterns analysed in this chapter are summarised in Table 8.1. Two-dimensional colour contour plots of the predicted vertical pressure distributions and geometry are shown in Fig. 8.1 which offer a global overview of the full system. The upper characteristic property values of wheat from EN 1991-4 (2007) Annex E were assumed in the calculation of the granular solid pressures, consistent with the set of granular solid properties used in the initial design of Silo B.

Table 8.1 – Flow patterns for the initial study of the mixed flow pressure theory

Acronym	Description	Eccentricity e_c / R	Outlet size r_0 / R	Channel power n
ConP	Concentric pipe flow (reference)	0.00	0.074 (0.25 m)	10.0
ConM	Concentric mixed flow	0.00	0.074	1.2
EccP	Eccentric pipe flow	0.74 (2.5 m)	0.074	2.0
EccM	Eccentric mixed flow	0.29 (1.0 m)	0.074	1.2

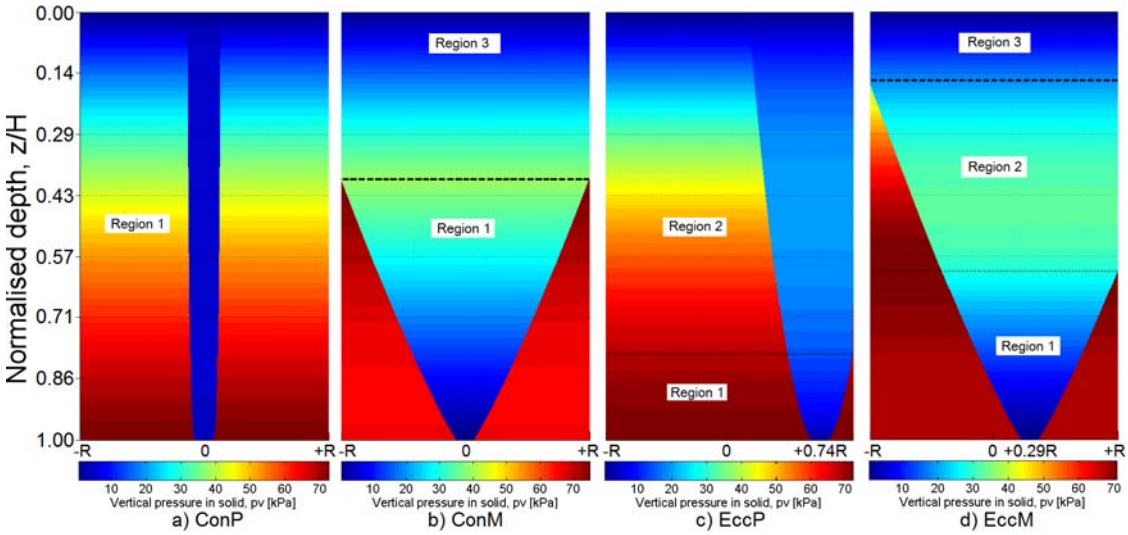

Fig. 8.1 – Colour contour plots of the vertical pressure distributions of the four flow patterns for the initial study of the mixed flow pressure theory

Silo B was designed with an aspect ratio of H/D = 2.06 (H = 14 m, R = 3.4 m) which places it on the boundary between the slender and intermediate slender categories (EN 1991-4, 2007). The choice of a relatively low aspect ratio was made here in order to justify the study of a wider range of different flow patterns. It was thought that silos of higher slenderness are less likely to develop a comparable range of flow patterns, and are more likely to exhibit effective transitions relatively low down the silo wall which span the entire circumference. Therefore the use of a more slender silo would probably reveal less in the present study. A similar concept was employed in the development of the slenderness categories prescribed in EN 1991-4 (2007), Fig. 4.1.

8.2.2 Concentric discharge patterns

The first of the concentric patterns was taken as internal pipe flow (ConP), consisting of a fully-internal steep-sided flow channel (n = 10) developing from a concentrically-located outlet. The effect of such a flow channel on the wall pressures is essentially negligible and the stationary solid exerts Janssen pressures throughout. The results for this pattern are therefore considered as a reference set, similar to the results for EN 1991-4 concentric discharge pressures in previous chapters. The flow is in Region 3 throughout (Fig. 7.3 defines the three regions of flow).

The second concentric pattern was taken as mixed flow (ConM), with an effective transition developing at a normalised depth of z_{13}/H = 0.39, at the boundary between Region 1 and 3 flow. Local equilibrium (BC2 - Fig. 7.10) predicts a sharp jump in wall pressures at the location of the effective transition up to approximately 1.94 times the local Janssen value. This may be expected to have a significant effect on the computed strength of the silo. The channel profile was assumed to be close to linear, with a value of steepness of n = 1.2. The predicted normal wall pressure distributions arising from the two concentric flow patterns are shown in Fig. 8.2.

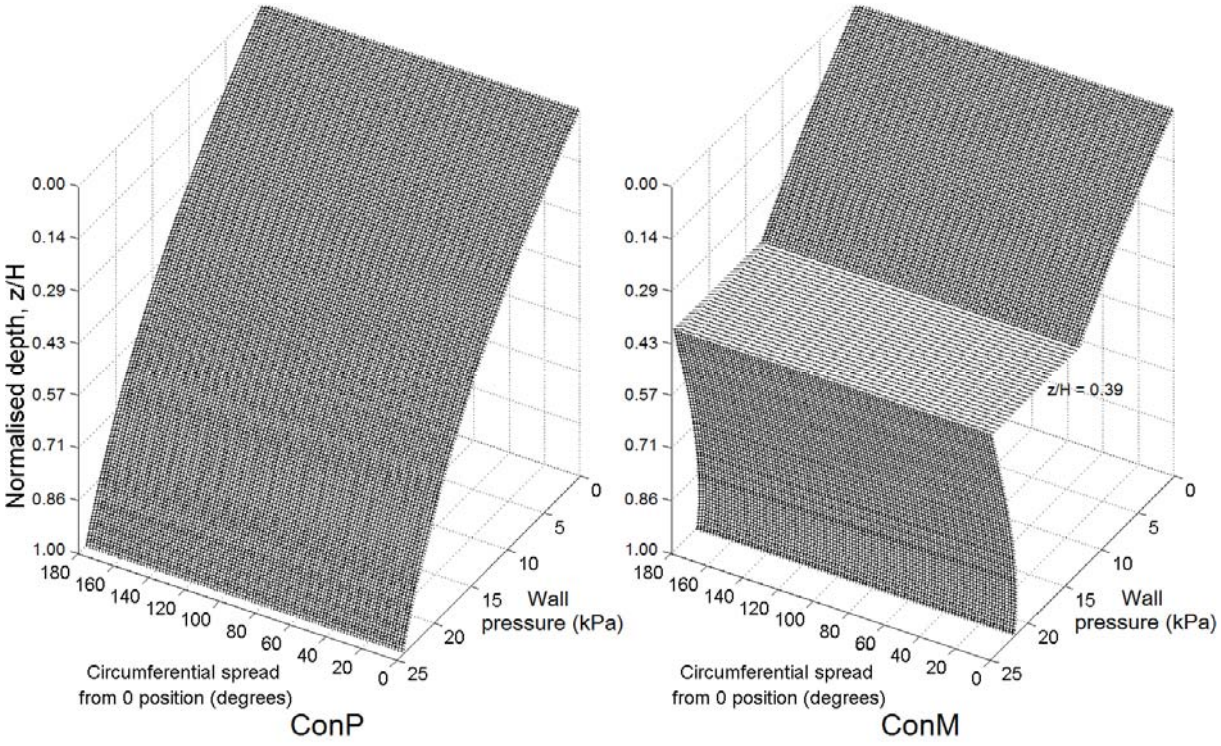

Fig. 8.2 – Surface plots of the normal wall pressure distributions of the concentric discharge flow patterns for the initial study of the mixed flow pressure theory

8.2.3 Eccentric discharge patterns

The first eccentric pattern was taken as a relatively steep-sided pipe flow channel (EccP), situated at a substantial eccentricity of $e_c/R = 0.74$. The value of $n = 2$ was considered sufficiently steep for this flow pattern. The channel is in contact with the silo wall for the majority of the silo height but in such a way that its wall contact half-angle (θ_c, Fig. 7.5) at any given level is rather modest, not exceeding 40°. There is a small zone below $z/H = 0.80$ where the flow channel is fully internal, and the stationary solid alone is in contact with the wall. Outside the circumferential extent of the flow channel, the stationary solid exerts wall pressures which are very close to the Janssen distribution. The EccP flow pattern is the closest of the four flow patterns to the EN 1991-4 parallel-sided eccentric discharge model.

The second of the unsymmetrical flow patterns was taken as eccentric mixed flow (EccM) with a rather small eccentricity of $e_c/R = 0.29$ and a profile that is close to linear ($n = 1.2$). This flow pattern exhibits a circumferentially-varying effective transition around the entire silo, from a depth of $z_{12}/H = 0.61$ adjacent to the outlet at $\theta = 0°$ (boundary between Region 1 and 2 flow) to a depth of $z_{23}/H = 0.16$ opposite the outlet at $\theta = 180°$ (boundary between Region 2 and 3 flow). A sharp local jump in wall pressures accompanies the circumferentially-varying effective transition, with the largest rise being to almost tripe the local value of vertical pressure in the flow channel occurring at z_{12}, adjacent to the outlet. The normal wall pressures arising from the eccentric flow patterns are shown in Fig. 8.3.

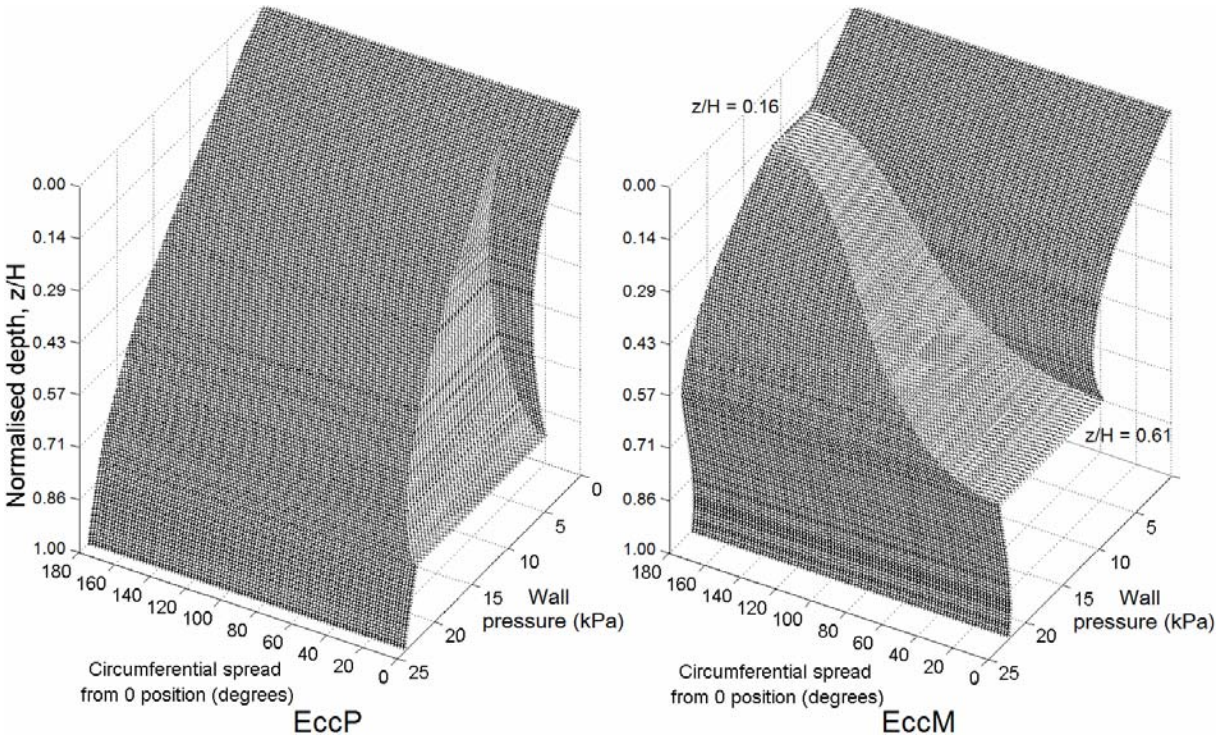

Fig. 8.3 – Surface plots of the normal wall pressure distributions of the eccentric discharge flow patterns for the initial study of the mixed flow pressure theory

8.3 Computational study

The standard suite of EN 1993-1-6 (2007) computational analyses were carried out on Silo B with the ABAQUS (2009) finite element software, using the predicted wall pressures presented in Fig. 8.2 and Fig. 8.3. This included LBA, MNA, GNA, GMNA and two different GMNIA analyses. In all cases, the frictional tractions were related to the local value of the normal wall pressure by the fully-developed upper characteristic value of the wall friction coefficient (EN 1991-4 (2007) Annex E), which for wheat was found to be 0.44 (Table 4.3). Both the uniform (6 mm wall throughout) and the more realistic stepwise-varying (6 mm wall at the base decreasing to 3 mm in the upper part, Fig. 4.2) wall thickness versions of Silo B were investigated to gain a deeper understanding of the behaviour of silos of both types of wall designs under the new pressure regimes. Material properties of mild steel were assumed to be the same as in all previous analyses of this nature (E = 200 GPa, ν = 0.3 and σ_y = 250 MPa).

In Chapter 4, it was shown that the axisymmetric circumferential weld depression (Type A from Rotter and Teng, 1989a) was not a suitable imperfection form for use with the EN 1991-4 eccentric discharge model. This was due to the inward depression feature of the imperfection resulting in an increased circumferential bending stiffness of the shell.

The drop in wall pressures adjacent to the flow channel was found to induce circumferential bending and the weld imperfection therefore resulted in significantly higher load factors for GMNIA analyses than for GMNA, a phenomenon further exacerbated by larger imperfection amplitudes.

The beneficial effect of the axisymmetric weld may well be unique to the pattern of pressures arising from a steep-sided flow channel forming against the wall of the silo (i.e. for the EN 1991-4 eccentric discharge model or EccP introduced above). However, for other flow patterns, including different forms of eccentric flow which do not have such localised features, it may be the case that the axisymmetric weld may be as damaging as it is for uniform axial compression. Considering that this is a relatively popular imperfection form that has been found to be very deleterious in a wide range of different studies (e.g. Rotter and Zhang, 1990; Teng and Rotter, 1992; Knödel & Ummenhofer, 1996; Ummenhofer & Knödel, 1996; Berry *et al.*, 1997; 2000; Pircher *et al.*, 2001), it was decided to verify its effects more closely under the mixed flow pressure theory. The axisymmetric weld depression was therefore employed as an imperfection form at 50% (GMNIA#1) and 100% (GMNIA#2) of the EN 1993-1-6 (2007) Section 8.7 special GMNIA amplitude (summarised in Table 4.6). It was intended that the two different amplitudes would act as a basic indicator of imperfection sensitivity. The weld depressions were located at numerous locations down the silo height including at changes of plate thickness, with the exception of the base or the top of the silo.

It should finally be noted that Silo B was originally designed to withstand the factored EN 1991-4 concentric discharge pressures for mass flow (with discharge factors C_h = 1.15 and C_w = 1.1) according to the EN 1993-1-6 (2007) and EN 1993-4-1 (2007) structural design procedure. The choice of thicknesses was therefore such that the wall was just critical at the base of each strake and should achieve a load factor of 1.65 or more. Though the same silo design was maintained here, the pressures predicted by the mixed flow theory have not been factored by the C_h or C_w discharge factors since factoring is only a conservative design procedure to compensate for uncertainty, not a scientific requirement. Indeed, for fully internal pipe flow, EN 1991-4 allows discharge pressures to be ignored and the C_h and C_w factors would not have been applied if Silo B had been designed for the concentric pipe flow pattern. Consequently, Silo B is

significantly overdesigned for concentric non-mixed flows and may be expected to exhibit very high load factors for the ConP flow pattern, higher than those for the factored EN 1991-4 concentric discharge pressures presented in Chapter 4. Additionally, comparisons of the predicted load factors to the 1.65 combined safety factor from the Eurocode assessment are no longer meaningful.

Many of the short-hand acronyms introduced in Table 4.8 of Chapter 4 are used throughout this chapter to describe the main features of the predicted failure modes. The relevant acronyms are reproduced in Table 8.2 below for convenience. The linear bifurcation eigenmode (LBA), the plastic collapse mode (MNA) and the incremental buckling mode (GNA-based analyses) are referred to in this chapter by the umbrella term 'failure modes'.

Table 8.2 – Description of short-hand acronyms to describe failure mode types

Acronym	Description
Axi-EF	Axisymmetric plastic elephant's foot buckling or yielding.
Axi-DD	Diamond pattern of deformation around the entire circumference, limited to being within a close distance of a wall strake or other boundary.
Axi-EL	Fully or partially axisymmetric elastic buckle.
Glb-EF	Global deformations, but with the main component of plastic elephant's foot-type buckling or yielding.
Glb-DD	Global diamond buckling mode
Glb-PL	Global plastic circumferential bending mode (the MNA mode).
Loc-CH	The characteristic or 'classic' mode associated with an eccentrically flowing channel: a local (predominantly) elastic buckle in the centre of the flow channel, at approximately midheight.
Loc-EG	This is also associated with this form of eccentric discharge, but seen more in squatter or uniform wall thickness silos as it requires a different location to be critical. A localised elastic or elastic-plastic buckle at or beneath the edge of the flow channel near the base of the silo.

8.4 Results for the uniform wall silo under the four flow patterns

8.4.1 Behaviour of the uniform wall silo under the ConP and ConM flow patterns

The uniform wall Silo B was first analysed under the axisymmetric wall pressures predicted by the mixed-flow theory for the concentric ConP and ConM flow patterns (Fig. 8.2). The resulting axial distributions of axial membrane stress resultants for the LA analyses at the LBA load factor (hereafter termed LA @ LBA) and the GNA or GMNA analyses at the instant before bifurcation (hereafter termed GNA or GMNA @ bifurcation) are shown in Fig. 8.4.

The ConM mixed flow pressure pattern differs considerably in certain places from the ConP pipe flow pattern (Fig. 8.2). There is an effective transition at a depth of z/H = 0.39 for ConM at which there is a jump in wall pressures up to 1.94 times the local Janssen value. Below the effective transition, the wall pressures are significantly higher for ConM than for ConP until just above the base of the silo, at which point the ConP pressures become higher instead. However, it appears from Fig. 8.4 that this does not lead to drastic changes in the axial membrane stress distributions, which would suggest that ConM is not predicted to be excessively more damaging to the strength of the silo than ConP. There is a noticeable change of slope for the ConM distribution of axial membrane stress resultants at a depth corresponding directly to the location of the effective transition due to the big increase in frictional tractions at this location. Yet beyond this feature, there appears to be little difference between the two predicted stress patterns.

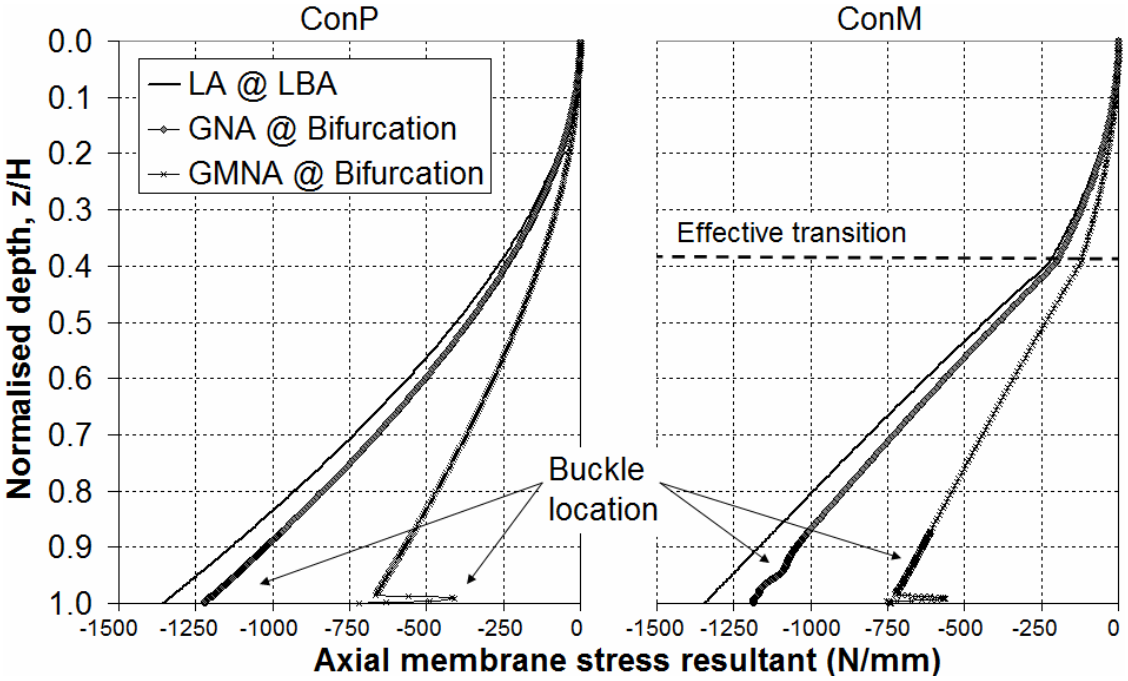

Fig. 8.4 – Axial distribution of LA, GNA and GMNA axial membrane stress resultants at bifurcation for the uniform wall Silo B under both ConP and ConM flow patterns

The sets of failure modes for the ConP and ConM flow patterns, illustrated in Fig. 8.5 and Fig. 8.6 respectively, show that both flow patterns result in very similar failure modes, all occurring at or very close to the base of the silo. For the MNA and GMNIA analyses, the failure modes under both concentric flow patterns are by axisymmetric plastic elephant's foot buckling or yielding (Axi-EF). The LBA, GNA and GMNA analyses predict instead an elastic axisymmetric buckle (Axi-EL), an elastic diamond buckle (Axi-DD) and a localised plastic buckle (Glb-EF) respectively.

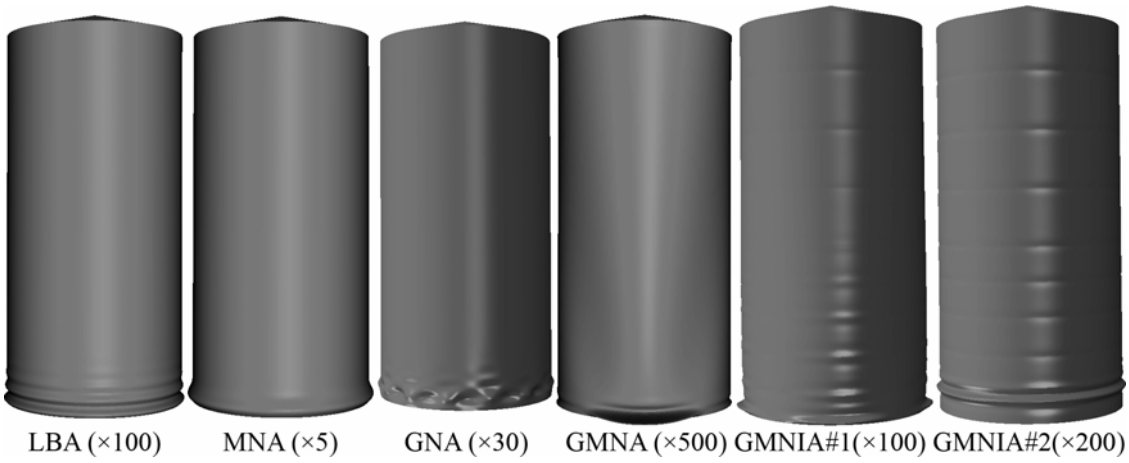

Fig. 8.5 – Uniform wall Silo B predicted failure modes under the ConP flow pattern

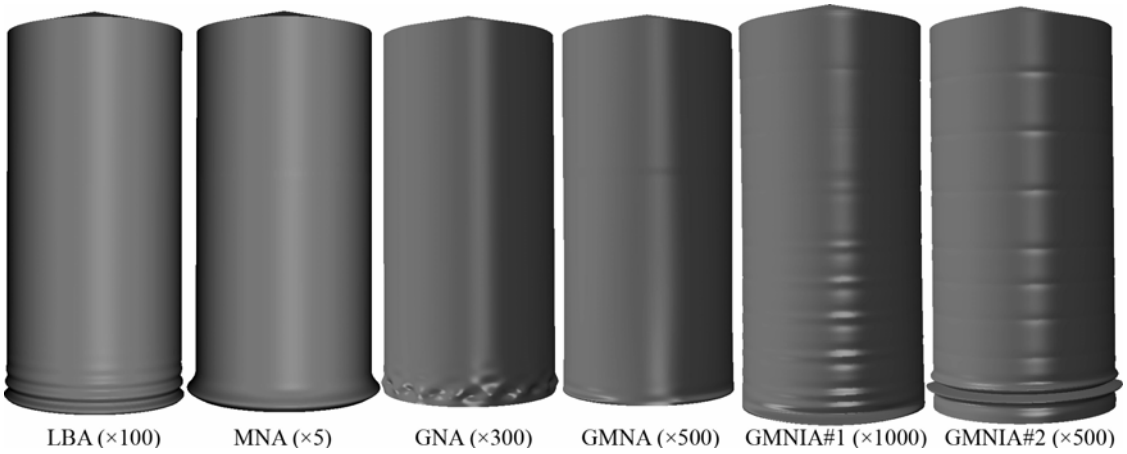

Fig. 8.6 – Uniform wall Silo B predicted failure modes under the ConM flow pattern

The load proportionality factors for the uniform wall Silo B under the ConP and ConM flow patterns are summarised in Table 8.3. The highest computed load factor is the LBA factor for ConP, a very high 15.22, whilst the lowest is GMNIA#2 for ConM, still a considerable value of 6.03. The predicted load factors are so high because the wall pressures applied in these analyses have not been increased by the discharge factors C_h and C_w, unlike the factored concentric EN 1991-4 pressures to which Silo B had been originally designed (Chapter 4). Furthermore, since the wall thickness is now uniform throughout, the load factors relate to failure modes at locations where the silo is actually strongest. As is usual under concentric loads (Rotter, 2004a), the inclusion of geometric or material nonlinearity in an analysis results in a lower predicted load factor.

Table 8.3 – Load proportionality factors and failure mode acronyms for the uniform wall Silo B under the ConP and ConM flow patterns

	LBA	MNA	GNA	GMNA	GMNIA#1	GMNIA#2
ConP	15.22	10.50	13.70	7.65	7.61	6.82
Failure mode	Axi-EL	Axi-EF	Axi-DD	Glb-EF	Axi-EF	Axi-EF
ConM	13.32	10.16	11.98	7.25	7.16	6.03
Failure mode	Axi-EL	Axi-EF	Axi-DD	Glb-EF	Axi-EF	Axi-EF
% change from ConP to ConM	– 12.5	– 3.3	– 12.6	– 5.2	– 5.9	– 11.6

The inclusion of axisymmetric weld depressions at 50% amplitude has an effectively negligible effect on the predicted silo behaviour, as the GMNIA#1 factor turns out to be 99% of the GMNA factor for both flow patterns. This was expected after examining

Fig. 8.5 and Fig. 8.6, as the buckling mode is in both cases the elephant's foot mode at the very base of the silo, and is thus effectively unaffected by weld imperfections as they are not present at this location. However, at 100% amplitude, the GMNIA#2 load factor drops noticeably to 89% and 83% of the GMNA load factors for the ConP and ConM flow patterns respectively. Considering the failure modes, the GMNIA#2 elephant's foot mode for both concentric flow patterns now forms at the lowest weld at a depth of $z/H = 0.95$, a more critical location at higher amplitudes than the base of the silo lacking the additional restraint that a boundary condition provides.

Despite the similarities in axial membrane stress distributions and failure modes, the predicted load factors are on average 8.8% lower for ConM than for ConP. The reason for this may be found in comparing the LA and GNA stresses for both flow patterns at a load factor of unity, shown in Fig. 8.7. The axial stresses are the same in the upper part of the silo for both patterns until the ConM effective transition at $z/H = 0.39$. At this point, the jump in frictional traction results in a change of slope of the ConM axial stresses and increased axial compression in the lower part of the silo. Thus the axial compression at the base of the silo is approximately 9% higher for ConM than for ConP, which is directly comparable with the average 8.8% reduction in load factor from ConM to ConP.

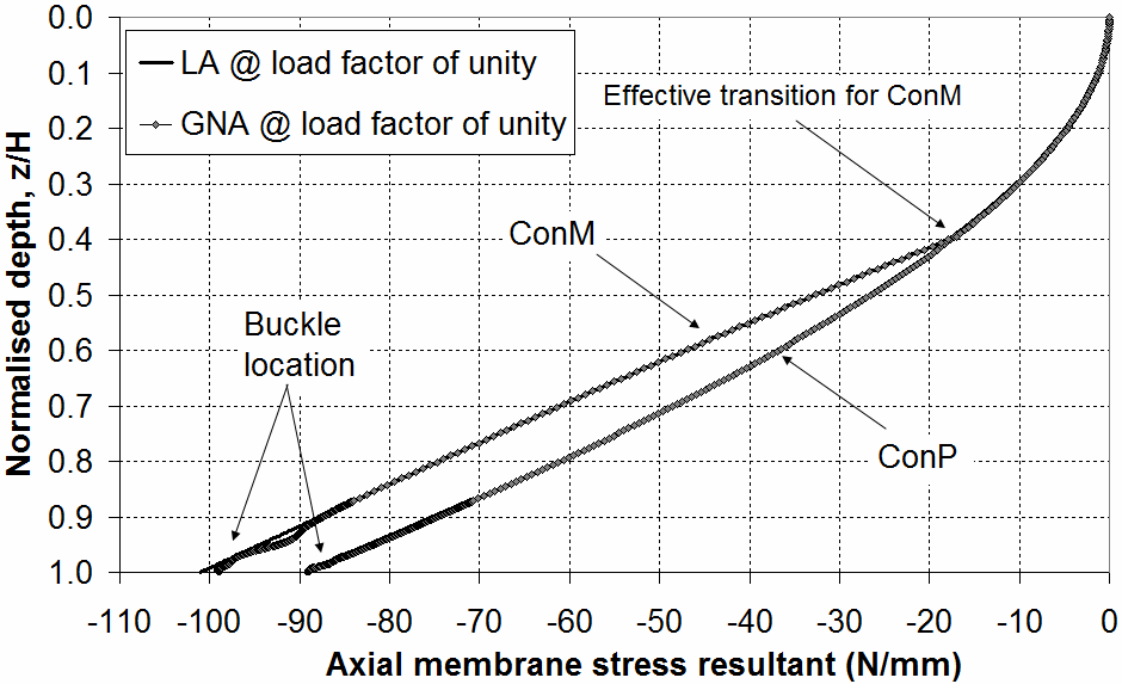

Fig. 8.7 – Axial distribution of LA and GNA axial membrane stress resultants at a load factor of unity for under both ConP and ConM flow patterns

8.4.2 Behaviour of the uniform wall silo under the EccP flow pattern

The uniform wall Silo B was analysed next under the non-symmetrical wall pressures predicted for the eccentric pipe flow pattern, EccP (Fig. 8.3). This flow pattern does not exhibit an effective transition around the entire silo circumference unlike ConM and EccM, and instead consists of a steep channel adjacent to a relatively narrow portion of the wall, covering at most 22% of the circumference over which it exerts very low pressures. Outside this zone, the wall pressures due to the stationary solid are very close to the Janssen values. The results for this suite of analyses are introduced here with an annotated three-dimensional global contour plot of the linear-elastic (LA) axial stresses, shown in Fig. 8.8.

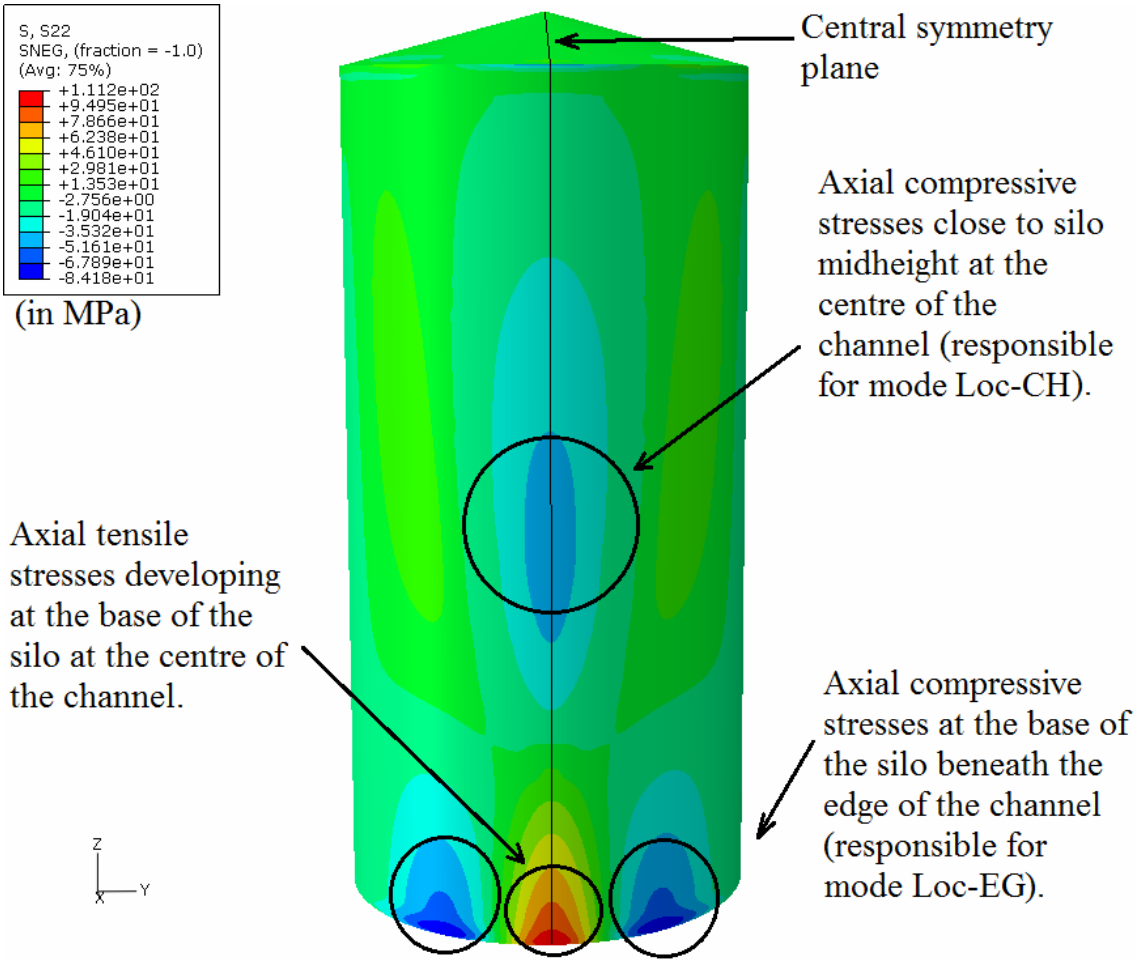

Fig. 8.8 – LA axial stresses for the uniform wall Silo B under the EccP flow pattern

The resulting pattern of axial stresses under EccP flow shares many of the same features seen in previous analyses of the EN 1991-4 eccentric discharge model. For example, a localised region of axial compressive membrane stresses develops in the silo wall across the flow channel at approximately midheight, becoming tensile at the base. These compressive membrane stresses are responsible for the elastic buckling mode Loc-CH. Additionally, high compressive membrane stresses also develop in the wall at the base of the silo slightly away from the centre, and these are responsible for the elastic-plastic buckling mode Loc-EG. In the case of EccP, the flow channel does not have parallel sides and does not actually reach the very bottom of the silo (Fig. 8.3), thus buckles which form in this location can only be described as being 'beneath' the edge of the flow channel, rather than 'at' the edge as was the case for the EN 1991-4 results.

The axial distributions of the axial membrane stress resultants for the GNA and GMNA analyses at bifurcation for the uniform wall Silo B under the EccP flow pattern are shown in Fig. 8.9 at four circumferential locations. The perturbations observed on some of the curves on this figure are due to the close proximity of the buckles. The distributions of axial membrane stress resultants at the positions θ = 0° and 45° correspond directly to the distributions at the flow channel centre and edge respectively from the analyses of the EN 1991-4 eccentric discharge distribution (compare, for example, with Fig. 2.9 and Fig. 2.13). However, for θ beyond approximately 60°, the distributions of the axial membrane stress resultants are again characteristic of Janssen-like wall pressures. The portion of the shell influenced by the flow channel is thus relatively small, though the structural consequences are very significant.

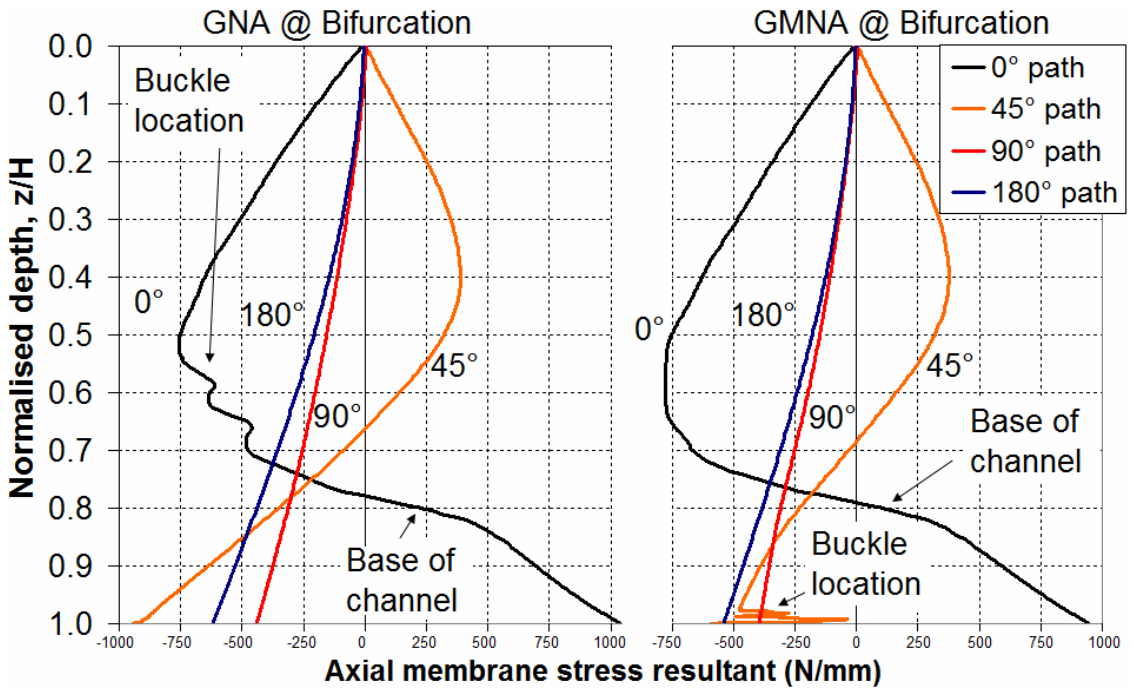

Fig. 8.9 – Axial distribution of the GNA and GMNA axial membrane stress resultants at bifurcation at four circumferential locations for the uniform wall Silo B under the EccP flow pattern

The predicted failure modes for the uniform wall Silo B under the EccP flow pattern are shown in Fig. 8.10 and the computed load proportionality factors are presented in Table 8.4. It was noted in Fig. 8.8 that two specific regions of high axial compressive membrane stresses become critical for buckling under the EccP flow pattern. These are the same critical regions as under the EN 1991-4 eccentric discharge model (Chapters 2 and 4). When the silo has a uniform wall throughout, the region at the base of the silo beneath the edge of the channel is most highly stressed and thus critical for buckling, especially when combined with the destabilising effect of the high internal pressure at this location (α_{xpp}, Eq. 1.20). This is indeed the case as the GMNA and both GMNIA analyses all result in the buckling mode Loc-EG. The LBA mode, which naturally does not include material plasticity, was nonetheless counted as mode Loc-EG as it is clearly caused by the compressive axial membrane stresses at this critical location (Table 8.2). The elastic midheight buckling mode Loc-CH (which forms in the silo wall within the region of low internal pressure) was obtained in the GNA analysis only, most likely because of the high internal pressure at the base providing a stabilising effect (α_{xpe}, Eq. 1.19) thus preventing a Loc-EG buckle from forming at the same location as for the GMNA, but *only* in the case of an elastic analysis.

Material plasticity has a significant influence on the predicted structural behaviour of the uniform wall Silo B under the EccP pattern. This is shown by the 13.5% drop in load factor from GNA to GMNA and the dominant presence of mode Loc-EG, which is accompanied by plasticity as the compressive stresses and internal pressure are usually very high at this location (Chapter 4). However, the associated load factor of the MNA mode, which corresponds to the circumferential bending plastic collapse mechanism, is higher than all the other factors. Thus an MNA analysis of the EccP flow pattern captures the plastic collapse mode due to circumferential bending, though however this does not reflect the true behaviour of the silo under eccentric discharge.

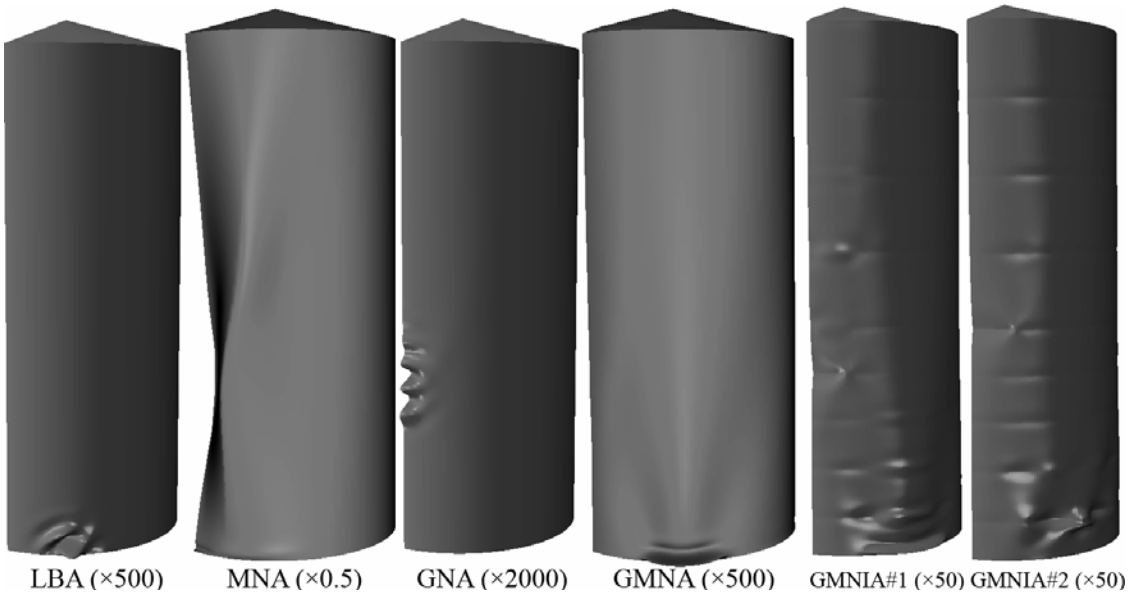

Fig. 8.10 – Uniform wall Silo B predicted failure modes under the EccP flow pattern

Table 8.4 – Load proportionality factors and failure mode acronyms for the uniform wall Silo B under the EccP flow pattern

	LBA	MNA	GNA	GMNA	GMNIA#1	GMNIA#2
ECCP	3.52	5.85	5.56	4.81	4.50	4.10
Failure mode	Loc-EG	Glb-PL	Loc-CH	Loc-EG	Loc-EG	Loc-EG
% change from ConP to EccP	– 76.9	– 44.3	– 59.4	– 37.1	– 40.9	– 39.9
% change from ConM to EccP	– 73.6	– 42.4	– 53.6	– 33.7	– 37.2	– 32.0

The load factors for the EccP flow pattern are clearly significantly lower than those for the ConP and ConM patterns (Table 8.3). Thus the EccP pattern is likely to be highly deleterious to the strength of the silo, and the corresponding structural behaviour correlates closely with what had been predicted previously for the EN 1991-4 eccentric discharge model which was based on an assumption of a similar flow pattern.

8.4.3 Behaviour of the uniform wall silo under the EccM flow pattern

The final suite of analyses for the uniform wall Silo B was performed using the non-symmetrical wall pressures predicted for the eccentric mixed flow pattern, EccM (Fig. 8.3). A three-dimensional colour contour plot of the resulting LA axial stresses is shown in Fig. 8.11 and serves as a useful introduction of the main features of the predicted structural response to the eccentric mixed flow which, it will be shown, is significantly different to that under eccentric pipe flow. This figure includes the approximate outline of the circumferentially-varying effective transition, but its position could actually be traced with relative ease by considering the patterns on the axial stress contours.

Examination of the axial stresses reveals that there is a region of high axial compressive membrane stress at the base of the silo on the side opposite the outlet at $\theta = 180°$. The stress at this location may cause elastic-plastic buckling of the silo which, in turn, may additionally cause the silo to overturn in the direction away from the outlet.

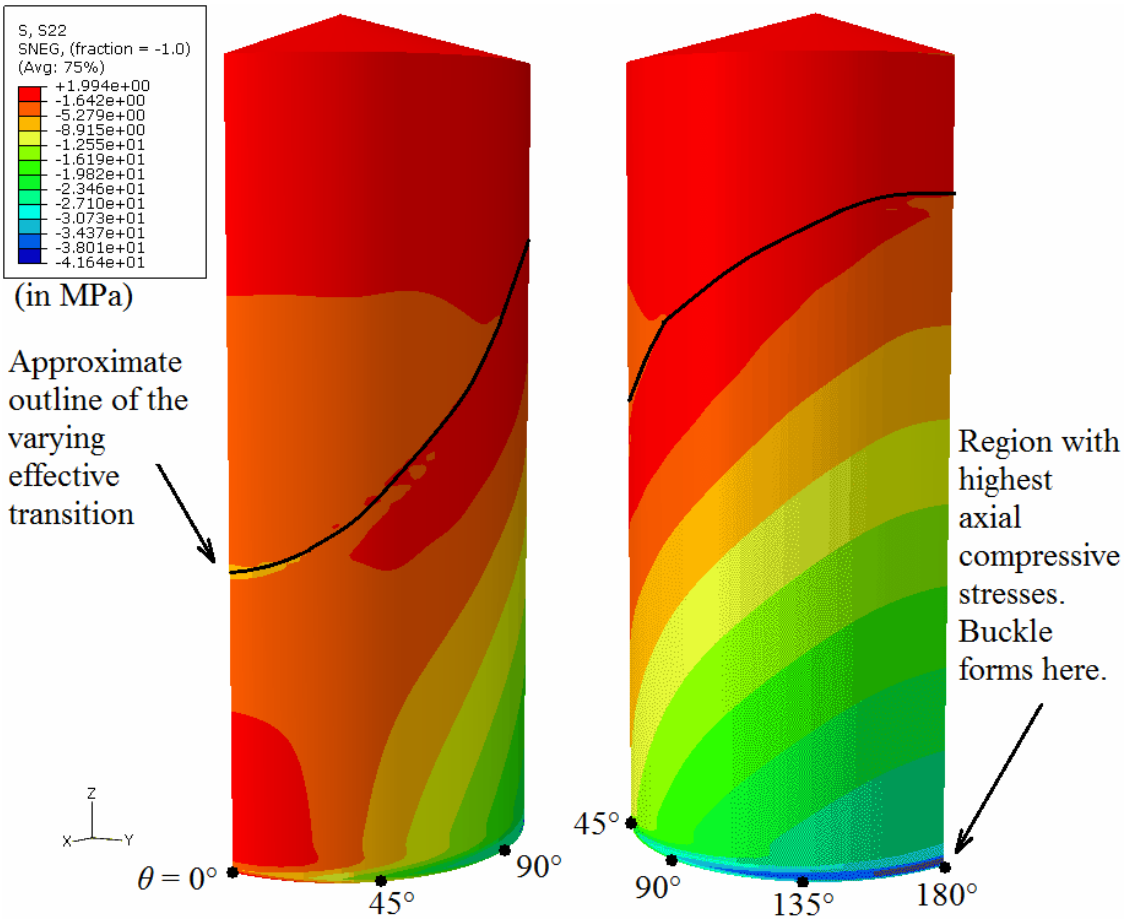

Fig. 8.11 – LA axial stresses for the uniform wall Silo B under the EccM flow pattern

The axial distributions of the axial membrane stress resultants for LA @ LBA and GMNA @ bifurcation are shown in Fig. 8.12. These curves reflect what is seen on Fig. 8.11, confirming that the magnitude of the compressive stress resultants at the base of the silo grows progressively around the circumference from $\theta = 0°$ to 180°. The axial membrane stresses are tensile at $\theta = 0°$, while at $\theta = 180°$ the axial compression is at a maximum. A slight perturbation may be seen at the base of the GMNA curve for $\theta = 180°$ due to the presence of a buckle at this location.

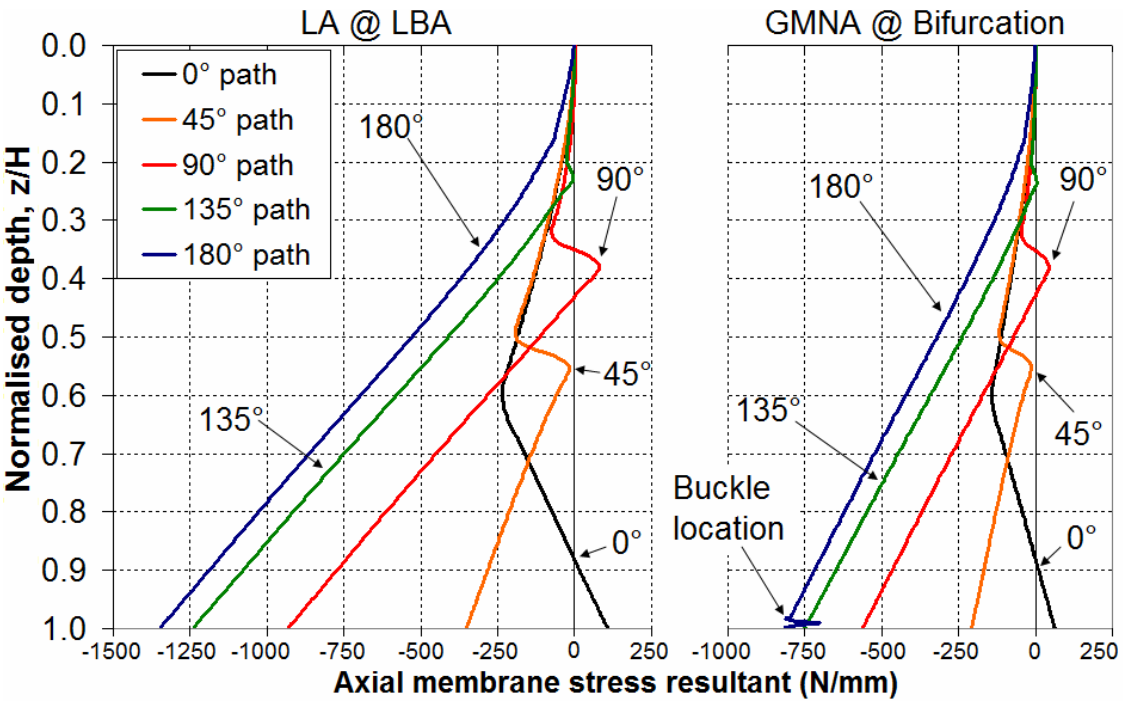

Fig. 8.12 – Axial distribution of the LA and GMNA axial membrane stress resultants at bifurcation at five circumferential locations for the uniform wall Silo B under the EccM flow pattern

To illustrate a further aspect of the silo behaviour, the axial distributions of the axial bending moments for GMNA @ bifurcation are shown in Fig. 8.13 for five different circumferential locations. Although this figure shows clearly that the silo is predominantly under axial membrane compression throughout, the bending moment at the base of the silo is seen to grow almost threefold from $\theta = 0°$ to 180° (it is assumed that a positive bending moment produces tension on the inner surface of the shell.). Thus the evidence so far suggest that the EccM flow pattern subjects the silo to a global overturning moment which in turn precipitates local plastic buckling failure opposite the outlet. There is also, interestingly, minor bending around the local circumferential position of the effective, but the magnitudes are very small. The predicted load proportionality factors are summarised in Table 8.5.

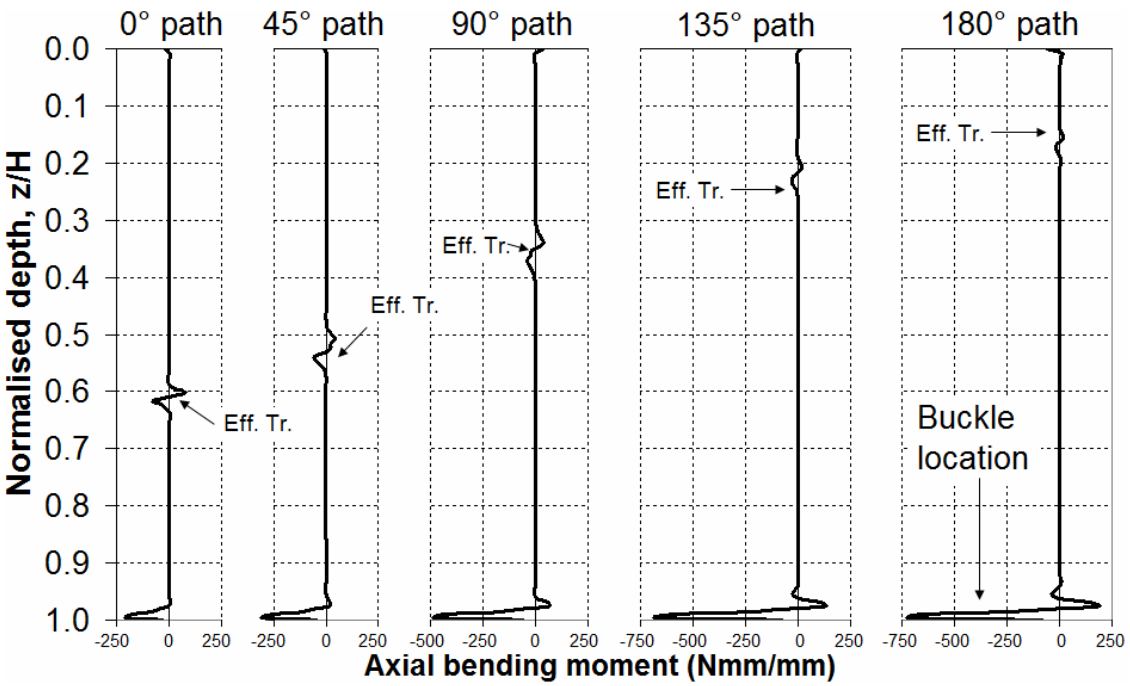

Fig. 8.13 – Axial distribution of the GMNA axial bending moments at bifurcation at five circumferential locations for the uniform wall Silo B under the EccM flow pattern (Note: Eff. Tr. = effective transition)

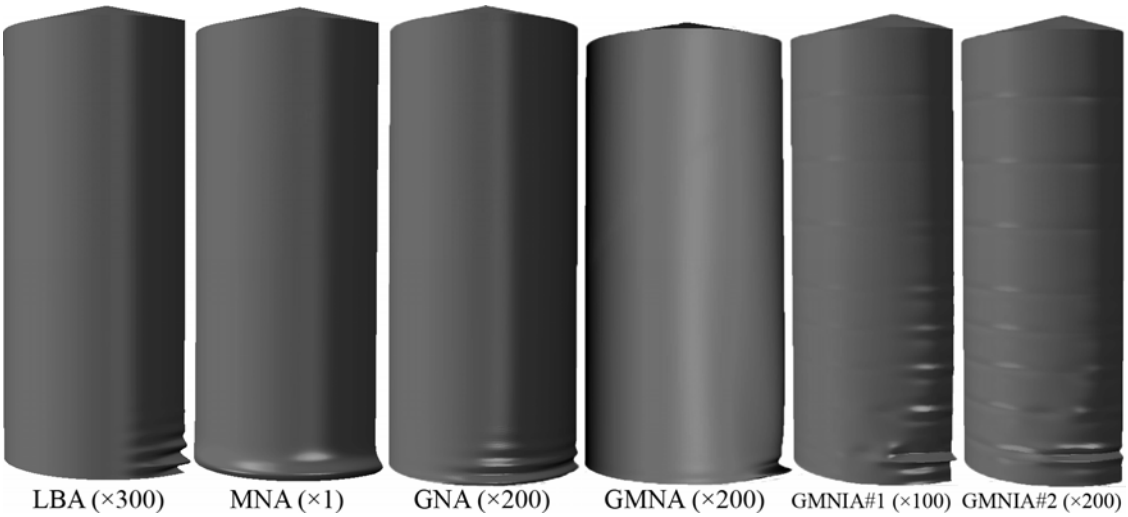

Fig. 8.14 – Uniform wall Silo B predicted failure modes under the EccM flow pattern

Table 8.5 – Load proportionality factors and failure mode acronyms for the uniform wall Silo B under the EccM flow pattern

	LBA	MNA	GNA	GMNA	GMNIA#1	GMNIA#2
ECCM	7.84	7.91	7.90	4.86	4.75	3.84
Failure mode	Axi-EL	Glb-EF	Axi-EL	Glb-EF	Glb-EF	Glb-EF
% change from ConP to EccM	– 48.5	– 24.7	– 42.3	– 36.5	– 37.6	– 43.7
% change from ConM to EccM	– 41.1	– 22.2	– 34.1	– 33.0	– 33.7	– 36.3
% change from EccP to EccM	+ 122.7	+ 35.2	+ 42.1	+ 1.0	+ 5.6	– 6.3

The definitions of the four flow patterns in Table 8.1 and Fig. 8.1 suggest that the only difference between the ConM and EccM patterns is the position of the central axis of the flow channel, placed at 0% and just over 25% eccentricity respectively. The outlet size r_0, channel steepness n and silo geometry are the same for both flow patterns. Yet the change in outlet eccentricity from 0% to just 25% is sufficient to warrant huge reductions in silo strength, and the geometrically nonlinear load factors (GNA, GMNA and both GMNIAs) are predicted to be on average 34% lower for EccM than for ConM. By contrast, the corresponding average reduction from ConP to ConM was a mere 8%. In light of the results in the previous section for the EccP pattern, this analysis additionally suggests that eccentric flow patterns in general may be disproportionately more damaging to silos than concentric patterns and that shell structures are thus rather inefficient at resisting unsymmetrical load patterns.

The inclusion of axisymmetric weld imperfections displaces the plastic buckling mode to the position of the lowest weld at a depth of $z/H = 0.95$, though still very close to the buckling locations for the LBA, GNA and GMNA analyses which occur at the base of the silo. An increased imperfection amplitude results in a 2.3% and 21% drop in load factor from GMNA to GMNIA#1 (50% amplitude) and GMNIA#2 (100% amplitude) respectively, and the buckling location remains the same at both imperfection amplitudes. The axisymmetric weld depression is therefore a deleterious imperfection form under eccentric mixed flow, and it is expected that the silo may have significant imperfection sensitivity under this flow pattern.

8.4.4 Global comparison of the results for the uniform wall silo

The entire set of computed load proportionality factors for the uniform wall Silo B is compared on a bar chart in Fig. 8.15. A schematic summarising the associated failure modes is shown in Fig. 8.16. The bar chart illustrates the global trend in terms of what the uniform wall silo is predicted to be most efficient at withstanding. It shows that concentric mixed flow is more serious than concentric pipe flow, that eccentric flows in general are significantly more serious than concentric flows, and that eccentric pipe flow is more serious than eccentric mixed flow. In terms of increasing structural severity: ConP < ConM < EccM < EccP.

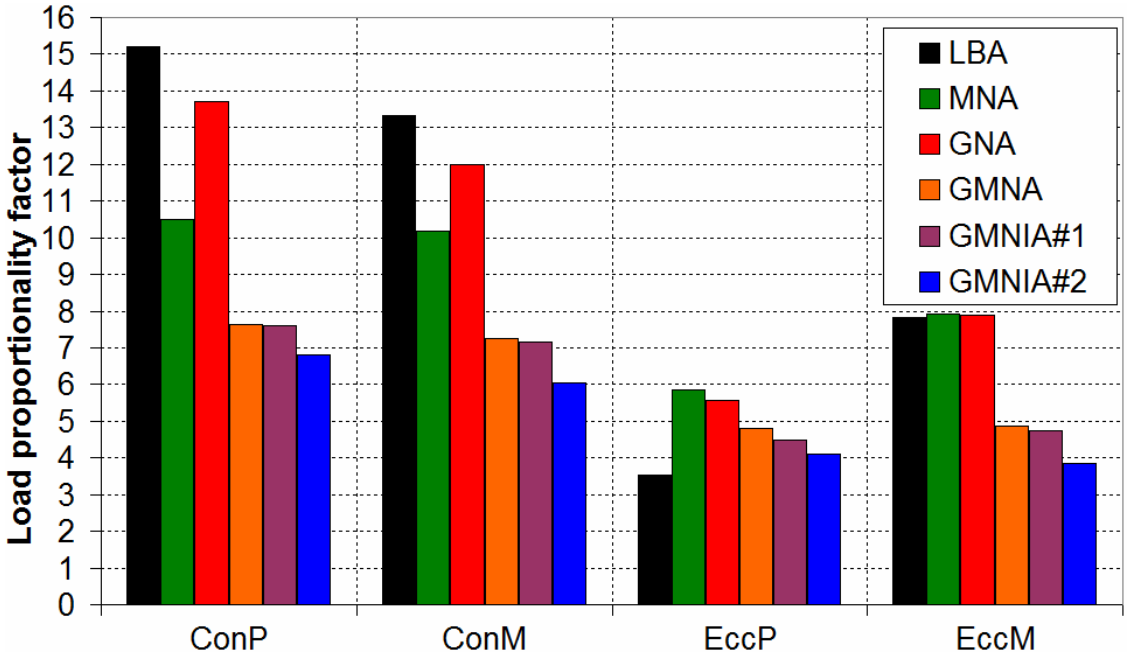

Fig. 8.15 – Bar chart comparison of the load factors for the four flow patterns for the uniform wall Silo B

The schematic in Fig. 8.16 suggests that, for uniform wall silos under concentric flows, the failure mode is likely to be by some form of buckling or yielding spanning the full circumference near the base of the silo. For eccentric flows, the failure mode and location are much harder to predict given the vast range of possible patterns. However, the current results which now span a much wider range of different flow patterns appear to confirm that eccentric pipe flow is rightly considered to be one of the most serious design conditions rightly meriting its own design scenario in the EN 1991-4 (2007) Standard. The critical location for buckling under mixed flow is predicted to be near the base of the silo opposite the outlet.

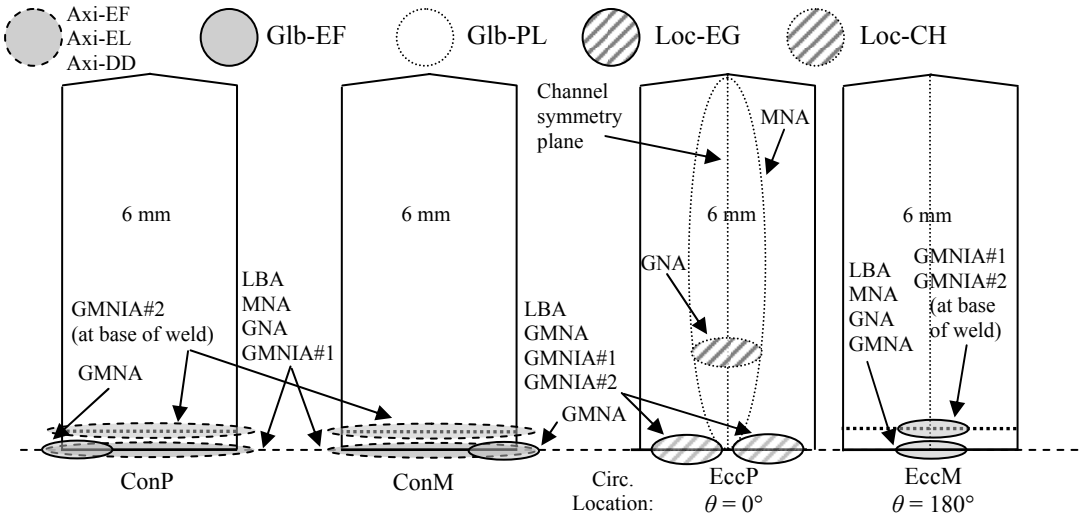

Fig. 8.16 – Summary of failure mode locations for the four flow patterns (uniform wall Silo B drawn to scale)

8.5 Results for the stepped wall silo under the four flow patterns

8.5.1 Behaviour of the stepped wall silo under the ConP and ConM flow patterns

The second half of this chapter is concerned with the analysis of the more realistic stepped wall thickness Silo B under the same four flow patterns and with their comparison to the results for the uniform wall Silo B. The first computational analyses of the stepped wall Silo B were performed using the wall pressures predicted for the concentric ConP and ConM flow patterns (Fig. 8.1). The axial distributions of axial membrane stress resultants for LA @ LBA, and GNA and GMNA @ bifurcation, are presented in Fig. 8.17. The critical values of the stress resultant N_{cl} at the classical buckling stress σ_{cl} for uniform axial compression, important in the context of stepped thickness designs, are summarised in Table 8.6.

Table 8.6 – Summary of critical N_{cl} values for each wall strake

Wall thickness (mm)	3	4	5	6
N_{cl} (N/mm)†	320.3	569.4	889.7	1281.2

† Note: $N_{cl} = t\sigma_{cl} \approx 0.605Et^2R^{-1}$ assuming $E = 200$ GPa and $R = 3400$ mm

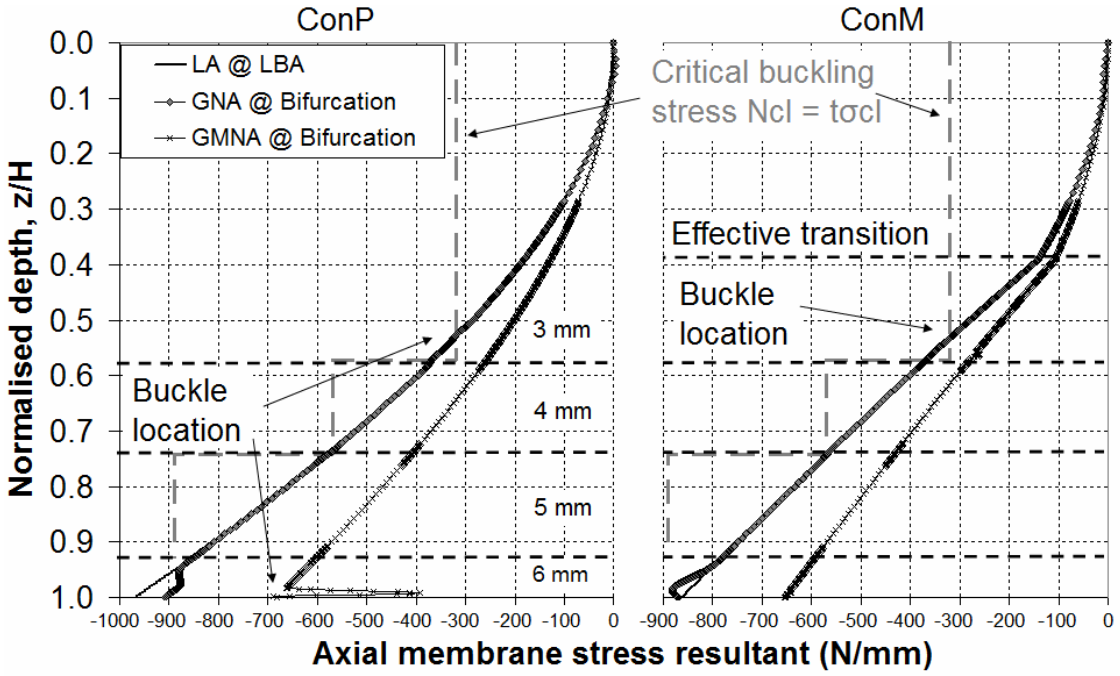

Fig. 8.17 – Axial distribution of LA, GNA and GMNA axial membrane stress resultants at bifurcation for the stepped wall Silo B under the ConP and ConM flow patterns

The above distributions of axial membrane stress resultants are very similar to those for the uniform wall silo in Fig. 8.5. Indeed, there again appears to be little difference between the curves for the ConP and ConM flow patterns, other than a clear change of slope at the location of the jump in wall pressures due to the effective transition at $z/H = 0.39$ and the rise in frictional tractions at this location. Additionally, the magnitudes of the stresses for LA @ LBA and GNA @ bifurcation are very similar for both ConP and ConM, suggesting very close load factors and a high degree of linearity in the behaviour of the silo under axisymmetric loads.

The failure modes of the stepped wall Silo B for the ConP are shown in Fig. 8.18. Similar to the corresponding results for the uniform wall Silo B, the MNA, GMNA and GMNIA analyses predict the plastic elephant's foot mode Axi-EF, while the LBA and GNA analyses predict the elastic modes Axi-EL and Axi-DD respectively. However, since the wall thickness is now stepped, the base of the silo is no longer exclusively critical.

For the ConP flow pattern, the base of every strake becomes critical for at least one of the computational analyses, but without exhibiting any obvious preference. Although the LA and GNA axial membrane stresses for ConP at the base of the 3 mm strake have

reached the critical value of N_{cl} = 320.3 N/mm (and thus duly buckle at this location, Fig. 8.17 and Table 8.6), the stress at the bases of the other strakes are also very close to their corresponding critical value of N_{cl}. Thus the remaining strakes may easily become critical for buckling under small changes in the conditions of the analysis, especially when plasticity is introduced, and the lack of a single critical location for failure shown in Fig. 8.18 seems to reflect this.

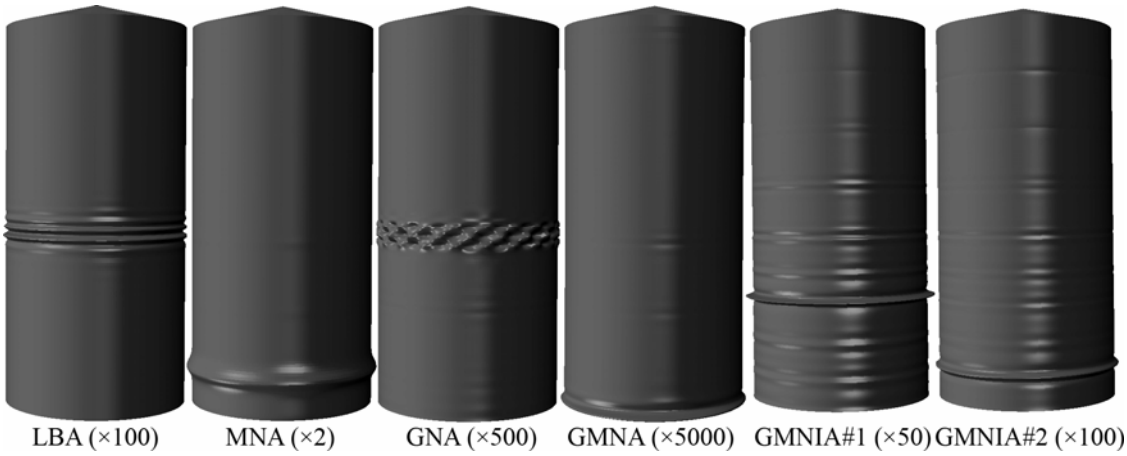

Fig. 8.18 – Stepped wall Silo B predicted failure modes under the ConP flow pattern

The failure modes for the stepped wall Silo B under the ConM flow pattern are shown in Fig. 8.19, where it is clear that the critical location is predicted to be consistently at the base of the thinnest 3 mm strake. The base of this strake occurs at z/H = 0.57 and is located very close to the axisymmetric effective transition at z_{13}/H = 0.39, at which there is a sudden increase in normal wall pressures and frictional tractions to 1.94 times the local Janssen value. It was discussed in Chapter 4, as the design of Silo B was being introduced, that the effect of internal pressure was included in design through the pressurised elastic imperfection factor α_{xp} of EN 1993-1-6 (2007; Eq. 1.17). As the internal pressure due to Janssen only was found not to be excessively high, it was deemed to be beneficial to the buckling strength and consequently α_{xp} was given by the elastic stabilisation factor α_{xpe} (Eq. 1.19). For the case of the effective transition of the ConM flow pattern, internal pressure as high as 1.94 times the original Janssen value is likely to contribute greatly to early yielding which is clearly no longer beneficial to the buckling strength, thus in design α_{xp} would be most likely be given instead by the plastic destabilisation factor α_{xpp} (Eq. 1.20). The plastic destabilisation effect of high internal pressure exacerbates the lower buckling resistance of the thinnest region of the silo, and consequently causes the MNA plastic collapse mode and GMN(I)A buckling modes to

shift from the base of the silo to the base of the thinnest strake. For the case of the elastic LBA and GNA analyses which cannot suffer from plastic destabilisation, a similar effect to that found in Fig. 8.7 sees higher axial compression below the effective transition at $z_{13}/H = 0.39$ firmly establishing the base of the 3 mm strake as the critical location for buckling. A full discussion of the design of silos for axial compression and the beneficial or detrimental effects of internal pressure may be found in Section 1.3.5 of the literature review.

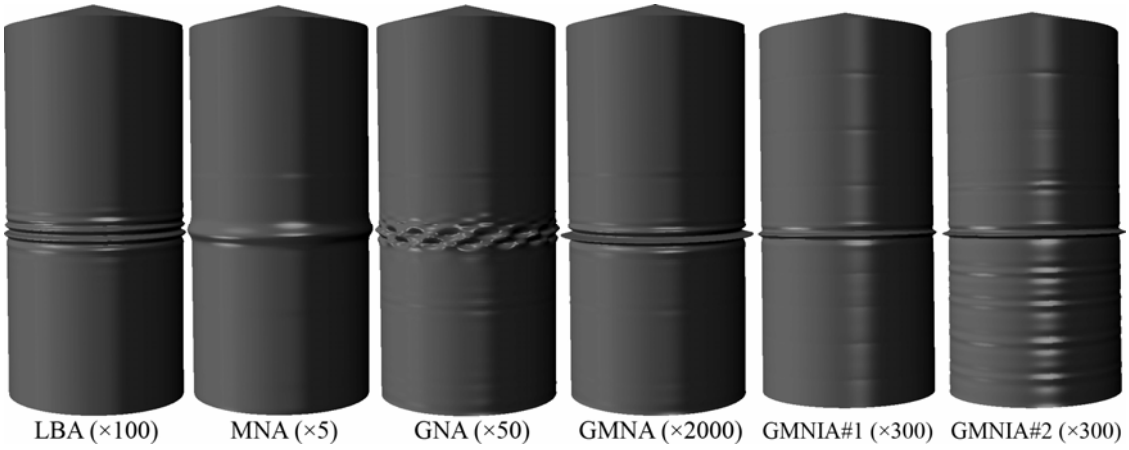

Fig. 8.19 – Stepped wall Silo B predicted failure modes under the ConM flow pattern

The computed load proportionality factors for the stepped wall Silo B under the two concentric flow patterns are summarised in Table 8.7. A similar pattern emerges as for the uniform wall Silo B (Table 8.3), except that the load factors are all significantly lower than before because the buckling or plastic collapse failure now occurs sooner in a thinner, weaker wall. The LBA and GNA load factors are very close indeed for both flow patterns suggesting that stepped wall silos behave in a very linear manner under axisymmetric loading and, where the weld imperfections are not explicitly modelled, any strength decreases occur as a result of material plasticity alone.

The stepped wall Silo B was originally designed for the EN 1991-4 concentric discharge pressures (Chapter 4), which included the C_h and C_w discharge factors which were equal to 1.15 and 1.1 respectively. The load factors for the ConP analyses using unfactored concentric pressures (Table 8.7) were found to be on average 1.12 times the corresponding load factors for the EN 1991-4 concentric discharge analyses (Table 4.11). This rise in buckling strength corresponds closely with the values of the missing discharge factors.

For the ConM flow pattern, the introduction of weld imperfections throughout the silo, including at all changes of strake thickness, leads to GMNIA load factors that are lower than the GMNA value and maintains the critical location at the base of the thinnest strake. For the ConP buckling modes, however, there is no such pattern and there does not appear to be any specific reason as to why one location becomes critical and not another.

Table 8.7 – Load proportionality factors and failure mode acronyms for the stepped wall Silo B under the ConP and ConM flow patterns

	LBA	MNA	GNA	GMNA	GMNIA#1	GMNIA#2
ConP	10.86	9.61	10.82	7.66	6.64	5.74
Failure mode	Axi-EL @ base of 3 mm	Axi-EF @ base of 5 mm	Axi-DD @ base of 3 mm	Axi-EF @ base of silo	Axi-EF @ base of 4 mm @ weld	Axi-EF @ base of 5 mm @ weld
ConM	8.51	7.22	8.48	6.46	5.10	4.42
Failure mode†	Axi-EL	Axi-EF	Axi-DD	Axi-EF	Axi-EF	Axi-EF
EN 1991-4 (2007)‡ concentric discharge	6.97	6.64	6.93	5.55	4.55	3.75
Failure mode	Axi-EL	Axi-EF	Axi-DD	Axi-EF	Glb-DD	Gbl-EF
% change from ConP to ConM	– 21.6	– 24.9	– 21.6	– 15.7	– 23.2	– 23.0

† the failure modes for ConM are all at the base of the 3 mm strake

‡ from the aspect ratio study of the *factored* EN 1991-4 concentric discharge pressures, Table 4.11, with $C_h = 1.15$ and $C_w = 1.1$

8.5.2 Behaviour of the stepped wall silo under the EccP flow pattern

The stepped wall Silo B was subsequently analysed under the non-symmetrical EccP flow pattern (Fig. 8.3). The global pattern of axial stresses was found to be very similar as for the uniform wall silo (Fig. 8.8), reproducing the same possible critical locations for buckling at the channel centre at midheight and beneath the edge of the channel near the base of the silo. The axial distributions of axial membrane stress resultants for LA and GNA/GMNA analyses at bifurcation are shown in Fig. 8.20 for four different circumferential positions. These curves reflect very closely what has been observed in the analyses of EN 1991-4 eccentric discharge model (e.g. Fig. 2.9).

The LA @ LBA axial compression consistently reaches the critical buckling value of N_{cl} = 320.3 N/mm just above the base of the 3 mm strake at the centre of the channel (Table 8.3 and Fig. 8.20). The GNA axial compression at buckling comes close to N_{cl} but does not reach it, a likely reason being due to the local flattening of the silo wall across the flow channel (see Chapters 3 and 6). Thus the corresponding location is critical for all buckling modes which are presented in Fig. 8.21 and may be compared directly with Fig. 2.13 which shows the elastic midheight buckling modes of Silo CVS under the EN 1991-4 eccentric discharge pressure model. The stepped wall Silo B was thus found to exhibit the fully-elastic midheight mode Loc-CH in all analyses of the EccP flow pattern, with the natural exception of the circumferential bending mode Glb-PL for the MNA analysis.

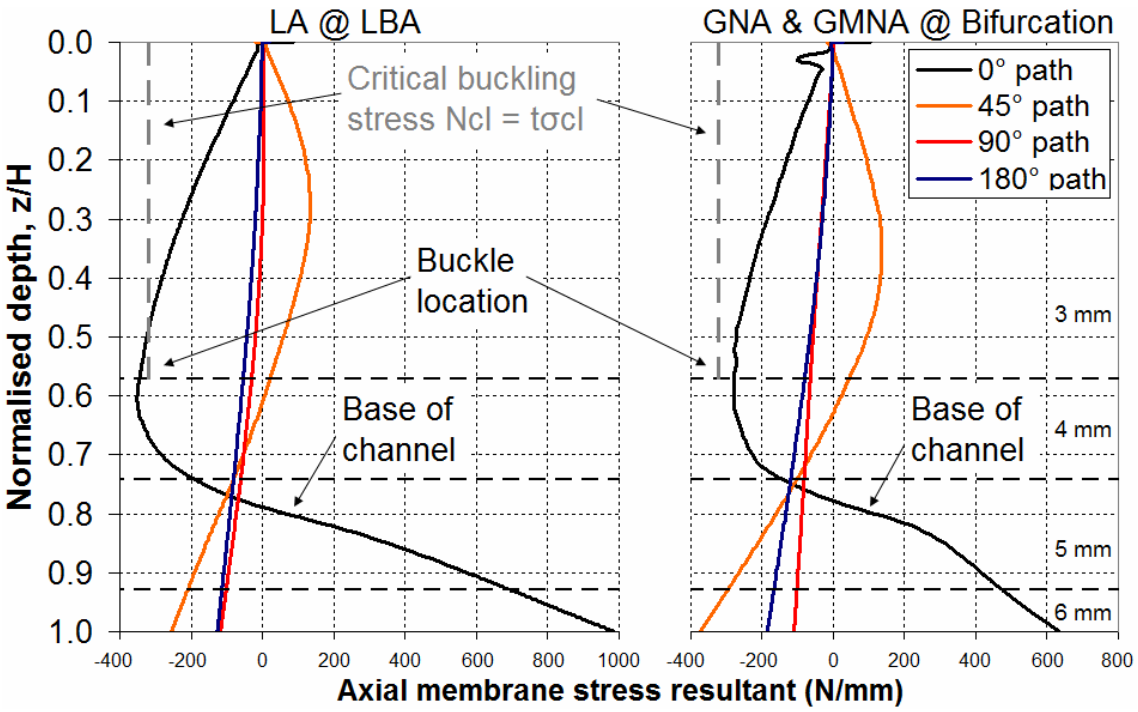

Fig. 8.20 – Axial distribution of the LA, GNA and GMNA axial membrane stress resultants at bifurcation at four circumferential locations for the stepped wall Silo B under the EccP flow pattern

The computed load proportionality factors are summarised in Table 8.8. The average reduction in geometrically nonlinear load factors from their ConP and ConM counterparts is a massive 84% and 79% respectively. Each of the computational analyses predicted fully elastic behaviour, with the natural exception of MNA. Additionally, all non-MNA load factors are within eyeshot of unity which, considering

that Silo B was significantly overdesigned for the reference ConP flow pattern, sees all conservatism in the design being wiped out and shows how destructive eccentric pipe flow is likely to be. Indeed, the lowest load factor was predicted to be 0.87 for the GMNIA#1 analysis, corresponding to the axisymmetric weld depression with an amplitude of 50% of the EN 1993-1-6 GMNIA requirement. At 100% amplitude, the weld depression exhibits a beneficial effect, raising the GMNIA#2 load factor by 20.7% from GMNIA#1 to 1.05. The beneficial effect of the axisymmetric weld depression under the EN 1991-4 eccentric discharge pressures has been discussed in the first half of this thesis, and it is apparent that the EccP flow pattern produces the same effect.

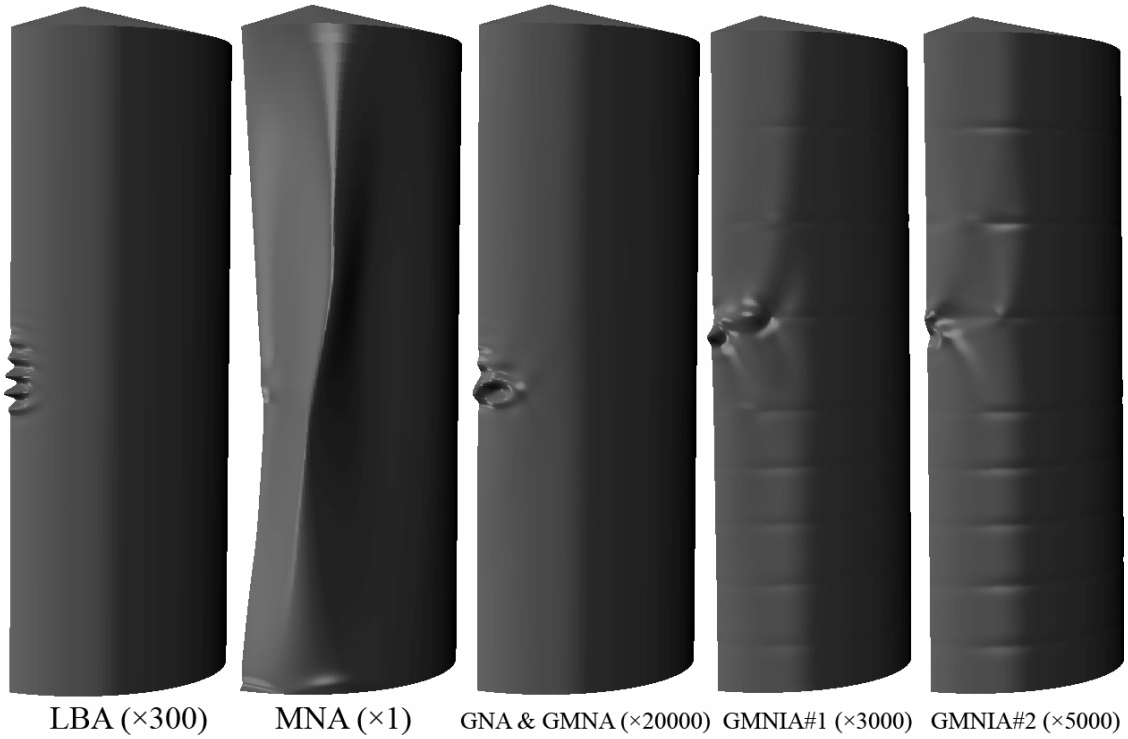

Fig. 8.21 – Stepped wall Silo B predicted failure modes under the EccP flow pattern

Table 8.8 – Load proportionality factors and failure mode acronyms for the stepped wall thickness silo under the EccP flow pattern

	LBA	MNA	GNA	GMNA	GMNIA#1	GMNIA#2
ECCP	1.07	3.35	1.58	1.58	0.87	1.05
Failure mode	Loc-CH	Glb-PL	Loc-CH	Loc-CH	Loc-CH	Loc-CH
% change from ConP to EccP	– 90.2	– 65.1	– 85.4	– 79.4	– 86.9	– 81.7
% change from ConM to EccP	– 87.4	– 53.6	– 81.4	– 75.5	– 82.9	– 76.2

8.5.3 Behaviour of the stepped wall silo under the EccM flow pattern

The stepped wall Silo B was analysed in this final study under the non-symmetrical wall pressures of the eccentric mixed flow pattern, EccM (Fig. 8.3). The three-dimensional global state of LA axial stresses is presented in Fig. 8.22 and shows very similar features to the corresponding figure for the uniform wall silo, Fig. 8.11. The outline of the position of the circumferentially-varying effective transition can be delineated with ease from the stress pattern and has not been marked on the figure.

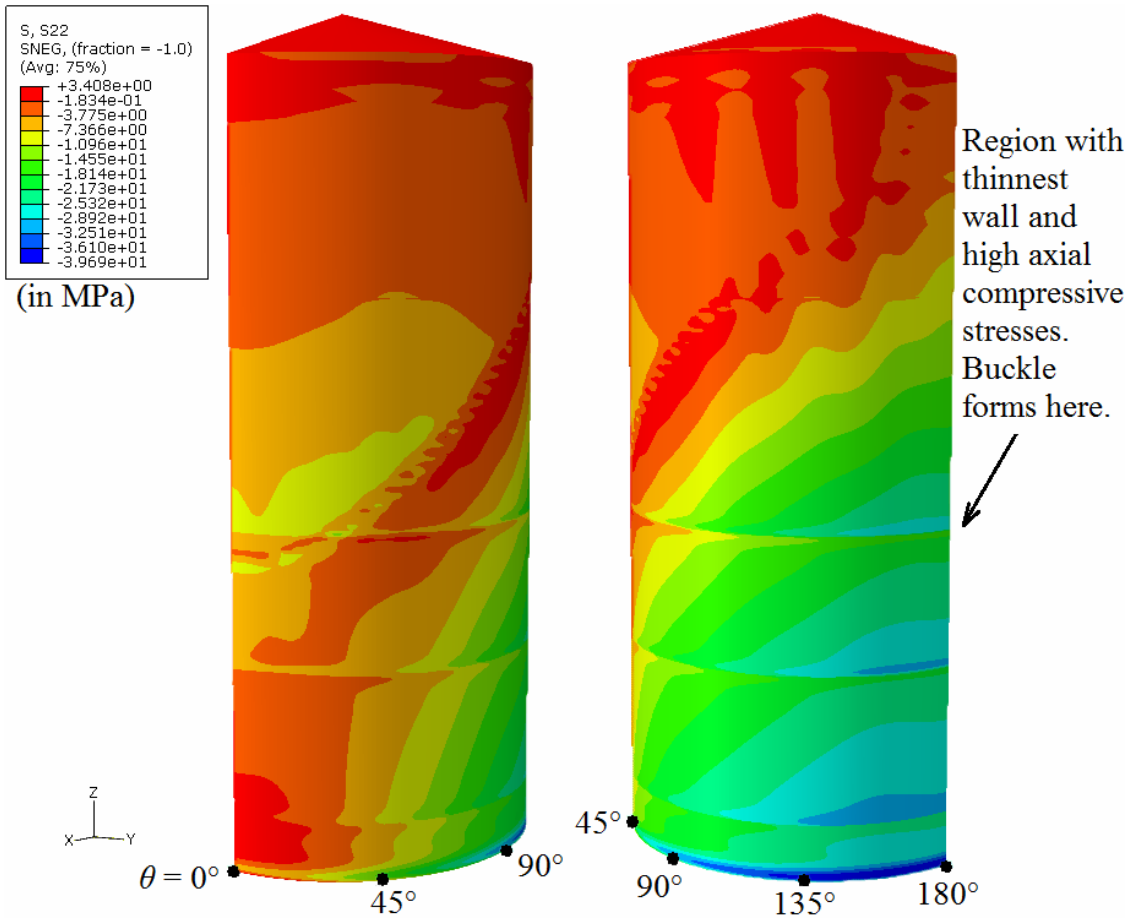

Fig. 8.22 – LA axial stresses for the stepped wall Silo B under the EccM flow pattern

The axial distributions of the axial membrane stress resultants and axial bending moments for the GMNA analysis at bifurcation are shown in Fig. 8.23 and Fig. 8.24 at five different circumferential locations. The magnitudes of axial compressive membrane stresses and bending moments at the base of the silo grow progressively from $\theta = 0°$ to 180°, and it is evident that the silo is subject to a global overturning moment which causes buckling in the wall opposite the outlet. However, unlike for the uniform wall design where the buckles were found to form at the base of the silo (Fig. 8.14), in the

case of the stepped wall Silo B buckling is predicted to occur at the base of the thinnest 3 mm strake due to its lower buckling resistance (Fig. 8.25). Indeed, the GMNA axial membrane stresses at buckling have reached the critical value of N_{cl} = 320.3 N/mm at this location (Fig. 8.23). The buckling modes in Fig. 8.25 were classified as according to Table 8.2 as modes Glb-EF for the materially nonlinear analyses (MNA, GMNA and GMNIA), and as modes Axi-EL for the elastic analyses (LBA and GNA).

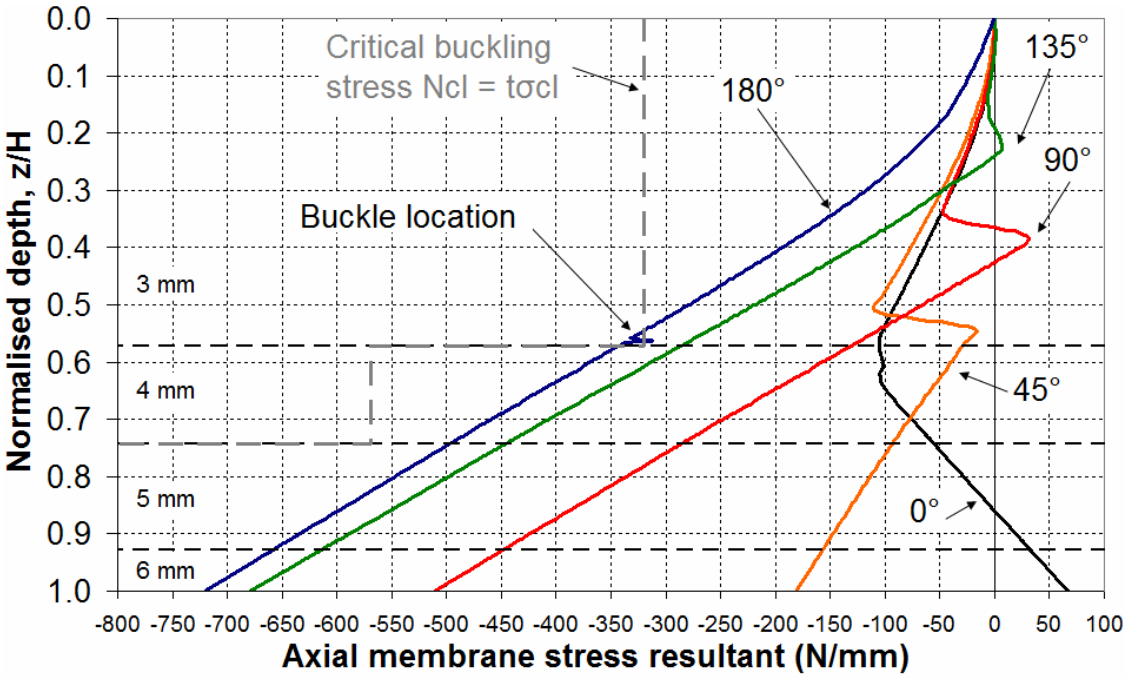

Fig. 8.23 – Axial distribution of the GMNA axial membrane stress resultants at bifurcation at five circumferential locations for the stepped wall Silo B under the EccM flow pattern

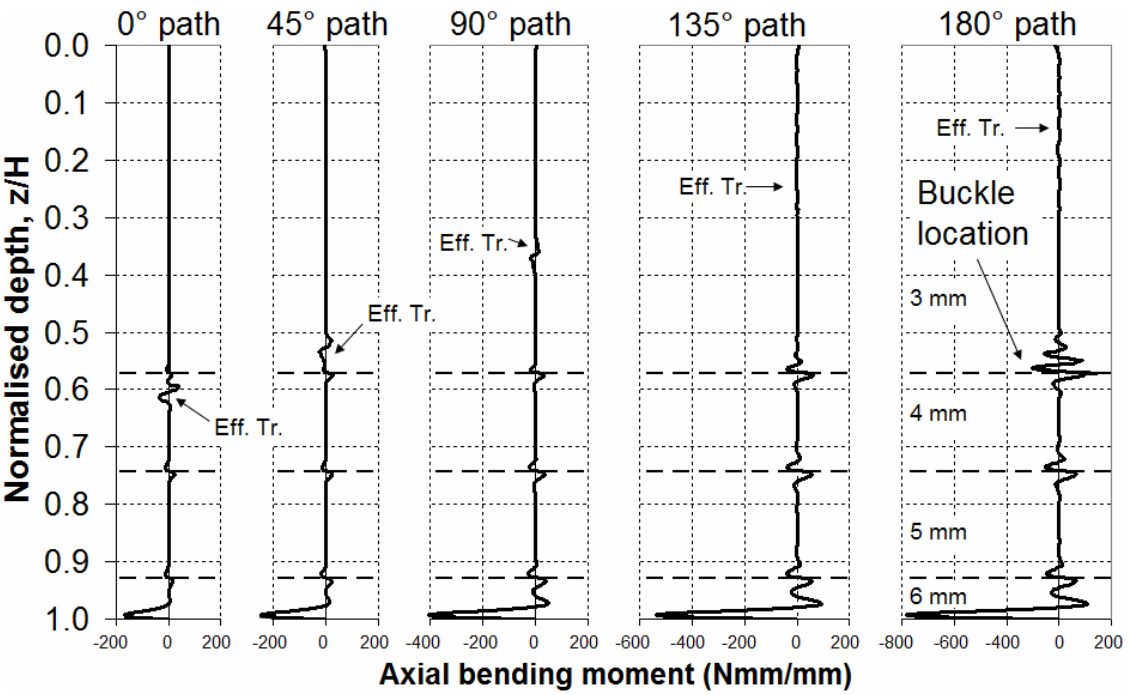

Fig. 8.24 – Axial distribution of the GMNA axial bending moments at bifurcation at five circumferential locations for the stepped wall Silo B under the EccM flow pattern (Note: Eff. Tr. = effective transition)

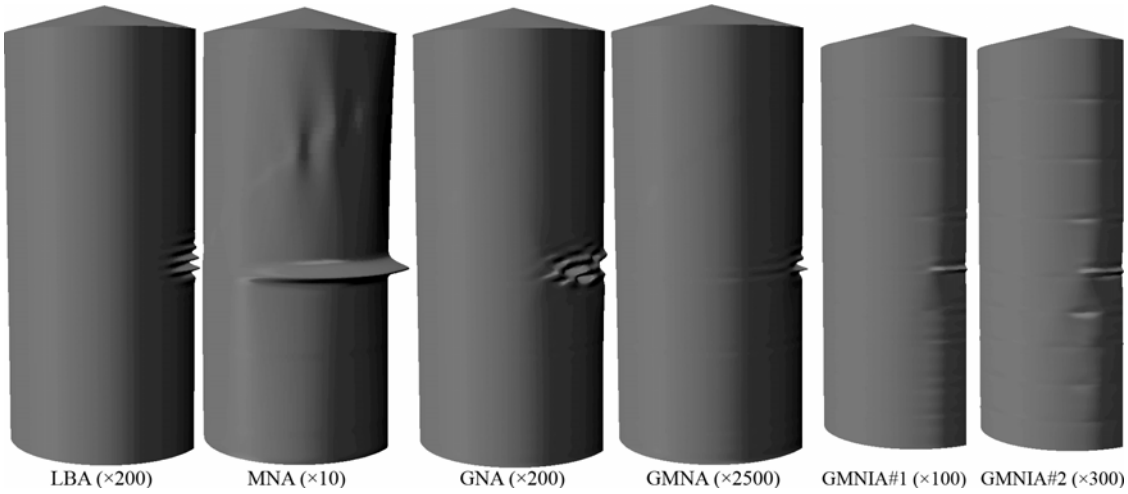

Fig. 8.25 – Stepped wall Silo B predicted failure modes under the EccM flow pattern

The predicted load proportionality factors for this suite of analyses are presented in Table 8.9. Comparing these to the load factors for the uniform wall silo in Table 8.5, it is clear that a stepped wall makes the silo more susceptible to early buckling failure under the EccM pattern, evidently due to the thinner wall at the new critical buckling location. The average of the geometrically nonlinear load factors is lower by 51% and 38% for EccM than for ConP and ConM respectively, but higher by a substantial 200% than for the EccP pattern. The lowest predicted load factor of 2.76 for GMNIA#2 is not as low as those obtained for EccP (Table 8.8), but this is nonetheless a very low result

for a silo that had been significantly overdesigned for the reference ConP pattern. Thus, for a more realistic stepped wall silo, eccentric mixed flow is predicted to be only a slightly less serious design condition than eccentric pipe flow.

The incorporation of axisymmetric weld imperfections results in a progressive reduction in the load factor from GMNA to GMNIA. This was expected as the buckling location in all analyses on the perfect shell is at the base of the 3 mm strake, and therefore also at the location of a weld. It is considered very unlikely that the axisymmetric weld will become beneficial at high amplitudes under the EccM pattern in a manner similar to its behaviour under the EccP pattern. The reason for this is most likely due to the fundamental difference in the structural response of the silo to the EccM and EccP patterns, as under EccM there is very little circumferential bending of the shell and thus little possibility that the weld depression may increase the bending stiffness of the structure. This aspect of the behaviour is explored shortly.

Table 8.9 – Load proportionality factors and failure mode acronyms for the stepped wall thickness silo under the EccM flow pattern

	LBA	MNA	GNA	GMNA	GMNIA#1	GMNIA#2
ECCM	4.54	6.30	4.75	4.31	3.21	2.76
Failure mode†	Glb-EF	Glb-EF	Glb-EF	Glb-EF	Glb-EF	Glb-EF
% change from ConP to EccM	– 58.2	– 34.4	– 56.1	– 43.7	– 51.7	– 51.9
% change from ConM to EccM	– 46.7	– 12.7	– 44.0	– 33.3	– 37.1	– 37.6
% change from EccP to EccM	+ 325.3	+ 88.1	+ 200.6	+ 172.8	+ 269.0	+ 162.9

† the failure modes for EccM are all at the base of the 3 mm strake opposite the outlet at $\theta = 180°$

8.5.4 Global comparison of the results for the stepped wall silo

A summary of the computational results for the stepped wall Silo B is presented on a bar chart in Fig. 8.26. The severity of each of the flow patterns follows a more obvious trend than for the uniform wall silo (Fig. 8.15) and a distinct hierarchy of ConP > ConM > EccM > EccP has clearly emerged.

The predicted failure modes for the stepped wall silo are summarised symbolically in Fig. 8.27. Under concentric pipe flow, the silo does not appear to exhibit a clear preference for a critical region depending on the analysis type. For concentric mixed flow, however, the bottom of the strake or weld depression closest to the effective transition is most likely to be the critical location for both buckling and plastic collapse, for reasons given previously. Although it was not found to be straightforward to predict the critical location for buckling of a uniform wall silo under eccentric flows (Fig. 8.16), for a stepped wall silo under eccentric pipe flow the critical location is likely to be at midheight at the centre of the channel, as discovered previously for the EN 1991-4 eccentric discharge pattern applied to stepped wall silos. For eccentric mixed flow, the critical location for buckling is likely to be the base of one of the thinner strakes opposite the outlet. The plastic collapse mechanism does not appear to play any role in the silo behaviour under either of the eccentric flow patterns.

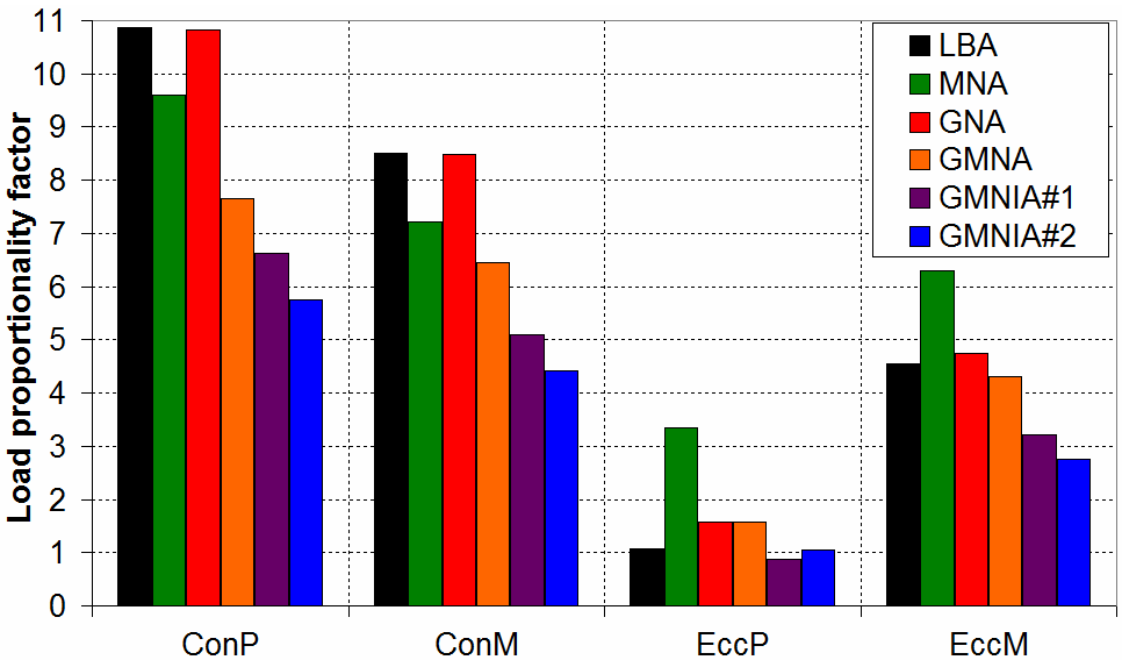

Fig. 8.26 – Bar chart comparison of the load factors for the four flow patterns for the stepped wall Silo B

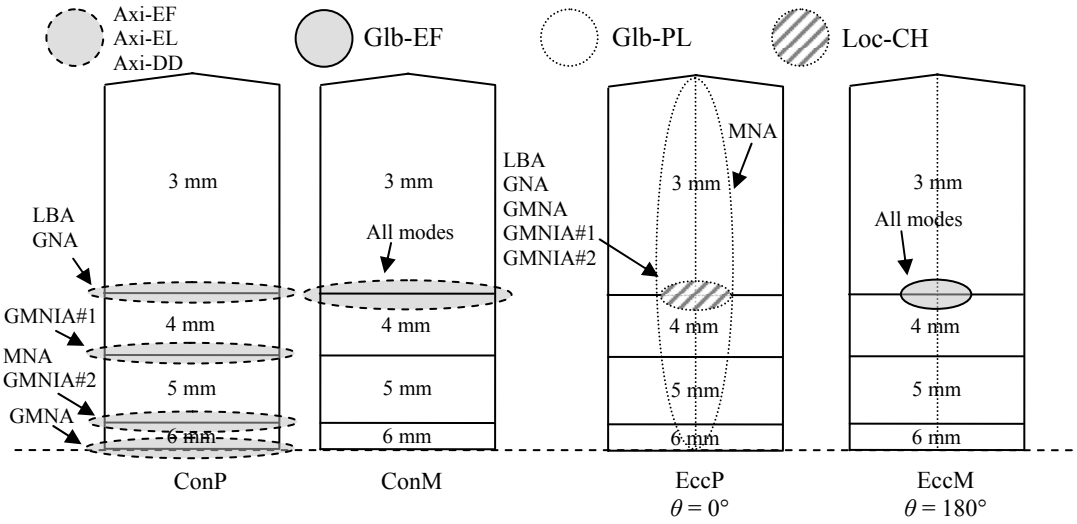

Fig. 8.27 – Summary of failure mode locations for the four flow patterns (stepped wall Silo B drawn to scale)

8.6 Comparison of changes of geometry for the stepped wall silo B under the EccP and EccM flow patterns

It was noted previously in this chapter that the structural behaviour of the silo is significantly different depending on whether the silo is subjected to eccentric mixed or pipe flow. For example, it was found that geometric nonlinearity results in significantly smaller buckling strength gains for the EccM flow pattern. Furthermore, although axisymmetric weld depressions were found to become beneficial under the EccP pattern at higher imperfection amplitudes, this was no longer the case under EccM where the weld depression was found to be consistently deleterious. To illustrate the differences in the behaviour, two main aspects of the structural response are presented in this section: circumferential bending and radial deformation, both closely related to each other.

The circumferential distribution of the circumferential bending moment for the stepped wall Silo B at midheight, close to the critical buckling location for both eccentric flow patterns, is shown in Fig. 8.28. The data shown is from the GNA analyses of both EccM and EccP flow patterns at the instant before buckling, and for the EccM pattern at a load factor close to the GNA buckling load factor of the EccP pattern. The convention assumes that a positive bending moment produces tension on the inner surface of the shell.

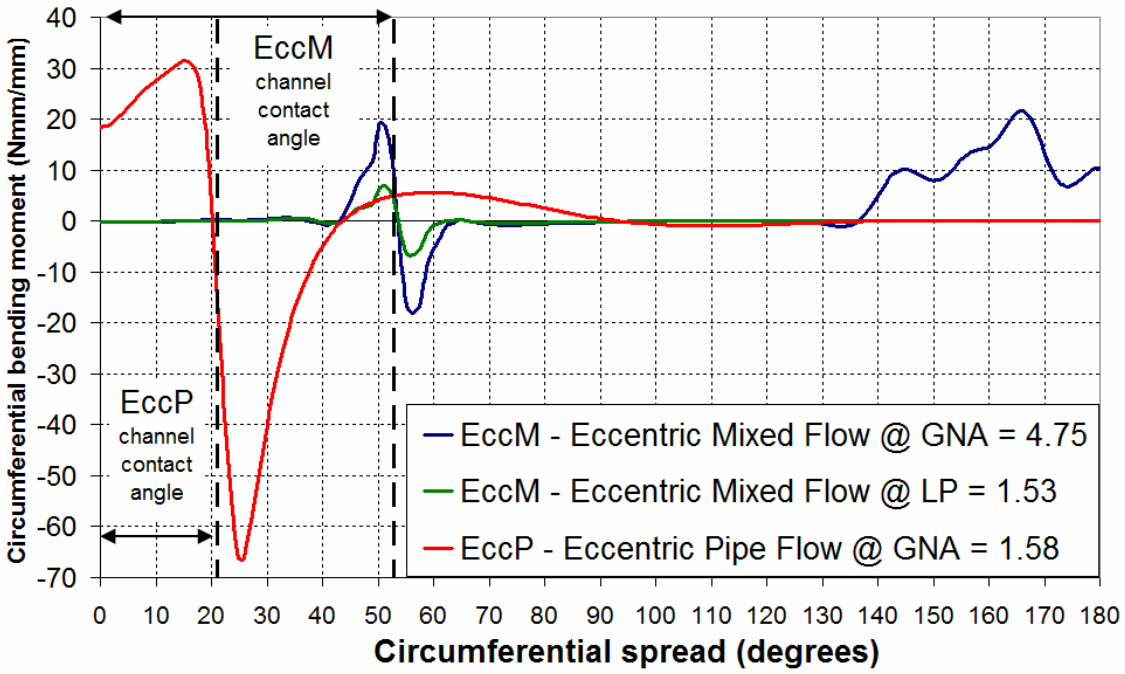

Fig. 8.28 – Circumferential distributions of the circumferential bending moment for both eccentric mixed flow patterns at midheight (GNA data)

Circumferential bending of the silo wall adjacent to the flow channel is a central component of the structural response of the silo under eccentric pipe flow (EccP). There is a large and sudden jump from positive to negative bending moment at the location of the channel wall contact angle θ_c (Fig. 7.5) which defines the circumferential position of the effective transition at which there is a steep rise in normal wall pressure. This sudden change in the sign of the bending moment corresponds to the change from inward to outward radial deformation of the silo wall adjacent to the flow channel (Fig. 8.29). Beyond $\theta > 90°$, the silo wall is under membrane action with virtually no bending and is no longer as affected by the flow channel.

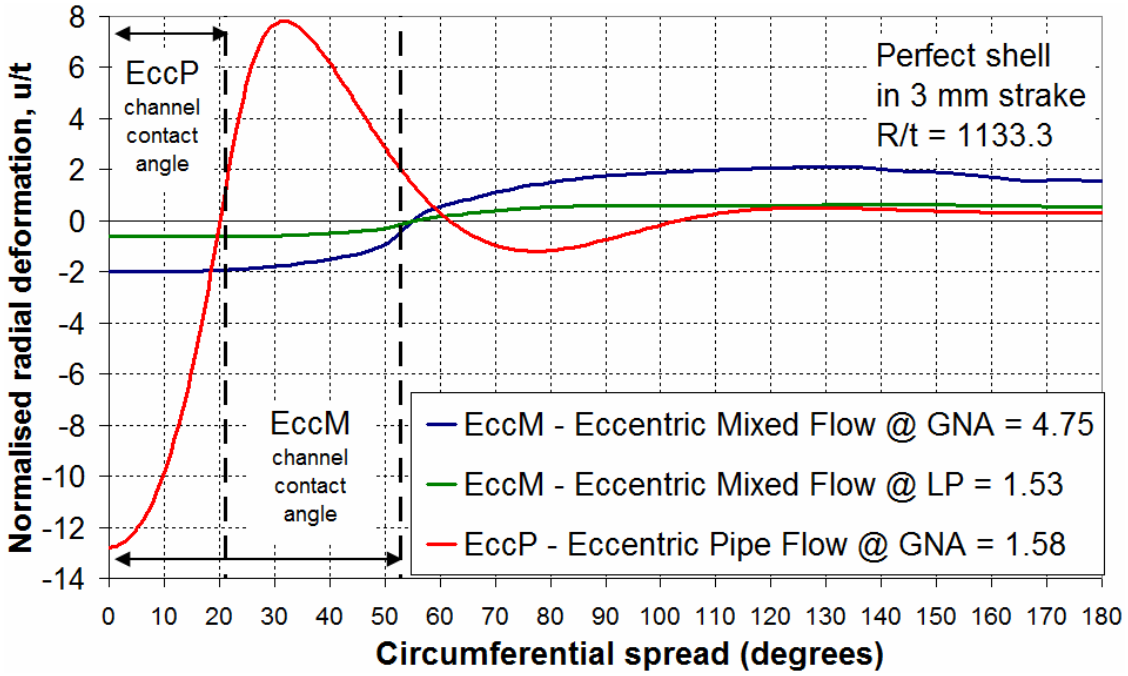

Fig. 8.29 – Circumferential distribution of the normalised radial deformation of the shell for both eccentric mixed flow patterns at midheight (GNA data)

Under eccentric mixed flow (EccM), the silo wall instead undergoes bending at the circumferential location of the effective transition and also opposite the outlet near θ = 180°, the critical buckling region for this flow pattern. However, the there is *very* little circumferential bending under EccM compared with EccP at approximately the same load factor (Fig. 8.28), as the peak bending moment for EccM is less than a tenth of what it is for EccP. Furthermore, the inward radial deformation at θ = 0° under the EccP pattern reaches almost 13t at buckling, whereas for EccM at the same load factor this appears to be no more than 0.8t at approximately the same load factor (Fig. 8.29).

The above two figures show that the silo undergoes significantly smaller changes of geometry under eccentric mixed flow than under eccentric pipe flow. This in turn directly affects the extent of circumferential bending caused by both flow patterns and therefore also the extent of the beneficial effect of geometric nonlinearity. Furthermore, as there is considerably less circumferential bending under EccM, any beneficial stiffening effect that may be provided by the axisymmetric weld depression (as was the case previously, e.g. Fig. 4.28) to increase the circumferential bending stiffness of the shell becomes negligible.

8.7 Conclusions

This chapter has presented the first known introductory finite element analysis of the effects of explicitely-defined concentric and eccentric pipe and mixed flow patterns on a thin-wall metal silo. The aspect ratio of the silo is on the boundary between the slender and intermediate slender EN 1991-4 aspect ratio ranges.

Two alternative designs were analysed, one with a uniform wall thickness and one with a stepped wall thickness. The silo was originally designed according to EN 1991-4, EN 1993-1-6 and EN 1993-4-1 for factored discharge loads arising from axisymmetric mass flow where the Janssen pressures were multiplied by a discharge factor of 1.15 for normal pressures and 1.1 for frictional tractions, C_h and C_w, respectively. The silo was therefore significantly overdesigned for the pressures arising from the reference *unfactored* concentric pipe flow pattern used in the present study.

For both silo designs under both concentric pipe and mixed flow patterns, there is a progressive decrease in computed load factor as the analysis becomes more sophisticated (LBA → GNA → GMNA → GMNIA, with the exception of MNA). The stepped wall silo design is weaker than the uniform design regardless of flow pattern, since the wall thicknesses are much lower throughout most of the silo height, and a thinner wall has a significantly lower resistance against both buckling and plastic collapse. This is in line with observations made previously in this thesis.

A concentric pipe flow channel has a negligible effect on the adjacent stationary solid, which basically exerts Janssen filling pressures on the silo wall. However, the effective transition present in the concentric mixed flow pattern results in a large and sudden rise in wall pressures, in this case to almost double the local Janssen value. This rise does not appear to be excessively damaging to either silo design, and results in an average decrease in the geometrically nonlinear load factor (GNA, GMNA or GMNIAs) of only 9% and 21% for the uniform and stepped wall silo designs respectively.

Both the buckling and plastic collapse modes under concentric flow relate to the elephant's foot mode at the base of the uniform wall silo, or, for the stepped wall design, usually at the base of the thinnest strake. The silo as a shell structure is therefore very efficient at resisting axisymmetric load patterns.

The results for the analyses of the eccentric pipe flow pattern closely reflect what has been previously reported in this thesis about the EN 1991-4 eccentric discharge pressure model. For the uniform wall design, a localised plastic buckle usually forms at the base of the silo, approximately 45° away from the axial plane through the outlet. This location corresponds loosely to the 'edge' of the flow channel in the EN 1991-4 model. The results of the stepped wall design, however, consistently reproduce the elastic midheight buckle across the flow channel. It has been reported previously that this type of buckle has been widely observed in practice.

The finite element analyses of eccentric mixed flow predict a global overturning moment on the silo which precipitates local elastic-plastic buckling failure on the side of the silo opposite the outlet. For the uniform wall design, this buckle is likely to form at the base, while for the stepped wall design, this buckle is likely to form instead at the base of the thinnest wall strake where buckling resistance is lowest.

The same overall trend has been identified for both silo designs which states that, in terms of increasing structural severity of each flow pattern, ConP < ConM < EccM < EccP.

Geometric nonlinearity has been found to have a much smaller beneficial effect on the predicted buckling strength under eccentric mixed flow than under eccentric pipe flow. The most likely reason for this is that the silo undergoes significantly circumferential bending and thus smaller changes of geometry under eccentric mixed flow than under eccentric pipe flow.

Chapter 9 – The structural consequences of flow channels with different steepness under mixed flow pressures

9.1 Introduction

The first half of this thesis introduced and explored the pressure distribution for eccentric discharge presented in the relatively recent European Standard EN 1991-4 (2007) through a series of parametric finite element studies. A new and more complete mixed flow discharge pressure theory was subsequently presented in Chapter 7 of this thesis, and a suite of introductory finite element studies was performed in Chapter 8. This produced the first set of preliminary predictions from the new theory, and showed that a realistic set of structural consequences might arise under a variety of different flow patterns.

This chapter presents the results and analysis of a parametric study into the structural effects of a range of flow channel profiles with varying degrees of steepness at a constant outlet eccentricity. As the steepness of the channel profile changes progressively, so does the nature of the discharge pressure pattern and so too does the associated structural behaviour of the silo. The results of the present study are compared with the results of the previous investigations that were presented in Chapters 4 and 5 where the flow channel size was varied according to the EN 1991-4 pressure model.

9.2 Predicted pressure distributions

9.2.1 Overview

The stepwise variable wall thickness Silo B (H = 14 m, R = 3.4 m, H/D = 2.06, Table 4.2) was employed in this parametric study. It was noted in Chapter 8 that the aspect ratio of Silo B, on the boundary between slender and intermediate slender categories of EN 1991-4, was considered to be the most suitable of the design silos presented in Chapter 4 for the analysis of a varied range of flow patterns. More slender silos are more likely to develop flow patterns that lead to effective transitions relatively low down the silo wall and which span the full circumference, a relatively limited range (Fig. 4.1).

A gradual change in the steepness of the eccentric flow channel profile was achieved by maintaining the eccentricity of the centre of the flow channel e_c at a constant value of 80% of the silo radius (2.72 m) while decreasing the power of the profile n gradually from 5.0 to 1.05 in intervals of 0.5. A value of $n = 5.0$ generates a flow channel that is only just fully internal, while $n = 1.05$ generates an eccentric mixed flow pattern with near-straight channel sides. Values of n between these limits generate eccentric taper pipe flow patterns of varying cross-section. The outlet size was maintained at a constant value of $r_0/R = 0.074$ (25 cm). Note that the vertical pressure in both the flow channel and stationary solid is independent of the eccentricity for the fully-internal pipe flow channel ($n = 5.0$) which, as discussed in Chapter 7, is a limitation of the mixed flow pressure theory because it considers only vertical, but not radial or circumferential, equilibrium.

The values of the flow channel steepness n and the cross-sectional areas at the solid surface ($z/H = 0$) are summarised in Table 9.1 as a percentage of the silo cross-sectional area. These serve as an initial comparison of the relative sizes of the different flow channels and show that the narrowest channels ($n \geq 3.5$) actually change very little with steepness. This is demonstrated more clearly by the axial distributions of the cross-sectional flow channel areas, shown in Fig. 9.1. The flow channel profiles are shown in Fig. 9.2 as a function of n and demonstrate the rather abrupt change from eccentric mixed to pipe flow and the gradual convergence of the channel sides to the vertical as $n \rightarrow \infty$.

Table 9.1 – Summary of chosen flow patterns ($e_c/R = 0.80$ and $r_0/R = 0.074$)

Channel power n	5.0†	4.5*	4.0*	3.5*	3.0*	2.5*	2.0*	1.5*	1.05‡
Max. silo cross-sectional area (%)	4.0	4.7	5.7	7.0	9.2	13.1	21.7	46.4	100.0

† equivalent to concentric pipe flow (ConP)

* eccentric pipe flow (EccP)

‡ eccentric mixed flow (EccM)

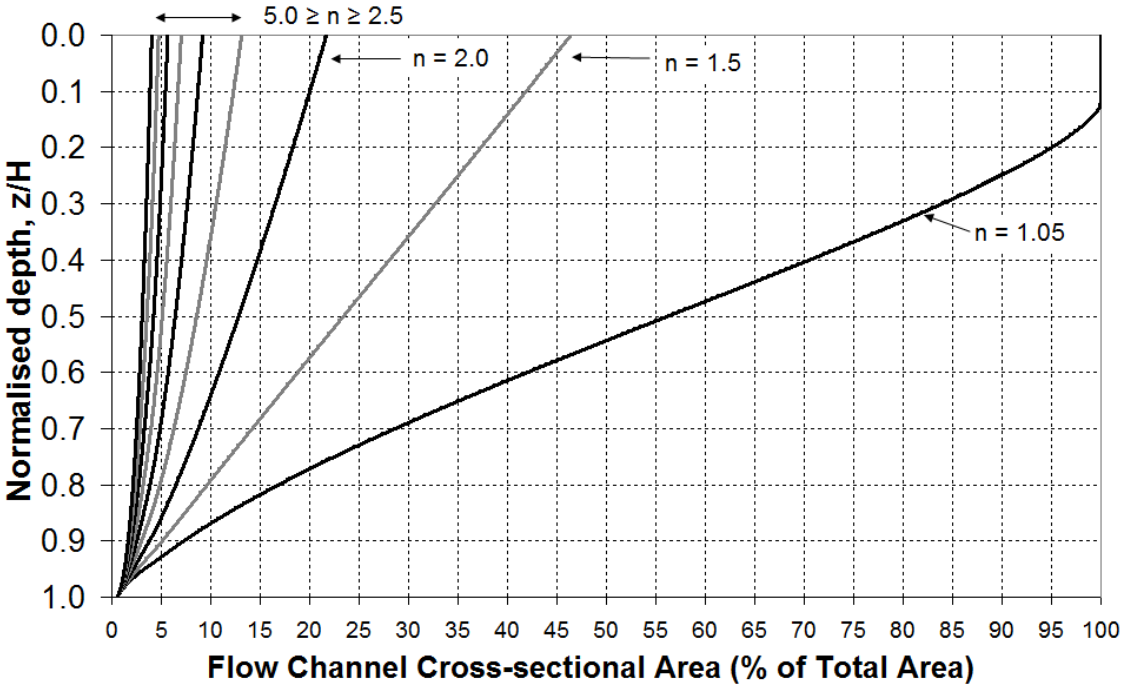

Fig. 9.1 – Flow channel cross-sectional areas as a function of the steepness *n*

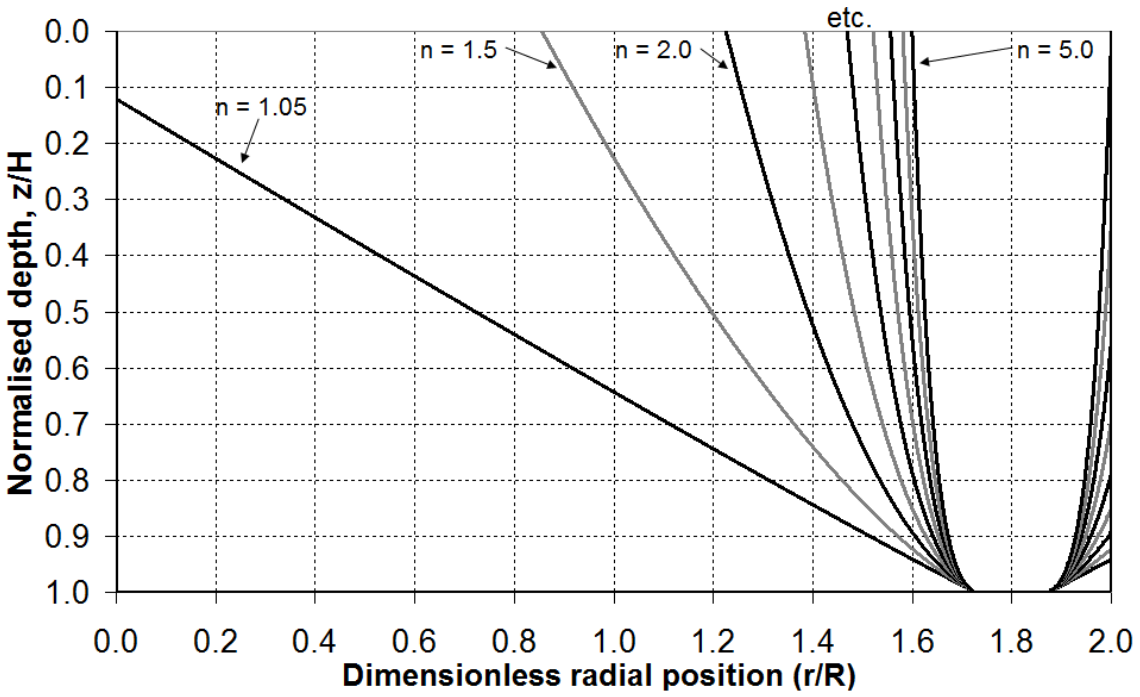

Fig. 9.2 – Flow channel geometry profiles as a function of the steepness *n*

9.2.2 The eccentric pipe flow channels, $5.0 \geq n \geq 1.5$

The distributions of vertical pressure in the flow channel and stationary solid are shown in Fig. 9.3 and Fig. 9.4 as a function of the steepness *n*. The pipe flow channels in the range $5.0 \geq n \geq 2.0$ exhibit a gradual and substantial increase in vertical pressure with decreased steepness and increased cross-sectional area, starting with a maximum value

of approximately 9.2 kPa for n = 5.0 (max. area cover 4.0%) and increasing to approximately 19.4 for n = 2.0 (max. area cover 21.7%). Yet the influence of a wider eccentric pipe flow channel, even one which covers over five times as large a cross-sectional area as another, appears to have a virtually negligible effect on the vertical pressure in the stationary solid which barely deviates from the local reference Janssen value (Fig. 9.4). The widest eccentric taper pipe flow channel of n = 1.5 has the largest influence on the adjacent stationary solid pressure, but even here the overpressure is still only of the order of 10%. Thus, considerable increases in the stationary solid pressure can only be achieved when the effective transition spans the entire circumference, as is the case for n = 1.05.

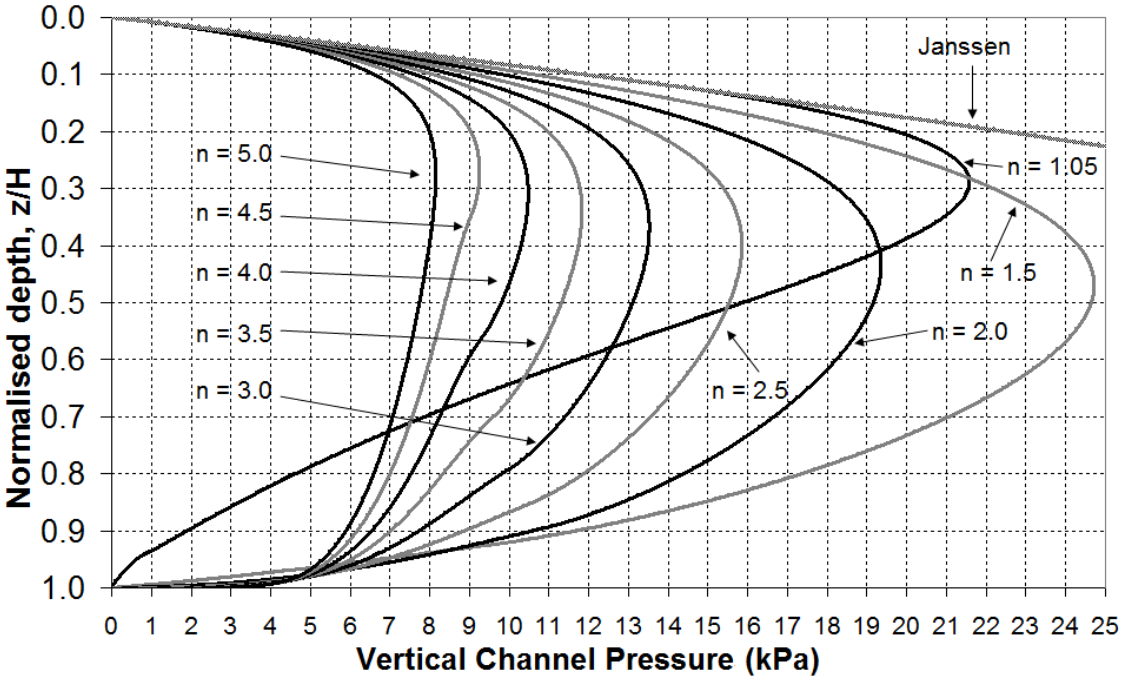

Fig. 9.3 – Vertical pressure in the flow channel as a function of the steepness n

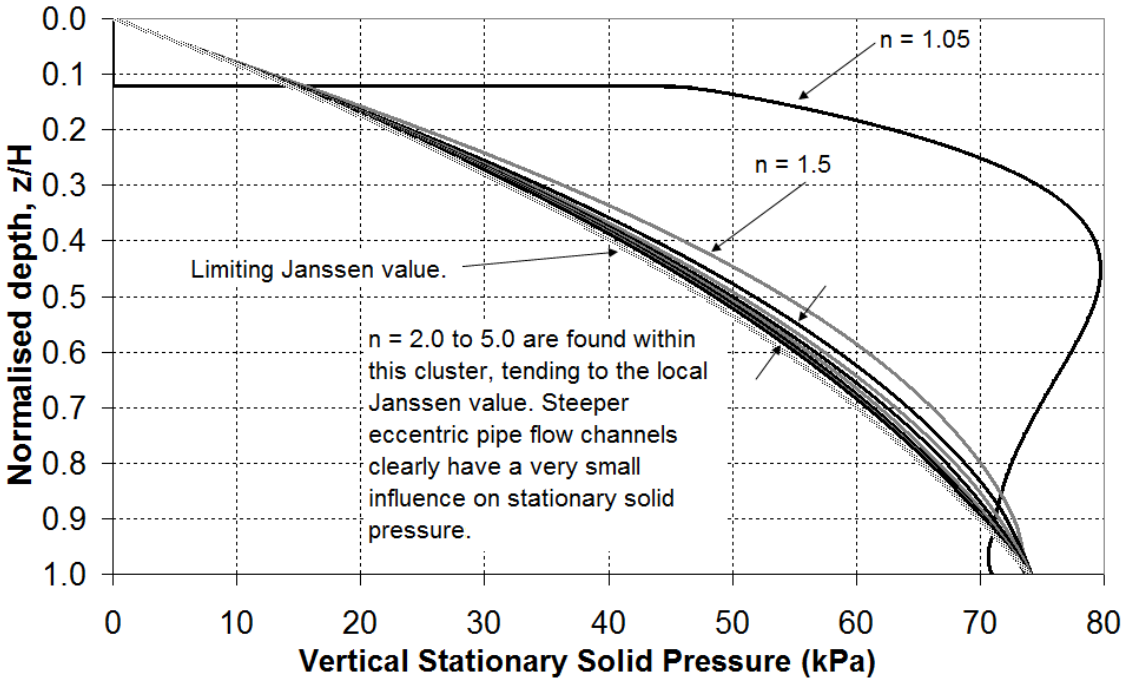

Fig. 9.4 – Vertical pressure in the stationary solid as a function of the steepness n

A series of three-dimensional surface plots illustrating the patterns of wall pressures applied to the silo wall are shown in Fig. 9.5. These focus on a 60º spread of the silo wall starting at the circumferential coordinate of the outlet, θ = 0º. The gradual widening and descent of the channel-wall contact and of the effective transition can be seen clearly. The variation of the lowest position of the effective transition z_{12}/H with n is summarised in Table 9.2. These values are important in relation to the location of the peak of the compressive axial membrane stress which, it will be shown in this chapter, develops in the silo wall adjacent to the centre of the flow channel and is responsible for the predicted buckling modes.

Table 9.2 – Variation of the lowest point of the effective transition with steepness n

Power n	5.0	4.5	4.0	3.5	3.0	2.5	2.0	1.5	1.05
Depth (z_{12}/H)	n/a	0.339	0.553	0.694	0.788	0.851	0.893	0.923	0.941
Within strake† (mm)	n/a	3	3	4	5	5	5	5	6

† only the stepped wall Silo B was analysed in this study

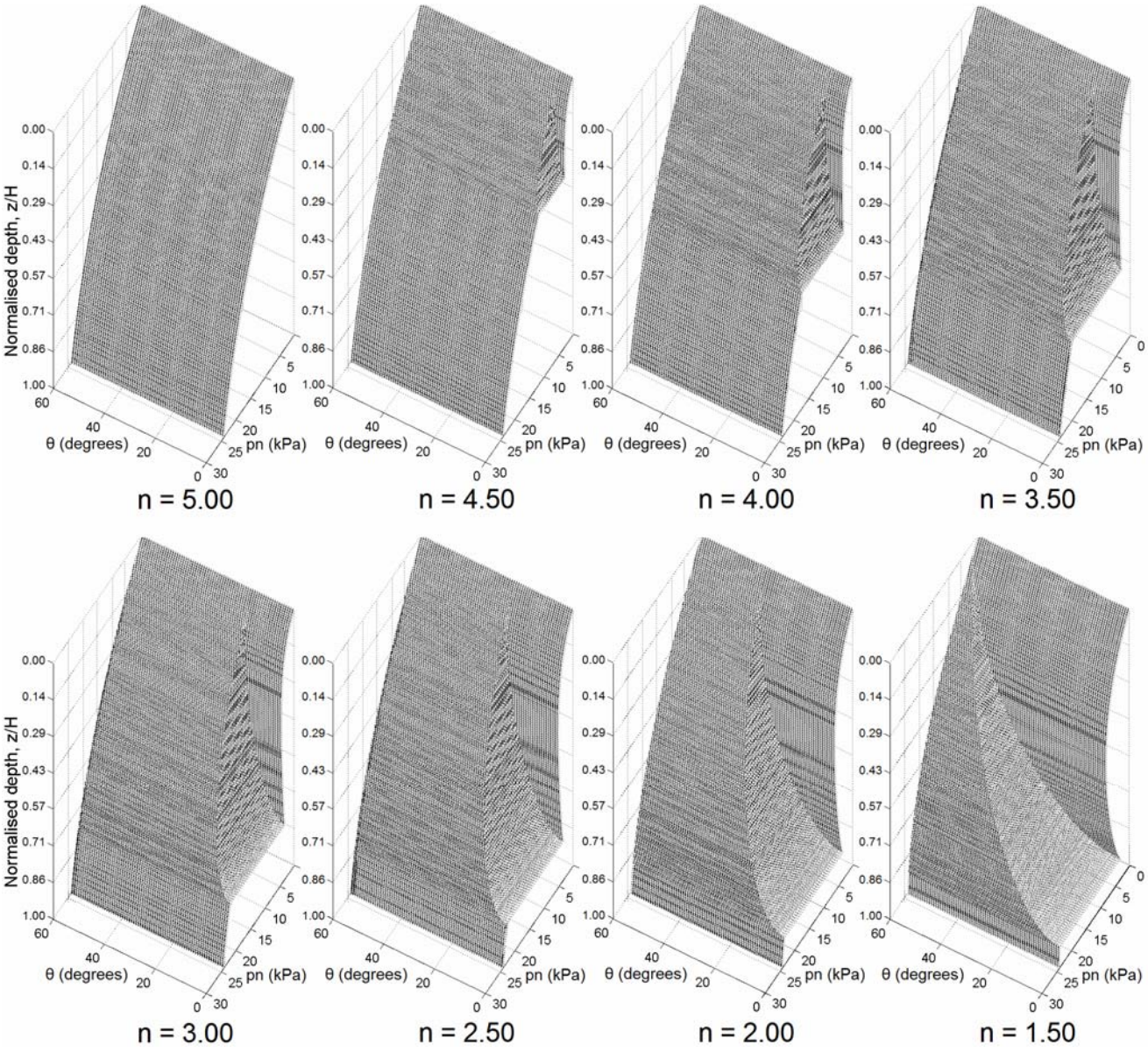

Fig. 9.5 – Three-dimensional surface plots of the normal wall pressure distributions for eccentric pipe flow patterns of varying steepness, $5.0 \geq n \geq 1.5$

9.2.3 The eccentric mixed flow channel, $n = 1.05$

The case of $n = 1.05$ deserves special attention, because the relatively minor change in the power of the channel profile from $n = 1.5$ to 1.05 alters the flow pattern fundamentally. The decreased steepness expands the flow channel to cover the entirety of the cross-section throughout the upper part of the silo and introduces a circumferentially-varying effective transition around the full perimeter, thus changing the flow pattern from eccentric taper pipe to eccentric mixed flow (from EccP to EccM, using the acronyms from Chapter 7).

The global distributions of vertical pressure within the solid and the normal wall pressure around the circumference for n = 1.05 are presented in Fig. 9.6 and Fig. 9.7 respectively. These distributions were additionally present in Fig. 9.3 and Fig. 9.4 where they allowed a direct comparison with the corresponding curves for higher values of n.

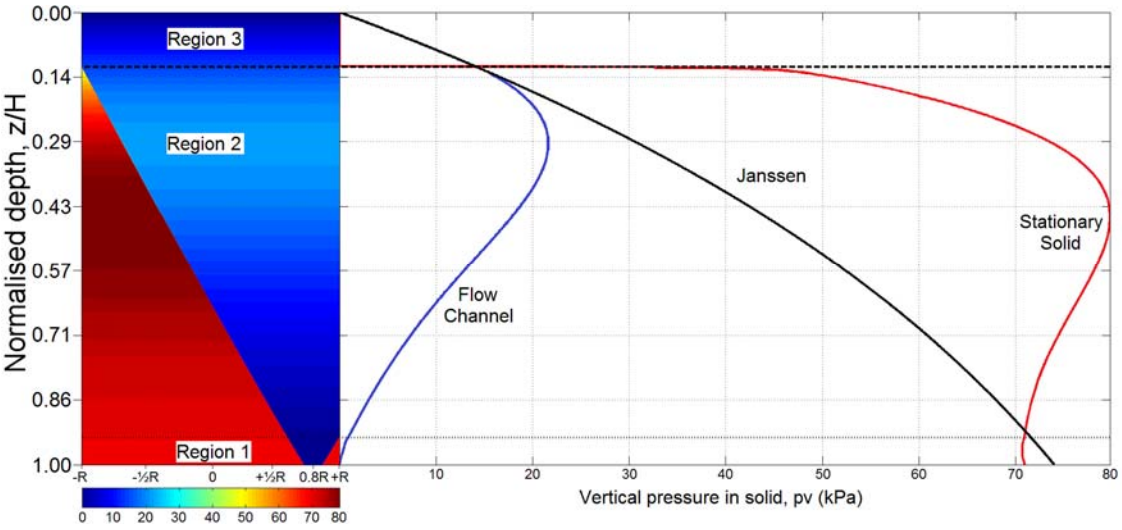

Fig. 9.6 – Two-dimensional contour and line plots of the vertical pressure distributions for the eccentric mixed flow pattern, n = 1.05

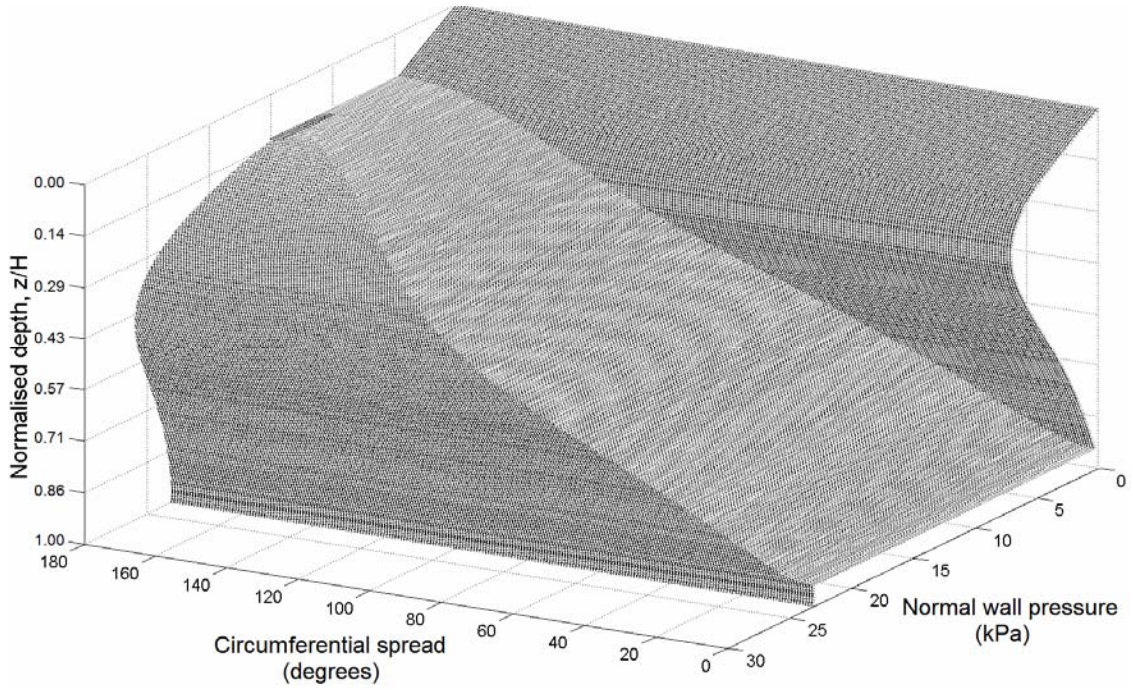

Fig. 9.7 – Three-dimensional surface plot of the normal wall pressure distribution for the eccentric mixed flow pattern, n = 1.05

The pressure in the stationary solid under eccentric mixed flow (EccM) is much higher than under eccentric pipe flow (EccP), where it remains very close to the Janssen value. This is a direct result of the boundary condition at the effective transition (BC2, Chapter 7), which produces a starting value for the stationary solid pressure based on local static equilibrium that is significantly higher than the local flow channel (Janssen) value. The integration of the equations governing the stationary solid pressure then continues from that boundary condition. For pipe flow, there is no effective transition and the starting value for the stationary solid pressure is zero due to the surface boundary condition (BC1). With no sharp rises in pressure elsewhere in the silo, the stationary solid pressure cannot possibly deviate considerably from the reference Janssen value.

It was explained in Chapter 7 that one of the properties of the mixed flow pressure theory was that the steepness of the channel introduces a singularity into the pressure distribution as n approaches unity. As a result, a steepness condition (BC4) was introduced which requires n to be at all times greater than unity. Yet, although a perfectly conical channel profile cannot be used, one may approach this limit very closely without experiencing the singularity effect, as can be seen for $n = 1.05$. The current theory is thus stable across the entire practical range of flow channel profiles $n > 1$. It was also noted in Chapter 7 that profiles with $n < 1$ do not appear to have been reliably measured and are thus not considered further here.

In the previous chapter, it was shown that the structural behaviour of a silo is very different depending on whether the granular solid flows in an eccentric mixed or pipe flow pattern. Perhaps counter-intuitively, it is the EccP flow pattern with low flow channel pressure, a narrow wall contact and barely any change in the stationary solid pressure that is often the most deleterious flow pattern that can develop inside a silo (Rotter, 1986; 2001a). This condition has the potential to result in elastic buckling of the silo (Fig. 9.8), which may develop into catastrophic global overturning in the direction of the outlet (Fig. 1.1). Eccentric mixed flow is also very damaging, though less so than pipe flow, and it was predicted to lead instead to global overturning in the direction opposite the outlet with localised plastic buckling in the silo wall at the base of the silo or the thinnest wall strake. It is expected that a similar behaviour will be reproduced in this study for both types of flow pattern.

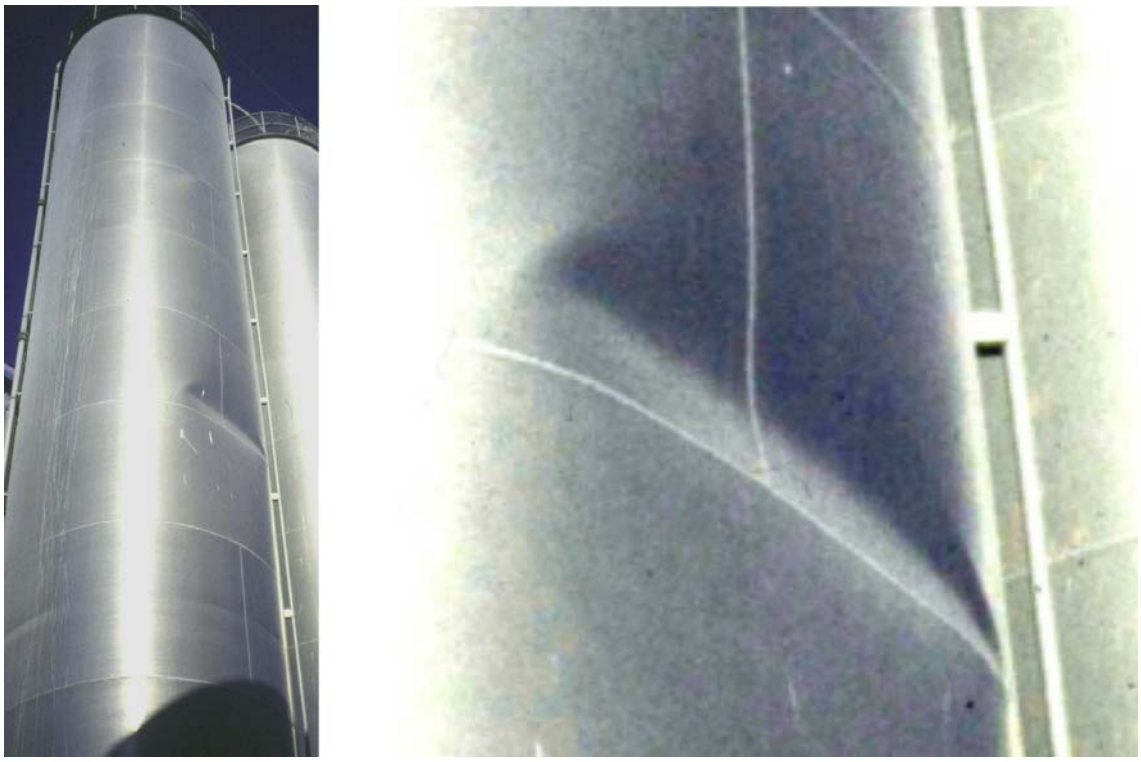

Fig. 9.8 – Local elastic buckling of a slender steel silo under fully eccentric discharge (courtesy of J.M. Rotter)

9.3 Introduction into the structural behaviour of the silo

9.3.1 Review of computational analyses undertaken in this study

The full suite of finite element analyses defined in EN 1993-1-6 (2007) was performed on the stepped wall Silo B with the ABAQUS (2009) software: LBA, MNA, GNA, GMNA and two GMNIA analyses. The imperfections used were the Type A axisymmetric weld depressions of Rotter and Teng (1989a) at 50% and 100% of the EN 1993-1-6 (2007) Section 8.7 GMNIA imperfection amplitude requirement. Material properties for mild steel were used as before (E = 200 GPa, ν = 0.3 and σ_y = 250 MPa). A similar suite of computational analyses was performed in Chapter 8.

No discharge factors C_h and C_w were applied to the wall pressures used in this study. It was explained in detail in Chapter 8 that this makes Silo B significantly overdesigned for unfactored concentric flow patterns and thus likely to result in higher than normal load factors. The short-hand acronyms describing the main features of the predicted failure modes obtained in this chapter are summarised in Table 9.3.

Table 9.3 – Description of short-hand acronyms to describe failure modes

Acronym	Description
Axi-EF	Axisymmetric plastic elephant's foot buckling or yielding.
Axi-DD	Diamond pattern of deformation around the entire circumference, limited to being within a close distance of a wall strake or other boundary.
Axi-EL	Fully or partially axisymmetric elastic buckle.
Glb-EF	Global deformations, but with the main component of plastic elephant's foot-type buckling or yielding.
Glb-DD	Global diamond buckling mode
Glb-PL	Global plastic circumferential bending mode (the MNA mode).
Loc-CH	The characteristic or 'classic' mode associated with an eccentrically flowing channel: a local (predominantly) elastic buckle in the centre of the flow channel, at approximately midheight.

9.3.2 Summary of the computed load proportionality factors

The variation of the computed LBA, MNA and G(M)NA load factors with channel steepness n is shown in Fig. 9.9. The load factors are additionally summarised in Table 9.4. The general pattern that emerges from this figure is very similar to that of Fig. 5.12, which showed the variation of the load factors with the flow channel size parameter ($k_c = r_c/R$) for the EN 1991-4 eccentric discharge pressure model.

The LBA load factor falls abruptly by 66% from $n = 5.0$ to 4.5 merely as a result of a flow channel with a very narrow and shallow contact with the wall (lowest point of the effective transition occurs at $z_{12}/H = 0.339$, Fig. 9.5). The LBA analyses predicted the characteristic elastic midheight buckling mode Loc-CH throughout the entire pipe flow range $4.5 \geq n \geq 1.5$ (Table 9.3). By contrast, the GNA and GMNA load factors are barely effected at $n = 4.5$, requiring a wider channel with $n = 4.0$ ($z_{12}/H = 0.553$) in order to fall significantly and produce the elastic midheight mode Loc-CH. At this point, the GNA and GMNA load factors also become equal to each another.

The axisymmetric weld depression was found to be beneficial to the buckling strength over most of the range of n values, shown by the fact that both GMNIA load factors are significantly higher than the perfect shell GMNA factors for steeper channels. Much shallower channels wich deeper effective transitions are required ($n \leq 3.5$, $z_{12}/H \geq$

0.694) to cause the imperfect GMNIA factors to fall considerably and for the buckling mode Loc-CH to be reproduced in a GMNIA analysis using axisymmetric weld depression imperfections. For the internal 'concentric' channel (n = 5), the lowest GMNIA load factor was found to be the very high value of 5.63, confirming that the current design of the stepped wall Silo B is overdesigned when analysed under axisymmetric pressures.

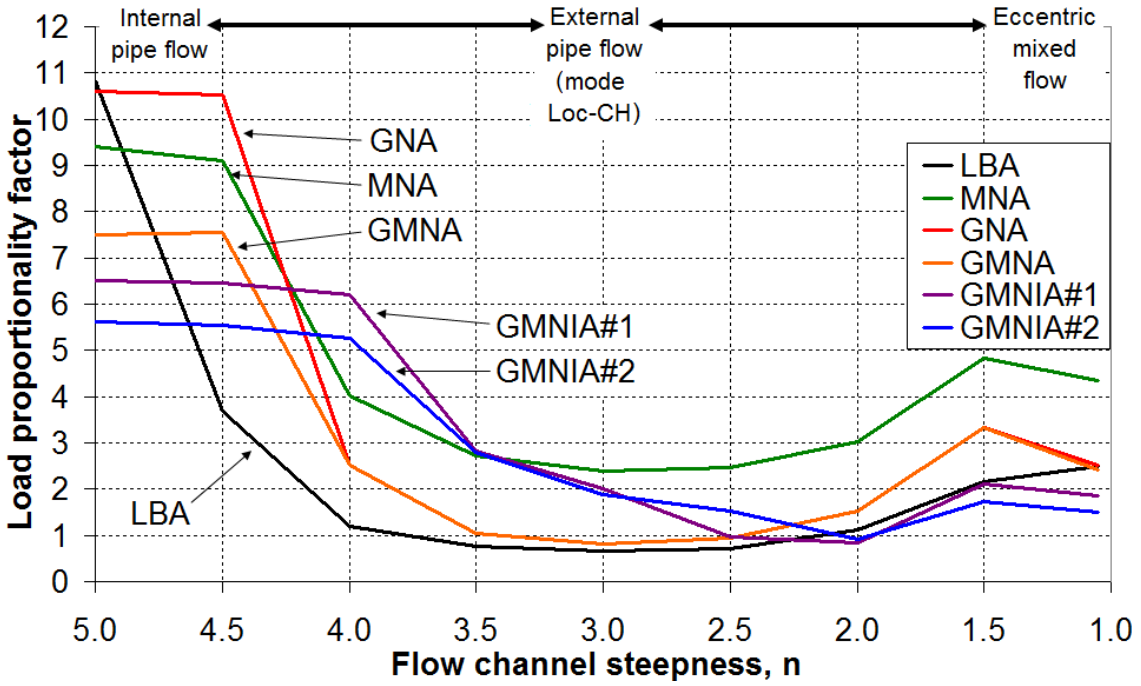

Fig. 9.9 – Predicted load proportionality factors of the steepness study

Table 9.4 – Summary of load proportionality factors for the steepness study

Power n	5.00	4.50	4.00	3.50	3.00	2.50	2.00	1.50	1.05
	Internal pipe flow (ConP)	External pipe flow (EccP)							External mixed flow (EccM)
LBA	10.82	**3.69†**	**1.19†**	**0.77†**	**0.65†**	**0.71†**	**1.12†**	**2.16†**	2.48
MNA	9.42	9.09	4.02	2.73	2.40	2.46	3.04	4.83	4.34
GNA	10.60	10.52	**2.53†**	**1.06†**	**0.80†**	**0.94†**	**1.52†**	**3.33†**	2.51
GMNA	7.50	7.54	**2.53†**	**1.06†**	**0.80†**	**0.94†**	**1.52†**	**3.33†**	2.42
GMNIA#1	6.50	6.47	6.21	**2.83†**	**2.01†**	**0.96†**	**0.83†**	**2.12†**	1.85
GMNIA#2	5.63	5.54	5.28	**2.79†**	**1.89†**	**1.53†**	**0.91†**	**1.73†**	1.51

† (**bold**) corresponds to the elastic midheight local buckling mode Loc-CH

The new mixed flow pressure theory successfully reproduces many the same nonlinear effects that were previously reported in the first half of this thesis for significantly more slender silo designs under a different eccentric discharge pressure model. There are many further similarities between the results of the current study and those presented in Chapters 4 and 5 in particular, where the effects of a varying the flow channel size in the EN 1991-4 eccentric discharge pressure model were examined. These will be explored shortly. The main reason for these similarities is that these studies effectively model the same thing despite any differences in the governing pressure theories: a shallower-sided eccentric pipe flow channel (lower n) also has a wider wall contact (higher $k_c = r_c/R$). However, the fact that the same patterns of behaviour and strength predictions may be extracted in both cases helps to support the validity of both theories.

Lastly, it is worth noting that the predictions for $n = 5.0$ are effectively the same as those for the concentric pipe flow channel (ConP) for the stepped wall Silo B in Chapter 8. The load factors in this study are however very marginally lower (compare with Table 8.7) due to the fact that the internal pipe flow channel in Chapter 8 was significantly steeper with a value of $n = 10.0$. Consequently, it was also slightly narrower and exerted a smaller influence on the stationary solid pressures, thus leading to slightly higher load factors.

9.4 Structural behaviour under eccentric pipe flow channels in the range $4.5 \geq n \geq 1.5$

9.4.1 Linear Elastic and Linear Bifurcation Analyses (LA & LBA)

The axial distributions of axial membrane stress resultants for the LA analyses at the LBA load factor are presented in Fig. 9.10 for the circumferential positions at $\theta = 0^o$ and 45^o. These correspond approximately to the distributions at the 'centre' and 'edge' of the eccentric pipe flow channel respectively. The pattern of stresses at $\theta = 0^o$ is closely reminiscent to that of Fig. 5.8 which showed the variation of the LA @ LBA axial membrane stress resultants with the EN 1991-4 flow channel size parameter, $k_c = r_c/R$.

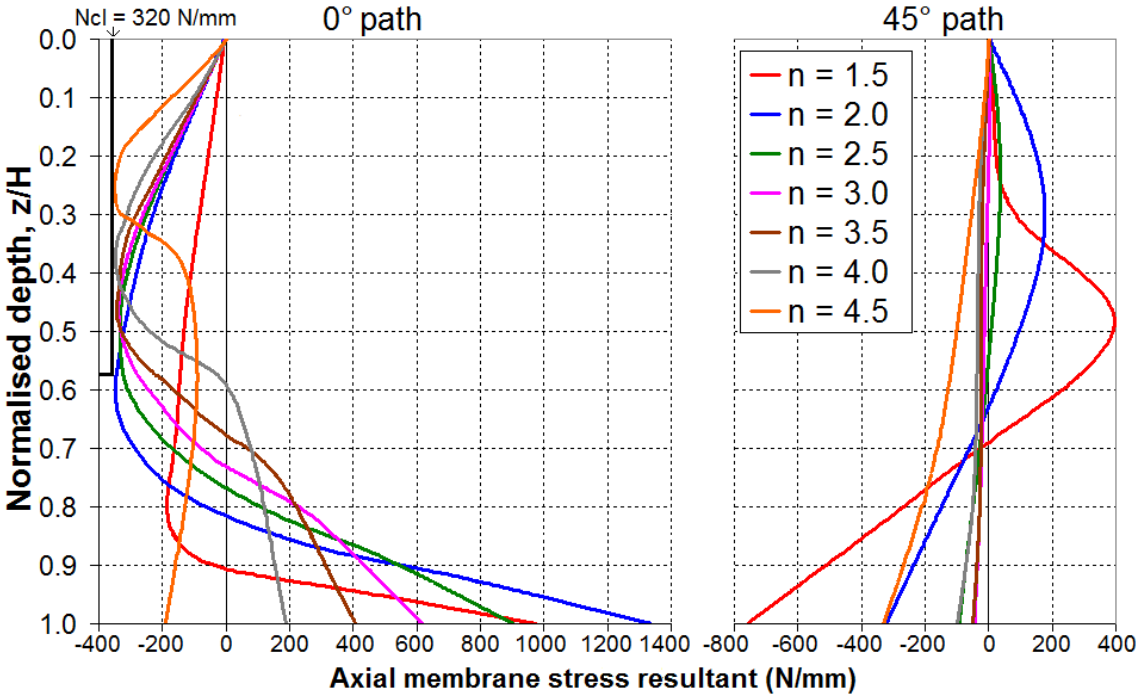

Fig. 9.10 – Axial distribution of the axial membrane stress resultants at θ = 0º and 45º from LA analyses at the LBA load factor

In both Fig. 5.8 and Fig. 9.10, the flow channel with the narrowest wall contact (k_c = 0.10 for the EN 1991-4 model or n = 4.5 here) already produces a pattern of LA stresses that is characteristic of eccentric pipe flow at the centre of the flow channel (e.g. Fig. 2.9). The n = 4.5 channel affects only a very small portion of the upper part of the silo wall (z_{12}/H = 0.339, Fig. 9.5), and although this is sufficient to cause a compressive peak at approximately z/H = 0.28 which in turn causes the elastic midheight buckle, it is insufficient to induce tensile stresses at the base of the silo. By contrast, the very small k_c = 0.10 channel of Fig. 5.8, which extended throughout the entire silo height, was sizeable enough to generate both compressive and tensile features of the characteristic stress distribution. Lastly, the peaks of the compressive axial membrane stresses in the upper part of the silo for all values of n were found to be limited by a value corresponding approximately to the classical buckling stress $N_{cl} = t\sigma_{cl} \approx 0.605Et^2R^{-1} \approx$ 320.3 N/mm of the 3 mm wall strake.

The distributions at θ = 45º are mostly typical of Janssen-like axial membrane stress patterns, since the narrower channels used in this study ($n \geq 2.5$) do not approach this circumferential coordinate and consequently the stresses here remain largely unaffected. Only the wider channels, n = 2.0 and 1.5, produced significant tensile membrane stresses near midheight at this location, characteristic of the 'channel edge' stress

distribution obtained when using the EN 1991-4 eccentric discharge pressure model (compare, for example, with Fig. 2.9 and Fig. 2.13).

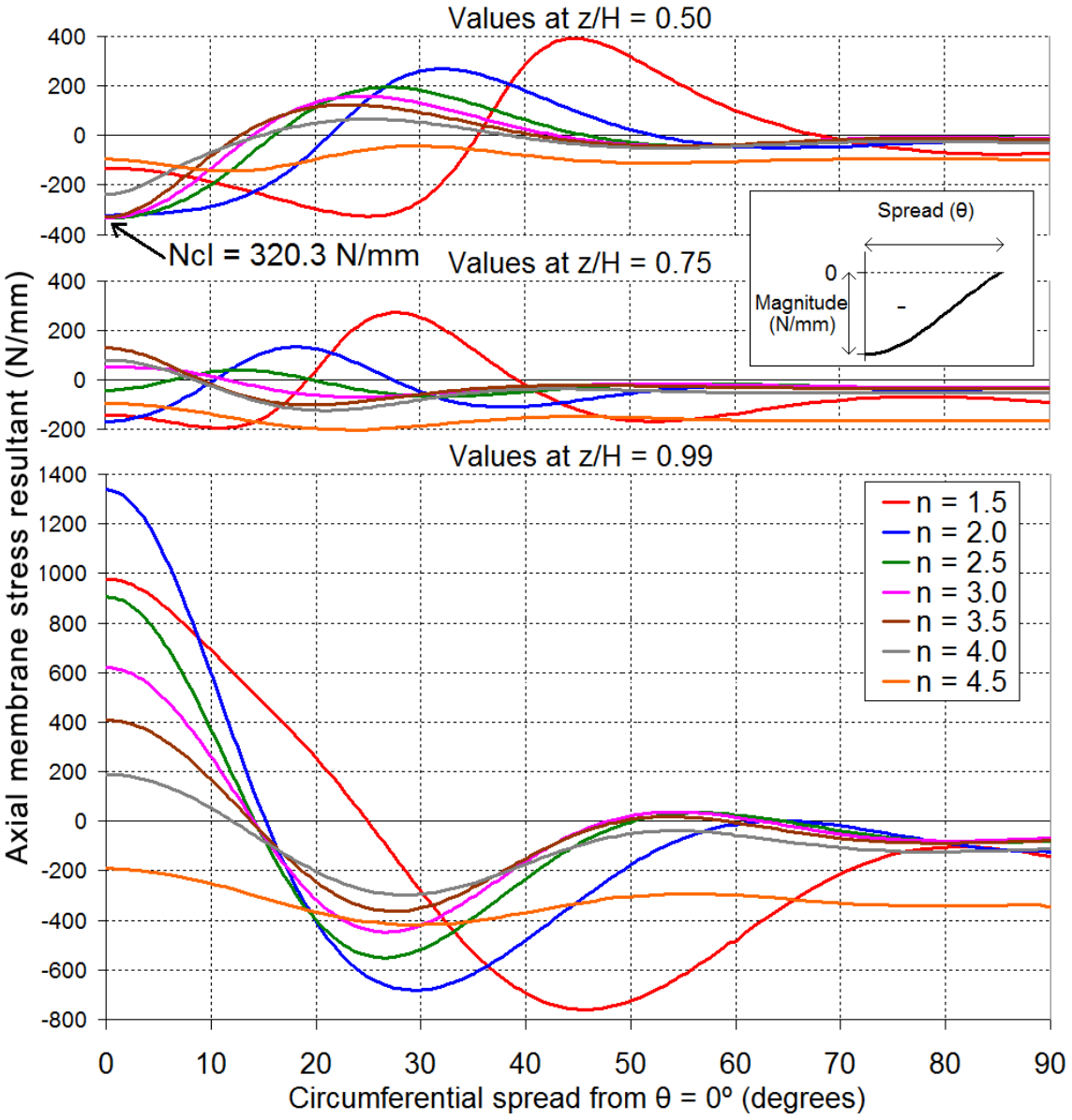

Fig. 9.11 – Circumferential distribution of the axial membrane stress resultants at z/H = 0.50, 0.75 and 0.99 from LA analyses at the LBA load factor

The circumferential distributions of the axial membrane stress resultants at z/H = 0.50, 0.75 and 0.99 are shown in Fig. 9.11. The midheight position corresponds closely to the critical buckling location at the base of the thinnest 3 mm strake, while the z/H = 0.75 and 0.99 positions correspond to the the base of the 4 mm strake and just above the base of the silo respectively. The circumferential distributions at midheight are very similar to those in Fig. 5.10, which showed the circumferential distributions of the axial

membrane stress resultant for different values of the EN 1991-4 flow channel size parameter $k_c = r_c/R$.

The midheight distributions (Fig. 9.11) of compressive axial membrane stresses exhibit a circumferential spread and peak magnitude. The spread is the circumferential extent of the compressive portion of the stresses and the magnitude is simply the maximum value of that compressive portion of the distribution, usually occurring at $\theta = 0^o$. Considering Fig. 9.11, the compressive region of the midheight distribution grows progressively with channel width and depth (decreased n). For the widest and deepest eccentric pipe flow channel of $n = 1.5$, however, the compressive peak appears to moves away from $\theta = 0^o$ to approximately 30^o, suggesting that the buckle instead forms away from the centre of the flow channel. An informative comparison of different values of the spread and magnitude of the compressive region of midheight axial membrane stresses is presented shortly in Section 9.4.4 for both LA and GNA analyses as a function of the channel steepness n.

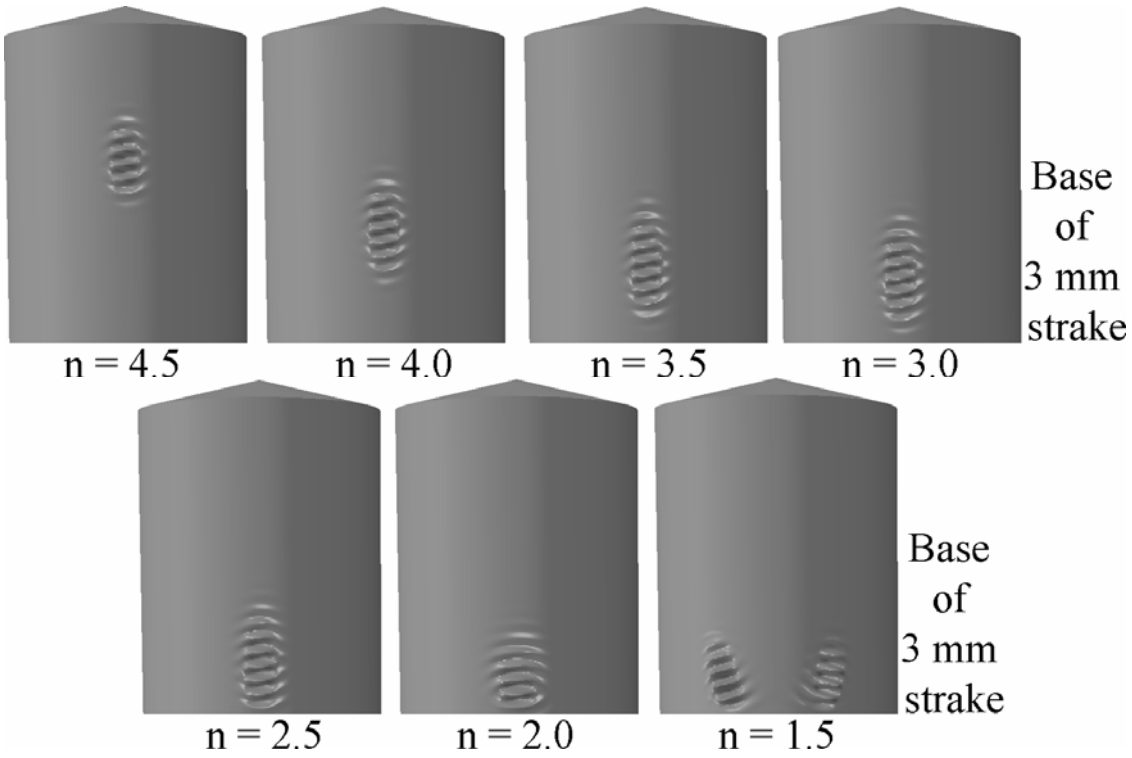

Fig. 9.12 – Progressive descent and expansion of the first LBA buckling mode with decreasing flow channel steepness n (geometric scale factor of 500)

The peak value of the midheight compression again does not go beyond $N_{cl} = t\sigma_{cl} \approx 320.3$ N/mm. Thus the criterion of buckling failure for all linear elastic analyses in the

present study appears to be that the wall of the silo will buckle locally when the local axial compression reaches the critical elastic buckling stress N_{cl}. For the distributions at z/H = 0.75 and 0.99 within the 4 mm and 6 mm strakes respecitively, the local respective buckling criteria of N_{cl} = 569.4 N/mm and 1281.2 N/mm have clearly not been reached at any point, hence the buckle cannot form within this part of the silo. The linear bifurcation eigenmodes in the range $4.5 \geq n \geq 1.5$ (Fig. 9.12) are thus naturally all elastic midheight modes Loc-CH within the 3 mm strake and correspond very closely in size, shape and location to previous observations in the EN 1991-4 flow channel size study (Fig. 5.6).

The LBA buckle gradually descends and expands both axially and circumferentially as n decreases (shallower channels), yet it remains at all times within the thinnest 3 mm strake. The buckling mode for n = 1.5 is a type of 'double buckle' caused by the non-central circumferential peak of axial membrane stresses seen in Fig. 9.11, and was observed previously for the EN 1991-4 pressure pattern with the widest flow channel with k_c = 0.90 in Fig. 5.6 and Fig. 5.7. In both cases, the migration of the peak away from θ = 0º appears to be characteristic of flow channels with a sufficiently wide circumferential wall contact angle at the level of the buckle, greater than approximately 50º from the symmetry axis.

The change in axial location and size of the LBA buckling mode corresponds directly to the varying position of the peak compressive LA axial membrane stress at θ = 0º (which has reached N_{cl}) in the wall adjacent to the flow channel. One may expect that there would be a relationship between the axial location of this peak and the lowest point of the effective transition z_{12}/H (Table 9.2 and Fig. 9.5). Such a relationship is illustrated in Fig. 9.13 and summarised in Table 9.5 for the range of values of n for which the elastic midheight mode Loc-CH was predicted in an LBA analysis, excluding the widest channel with n = 1.5.

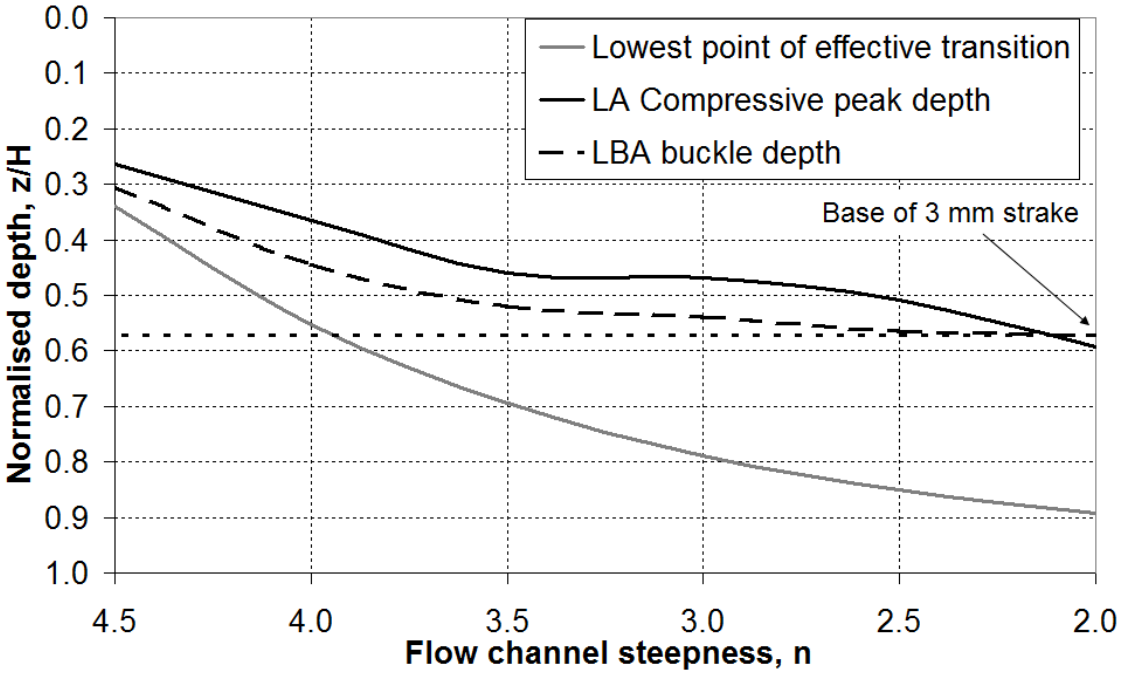

Fig. 9.13 – Variation of the axial locations of LA parameters with depth z and channel steepness n at $\theta = 0^{o}$

Table 9.5 – Summary of lowest flow channel wall contact, LA axial compressive membrane stress peaks and LBA buckle positions†

Power n	4.5	4.0	3.5	3.0	2.5	2.0
Lowest point of effective transition (z_{12}/H)	0.339	0.553	0.694	0.788	0.851	0.893
Within wall strake (mm)	3	3	4	5	5	5
Compressive peak N_{cl} depth (z/H)	0.263	0.365	0.460	0.468	0.508	0.593
Within wall strake (mm)	3	3	3	3	3	4
LBA buckle depth (z/H)	0.304	0.444	0.518	0.537	0.564	0.571
Within wall strake (mm)	3	3	3	3	3	3

† All axial positions refer to the channel centre meridian at $\theta = 0^{o}$

It is likely that the three axial locations are closely correlated (Fig. 9.13). The compressive peak in a linear analysis (N_{cl}) tends to be reached just above the lowest point of the effective transition where there is a sudden rise in wall pressure and frictional traction. However, it is important to note that this result has been obtained for a stepped wall silo design and both the compressive peak and LBA buckle do not descend below the boundary of the 3 mm strake, which has the lowest buckling resistance. It is likely, though not certain, that if a uniform wall silo design had been used, the compressive peaks and associated buckles might well have formed just above

the lowest point of the effective transition for a much wider range of *n*. The position of the LBA buckle was assumed here to be at the axial position of the maximum radial displacement associated with the LBA mode.

9.4.2 Materially Nonlinear Analyses (MNA)

The plastic collapse mode does not play any role in the silo behaviour for flow channels shallower than $n = 4.0$, with the predicted MNA load factors being on average 2.2 times higher than the GMNA load factors in this range. The plastic deformation modes are shown in Fig. 9.14 (all are mode Glb-PL, Table 9.3). These follow the outline of the effective transition rather closely (Fig. 9.5), and the gradual axial and circumferential growth with *n* of the portion of the wall which undergoes extensive circumferential yielding can be seen clearly.

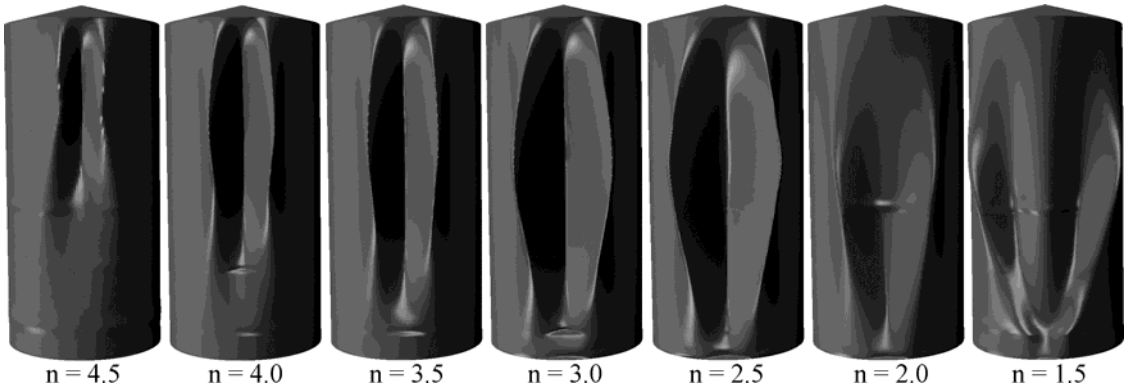

Fig. 9.14 – Progressive expansion of MNA plastic collapse mode with decreasing flow channel steepness *n* (geometric scale factor of 0.5)

It is important to reiterate at this point that a huge portion of the literature on structural behaviour under eccentric discharge identifies this plastic collapse mode as the failure mechanism. A long list of these may be found in Section 1.2.8 of the literature review and includes, amongst others, Jenike (1967), Bucklin *et al.* (1980), Colijn and Peschl (1981), Wood (1983), Roberts and Ooms (1983), Safarian and Harris (1985) and Ooms and Roberts (1986). These were all fundamentally wrong.

9.4.3 Geometrically and Materially Nonlinear Analyses (GNA & GMNA)

The distributions of GNA axial membrane stress resultants at bifurcation are shown in Fig. 9.15 for the circumferential positions at $\theta = 0^\circ$ and 45º. The overall stress patterns are generally similar to their LA equivalents in Fig. 9.10. The GNA axial membrane

stresses for the steepest channel for n = 4.5 follow a Janssen-like distribution throughout, save for a minor perturbation near z/H = 0.30 where the compression has increased locally due to the lowest point of the effective transition at z_{12}/H = 0.339. However, this rise in compression is insufficient to cause any significant peak that would change the buckling behaviour from the circumferendial diamond buckling mode Axi-DD that was predicted for the 'concentric' case of n = 5 into the elastic midheight mode Loc-CH. Indeed, the axial compression near the base of the 3 mm strake strake (z/H = 0.57) is higher than at z_{12}/H = 0.339 by more than a factor of two and has reached the elastic critical stress value $N_{cl} = t\sigma_{cl}$ = 320.3 N/mm. The GNA buckling mode for n = 4.5 thus remains at what it was for n = 5 (mode Axi-DD), accompanied by a near-negligible drop in load factor from 10.60 to 10.52. This was not the case for the LA analysis for n = 4.5 (Fig. 9.12), which predicted a well-defined peak near z/H = 0.30 that reached the critical value of N_{cl} and resulted in the corresponding buckling mode Loc-CH as well as a considerable drop in LBA load factor from 10.82 to 3.69.

The lower portions of the curves for n = 4.5 at both θ = 0º and 45º are furthermore very similar to each other, tending almost to the same base value and sharing a similar slope. The stresses throughout the vast majority of the silo are thus largely unaffected by very small flow channels in a GNA analysis, and geometric nonlinearity seems to limit the impact of relatively minor asymmetries in applied pressure patterns to their local contact vicinity of the silo wall. A much wider channel with $n \leq 3.5$ was thus found to be necessary to reduce the axial compressive membrane stresses at the base of the silo to the point at which they turned tensile, whereas a linear analysis predicted that this would already occur for a steeper channel with n = 4.0. The characteristic stress patterns under eccentric pipe flow therefore require significantly wider channels in order to develop in a geometrically nonlinear analysis. A similar conclusion was reached in the study of the EN 1991-4 flow channel size in Chapter 5.

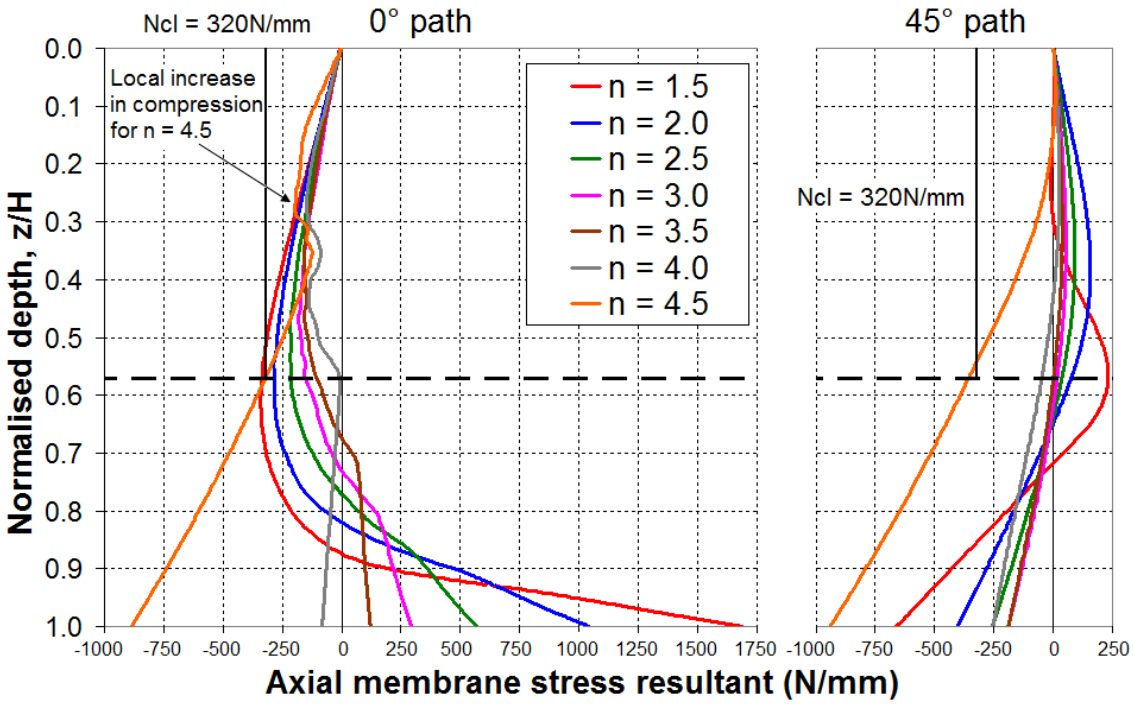

Fig. 9.15 – Axial distribution of the axial membrane stress resultants at $\theta = 0^{\circ}$ and 45° from GNA analyses at bifurcation

For the GNA analyses of the wider channels ($n \leq 4.0$), the peak values of axial compression at buckling failure for no longer attain the critical elastic value of N_{cl} = 320.3 N/mm. This value *had* been reached for the GNA analysis of $n = 4.5$ only because the silo under concentric discharge still behaves in a remarkably linear manner. Under eccentric discharge, however, geometric nonlinearity has been found to be beneficial in all analyses presented in this thesis so far and the predicted peak values of the GNA axial compression are thus significantly below the limiting value of N_{cl}. This aspect of the behaviour is demonstrated in the next section through a comparison of the varying circumferential extents and peak magnitudes of the compressive regions at $z/H = 0.50$ for both LA and GNA analyses.

The incremental GNA buckling modes are presented in Fig. 9.16 in the range $4.5 \geq n \geq 1.5$. The GNA analyses predict the elastic midheight buckling mode Loc-CH across the whole range of eccentric pipe flow channels with the exception of the steepest channel with $n = 4.5$ (see above discussion). The GMNA buckling mode for $n = 4.5$ (not shown) is the axisymmetric elephant's foot mode Axi-EF and occurs at the same location as the GNA mode Axi-DD. For all $n \leq 4.0$, the GNA and GMNA analyses are the same.

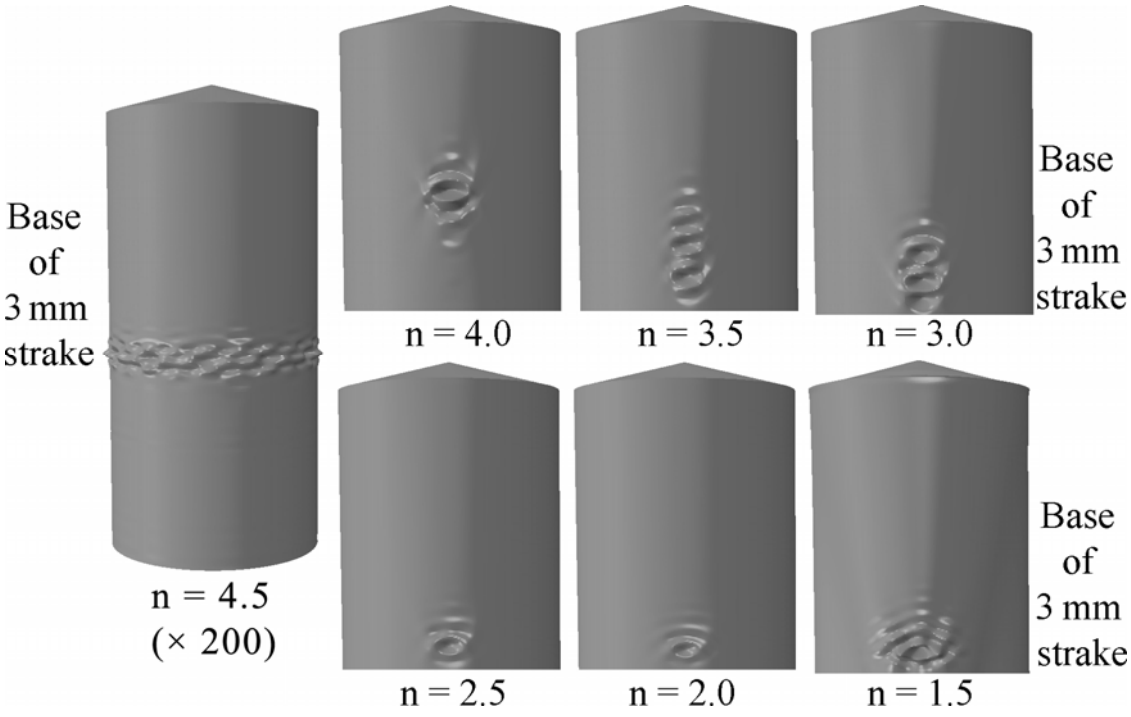

Fig. 9.16 – Progressive descent and expansion of the GNA and GMNA incremental buckling modes with decreasing flow channel steepness *n* (geometric scale factor of 5000 for all except *n* = 4.5 which is GNA only × 200)

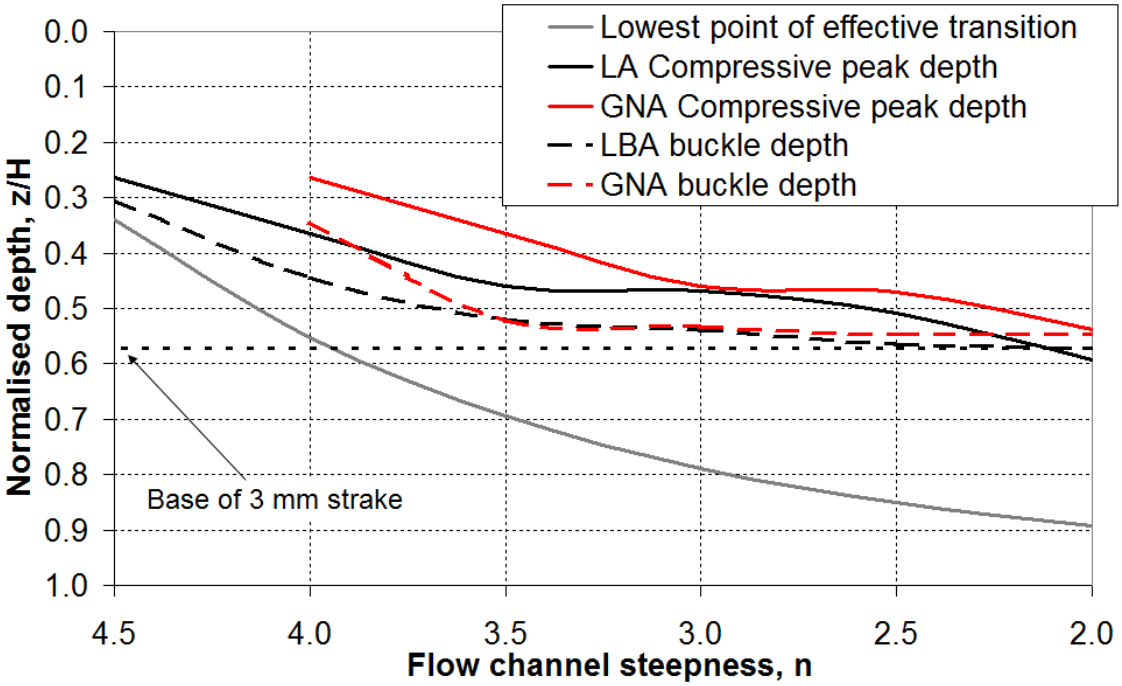

Fig. 9.17 – Variation of the axial locations of LA and GNA parameters with depth *z* and channel steepness *n* at $\theta = 0^{o}$

Table 9.6 – Summary of lowest flow channel wall contact, GNA axial compressive membrane stress peaks and GNA buckle positions†

Power n	4.5	4.0	3.5	3.0	2.5	2.0
Lowest point of effective transition (z_{12}/H)	0.339	0.553	0.694	0.788	0.851	0.893
Within wall strake (mm)	3	3	4	5	5	5
Compressive peak depth (z/H)	n/a	0.263	0.365	0.460	0.470	0.537
Within wall strake (mm)	n/a	3	3	3	3	3
GNA buckle depth (z/H)	n/a	0.343	0.522	0.531	0.546	0.547
Within wall strake (mm)	n/a	3	3	3	3	3

† All axial positions refer to the channel centre meridian at $\theta = 0^o$

Both the LA and GNA analyses predict similar buckle locations as a function of the channel steepness n (Fig. 9.17 and Table 9.6), regardless of the local position of the effective transition. The buckle is thus most likely to form at the base of the thinnest wall strake, presumably as long as this is reasonably close to midheight of the silo. Had the silo wall been of uniform thickness throughout, there would most likely have been a closer correlation between the axial locations of the lowest point of the effective transition and the LBA and GNA buckles over more of the silo height, as long as the other highly-stressed location at the base of the silo beneath the edge of the flow channel did not become critical.

9.4.4 The effect of geometric nonlinearity based on the steepness study of the mixed flow pressure theory

The comparison of the midheight circumferential forms of the LA and GNA axial membrane stress distributions presented in this section closely reflects a similar exercise performed for the flow channel size study of the EN 1991-4 eccentric discharge model (Section 5.5). Returning to the discussion of Fig. 9.11, it was noted that the shape of the central compressive feature of a typical circumferential distribution of axial membrane stresses at $z/H = 0.50$ may be characterised in terms of an angular spread from $\theta = 0^o$ and a peak magnitude. The result is shown in Fig. 9.18 for LA analyses @ LBA in the range $4.5 \geq n \geq 2.0$ and for the GNA analyses at bifurcation in the range $4.0 \geq n \geq 1.5$. Both of these correspond to the respective ranges of n where the elastic midheight Loc-CH mode was predicted (excluding the LBA 'double buckle' for $n = 1.5$). The similarity to Fig. 5.14 is quite striking.

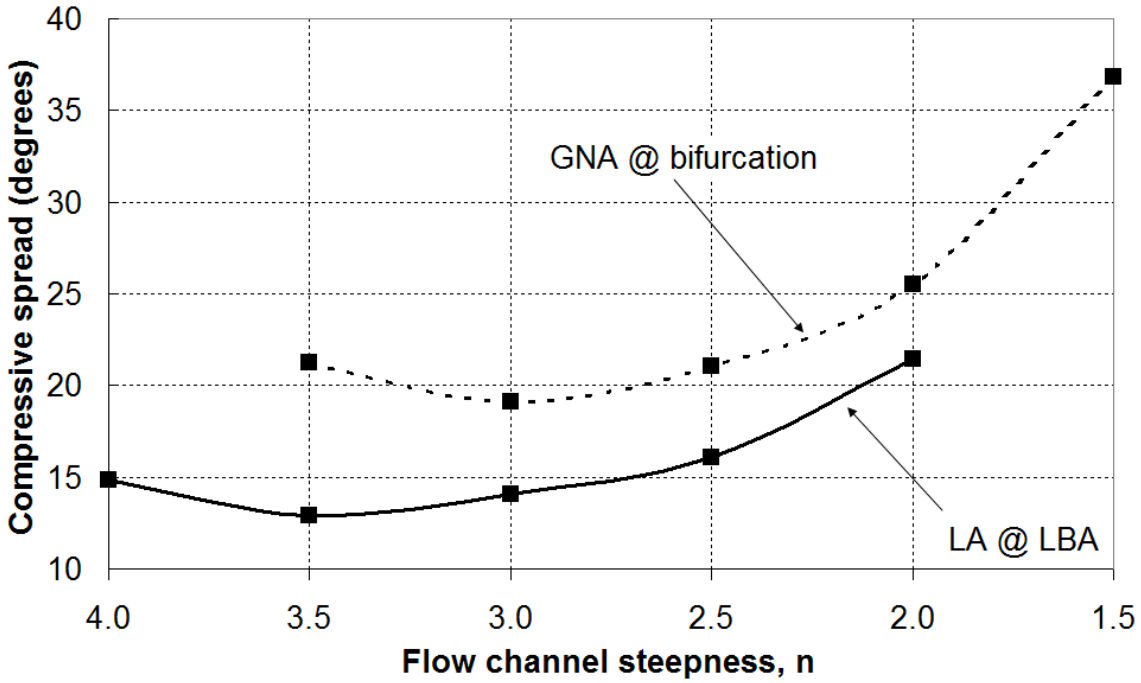

a) Variation of the compressive spread with flow channel steepness *n*

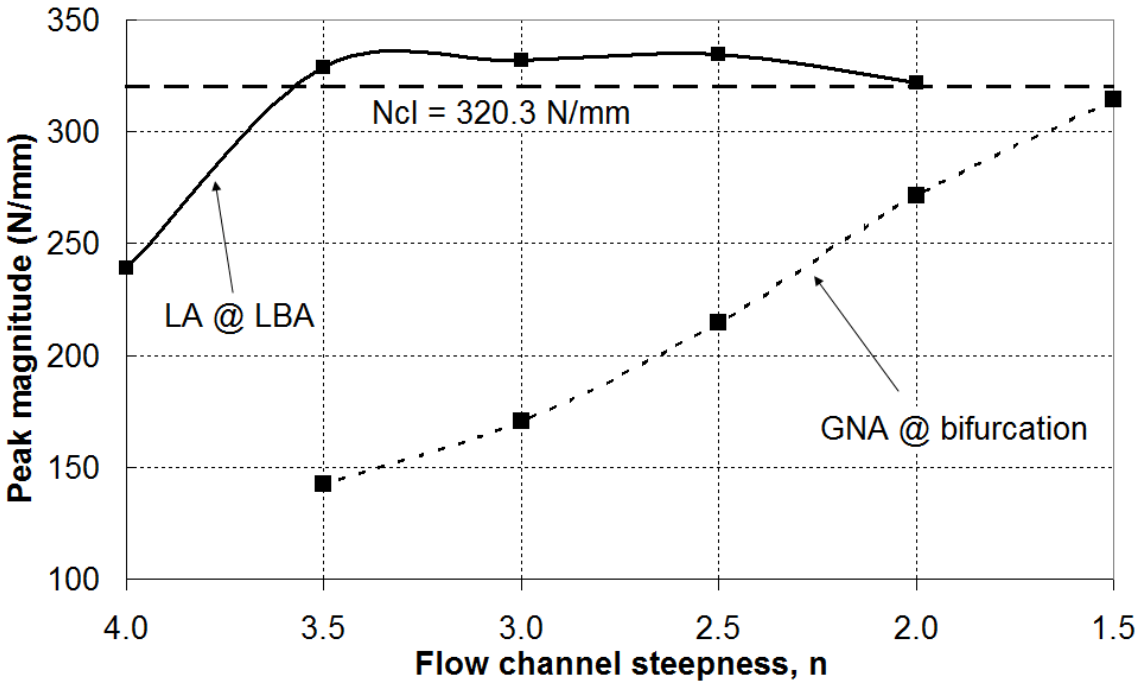

b) Variation of the peak compressive magnitude with flow channel steepness *n*

Fig. 9.18 – Variation of two measures of the central compressive region of axial membrane stresses at midheight with flow channel steepness *n* for eccentric pipe flows

This comparison confirms once again that a greater circumferential portion of the silo wall is mobilised by changes of geometry to resist the eccentric pipe flow channel

pressures. In turn, this leads to significantly lower peak axial compressive stresses and consequently higher load factors for GNA/GMNA than LBA (Table 9.4). Interestingly, the LA stresses quickly reach a plateau that is approximately 20 N/mm above the critical value of N_{cl} = 320.3 N/mm for the 3 mm strake, while the GNA stresses approach this limiting value more gradually for shallower channels. An interesting direction for future research would be to investigate the changes in local R/t ratio near the peak compressive magnitude in a GNA analysis and to relate the low buckling stresses to local wall flattening to see how big an influence an increased R/t may have (Rotter, 1985a).

The LA stresses in the perfect shell reach a peak compressive value at buckling that is slightly higher than N_{cl}, most likely because of the beneficial stabilising effect of internal pressure. The classical elastic critical stress σ_{cl} was derived for a state of uniform axial compression only, and a gradual increase in internal pressure is known to be beneficial to the elastic buckling strength of a silo both with and without geometric imperfections (e.g. Harris *et al.*, 1957; Schnell, 1959; Weingarten *et al.*, 1965; Saal *et al.*, 1979; Rotter, 2004; EN 1993-1-6, 2007).

Additionally, many numerical studies of linear bifurcation buckling of perfect cylinders under circumferentially varying axial loads (e.g. Abir and Nardo, 1958; Bijlaard and Gallagher, 1959; Johns, 1966; Libai and Durban, 1973; 1977; Cai, 2003) also suggest that the perfect shell buckles at local values of axial membrane stress that are may be significantly higher than σ_{cl}, especially for circumferentially narrow localisations of compressive stresses close to the axial half-wavelength of an axisymmetric buckle $\lambda_{cl} \approx 1.278(Rt)^{½}$ (Cai *et al.*, 2002; 2003a,b; Rotter, 2004a). However, it should be noted concerning Fig. 9.18a that the circumferential arc length of axial compressive stresses near the region of the buckle may be several times the relatively small value of λ_{cl} which corresponds to an equivalent spread of 2.18°, and within this range they are of a magnitude that is comparable with N_{cl}. Therefore, in the vicinity of the buckle, there is a condition close to that of uniform compression, and buckling should occur at stresses close to N_{cl} (Cai, 2003).

The above effects of geometric nonlinearity and buckling under local axial compression is not limited to the present comparison but has been found to be a recurring feature of

the finite element analyses of eccentric discharge presented in this thesis, and is a topic for further investigations.

9.4.5 Imperfect shells: the effect of axisymmetric weld depressions (GMNIA)

The effect of the axisymmetric weld imperfections on the structural behaviour is similar to that seen in Section 4.8.4 for the EN 1991-4 study of silos of different aspect ratio. It was suggested in that study that the substantial stiffening effect of the axisymmetric weld imperfection against circumferential bending, combined with a complementary beneficial effect due to geometric nonlinearity, prevented the characteristic elasitc midheight buckling mode Loc-CH from developing before the eccentric pipe flow channel reached a rather large size, with $k_c = r_c/R = 0.60$ being required to achieve this (Fig. 4.29).

A similar pattern is visible on Fig. 9.10 and Fig. 9.19 which show that the transition in characteristic discharge behaviour from concentric to eccentric occurs only at $n = 3.5$ for the imperfect shell. At $n = 3.5$, the flow channel has a significantly deeper and wider wall contact than at higher values of n (Fig. 9.5). The GNA analysis predicted that this transition in behaviour would occur already at $n = 4.0$, while the LA/LBA analyses exhibited the elastic midheight buckle as soon as $n = 4.5$. For $n = 4.5$ and 4.0, both GMNIA analyses predicted a local plastic elephant's foot mode Glb-EF at the base of the 3 mm strake, opposite the outlet. For the two imperfection amplitudes chosen in this study, the buckling modes are very similar, hence only those for the GMNIA#1 suite of analyses at 50% amplitude are shown in Fig. 9.19. The results of this study therefore confirm the previous findings in this thesis which suggest that the axisymmetric weld imperfection may be beneficial to the buckling strength of the silo under certain channel geometries of eccentric pipe flow.

The load factors for the geometrically nonlinear analyses of the imperfect shell are higher than those of the perfect shell in the range $4.5 \geq n \geq 2.0$. Additionally, in the range $3.5 \geq n \geq 2.0$, the two GMNIA load factors are very close to each other, and at $n = 2.0$ and 2.5 the load factor for the 100% amplitude imperfection is higher than that for the 50% amplitude imperfection. The phenomenon of a deeper imperfection amplitude resulting in higher buckling strengths has been documented before (Yamaki, 1984; Rotter, 2007b), and the results in this section support previous findings obtained using

the EN 1991-4 eccentric discharge pressure model (e.g. Fig. 2.15). However, the mechanics of this nonlinear behaviour is highly complex, and merits further study.

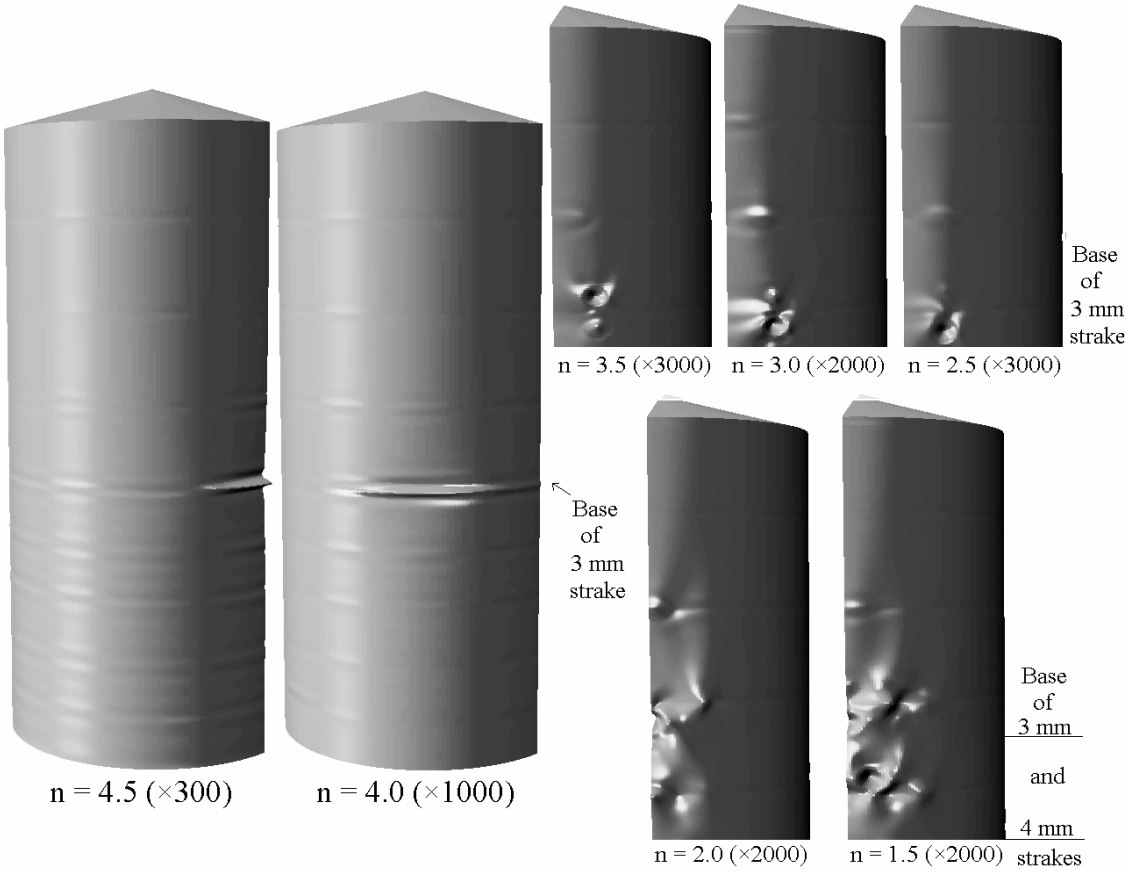

Fig. 9.19 – Variation of the incremental buckling modes with channel steepness n for the GMNIA#1 analyses

9.5 Structural behaviour under eccentric mixed flow channels

9.5.1 Comparison of geometry and pressure patterns

The structural behaviour of the stepped wall Silo B under the wide near-conical flow channel with n = 1.05 and e_c/R = 0.80 has been found to resemble qualitatively the behaviour of the eccentric mixed flow pattern analysed in Chapter 8 with n = 1.2 and e_c/R = 0.29. Both channels share the same outlet size of r_0/R = 0.074. The similarity in behaviour is plausible, since in both cases Silo B was analysed under a set of wall pressures predicted for a similar pattern of eccentric mixed flow (EccM). However, these flow patterns are far from being the same, as illustrated by the geometry and pressure patterns in Figs 9.20 to 9.22.

The three-dimensional geometry of both eccentric mixed flow patterns is shown in Fig. 9.20. Although in both cases the effective transition begins at approximately the same axial location opposite the outlet at $\theta = 180º$, its circumferential variation is significantly steeper for $n = 1.05$ and $e_c/R = 0.80$ than for $n = 1.2$ and $e_c/R = 0.29$, and also covers a much greater portion of the silo height. Values of $n = 1.05$ and 1.2 generate flow channel profiles of similar steepness, thus the main cause of any differences in wall pressure and consequent structural behaviour between both flow patterns is likely to be due to the different values of the outlet eccentricity. The distributions of vertical pressure for both eccentric mixed flow patterns are shown in Fig. 9.21. The three-dimensional distributions of normal pressure applied on the silo wall are shown in Fig. 9.22.

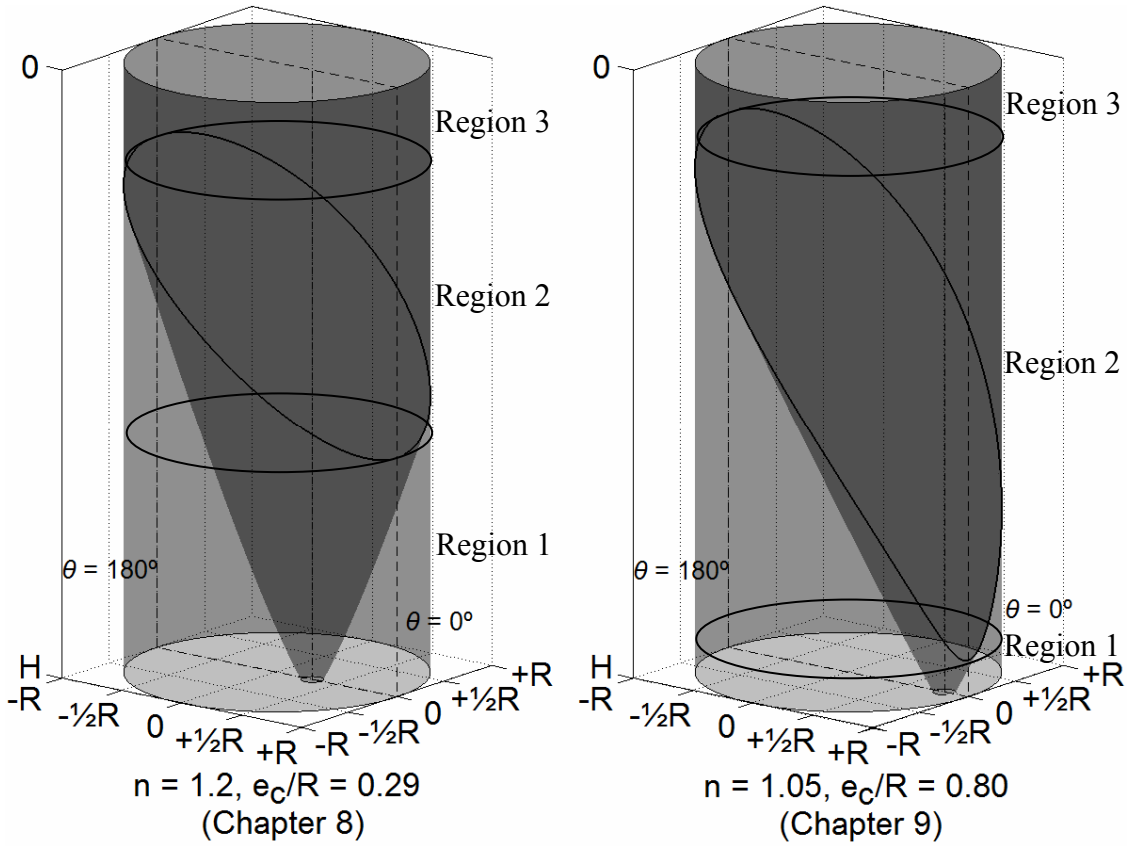

Fig. 9.20 – Comparison of the geometry of two different eccentric mixed flow patterns and flow regions

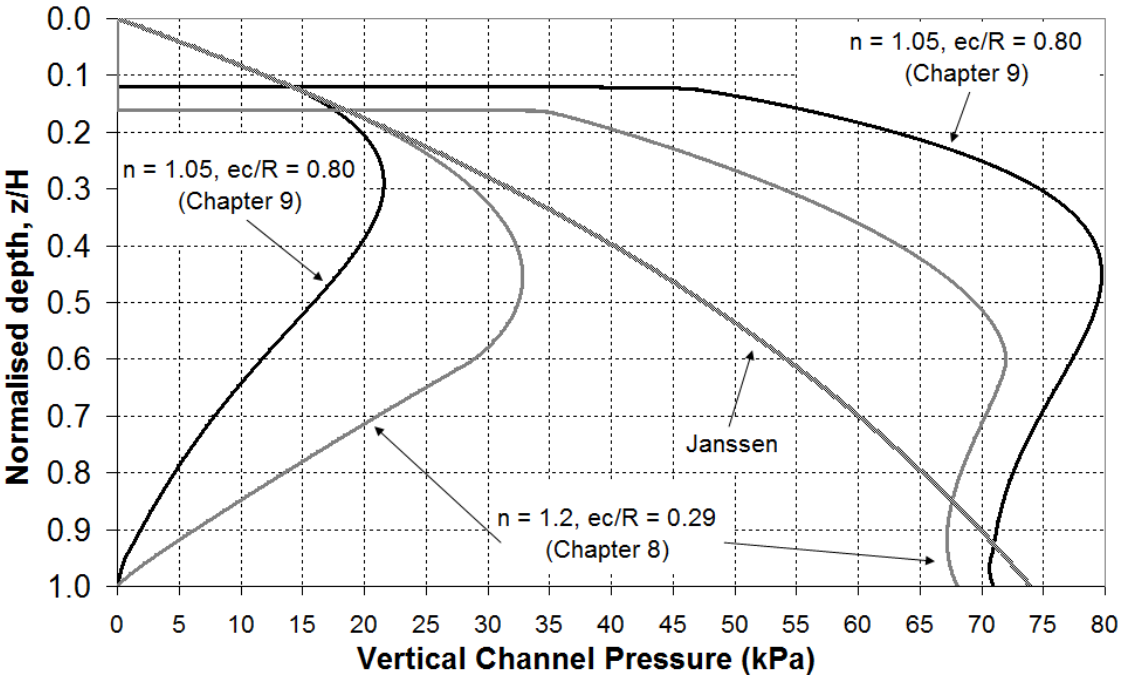

Fig. 9.21 – Comparison of vertical pressure distributions for two different eccentric mixed flow patterns

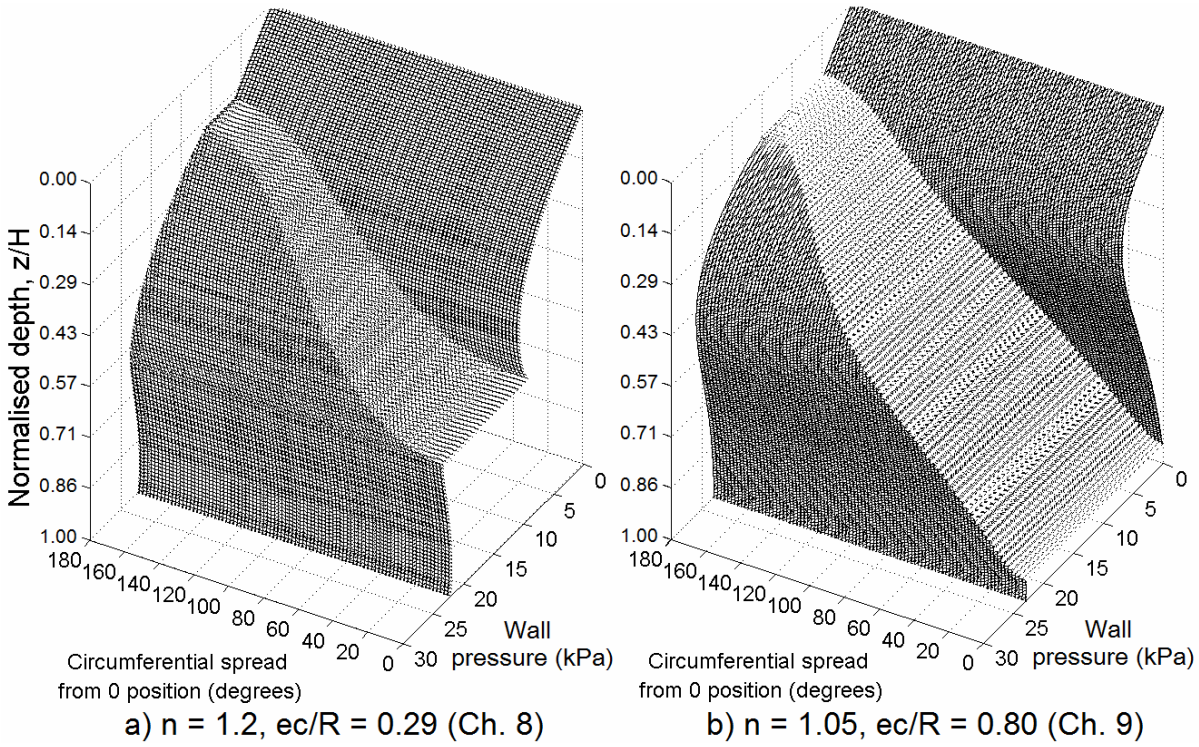

Fig. 9.22 – Comparison of three dimensional surface plots of the normal wall pressure distributions of two different eccentric mixed flow patterns

According to the mixed flow theory presented in Chapter 7, there is an imbalance in normal wall pressure for the portion of the silo under Region 2 flow in which the flow

channel is partially internal. This imbalance results in a net horizontal force acting through the symmetry axis and contributes to a global overturning moment on the silo in the direction away from the outlet (Fig. 9.23). There is no such imbalance in Region 1 because the model assumes that the pressure in the stationary solid is constant around the circumference and independent of the outlet eccentricity once the flow channel is fully internal. The pressure in Region 3 is balanced as it is under axisymmetirc mass flow. In reality, however, it is possible that the drop in pressure in the channel would be balanced by a rise in pressure adjacent to the edge of the channel in such a way that there would be no net force.

The magnitude of the difference between the vertical pressure in the stationary solid and flow channel at any level is significantly higher for n = 1.05 and e_c/R = 0.80 than for n = 1.2 and e_c/R = 0.29 (Fig. 9.21). Thus the n = 1.05 and e_c/R = 0.80 pattern exhibits a higher imbalance in vertical pressure and therefore a larger net horizontal force at any level in Region 2 flow. Additionally, the axial range covered by the effective transition, and therefore by the jump in normal wall pressure and net horizontal force, is significantly greater for n = 1.05 and e_c/R = 0.80 than for n = 1.2 and e_c/R = 0.29 (Fig. 9.22). Consequently, the wall pressures exerted by the mixed flow pattern with n = 1.05 and e_c/R = 0.80 lead to a significantly higher overturning moment on the silo and therefore constitute a more dangerous load condition. This is illustrated in Fig. 9.24 through the approximate analogy of the silo under eccentric mixed flow with a cantilever beam under a partially-distributed load.

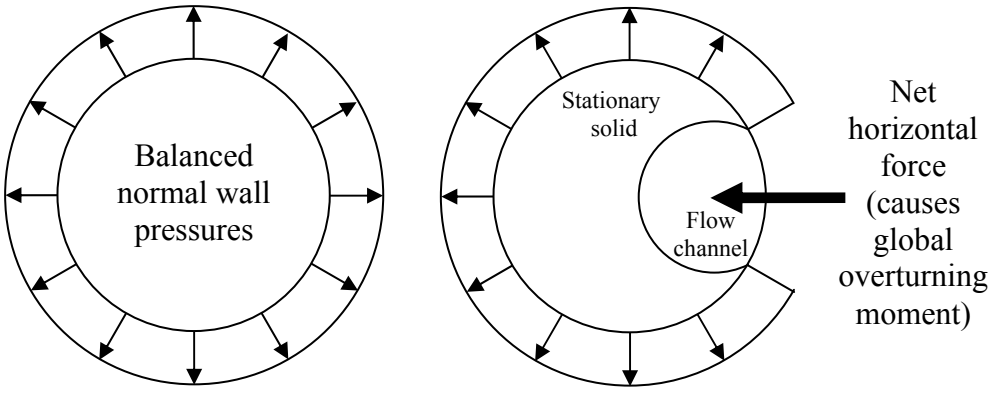

a) Balanced axisymmetric normal pressures

b) Unbalanced eccentric flow channel pressures

Fig. 9.23 – Net horizontal force under eccentric discharge (Region 2 flow only)

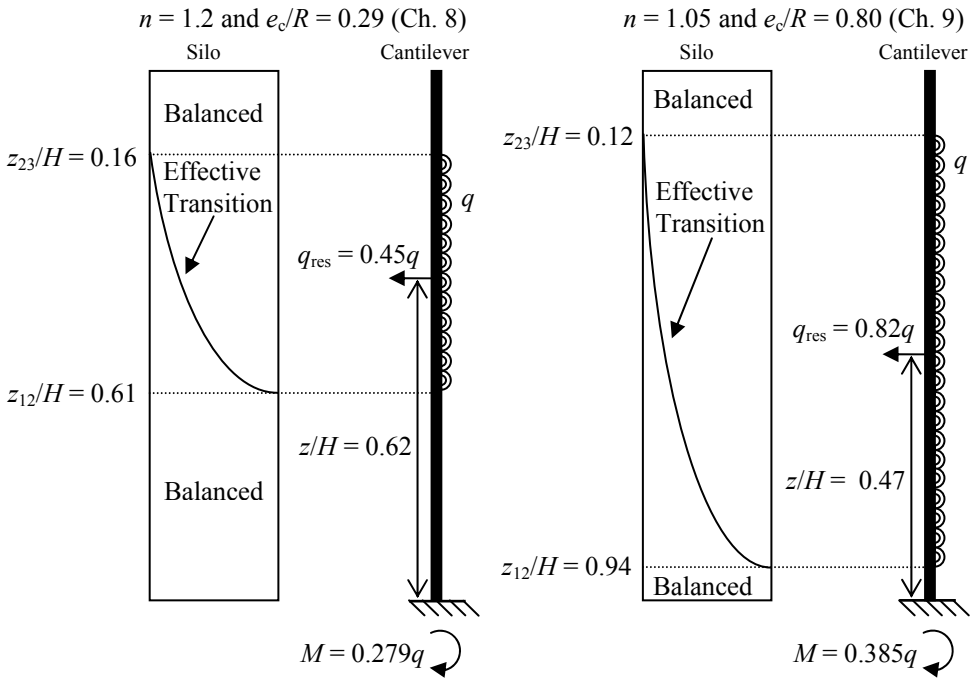

Fig. 9.24 – Illustration of the global overturning moment of the two eccentric mixed flow patterns by approximate analogy to a cantilever beam under a partially-distributed load

9.5.2 Comparison of axial distributions of axial membrane stresses

The axial distributions of the axial membrane stress resultants at bifurcation at five different circumferential locations are shown in Fig. 9.25 and Fig. 9.26 for n = 1.2 and e_c/R = 0.29 (GMNA data from Fig. 8.23) and n = 1.05 and e_c/R = 0.80 (LA and GMNA data) respectively. Both sets of curves exhibit a sudden change in slope due to the large increase in normal pressure and frictional traction at the local position of the effective transition (Fig. 9.20). Additionally, the critical buckling location for both flow patterns occurs opposite the outlet at the base of the 3 mm strake, where the axial compression reaches the critical elastic stress $N_{cl} = t\sigma_{cl}$ = 320.3 N/mm.

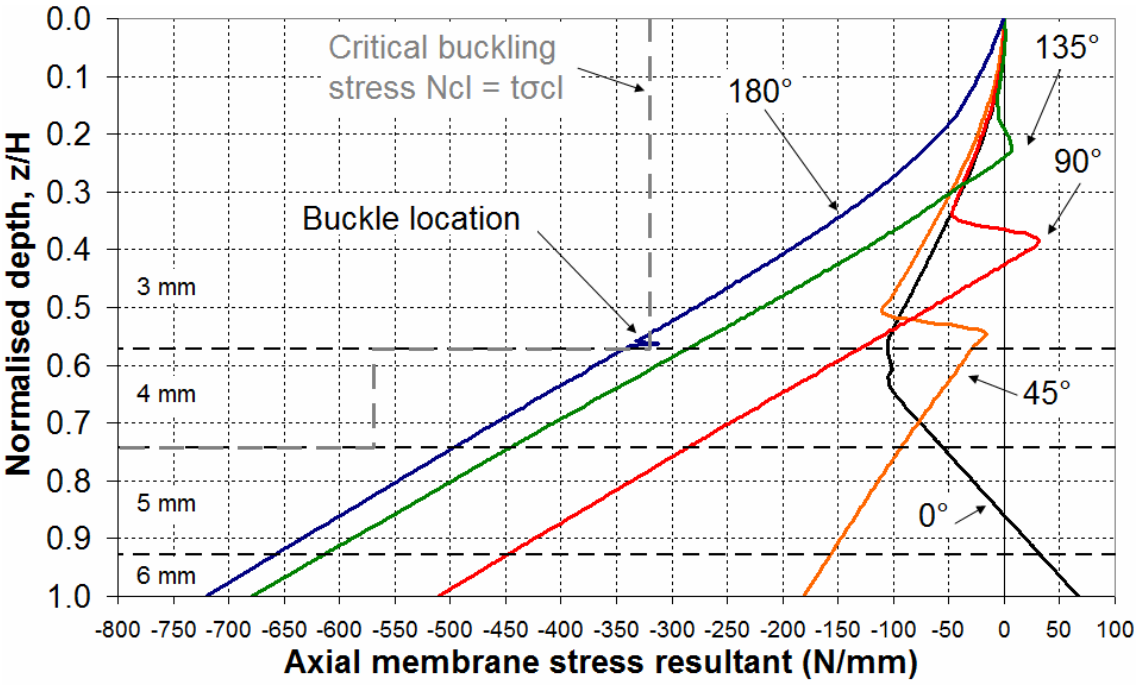

Fig. 9.25 – Axial distribution of the axial membrane stress resultants from GMNA analyses at bifurcation for n = 1.2 and e_c/R = 0.29 (from Fig. 8.23)

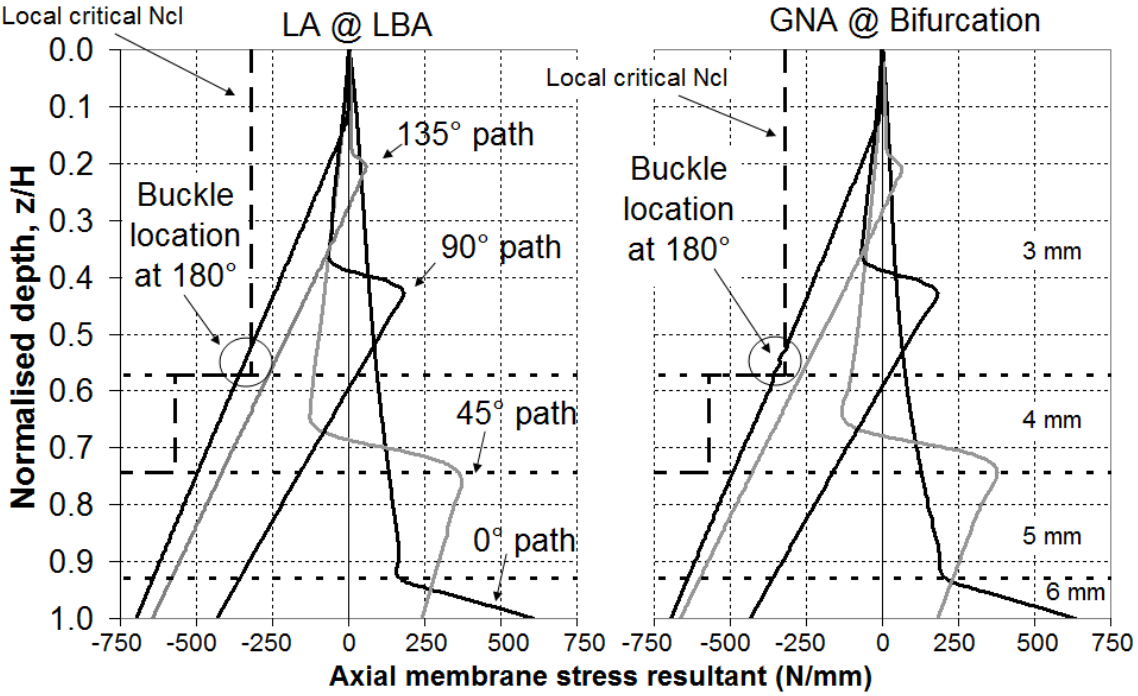

Fig. 9.26 – Axial distribution of the axial membrane stress resultants from LA and GMNA analyses at bifurcation for n = 1.05 and e_c/R = 0.80

The LA and GMNA stress distributions for n = 1.05 and e_c/R = 0.80 are very similar at all circumferential positions (Fig. 9.26), and the critical value of N_{cl} is reached at the buckling load factor even in a geometrically nonlinear analysis with plasticity. This was

not the case for geometrically nonlinear analyses of eccentric pipe flow, which predicted elastic buckling failure at values of local axial compression that were significantly below N_{cl} (Fig. 9.15). Geometric nonlinearity under eccentric mixed flow nonetheless results in *slight* overall reductions in stress magnitudes and marginally higher buckling strengths (e.g. 2-5% increase from LBA to GNA), and thus may be considered to have a minor beneficial effect. However, this beneficial effect is indeed minor when compared to the possible strength gains under eccentric pipe flow, where the increase in load factor from LBA to GNA was found to be anything from 50% to several hundred percent depending on the flow channel size (Table 9.4). This major difference in behaviour is most likely because the structural response to eccentric mixed flow includes significantly less circumferential bending, which in turn results in much smaller (beneficial) changes of geometry and was explored in Section 8.6. The full set of computed load factors illustrates the above discussion (Table 9.7).

Table 9.7 – Comparison of load proportionality factors at failure Silo B under two different eccentric mixed flow patterns

	LBA	MNA	GNA	GMNA	GMNIA#1	GMNIA#2
n = 1.2, e_c/R = 0.29 (from Table 8.8)	4.54	6.30	4.75	4.31	3.21	2.76
Failure mode	Axi-EL†	Glb-EF†	Axi-EL†	Glb-EF†	Glb-EF†	Glb-EF†
n = 1.05, e_c/R = 0.80	2.48	4.34	2.51	2.42	1.85	1.51
Failure mode	Axi-EL†	Glb-EF†	Axi-EL†	Glb-EF†	Glb-DD	Glb-DD
% change from e_c/R = 0.29 to 0.80	– 45.4	– 31.1	– 47.2	– 43.9	– 42.4	– 45.3

† these failure modes are at the base of the 3 mm strake opposite the outlet at θ = 180°

9.5.3 Comparison of failure modes

The predicted failure modes are shown in Fig. 9.27 and Fig. 9.28 for n = 1.2 and e_c/R = 0.29, and n = 1.05 and e_c/R = 0.80 respectively. For the LBA, MNA, GNA and GMNA analyses under both eccentric mixed flow patterns, the failure modes are predicted to occur opposite the outlet at θ = 180° at the base of the thinnest 3 mm strake. Both buckling and plastic collapse at this location are caused by the high magnitudes of axial membrane stresses, and by the weaker buckling and yielding resistance of the thinnest strake. The buckling mode in both GMNIA analyses is predicted to be a local plastic

elephant's foot mode Glb-EF for n = 1.2 and e_c/R = 0.29, however the GMNIA analyses of n = 1.05 and e_c/R = 0.80 show a more global diamond pattern concentrated near θ = 180° instead (best described by mode Glb-DD, Table 9.3).

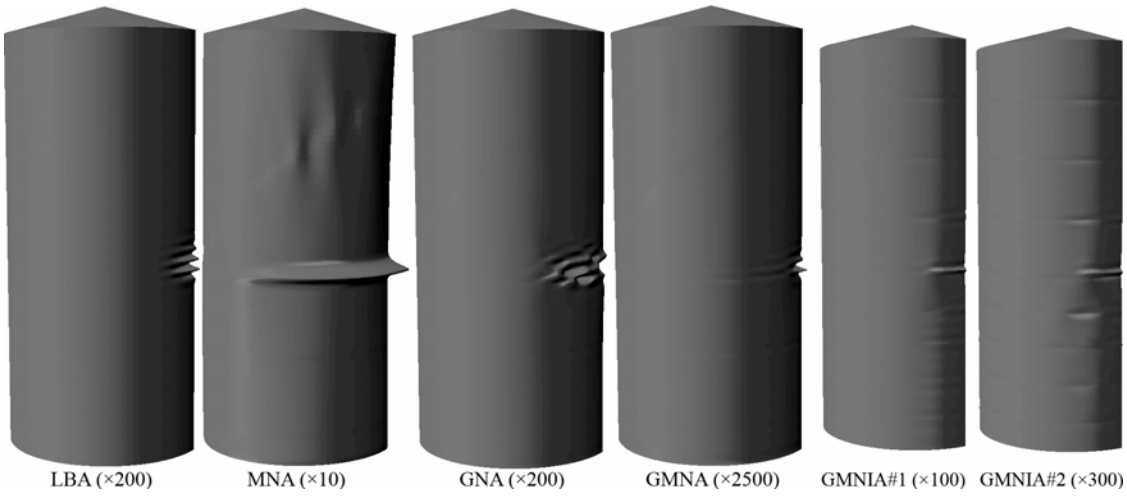

Fig. 9.27 – Predicted failure modes for the stepped wall B silo under the eccentric mixed flow pattern, n = 1.2 and e_c/R = 0.29 (from Fig. 8.25)

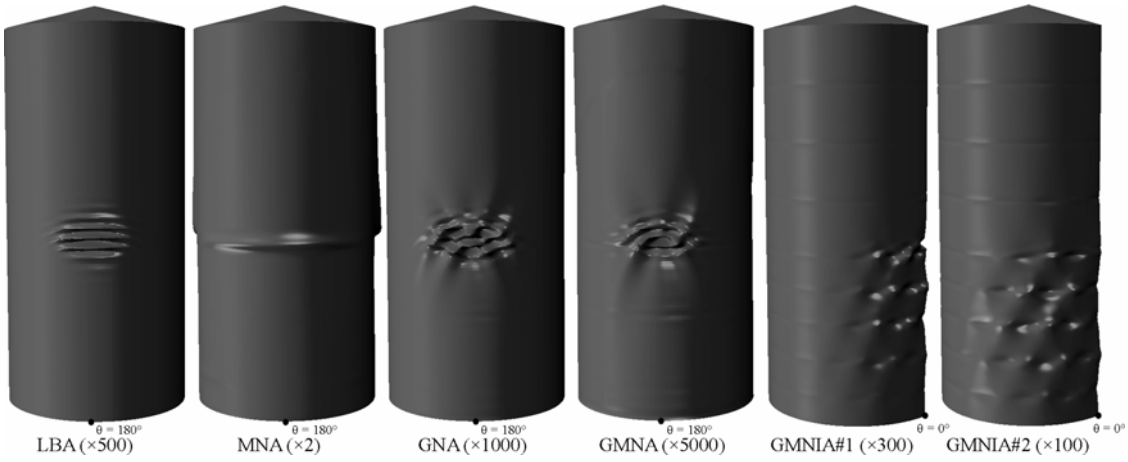

Fig. 9.28 – Predicted failure modes for the stepped wall B silo under the eccentric mixed flow pattern, n = 1.05 and e_c/R = 0.80

9.5.4 Comparison of circumferential distributions of axial membrane stresses

Despite the apparent similarities in axial membrane stress distributions and failure mode for both sets of analyses, the load factors are failure were found to be significantly lower for n = 1.05 and e_c/R = 0.80 than for n = 1.2 and e_c/R = 0.29 (Table 9.7). A likely reason for this may be found in the circumferential distribution of the axial membrane stress resultants at midheight, presented in Fig. 9.29. The data shown here is for both eccentric mixed flow patterns at their respective GNA buckling load factors, and for the pattern

with n = 1.2 and e_c/R = 0.29 at close to the buckling load factor of the pattern with n = 1.05 and e_c/R = 0.80 to allow a comparison of the behaviour of the silo under both flow patterns at approximately the same load factor.

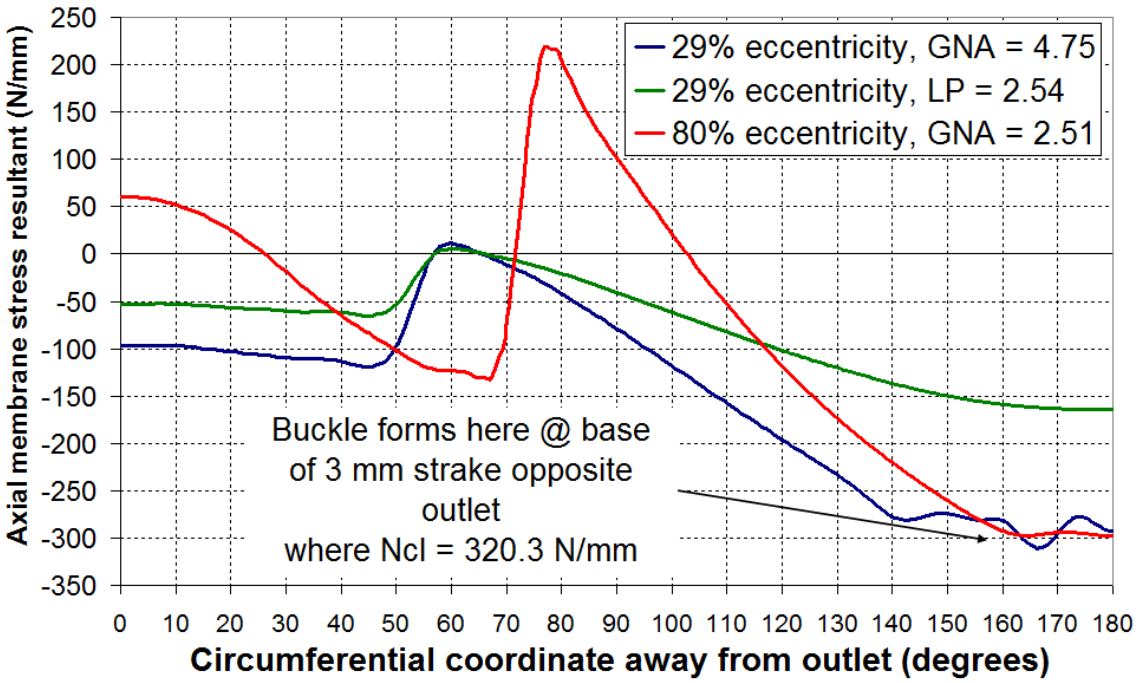

Fig. 9.29 – Circumferential distribution of axial membrane stresses at midheight for two different eccentric mixed flow patterns (GNA-analysis data)

The compressive axial membrane stresses near the buckle are of a very similar magnitude for both patterns regardless of the GMNA load factor at buckling, corresponding to the familiar value of $N_{cl} = t\sigma_{cl} \approx 0.605Et^2R^{-1} \approx 320.3$ N/mm (Fig. 9.25, Fig. 9.26 and Fig. 9.29). Both flow patterns share almost the same depth of the effective transition opposite the outlet at θ = 180° (Fig. 9.20 and Fig. 9.22), occuring approximately the same distance above the common critical location for buckling at the base of the 3 mm strake. Thus the buckle is caused in both cases by high axial membrane stresses which grow progressively with depth due to friction between the stationary solid and the wall, and because this growth covers approximately the same distance, the axial membrane stresses reach approximately the same critical value at buckling which happens to be N_{cl}.

Both eccentric mixed flow patterns apply a global moment on the silo causing it to overturn away from the outlet, but it was noted in Fig. 9.24 that the channel with n = 1.2 and e_c/R = 0.29 applies a significantly lower global moment. Indeed, when considering

the circumferential distribution of midheight axial membrane stresses at approximately the same load factor (Fig. 9.29), it is clear that the flow pattern with n = 1.2 and e_c/R = 0.29 results in much lower magnitudes of these stresses than the channel with n = 1.05 and e_c/R = 0.80. The flow pattern with n = 1.2 and e_c/R = 0.29 therefore requires a significantly higher load factor to reach the critical buckling value of axial membrane stress N_{cl}.

9.6 Criterion of failure for high local axial compression

9.6.1 Background literature

The discussion in Section 9.4.4 concerning the peak magnitude and circumferential spread of the axial compressive membrane stresses near the critical buckling region lends itself naturally to the consideration of a criterion of failure, such as the one currently in the EN 1993-4-1 (2007) standard. This method of characterising local peaks of axial compression and coupling it with a criterion to assess the buckling strength was originally devised by Rotter (1986). For the failure criterion, he assembled key items relating to different buckling design conditions from Libai and Durban (1973, 1977), the ECCS Recommendations 2nd Edition (1983) and Rotter (1985c).

This process was adopted into Section 5.3.2.4 of EN 1993-4-1 to provide a method for assessing the buckling resistance of a silo under axial compression. The resistance is assessed by using an amended version (Rotter, 1986) of the unpressurised elastic imperfection reduction factor α_0 (EN 1993-1-6, 2007; Eq. 1.17 introduced in Section 1.3.5 of the literature review) that includes a stress non-uniformity parameter ψ in the denominator:

$$\alpha_0 = \frac{0.62}{1 + 1.91\psi\left(\frac{\Delta w_0}{t}\right)^{1.44}} \tag{9.1}$$

where $\frac{\Delta w_0}{t} = \frac{1}{Q}\sqrt{\frac{R}{t}}$ is the representative imperfection amplitude and Q is the Quality Parameter dependent on the Fabrication Tolerance Quality Class of the structure.

The evaluation of the stress non-uniformity parameter ψ is central to the present discussion. The design value of the compressive axial membrane stress $\sigma_{x,Ed}$ at the most highly stressed point in a linear elastic (LA) analysis is defined as $\sigma_{x0,Ed}$ in the

compression-positive convention. Rotter (1986) based the assessment of the localisation in the stress distribution on a second value of the axial membrane stress $\sigma_{x1,Ed}$ at a point at the same axial coordinate adjacent to the peak stress separated from $\sigma_{x0,Ed}$ by a circumferential arc length $R\Delta\theta_g$ (Fig. 9.30).

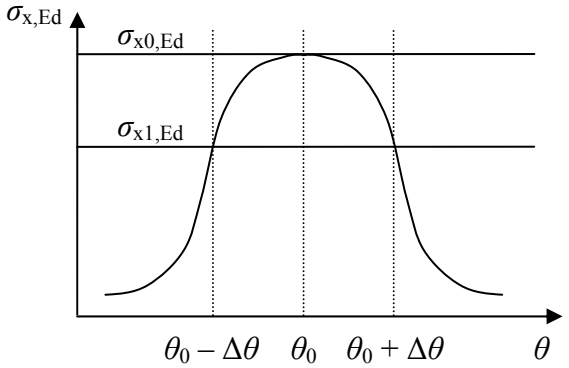

Fig. 9.30 – Representation of the local distribution of axial compressive membrane stresses around the circumference, from EN 1993-4-1 (2007)

The best value for $\Delta\theta_g$ has been chosen somewhat differently in the various formulations of the theory (Rotter, 1986; 2001a; 2001b; EN 1993-4-1, 2007; Schmidt and Rotter, 2008), but in all cases an equivalent harmonic for the peak of the stress pattern is determined as:

$$j = 0.25\sqrt{\frac{R}{t}}\cos^{-1}\left(\frac{\sigma_{x1,Ed}}{\sigma_{x0,Ed}}\right) \tag{9.2}$$

The condition of uniform axial compression is represented by $j = 0$. A value of $j = 1$ represents pure bending. Values of $j > 1$ represent progressively sharper and more localised peaks, so that finally as $j \to \infty$, or $1/j \to 0$, the buckling stress should rise to the classical elastic critical stress. Indeed, the buckling stress should reach this value when the local peak in the stress distribution still covers a zone that exceeds the size of a typical axial compression buckle ($\lambda_{cl} \approx 1.278(Rt)^{½}$, Rotter 2004a), so this condition must be attained whilst the value of j is only moderate.

The location of the second stress point, defined by $\Delta\theta_g$, was chosen differently in different publications, as noted above. In Rotter (2001a), it is defined as $R\Delta\theta_g = 4(Rt)^{½}$ with the restriction that $0.2 < \sigma_{x1,Ed}/\sigma_{x0,Ed} < 0.8$ to ensure that a reasonable separation in the values of $\sigma_{x1,Ed}$ and $\sigma_{x0,Ed}$ is achieved, though the buckling strength outcome is not

sensitive to the chosen value of $\Delta\theta_g$. Otherwise, $R\Delta\theta_g$ should be adjusted so that $\sigma_{x1,Ed}/\sigma_{x0,Ed} \approx 0.5$. Note that EN 1993-4-1 prescribes instead $0.3 < \sigma_{x1,Ed}/\sigma_{x0,Ed} < 1.0$.

The stress non-uniformity parameter was chosen by Rotter (1986) to take the following form:

$$\psi = \frac{1 - b_1 j}{1 + b_2 j} \tag{9.3}$$

where

$$b_1 = 0.5\sqrt{\frac{t}{R}} \tag{9.4}$$

$$b_2 = \frac{(1 - b_1)}{\psi_b} - 1 \tag{9.5}$$

and ψ_b is the value that yields an appropriate gain in buckling strength from the uniform compression value to that for global bending. In Rotter (2001a) and EN 1993-4-1, the value of $\psi_b = 0.4$ is recommended (based on the assumption of global bending), but this value is based on rather limited information. A better value may be obtained from the more recent work of Chen *et al.* (2008). The harmonic localisation at which there is no reduction in buckling strength below the classical elastic critical stress as a result of imperfections is $j_\infty = 1/b_1$. The value given in Eq. 9.4 was chosen by Rotter (1986) based on the buckling of longitudinal stiffened shells and the criterion of shell buckling (e.g. Schmidt and Samuelsen, 2008). Once again, the relationship for this parameter b_1 could be improved following further research. Whatever the individual components of the evaluation, it is clear that this is an effective way of describing the loss of imperfection sensitivity under non-uniform axial compressive stress around the circumference.

It was discussed in Section 1.3.5 of the literautre review that the factor α_0 may subsequently be upgraded to α_{pe} (Eq. 1.19) to account for the elastic sabilising effect of internal pressure which significantly reduces the effects of geometric imperfections, leading to the attainment of the classical elastic critical stress at higher pressures (as has been found to be the case in the present analyses, e.g. Fig. 9.11 and Fig. 9.29). However, at very high internal pressures, plasticity causes destabilisation that is not associated with the geometric imperfections and the α_0 must be downgraded to α_{pp} (Eq. 1.20), but this is not a key aspect in the present discussion.

Assuming fully-elastic unpressurised behaviour such that α_0 gives the dimensionless buckling stress of the imperfect shell directly ($\alpha_0 = \sigma_{x,Rk}/\sigma_{x,Rcr}$ where $\sigma_{x,Rcr} = \sigma_{cl} \approx 0.605Et/R^{-1}$), the relationship between j and α_0 is shown in Fig. 9.31 for different values of the R/t ratio. A 'Normal' Fabrication Tolerance Quality Class was assumed. The EN 1993-4-1 (2007) design procedure therefore predicts buckling of the imperfect shell to occur at very low stresses under uniform axial compression, at higher stresses under global bending where half of the circumference is in tension and half is in compression, and at significantly higher stresses if they are very local. In the case of high localisation, the stressses approach the classical buckling stress actually rather slowly and, according to this relationship, the critical buckling stress (more specifically, $\alpha_0\sigma_{cl}$) is reached when $j = j_\infty = 1/b_1$.

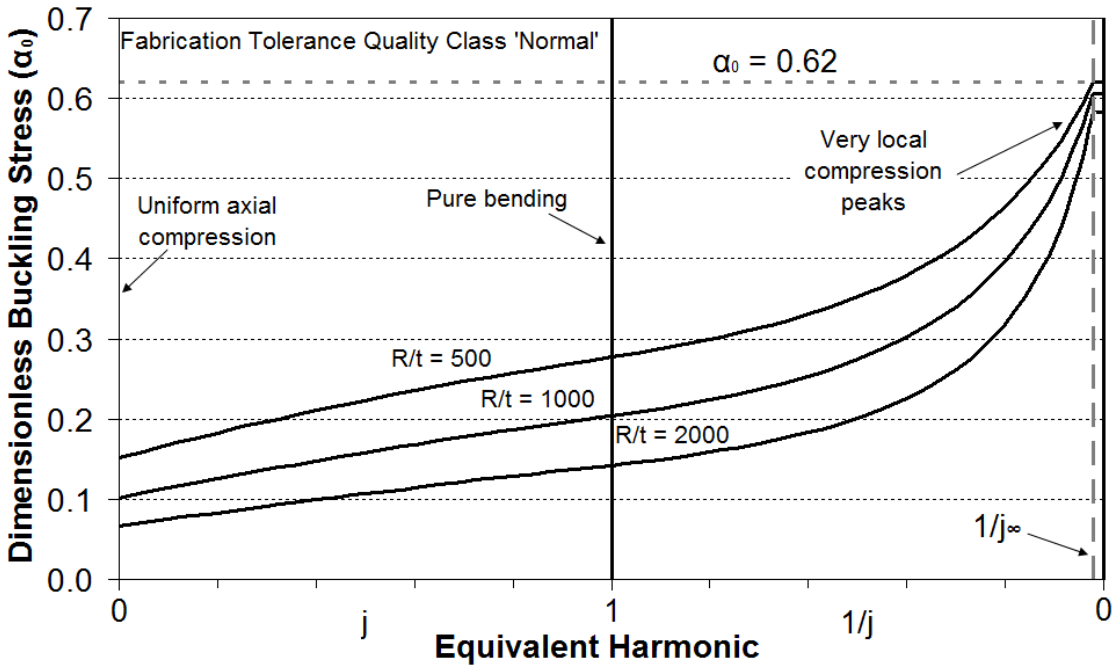

Fig. 9.31 – Effect of compressive stress peak localisation on the buckling stress according to EN 1993-4-1 (2007)

9.6.2 Example application of the failure criterion to the present results of eccentric pipe and mixed flow

The EN 1993-4-1 design procedure was applied to the results presented in this chapter for the LA analyses under eccentric mixed (EccM) and pipe flow (EccP) assuming n = 1.05 and 3.0 respectively (Fig. 9.32). The angular separation $\Delta\theta_g = 4(t/R)^{½}$ was found to be 6.8°. The resulting calculations are summarised in Table 9.8.

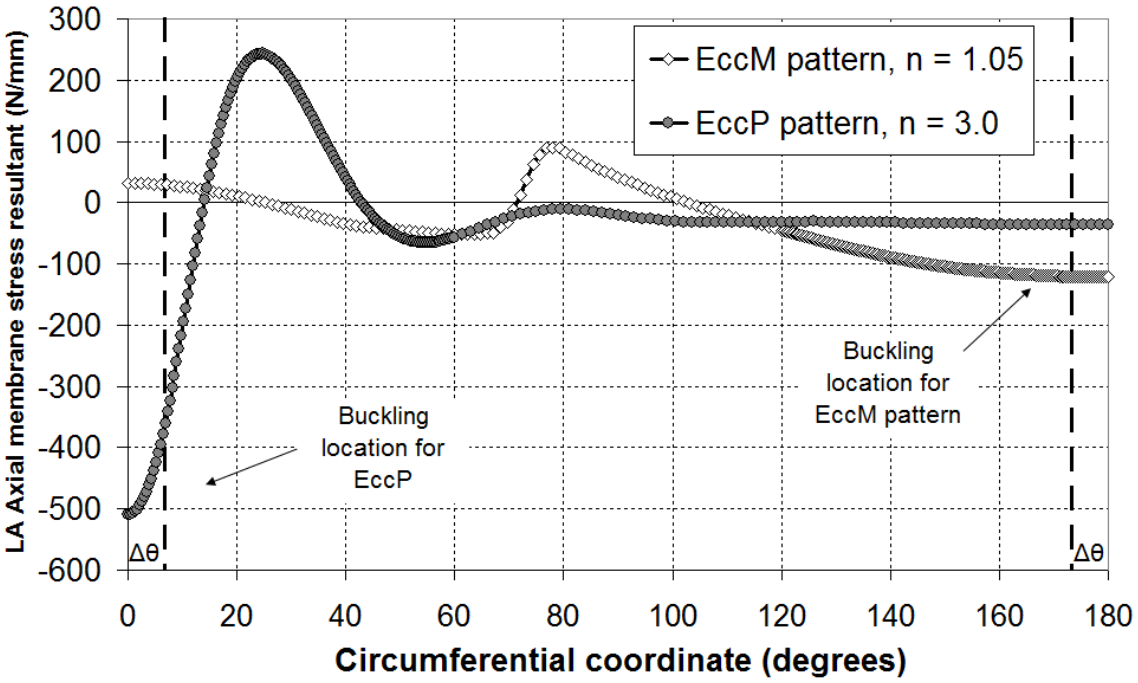

Fig. 9.32 – Circumferential distribution of (unfactored) LA axial membrane stress resultants at midheight for the EccM (n = 1.05) and EccP (n = 3.0) flow patterns

Table 9.8 – Application of the EN 1993-4-1 (2007) failure criterion to the EccM (n = 1.05) and EccP (n = 3.0) flow patterns

	$N_{x0,Ed}$ (N/mm)†	$N_{x1,Ed}$ (N/mm)†	$N_{x1,Ed}$ / $N_{x0,Ed}$	j	ψ	α_0	$N_{x,Rk}$ (N/mm)†	N @ LBA (N/mm)†
EccM	121.75	120.75	0.99	1.08	0.381	0.198	63.52	302.17
EccP	510.17	360.54	0.71	6.62	0.085	0.422	135.02	332.13
Reference	n/a	n/a	n/a	j_∞	0	0.094	30.20	n/a

† compression positive

For the EccM flow pattern, the equivalent harmonic j = 1.08 was found to be very close to the value for pure bending (j = 1) and reflects the fact that the spread of the compressive region from the axis of symmetry is approximately 80° at midheight (pure bending would give 90°). The unpressurised imperfection factor α_0 thus rises from 0.094 to 0.198, which increases the characteristic value of the axial membrane stress resultant at buckling $N_{x,Rk}$ from 30.20 to 63.52, an increase by a factor of 2.1.

By contrast, the equivalent harmonic for the EccP flow pattern was found to be the much higher value of j = 6.62 which reflects the highly localised nature of this

compressive peak (Fig. 9.32). The corresponding value of $N_{x,Rk}$ thus increases from 30.20 to 135.02 by a factor of 4.5.

The above procedure is highly conservative for four reasons. Firstly, the buckling stress can only ever reach approximately 60% of the classical value σ_{cl} because of a safety factor of $^4/_3$ and low reference strength built into the expression for α_0 (ECCS, 1988). Secondly, buckling is predicted to occur already when a single point reaches the buckling stress. However, considering the circumferential distribution of the axial membrane stresses for eccentric mixed flow (Fig. 9.29 and Fig. 9.32), it was found that a significant portion of the shell must first reach approximately the same critical stress in order for the LBA buckling mode to have enough space to form. Thirdly, the characteristic buckling stress resultants $N_{x,Rk}$ are significantly below the values at which both flow patterns were actually predicted to buckle in an LBA analysis, which instead found that the LA stress resultants at buckling almost always reached the classical value $N_{cl} = t\sigma_{cl}$ regardless of how localised they are. Lastly, the above conservatism is amplified in light of the discovery of the beneficial effect of geometric nonlinearity, whereby the predicted GNA buckling loads were often found to be over 50% higher than their LBA counterparts.

9.7 Conclusions

This chapter has provided strong evidence that the new mixed flow pressure theory may give credible predictions of silo behaviour. There are close similarities in terms of structural consequences predicted for the eccentric pipe flow patterns investigated in this study and the previous studies of Chapters 4 and 5 which investigated the structural effects of variations in flow channel size using the EN 1991-4 eccentric discharge pressure model. The EN 1991-4 model is effectively a special case of the mixed flow theory in which an eccentric pipe flow channel is assumed to extend over the entire height of the silo and to have parallel sides (i.e. infinitely steep, $n \rightarrow \infty$). This is a remarkable finding which supports the mixed flow pressure theory, because the two sets of flow channel geometries and their associated wall pressures are significantly different.

The supporting evidence works both ways. It may also be considered that the great simplifications of the EN 1991-4 pressure model are not invalid, since its predicted

structural consequences are very closely reproduced by a more complex and complete theory. Thus what is already in EN 1991-4 is not inappropriate as an aid to design against eccentric discharge.

The results of this study uphold the proposition that changes in geometry are beneficial under eccentric discharge. This proposition is supported by the results of a wide range of different flow channel geometries in which a relatively narrow strip of low pressure acts on the silo wall which is otherwise under a relatively uniform state of high internal pressure. However, the extent of this beneficial effect depends strongly on the flow pattern.

It was found that, under two mixed flow patterns of similar steepness but different outlet eccentricity, the silo buckles at almost the same critical value of the local axial membrane stress which corresponds approximately to the elastic critical buckling stress, even in a geometrically nonlinear analysis. This is despite the fact that the predicted buckling strength under the more eccentric channel is almost double the predicted buckling strength under the less eccentric channel. The mixed flow pattern which covers a smaller portion of the silo height applies a lower global overturning moment on the silo than the one which covers a larger portion and causes significantly lower magnitudes of compressive axial membrane stresses in the critical buckling location of the silo at the same load factor. Consequently, it requires a higher load factor to reach the critical value of the axial membrane stress.

An appropriate failure criterion found in EN 1993-4-1 (2007) based on the work of Rotter (1986) and others was explored in the context of providing a design procedure for highly localised axial compression, such as that caused by both eccentric pipe and mixed flow. The criterion is based on the concept of a significantly decreased elastic imperfection sensitivity under progressively more localised axial compression. It was found that this innovative procedure is a very conservative assessment of the linear buckling stress under high local axial compression, and the reasons for this conservatism were discussed. More work needs to be done to calibrate the various parameters in this criterion to the results of more recent research.

Chapter 10 – The structural consequences of flow channels with different eccentricity under mixed flow pressures

10.1 Introduction

This chapter presents the results of a parametric study into the structural effects of taper pipe flow channels with different values of outlet eccentricity. As the eccentricity of flow patterns is the central theme of this thesis, this final study sheds some light on the direct relationship between the predicted silo strength and the eccentricity of the channel, and investigates the associated changes in global pressure and stress patterns. The findings are finally discussed in the context of the prescribed rules for eccentric discharge present in some of the more common design standards.

10.2 Predicted pressure distributions and analyses

The stepped wall thickness Silo B (H = 14 m, R = 3.4 m, H/D = 2.06) was analysed under the wall pressures predicted by the mixed flow pressure theory presented in Chapter 7 for five taper pipe flow channels with different values of outlet eccentricity. The channel was assigned a constant outlet size of r_0/R = 0.074 (0.25 m) and a constant steepness of n = 1.5. The eccentricity of the outlet was varied in intervals of e_c/R = 0.25 from e_c/R = 0.00 to a value corresponding to an outlet whose outer edge just touches the silo wall, placed at one outlet radius short of the full radius; $e_c/R = (R - r_0)/R$ = 0.93. The granular material was assumed to be wheat, with the relevant material properties taken from Annex E of EN 1991-4 (2007). The properties of the stepped wall Silo B and wheat are summarised in Table 4.2 and Table 4.3. Both were used previously in the parametric finite element studies presented in Chapters 8 and 9.

The three and two-dimensional geometries of the full suite of flow channels are presented in Fig. 10.1 and Fig. 10.2 respectively. At zero eccentricity, the flow is concentric and fully internal, and therefore in Region 1 only. However, at maximum eccentricity, the flow is in Region 2 only. Between these two limits, both Regions 1 and 2 are present. The lowest depth of the effective transition, on the boundary between Regions 1 and 2, decreases progressively with outlet eccentricity (z_{12}/H = 0.30, 0.63 and 0.88 for e_c/R = 0.25, 0.50 and 0.75 respectively) and the channel passes gradually from concentric to eccentric taper pipe flow (ConP to EccP, Fig. 7.1). The flow regions are

defined in full in Section 7.2.2. The stationary solid is present down the entire height of Silo B in all channels investigated in this study, hence there is no Region 3 flow or mixed flow anywhere (EccM, Fig. 7.1).

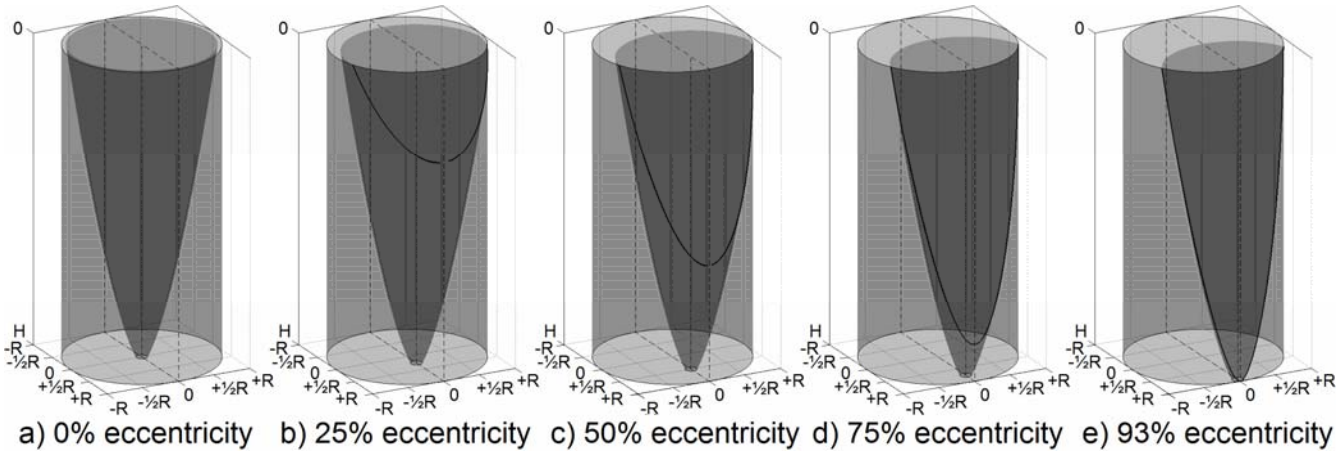

Fig. 10.1 – Three-dimensional channel and silo surfaces for Silo B as a function of the outlet eccentricity

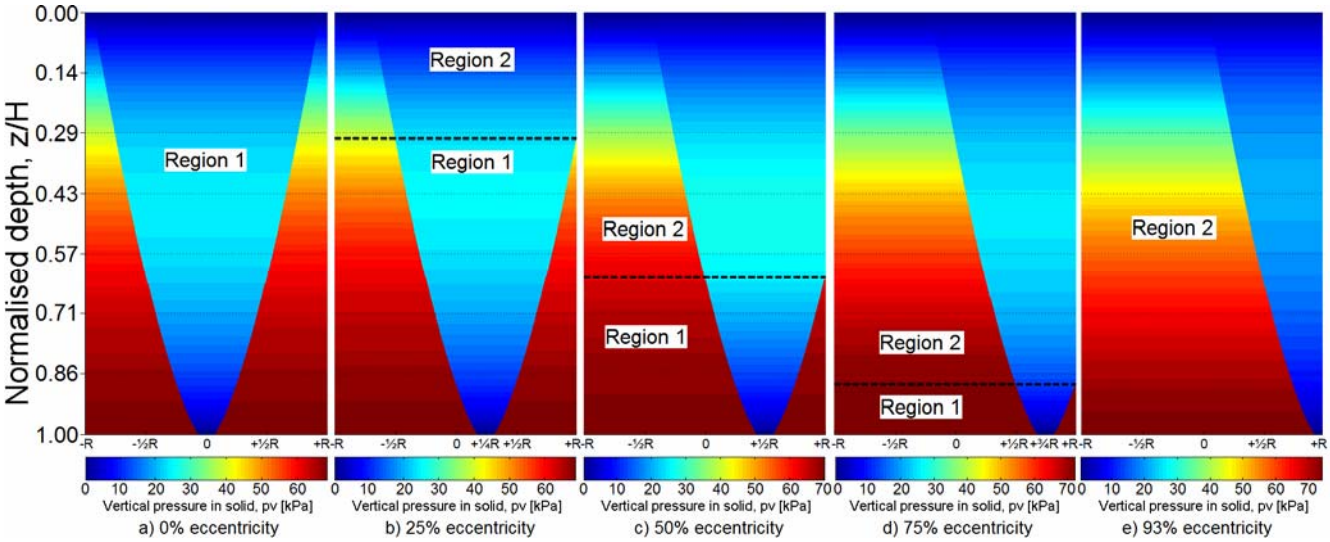

Fig. 10.2 – Colour contour plots of the vertical pressure distributions of the five taper pipe flow patterns as a function of the outlet eccentricity

The vertical distributions of the predicted vertical pressure in the flow channel and stationary solid as a function of the outlet eccentricity e_c/R are presented in Fig. 10.3 and Fig. 10.4 respectively. As there is no Region 3 present in any of the channels, BC2 is not invoked at any point (Fig. 7.10) and consequently there are no sudden jumps in vertical pressure in the stationary solid. Furthermore, although the channel geometries are very different for all five values of e_c/R, the predicted vertical pressure in both the

static and flowing solid does not vary significantly at all with eccentricity. The peak vertical pressure in the flow channel and stationary solid does not vary by more than approximately 10% of the local Janssen value (4.5 kPa and 6 kPa respectively) across the entire range of investigated eccentricities.

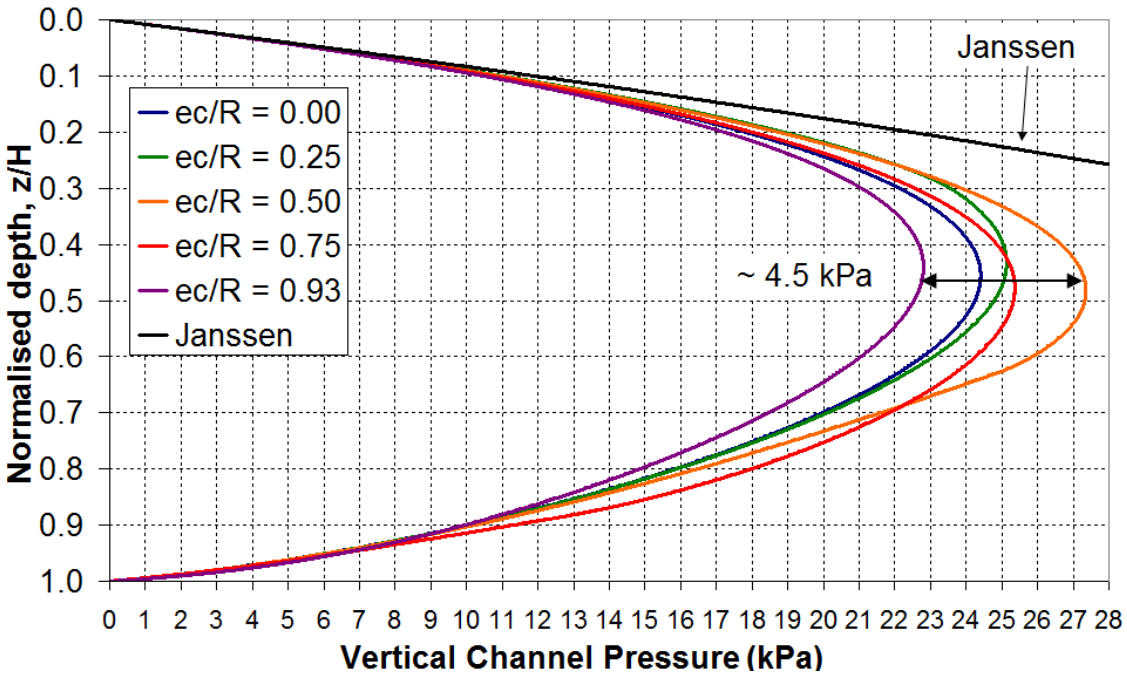

Fig. 10.3 – Vertical pressure in the flow channel as a function of the outlet eccentricity

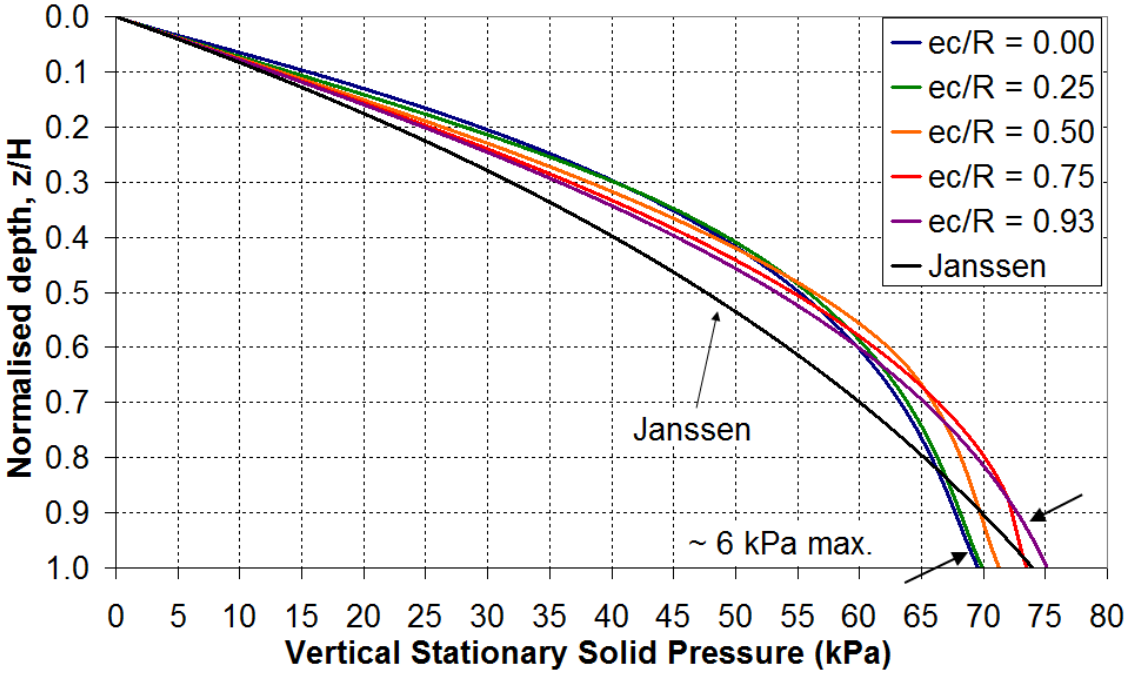

Fig. 10.4 – Vertical pressure in the stationary solid as a function of the outlet eccentricity

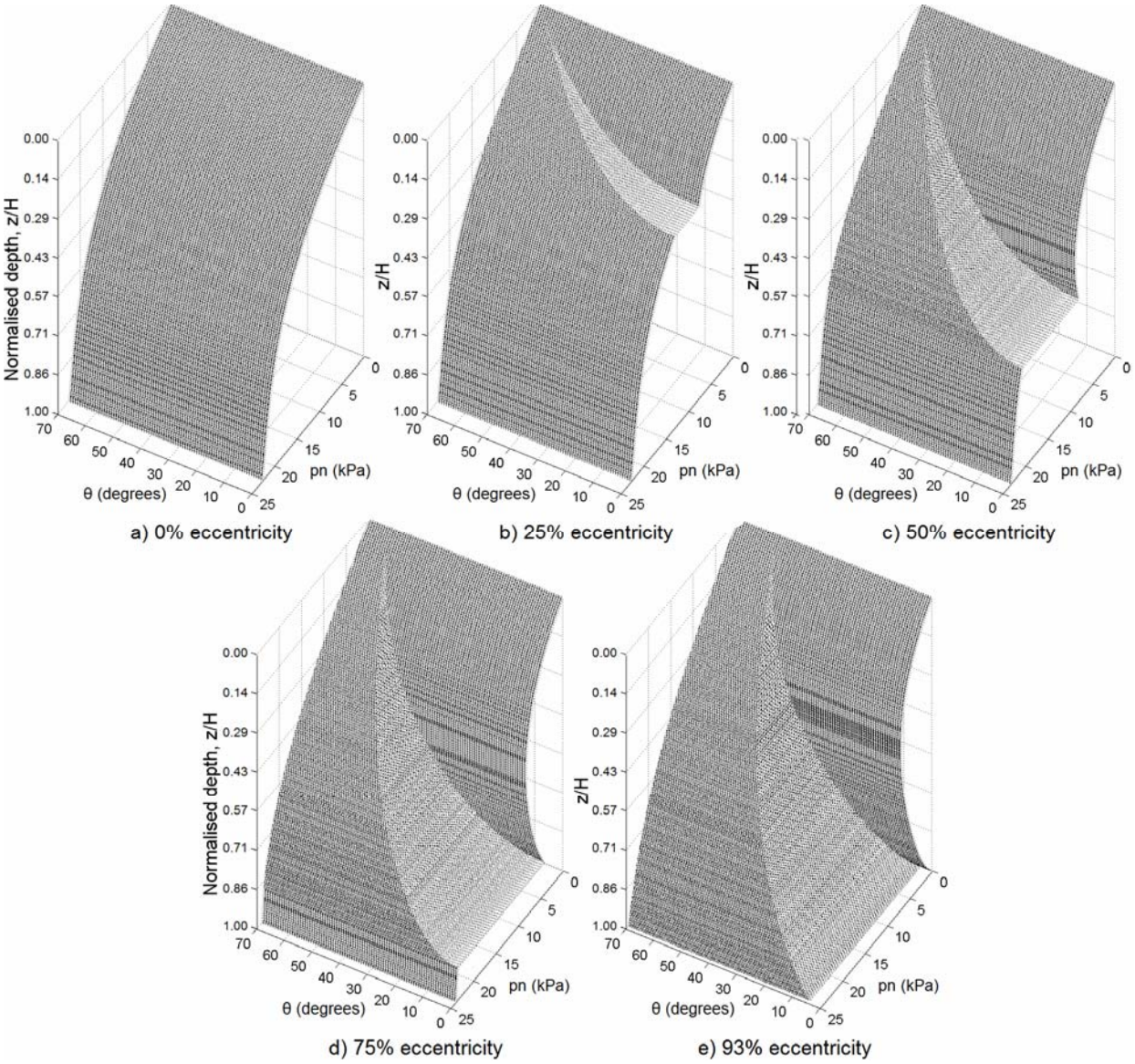

Fig. 10.5 – Three-dimensional surface plots of the normal wall pressure distributions for eccentric pipe flow patterns as a function of the outlet eccentricity

The global distributions of normal wall pressures for the five flow channels are presented in Fig. 10.5, showing the circumferential range within 70° of the outlet. Although the patterns of vertical pressure in the both the stationary and flowing solid are predicted to be very similar for all values of the outlet eccentricity, the patterns of normal wall pressure are not. As the eccentricity increases, a progressively deeper portion of the wall comes into contact with the flow channel (higher z_{12}/H) and experiences its associated low pressures. However, the contact between the flowing solid and the silo wall does *not* become significantly more circumferentially extensive, and the maximum flow channel wall contact angle stays at approximately 60° for all eccentricities. It is expected that in the current study a larger outlet eccentricity will

become gradually more deleterious to the strength of the silo, though experimental studies have shown that the most damaging outlet eccentricities are those near the middle of the range; approximately $0.50 \leq e_c/R \leq 0.80$ (Fleming, 1985; Fitz-Henry, 1986; Rotter, 2001b; Watson, 2010).

The full suite of computational analyses according to the EN 1993-1-6 (2007) framework was performed on the stepped wall Silo B for each value of the outlet eccentricity. This included the LBA, MNA, GNA, GMNA analyses and two different GMNIA analyses, using the same material properties for mild steel as in Chapters 8 and 9 (E = 200 GPa, ν = 0.3 and σ_y = 250 MPa). The imperfections used were the Type A axisymmetric weld depressions of Rotter and Teng (1989a) at 50% and 100% of the EN 1993-1-6 Section 8.7 imperfection amplitude for GMNIA analyses (Table 4.6). These imperfections were placed at regular intervals down the silo wall, including at changes of wall thickness. The frictional tractions were calculated directly from the predicted normal wall pressures using the upper characteristic value of the wall friction coefficient for wheat. No discharge factors C_h or C_w were applied to the wall pressures. A summary of failure mode acronyms used in this chapter is presented in Table 10.1.

Table 10.1 – Description of short-hand acronyms to describe failure modes

Acronym	Description
Axi-EF	Axisymmetric plastic elephant's foot buckling or yielding.
Axi-DD	Diamond pattern of deformation around the entire circumference, limited to being within a close distance of a wall strake or other boundary.
Axi-EL	Fully or partially axisymmetric elastic buckle.
Glb-EF	Global deformations, but with the main component of plastic elephant's foot-type buckling or yielding.
Glb-DD	Global diamond buckling mode
Glb-PL	Global plastic circumferential bending mode (the MNA mode).
Loc-CH	The characteristic or 'classic' mode associated with an eccentrically flowing channel: a local (predominantly) elastic buckle in the centre of the flow channel, at approximately midheight.

10.3 Investigation of the elastic buckling behaviour using geometrically linear and nonlinear analyses (LA, LBA and GNA)

10.3.1 Overview

The eccentric taper pipe flow patterns investigated in this study share many features with the EN 1991-4 eccentric discharge pressure model. These include a relatively steep flow channel with low pressures, a relatively narrow channel-wall contact, an effective transition that does not span the entire circumference, and Janssen-like stationary solid pressures applied to the greater majority of the silo wall. Naturally, there are important differences too, as the EN 1991-4 flow channel assumes parallel sides and covers the entire height of the silo, which is not the case for the present taper pipe flow patterns.

In previous studies presented in this thesis, the predicted failure modes of eccentric pipe flow patterns and the EN 1991-4 eccentric discharge model have been found to be solely by (predominantly elastic) buckling under compressive axial membrane stresses. The other stress components have not been found to be relevant to the same degree, hence it was decided that the descriptions presented here should focus on the axial membrane stress component. Furthermore, it will be shown that all LBA and GNA buckling modes are predicted to occur near the base of the thinnest 3 mm strake at a depth of $z/H = 0.57$ regardless of eccentricity, thus the approximate midheight region was considered most important when comparing stresses.

10.3.2 LBA and GNA load proportionality factors at failure

The computed LBA and GNA load proportionality factors are presented in Table 10.2 and plotted in Fig. 10.6 and Fig. 10.7. There is a small reduction in buckling strength from $e_c/R = 0.00$ to 0.25, followed by a very large drop in strength at an eccentricity of $e_c/R = 0.50$, then followed by a further but much smaller decrease in buckling strength up to the maximum eccentricity of $e_c/R = 0.93$ (Fig. 10.6). At the same time, the effect of geometric nonlinearity becomes progressively more beneficial with increasing outlet eccentricity, resulting in buckling strength gains of up to 55% at maximum eccentricity according to a GNA analysis (Fig. 10.7). The reported finding that medium values of the eccentricity cause the greatest reductions in the buckling strength has *not* been reproduced (Fleming, 1985; Fitz-Henry, 1986; Rotter 2001b; Watson, 2010). This is possibly due to the fact that the steepness of the channel n was kept constant at all eccentricities, but in reality it is likely that n depends on the the extent of the channel-

wall contact and is not constant with e_c/R. More research is needed to calibrate the different parameters in the mixed flow theory presented in Chapter 7.

Table 10.2 – Summary of computed LBA and GNA load proportionality factors as a function of the outlet eccentricity

Outlet eccentricity e_c/R	0.00 ConP	0.25	0.50 →	0.75	0.93 EccP
LBA	8.947	8.037	3.305	2.275	1.946
Failure mode†	Axi-EL @ all θ	Axi-EL @ $\theta = 180°$	Loc-CH @ $\theta = 0°$	Loc-CH @ $\theta = 0°$	Loc-CH @ $\theta = 0°$
GNA	8.915	8.280	3.905	3.408	3.027
Failure mode†	Axi-DD @ all θ	Axi-DD @ $\theta = 180°$	Loc-CH @ $\theta = 0°$	Loc-CH @ $\theta = 0°$	Loc-CH @ $\theta = 0°$
GNA / LBA	0.996	1.030	1.182	1.498	1.556

† all failure modes occur at the base of the 3 mm strake

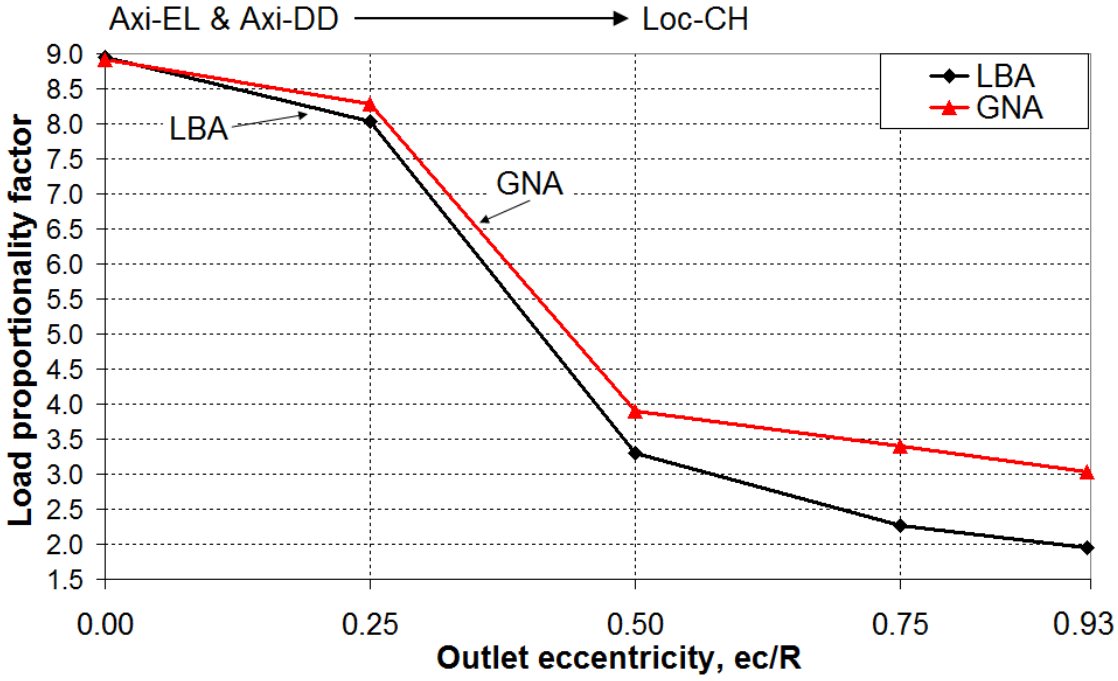

Fig. 10.6 – Distribution of computed LBA and GNA load factors with outlet eccentricity

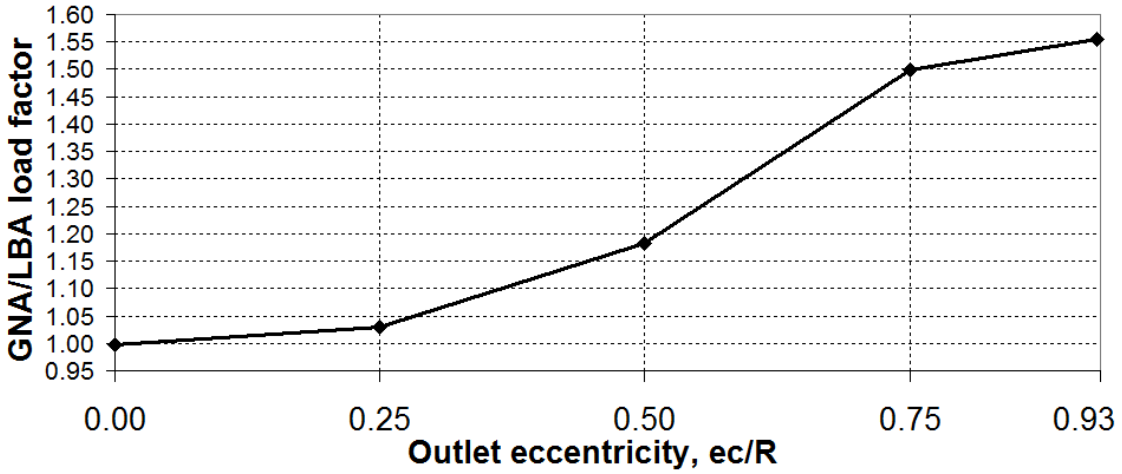

Fig. 10.7 – Distribution of the GNA load factor normalised by the LBA factor with outlet eccentricity; shows the gradual development of the beneficial effect of geometric nonlinearity

Each of the LBA and GNA load factors refers to elastic buckling failure at the base of the 3 mm strake, though at varying circumferential positions. For concentric flow, the LBA analysis predicts an axisymmetric elastic buckling mode (Axi-EL), while the GNA analysis predicts a diamond buckling mode (Axi-DD) present around the entire circumference. This is consistent with all analyses on concentric discharge performed in this thesis. As the eccentricity increases to e_c/R = 0.25, the LBA mode turns into a partially-axisymmetric elastic buckle opposite the outlet at θ = 180° (also mode Axi-EL), and similarly the GNA buckling mode predicts a diamond buckling mode that is concentrated around θ = 180° (mode Axi-DD). For outlet eccentricities beyond e_c/R = 0.50, the LBA and GNA analyses both predict the elastic midheight buckling mode Loc-CH across the channel, which has been shown to be characteristic of eccentric pipe flow throughout this thesis. The LBA linear bifurcation modes and GNA incremental buckling modes are shown in Fig. 10.8 and Fig. 10.9 respectively.

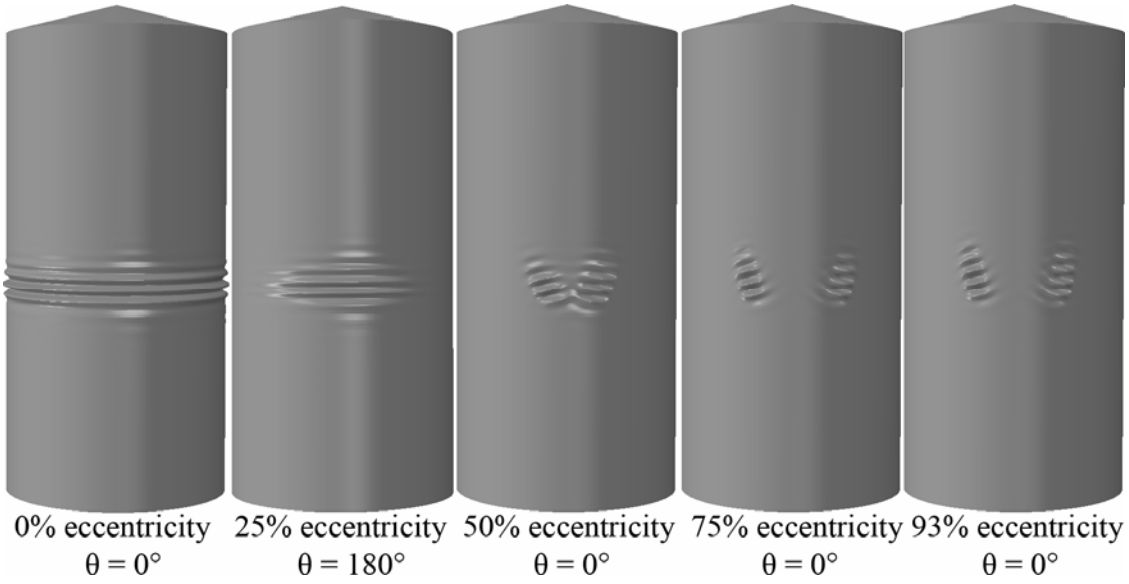

Fig. 10.8 – Predicted LBA buckling modes as a function of the outlet eccentricity (all at a geometric scale factor of 200)

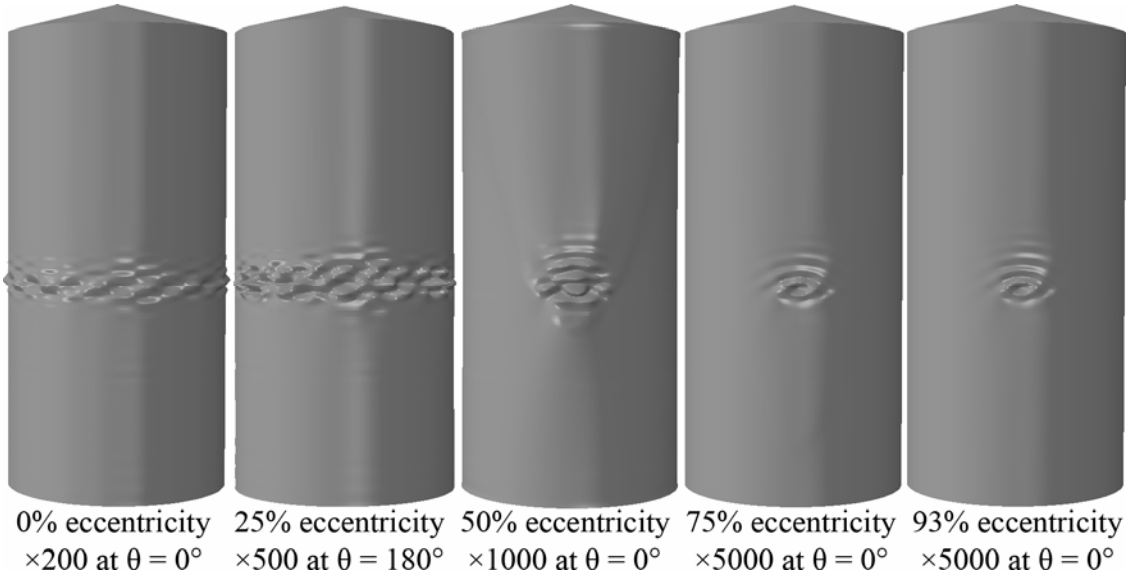

Fig. 10.9 – Predicted GNA buckling modes as a function of the outlet eccentricity

10.3.3 Linear and nonlinear axial membrane stress distributions at midheight

The preceding section clearly identifies the base of the 3 mm strake as critical for every buckling mode in this study. The base of this strake occurs at a depth of $z/H = 0.57$, but the buckling modes are naturally not confined to just this location, covering a finite portion of the wall up to a depth of approximately $z/H = 0.45$. The circumferential distributions of the LA and GNA axial membrane stress resultants at buckling failure were thus extracted at midheight ($z/H = 0.50$), which is very close to the middle of the

portion of the silo wall affected by each of the buckling modes. These are presented in Fig. 10.10 and Fig. 10.11.

Considering the distributions of LA axial membrane stress resultants at the LBA load factor for the five outlet eccentricities (Fig. 10.10), every one of these curves shows that buckling occurs when the axial membrane stress resultants have reached approximately the same value: ~ 290 N/mm for $e_c/R \leq 0.25$ and ~ 320 N/mm for $e_c/R \geq 0.50$. This value corresponds very closely to the stress resultant at to classical buckling stress for the 3 mm strake, $N_{cl} = t\sigma_{cl} \approx 0.605Et^2R^{-1} \approx 320.3$ N/mm. Thus it is clear that the buckles form where the stresses in the wall reach the classical buckling stress. The corresponding distributions of GNA axial membrane stress resultants in Fig. 10.11 show almost the same story.

The value of the LA and GNA axial compression is 290 N/mm at $z/H = 0.50$ for $e_c/R \leq 0.25$, slightly less than 320 N/mm. However, since the buckling mode covers a finite portion of the silo depth, the slightly higher critical value of N_{cl} *is* reached somewhere nearby where the largest displacements associated with the buckling mode are predicted to occur. The exact location where this does occur is different for every outlet eccentricity. Furthermore, the LA stress distribution for $e_c/R = 0.25$ shows that N_{cl} is close to being reached at two locations, both at $\theta = 0°$ and 180°, and it seems more due to coincidence that $\theta = 180°$ became critical first. At a slightly higher value of e_c/R, it is likely that the location at $\theta = 0°$ would instead have become critical. For the corresponding GNA stress distribution at $e_c/R = 0.25$, the position at $\theta = 180°$ is clearly the critical one. The question therefore remains as to why the load factors were so much lower for the flow patterns at higher eccentricities if all buckles formed at approximately the same value of the critical stress.

It is interesting to note that the compressive peak in an LA analysis occurs approximately 25° off-centre, resulting in a type of LBA ‘double buckle’ (Fig. 10.8). A similar result was previously reported for $k_c = r_c/R = 0.90$ in Fig. 5.6 for the EN 1991-4 flow channel size study, and for $n = 1.5$ in Fig. 9.12 for the mixed flow theory channel steepness study. It appears to be a recurring finite element prediction for eccentric pipe flow channels with wide wall contact angles, but it is not known whether such a buckle has been observed in practice.

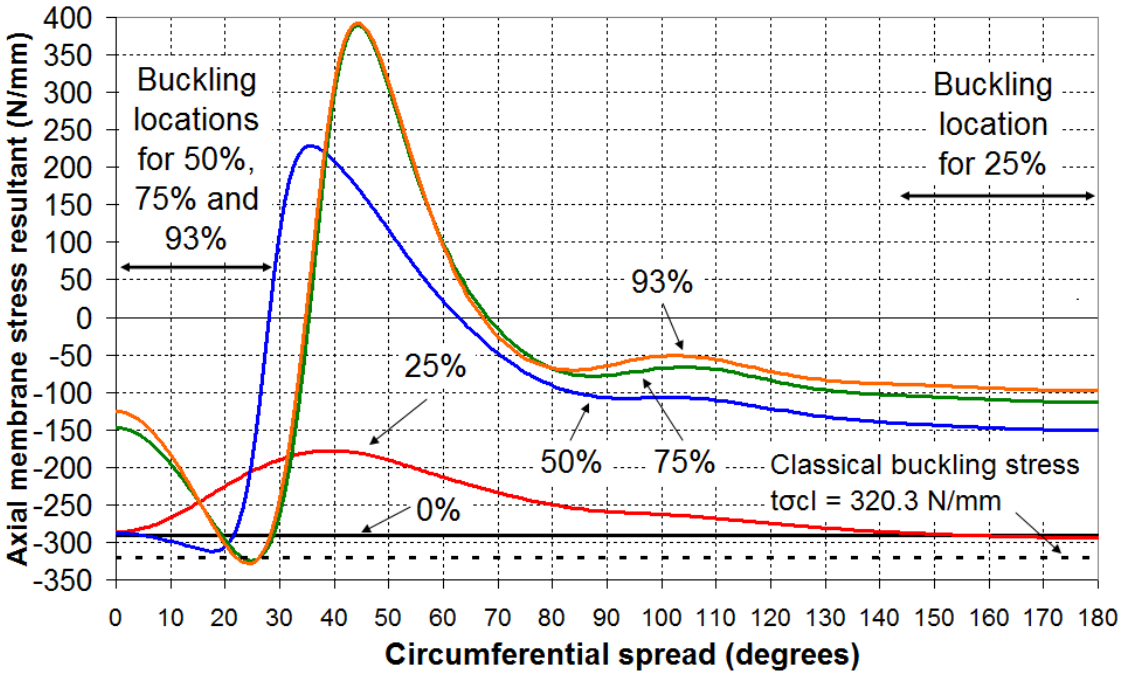

Fig. 10.10 – Circumferential distribution of axial membrane stress resultants at midheight within the 3 mm strake for LA @ LBA

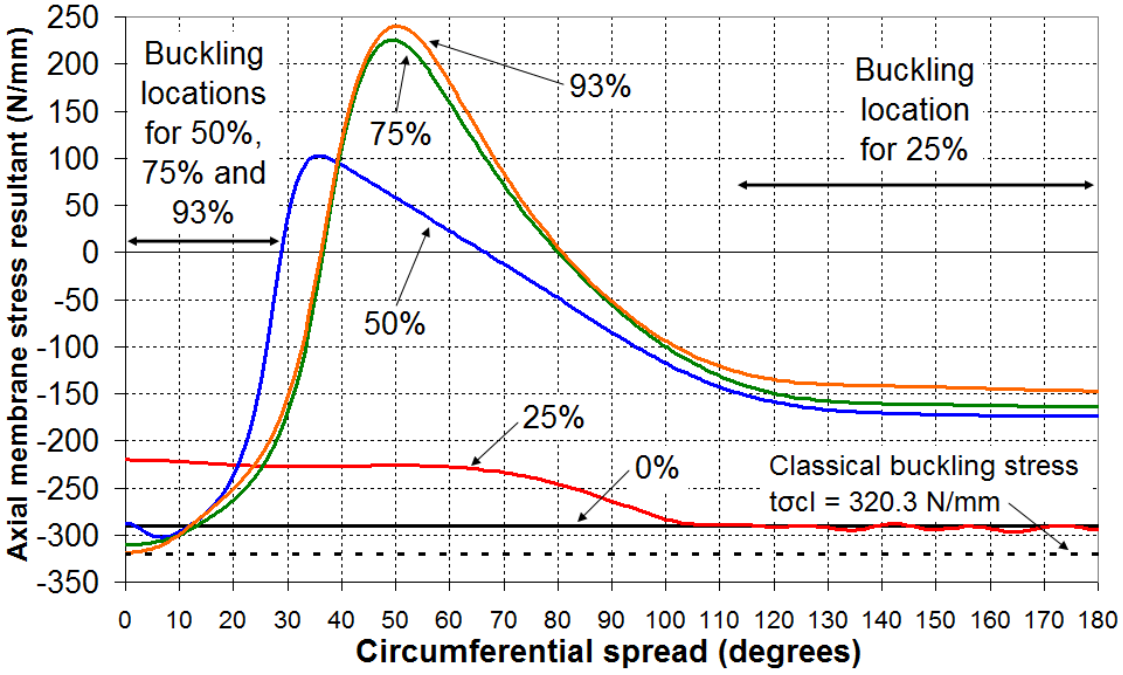

Fig. 10.11 – Circumferential distribution of axial membrane stress resultants at midheight within the 3 mm strake for GNA @ bifurcation

10.3.4 Investigation of the sudden drop in load factor from e_c/R = 0.25 to 0.50

The LA and GNA axial membrane stresses at z/H = 0.50 are shown in Fig. 10.12 and Fig. 10.13, at the same load factor of *unity*. Both of these sets of distributions suggest that the pattern of stresses near the critical buckling location changes drastically with

increasing eccentricity as the flow channel comes into contact with a progressively deeper portion of the silo wall. The low normal wall pressure associated with the flow channel increases the axial compression locally to a progressively higher value. Consequently, whichever value of the outlet eccentricity results in the highest magnitude of axial compression at the same load factor of unity, the stresses at that eccentricity require multiplication by a lower load factor to reach the critical value of the elastic buckling stress N_{cl}.

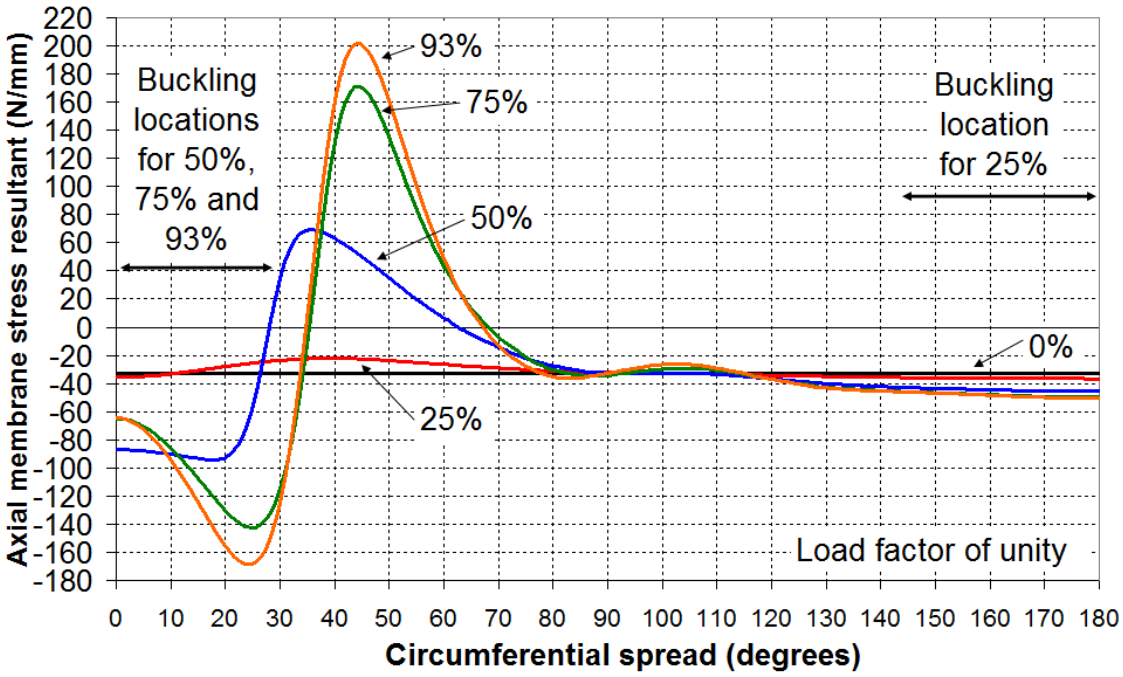

Fig. 10.12 – Circumferential distribution of midheight LA axial membrane stress resultants at a load factor of unity

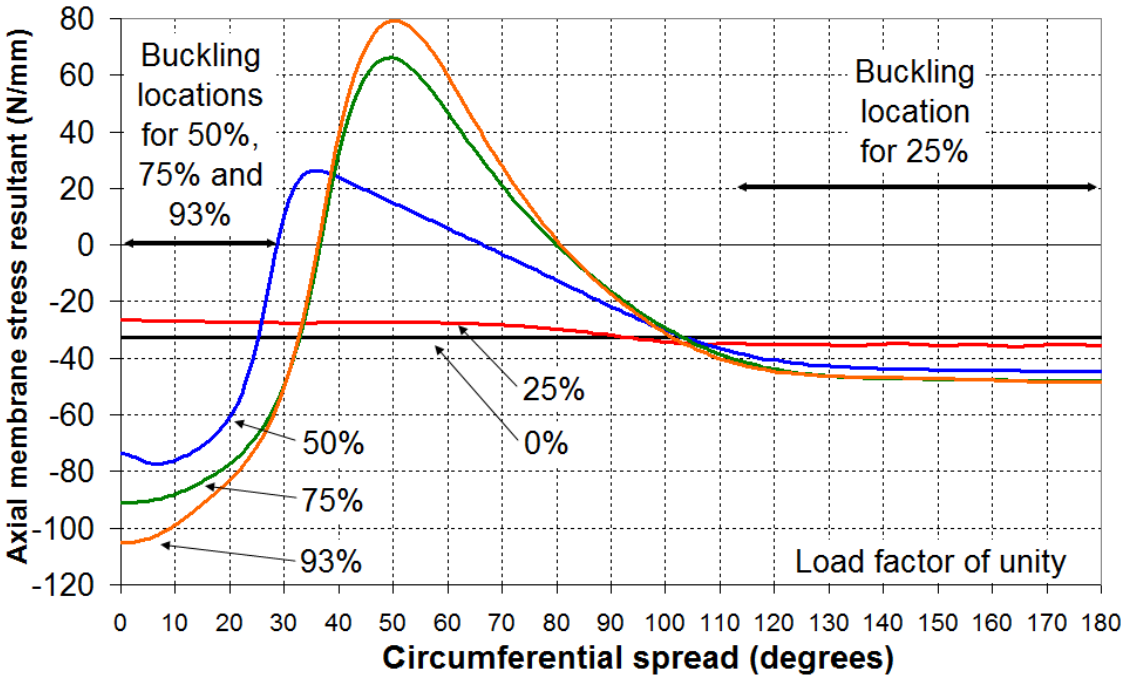

Fig. 10.13 – Circumferential distribution of midheight GNA axial membrane stress resultants at a load factor of unity

At e_c/R = 0.25, the contact of the channel with the wall is too small to cause any significant increases in axial compression at z/H = 0.50 because the lowest point of the effective transition has not yet reached this level, occurring much higher at z_{12}/H = 0.30 (Fig. 10.5). But for $e_c/R \geq 0.50$, $z_{12}/H \geq 0.63$ hence the region of the wall near the base of the 3 mm strake at z/H = 0.57 is now affected by the low wall pressure, and the local axial compression increases accordingly. Thus the rather steep drop in load factor from e_c/R = 0.25 to 0.50 (Table 10.2) appears to correspond to the change in the location of the lowest point of the effective transition z_{12}/H, which descends from being above to below the critical buckling region at the base of the 3 mm strake respectively. Thus once the effective transition is within the 4 mm strake, any subsequent increase in eccentricity only results in relatively minor increases in the magnitude of the drop in normal wall pressure from stationary to flowing solid at the critical location, and the consequent increase in axial compression and decrease in load factor is small.

10.3.5 The effect of geometric nonlinearity

Considering again the midheight distributions of LA and GNA axial membrane stresses at a load factor of unity (Fig. 10.12 and Fig. 10.13), the peak compressive value was extracted as a function of the outlet eccentricity e_c/R and compared for both sets of analyses. The GNA analyses were found to predict significantly lower peak

compressive stresses at the same load factor than the LA analyses, thus supporting the finding that geometric nonlinearity has an important beneficial effect. An interesting pattern emerges when the ratios of the peak LA to GNA compressive axial membrane stresses are plotted against the outlet eccentricity (Fig. 10.14), as it shows that the progressive growth of the extent to which the LA analysis overestimates this peak, reaching almost 60% for maximum eccentricity. When compared to the variation of the GNA/LBA load factor ratio with eccentricity, the relationship is very similar indeed. The most likely reason for the beneficial effect of changes of geometry may be found in the context of a beam theory analogy in Chapter 3.

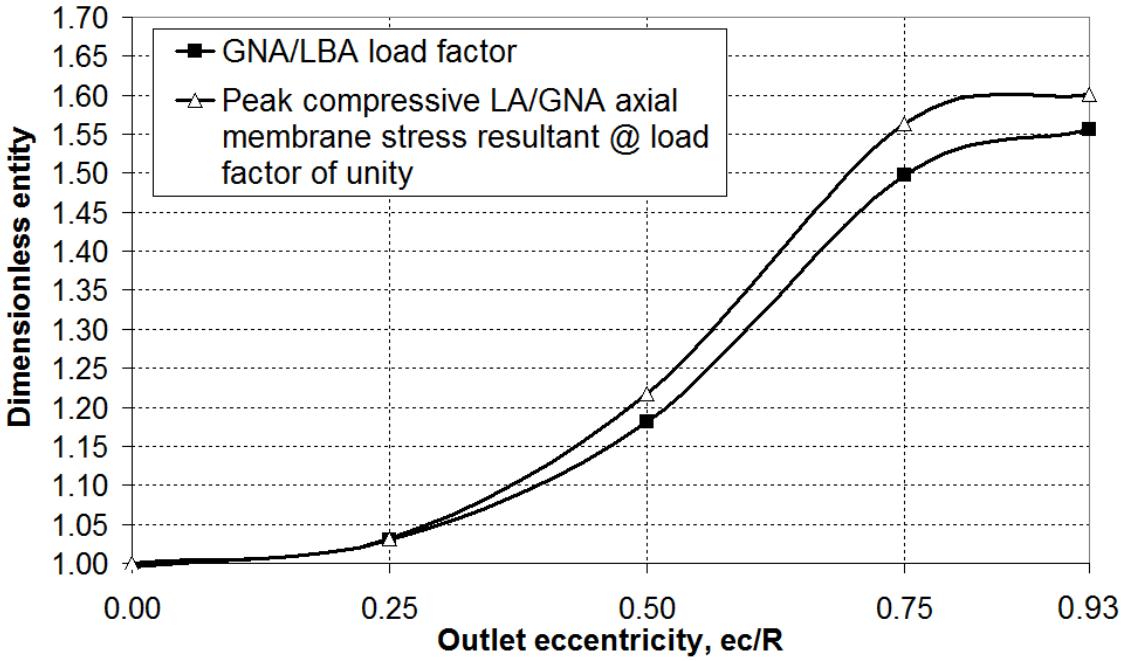

Fig. 10.14 – Distribution of two dimensionless entities with outlet eccentricity

10.4 Presentation of the geometrically linear and nonlinear axial membrane stress distributions at additional circumferential locations

The evidence presented in the previous section attempted to explain the predicted buckling behaviour of the stepped wall Silo B under eccentric taper pipe flow of increasing outlet eccentricity. For the purposes of completeness, this section presents some of the rather exotic axial distributions of LA and GNA axial membrane stresses that occur at various circumferential locations and the progressive development with e_c/R of the characteristic pattern of axial membrane stresses associated with eccentric pipe flow. The characteristic pattern was first introduced in Chapter 2 for the EN 1991-4 eccentric discharge pressure model (Fig. 2.9 and Fig. 2.13).

The axial distributions of axial membrane stress resultants at $\theta = 0°$, 45° and 90° for the LA and GNA analyses at buckling are shown in Figs 10.15 to 10.20. These three circumferential locations correspond to the flow channel centre, edge and significantly away from the flow channel respectively. The curves for $e_c/R = 0.00$ (Fig. 10.15 and Fig. 10.16) show the expected response to axisymmetric Janssen-like wall pressures, and are naturally independent of the circumferential position. They are thus the same on all three figures. These distributions confirm that the classical buckling stress N_{cl} is only ever reached at the base of the 3 mm strake in all analyses, though the LA and GNA axial membrane stress resultant for $e_c/R = 0.00$ also appears to be very close to the value of N_{cl} at the base of the 4 mm strake. The values of N_{cl} for each wall thickness strake are summarised in Table 10.3.

Table 10.3 – Summary of critical N_{cl} values for each wall strake

Wall thickness (mm)	3	4	5	6
N_{cl} (N/mm)†	320.3	569.4	889.7	1281.2

† Note: $N_{cl} = t\sigma_{cl} \approx 0.605Et^2R^{-1}$ assuming $E = 200$ GPa and $R = 3400$ mm

For the LA and GNA analyses at $e_c/R = 0.25$, the compression at the base of the silo has decreased significantly from its value at $e_c/R = 0.00$. A compressive peak is also beginning to develop at $z_{12}/H = 0.30$, very close to the local position of the effective transition at the boundary between Region 1 and 2. This location corresponds to a sudden rise in wall pressures. At higher eccentricities, the location of this compressive peak continues to follow the descending z_{12}/H boundary very closely. For $e_c/R \geq 0.50$, the axial membrane stress at the base of the silo has become tensile and becomes more so as e_c/R increases further. In this range, the distribution of axial membrane stresses throughout the silo height becomes similar to the characteristic EN 1991-4 flow channel 'centre' distribution (compare with Fig. 2.9 and Fig. 2.13).

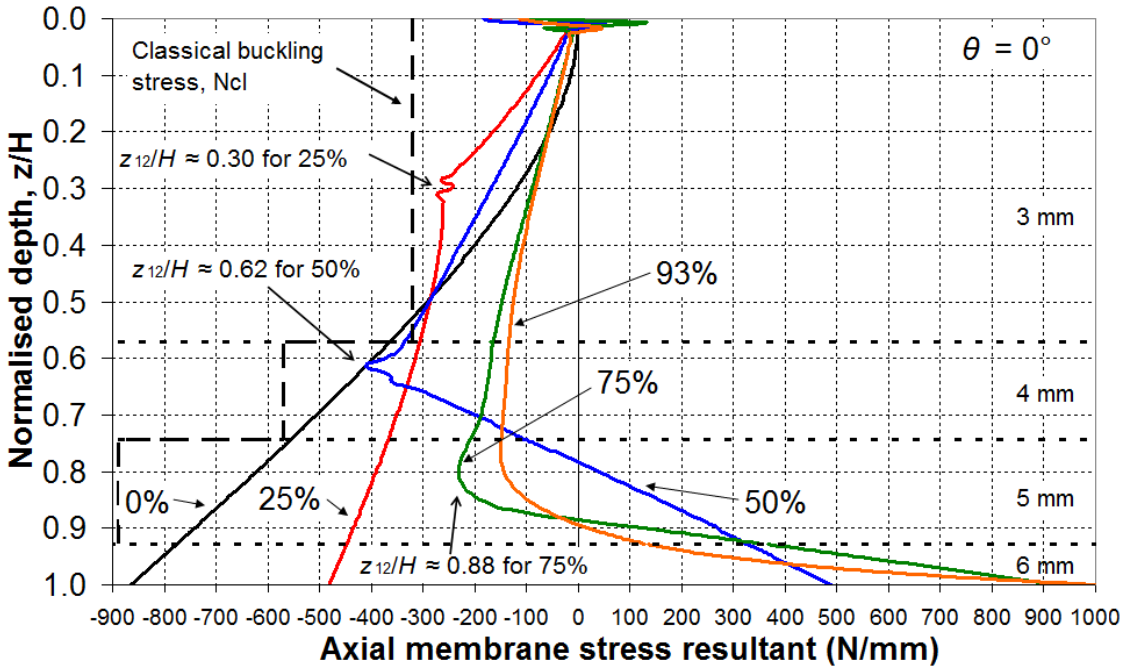

Fig. 10.15 – LA @ LBA axial membrane stress resultants at $\theta = 0°$

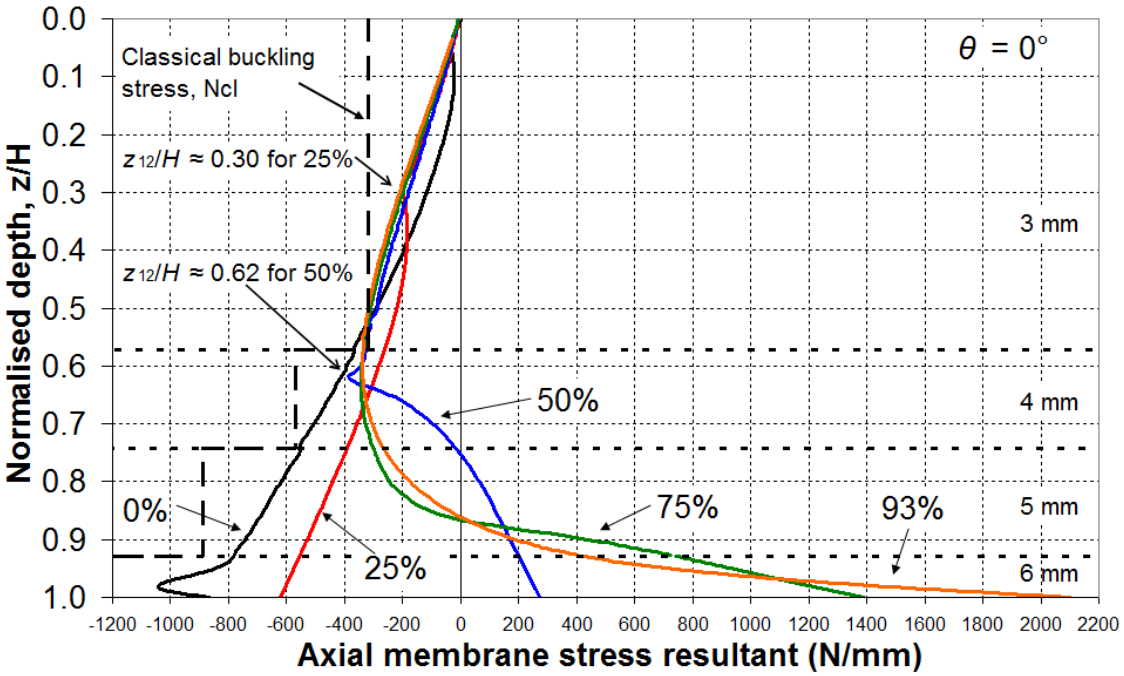

Fig. 10.16 – GNA @ bifurcation axial membrane stress resultants at $\theta = 0°$

The distributions of the LA and GNA axial membrane stress resultants at buckling for the circumferential position at $\theta = 45°$ are presented in Fig. 10.17 and Fig. 10.18 respectively. The position $\theta = 45°$ is close to the edge of the portion of the silo wall that is covered by the flow channel. With increasing outlet eccentricity, tensile peaks develop in these curves, rather than compressive peaks as seen for $\theta = 0°$ in Fig. 10.15

and Fig. 10.16. The positions of these tensile peaks also correspond closely to the local positions of the effective transition $z_{\text{Eff.Tr}}/H$, as annotated in the figures. For $e_c/R \geq 0.50$, the distribution of axial membrane stresses begins to be very similar to the characteristic EN 1991-4 flow channel 'edge' distribution (compare again with Fig. 2.9 and Fig. 2.13).

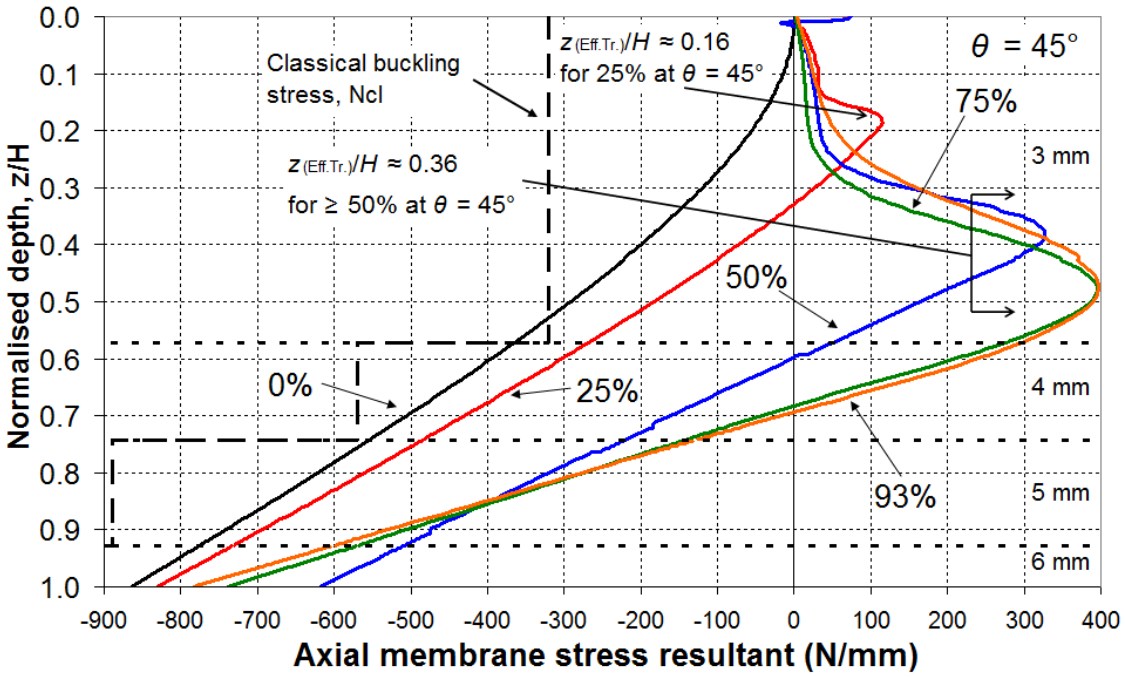

Fig. 10.17 – LA @ LBA axial membrane stress resultants at $\theta = 45°$

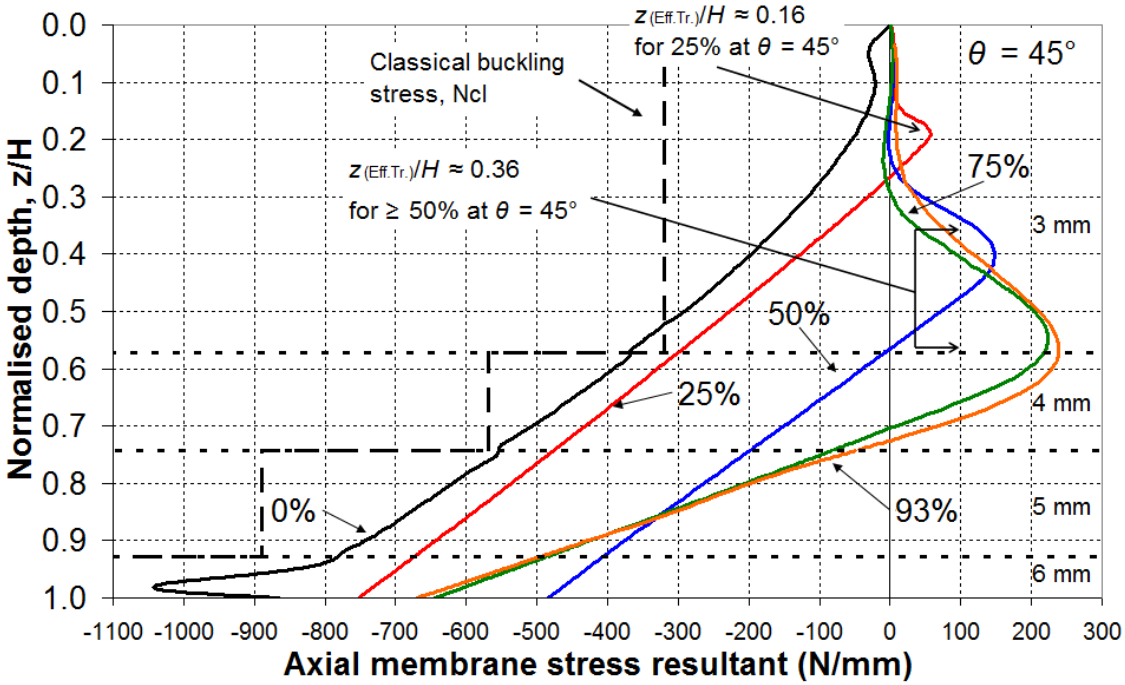

Fig. 10.18 – GNA @ bifurcation axial membrane stress resultants at $\theta = 45°$

Lastly, the LA and GNA axial membrane stress resultants for $\theta = 90°$ at buckling (Fig. 10.19 and Fig. 10.20) seem largely unaffected by the flow channel and show Janssen-like distributions throughout without any apparent anomalies. Thus all five flow channels are predicted to have a mostly local influence on the axial membrane stresses in the shell.

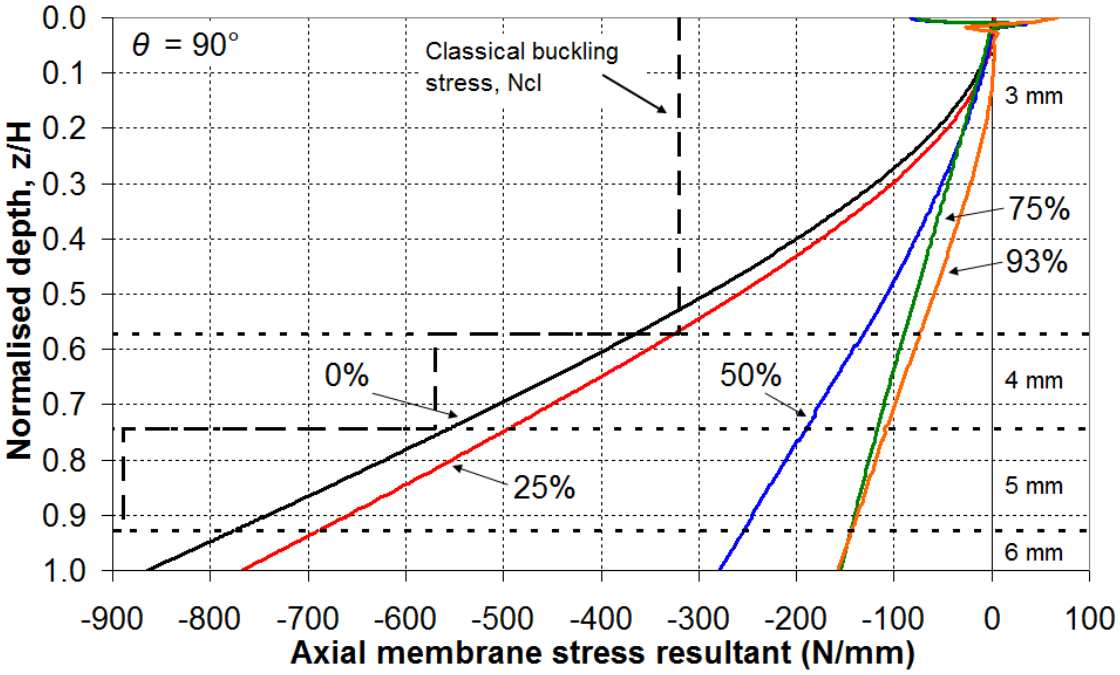

Fig. 10.19 – LA @ LBA axial membrane stress resultants at $\theta = 90°$

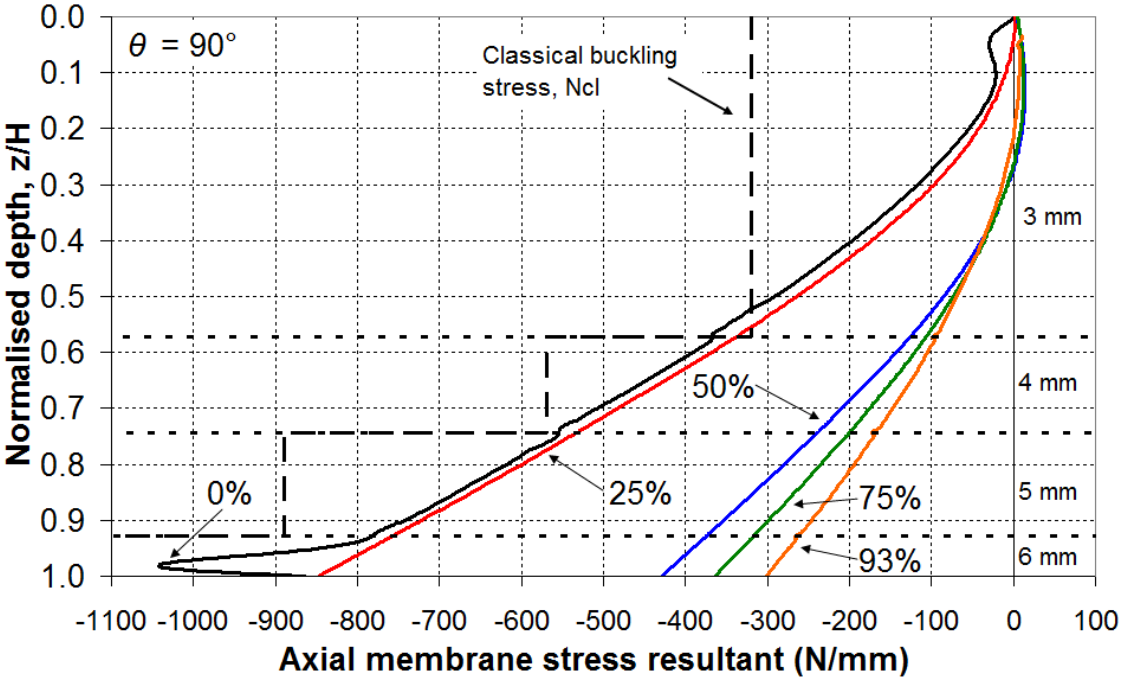

Fig. 10.20 – GNA @ bifurcation axial membrane stress resultants at $\theta = 90°$

10.5 Materially nonlinear analyses (MNA)

The predicted load proportionality factors for the MNA analyses are listed in Table 10.4 and plotted in Fig. 10.21, together with the corresponding LBA and GNA load factors for comparison. Although the MNA factor is smaller than both the LBA and GNA factors for $e_c/R = 0.00$, it becomes larger than all other factors when $e_c/R \geq 0.25$, especially so for $e_c/R \geq 0.50$ where a significant contact has developed between the eccentric taper pipe flow pattern and the silo wall.

Table 10.4 – Summary of computed LBA, MNA and GNA load proportionality factors as a function of the outlet eccentricity

Outlet eccentricity	0.00	0.25	0.50	0.75	0.93
e_c/R	ConP		→		EccP
LBA	8.947	8.037	3.305	2.275	1.946
GNA	8.915	8.280	3.905	3.408	3.027
MNA &	8.591	8.370	7.852	5.487	4.290
Collapse mode	Axi-EF†	Glb-EF†	Glb-PL	Glb-PL	Glb-PL

† at the base of the 3 mm strake

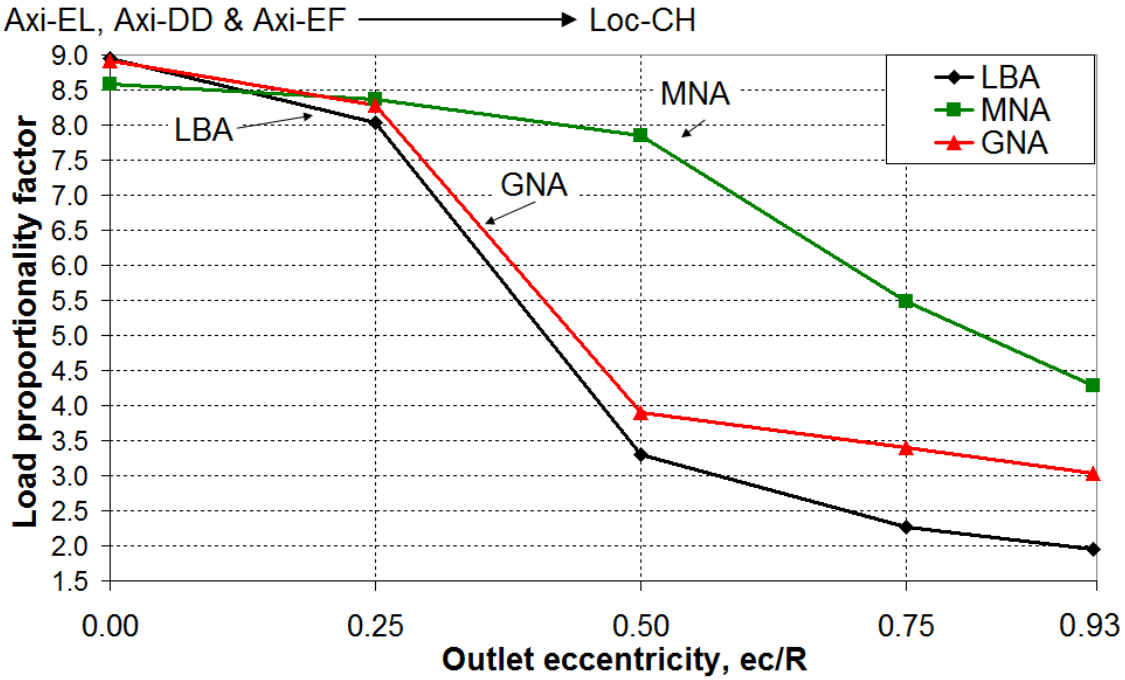

Fig. 10.21 – Distribution of computed LBA, MNA and GNA load factors with outlet eccentricity

The predicted MNA plastic collapse modes are presented in Fig. 10.22, showing very extensive circumferential bending at higher eccentricities. For e_c/R = 0.00 and 0.25, both MNA analyses result in an elephant's foot plastic collapse mode at the base of the 3 mm strake. This mode is fully axisymmetric for e_c/R = 0.00 but locally centred near θ = 180° for e_c/R = 0.25, and may be classified as Axi-EF and Glb-EF respectively (Table 10.1). For $e_c/R \geq 0.50$, the plastic collapse modes may be classified instead as Glb-PL, but these are not expected to play any further role in the behaviour of the silo. It has been discussed consistently throughout this thesis that the analyses of many authors including Jenike (1967), Bucklin *et al.* (1980), Colijn and Peschl (1981), Wood (1983), Roberts and Ooms (1983), Safarian and Harris (1985) and Ooms and Roberts (1986) were incorrect in their assumption that the silo under eccentric discharge fails through circumferential bending. This is confirmed once again in this set of MNA analyses.

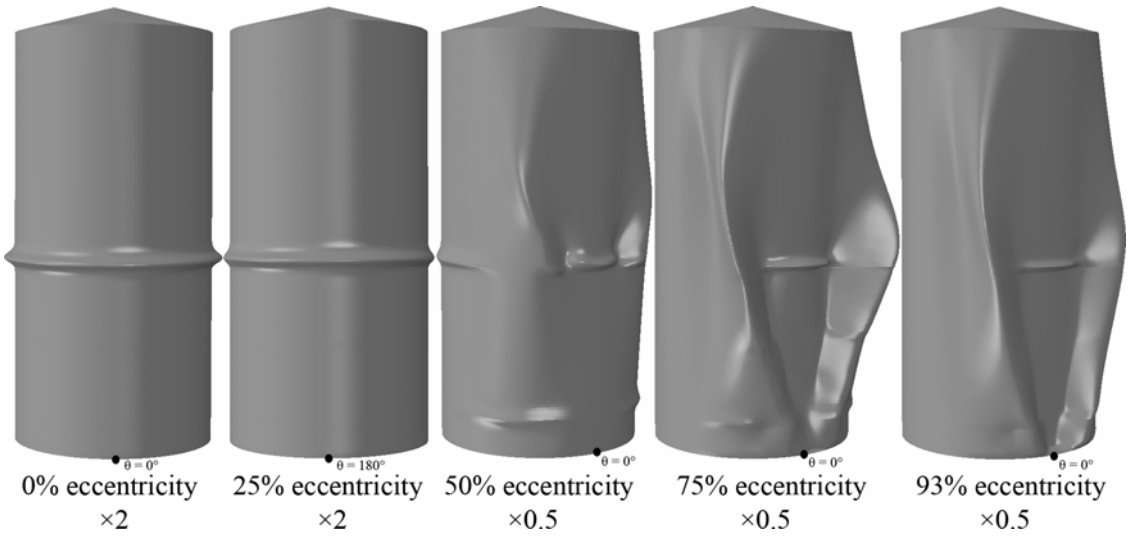

Fig. 10.22 – Predicted MNA plastic collapse modes as a function of the outlet eccentricity

10.6 Geometrically and materially nonlinear analyses (GMNA)

Material plasticity was found to have a negligible influence on the buckling behaviour for flow patterns with outlet eccentricities greater than e_c/R = 0.50, consistent with previous findings in this thesis for plasticity under eccentric pipe flow. At eccentricities of $e_c/R \leq 0.25$, where the characteristic concentric discharge behaviour still dominates, material plasticity was found to be responsible for reductions in buckling strength of up to 17%. The predicted GMNA load factors are thus shown in Table 10.5 and plotted in Fig. 10.23 and Fig. 10.24. The buckling modes are shown in Fig. 10.25.

Table 10.5 – Summary of computed LBA, GMNA and GNA load proportionality factors as a function of the outlet eccentricity

Outlet eccentricity e_c/R	0.00	0.25	0.50	0.75	0.93
	ConP		→		EccP
LBA	8.947	8.037	3.305	2.275	1.946
GNA	8.915	8.280	3.905	3.408	3.027
GMNA & Buckling mode	7.334	6.859	3.905	3.408	3.009
	Axi-EF† @ all θ	Glb-EF‡ @ $\theta = 180°$	Loc-CH‡ @ $\theta = 0°$	Loc-CH‡ @ $\theta = 0°$	Loc-CH‡ @ $\theta = 0°$

† at the base of the silo

‡ at the base of the 3 mm strake

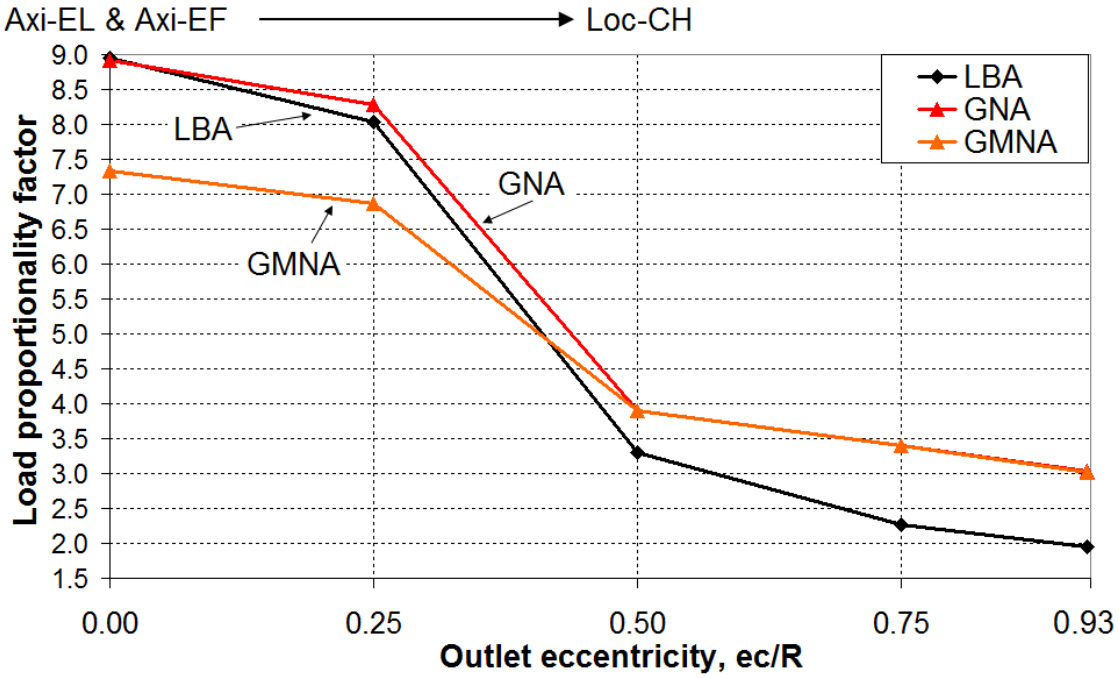

Fig. 10.23 – Distribution of computed LBA, GNA and GMNA load factors with outlet eccentricity

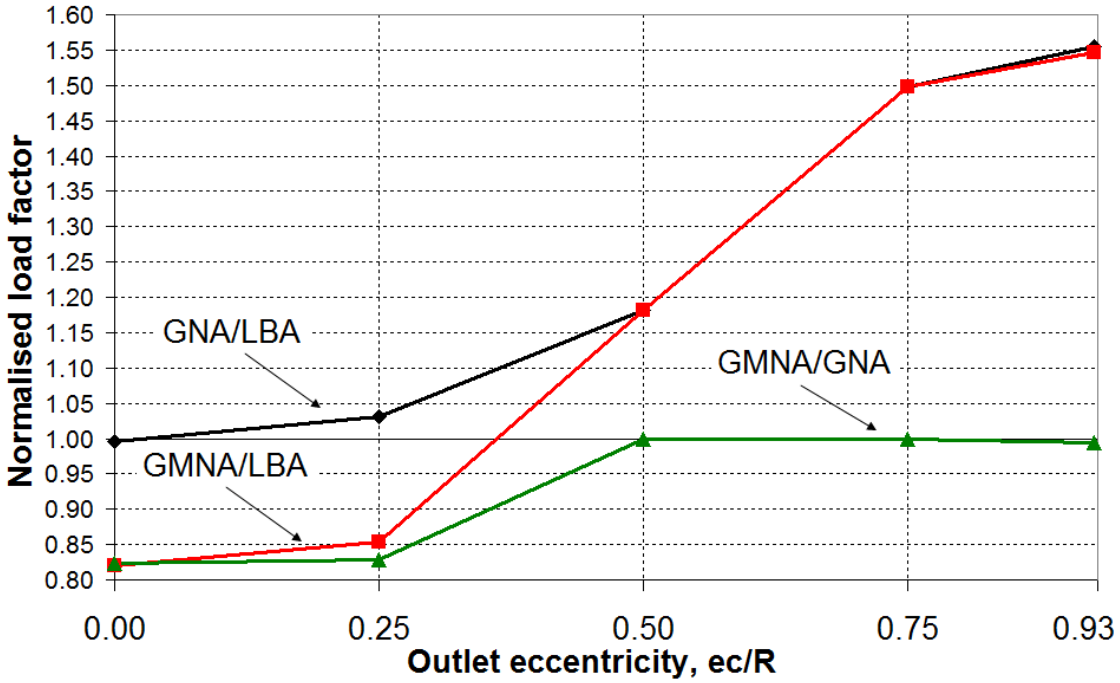

Fig. 10.24 – Distribution of the different normalised load factors with outlet eccentricity

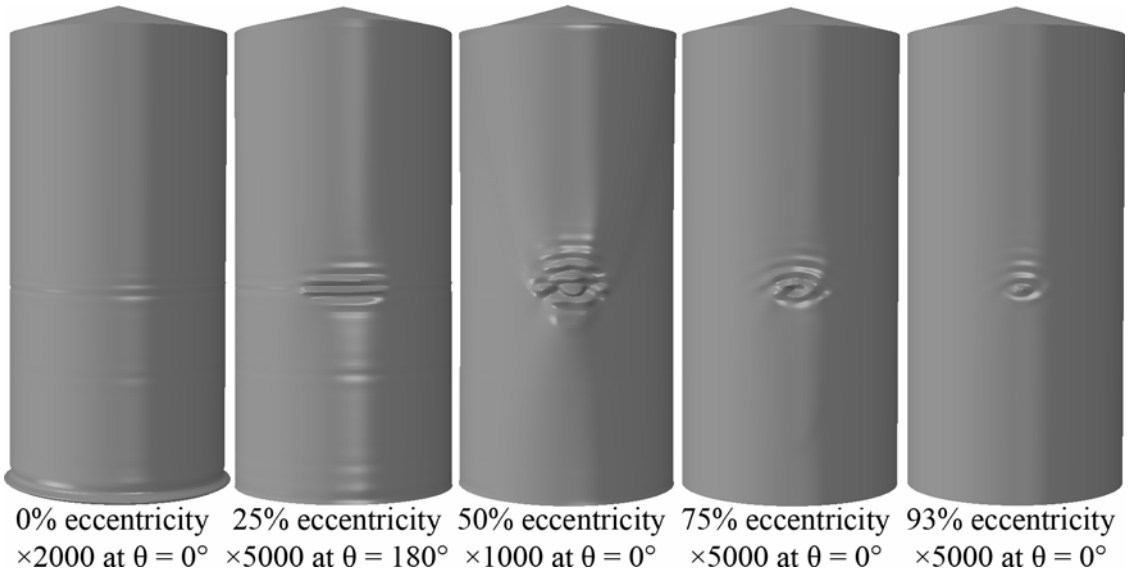

Fig. 10.25 – Predicted GMNA buckling modes as a function of the outlet eccentricity

The GMNA buckling mode for e_c/R = 0.00 is axisymmetric plastic elephant's foot (mode Axi-EF) at the base of the silo, not at the 3 mm strake. At e_c/R = 0.25, the elephant's foot buckling mode is predicted to occur more locally, this time opposite the outlet but at the base of the same strake (mode Glb-EF). For higher eccentricities, the GMNA buckling modes very closely reflect the type, location and overall size of the GNA buckling modes shown in Fig. 10.9. Indeed, the GMNA load factors and buckling

modes at e_c/R = 0.50, 0.75 and 0.93 are almost identical to those of the GNA, suggesting fully elastic behaviour once eccentric taper pipe flow has developed.

10.7 Geometrically nonlinear analyses with weld imperfections (GMNIA)

The full set of load proportionality factors at failure are summarised in Table 10.6 and plotted in Fig. 10.26 and Fig. 10.27 as a function of the outlet eccentricity. These results include both GMNIA analyses which used the axisymmetric weld imperfection of Rotter and Teng (1989a) at 50% and 100% of the EN 1993-1-6 Section 8.7 amplitude requirement (Table 4.6).

The two sets of GMNIA load factors were found to be consistently lower than the GMNA load factors for all eccentricities, thus the effect of axisymmetric weld imperfections was found to be consistently deleterious for all eccentric taper flow channels investigated in this study, going against the results of Chapters 8 and 9. At e_c/R = 0.50 only, the 50%-amplitude GMNIA#1 load factor is actually higher than the 100%-amplitude GMNIA#2 load factor, suggesting that a deeper imperfection is less detrimental to the predicted strength of the silo for this eccentricity, a feature known to occur elsewhere (e.g. Yamaki, 1984), but it is not known why this occurs specifically at that value of e_c/R and not at another. The weld depression is responsible for a reduction in the predicted buckling strength of up to 45% for concentric discharge, but this reduction becomes progressively smaller at higher eccentricities, and at e_c/R = 0.93 it is only 21%. Thus where the silo under uniform stress states exhibits very acute imperfection sensitivity, this appears to be no longer the case for stress states with more localised compressive peaks, a feature exploited in the formulation of a failure criterion in Section 9.6 (e.g. Libai and Durban, 1973; 1977; Rotter, 1986).

Table 10.6 – Summary of the full set of computed load proportionality factors as a function of the outlet eccentricity

Outlet eccentricity e_c/R	0.00	0.25	0.50	0.75	0.93
	ConP		→		EccP
LBA	8.947	8.037	3.305	2.275	1.946
MNA	8.591	8.370	7.852	5.487	4.290
GNA	8.915	8.280	3.905	3.408	3.027
GMNA	7.334	6.859	3.905	3.408	3.009
GMNIA#1	5.635	5.205	2.399	2.054	1.720
GMNIA#2	4.819	4.447	3.826	1.785	1.531
Buckling mode†	Axi-EF	Glb-EF	Loc-CH		

† at the base of the 3 mm strake for both GMNIA analyses

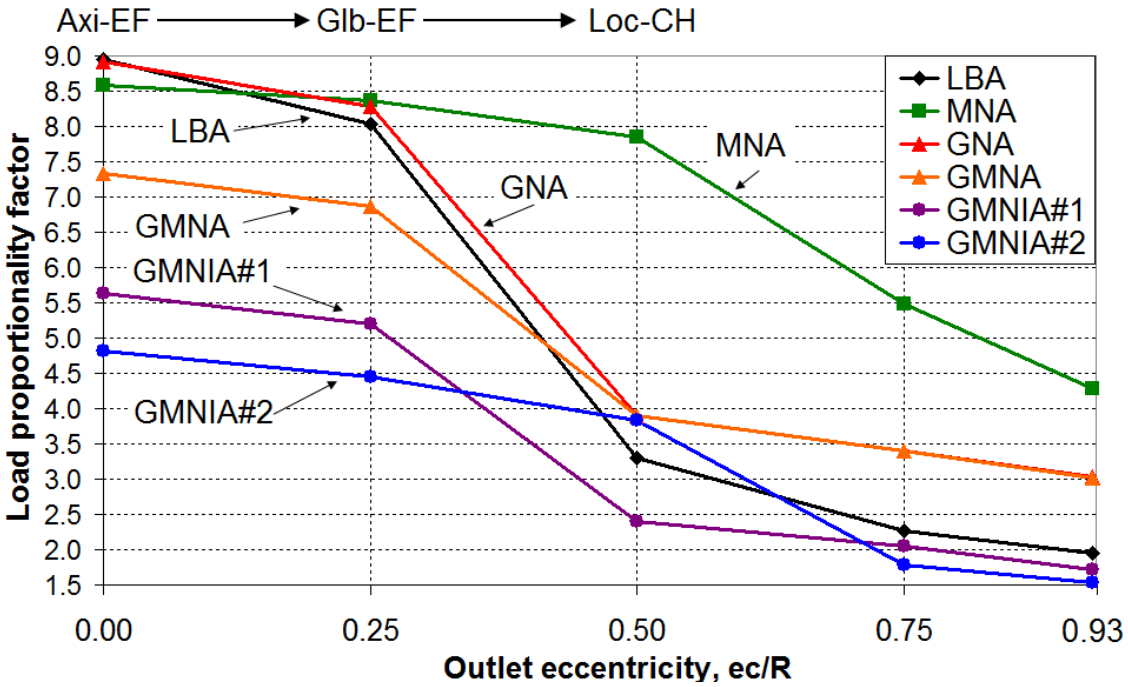

Fig. 10.26 – Distribution of computed load proportionality factors as a function of the outlet eccentricity

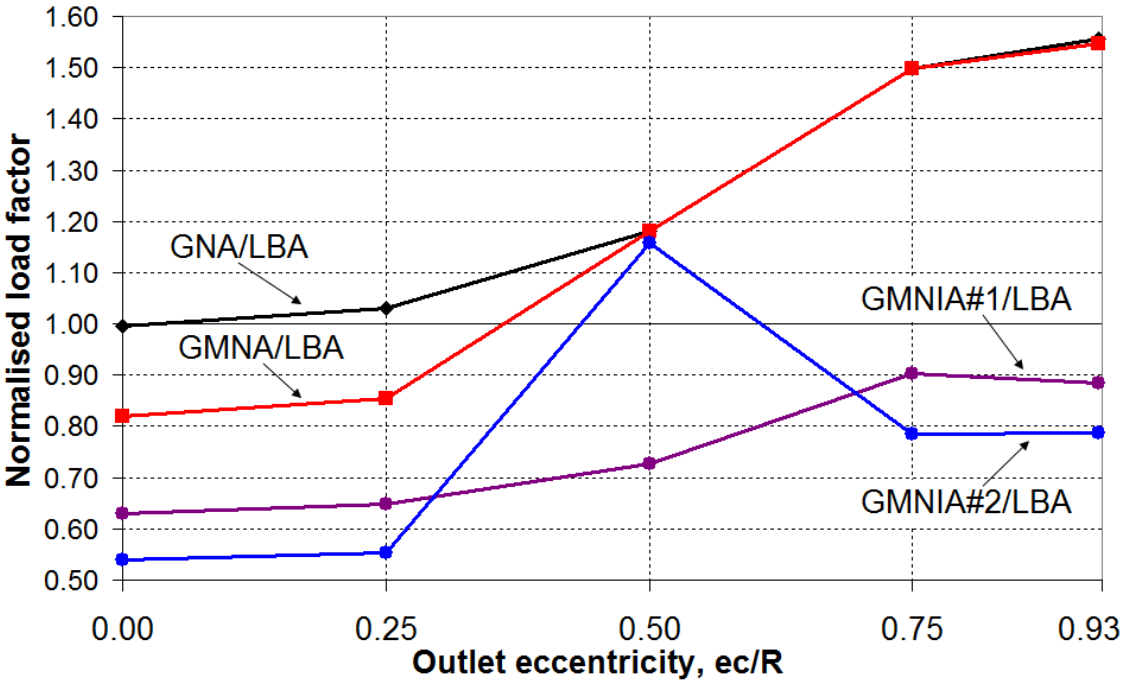

Fig. 10.27 – Distribution of the all normalised GNA-based load factors with outlet eccentricity

The predicted incremental buckling modes for both GMNIA analyses (Fig. 10.28 and Fig. 10.29) are similar to each other and to the GMNA buckling modes (Fig. 10.25), and occur at the same locations in the silo wall. The GMNA analyses predict failure by plastic elephant's foot buckling at the base of the 3 mm strake for $e_c/R \leq 0.25$, and the introduction of a weld imperfection at this same location naturally results in a decreased GMNIA load factor. However, once the outlet eccentricity has increased beyond $e_c/R = 0.50$ and the GMNIA analysis predicts a predominantly elastic midheight buckling mode at the centre of the flow channel (with only very local plasticity effects), the detrimental effect of the axisymmetric weld depression becomes harder to explain.

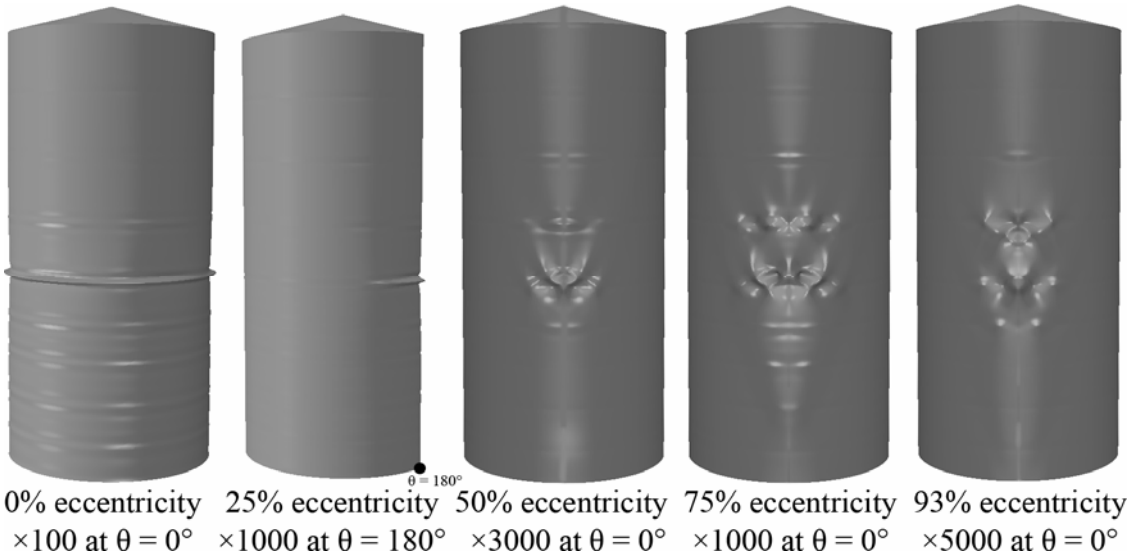

Fig. 10.28 – Predicted GMNIA#1 buckling modes as a function of the outlet eccentricity

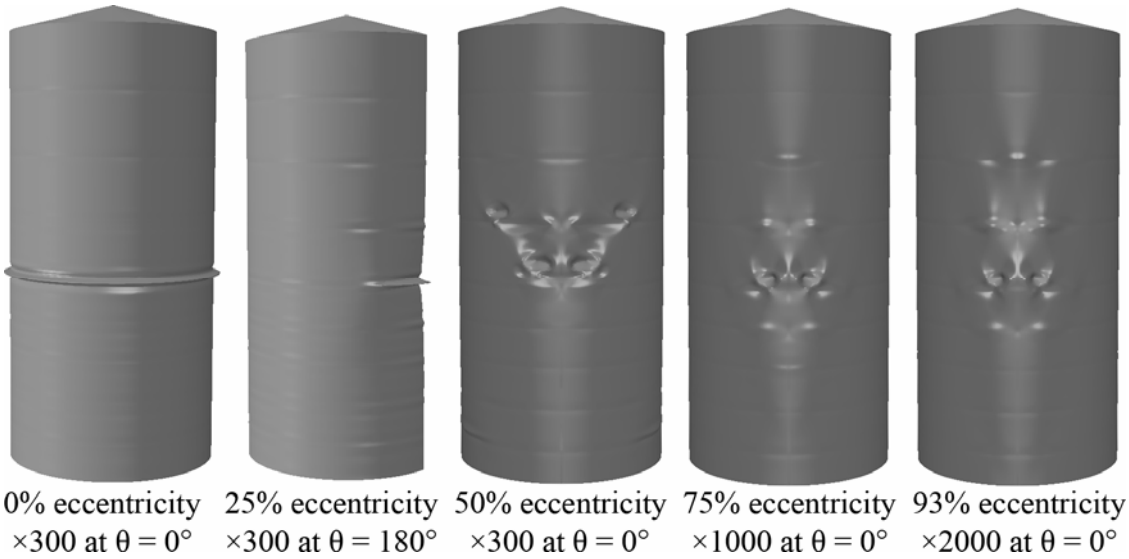

Fig. 10.29 – Predicted GMNIA#2 buckling modes as a function of the outlet eccentricity

The results of this study do not support the previous findings where the axisymmetric weld depressions were reported to be beneficial to the predicted buckling strength (Chapters 4, 8 and 9). The most likely reason for this may be found by looking in Fig. 4.29 (reproduced here as Fig. 10.30) which showed that, although the weld depression was found to be significantly beneficial for small and medium-sized EN 1991-4 eccentric discharge flow channels ($k_c = r_c/R = 0.25$ and 0.40), this was no longer the case for the flow channel with the widest wall contact ($k_c = 0.60$). The contact angle of the channel with the wall θ_c was found to be 28.73° for $k_c = 0.60$ (Table 4.7), whereas in

the present study, each eccentric taper pipe flow channel has a wall contact of approximately 40° near the critical buckling location at the base of the 3 mm strake. Thus the eccentric taper pipe flow channels analysed in this study may simply have too wide a contact with the silo wall for the weld depressions to be beneficial, as was the case of the study in Chapter 4. However, this is a complicated aspect which merits further study.

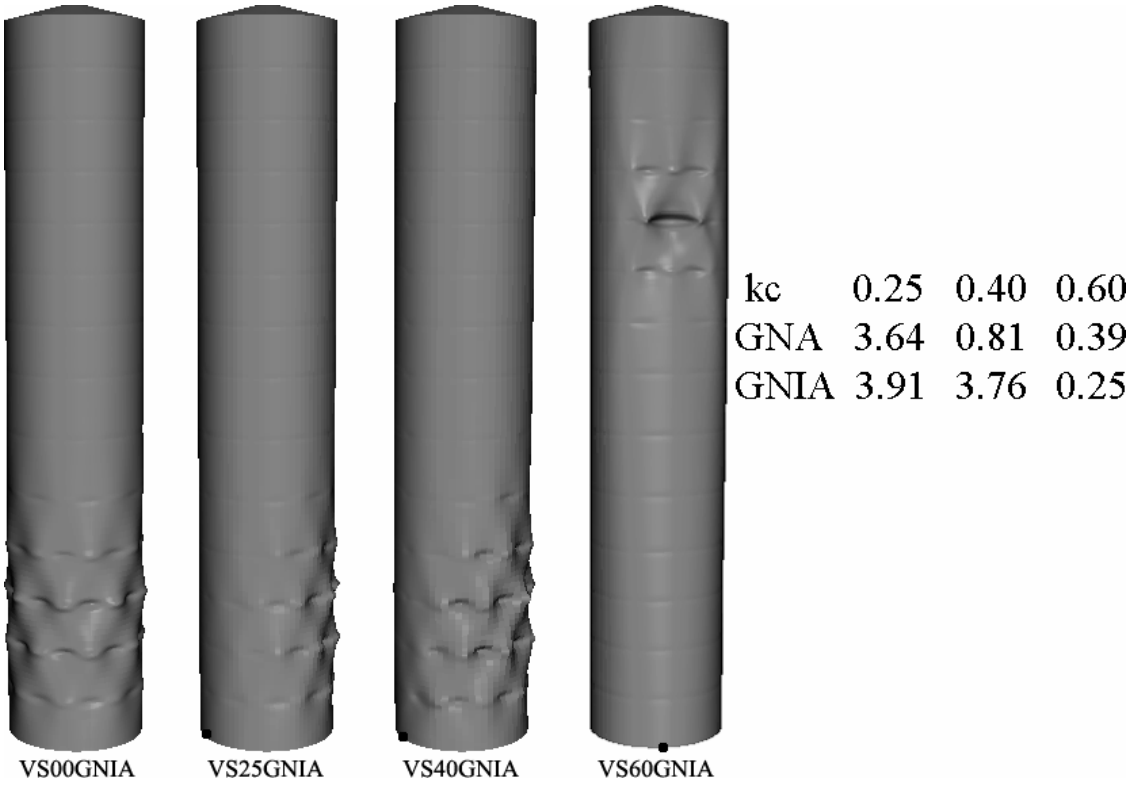

Fig. 10.30 – Reproduction of Fig. 4.29 showing the GNIA buckling modes of silo VS (H/D = 5.2) for $k_c = r_c/R$ = 0.00, 0.25, 0.40 and 0.60 and associated GNA and GNIA load factors

10.8 Relationship to the Standards

The Australian Standard (AS 3774, 1996) specifies that discharge eccentricities smaller than 0.2R may be treated as concentric and a special procedure for eccentric flows need not be invoked. The European Standard (EN 1991-4, 2007) specifies instead that the large outlet eccentricity procedure (the focus of Chapters 2 to 6) does not need to be applied where the outlet eccentricity is less than 0.5R. The German and ISO Standards (DIN 1055-6, 1987; ISO 11697, 1995) only treat filling and discharge eccentricity through 'patch' loads (discussed in Section 1.2.6 of the literature review) and no special value of eccentricity is defined.

The load factors predicted in this study for $e_c/R = 0.25$ (close to $0.2R$) have indeed been found to be very similar to the concentric values, while a significant drop in buckling strength was found for outlet eccentricities greater than $e_c/R = 0.50$ (Table 10.6). Based on the results presented in this chapter, it therefore appears that the Australian and European Standards were spot on.

10.9 Conclusions

This chapter has presented the results of a computational study into the structural effects of taper pipe flow channels with five different outlet eccentricities, assuming a constant outlet size and channel steepness. The wall pressures were predicted by the mixed flow pressure theory introduced earlier in this thesis. The analyses were performed on a single stepped-wall thickness silo of intermediate slenderness. This is the final study to be presented in this thesis.

The mixed flow pressure theory predict very similar distributions of vertical pressure in both the flow channel and stationary solid regardless of outlet eccentricity. An increasingly eccentric taper pipe flow channel was found to result in a larger vertical, but not circumferential, contact with the silo wall over which low wall pressures are applied.

The finite element analyses predict a minor fall in buckling strength from 0% to 25% eccentricity, followed by a significant fall in the buckling strength from 25% to 50%. For even higher eccentricities, the buckling strength continues to fall further, but only by very little. The reported result of a rise in buckling strength after a certain middle value of the eccentricity (approximately 80%) has not been reproduced. The plastic collapse mechanism was not found to play any role in the behaviour of medium and high eccentricities.

Axisymmetric weld imperfections were found to be detrimental to the predicted buckling strength at all values of outlet eccentricity. This is likely to be due to the relatively wide contact between the flow channel and the wall, which seems to negate any strengthening effects in terms of the circumferential bending stiffness that a narrower channel-wall contact may have. A similar finding was presented in a previous study in this thesis, but the mechanics is complex and requires further study.

The relationship between the predicted load factors at buckling failure with the outlet eccentricity was found to correspond remarkably well to the provisions of the Australian and European Standards, AS 3774 and EN 1991-4 respectively.

Chapter 11 – Conclusions and further research

11.1 Introduction

This thesis has presented a series of detailed numerical investigations into the structural effects of concentric and eccentric discharge of granular solids in slender and intermediate slender metal silos. Seven silos of varying aspect ratio were custom designed for this purpose according to the EN 1993-1-6 (2007) and EN 1993-4-1 (2007) European Standards using the prescribed concentric discharge loads and material properties of EN 1991-4 (2007) for two different granular solids: wheat and cement. The custom designs offered full freedom in the control and understanding of the system that was being analysed and helped explain the type and location of many of the predicted buckling and plastic collapse modes.

The numerical studies were all carried out with the powerful ABAQUS finite element software, which is capable of all of the computational analyses within the framework of the EN 1993-1-6 Standard. Due to the high complexity involved in preparing and programming the finite element models (which was done with custom-written software), the long run times of over a thousand nonlinear analyses and the considerable effort required to process the resulting output data, there was unfortunately no scope in the time available to undertake experimental studies.

11.2 Literature on granular solids flows in silos and on shell structures

The literature on experimental studies of granular solids flows in silos is vast. It includes very extensive measurements of filling, storage and discharge pressures, though measurement of flow channel profiles are much rarer due to the difficulties of observation. Unfortunately, these studies have been carried out over the course of many decades by researchers all over world who naturally used different granular materials and measuring techniques, assumed different eccentricities of flow, employed different example silos of varying aspect ratios built with different construction techniques (both model and full-scale), or simply had a different philosophy within which the experiments were carried out, all of which influenced either the focus or the conclusions of the research. Consequently, it is extremely difficult to extract any systematic conclusions from this vast volume of research other than rather vague qualitative generalities such as ‘eccentric discharge is bad’.

It has become apparent over the course of this research that the even larger literature on shell structures is equally lacking in clarity on the subject of the effects of non-symmetrical pressures, such as those occurring under eccentric mixed and pipe flows and especially so under geometric nonlinearity. This is party due to the algebraic character of most texts on shell theory, whose mathematical analyses of linear shell behaviour already approach the limit of what can be achieved algebraically. Analytical studies of nonlinear shell behaviour under unsymmetrical using algebraic treatments are simply too complex. It has really only been possible to begin to unlock the secrets of nonlinear shell behaviour in recent years, with the advance of cheap computing power and the development of nonlinear finite element software. For many reasons, it would not have been possible to carry out the research presented in this thesis even ten years ago.

11.3 Analyses of the EN 1991-4 eccentric discharge model

The natural place to begin an investigation of the effects of eccentric discharge is with the provisions of the relatively recent European Standard EN 1991-4. Published only in 2007, the design procedure for large eccentricities found therein is a milestone in the codified treatment of this design condition and its structural effects have not been explored in any known study preceding this thesis. The EN 1991-4 eccentric discharge model uses an eccentric pipe flow channel with parallel sides and a truncated circular cross-section down the entire height of the silo. The necessary change to this shape near the outlet is ignored.

The first half of this thesis was dedicated to parametric studies of the EN 1991-4 eccentric discharge model using the full range of computational analyses introduced in EN 1993-1-6. These included an initial study into the structural effects of this model on a slender silo, a second study which investigated different circumferential forms of the distribution (there are considerable doubts about the magnitudes of high pressures on either side of the flow channel), a third study of the suitability of the model for silos of different aspect ratios and a final study of the effects of varying the flow channel size.

It was found that there are two critical buckling regions under eccentric pipe flow. At the base of the silo near the edge of the flow channel, high compressive axial membrane stresses develop which usually result in a plastic buckle. Alternatively, at approximately

silo midheight, relatively low magnitudes of axial compressive stresses develop at the centre of the flow channel which usually result in an elastic buckle. For silos which have a uniformly thick wall and thus the same buckling resistance throughout, the base edge buckle mode was found to be the most commonly critical one. However, in a more realistic silo with a stepwise varying wall thickness, buckling occurred slightly above midheight where the wall was thinner. The predominant buckling under eccentric pipe flow for realistic silo wall geometries was thus found to be the elastic midheight buckle.

When analysing slender silos subject to the EN 1991-4 eccentric discharge pressures, it was found that the *only* buckling modes obtained in finite element analyses were the two mentioned above. However, since silos with stepwise varying wall thicknesses are the only ones used in practice, it is evident that the midheight buckle is the most 'representative' or 'characteristic' mode associated with eccentric discharge. Many observations of such buckles have been made on silos in service. However, though it is uncertain whether in practice this is the *only* possible mode (an aspect which requires verification), the midheight buckle is a valuable concept for the purposes of conservative structural design since nevertheless the predicted load factors associated with this buckle are always the lowest. Not all channel sizes recommended by EN 1991-4 resulted in this buckling mode, and it was found that small flow channels should probably be omitted for conservative design calculations because the predicted load factors are very high. Thus it was suggested that, if a design calculation process leads to a predicted midheight buckle, one may be confident that a conservative design for eccentric pipe flow may probably be achieved. The most secure way of ensuring this is to choose a mid-sized flow channel.

11.4 Development of a new mixed flow eccentric discharge pressure model

The EN 1991-4 eccentric discharge model is based on the assumption of eccentric pipe flow. This is the only simple algebraic model known, and it is thought to be the most damaging pattern of pressures for thin-walled silos. However, flow channels of this geometry only form in slightly cohesive solids or in tightly packed rough solids (Rotter, 2001a). Most stored bulk solids develop flow channels that progressively spread out from the outlet, though the precise shape of these channels cannot yet be predicted with any certainty. These expanding mixed flow channels leads to structural conditions that are only slightly less dangerous than those associated with eccentric pipe flow, but the

condition is not covered by EN 1991-4 because no simple theory for the associated pressure pattern has been available.

To address this issue, and to expand the range of flow patterns which may be analysed numerically, a mixed flow pressure theory was developed based on a generalisation of the slice equilibrium analyses of hoppers with sloped sides. The basic concepts were originally developed by Berry (1988) and Rotter *et al*. (1990) but have not been used again since. Here, the equilibrium concept was applied to channel sides of varying slope and outlets of varying eccentricity, making the theory potentially much more powerful than any previous treatment, as it can be applied to a vast range of different geometries though at the cost of necessitating a numerical solution to the resulting differential equations. Such a solution is not a hindrance, however, and may be done with relative ease in a spreadsheet.

Subsequent finite element studies of wall pressures predicted by this theory covered a wide range of different flow patterns. These included concentric pipe flow, concentric mixed flow, eccentric parallel or taper pipe flow and eccentric mixed flow. Concentric pipe flow was found to have a negligible effect on the stationary Janssen pressures for narrow channels, while concentric mixed flow was found to predict sudden wall pressure increases adjacent to the effective transition that were of a realistic order of magnitude (discrediting the 'switch' theory for the lateral pressure ratio K). Eccentric pipe flow expressed with the mixed flow theory was predicted to result in very similar structural consequences as the EN 1991-4 eccentric discharge model, reproducing the elastic midheight buckle. Finally, eccentric mixed flow was found to be only slightly less destructive than eccentric pipe flow, despite a fundamentally different predicted structural response. The hierarchy, in terms of increasing structural severity, was found to be: concentric pipe flow < concentric mixed flow < eccentric mixed flow < eccentric pipe flow.

The mixed flow pressure theory was developed with only the simplest of assumptions for the lateral pressure ratio K, which was taken to be constant throughout the silo. Indeed, it does not really matter which equation is assumed for K if it is to be constant, since the predicted *patterns* of wall pressure are then effectively independent of it. Probably most importantly of all, large and sudden rises in wall pressure at the effective

transition between the flowing and stationary solid were found to be caused be local equilibrium considerations, and not by a 'switch' in K as previously advocated by Jenike *et al.* (1967) and many others. The predicted magnitude of these rises was found to be moderate, approximately of the order of 2 (as opposed to almost 10 according to the 'switch' theory), and has been found to correlate surprisingly closely with reported measurements as well as the prescribed concentric discharge factors in EN 1991-4 for silos in (the most demanding) Action Assessment Class 1. However, it is recognised that K is almost certainly not constant throughout the whole silo, and an experimental programme designed specifically to calibrate K depending on flow pattern and location is highly recommended.

In addition to an initial probing computational study, two parametric studies were carried on sets of flow patterns with pressures predicted the mixed flow pressure theory using linear and nonlinear finite element analyses. The first study investigated the effect of increasing the steepness of a flow channel of constant eccentricity and outlet size. The flow pattern passed from eccentric mixed to pipe flow, resulting in a fundamental change in the structural response. The second study investigated the effect of increasing the eccentricity of a flow channel of constant steepness and outlet size. The flow patterns this time passed from concentric pipe to eccentric taper pipe flow, with a progressive decrease in load factor that was found to correspond remarkably well to the provisions of the Australian and European Standards, AS 3774 (1996) and EN 1991-4 (2007), respectively.

11.5 The dual effect of geometric nonlinearity

It was discovered very early in the research that buckling loads under eccentric pipe flow predicted by a geometrically nonlinear analysis were significantly higher than those predicted by a linear bifurcation analysis. At first, it was uncertain if beneficial geometric nonlinearity was a genuine phenomenon and many of the initial finite element analyses were rerun many times using different elements and changing other conditions in order to test for errors in the model, but the effect reappeared consistently for every single finite element analysis of an eccentric mixed or pipe flow channel.

An initial explanation supporting the above phenomenon was found in the context of a propped cantilever analogy, whereby a wider portion of the shell acts like an arc-profile

beam with a higher section modulus in a geometrically nonlinear analysis, consequently resulting in lower extreme fibre stresses. Thus changes of geometry mobilise a greater circumferential portion of the shell to carry the non-symmetrical stresses that occur under eccentric discharge, which in turn reduces their peak magnitudes both in tension and compression and consequently increases the load factor at buckling. However, there is still much to be done to determine why exactly this phenomenon occurs.

Geometric nonlinearity has also been found to cause local circumferential flattening of the silo wall adjacent to the low pressure in the flow channel. This increases the local radius of curvature of the shell, an affect known to result in lower buckling strengths (Rotter, 1985), directly countering the beneficial effect described above. These two opposing effects were able to be isolated thanks to the chance discovery of the same linear and nonlinear elastic buckling load factor for a slender silo under the same flow pattern.

11.6 The minor effect of material nonlinearity

It was found that the buckling behaviour under eccentric pipe flow occurs predominantly in the elastic material range of the silo wall under compressive axial membrane stresses. If material plasticity was detected, it was usually very minor. This was of course not the case for concentric discharge, where plasticity was found to play a central role in the dominant global bursting or elephant's foot buckling behaviour. Additionally, failure under eccentric mixed flow was also found to involve local plastic elephant's foot buckling.

The predominantly elastic behaviour of the most serious condition of eccentric pipe flow allowed a potential layer of additional complexity to be removed, for now, and thus spared the need to investigate plastic hardening, softening or any other nonlinear plasticity law beyond ideal elastic-plastic. Naturally, the use of more complex material laws for structural analysis under concentric discharge or eccentric mixed flow may be considered as a topic for further research.

11.7 Those elusive imperfections!

The popular Type A axisymmetric weld depression of Rotter and Teng (1989a), very serious under uniform axial compression and internal pressure, was put through rigorous testing. Due to the nature of the deformation response of the silo under eccentric pipe flow, it was found that the weld depression consistently enhanced the circumferential bending stiffness of the silo for small and medium-sized EN 1991-4 flow channels, leading to higher predicted buckling strengths. For larger-sized flow channels with a wider circumferential contact with the silo wall, it was still not possible to ascertain whether the weld depressions were a reliably deleterious imperfection form because the amplitude of the imperfection (as required by EN 1993-1-6) was so deep that it often eliminated the bifurcation point. Thus the silo passed from pre- to post-buckling yet the deformations remained stable, and the reported load factor corresponded to a change of slope on the load-displacement path at which no negative eigenvalues had been reported by the finite element software. Similarly conflicting evidence was obtained in studies of more realistic flow patterns in the second half of this thesis. Thus the axisymmetric weld depression cannot be relied on to give a conservative estimate under eccentric parallel and taper pipe flows. For concentric flows and eccentric mixed flows, however, the weld depression is reliably deleterious and may probably be the most damaging possible imperfection form (Rotter, 2004).

The more traditional eigenmode-affine imperfection forms were found to be equally inadequate at predicting consistent decreases in the corresponding load factor. This was due to the shape of the linear bifurcation eigenmode or the geometrically nonlinear pre-buckling deformations. When applied as an imperfection form to the silo, eigenmode-affine imperfections were found to result in an increased buckling strength. The shape of this imperfection form was found to be composed of tightly-packed alternating inward and outward indentations located close to the critical buckling location. It is thus likely that these indentations increase the circumferential bending stiffness of the shell near the critical location in a similar manner to the axisymmetric weld depression for small and mid-sized eccentric pipe flow channels. However, the strength gains for the eigenmode-affine imperfection were not as large as for the axisymmetric weld depression.

Thus where the silo under uniform loading conditions exhibits very high imperfection sensitivity, responding negatively even to minor perturbations at very low imperfection amplitudes of less than one wall thickness, under localised loads this imperfection sensitivity has been found to be significantly reduced. Indeed, it was found that a large-scale deviation from the perfect shape was necessary in order to produce buckling strength decreases under eccentric discharge. Thus a novel and rather exotic *global* imperfection form was proposed based on the deformed radial shape of the shell at buckling. Dubbed 'superelliptical flattening', it exploited the feature of a flattened wall adjacent to the centre of the flow channel and achieved consistent predicted decreases in buckling strength. This imperfection may be likened to a global out-of-roundness deformation or a long-wave circumferential dimple, as the imperfection amplitudes required to attain non-trivial buckling strength reductions are comparable to the corresponding EN 1993-1-6 tolerance requirements, easily reaching 20 or more wall thicknesses. However, even this imperfection form exhibits a strengthening effect above a certain imperfection amplitude, and it is not yet understood why this is so. It was therefore recommended that the computational calculations required for the design for eccentric discharge should be limited to perfect shells, since these already exhibit very low predicted buckling strengths under this load condition.

11.8 Further research

There are many loose ends in the research presented in this thesis and consequently many directions in which further work may be taken, an exciting prospect for a researcher in this field. Firstly, one of the main features missing from all of the finite element models in this thesis is the effect of the stiffness of the stationary solid. This may be implemented in a finite element analysis with spring elements, but a methodology must be worked out to reliably relate the local normal wall pressure to the stiffness constant of every one of these spring elements.

The vast majority of the buckling failures in stepped wall silos analysed in this thesis have been predicted to occur in the wall adjacent to the flow channel, where the solid may be assumed to have little or no stiffness. It is therefore difficult to say what effect, if any, the incorporation of spring elements within the stationary solid may have on the elastic midheight buckling mode within the flow channel.

However, many experiments were performed in the past on model silos with uniformly thick walls, for which the current finite element analyses would predict a (plastic, if the analysis allows it) base buckling mode to the edge of the channel. It is not known whether this base buckling mode has actually been observed in practice, but it is known that the stationary solid at the base of the silo has considerable stiffness and consequently provides a high restraint against buckling, which suggests that a buckle is unlikely to form anywhere at the base of the silo under eccentric pipe flow. A much more likely location for buckling, as suggested by some studies, is at the foot of the flow channel in the form of a 'smile' buckle, just above the effective transition before the channel becomes internal (Fleming, 1985; Fitz-Henry, 1986). However, such a buckling mode has not yet been reproduced in any known finite element analysis.

A potentially very powerful mixed flow pressure theory was considered in this thesis, one which predicts the vertical pressures in the flow channel and stationary solid for a vast range of geometries and material properties. Although the finite element analyses on example silos subjected to wall pressures predicted by this theory yielded credible results, the theory itself lacks extensive experimental evidence. It is therefore considered that an experimental programme tailor-made to verify specific aspects of this theory would be of utmost importance.

In addition to the above, there are clearly very many further parametric studies which may be undertaken using finite element analyses of the new mixed flow pressure theory. These include investigating the structural effects of eccentric mixed flow channels with different eccentricities (the focus so far has been mostly on eccentric pipe flow because it was considered to be the most dangerous flow pattern) and the consequences of the effective transition (axisymmetric or not) on silos of different aspect ratios. Furthermore, the EN 1993-4-1 (2007) failure criterion for local axial compression has been found to be a very conservative one under eccentric mixed and pipe flow and further research is needed to calibrate the various parameters to give a more reasonable correlation with predicted buckling strengths, though for a phenomenon as dangerous as eccentric discharge a conservative failure criterion may not be such a bad idea.

A final important point is the philosophical question of how to define structural failure. Throughout this thesis, the definition of failure of the EN 1993-1-6 Standard was

followed consistently. Hence, in all cases, the lowest bifurcation point, limit point or inflection point on the load-displacement curve was assumed to be the point of structural failure by buckling, and the behaviour beyond this was not considered. This is of course a gross simplification, but also an important one, as it offers a consistent frame of reference and a conservative assessment of the structural strength. It is therefore not known whether the very low load factors predicted in this thesis for eccentric pipe flow are indeed those at which the silo would fail catastrophically in reality, and it may be possible that the structure is able to sustain significantly higher loads in the post-buckling range.

References

ABAQUS (2009). "ABAQUS Version 6.9" *Dassault Systèmes Simulia Corp.*, Providence, RI, USA. www.simulia.com

Abir D. & Nardo S.V. (1958). "Thermal buckling of circular cylindrical shells under circumferential temperature gradients." *Journal of the Aerospace Sciences*, 26(12), 803-808.

ACI 313-77 (1983). "Recommended practice for design and construction of concrete bins, silos and bunkers for storage of granular materials (ACI 313-77, revised 1983) and Commentary (ACI 313R-77)." *ACI Committee 313 on Concrete Bins, Silos and Bunkers for Storing Granular Materials*, American Concrete Institute, Detroit, Michigan, USA.

ACI 313 ADP (1989). "Alternate Design Procedure – Discussion Document." *ACI Committee 313 on Concrete Bins, Silos and Bunkers for Storing Granular Materials*, American Concrete Institute, Detroit, Michigan, USA.

Aldrich R.A. (1963). "Tower silos: unit weight of silage and silo capacities." *Agr. Eng. Yearbook*, ASAE, St. Joseph, Michigan, USA, 49085.

Almroth B.O. (1963). "Postbuckling behaviour of axially compressed circular cylinders." *AIAA Journal*, 1(3), 630-633.

Almroth B.O. (1966). "Influence of edge conditions on the stability of axially compressed cylindrical shells." *AIAA Journal*, 4(1), 143-140.

Amundson L.R. (1945). "Determination of band stresses and lateral wheat pressures for a cylindrical grain bin." *Agr. Eng.*, 26(8), 321-324.

Ansourian P. (2004). "Cylindrical shells under non-uniform external pressure." Chapter 6 in *Buckling of Thin Metal Shells*, eds J.G. Teng & J.M. Rotter, Spon, London, pp 175-197.

ANSYS (2009). "ANSYS Version 12.0." *ANSYS Inc.*, Canonsburg, PA, USA. www.ansys.com

Arbocz J. & Sechler E.E. (1974). "On the Buckling of Axially Compressed Imperfect Shells ." *Jnl. Appl. Mech.*, Vol. 41, 737-743.

Arnold P.C. & McLean A.G. (1976). "Prediction of Cylinder Flow Pressures in Mass Flow Bins using Minimum Strain Energy." *Jrnl. of Eng. for Industry*, Trans ASME, Series B, Vol. 98, N. 4, 1370-1374.

Arnold P.C., McLean A.G. & Roberts A.W. (1980). "Bulk Solids: Storage, Flow and Handling, 2nd Edition." *Tunra Bulk Solids Handling Research Associates*, University of Newcastle, Australia.

AS 3774 (1996). "Loads on bulk solids containers." *Standards Australia*, Sydney.

Ayuga F., Guaita M., Aguado P.J. & Couto A. (2001). "Discharge and Eccentricity of the Hopper Influence on the Silo Wall Pressures." *Jrnl. of Eng. Mech.*, ASCE, 127(10), 1067-1074.

Baker E.H., Kovalevksy L. & Rish F.L. (1972). "Structural Analysis of Shells." *McGraw-Hill*, New York.

Berry P.A. (1988). "Flow Channel Geometry and Silo Pressures under Eccentric Discharge." *BSc Thesis*, The University of Sydney, Australia.

Berry P.A. & Rotter J.M. (1996). "Partial axisymmetric imperfections and their effect on the buckling strength of axially compressed cylinders." *Proc. of the Int. Workshop on Imperfections in Metal Silos: Measurement, Characterisation and Strength Analysis*, CA-Silo, Lyon, France, 199-216.

Berry P.A., Bridge R.Q. & Rotter J.M. (1997). "Experiments on the buckling of axially compressed fabricated steel cylinders with axisymmetric imperfections." *Proc., Int. Conf. on Carrying Capacity of Steel Shell Structures*, Brno, Czech Republic, 1-3 October 1997, pp 347-353.

Berry P.A., Rotter J.M. & Bridge R.Q. (2000). "Compression tests on cylinders with circumferential weld depressions." *Jrnl. of Eng. Mech.*, ASCE, 126(4), 405-413.

Bijlaard D.L. & Gallagher R.H. (1959). "Elastic instability of a cylindrical shell under arbitrary circumferential variation of axial stresses." *Journal of the Aerospace Sciences*, 27(11), 854-858, 866.

Blachut J. & Galletly G.D. (1987). "Externally pressurised hemispheres and shallow torispheres." *Proc. Int. Colloquium on the Stability of Plate and Shell Structures*, Gent, Belgium, 6-8 April, ECCS, 361-366.

Blachut J. & Galletly G.D. (1990). "Buckling Strength of Imperfect Spherical Caps - Some Remarks." *AIAA Journal*, Vol. 28, N. 7, July, 1314-1319.

Blachut J., Galletly G.D. & Moreton D.N. (1990). "Buckling of Near-Perfect Steel Torispherical and Hemispherical Shells subjected to external pressure." *AIAA Journal*, Vol. 28, N. 11, November, 1971-1975.

Blight G. (2006). "Assessing Loads on Silos and Other Bulk Storage Structures - Research Applied to Practice." *Taylor and Francis*, New York.

Borcz A. & Marcinkowski Z. (1974). "Measuring stand and preliminary results of the cement pressure investigation in a silo in a natural scale." *Prace Naukowe Instytutu Budownictwa Politechniki Wrocławskiej*, N. 14, Conferences N. 1, Poland.

Bornscheuer F.W. (1982). "To the problem of buckling safety of shells in the plastic range." *Buckling of Shells, Proceedings of a State-of-the-Art Colloquium*, ed. E. Ramm, Springer-Verlag, Berlin, 601-619.

Bornscheuer F.W. & Hafner L. (1983). "The influence of an imperfect circumferential weld on the buckling strength of axially loaded circular cylindrical shells." *Preliminary Report, 3rd Int. Colloquium on the Stability of Metal Structures*, Paris, France, 407-414.

Bornscheuer F.W., Hafner L. & Ramm E. (1984). "Zur Stabilität eines Kreiszylinders mit einer Rundschweissnaht under Axialbelastung." *Der Stahlbau*, 52(10), 313-318.

Bovey H.T. (1904). "Experiments on grain pressures in deep bins and the strength of wooden bins." *Engineering News*, 52, 32-34.

Britton M.G. & Hawthorne C.R.J. (1984). "Dynamic behaviour of wheat in a lamellar bin." *ASAE Paper No. NCR-84-501*, Amer. Soc. of Agric. Engrs., St. Joseph, Michigan, USA,

Brush D.O. & Almroth B.O. (1976). "Buckling of Bars, Plates and Shells." *McGraw-Hill*, New York.

Budiansky B. & Sanders J.L. (1963). "On the 'Best' First-Order Linear Shell Theory." *Progress in Applied Mechanics*, The Prager Anniversary Volume, Macmillan, 129-140.

Bucklin R.A., Thompson S.A. & Ross I.J. (1990). "Bin-Wall Failure Caused by Eccentric Discharge of Free-Flowing Grain." *Jrnl. of Struct. Eng.*, ASCE, 116(11), 3175-3189.

Cai M. (2003). "Buckling of cylindrical shells under non-uniform loads." *PhD Thesis*, The University of Edinburgh, UK.

Cai M., Holst J.M.F.G. & Rotter J.M. (2002). "Buckling strength of thin cylindrical shells under localised axial compression." *15th ASCE Engineering Mechanics Conference*, Columbia University, New York. Also in *Research Report R02-002*, The University of Edinburgh, School of Civil and Environmental Engineering.

Cai M., Holst J.M.F.G. & Rotter J.M. (2003a). "Parametric study on the buckling of thin steel cylindrical shells under elevated axial compression stresses." *16th ASCE Engineering Mechanics Conference*, University of Washington, Seattle.

Cai M., Holst J.M.F.G. & Rotter J.M. (2002). "Buckling of cylindrical tank shells under local axial compression stresses." *Int. Conf. on Design, Inspection, Maintenance and Operation of Cylindrical Steel Tanks and Pipelines*, ECCS, Prague, Czech Republic, 70-76.

Calladine C.R. (1983). "Theory of Shell Structures." *Cambridge University Press*, Cambridge.

Carson J.W., Goodwill D.J. & Bengston K.E. (1991). "Predicting the shape of flow channels in funnel flow bins and silos." *Proc. ACI Convention*, Boston, Massachussetts, p. 12.

Chatlynne C.J. & Resnick W. (1973). "Determination of Flow Patterns for Unsteady-State Flow of Granular Materials." *Powder Technology*, Vol. 8 N. 3-4, 177-182.

Chen J.F. (1996). "Granular Solid – Structure Interaction in Silos." *PhD Thesis*, The University of Edinburgh, UK.

Chen J.F., Rotter J.M. & Ooi J.Y. (1998). "Statistical inference of unsymmetrical silo pressures from comprehensive wall strain measurements." *Thin-Walled Structures*, 31, 117-136.

Chen L., Doerich C. & Rotter J.M. (2008) . "A study of cylindrical shells under global bending in the elastic-plastic range." *Steel Construction - Design and Research*, Stahlbau, 1(1), 59-65.

Chrisp T.M., Wood J.G.M. & Blacker M.J. (1988). "Comparison of model and full-scale test results with simplified and finite element analyses of eccentrically discharged silos." *Silos – Forschung und Praxis*, University of Karlsruhe, Germany.

Clarke M.J. (1987). "Measurement and analysis of imperfections in full scale silos." *BEng Thesis*, The University of Sydney, Australia.

Clarke M.J. & Rotter J.M. (1988). "A technique for the measurement of imperfections in prototype silos and tanks." *Research Report R565*, University of Sydney, School of Civil and Mining Engineering, Australia.

Cohen G.A. (1971). "Computer analysis of imperfection sensitivity of ring-stiffened orthotropic shells of revolution." *Journal of the American Institute of Aeronautics and Astronautics*, 9, 1032-1039.

Colijn H. & Peschl I.A.S.Z. (1981). "Non-symmetrical bin flow problems." *Bulk Solids Handling*, Vol. 1 N. 3, 337.

Cook R.D., Malkus D. S., Plesha M. E. & Witt R. J. (2002). "Concepts and Applications of Finite Element Analysis, 4th Edition." *John Wiley & Sons*, USA. (1st edition in 1974).

Dąbrowski A. (1957). "Parcie Materiałów Sypkich w Leju." *Archiwum Inżynierii Lądowej*, Warsaw, Poland, Z.3, 325-328.

Darcourt C., Roelandt J.M., Rachik M., Deloison D. & Journet B. (2004). "Thermomechanical analysis applied to the laser beam welding simulation of aeronautical structures." *Journal de Physique IV*, 120, 785-792.

Deml M. & Wunderlich W. (1997). "Direct evaluation of the 'worst' imperfection shape in shell bucklins." *Computer Methods in Applied Mechanics and Engineering*, 149, 201-222.

Deutsch G.P. & Clyde D.H. (1967). "Flow and pressure of granular materials in silos." *Jrnl. of Eng. Mech.*, ASCE, 93, 103-125.

DIN 1055-6 (1987). "Design loads for buildings: loads in silo bins." *Deutsches Institut für Normung*, Berlin, Germany.

Ding X.L., Coleman R.D. & Rotter J.M. (1996). "Technique for precise measurement of large-scale silos and tanks." *Jrnl. of Surveying Eng.*, ASCE, 122, 14-25.

Doerich C. (2007). "Strength and stability of locally supported cylinders." *PhD Thesis*, The University of Edinburgh, UK.

Doerich C. (2008). "Effect of geometric nonlinearity of locally supported cylinders." *Proc. of the Int. Conf. on Structures and Granular Solids: From Scientific Principles to Engineering Applications*, The Royal Society of Edinburgh, UK, 1-2 July 2008. Festschrift edited by J.F. Chen, J.Y Ooi & J.G. Teng, pp. 183-197.

Donnell L.H. (1934). "A New Theory for the Buckling of Thin Cylinders under Axial Compression and Bending." *Trans. ASME*, 56, 795-806.

Donnell L.H. & Wan C.C. (1950). "Effect of Imperfections on Buckling of Thin Cylinders and Columns under Axial Compression." *Jnl. Appl. Mech.*, Vol. 17, 73-83.

Drescher A. (1991). "Analytical Methods in Bin-Load Analysis", *Elsevier*, New York.

Emanuel J.H., Best J.L., Mahmoud M.H. & Hasanain G.S. (1983). "Parametric Study of Silo-Material Interaction." *Powder Tech.*, Vol. 36, 223-233.s

ECCS (1983). "European Recommendations for Steel Construction: Buckling of Shells, 2nd edition." *European Convention for Constructional Steelwork*, Brussels.

ECCS (1988). "European Recommendations for Steel Construction: Buckling of Shells, 4th edition." *European Convention for Constructional Steelwork*, Brussels.

EN 1991-4 (2007). "Eurocode 1: Actions on Structures, Part 4: Silos and Tanks." *European Committee for Normalisation,* Brussels.

EN 1993-1-6 (2007). "Eurocode 3: Design of Steel Structures, Part 1-6: Strength and Stability of Shell Structures." *Comité Européen de Normalisation*, Brussels.

EN 1993-4-1 (2007). "Eurocode 3: Design of Steel Structures, Part 4-1: Silos." *Comité Européen de Normalisation*, Brussels.

Esslinger M. (1973). "Buckling Loads of Steel Metal Silos with Overlapping Circumferential Seams." *Deutscher Forschungs- und Versuchsanstalt für Luft- und Raumfahrt*, Rep. DLR-FB 73-36, Braunschweig.

Esslinger M. & Geier B. (1972). "Gerechnete Nachbeulasten als untere Grenze der experimentellen axialen Beulasten von Kreiszylindern." *Der Stahlbau*, 41(12), 353-360.

Esslinger M. & Geier B. (1977). "Buckling Loads of Thin-Walled Circular Cylinders with Axisymmetric Irregularities." *Steel Plate Structures: An International Symposium*, edited by P.J. Dowling, J.E. Harding and P.A. Frieze, London, pp. 865-88.

FBIC (1981). "A guide for the design and construction of agricultural grain bins." *Farm Building Information Centre*, Stoneleigh, UK.

Fitz-Henry J.O.D. (1986). "Buckling Failures of Eccentrically-Discharged Silos." *BE Thesis*, The University of Sydney, Australia.

Flemig S.P. (1985). "The Buckling and Collapse of Silos under Eccentric Discharge." *BE Thesis*, The University of Sydney, Australia.

Flügge W. (1957). "Statik und Dynamik der Schalen, zweite Auflage." *Springer-Verlag*, Berlin, Göttingen & Heidelberg.

Frese B. (1977). "Drückverhältnisse in Silozellen." *Dissertation*, TU Karlsruhe.

Galambos T.V. (1988). "Guide to stability design criteria for metal structures." *John Wiley & Sons*, New York.

Gale B.R., Hoadley P.J. & Schmidt L.C. (1986). "Aspects of Eccentric Discharge of Granular Material from a Circular Silo." *Proc. of the 2nd Int. Conf. on Bulk Materials Storage, Handling and Transportation,* IEAustralia, Wollongong, 258-263.

Gaylord E.H. & Gaylord C.N. (1984). "Design of Steel Bins for Storage of Bulk Solids." *Prentice Hall*, New Jersey.

Gielis J. (2003). "A generic geometric transformation that unifies a wide range of natural and abstract shapes." *American Journal of Botany*, 90(3), 338-338.

Gillie M. & Rotter J.M. (2002). "The effects of patch loads on thin-walled steel silos." *Thin-Walled Structures* 40, 835-852.

Gillie M. & Holst J.M.F.G. (2003). "Structural behaviour of silos supported on discrete, eccentric brackets." *Journal of Constructional Steel Research* 59, 887-910.

Gopalakrishnan S. (1978). "Bestimmung von Silowandlasten durch experimentelle Untersuchungen am Modellsilo." *IASS-Tagung*, Braunschweig, Germany.

Gorenc B.E., Hogan T.J. & Rotter J.M. (1986). "Guidelines for the assessment of loads on bulk solids containers." *Inst. Engineers*, Sydney, Australia.

Gould P. L. (1977). "Static analysis of shells." *Lexington Books*, *D.C. Heath & Co.*, Lexington.

Green A.E. (1945). "Stress Systems in Aelotropic Plates." *Proc. Royal Soc. London*, Series A, Vol. 184, N. 998, 231-252.

Greiner R. (1980). "Ingenieurmäßige Berechnung dünnwandiger Kreiszylinderschalen." *Veröffentlichung des Instituts für Stahlbau, Holzbau und Flächentragwerke*, TU Graz.

Greiner R. & Guggenberger W. (1998). "Buckling Behaviour of Axially Loaded Steel Cylinders on Local Supports – with and without internal pressures." *Thin-Walled Structures*, 31, 159-167.

Gridgeman N. T. (1970). "Lamé ovals." *Math. Gaz.*, 54, 31-37.

Guggenberger W., Greiner R & Rotter J.M. (2004). "Cylindrical shells above local supports." Chapter 3 in *Buckling of Thin Metal Shells*, eds J.G. Teng & J.M. Rotter, Spon, London, pp 88-128.

Hampe E. (1987). "Silos, Band 1 - Grundlagen." *VEB Verlag für Bauwerke*, Berlin.

Hampe E. & Kamiński M. (1984a). "Der Einfluß exzentricher Entleerung auf die Drückverhältnisse in Silos." *Bautechnik*, 61(3), 73-82, Germany.

Hampe E. & Kamiński M. (1984b). "Der Einfluß exzentricher Entleerung auf die Drückverhältnisse in Silos." *Bautechnik*, 63(4), 136-142, Germany.

Harris L.A., Suer H.S., Skene W.T. & Benjamin R.J. (1957). "The stability of thin-walled unstiffened circular cylinders under axial compression including the effects of internal pressure." *Jrnl. of Aeronautical Science*, 24(8), 587-596.

Hartlén J., Nielsen J., Ljunggren L., Mårtensson G. & Wigram S. (1984). "The Wall Pressure in Large Grain Silos." *Swedish Council for Building Research*, Stockholm, Document D2:1984.

Holst J.M.F.G. (2008). "Local dimpling of the shell surface of a tank due to shrinkage effects." *Proc. of the Int. Conf. on Structures and Granular Solids: From Scientific Principles to Engineering Applications*, The Royal Society of Edinburgh, UK, 1-2 July 2008. Festschrift edited by J.F. Chen, J.Y Ooi & J.G. Teng.

Holst J.M.F.G., Rotter J.M. & Calladine C.R. (1996). "Geometric imperfections and consistent residual stress fields in elastic cylinder buckling under axial compression." *Proc. of the Int. Workshop on Imperfections in Metal Silos: Measurement, Characterisation and Strength Analysis*, CA-Silo, Lyon, France, 199-216.

Holst J.M.F.G., Rotter J.M. & Calladine C.R. (1999). "Imperfections in cylindrical shells resulting from fabrication misfits." *Jrnl. of Eng. Mech.*, ASCE, 125(4), 410-418.

Holst J.M.F.G., Rotter J.M. & Calladine C.R. (2000). "Imperfections and buckling in cylindrical shells with consistent residual stresses." *Jrnl. of Constructional Steel Research*, 54, 265-282.

Holst J.M.F.G & Rotter J.M. (2002). "Buckling strength of cylinders with a consistent residual stress state." *3rd Int. Conf. on Advances in Steel Structures*, Hong-Kong, 9-11.

Holst J.M.F.G. & Rotter J.M. (2003). "Nonlinear response and buckling of cylindrical tanks due to foundation settlement." *Proc. Int. Conf. on Design, Inspection, Maintenance and Operation of Cylindrical Steel Tanks and Pipelines*, Prague, Czech Republic, ed. V. Krupka, 29-35.

Holst J.M.F.G. & Rotter J.M. (2004). "Settlement beneath cylindrical shells." Chapters 4 in *Buckling of Thin Metal Shells*, eds J.G. Teng & J.M. Rotter, Spon, London, pp 129-153.

Hoppe H. (1979). "Experimentelle Darstellung der Spannungsverteilung in Bunkern mit Silos in Abhängihkeit vom Fließbild der Anlage." *Dissertation*, TU Clausthal.

Horabik J.A., Ross I.J. & Schwab C.V. (1988). "Effects of spatial orientation on grain load distribution." *Trans. Amer. Soc. Agric. Engrs.*, 31(6), 1787-1793.

Hübner A., J.G. Teng & Saal H. (2006). "Buckling behaviour of large steel cylinders with patterned welds." *Int. Jrnl. of Pressure Vessels and Piping*, 83, 13-26.

Hübner A., Albiez M., Kohler D. & Saal H. (2007). "Buckling of long steel cylindrical shells subjected to external pressure." *Thin-Walled Structures*, 45, 1-7.

Hutchinson J.W. (1965). "Axial buckling of pressurised imperfect cylindrical shells." *AIAA Journal*, 3, 1461-1466.

Hutchinson J.W. & Koiter W.T. (1970). "Postbuckling theory." *Appl. Mech. Rev.*, Vol. 23, 1353-1366.

Hutchinson J.W., Tennyson R.C. & Muggeridge D.B. (1971). "Effect of a Local Axisymmetric Imperfection on the Buckling Behaviour of a Circular Cylindrical Shell under Axial Compression." *AIAA Jnl.*, Vol. 9, 48-53.

ISO 11697 (1995). "Basis for design of structures – loads due to bulk materials." International Standard.

Jaky J. (1948). "Pressures in Silos." *Proc. 2nd Int. Conf. On Soil Mechanics and Foundation Engineering*, Rotterdam, Vol. 1, 103-107.

Jamieson J.A. (1903). "Grain pressures in deep bins." *Trans. Can. Soc. Civil. Eng.*, 17, 554-607.

Jamieson J.A. (1904). "Grain pressures in deep bins." *Eng. News*, 51(10), 236-243.

Janssen H.A. (1895). "Versuche über Getreidedrück in Silozellen." *Zeitschrift des Vereines Deutscher Ingenieure*, Vol. 39, N. 35, 1045-1049.

Jenike A.W. (1967). "Denting of Circular Bins with Eccentric Drawpoints." *J. of the Sruct. Div.,* ASCE, 93 (ST1) 27-35.

Jenike A.W., Johanson J.R. and Carson J.W. (1973) "Bin Loads - Parts 2, 3 and 4: Concepts, Mass Flow Bins, Funnel Flow Bins", *J. of Eng. for Industry*, Trans. ASME, Vol. 95, Series B, No. 1, Feb 1973, pp 1-5, 6-12, 13-16.

Johns D.J. (1966). "On the linear buckling of circular cylindrical shells under asymmetric axial compressive stress distribution." *Journal of the Royal Aeronautical Society*, 1095-1097.

Josserand E., Jullien J.F., Nelias D. & Deloison D. (2007). "Numerical simulation of welding-induced distortions taking into account industrial clamping conditions." *Mathematical Modelling of Weld Phenomena*, 8, 1105-1124.

Jullien J.F., Combescure A. & Zain-ul-abdein M. (2008). "Investigation of laser-beam welding induced distortions in thin sheets of Al 6056T4." *Proc. of the Int. Conf. on Structures and Granular Solids: From Scientific Principles to Engineering Applications*, The Royal Society of Edinburgh, UK, 1-2 July 2008. Festschrift edited by J.F. Chen, J.Y Ooi & J.G. Teng, pp. 145-151.

Kaldenhoff M. (2008). "Experience with funnel flow." *Proc. of the Int. Conf. on Structures and Granular Solids: From Scientific Principles to Engineering Applications*, The Royal Society of Edinburgh, UK, 1-2 July 2008. Festschrift edited by J.F. Chen, J.Y Ooi & J.G. Teng, pp. 59-66.

Kamiński M. (1981). "Untersuchungen des Getreidedrücks in Silozellen." *Bautechnik*, 1, 19-22.

Kamiński M. & Zubrzycki N. (1981). "Untersuchungen des Getreidedrücks in der Zelle eines Großsilos." *IASS-Tagung*, Technische Hochschule Wrocław, Poland.

Ketchum M.S. (1907). "Design of Walls, Bins and Grain Elevators, 1st Edition." *McGraw-Hill*, New York (2nd edn 1911, 3rd edn 1919).

Klopsch E. (1972). "Zur Bemessung prismatischer Silos mit Wänden aus Wellblech und starr gestützten Ecken." *Dissertation*, TU Braunschweig.

Knödel P. & Ummenhofer T. (1996). "Substitute Imperfections for the Prediction of Buckling Loads in Shell Design." *Proc. of the Int. Workshop on Imperfections in Metal Silos: Measurement, Characterisation and Strength Analysis*, CA-Silo, Lyon, France, 87-101.

Knödel P. & Ummenhofer T. (1998). "Ein einfaches Modell zum Stabilitätsnachweis zylindrischer Schalentragwerke auf Einzelstützen." *Der Stahlbau*, 67, Heft 6, 425-429.

Knödel P., Ummenhofer T. & Brenner J. (1994). "Zur Stabilität dünnwandiger Zylinderschalen unter längsgerichteten Einzellasten." in Saal H. & Bucak Oe (eds.) *Neue Entwicklungen in Konstruktiven Ingenieurbau*, Festschrift Mang/Steinhardt, Versuchsanstalt für Stahl, Holz und Stein, TU Karlsruhe.

Knödel P., Ummenhofer T. & Schulz U. (1995). "On the modelling of different types of imperfections in silo shells." *Thin-Walled Structures*, 23, 283-293.

Koenen M. (1895). "Berechnung des Seiten- und Bodendrücks." *Zentralbl. Bauverwaltung*, Vol. 16, 446-449.

Koiter W.T. (1945). "On the stability of elastic equilibrium." *PhD Thesis*, Delft University, Holland.

Koiter W.T. (1963). "The effect of axisymmetric imperfections on the buckling of cylindrical shells under axial compression." *Proc. Kon. Ned. Akad. Wet.*, B66, 265-279. (See also *Appl. Mech. Rev.*, 18, Review 3387, 1965).

Kraus H. (1967). "Thin Elastic Shells." *Wiley and Sons*, New York.

Kroll D. (1975). "Untersuchungen über die Belastung horizontaler Zuganker sowie vertikaler Hängepedel und Gehänge durch Schüttgüter in Silozellen." *Disseration*, TU Braunschweig.

Kvapil R. (1959). "Theorie der Schüttgutbewegung - Auslaufverhalten von Schüttgütern in Bunkern." *VEB Verlag Technik*, Berlin.

Lamé G. (1818). "Examen des différentes méthodes employées pour résoudre les problèmes de géométrie." *Vve Courcier Imprimeur-Libraire*, Paris.

Leczner D. (1963). "Untersuchung des Verhaltens von Sand im Modellsilo." *The Structural Engineer.*, N. 12 Vol. 11.

Li H.Y (1994). "Analysis of Steel Silo Structures on Discrete Supports." *PhD Thesis*, The University of Edinburgh, UK.

Libai A. & Durban D. (1973). "A method for approximate stability analysis and its application to circular cylindrical shells under circumferentially-varying loads." *J. Appl. Mech*, Vol. 40, Trans. ASME, 971-976.

Libai A. & Durban D. (1977). "Buckling of Cylindrical Shells Subjected to Non-uniform Axial Loads." *J. Appl. Mech*, Vol. 44, Trans. ASME, 714-720.

Lo H., Crate H. & Schwartz E.B. (1951). "Buckling of thin-walled cylinders under axial compression and internal pressure." *NACA Report No. 1027*, National Advisory Committee for Aeronautics, Washington D.C., USA.

Lockwood E.H. (1967). "Bipolar coordinates." Chapter 25 in *A Book on Curves*, Cambridge University Press, 186-190.

Lorenz Z. (1908). "Achsensymmetrische Verzerrungen in dunwandigen Hohlzylinder." *Zeitschrift des Vereines Deutscher Ingenieure* 52, 1766-1793.

MacNeal R. (1994). "Finite Elements: Their Design and Application." *Marcel Dekker*, New York.

McLean A.G. & Bravin B. (1985). "Wall loads in eccentric discharge silos." *Int. J. Bulk Solids Storage in Silos*, 1(1), 12-24.

Martens P. (1988). "Silo-Handbuch." *Ernst und Sohn*, Berlin.

McCabe R.P. (1974). "Flow Patterns in Granular Material in Circular Silos." *Géotechnique*, Vol. 24 N. 1, 45-62.

Moriyama R. & Jotaki T. (1980). "An investigation of wall pressures in flowing and static bulk materials in model bins." *Proc. Int. Conf. on Design of Silos for Strength nad Flow*, Lancaster, Proc. Vol 1, 1-12.

Motzkus U. (1974). "Belastung von Siloboden und Auslauftrichtern durch kornige Schuttguter." *Dr.-Ing. Dissertation*, Technical University of Braunschweig, Germany.

MSC NASTRAN (2009). "MSC Nastran FEA solver." *MSC Software Corporation*, California, USA. www.mscsoftware.com

Muir-Wood D. (1990). "Soil behaviour and critical state solid mechanics." *Cambridge University Press*, Cambridge.

Munch-Andersen J. & Nielsen J. (1990). "Pressures in Slender Grain Silos." *Second European Symposium on Stress and Strain in Particulate Solids*, CHISA 1990, Prague, August, 26-31, pp. 9.

Muskhelishvili N. I. (1953). "Some Basic Problems of the Mathematical Theory of Elasticity, 3rd Edition." *P. Noordhoff Ltd.*, Groningen-Holland.

Nanninga N. (1956). "Gibt die übliche Berechnungsart der Drücke auf die Wände und den Boden von Silobauten Sichere Ergebnisse?" *Die Ingenieur*, Vol. 68, N. 44, Nov.

Navier C.L.M.H (1822). "Mémoire sur les lois du mouvement des fluides." *Mém. Acad. Sci. Inst. France*, 6, 389-440.

Nedderman R.M. (1992). "Statics and kinematics of granular materials", *Cambridge University Press*, Cambridge, UK.

Nielsen J. (1983). "Load distribution in silos influenced by anisotropic grain behaviour." *Proc. Int. Conf. on Bulk Materials Storage, Handling & Transporation*, I.E. Aust., Newcastle, 226-230.

Nielsen J. (1998). "Pressures from flowing granular solids in silos", *Phil. Trans. Royal Society of London: Philosophical Transactions: Mathematical, Physical and Engineering Sciences*, Series A, 356 (1747) 2667-2684.

Nielsen J. & Askegaard V. (1977). "Scale errors in model tests on granular media with special reference to silo models", *Powder Technology*, 16, 123-130.

Nielsen J. & Andersen E.Y. (1981). "Silotrykmålinger i Karpalund 1980." *Dept. Struct. Eng. Tech. Univ. Denmark*, Lyngby.

Nielsen J. & Andersen E.Y. (1982). "Loads in grain silos." *Bygningsstatiske Meddelelser*, 53(4), 123-135.

Nielsen J. & Kristiansen N.O. (1979). "Trykmåling på silo i Karpalund." *Dept. Struct. Eng. Tech. Univ. Denmark*, Lyngby.

Nielsen J. & Kristiansen N.O. (1980). "Related measurements of pressure conditions in full-scale barley silo and in model silo." *Proc. Int. Conf. on Design of Silos for Strength and Flow*, Lancaster, UK, 1-23.

Nothdurft H. (1976). "Schüttgutlasten in Silozellen mit Querschnittsverengungen" *Dissertation*, TU Braunschweig.

NRCC (1969). "Canadian farm building code: NRCC No. 21312." *Nat. Res. Council of Canada*, Ottawa, Canada.

Ooi J.Y., Pham L. & Rotter J.M. (1990). "Systematic and random features of measured pressures on full-scale silos." *Eng. Struct.*1990, Vol. 12, No. 2, 74-87.

Ooi J.Y., Rotter J.M. & Zhong Z. (2005). "A statistical evaluation of filling and discharging pressures on silo walls." *Proc. 7th World Congress on Chemical Engineering*, Glasgow, UK, 13-15 July, p. 10.

Ooms M. & Roberts A.W. (1986) . "A Study of Flow Patterns and Wall Pressures in Large Scale Model Storage Silos." *Proc. of the 2nd Int. Conf. on Bulk Materials Storage, Handling and Transportation,* IEAustralia, Wollongong, 143-152.

Otis C.K. & Pomroy J.H. (1957). "Density: a tool in silo research." *Agr. Eng.*, 38(11), 806-807.

Pieper K. (1969). "Investigation of Silo Loads in Measuring Models." *J. of Engrg. for Ind.*, ASME, Series B, Vol. 91, N.2, 365-372.

Pieper. K & Wenzel F. (1964). "Drückverhältnisse in Silozellen." *Wilhelm Ernst und Sohn*, Berlin.

Pieper K. & Wagner K. (1969). "Der Einfluß verschiedener Auslaufarten auf die Seitendrücke der Silozellen." *Aufbereitungs-Technik*, 10, 542-546, Germany.

Pirscher M., Berry P.A., Ding X.L. & Bridge R.Q. (2001). "The shape of circumferential weld-induced imperfections in silos and tanks." *Thin-Walled Structures*, 39, 999-1014.

Pleißner J. (1906). "Versuche zur Ermittlung der Boden und Seitwanddrücke in Getreidesilos." *Zeitschrift des VDI*, 50(1), 976ß986.

PN-B-03202 (1996). "Konstrukcje stalowe. Silosy na materiały sypkie – Obliczenia statyczne i projektowanie." *Polski Komitet Normalizacyjny*, Warsaw, Poland.

Prante N.I. (1896). "Messungen des Getreidedrückes gegen Silowandungen." *Zeitschrift des Verein Deutscher Ingenieure*, 40(39), 112-125, Germany.

Przemieniecki J. S. (1967). "Theory of matrix structural analysis." *McGraw-Hill Book Company*, Singapore.

Rankine W.J.M. (1857). "On the stability of loose earth." *Phil. Trans. Roy. Soc.*, London, VOl. 147, p. 9.

Ravanet J. (1976). "Overpressures in silos with off-centre emptying." *Acier-Stahl-Metal*, V. 41, N. 3, March, 109-113.

Reimbert M. & Reimbert A. (1961). "Silos." *Bauverlag*, Wiesbaden, Berlin. (2nd ed. 1976).

Reimbert M. & Reimbert A. (1976). "Silos: Theory and Practice." *Trans. Tech. Publications*, Clausthal, Bay Village, Ohio, USA.

Riks E. (1979). "An incremental approach to the solution of snapping and buckling problems." *Int. J. of Solids and Structures*, 15, 529-551.

Riks E., Rankin C.C. & Brogan F.A. (1996). "On the solution of mode jumping phenomena in thin-walled shell structures." *Computer Methods in Applied Mechanics and Engineering*, 136, 59-92.

Roberts I. (1882). "Pressures of stored grain." *Engineering*, 34, 399.

Roberts I. (1884). "Determination of the vertical and lateral pressure of granular substances." *Proc. Royal Society of London*, 36, 225-240.

Roberts A.W. & Ooms M. (1983). "Wall Loads in Large Metal and Concrete Silos and Silos due to Eccentric Draw-Down and other Factors." *Proc. 2nd Int. Conf. on Design of Silos for Strength and Flow*, 151-170.

Robertson A. (1928). "The strength of tubular struts." *Proc. of the Royal Society of London*, Series A 121, 558.

Ross I.J., Moore D.W., Loewer O.J. & White G.M. (1980). "Model studies on grain bin failures." *ASAE Paper No. 80-2-264*, Amer. Soc. Of Agric. Eng, St. Joseph, Michigan, USA.

Rotter J.M. (1983a). "Stress Amplification in Unstiffened Steel Silos and Tanks." *Research Report R437*, University of Sydney, School of Civil and Mining Engineering, Australia.

Rotter J.M. (1983b). "Structural Effects of Eccentric Loading in Shall Steel Bins." *Proc. 2nd Int. Conf. on the Design of Silos for Strength and Flow*, Stratford upon Avon, November, 446-463.

Rotter J.M. (1985a). "Design under axial compression." *Design of Steel Bins for the Storage of Bulk Solids*, J.M. Rotter Ed., The University of Sydney, School of Civil and Mining Engineering, Australia, 122-137.

Rotter J.M. (1985b). "Local Inelastic Collapse of Pressurised Thin Cylindrical Shells under Axial Compression." *Research Report R502*, University of Sydney, School of Civil and Mining Engineering, Australia.

Rotter J.M. (1985c). "Buckling of Ground-Supported Cylindrical Steel Bins under Compressive Wall Loads." *Proc. Metal Structs. Conf*, IE Australia, Melbourne, 71-81.

Rotter J.M. (1986). "The analysis of steel bins subject to eccentric discharge." *Proc. of the 2nd Int. Conf. on Bulk Materials Storage, Handling and Transportation,* IEAustralia, Wollongong, 264-271.

Rotter J.M. (1987a). "Membrane Theory of Shells for Bins and Silos." *Trans. of Mech. Eng*., IE Aust, ME12 (3), 135-146.

Rotter J.M. (1987b). "Bending Theory of Shells for Bins and Silos." *Trans. of Mech. Eng*., IE Aust, ME12 (3), 147-159.

Rotter J.M. (1988). "Final stability assessment for 10,000 tonne silos at Port Kembla." *Investment Report S684*, University of Sydney, School of Civil and Mining Engineering, Australia.

Rotter J.M. (1989). "Stress Amplification in Unstiffened Cylindrical Steel Silos and Tanks." *Civil Eng. Transactions*, IE Aust, CE31(3), 142-148.

Rotter J.M. (1990). "Local inelastic collapse of pressurised thin cylindrical steel shells under axial compression." *Jrnl. of Struct. Eng.*, ASCE, 116(7), 1955-1970.

Rotter J.M. (1996). "Elastic plastic buckling and collapse in internally pressurised axially compressed silo cylinders with measured axisymmetric imperfections: interactions between imperfections, residual stresses and collapse." *Proc. Int. Workshop of Imperfections in Metal Silos: Measurement, Characterisation and Strength Analysis*, CA-Silo, Lyon, France, 119-140.

Rotter J.M. (1997). "Design standards and calculations for imperfect pressurised axially compressed cylinders." *Proc., Int. Conf. on Carrying Capacity of Steel Shell Structures*, Brno, Czech Republic, 1-3 October 1997, pp 354-360.

Rotter J.M. (1998). "Development of proposed European design rules for buckling of axially compressed cylinders." *Advances in Structural Engineering*, 1(4), 273-286.

Rotter J.M. (1999a). "Flow and Pressures in Silo Structural Integrity Assessments." *Proc. Int. Symposium: Reliable Flow of Particulate Solids III*, Porsgrunn, Norway, 281-292.

Rotter J.M. (1999b). "Proposal for generalisation of the elastic-plastic buckling interaction rule from Eurocode 3 Part 1.6." submission to *CEN TC250/SC3/PT4 and ECCS TWG8.4 Buckling of Shells*, March 1999, pp 8.

Rotter J.M. (2000). "Background Document for the Guide to the Economic Design of Circular Metal Silos." *Research Report R0-021*, The University of Edinburgh, School of Civil and Environmental Engineering.

Rotter J.M. (2001a). "Guide for the Economic Design of Circular Metal Silos.", *Spon Press*, London & New York.

Rotter J.M. (2001b). "Pressures, Stresses and Buckling in Metal Silos containing Eccentrically Discharging Solids." *Festschrift Richard Greiner*, Celebration volume for the 60th birthday of Prof. Richard Greiner, TU Graz, Austria, October, 85-104.

Rotter J.M. (2002). "Shell Buckling and Collapse Analysis for Structural Design: The New Framework of the European Standard." *New Approaches to Structural Mechanics, Shells & Biological Structs*, Eds H. R. Drew & S. Pellegrino, Kluwer Academic, London, 355-378.

Rotter J.M. (2004). "Buckling of cylindrical shells under axial compression." Chapters 1 & 2 in *Buckling of Thin Metal Shells*, Eds J.G. Teng & J.M. Rotter, Spon, London, pp 1-87.

Rotter J.M. (2006). "Elephant's foot buckling in pressurised cylindrical shells." *Stahlbau*, Vol 75, Heft 9, 742-747.

Rotter J.M. (2007a). "Silo and hopper design for strength." Chapter 4 in *Bulk Solids Handling Equipment Selection and Operation*, Ed. D. McGlinchey, Blackwell, Oxford, UK.

Rotter J.M. (2007b). "A framework for exploiting different computational assessments in structural design." *Proc. 6th Int. Conf. on Steel and Aluminium Structures*, 6th ICSAS 07, Oxford, UK.

Rotter J.M. (2008). "The Elastic-Plastic Imperfection Sensitivity of Axially Compressed Cylinders with Weld Depressions." *Proc. Eurosteel 2008 Conference*, 3-5 September, Graz, Austria, 1497-1502.

Rotter J.M., Ansourian P. & Trahair N. S. (1986). "A Survey of Recent Buckling Research on Steel Silos." *Proc. of the 2nd Int. Conf. on Bulk Materials Storage, Handling and Transportation,* IEAustralia, Wollongong, 68-75.

Rotter J.M. & Teng J.G. (1989a). "Elastic stability of cylindrical shells with weld depressions." *Jrnl. of Struct. Eng.*, ASCE, 115(5), 1244-1263.

Rotter J.M. & Teng J.G. (1989b). "Elastic stability of lap-jointed cylinders." *Jrnl. of Struct. Eng.*, ASCE, 115(3), 683-697.

Rotter J.M. & Zhang Q. (1990). "Elastic buckling of imperfect cylinders containing granular solids." *Jrnl. of Struct. Eng.*, ASCE, 116(8), 2253-2271.

Rotter J.M., Berry P.A. & Ooi J.Y. (1990). "The Discrete Rupture Surface Theory applied to Silos under Eccentric Discharge." *Proc. 2nd European Symposium on the Stress and Strain Behaviour of Particulate Solids and Silo Stresses*, Prague, Czechoslovakia, 1-6.

Rotter J.M., Coleman R., Ding X.L. & Teng J.G. (1992). "The measurement of imperfections in cylindrical silos for buckling strength assessment." *Proc. of the 4th Int. Conf. on Bulk Materials Storage, Handling and Transportation,* IEAustralia, Wollongong, 473-479.

Rotter J.M., Ooi J.Y. & Zhong Z. (2006). "Critical pressure conditions in silos." *Proc. 5th Int. Conf. for Conveying and Handling of Particulate Solids*, Sorrento, Italy, 27-31.

Saal H., Kahmer H. & Reif A. (1979). "Beullasten axial gedrückter Kreiscylinderschalen mit Innendruck - Neue Versuche und Vorschriften." *Der Stahlbau*, 48(9), 262-269.

Sadowski A.J. & Rotter J.M. (2008). "A Study of Buckling in Steel Silos under Eccentric Discharge Flows of Stored Solids." *Proc. Eurosteel 2008 Conference*, 3-5 September, Graz, Austria, 1509-1514.

Sadowski A.J. & Rotter J.M. (2009). "Eccentric discharge buckling of a very slender silo." *Proc. IASS 2009 Symposium*, 28 September – 2 October, Valencia, Spain.

Sadowski A.J. & Rotter J.M. (2010). "A Study of Buckling in Steel Silos under Eccentric Discharge Flows of Stored Solids." *Jrnl. of Eng. Mech.*, ASCE, 136(6), 769-776.

Safarian S. S. & Harris E.C. (1985). "Design and Construction of Silos and Bunkers." *Van Nostrand Reinhold Co.*, New York.

Saul R.A. (1953). "Measurement of grain pressures on bin walls and flows." *Agr. Eng.*, 34(4), 231-234.

Schmidt H. & Rotter J.M. (2008). "Cylindrical shells of constant wall thickness under general loading." Chapter 10 in *Stability of Steel Shells: European Design Recommendations 5th edition 2008*, European Convention for Constructional Steelwork, Brussels, 167-216.

Schmidt H. & Samuelsen L. (2008). "Cylindrical shells with longitudinal stiffeners under meridional compression." Chapter 18 in *Stability of Steel Shells: European Design Recommendations 5th edition 2008*, European Convention for Constructional Steelwork, Brussels, 353-364.

Schmidt H. & Winterstetter T.A. (2004a). "Cylindrical shells under torsion and transverse shear." in *Buckling of Thin Metal Shells*, Eds J.G. Teng & J.M. Rotter, Spon, London, pp 207-229.

Schmidt H. & Winterstetter T.A. (2004b). "Cylindrical shells under combined loading: axial compression, external pressure and transverse shear." in *Buckling of Thin Metal Shells*, Eds J.G. Teng & J.M. Rotter, Spon, London, pp 261-285.

Schnell W. (1959). "Zur Stabilität dunnwandiger Langsgedruckter Kreiszylinderschalen bei Zusatzlichem Innendruck." *Proc. of the IUTAM Symposium on the Theory of Thin Elastic Shells*, Delft, 167-188.

Seide P. (1975). "Small elastic deformations of thin shells." *Noordhoff International*, Leyden.

Sielamowicz I. & Kowalewski T. (2007). "Eccentric Flows Registered by DPIV in a Model of Silo." *IUTAM Symposium on Multiscale Problems in Multibody System Contacts*, Ed. P. Eberhard, Springer, Netherlands, 281-290.

Singer J. (1980). "Buckling Experiments on Shells: A Review of Recent Developments." *TAE Rep. 43*, Dept. Aero. Eng. Technion, Israel Inst. of Tech.

Singer J. (1982). "The status of buckling investigations of shells." In *Buckling of Shells, Proceedings of a State-of-the-Art Colloquium*, ed. E. Ramm, Springer-Verlag, Berlin.

Song C.Y. (2004). "Effects of patch loads on structural behaviour of circular flat-bottomed steel silos." *Thin-Walled Structures* 42, 1519-1542.

Song C.Y. & Teng J.G. (2003). "Buckling of steel silos subject to code-specified eccentric discharge pressures." *Engineering Structures* 25, 1397-1417.

Song C.Y., Teng J.G. & Rotter J.M. (2004). "Imperfection sensitivity of thin elastic cylindrical shells subject to partial axial compression." *Int. Jrnl. Of Solids and Structures*, 41, 7155-7180.

Southwell R. V. (1914). "On the general theory of elastic stability." *Philosophical Transactions of the Royal Society*, London, Series A 213, 187-202.

Steinhardt O. & Schulz V. (1971). "Zum Beulverhalten von Kreiszylinderschalen." *Schweize Bauzeitung*, 89(1).

Sugden M.B. (1980). "Effect of Initial Density on Flow Patterns in Circular Flat Bottomed Silos." *Proc. Int. Conf. on Design of Silos for Strength and Flow*, University of Lancaster, 11-28.

Takhtamishev S.G. (1953). "Experimental values of silo pressures." *Central Research Institute of Industrial Buildings (ZNIPS)*, Moscow, U.S.S.R. (in Russian)

Teng J.G., Lin X. & Rotter J.M. (2005). "Analysis of geometric imperfections in full-scale welded steel silos." *Eng. Struct.*, 27(6), 938-950.

Teng J.G. & Rotter J.M. (1992). "Buckling of Pressurised Axisymetrically-Imperfect Cylinders under Axial Loads." *Jrnl. of Eng. Mech.*, ASCE, 118, 229-247.

Teng J.G. & Song C.Y. (2001). "Numerical models for nonlinear analysis of elastic shells with eigenmode-affine imperfections." *Int. Jrnl. of Solids and Structures.*, 38(18), 3263-3280.

Thompson S.A., Usry J.L. & Legg J.A. (1986). "Loads in a model grain bin as affected by various unloading techniques." *Trans. Amer. Soc. Agric. Engrs.*, 29(2), 556-561.

Timoshenko S. P. (1910). "Einige Stabilitätsprobleme der Elastizitätstheorie." *Zeischrift für Angewandte Mathematik und Physik* 58, 337-357.

Timoshenko S. P. & Woinowsky-Krieger S. (1959). "Theory of Plastes and Shells, 2nd Edition." *McGraw-Hill Book Company*, Singapore.

Timoshenko S.P. & Gere J. M. (1963). "Theory of Elastic Stability." *McGraw-Hill Book Company*, Singapore

Timoshenko S.P. & Goodier J.N. (1970). "Theory of Elasticity, 3rd Edition." *McGraw-Hill Book Company*, Singapore.

Tolz M. (1903). "Discussion on grain pressures in deep bins." *Trans. Can. Soc. Civil Eng.*, 17, 641-644.

Trahair N.S., Abel A., Ansourian P., Irvine H.M. & Rotter J.M. (1983). "Structural Design of Steel Bins for Bulk Solids." *Aust. Inst. Steel Constr.*, Sydney.

Ummenhofer T. (1996). "Stability behaviour of imperfect silo shells." *PhD Thesis*, TU Karlsruhe.

Ummenhofer T. & Knödel P. (1996). "Typical Imperfections of Steel Silo Shells in Civil Engineering." *Proc. of the Int. Workshop on Imperfections in Metal Silos: Measurement, Characterisation and Strength Analysis*, CA-Silo, Lyon, France, 103-118.

Urugal A.C. & Fenster S.K. (1977). "Advanced Strength and Applied Elasticity." *Elsevier*, USA.

Vidal P., Couto A., Ayuga F. & Guaita M. (2006). "Influence of hopper eccentricity on discharge of cylindrical mass flow silos with rigid walls." *Jrnl. of Eng. Mech.*, ASCE, 132(9), 1026-1033.

Walker D.M. (1966). "An Approximate Theory for Pressure and Arching in Hoppers." *Chem. Eng. Science*, Vol. 21, 957-997.

Walters J.K. (1973). "A Theoretical Analysis of Stresses in Silos with Vertical Walls." *Chem. Eng. Science*, 28, 13-21.

Watson D. (2010). "Buckling Experiments on Silos under Eccentric Discharge." *BEng Thesis*, The University of Edinburgh, UK.

Weingarten V.I., Morgan E.J. & Seide P. (1965). "Elastic stability of thin-walled cylindrical and conical shells under combined internal pressure and axial compression." *AIAA Journal*, 3(6), 1118-1125.

Wilson W.M. & Newmark N.W. (1933). "The strength of thin cylindrical shells as columns." *Bulletin N. 255*, Univ. Illinois Engg Exptl Sta.

Wood J.G.M. (1983). "The Analysis of Silo Structures Subject to Eccentric Discharge." *Proc. of the 2nd Int. Conf. on Design of Silos for Strength and Flow*, Stratford-upon-Avon, 132-144.

Wright A.W.S. (1979). "Silos – model and field studies." *PhD Thesis*, The University of Manchester, UK, pp. 480.

Yamaki N. (1984). "Elastic Stability of Circular Cylindrical Shells." *North-Holland*, Amsterdam.

Zakrzewski M.S. (1959). "Design of silos for grain storage." *Trans. S. Afr. Ins. Civil. Eng.*, 1, 69-89-.

Zienkiewicz O.C. & Taylor R. L. (2006). "The Finite Element Method for Solid and Structural Mechanics, 6th Edition." *Butterworth-Heinemann*, UK. (1st edition in 1967, McGraw-Hill).

Zhong Z., Ooi J.Y. & Rotter J.M. (1996). "The Sensitivity of Silo Flow and Wall Pressures in to Filling Method." *Proc. 12th Int. Congress of Chemical and Process Engineering*, CHISA 1996, Prague, August, pp. 10.

Zhong Z., Ooi J.Y. & Rotter J.M. (2001). "The Sensitivity of Silo Flow and Wall Stresses to Filling Method." *Engineering Structures*, 23, 756-767.

Zhong Z., Rotter J.M. & Ooi J.Y. (2010). “Estimation of eccentric flow channel dimensions in funnel flow silos.” Experimental report, The University of Edinburgh.

Appendix A – Stress patterns in silos subject to eccentric discharge using a propped cantilever analogy

A.1 Introduction: the 'arc-beam'

Certain aspects of the mechanics of behaviour of a silo under eccentric pipe flow are explored in this appendix through the analogy of the silo with a propped cantilever using simple beam theory. The portion of the shell which is most influenced by the flow channel may be conceptually isolated and treated as an independent 'arc-beam' (Fig. A.1), whose cross-section consists of a an arc of finite wall thickness t and a circumferential spread $2\theta_c$, which may or may not be related to the flow channel wall contact angle θ_c of the Rotter (1986) and EN 1991-4 (2007) eccentric discharge pressure models.

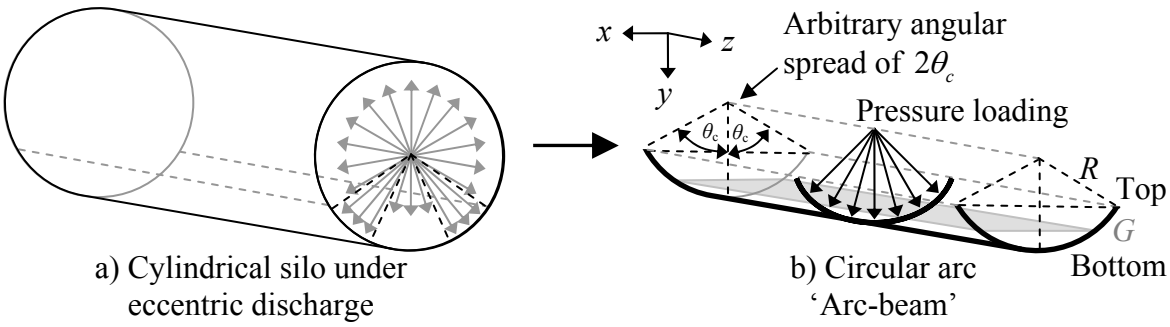

Fig. A.1 – Silos under eccentric discharge by beam theory analogy

The stress distribution which arises in the silo wall adjacent to the centre and edges of a flow channel under eccentric pipe flow using shell theory (e.g. Fig. 2.9 and Fig. 2.13) is very similar in form to that which arises in the extreme fibres of a propped cantilever under a uniformly distributed load using Euler beam theory, as illustrated in Fig. A.2. There are of course paramount limitations to this analogy and the stresses do not directly correspond to each other, but the comparison may nonetheless provide useful insights into the far more complex behaviour of the silo under eccentric discharge. Additionally, the analogy presented here was instrumental to the development of the superelliptical flattening imperfection form presented in Chapter 6.

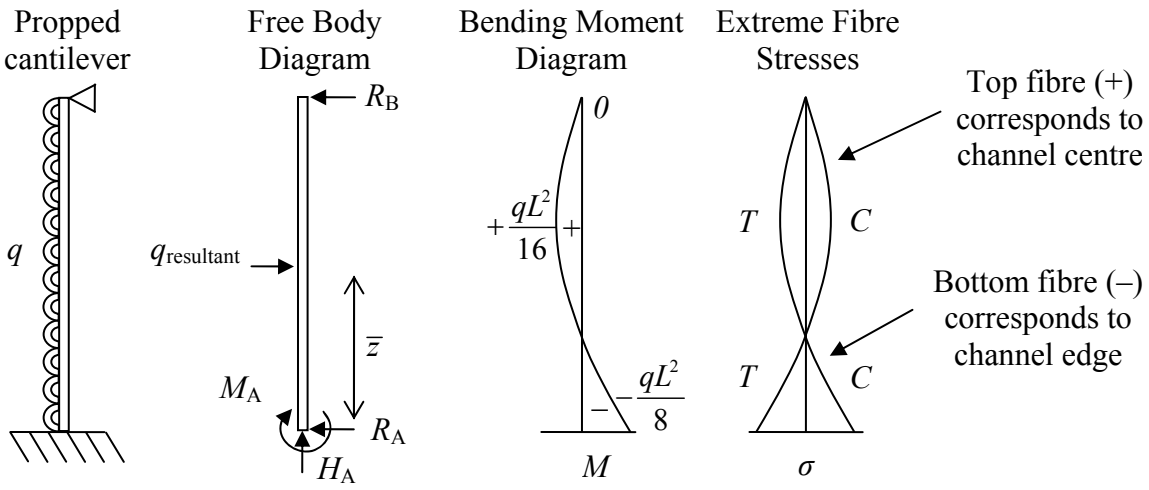

Fig. A.2 – System diagrams for a propped cantilever with uniformly distributed load

The extreme fibre stresses are given by $\sigma(y,z)_{\pm} = \frac{M(z)}{Z_{\pm}}$ (A.1)

where $Z_{\pm}$ is the section modulus for the top (+) or bottom (–) fibres, while I is the second moment of area through the centroid of the arc-beam:

$$Z_{+} = \frac{I_{centroid}}{y_{+}} = \frac{I_G}{y_{top}} \text{ and } Z_{-} = \frac{I_{centroid}}{y_{-}} = \frac{I_G}{y_{bot}} \quad \text{(A.2)}$$

The bending moment distribution is given by the following general expression which depends on the form of the distributed load:

$$M(z) = R_B L - q_{\text{resultant}}\bar{z} = -\frac{q}{8}\left(4z^2 - 5zL + L^2\right) \text{ for a uniformly distributed load.} \quad \text{(A.3)}$$

More comprehensive 'Janssen-like' load distributions may be explored if a closer numerical correlation between the two different theories is desired. This may pave the way for a short-hand, semi-empirical method to obtain an approximation of the shell stresses directly for design purposes, without resorting to an onerous finite element analysis or Fourier series-based membrane theory analysis.

If the section modulus on either extreme fibre increases, the stresses on that fibre decrease. This is important in the context of determining whether a change in the cross-sectional geometry of the arc-beam, based on this relatively simple assessment, is likely to lead to an increase or reduction in extreme fibre stresses. By analogy, this corresponds to the consideration whether a change in geometry the silo wall under eccentric discharge leads to a reduction in the membrane stresses. Such an analogy was

extremely helpful in Chapter 3 in supporting the finding that GNA load factors have been consistently higher than the LBA load factors under eccentric pipe flow throughout this thesis.

A.2 Arc-beam segment properties

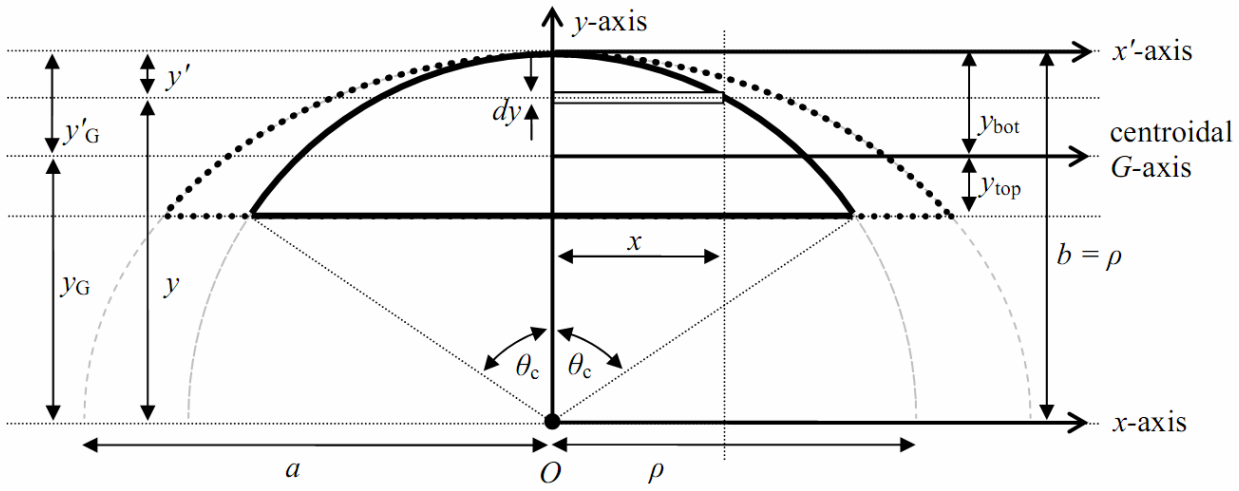

Fig. A.3 – Circular and elliptical arc segments

Circular and elliptical segments of angular spread $2\theta_c$, where θ_c *always* $\leq \frac{1}{2}\pi$.

Circular radius: ρ.

Elliptical major axis: a.

Elliptical minor axis: $b = \rho$.

The coordinates are expressed parametrically in terms of the angle θ, which is taken as zero on the vertical y axis and may be taken to go either clockwise or anti-clockwise. When considering deformed geometries, the general superellipse equations (Lamé, 1818; Gridgeman, 1970) allow direct control over the flatness of the geometry through variation of the parameters p and q (> 0, $= 2$ for ellipse).

Ellipse: $\left(\frac{x}{a}\right)^2 + \left(\frac{y}{b}\right)^2 = 1$ and $x = a\sin\theta,\ y = b\cos\theta,\ y' = b\left(1-\cos\theta\right)$

Superellipse: $\left(\frac{x}{a}\right)^p + \left(\frac{y}{b}\right)^q = 1$ and $x = a\sin^{\frac{2}{p}}\theta,\ y = b\cos^{\frac{2}{q}}\theta,\ y' = b\left(1-\cos^{\frac{2}{q}}\theta\right)$

The area of a segment is given by $A = \int dA = \int x dy$.

The centroid of a segment about the *x*-axis is given by $y_G = \frac{\int ydA}{\int dA} = \frac{\int yxdy}{\int xdy}$, and about the *x*'-axis by $y'_G = \rho - y_G$.

The second moment of area about the *x*-axis is given by $I_x = \int y^2 dA = \int y^2 xdy$, about the *x*'-axis by $I_{x'} = \int y'^2 dA = \int y'^2 xdy'$ and about the centroidal *G*-axis by $I_G = I_x - Ay_G^2 = I_{x'} - Ay_G'^2$ using the Parallel Axis Theorem. The integrals are computed in the range $0 \le \theta \le \theta_c$ and are multiplied by a factor of 2 to account for symmetry about the *y* axis.

For a circular arc segment as a function of the radius and half-spread angle θ_c, the properties are:

$$A(\rho,\theta_c) = \frac{1}{2}\rho^2(2\theta_c - \sin 2\theta_c) \tag{A.4}$$

$$y_G(\rho,\theta_c) = \frac{4\rho\sin^3\theta_c}{3(2\theta_c - \sin 2\theta_c)} \tag{A.5}$$

$$y'_G(\rho,\theta_c) = \rho - \frac{4\rho\sin^3\theta_c}{3(2\theta_c - \sin 2\theta_c)} \tag{A.6}$$

$$I_x(\rho,\theta_c) = \frac{\rho^4}{16}(4\theta_c - \sin 4\theta_c) \tag{A.7}$$

$$I_{x'}(\rho,\theta_c) = \frac{\rho^4}{16}\left(20\theta_c - 16\sin\theta_c - 8\sin 2\theta_c + \frac{16}{3}\sin 3\theta_c - \sin 4\theta_c\right) \tag{A.8}$$

Similarly, for an elliptical arc segment as a function of the minor and major axes and half-spread angle θ_c, the properties are:

$$A(a,b,\theta_c) = \frac{1}{2}ab(2\theta_c - \sin 2\theta_c) \tag{A.9}$$

$$y_G(b,\theta_c) = \frac{4b\sin^3\theta_c}{3(2\theta_c - \sin 2\theta_c)} \tag{A.10}$$

$$y'_G(b,\theta_c) = b - \frac{4b\sin^3\theta_c}{3(2\theta_c - \sin 2\theta_c)} \tag{A.11}$$

$$I_x(a,b,\theta_c) = \frac{ab^3}{16}(4\theta_c - \sin 4\theta_c) \tag{A.12}$$

$$I_{x'}(a,b,\theta_c) = \frac{ab^3}{16}\left(20\theta_c - 16\sin\theta_c - 8\sin 2\theta_c + \frac{16}{3}\sin 3\theta_c - \sin 4\theta_c\right) \tag{A.13}$$

When θ_c is set to ½π, the familiar results for a half-circle and half-ellipse are obtained:

$$A(\rho)=\frac{\pi\rho^2}{2},\ y_G(\rho)=\frac{4\rho}{3\pi},\ y'_G(\rho)=\frac{\rho(3\pi-4)}{3\pi}\ \text{and}\ I_x(\rho)=\frac{\pi\rho^4}{8} \tag{A.14}$$

$$A(a,b)=\frac{\pi ab}{2},\ y_G(b)=\frac{4b}{3\pi},\ y'_G(b)=\frac{b(3\pi-4)}{3\pi}\ \text{and}\ I_x(a,b)=\frac{\pi ab^3}{8} \tag{A.15}$$

For superelliptical geometries, a closed-form solution is available only for the integral in the range $0 \le \theta \le ½\pi$ albeit in terms of the gamma function, $\Gamma(x)$. Hence, only a full semi-superellipse may be considered as a geometrical feature of an arc-beam section. The gamma function is defined as $\Gamma(x)=\int_0^\infty e^{-t}t^{x-1}dt$. It is evaluated numerically by many professional software packages, i.e. Excel, Matlab, Maple etc., and may be easily invoked.

$$A(a,b,p,q)=\frac{2ab}{q}\frac{\Gamma\left(\frac{1}{q}\right)\Gamma\left(\frac{1+p}{p}\right)}{\Gamma\left(\frac{p+pq+q}{pq}\right)} \tag{A.16}$$

$$y_G(b,p,q)=\frac{4^{\frac{1}{q}}b}{2\sqrt{\pi}}\frac{\Gamma\left(\frac{2+q}{2q}\right)\Gamma\left(\frac{p+pq+q}{pq}\right)}{\Gamma\left(\frac{2p+pq+q}{pq}\right)}\ \text{and}\ y'_G(b,p,q)=b-y_G(b,p,q) \tag{A.17}$$

$$I_x(a,b,p,q)=\frac{2ab^3}{q}\frac{\Gamma\left(\frac{3}{q}\right)\Gamma\left(\frac{1+p}{p}\right)}{\Gamma\left(\frac{3p+pq+q}{pq}\right)} \tag{A.18}$$

When $p = q = 2$, Eqs A.16 to A.18 reduces to those in Eq. A.15. The equations presented in this section are thus left in the general form *f*(radius, angle) as this allows their direct implementation as functions or subroutines in a computer algorithm. It allows the isolation of the contributions of the various geometric components of the given cross-sectional geometry to the properties of that geometry (i.e. area, centroid, second moment of area), which becomes very important for more complex shapes, as presented shortly.

A.3 Proposed arc-beam geometries

The equations derived in this section are algebraically very protracted. They are left as composite functions of the section properties of the individual geometric features which

form the given beam geometry, thus allowing them to be as clear as possible and valid for finite 'shell' thicknesses. Note that in these derivations it is assumed that the inner geometric feature (i.e. the inner arc) terminates at the same y coordinate as the outer feature, rather than at the same angle θ to the vertical axis. This allows for greater freedom in deriving more complex sections, such as semielliptical arcs, full semiellipses and elliptical indentations. The section properties derived in this appendix may additionally prove useful for structural engineers designing unusually-shaped thin-walled circular members, usually from cold-formed steel.

A.3.1 Circular arc-beam (undeformed reference case)

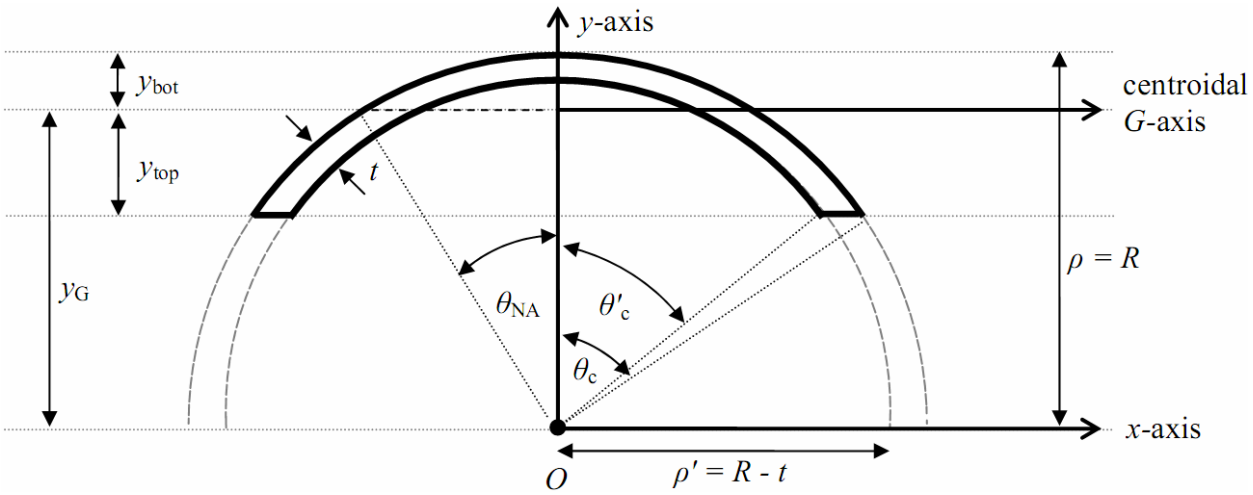

Fig. A.4 – Undeformed circular arc-beam of thickness t

Outer circular segment: radius $\rho = R$; spread $2\theta_c$.

Inner circular segment: radius $\rho' = R - t$; spread $2\theta'_c$.

Extreme fibre distances: $y_{top} = y_G - R\cos\theta_c$, $y_{bot} = R - y_G$

Relation: $\theta'_c = \cos^{-1}\left[\dfrac{R}{R-t}\cos\theta_c\right]$

The properties of the shell are as follows:

$$A_{shell} = A\left(R,\theta_c\right) - A\left(R-t,\theta'_c\right) \tag{A.19}$$

$$y_{G,shell} = \frac{y_G\left(R,\theta_c\right)A\left(R,\theta_c\right) - y_G\left(R-t,\theta'_c\right)A\left(R-t,\theta'_c\right)}{A_{shell}} \tag{A.20}$$

$$I_{G,shell} = I_x\left(R,\theta_c\right) - I_x\left(R-t,\theta'_c\right) - A_{shell}y^2_{G,shell} \tag{A.21}$$

An alternative treatment, considered for this reference geometry only, may be made in terms of a different input parameter, the angle to the elastic neutral axis, here denoted as θ_{NA}, which gives the location of the section centroid directly. However, this requires that the value of θ_c be deduced numerically through the solution of the following transcendental equation:

$$y_{G,shell} = R\cos\theta_{NA} = \frac{y_G(R,\theta_c)A(R,\theta_c) - y_G(R-t,\theta_c')A(R-t,\theta_c')}{A_{shell}} \tag{A.22}$$

The values of A_{shell} and $I_{G,shell}$ may be found as above using the new values of θ_c. This procedure was employed in Chapter 3.

A.3.2 Elliptical arc-beam

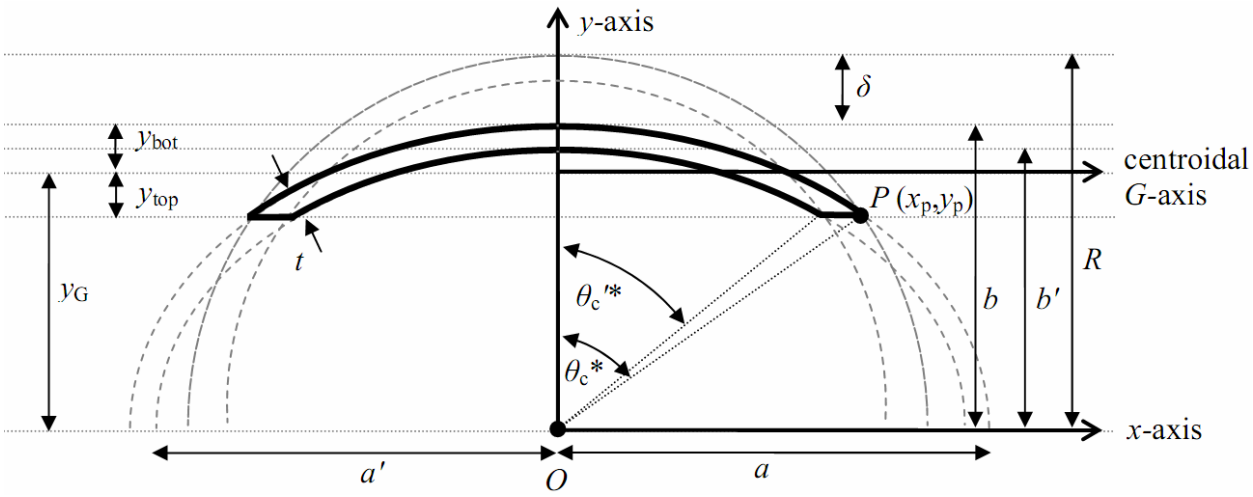

Fig. A.5 – Deformed elliptical arc-beam of thickness t

The point P is on both the circle and the ellipse: $(x_p,y_p) = (R\sin\theta_c, R\cos\theta_c) = (a\sin\theta_c^*, b\cos\theta_c^*)$.

Hence: $\theta_c^* = \cos^{-1}\left[\frac{R}{R-\delta}\cos\theta_c\right]$ and $a = R\frac{\sin\theta_c}{\sin\theta_c^*}$. The parametric angle of the ellipse, centred at O, is denoted with a '*', while that of the circle is without this.

Outer elliptical arc: major axis a; minor axis $b = R - \delta$; spread $2\theta_c^*$.

Inner elliptical arc: major axis $a' = a - t$; minor axis $b' = b - t$; spread $2\theta'^*_c$.

Extreme fibre distances: $y_{top} = y_G - R\cos\theta_c = y_G - b\cos\theta_c^*$, $y_{bot} = R - \delta - y_G$

Relations: $\theta_c^* = \cos^{-1}\left[\frac{R}{R-\delta}\cos\theta_c\right]$ and $\theta_c' = \cos^{-1}\left[\frac{R}{R-t}\cos\theta_c\right]$

The properties of the shell are as follows:

$$A_{shell} = A\left(a,b,\theta_c^*\right) - A\left(a',b',\theta_c^{*\prime}\right) \tag{A.23}$$

$$y_{G,shell} = \frac{y_G\left(b,\theta_c^*\right)A\left(a,b,\theta_c^*\right) - y_G\left(b',\theta_c^{*\prime}\right)A\left(a',b',\theta_c^{*\prime}\right)}{A_{shell}} \tag{A.24}$$

$$I_{G,shell} = I_x\left(a,b,\theta_c^*\right) - I_x\left(a',b',\theta_c^{*\prime}\right) - A_{shell}y_{G,shell}^2 \tag{A.25}$$

A.3.3 Semielliptical (or semi-superelliptical) arc-beam

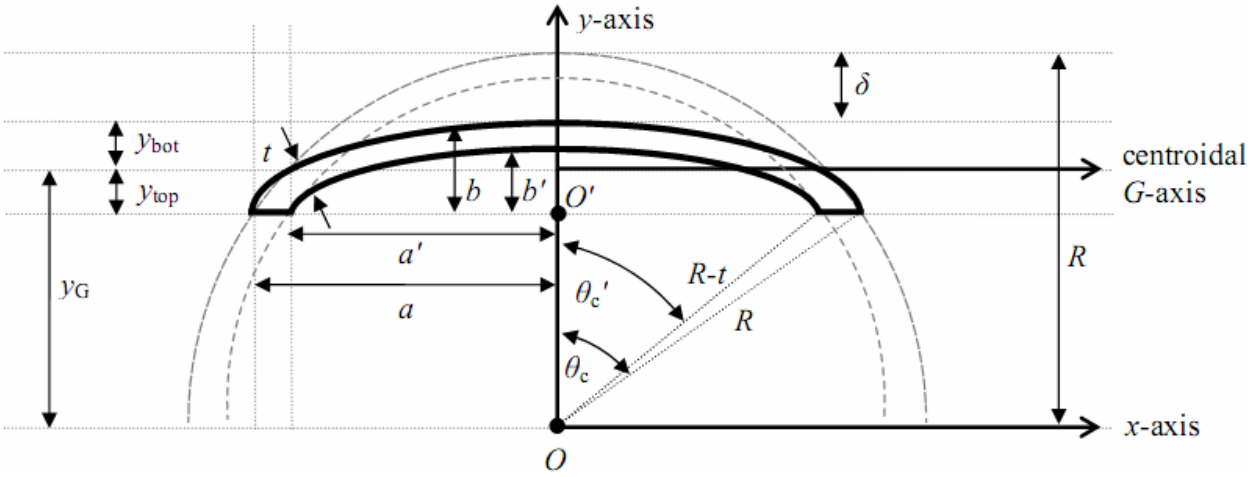

Fig. A.6 – Deformed semielliptical arc-beam of thickness t

Outer semiellipse: major axis $a = R\sin\theta_c$; minor axis $b = R(1 - \cos\theta_c) - \delta$.

Inner semiellipse: major axis $a' = a - t$; minor axis $b' = b - t$.

Extreme fibre distances: $y_{top} = y_G - R\cos\theta_c$, $y_{bot} = b - y_G + R\cos\theta_c$

Relation: $\theta_c' = \cos^{-1}\left[\frac{R}{R-t}\cos\theta_c\right]$

Note that although the arc-beam itself only covers a spread of $2\theta_c$ with respect to the global origin O, the semiellipse has a full spread of π with respects to its own origin O'. The properties of the shell are therefore as follows:

$$A_{shell} = A\left(a,b\right) - A\left(a',b'\right) \tag{A.26}$$

$$y_{G,shell} = \frac{y_G\left(b\right)A\left(a,b\right) - y_G\left(b'\right)A\left(a',b'\right)}{A_{shell}} + R\cos\theta_c \tag{A.27}$$

$$I_{G,shell} = I_x\left(a,b\right) - I_x\left(a',b'\right) - A_{shell}\left(y_{G,shell} - R\cos\theta_c\right)^2 \tag{A.28}$$

The flatness may be additionally controlled with the p and q parameters using for the properties of the superellipse in Eqs A.16 to A.18 instead of Eq. A.15. If this is the case, the shape must be extended fully so that $\theta_c = \theta'_c = ½\pi$, and the above equations become:

$$A_{shell} = A(a,b,p,q) - A(a',b',p,q) \tag{A.29}$$

$$y_{G,shell} = \frac{y_G(b,p,q)\,A(a,b,p,q) - y_G(b',p,q)\,A(a',b',p,q)}{A_{shell}} \tag{A.30}$$

$$I_{G,shell} = I_x(a,b,p,q) - I_x(a',b',p,q) - A_{shell}\,y_{G,shell}^2 \tag{A.31}$$

where $a = R$, $b = R - \delta$, and a' and b' as before.

A.3.4 Circular arc with elliptical indentation and reversal of curvature: Indented arc-beam

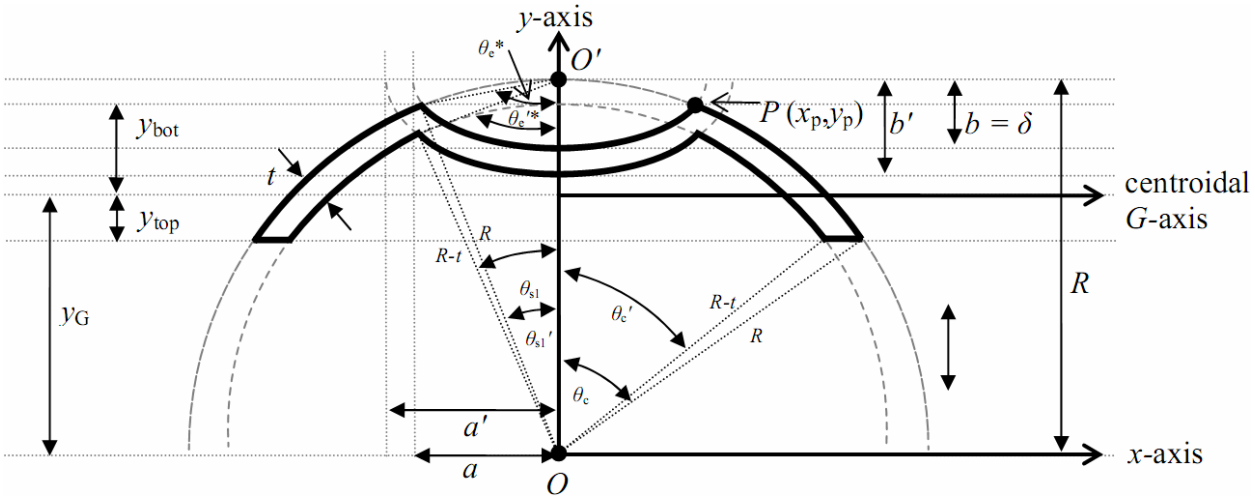

Fig. A.7 – Deformed circular arc-beam with elliptical indentation of thickness t

The point P is on both the circle and the ellipse: $(x_p,y_p) = (R \sin\theta_{s1}, R\cos\theta_{s1}) = (a \sin\theta_e^*, R - \delta\cos\theta_e^*)$.

Hence: $\theta_e^* = \cos^{-1}\left[\frac{R}{\delta}\left(1-\cos\theta_{s1}\right)\right]$, $\theta_e^{*\prime} = \cos^{-1}\left[\frac{R}{\delta}\left(1-\cos\theta_{s1}'\right)\right]$ and $a = R\frac{\sin\theta_{s1}}{\sin\theta_e^*}$.

The parametric angle of the ellipse about its own origin O' is denoted with a '*', while that of the circle is without this symbol. The extent of the indentation is limited to $\delta \geq R(1 - \cos\theta_{s1})$.

Outer circular segment #1: radius $\rho = R$; spread $2\theta_c$.

Inner circular segment #1: radius $\rho' = R - t$; spread $2\theta_c'$.

Outer circular segment #2: radius $\rho = R$; spread $2\theta_{s1}$.

Inner circular segment #2: radius $\rho' = R - t$; spread $2\theta_{s1}'$.

Outer elliptical arc: major axis a; minor axis $b = \delta$; spread $2\theta_e$.

Inner elliptical arc: major axis $a' = a + t$; minor axis $b' = b + t$; spread $2\theta'_e$.

The angle θ_{s1} may be chosen freely.

Extreme fibre distances: $y_{top} = y_G - R\cos\theta_c$, $y_{bot} = R\cos\theta_{s1} - y_G$

Relations: $\theta_c' = \cos^{-1}\left[\frac{R}{R-t}\cos\theta_c\right]$ and $\theta_{s1}' = \sin^{-1}\left[\frac{R}{R-t}\sin\theta_{s1}\right]$

The properties of the shell are as follows:

$$A_{out} = A(\rho,\theta_c) - A(\rho,\theta_{s1}) - A\left(a,b,\theta_e^*\right) \text{ and } A_{in} = A(\rho',\theta_c') - A(\rho',\theta_{s1}') - A\left(a',b',\theta_e^{*\prime}\right)$$

$$A_{shell} = A_{out} - A_{in} \tag{A.32}$$

$$y_{G,out} = \frac{y_G(\rho,\theta_c)A(\rho,\theta_c) - y_G(\rho,\theta_{s1})A(\rho,\theta_{s1}) - \left(\rho - y_G\left(b,\theta_e^*\right)\right)A\left(a,b,\theta_e^*\right)}{A_{out}}$$

$$y_{G,in} = \frac{y_G(\rho',\theta')A(\rho',\theta_c') - y_G(\rho',\theta_{s1}')A(\rho',\theta_{s1}') - \left(\rho - y_G\left(b',\theta_e'^*\right)\right)A\left(a',b',\theta_e'^*\right)}{A_{in}}$$

$$y_{G,shell} = \frac{y_{G,out}A_{out} - y_{G,in}A_{in}}{A_{shell}} \tag{A.33}$$

$$I_{x,out} = I_x(\rho,\theta_c) - I_x(\rho,\theta_{s1}) - \left[I_{x'}\left(a,b,\theta_e^*\right) + A\left(a,b,\theta_e^*\right)\left[\left(\rho - y_G\left(b,\theta_e^*\right)\right)^2 - \left(y_G'\left(b,\theta_e^*\right)\right)^2\right]\right]$$

$$I_{x,in} = I_x(\rho',\theta_c') - I_x(\rho',\theta_{s1}') - \left[I_{x'}\left(a',b',\theta_e'^*\right) + A\left(a',b',\theta_e'^*\right)\left[\left(\rho - y_G\left(b',\theta_e^{*\prime}\right)\right)^2 - \left(y_G'\left(b,\theta_e^*\right)\right)^2\right]\right]$$

$$I_{G,shell} = I_{x,out} - I_{x,in} - A_{shell}y_{G,shell}^2 \tag{A.34}$$

A.3.5 Circular arc with localised semielliptical flattening: Flattened arc-beam

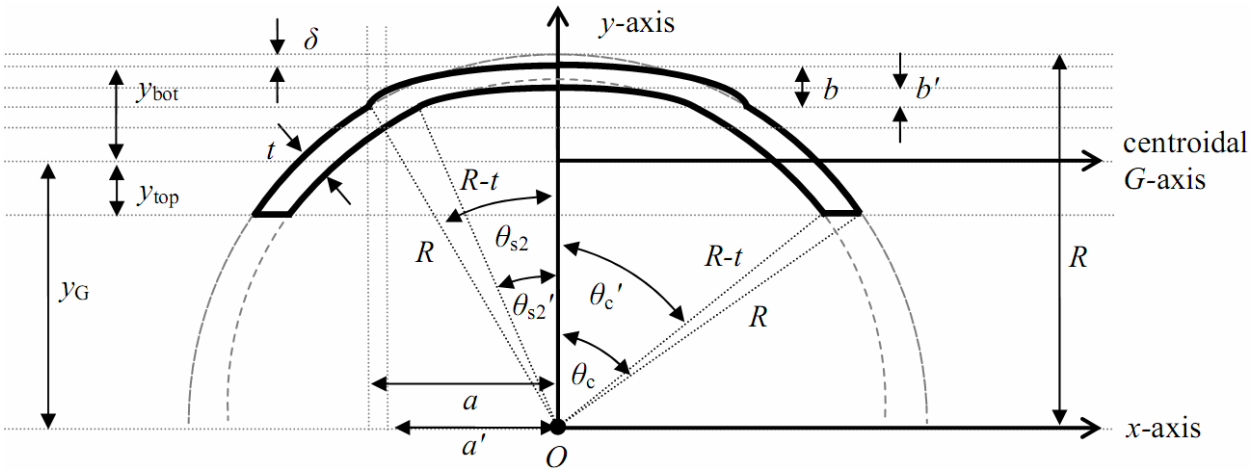

Fig. A.8 – Deformed circular arc-beam with semielliptical flattening of thickness t

Outer circular segment #1: radius $\rho = R$; spread $2\theta_c$.

Inner circular segment #1: radius $\rho' = R - t$; spread $2\theta_c'$.

Outer circular segment #2: radius $\rho = R$; spread $2\theta_{s2}$.

Inner circular segment #2: radius $\rho' = R - t$; spread $2\theta_{s2}'$.

Outer semiellipse: major axis $a = R \sin\theta_{s2}$; minor axis $b = R\,(1 - \cos\theta_{s2}) - \delta$.

Inner semiellipse: major axis $a' = (R - t) \sin\theta_{s2}'$; minor axis $b' = b - t$.

Extreme fibre distances: $y_{top} = y_G - R\cos\theta_c$, $y_{bot} = R - \delta - y_G$

Relation: $\theta_c' = \cos^{-1}\left[\frac{R}{R-t}\cos\theta_c\right]$ and $\theta_{s2}' = \cos^{-1}\left[\frac{R}{R-t}\cos\theta_{s2}\right]$

The properties of the shell are as follows:

$$A_{out,circ} = A(\rho,\theta_c) - A(\rho,\theta_{s2}) \text{ and } A_{in,circ} = A(\rho',\theta_c') - A(\rho',\theta_{s2}')$$

$$A_{out,ell} = A(a,b) \text{ and } A_{in,ell} = A(a',b')$$

$$A_{circ} = A_{out,circ} - A_{in,circ} \text{ and } A_{ell} = A_{out,ell} - A_{in,ell}$$

$$A_{shell} = \left[A_{out,circ} + A_{out,ell}\right] - \left[A_{in,circ} + A_{in,ell}\right] \tag{A.35}$$

$$y_{G,out,circ} = \frac{y_G(\rho,\theta_c)\,A(\rho,\theta_c) - y_G(\rho,\theta_{s2})\,A(\rho,\theta_{s2})}{A_{out,circ}}$$

$$y_{G,in,circ} = \frac{y_G(\rho',\theta_c')\,A(\rho',\theta_c') - y_G(\rho',\theta_{s2}')\,A(\rho',\theta_{s2}')}{A_{in,circ}}$$

$$y_{G,out,ell} = y_G(b) + \rho\cos\theta_{s2} \text{ and } y_{G,in,ell} = y_G(b') + \rho'\cos\theta_{s2}'$$

$$y_{G,circ} = \frac{y_{G,out,circ}A_{out,circ} - y_{G,in,circ}A_{in,circ}}{A_{circ}} \text{ and } y_{G,ell} = \frac{y_{G,out,ell}A_{out,ell} - y_{G,in,ell}A_{in,ell}}{A_{ell}}$$

$$y_{G,shell} = \frac{\left[y_{G,out,circ}A_{out,circ} + y_{G,out,ell}A_{out,ell}\right] - \left[y_{G,in,circ}A_{in,circ} + y_{G,in,ell}A_{in,ell}\right]}{A_{shell}} \tag{A.36}$$

$$I_{x,out,circ} = I_x(\rho,\theta_c) - I_x(\rho,\theta_{s2}) \text{ and } I_{x,in,circ} = I_x(\rho',\theta_c') - I_x(\rho',\theta_{s2}')$$

$$I_{x,out,ell} = I_x(a,b) + A(a,b)\left(\rho\cos\theta_{s2}\right)^2 \text{ and } I_{x,in,ell} = I_x(a',b') + A(a',b')\left(\rho'\cos\theta_{s2}'\right)^2$$

$$I_{G,circ} = I_{x,out,circ} - I_{x,in,circ} - A_{circ}y_{G,circ}^2$$

and $I_{G,ell} = I_x(a,b) - I_x(a',b') - A_{ell}\left(y_{G,ell} - \rho\cos\theta_{s2}\right)^2$

$$I_{G,shell} = \left[I_{G,circ} + A_{circ}\left(y_{G,shell} - y_{G,circ}\right)^2\right] + \left[I_{G,ell} + A_{ell}\left(y_{G,shell} - y_{G,ell}\right)^2\right] \tag{A.37}$$

Once again, the semielliptical flattening may be generalised to the form of the semi-superellipse, allowing the exact form of the flattening to be controlled directly. The equations are thus modified in a manner similar to those in Section A.3.3.

A.3.6 Extension of properties to the full 360 degrees

For arc-beams which extend to the full half-circumference, $\theta_c = ½\pi$, the properties may be combined with those of an undeformed semi-circular arc to make a complete deformed cylindrical tube.

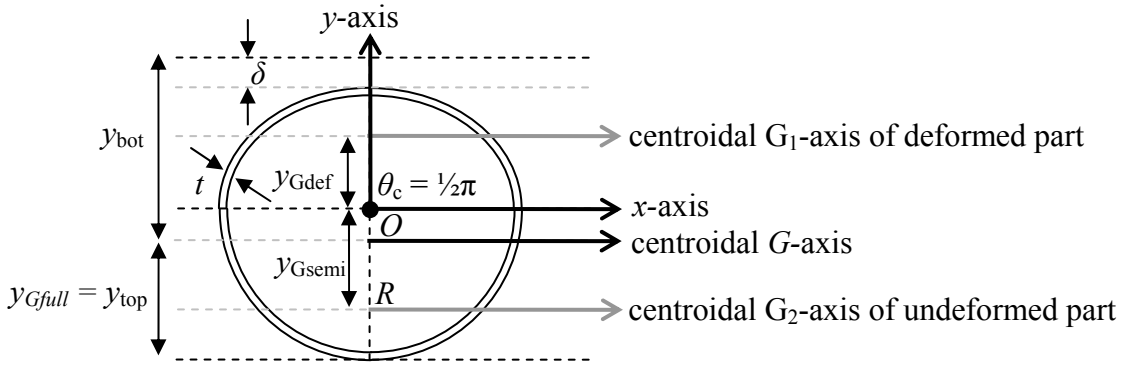

Fig. A.9 – Extension to a fully cylindrical arc-beam

The properties of an undeformed semi-circular shell are as follows:

$$A_{semi} = \frac{\pi}{2}\left(R^2 - \left(R-t\right)^2\right) \text{ and } y_{Gsemi} = \frac{4}{3\pi}\left(\frac{R^3 - \left(R-t\right)^3}{R^2 - \left(R-t\right)^2}\right)$$

$$I_{xsemi} = \frac{\pi}{8}\left(R^4 - \left(R-t\right)^4\right) \text{ and } I_{Gsemi} = \frac{\pi}{8}\left(R^4 - \left(R-t\right)^4\right) - \frac{8}{9\pi}\frac{\left(R^3 - \left(R-t\right)^3\right)^2}{R^2 - \left(R-t\right)^2} \quad \text{(A.38)}$$

From other geometries:

$A_{def} = A_{shell}$, $y_{G,def} = y_{G,shell}$, $I_{x,def} = I_{x,shell}$ and $I_{G,def} = I_{G,shell}$

Hence:

$$A_{full} = A_{def} + A_{semi} \quad \text{(A.39)}$$

$$y_{G,full} = \frac{A_{def}\left(y_{G,def} + R\right) + A_{semi}\left(R - y_{G,semi}\right)}{A_{full}} \quad \text{(A.40)}$$

$$I_{G,full} = \left[I_{x,def} + A_{def}\left(R - y_{G,full}\right)^2\right] + \left[I_{x,semi} - A_{semi}\left(R - y_{G,full}\right)^2\right]$$

OR

$$I_{G,full} = \left[I_{G,def} + A_{def}\left(y_{G,def} + R - y_{G,full}\right)^2\right] + \left[I_{G,semi} + A_{semi}\left(y_{G,full} - R + y_{G,semi}\right)^2\right] \quad \text{(A.41)}$$

A.4 Select investigations

A.4.1 Overview

Each one of the different geometries presented in Figs A.5 to A.8 may be considered as alternative suggestions for what the deformed radial shape of the silo wall near the critical buckling region under eccentric pipe flow may best resemble. The undeformed circular arc (Fig. A.4) is naturally the reference geometry. However, it is thought that the arc-beam geometry which most accurately corresponds to the deformed radial shape of the silo at bifurcation is that of the semi-superellipse (Fig. A.6) or alternatively the circular arc with local (super-) elliptical flattening at the tip (Fig. A.8), both assuming appropriate values for the set of powers p and q.

It was thought at an early point in the investigation of the beneficial effect of geometric nonlinearity under eccentric discharge that the radial deformation of the silo may be such that the shell actually inverts inwards near the channel (with a reversal of curvature), and thus an arc-beam in the form of a circular arc with an inward indentation in the shape of an elliptical arc was conceived (Fig. A.7). According to beam theory (presented shortly), this type of deformation would indeed result in noticeable reductions in extreme fibre stresses (due to increased section moduli), but this is not a true representation of the deformed radial shape of the silo at buckling.

The two following analyses into extreme fibre stresses under changes of beam geometry are thus very useful to show what is *not* the cause of beneficial geometric nonlinearity in shells under eccentric discharge. However, over the course of this side study it became apparent that a much simpler interpretation of beam theory may help to explain what *is* the cause. This may be found in Chapter 3.

A.4.2 Investigation of the circular arc-beam with superelliptical flattening at the tip

The trigonometric term powers p and q of the superelliptical shape allow excellent control of the exact shape, size and flatness of the radial coordinate of the shell, a feature exploited in the novel imperfection form for eccentric discharge presented in Chapter 6. Using data extracted from ABAQUS and Excel's nonlinear SOLVER functionality, it was possible to deduce the most representative values for p, q and θ_{s2} (the angular spread of the superellipse with respect to the full circular cross-section if to

assume the arc beam of Fig. A.8). Values for δ (the central radial deformation) were read directly from the ABAQUS results.

The circumferential deformations for the stepped wall Silo S (H = 18 m, R = 3 m; critical buckling location within 3 mm wall strake near midheight) analysed under the full EN 1991-4 (2007) eccentric discharge pressures (Chapter 4) were extracted from the ABAQUS models at three conditions for the three recommended EN 1991-4 flow channel sizes; $k_c = r_c/R$ = 0.25, 0.40 and 0.60. These are: 1) the LA displacements at the LBA load factor, 2) the GNA displacements at the LBA factor and 3) the GNA displacements at the instant before bifurcation. Recall that the LBA load factors for the three channels were 0.46, 0.25 and 0.42 respectively, while the GNA load factors were 4.11, 0.37 and 0.66 respectively (Table 4.10). In all cases, geometric nonlinearity was beneficial to the structure (respective buckling strength increases of 793%, 48% and 57% from LBA to GNA), especially for very small flow channels. The values were extracted at midheight as this location was close to the base of the thinnest 3 mm strake which was found to be critical for buckling.

The typical midheight circumferential deformations of Silo S are shown in Figs A.10 and A.11 for the GNA analysis at the LBA factor for the flow channel with k_c = 0.25. The shell remains circular around the majority of the circumference except where it is flattened near the flow channel due to the circumferential bending associated with low flow channels pressures. The deformed shape is surprisingly well described by the general superelliptical equation, applied in the context of the flattened tip arc-beam (Fig. A.8).

The radial deviation was identified to have three basic features; a large primary inward deformation adjacent to the low pressures of the channel centre, a large primary outward deformation adjacent to the high pressures of the channel edge, and a much smaller secondary inward deformation which decays around the shell circumference away from the channel. These are annotated in Figs A.10 and A.11. The circular arc-beam with local tip superelliptical flattening (Fig. A.8) only manages to capture the primary inward and outward radial features to any degree, and it will be shown that this is a significant limitation.

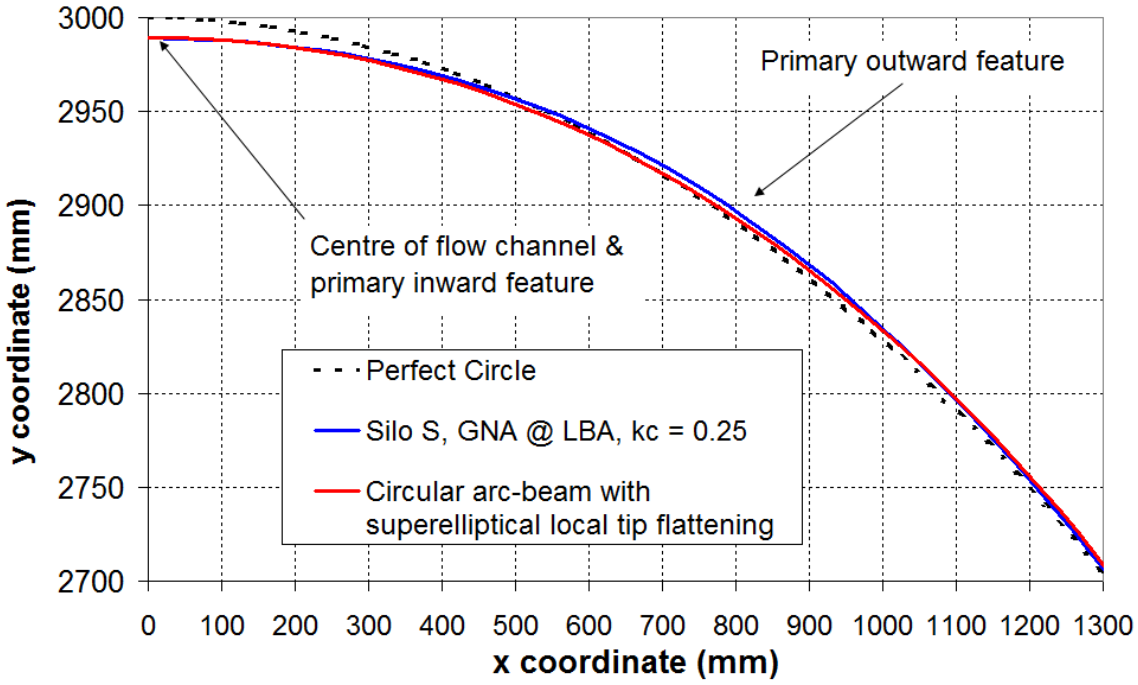

Fig. A.10 – Deformed shape at midheight of Silo S for the GNA analysis at the LBA factor for $k_c = 0.25$ in Cartesian coordinates

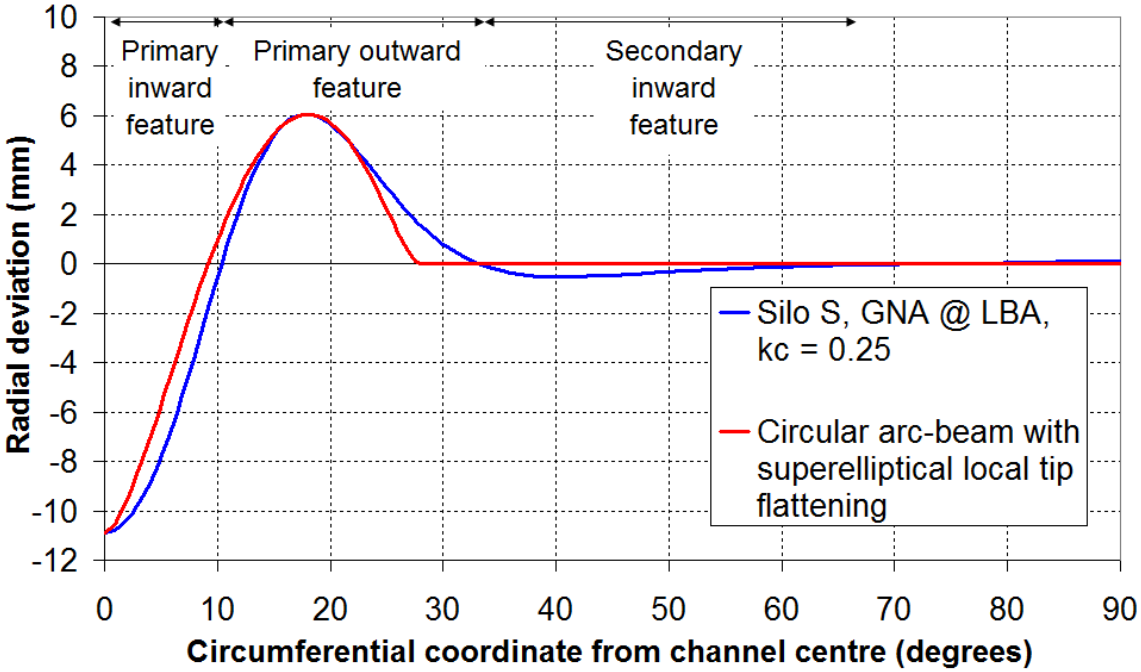

Fig A.11 – Radial deviation at midheight of Silo S for the GNA analysis at the LBA factor for $k_c = 0.25$

Table A.1 – Summary of the representative values of the p, q, θ_{s2} and δ for the flattened superelliptical arc

Analysis	k_c	p	q	θ_{s2} (degrees)			δ (mm)		
LA @ LBA	0.25	2.29	1.06	36.81			19.94		
GNA @ LBA		2.12	1.08	27.21			10.88		
GNA @ Bifurcation		2.15	1.29	27.83			38.29		
LA @ LBA	0.40	2.09	2.10	44.68			134.75		
GNA @ LBA		2.02	1.35	43.51			61.53		
GNA @ Bifurcation		1.99	1.43	43.51			74.64		
LA @ LBA	0.60	1.54	1.81	61.00			55.68		
GNA @ LBA		1.99	1.46	66.27			39.92		
GNA @ Bifurcation		1.97	1.61	72.24			54.98		
Mean for ALL values (GNA only)	0.25	2.19 (2.13)	1.14 (1.19)	30.61 (27.52)			23.04 (24.59)		
	0.40	2.03 (2.00)	1.63 (1.39)	43.90 (43.50)			90.31 (68.08)		
	0.60	1.83 (1.98)	1.63 (1.54)	66.50 (69.25)			50.19 (47.56)		
Standard deviation for ALL values (GNA only)	0.25	0.09 (0.02)	0.13 (0.15)	5.37 (0.44)			13.97 (19.38)		
	0.40	0.05 (0.02)	0.41 (0.05)	0.68 (0.00003)			39.04 (9.27)		
	0.60	0.26 (0.01)	0.18 (0.11)	5.62 (4.22)			8.90 (10.65)		
Overall mean for ALL values (GNA only)		2.02 (2.04)	1.47 (1.37)	k_c			k_c		
				0.25	*0.40*	*0.60*	*0.25*	*0.40*	*0.60*
Final choice		**2.0**	**1.4**	**30**	**45**	**70**	**25**	**70**	**50**

The local superelliptical shape (Fig. A.8) was thus fitted to the circumferential distributions of radial displacements for Silo S using the SOLVER functionality in Excel. The results are summarised in Table A.1. It appears that the mean powers of p and q which best represent the primary features of the deformed shape are 2.0 and 1.4

respectively regardless of channel size or analysis type (with surprisingly low standard deviations). However, the parameters θ_{s2} and δ, governing the magnitude of the flattening, are dependent on the flow channel size

The shapes of an arc-beam with the same values of R and t as Silo S and superelliptical flattening at the tip (Fig. A.8) generated with the above fitted values for the parameters p, q, θ_{s2} and δ are shown in Fig. A.12 for the three flow channel sizes. The resulting section moduli at both extreme fibres are presented in Tables A.2 to A.4, calculated according to the corresponding section property equations derived in Section A.3.5 for three different circumferential spreads of the arc-beam: partial arc (with, say, $\theta_c = 5\delta/R < ½\pi$), half arc ($\theta_c = ½\pi$) and full circle ($\theta_c = \pi$). The results for the other arc-beam cross-sectional geometries derived in Section A.3, assuming the same spread and deformation amplitudes θ_{s2} and δ (if applicable), are included for comparison. The section modulus for the bottom fibre (Z_{bot}) corresponds to the centre of the flow channel.

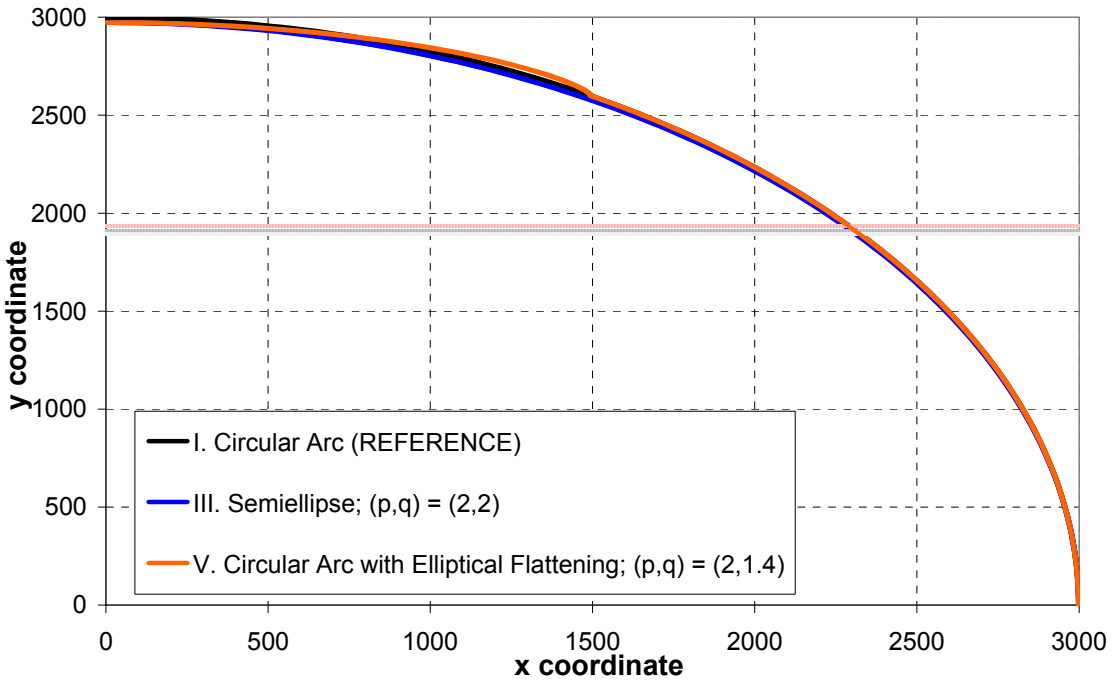

a) $k_c = 0.25$

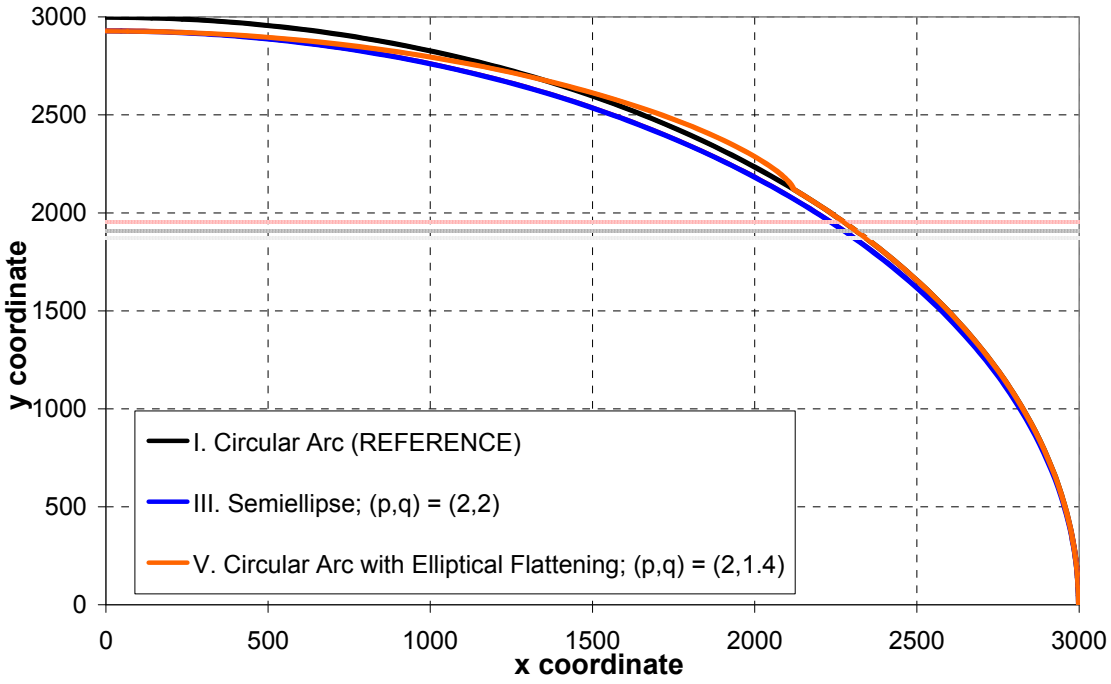

b) $k_c = 0.40$

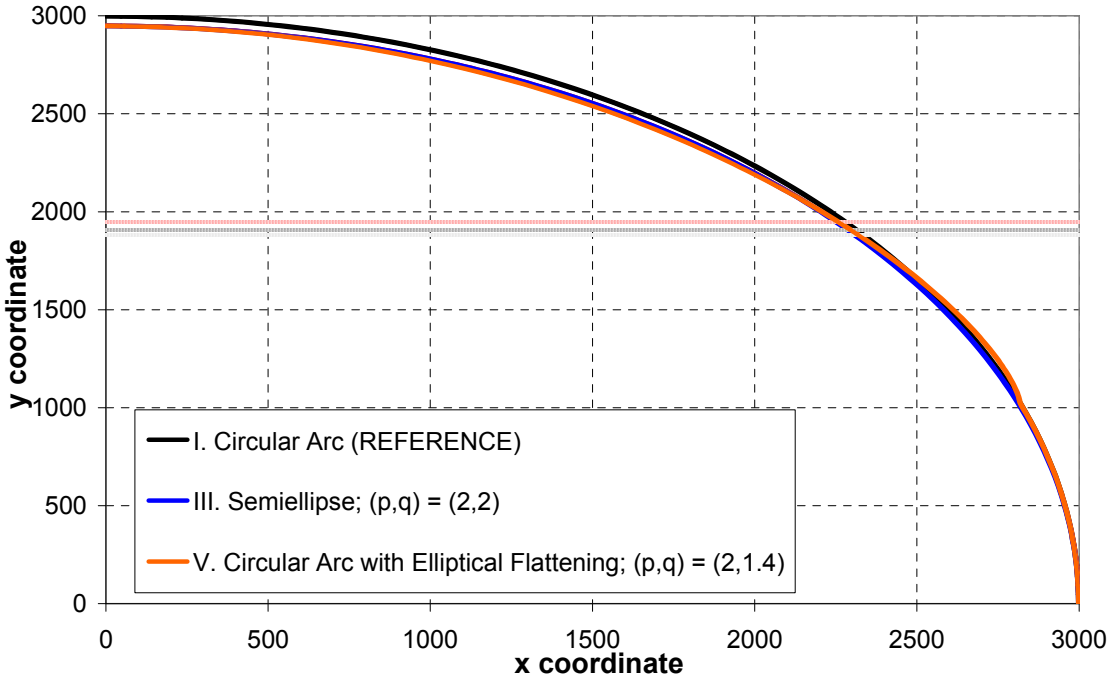

c) $k_c = 0.60$

Fig A.12 – Changes of geometry covering an increasing portion of the circumference with a larger channel

Table A.2 – Section moduli ratios for the partial circumference arc-beam ($\theta_c < ½\pi$)

	$k_c = 0.25$			$k_c = 0.40$			$k_c = 0.60$		
Partial arc $\theta_c = \theta_{s2}$, $\theta_{s1} = 5\delta/R$	Z_{top} / Z_{ref}	Z_{bot} / Z_{ref}	% change in bottom fibre stresses	Z_{top} / Z_{ref}	Z_{bot} / Z_{ref}	% change in bottom fibre stresses	Z_{top} / Z_{ref}	Z_{bot} / Z_{ref}	% change in bottom fibre stresses
Circular Arc (Fig. A.3.1)	1	1		1	1		1	1	
Elliptical Arc (Fig. A.3.2)	0.891	0.913	+ 9.57	0.817	0.865	+ 15.55	0.935	0.955	+ 4.68
Semiellipse ($p = 2$, $q = 2$) (Fig. A.3.3)	0.568	0.926	+ 8.02	0.688	0.966	+ 3.47	0.920	1.040	– 3.87
Indented Arc (Fig. A.3.4)	1.026	1.132	– 11.68	1.013	1.190	– 15.97	1.028	1.115	– 10.31
Flattened Arc ($p = 2$, $q = 1.4$) (Fig. A.3.5)	**0.583**	**0.839**	**+ 19.23**	**0.689**	**0.867**	**+ 15.34**	**0.899**	**0.927**	**+ 7.90**

Table A.3 – Section moduli ratios for the half circumference arc-beam ($\theta_c = ½\pi$)

	$k_c = 0.25$			$k_c = 0.40$			$k_c = 0.60$		
Half circle $\theta_c = ½\pi$	Z_{top} / Z_{ref}	Z_{bot} / Z_{ref}	% change in bottom fibre stresses	Z_{top} / Z_{ref}	Z_{bot} / Z_{ref}	% change in bottom fibre stresses	Z_{top} / Z_{ref}	Z_{bot} / Z_{ref}	% change in bottom fibre stresses
Circular Arc (Fig. A.3.1)	1	1		1	1		1	1	
Semiellipse ($p = 2$, $q = 2$) & Elliptical Arc (Figs A.3.2 & A.3.3)	0.985	0.989	+ 1.11	0.959	0.969	+ 3.16	0.971	0.978	+ 2.24
Indented Arc (Fig. A.3.4)	1.017	1.054	– 5.11	1.027	1.115	– 10.32	1.025	1.093	– 8.50
Flattened Arc ($p = 2$, $q = 1.4$) (Fig. A.3.5)	**0.978**	**0.945**	**+ 5.83**	**0.966**	**0.969**	**+ 3.16**	**0.957**	**0.954**	**+ 4.82**

Table A.4 – Section moduli ratios for the full circumference arc-beam

	$k_c = 0.25$			$k_c = 0.40$			$k_c = 0.60$		
Full circle $\theta_c = \pi$	Z_{top} / Z_{ref}	Z_{bot} / Z_{ref}	% change in bottom fibre stresses	Z_{top} / Z_{ref}	Z_{bot} / Z_{ref}	% change in bottom fibre stresses	Z_{top} / Z_{ref}	Z_{bot} / Z_{ref}	% change in bottom fibre stresses
Circular Arc (Fig. A.3.1)	1	1		1	1		1	1	
Semiellipse ($p = 2$, $q = 2$) &Elliptical Arc (Figs A.3.2 & A.3.3)	0.994	0.995	+ 0.46	0.984	0.987	+ 1.30	0.988	0.991	+ 0.92
Indented Arc (Fig. A.3.4)	1.011	1.042	– 4.00	1.020	1.091	– 8.31	1.017	1.073	– 6.78
Flattened Arc ($p = 2$, $q = 1.4$) (Fig. A.3.5)	**0.982**	**0.950**	**+ 5.26**	**0.979**	**0.958**	**+ 4.34**	**0.981**	**0.958**	**+ 4.40**

The above results suggest that, for changes of cross-sectional beam geometry which result in the flattening of only the tip of the arc-beam (corresponding to all proposed deformed arc-beams except the indented arc-beam in Fig. A.7), the bottom section moduli consistently decrease resulting in an *increase* in bottom extreme fibre stresses. By analogy, this corresponds to increased stresses in the silo wall adjacent to the centre flow channel under eccentric discharge. Thus the circular arc-beam with tip flattening only (Fig. A.8), marked in bold in the above tables, is not a satisfactory analogy to approximate the deformed midheight shape of the silo under eccentric discharge.

The indented arc-beam (Fig. A.7), which includes a reversal of in the radius of curvature at the tip, does consistently result in increased section moduli and thus a *decrease* in extreme fibre stresses. This may have been an fortunate piece of early evidence for beneficial geometric nonlinearity if the indented arc did indeed reflect the true deformed shape of the silo under eccentric pipe flow, but this is not the case because the shell exhibits no such reversal of curvature. Furthermore, the percentage decreases in section modulus predicted for the indented arc-beam are rather modest, some 15% at most, which do not explain the much higher reductions of stresses (over 50%) that have been found to occur with geometric nonlinear finite element analyses. A different explanation was therefore required.

A.4.3 Investigation of the superellipse to describe the entire arc-beam geometry

In the previous section, only the primary inward and outward radial deformation features (Fig. A.11) could be modelled by the arc-beam geometry with superelliptical tip flattening (Fig. A.8). In this section, a superellipse is used instead to model the whole arc-beam (Fig. A.6), which manages to capture the smaller secondary inward deformation to a much greater extent. The semi-superellipse, however, can only be fitted to a maximum spread of ½π of the circumference, and cannot be fitted to deformations beyond this. An example of the measured radial deviations from LA and GNA analyses of Silo CS and their superelliptical fits (Fig. A.6), extracted from the base of the thinnest 3 mm strake at buckling, is shown in Fig. A.13.

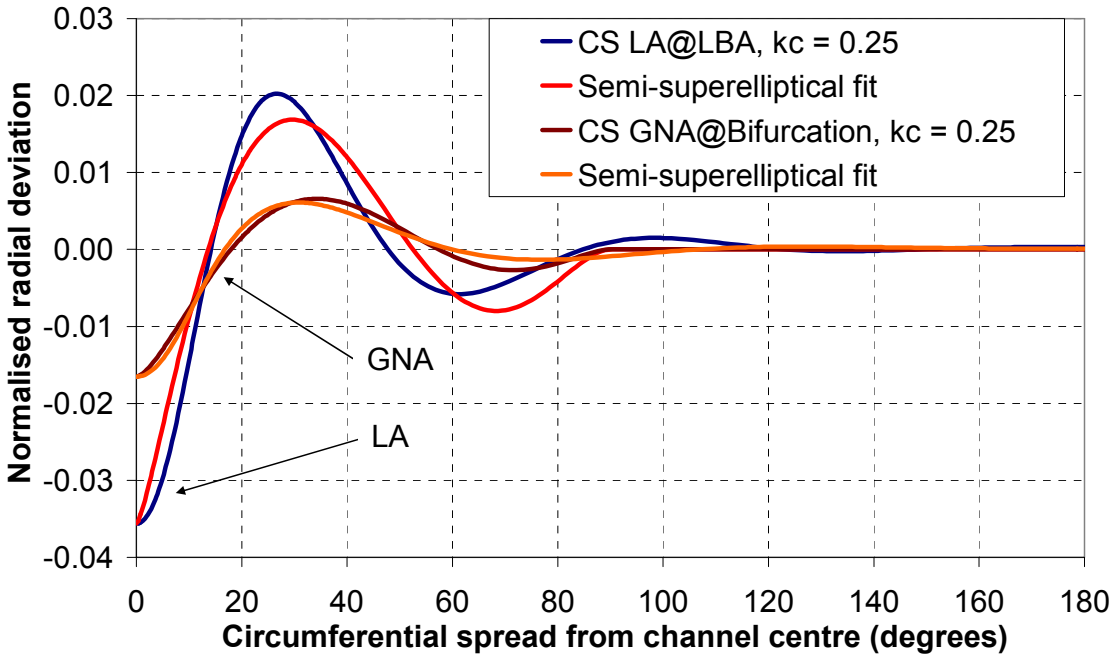

Fig A.13 – Normalised radial deviation at the base of the thinnest respective strake for the k_c = 0.25 flow channel in Silo CS

A set of representative values for the parameters p, q and δ were obtained using a similar fitting procedure as in the previous section. This was carried out using LA and GNA data from Silos CS and CVS extracted at the base of the respective thinnest 3 mm strake under the Rotter (1986) model without the regions of high normal wall pressures adjacent to the edge of the flow channel (Chapter 3). The value of k_c used was 0.25, since at this flow channel size the LBA and GNA and load factors were predicted to be the same (Table 3.4 and Table 3.5). The analysis is summarised in Table A.5.

Table A.5 – Summary of the representative values of the p, q and δ for the superelliptical arc-beam

	LA @ LBA	p	q	δ (mm)	GNA @ Bifurcation	p	q	δ (mm)
EN 1991-4 (2007)	Silo CS	2.86	1.64	106.88	Silo CS	2.32	1.86	49.55
	Silo CVS	2.91	1.60	109.49	Silo CVS	2.30	1.86	47.11
Rotter (1986)	Silo CS	2.93	1.86	142.53	Silo CS	2.32	1.95	63.58
	Silo CVS	2.96	1.85	146.01	Silo CVS	2.31	1.95	61.63
	Mean	2.91	1.73	126.23		2.31	1.90	55.47
	St. Deviation	0.04	0.14	20.91		0.01	0.05	8.34
	Final Choice	**2.9**	**1.7**	**125**		**2.3**	**1.9**	**55**

It is clear from Table A.5 that the main feature of the GNA deformations is that they are lower in amplitude and extend further into the shell. This is represented by a fall in the power of p, a rise in the power of q, and naturally by a lower central deformation δ. The resulting section moduli at both extreme fibres for a superellipse with $\theta_c = ½\pi$ (Fig. A.3.3) are shown in Table. A.6, based on the equations derived in Section A.3.3.

Table A.6 – Section moduli ratios for the superelliptical arc-beam

	LA @ LBA	Z_{top} / Z_{ref}	Z_{bot} / Z_{ref}	% change in bottom fibre stresses	GNA @ Bifurcation	Z_{top} / Z_{ref}	Z_{bot} / Z_{ref}	% change in bottom fibre stresses
	Semicircle	1	1		Semicircle	1	1	
EN 1991-4 (2007)	Silo CS	0.977	**1.088**	– 8.1	Silo CS	0.989	**1.038**	– 3.7
	Silo CVS	0.976	**1.089**	– 8.2	Silo CVS	0.990	**1.034**	– 3.3
Rotter (1986)	Silo CS	0.965	**1.116**	– 10.4	Silo CS	0.984	**1.045**	– 4.3
	Silo CVS	0.964	**1.118**	– 10.6	Silo CVS	0.985	**1.044**	– 4.2

Clearly, there is some progress. For the LA parameters, which give a ‘more deformed’ shape than the GNA parameters, the bottom extreme fibre (analogous to the silo wall at the flow channel centre) shows a reduction in stresses of approximately 10%, while for the GNA deformed shape this is approximately only 4%. The GNA deformed shape is ‘less deformed’, thus the stress reductions are predicted to be smaller.

The above analysis certainly seems to support the idea that a change in geometry of the arc-beam from a semicircle to a flattened superellipse reduces at least one of the extreme fibre stresses, but the scale of the reductions is nothing close to that which is expected based on the finite element results (over 55%). However, the importance of modelling the secondary inward deformation feature (Fig. A.11) has been shown, since without this feature there is no reduction in extreme fibre stresses at all.

A.5 Conclusions

A flattened arc-beam modelled with the superellipse has not been found to exhibit a reduction in extreme fibre stresses of a magnitude that would enable the beam theory analogy to support directly the geometrically nonlinear finite element observations of the behaviour of the silo under eccentric discharge.

However, the simple beam analogy presented in this appendix has yielded an explicit mathematical form (the superellipse) with which to define the deformed shape of a flattened silo wall at buckling under eccentric discharge. The superellipse has since proved to be instrumental in the development of a global geometric imperfection form that has been found to be deleterious for silos under eccentric discharge. A full study of the superellipse as an imperfection form was presented in Chapter 6.

Appendix B – Elasticity solution for the circumferential distribution of stresses in the eccentric flow channel geometry

B.1 Introduction

It was discussed in Section 1.2.8 of the literature review that the stationary granular solid is likely to exert a high normal pressure against the wall due to the arching effect of the ring of static material in the region immediately adjacent to the flow channel (Jenike, 1967; Rotter, 1986; Wood, 1983; Chrisp *et al.*, 1988; Chen, 1996). This rise in normal pressure is necessary to maintain horizontal equilibrium, but there is no consensus on what circumferential form this rise should take. The original working of the pressure theory for eccentric parallel pipe flow of Rotter (1986) assumed no such rise for the purposes of simplicity, while the implementation of this theory in the EN 1991-4 (2007) standard assumed a form (Fig. B.1b) that is unduly severe on the structure.

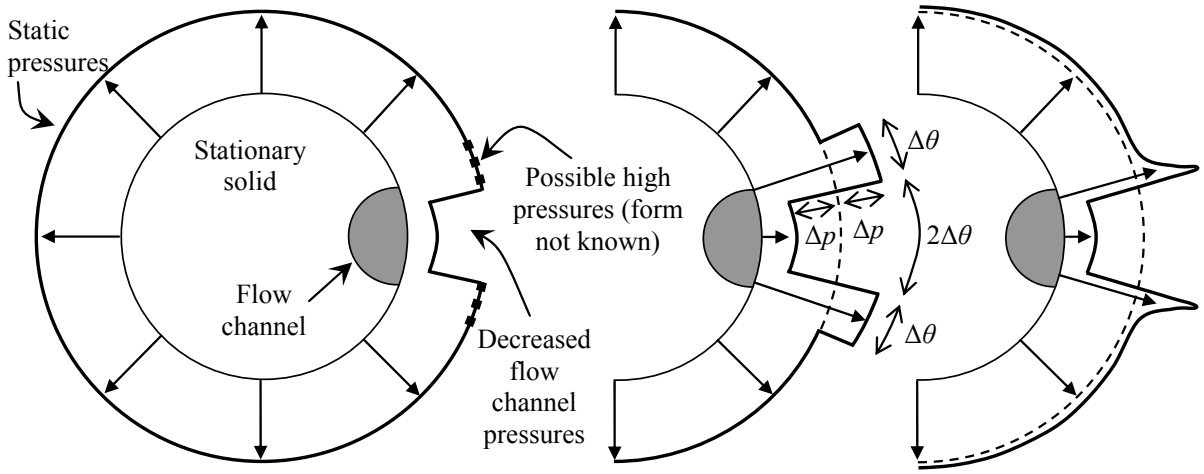

Fig. B.1 – Suggestions for the form of normal pressures against the wall of an eccentrically discharging silo

The brief study presented in this appendix attempts to model the static granular solid as an elastic planar body under a prescribed unit compressive out-of-plane strain. The mass of particulate granular material is naturally not a solid elastic body as it is subject to complex phenomena of friction and plasticity. However, an elastic solution may nonetheless offer a valuable insight into the elusive response of the stationary solid immediately adjacent to a region of low pressure, both fully internal and external. This

is a very difficult problem to treat analytically, and it was necessary to make certain assumptions in the present study in order to obtain a solution. The resulting algebraic form of the solution was unfortunately found to be highly unwieldy and utterly impractical for application in any design scenario.

B.2 Presentation of an elasticity theory solution for a curved planar body

B.2.1 The bipolar coordinate system

The orthogonal bipolar coordinate system is related to the Cartesian coordinate system as follows (Lockwood, 1967; Timoshenko and Goodier, 1970):

$$x = \frac{a \sinh \xi}{\cosh \xi - \cos \eta} \text{ and } y = \frac{a \sin \eta}{\cosh \xi - \cos \eta} \tag{B.1}$$

In this system, curves (isosurfaces) of constant ξ represent non-concentric, non-intersecting circles that share the same focus point F on the Cartesian x axis, while curves of constant η represent non-concentric, intersecting circles which intersect at the two foci, symmetric about the Cartesian y axis. The x and y axes represent curves with $\eta = 0$ and $\xi = 0$ respectively (circles with infinite radii). The ξ coordinate ranges from $-\infty$ to ∞ at both foci, whilst the η coordinate ranges from 0 to 2π. Both are periodic and symmetric about both Cartesian axes. The fact that one single coordinate represents a well-defined circular curve makes this coordinate system very advantageous indeed for the study of complex curved geometries with elasticity theory.

In applying this coordinate system to the study of a plane through the stationary and flowing solid, a distinction must be made with respects to the positioning of the geometric system in the x-y plane. If the flow channel is fully internal (Fig. B.2), the system is represented by two ξ isosurfaces and both circles are positioned on the x axis. If, however, the flow channel touches the silo wall (Fig. B.3), the system consists of two circles truncated at their overlap which occurs at the foci, and is instead represented by two η isosurfaces, with both circles positioned on the y axis. The fact that this intersect occurs at a focus point F where $\xi \rightarrow \infty$ makes this location a sharp edge in the elastic body which, as will be shown in this study, has a serious effect on the stress distribution at this point.

B.2.2 System geometry: internal flow channel

The first case, that of the fully internal channel (limited to $r_c + e_c < R$), is illustrated in Fig. B.2.

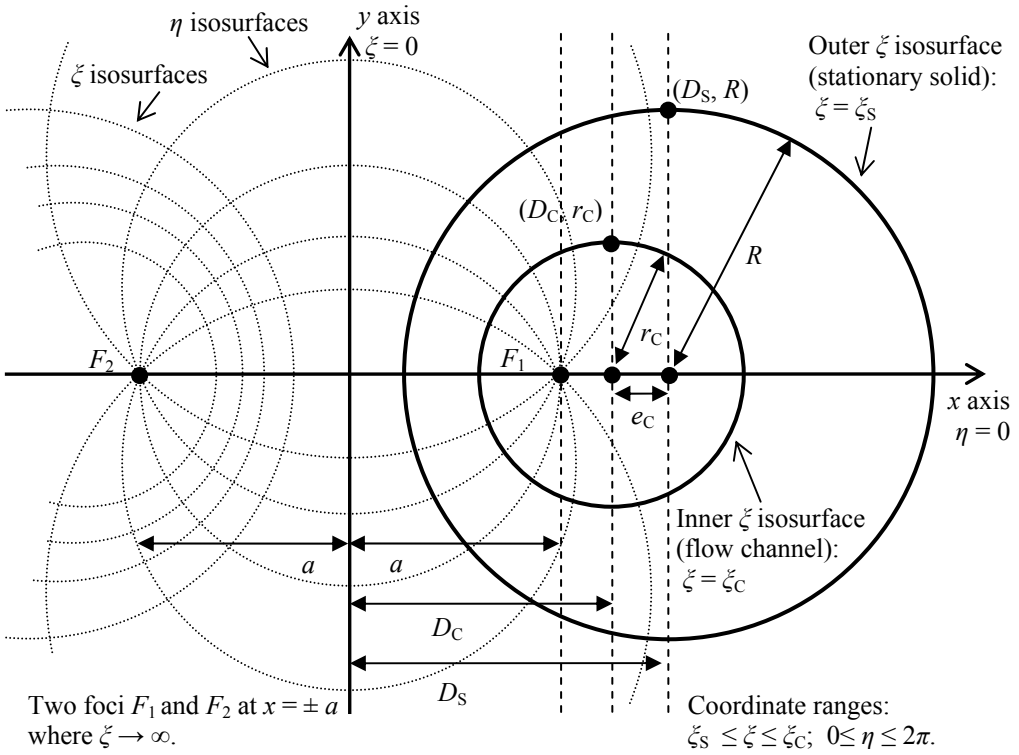

Fig. B.2 – System centred on the $\eta = 0$ plane in bipolar coordinates for a fully internal flow channel

Considering the coordinate relations in Eq. B.1 and the geometry of Fig. B.2, the two circles the following radii and centres:

$$R = a\,\mathrm{cosech}\,\xi_S \text{ and } r_C = a\,\mathrm{cosech}\,\xi_C \tag{B.2}$$

$$D_S = a\coth\xi_S \text{ and } D_C = a\coth\xi_C \text{ where } e_C = D_S - D_C \tag{B.3}$$

Since the two radii and the distance between the centres (the flow channel eccentricity e_c) are known, the values of a, ξ_S and ξ_C may be found numerically from the above relations, taking care that the correct root is found so that the smaller circle ends up inside the larger one. The numerical procedure becomes increasingly ill-conditioned as $r_c + e_c \to R$ or $e_c \to 0$.

B.2.3 System geometry: truncated flow channel

The second, more important case, is that of the truncated flow channel which touches the wall (limited to $r_c + e_c > R$), is illustrated in Fig. B.3.

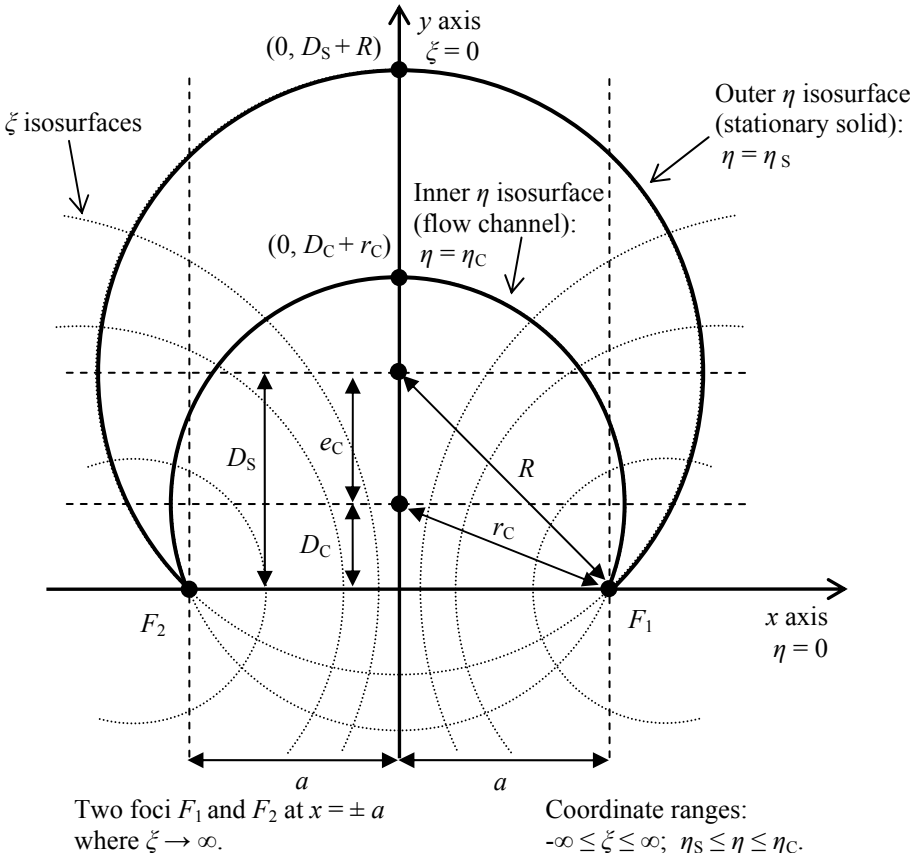

Fig. B.3 – System centred on the $\xi = 0$ plane in bipolar coordinates for a truncated flow channel

From the coordinate relations in Eq. B.1 and the information on Fig. B.3, two points on the y axis lead to the following relations:

$$D_S + R = \frac{a \sin \eta_S}{1 - \cos \eta_S} \text{ and } D_C + r_C = \frac{a \sin \eta_C}{1 - \cos \eta_C} \tag{B.4}$$

$$\text{where } D_S = \left(\frac{R^2 - r_C^2 + e_C^2}{2e_C} \right) \text{ and } D_C = \left(\frac{R^2 - r_C^2 - e_C^2}{2e_C} \right)$$

Additionally, using Pythagoras's theorem:

$$a = \sqrt{R^2 - D_S^2} = \sqrt{r_C^2 - D_C^2} \tag{B.5}$$

Once again the known values of the radii and eccentricity allow the values of a, η_S and η_C to be found numerically from the above relations. This procedure again becomes ill-conditioned as $r_c + e_c \to R$.

An additional useful parameter for the truncated channel is the angle of intersection of the two tangent lines at the foci F_1 and F_2. Used as a measure of the 'sharpness' of the edge of the truncated elastic body and assigned the notation α, it is derived as follows:

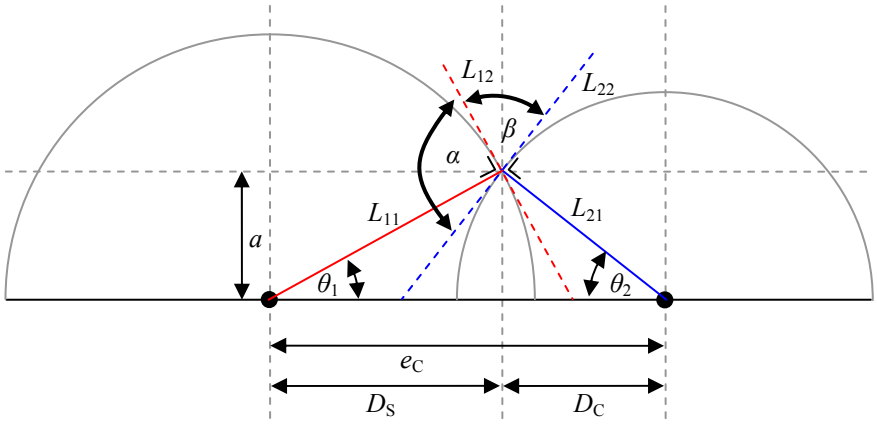

Fig. B.4 – Derivation diagram for the tangent intersection angle

The slopes of lines L_{11} and L_{21} are, respectively:

$$m_{11} = \tan\theta_1 = \frac{a}{D_S} \text{ and } m_{21} = \tan(\pi - \theta_2) = -\tan\theta_2 = -\frac{a}{D_C}$$

The slopes of the tangent lines L_{12} and L_{22} are, therefore:

$$m_{12} = \tan\left(\theta_1 + \frac{\pi}{2}\right) = -\cot\theta_1 = -\frac{D_S}{a} \text{ and } m_{22} = \tan\left(\frac{\pi}{2} - \theta_2\right) = \cot\theta_2 = \frac{D_C}{a}$$

The angle of intersection is now obtained by the familiar formula:

$$\tan\beta = \frac{m_{12} - m_{22}}{1 + m_{12}m_{22}} = \frac{(D_S + D_C)a}{D_S D_C - a^2} \text{ (taking care to obtain the correct quartile)}$$

Thus $\alpha = \pi - \beta$. (B.6)

Note that the above treatment is not defined for an internal channel with zero eccentricity (e_c = 0) as the two ξ circles cannot be concentric, nor is the treatment defined for the boundary between internal and truncated channels where $r_c + e_c = R$, as no ξ circles may intersect.

B.2.4 Elasticity theory equations

The analysis of the elastic body was performed according to Chapter 6 of Timoshenko and Goodier (1970) on two-dimensional problems in curvilinear coordinates. The stress and displacements for a condition of plane strain are given by:

$$\sigma_\xi + \sigma_\eta = 4\,\mathrm{Re}\left[\psi'(z)\right]$$

$$\sigma_\eta - \sigma_\xi + 2i\tau_{\xi\eta} = 2e^{2i\alpha}\left[\bar{z}\psi''(z) + \chi''(z)\right]$$

$$2G\left(u_\xi - iu_\eta\right) = e^{i\alpha}\left[(3-4\nu)\bar{\psi}(\bar{z}) - \bar{z}\psi'(z) - \chi'(z)\right]$$

so that:

$$\sigma_\eta = \mathrm{Re}\left[2\psi'(z) + e^{2i\alpha}\left(\bar{z}\psi''(z) + \chi''(z)\right)\right] \tag{B.7}$$

$$\sigma_\xi = \mathrm{Re}\left[2\psi'(z) - e^{2i\alpha}\left(\bar{z}\psi''(z) + \chi''(z)\right)\right] \tag{B.8}$$

$$\tau_{\xi\eta} = \mathrm{Im}\left[e^{2i\alpha}\left(\bar{z}\psi''(z) + \chi''(z)\right)\right] \tag{B.9}$$

$$u_\xi = \frac{1}{2G}\mathrm{Re}\left[e^{i\alpha}\left((3-4\nu)\bar{\psi}(\bar{z}) - \bar{z}\psi'(z) - \chi'(z)\right)\right] \tag{B.10}$$

$$u_\eta = -\frac{1}{2G}\mathrm{Im}\left[e^{i\alpha}\left((3-4\nu)\bar{\psi}(\bar{z}) - \bar{z}\psi'(z) - \chi'(z)\right)\right] \tag{B.11}$$

In the above, z is the complex variable $x + iy$, where $i^2 = -1$. *Re* and *Im* thus correspond respectively to the real and imaginary parts of the entities in brackets. The complex variable z is defined in bipolar coordinates as follows:

$$z = ia\coth\frac{\zeta}{2} \text{ where } \zeta = \xi + i\eta = 2\coth^{-1}\left(\frac{z}{ia}\right) \tag{B.12}$$

The exponents in the above are given by:

$$e^{i\alpha} = \frac{1}{\cosh\xi - \cos\eta}\left[\sinh\xi\sin\eta + i\left(\cosh\xi\cos\eta - 1\right)\right] \tag{B.13}$$

$$e^{2i\alpha} = \frac{1-\cosh\left(-\xi + i\eta\right)}{\cosh\left(\xi + i\eta\right) - 1} \tag{B.14}$$

where α is the angle between the tangent to the a curve of constant η in the increasing ξ direction and the x axis (*not* the 'sharpness' angle in Fig. B.4).

Where analytical solutions to difficult problems in elastic bodies are usually solved with the help of real-valued stress functions, these are replaced here by two complex potentials $\psi(z)$ and $\chi(z)$ which, though more difficult to conceptualise, are mathematically more advantageous. The rationale may be found in the above reference, while the original treatment is given in Muskhelishvili (1953). As per standard complex notation, a bar across a symbol denotes its complex conjugate, where i is replaced by $-i$.

The stress components σ_ξ and σ_η are defined as the stresses normal to the curves of constant ξ and η respectively, while $\tau_{\xi\eta}$ is the shear stress on either ξ or η. If the system is centred on the Cartesian x axis (internal channel), σ_ξ and σ_η correspond to the radial and circumferential stresses respectively. If, however, the system is centred on the Cartesian y axis (truncated channel), it is the other way round. The displacements u_ξ and u_η are similarly defined. The entity G is the shear modulus, found only in the displacement equations. The complexity of the system requires the boundary conditions and the forms of the complex potentials $\psi(z)$ and $\chi(z)$ to be chosen with great care.

B.2.5 Boundary conditions and stress functions

The current problem is that of a two-dimensional plane strain elastic body. It is, however, subjected to a prescribed strain ε_0 acting normal to the ξ-η (r-θ) plane which develops a corresponding 'vertical' stress σ_V and, through Poisson effects, causes the material to deform in the ξ-η plane. This effectively turns the problem into a three-dimensional one, and goes significantly beyond what is covered in the Timoshenko and Goodier (1970) and Muskhelishvili (1953) texts. The strain ε_0 is assigned a value of positive unity, representing a unit compressive strain in the compression-positive convention. The applied out-of-plane strain and stress corresponds to the compressive loading on a slice of granular solid within a silo.

It is important to ensure that the curved body maintains its shape (i.e. the silo wall is assumed to be a rigid boundary), thus the radial displacements on the outer isosurface must be clearly constrained. The radial stresses cannot be set to zero at the outer boundary because they are of greatest interest, corresponding to the normal pressure exerted by the stationary solid on the silo wall. However, the flow channel isosurface effectively represents a hole in a body with no restraint, thus the opposite condition of zero radial and circumferential shear stress must be enforced here instead. The first three boundary conditions were therefore assumed to be as follows:

BC1) Zero radial displacement in the outer isosurface: $u\left(R,\theta\right)=0$

Internal flow channel system: $u_\xi\left(\xi_S,\eta\right)=0$

Truncated flow channel system: $u_\eta\left(\xi,\eta_S\right)=0$

BC2) Zero shear stress on the inner isosurface: $\tau\left(r_C,\theta\right)=0$

Internal flow channel system: $\tau_{\xi\eta}\left(\xi_C,\eta\right)=0$

Truncated flow channel system: $\tau_{\xi\eta}\left(\xi,\eta_C\right)=0$

BC3) Zero radial stress in the inner isosurface: $\sigma_R\left(r_C,\theta\right)=0$

Internal flow channel system: $\sigma_\xi\left(\xi_C,\eta\right)=0$

Truncated flow channel system: $\sigma_\eta\left(\xi,\eta_C\right)=0$

The fourth boundary condition, governing the straining of the body out of its plane, requires more care and is the weakest link in this analysis, for reasons given below. This boundary condition is effectively a load case. It is assumed that a strain ε_0 applied throughout the body in the out-of-plane axis is related to the orthogonal in-plane strains by Poisson's ratio, such that $\varepsilon_R = \varepsilon_\theta = v\varepsilon_0$. Generalised Hooke's Law in cylindrical coordinates thus gives:

$$E\varepsilon_R=\sigma_R-\nu\left(\sigma_\theta+\sigma_V\right)=E\nu\varepsilon_0 \tag{B.15}$$

$$E\varepsilon_\theta=\sigma_\theta-\nu\left(\sigma_R+\sigma_V\right)=E\nu\varepsilon_0 \tag{B.16}$$

$$E\varepsilon_V=\sigma_V-\nu\left(\sigma_\theta+\sigma_R\right)=E\varepsilon_0 \tag{B.17}$$

Solving the above directly for the axisymmetric case (planar elastic body with no hole) gives:

$$\sigma_{V,axi}=\frac{\left(2\nu^2-\nu+1\right)E\varepsilon_0}{\left(1+\nu\right)\left(1-2\nu\right)}\approx 1.69E\varepsilon_0 \text{ and} \tag{B.18}$$

$$\sigma_{\theta,axi}=\sigma_{R,axi}=\frac{2\nu E\varepsilon_0}{\left(1+\nu\right)\left(1-2\nu\right)}\approx 1.15E\varepsilon_0 \tag{B.19}$$

The imposition of ε_0 is by itself not sufficient to be able to solve for all of the unknowns. It was thus further assumed that a uniform compressive out of plane stress given by σ_V (Eq. B.18) also acts throughout the body. Consequently, Eq. B.17 may be solved for the sum of σ_R and σ_θ, thus giving the fourth boundary condition:

BC4) Prescribed out-of-plane strain condition throughout the body (for both systems):

$$\sigma_\eta(\xi,\eta)+\sigma_\xi(\xi,\eta)=\frac{\sigma_{V,axi}-E\varepsilon_0}{\nu}\approx 2.3E\varepsilon_0$$

However, with only four boundary conditions, there are *still* not enough degrees of freedom in the system to adequately satisfy all three of Hooke's Law relations, which would naturally be satisfied in a finite element analysis. It was thus decided to solve for the radial stresses, which are of greatest interest, from the complex potentials by means of Eqs B.7 or B.8 so that the chosen boundary conditions were satisfied. The circumferential stresses, however, were to be calculated directly from Eq. B.16 so as to satisfy Hooke's Law, otherwise there is no possibility of implementing this relation. However, this is clearly not a fully satisfactory treatment.

It was found that an adequate result (free from singularities) was obtained for a reasonable range of geometry configurations when the following complex potentials were chosen:

Internal flow channel system:

$$\psi(z)=iB\cosh\zeta+aC\sinh\zeta+Dz \tag{B.20}$$

$$\chi(z)=Az+B\sinh\zeta+C\cosh\zeta \tag{B.21}$$

Truncated flow channel system:

$$\psi(z)=Aaz+B\cosh\zeta+C\sinh\zeta \tag{B.22}$$

$$\chi(z)=B\sinh\zeta+iC\cosh\zeta+D\zeta \tag{B.23}$$

In the above, A, B, C and D are integration constants which are dependent on Eq. B.7 and the boundary conditions. They are solved for numerically in real time for every geometric coordinate through the inversion of a matrix in the form:

$$\begin{bmatrix} f(u_{R,A\_out}) & f(u_{R,B\_out}) & f(u_{R,C\_out}) & f(u_{R,D\_out}) \\ f(\tau_{R\theta,A\_in}) & f(\tau_{R\theta,B\_in}) & f(\tau_{R\theta,B\_in}) & f(\tau_{R\theta,B\_in}) \\ f(\sigma_{R,A\_in}) & f(\sigma_{R,B\_in}) & f(\sigma_{R,C\_in}) & f(\sigma_{R,D\_in}) \\ f(\sigma_{R,A}+\sigma_{\theta,A}) & f(\sigma_{R,B}+\sigma_{\theta,B}) & f(\sigma_{R,C}+\sigma_{\theta,C}) & f(\sigma_{R,D}+\sigma_{\theta,D}) \end{bmatrix} \begin{Bmatrix} A \\ B \\ C \\ D \end{Bmatrix} = \begin{Bmatrix} 0 \\ 0 \\ 0 \\ \dfrac{\sigma_{V,axi}-E\varepsilon_0}{\nu} \end{Bmatrix}$$

where, for example, $f(\sigma_{R,A\_out})$ is the component of the radial stress that is the coefficient of A, calculated at the outer edge. The f coefficients are *extremely* onerous and take up several screens of Maple output, and it is recommended that they be rederived from Eq. B.7 with a symbolic computer package should the need arise to reproduce the analysis presented here.

B.3 Analytical solution for the radial stresses in a circular elastic body with an internal hole

The select analyses presented in this section correspond to the internal flow channel (Fig. B.2). A unit circle was assumed. The hole (i.e. flow channel) was located at a very small value of the eccentricity of $e_c/R = 0.01$ within the elastic body. The eccentricity cannot be zero because two ξ circles cannot be concentric, hence it was chosen as $e_c/R = 0.01$. A smaller value was found to cause the complex potentials $\psi(z)$ and $\chi(z)$ (Eqs B.20 and B.21) to exhibit singularities. A cross-section of radial stresses in terms of $E\varepsilon_0$ through the symmetry axis (the x axis, Fig. B.2) is shown in Fig. B.5 for a range of internal holes of increasing radius in the range $0.01 \leq r_c/R \leq 0.95$.

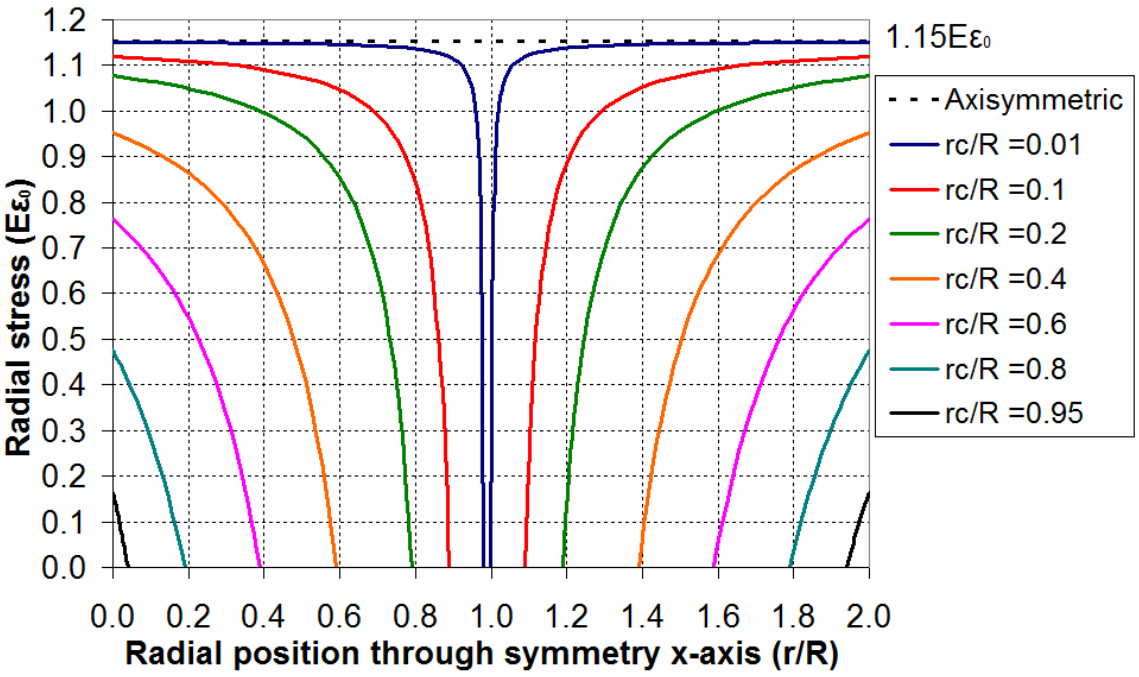

Fig. B.5 – Distribution of radial stresses through the symmetry axis for a near-concentric internal hole, $e_c/R = 0.01$

For the smallest hole ($r_c/R = 0.01$), the radial stresses in the body are at mostly at the axisymmetric value of $1.15E\varepsilon_0$ (Eq. B.19). There is a very steep drop down to zero

approaching the sides of the hole to satisfy the boundary condition (BC3). As the hole becomes larger, the drop becomes progressively smoother and the value of $1.15E\varepsilon_0$ is no longer reached at the outer boundary. This is because, for larger r_c/R, the elastic body becomes ever freer to deform radially inwards at the inner boundary which reduces the radial stress on the outer rigid boundary. For the largest hole with radius $r_c/R = 0.95$, the radial stresses become very small and as $r_c/R \rightarrow 1$ they are expected to become negligible. Thus for a very thin elastic body with an near-concentric internal hole, the behaviour approaches that of a thin shell in which radial stresses can be ignored.

A subsequent study investigated the effect of an internal hole of constant size $r_c/R = 0.4$ placed at varying eccentricities in the range $0.01 \leq e_c/R \leq 0.55$ (i.e. $0 \leftarrow e_c/R \rightarrow r_c/R$), shown in Fig. B.6. Values of e_c/R close to the boundaries of this range resulted in singularities in the solution. The distribution of the radial stress around the circumference is shown in Fig. B.7, where $\theta = 0°$ starts on the x axis. Thus the elastic solution predicts a significant drop in radial pressure on the outer boundary of the solid closest to the hole. For the largest value of e_c/R, where the solid body has a thickness of $0.05R$ adjacent to the hole, the drop in radial pressure is 84%. Opposite the reduction, there is clearly a rise in radial stress. The integral of the rise in radial stresses approximately equals the integral of the fall in radial stresses.

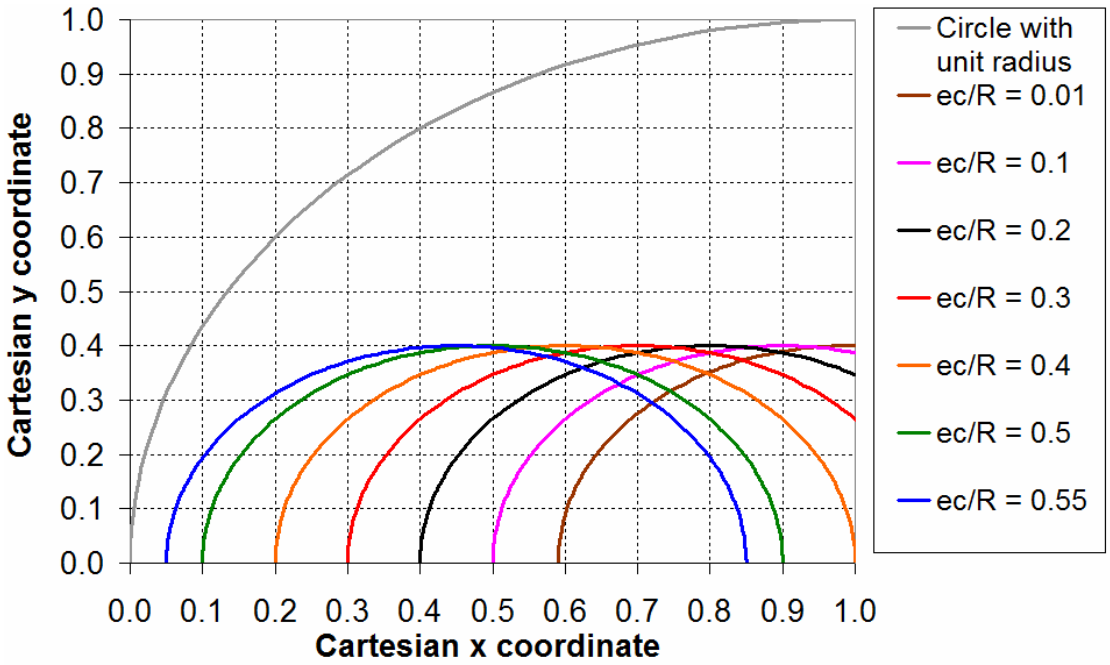

Fig. B.6 – Geometry of an internal hole of constant size placed at different eccentricities, $r_c/R = 0.4$

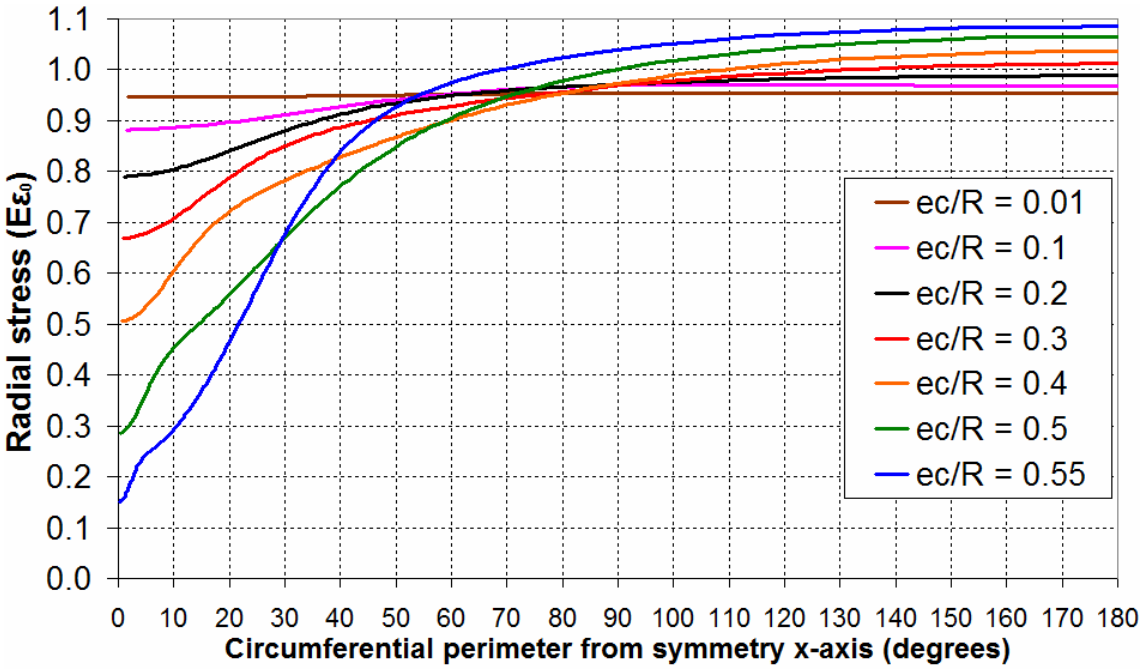

Fig. B.7 – Distribution of radial stresses around the outer circumference of the elastic body, $r_c/R = 0.4$

Extending the elastic solution to the context of the internal non-concentric flow channel, it is clear that larger flow channel eccentricities cause progressively larger reductions in normal wall pressure on the side adjacent to the outlet even when the channel is internal. Furthermore, the fall in normal pressure at the outlet is balanced by a rise in normal pressure opposite the outlet to maintain horizontal equilibrium. This is an important feature that the mixed flow pressure theory presented in Chapter 7 (or indeed *any* slice-based granular solid pressure theory) is unable to capture because it considers vertical equilibrium only and thus predicts a circumferentially-constant pressure in the static solid regardless of the interal position of the flow channel (Region 1, Fig. 7.3 and Fig. 7.4). However, it is not possible to address this limitation of the mixed flow theory without going into a similar onerous level of detail as is done in the present analysis.

The present study supports the observations of many researchers who also reported decreased wall pressures adjacent to the outlet, including Ravenet (1976), Frese (1977), Nielsen and Askegaard (1977), Gale *et al.* (1986) and many others. A more comprehensive discussion may be found in Section 1.2.8 of the literature review.

B.4 Analytical solution for the radial stresses in a crescent-shaped elastic body

The select analyses presented in this section correspond to the truncated circular flow channel (Fig. B.3). A unit circle was again assumed. The hole was assigned a constant radius $r_c/R = 0.6$ and placed at varying eccentricities in the range $0.9 \leq e_c/R \leq 1.5$, all of which result in a non-internal hole in the elastic body (Fig. B.8). As the eccentricity increases, the sharpness of the edge decreases, expressed through a higher 'sharpness angle' α introduced in Fig. B.4 and Eq. B.6.

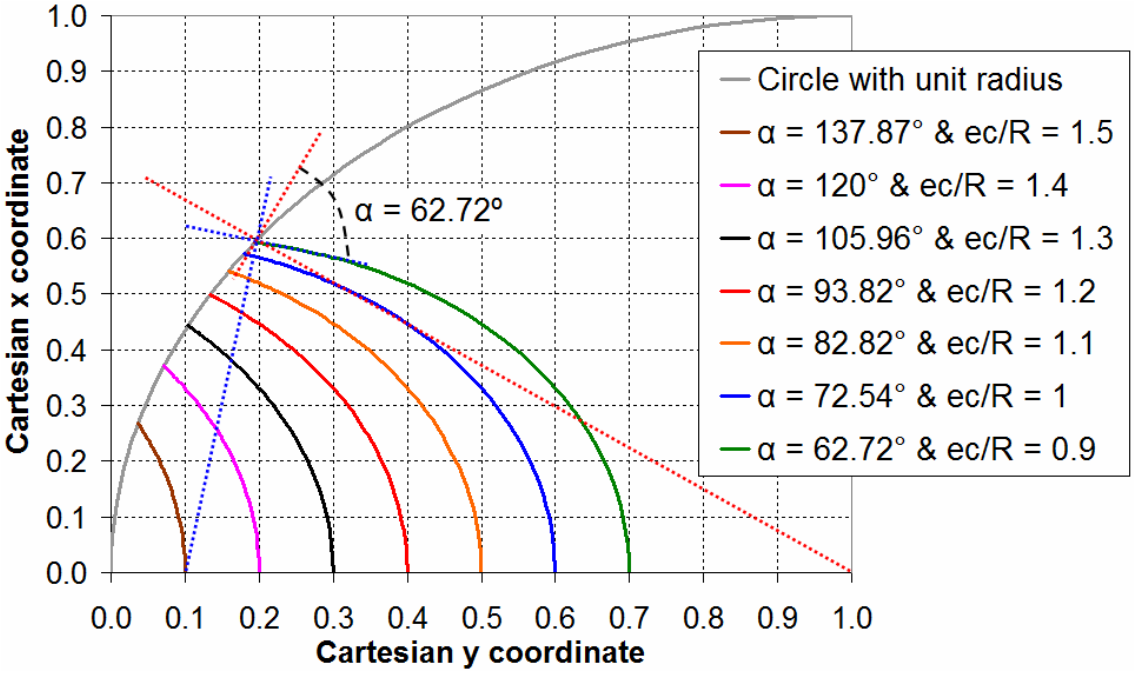

Fig. B.8 – Geometry of an external hole of constant size placed at different eccentricities, $r_c/R = 0.6$ (α marked for $e_c/R = 0.9$)

The distribution of radial stresses through the symmetry axis (the y axis, Fig. B.3) is shown in Fig B.9. Adjacent to the hole, the radial stress is zero due to the boundary condition BC3. Moving away from the hole along the y axis, the radial stress tends to the axisymmetric value of $1.15E\varepsilon_0$ (Eq. B.19). Smaller eccentricities of the hole produce patterns of radial stress which rise gradually towards $1.15E\varepsilon_0$ but do not exceed it. Larger eccentricities, corresponding to a sharper solid edge, exhibit instead a very steep initial rise in radial stress to well above $1.15E\varepsilon_0$ (significantly increased compression), followed by a gradual descent towards $1.15E\varepsilon_0$. The physical explanation for this is that the line of thrust in a compressed steep arch is transmitted almost directly into the supports, but a compressed shallow arch is substantially more ill-conditioned and the

line of thrust reaches the crown of the arch (thus increasing the local compression) and subsequently must be 'channelled' outwards into the supports.

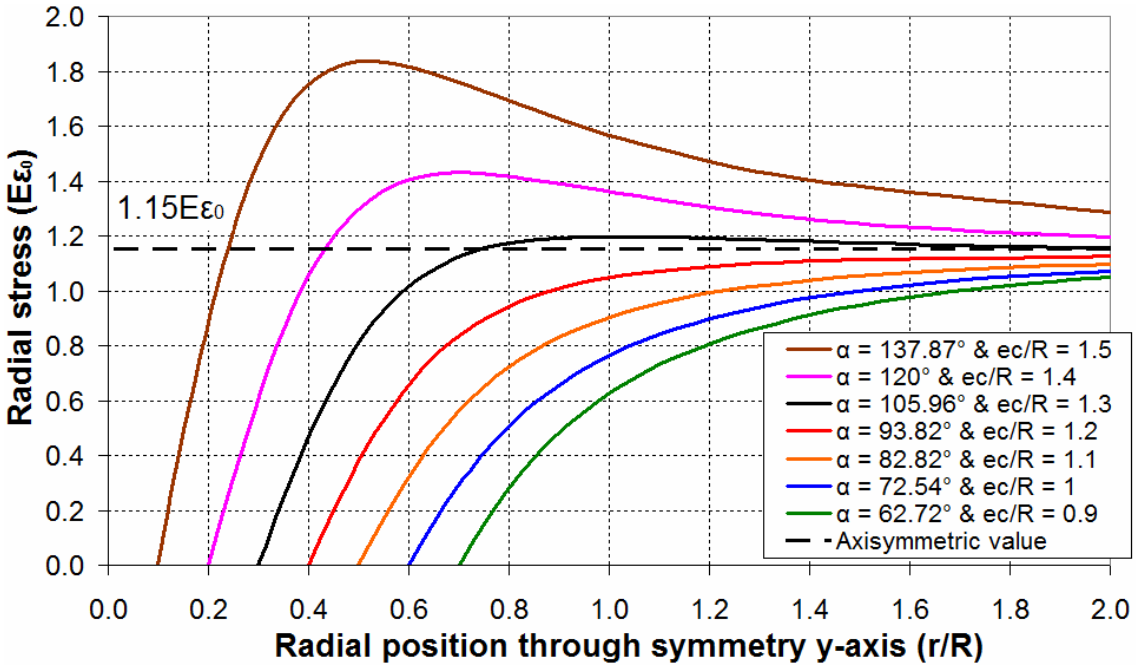

Fig. B.9 – Distribution of radial stresses through the symmetry axis for the truncated elastic body, $e_c/R = 0.01$

The circumferential distribution of radial stress on the outer boundary is shown in Fig. B.10, perhaps the most important diagram of the entire analysis. The sharp edge corresponds to an asymptote and produces an infinite concentration of radial stress. The reason for this, it was noted, is that the sharp edge corresponds to a focus point F where $\xi \rightarrow \infty$ (Fig. B.3). In their chapter on two-dimensional problems in curvilinear coordinates, Timoshenko and Goodier (1970) report an analysis by Green (1945) who obtained an elastic solution for a plate with an exactly rectangular hole and similarly found infinite stress concentrations at the sharp corners.

There is a significant increase in the magnitude of the radial stress for larger values of e_c/R. Away from the sharp edge, $\theta > 5°$, the radial stress for $e_c/R = 1.5$ is approximately double what it is for $e_c/R = 0.9$. The increased eccentricity corresponds to a larger value of the sharpness angle α. The inner circular boundary of the elastic body forms an arch of material which becomes progressively shallower with increased α. Since shallow arches are known to exhibit higher horizontal thrusts than steeper arches, the radial stress near the sharp edge are thus progressively larger at higher values of α.

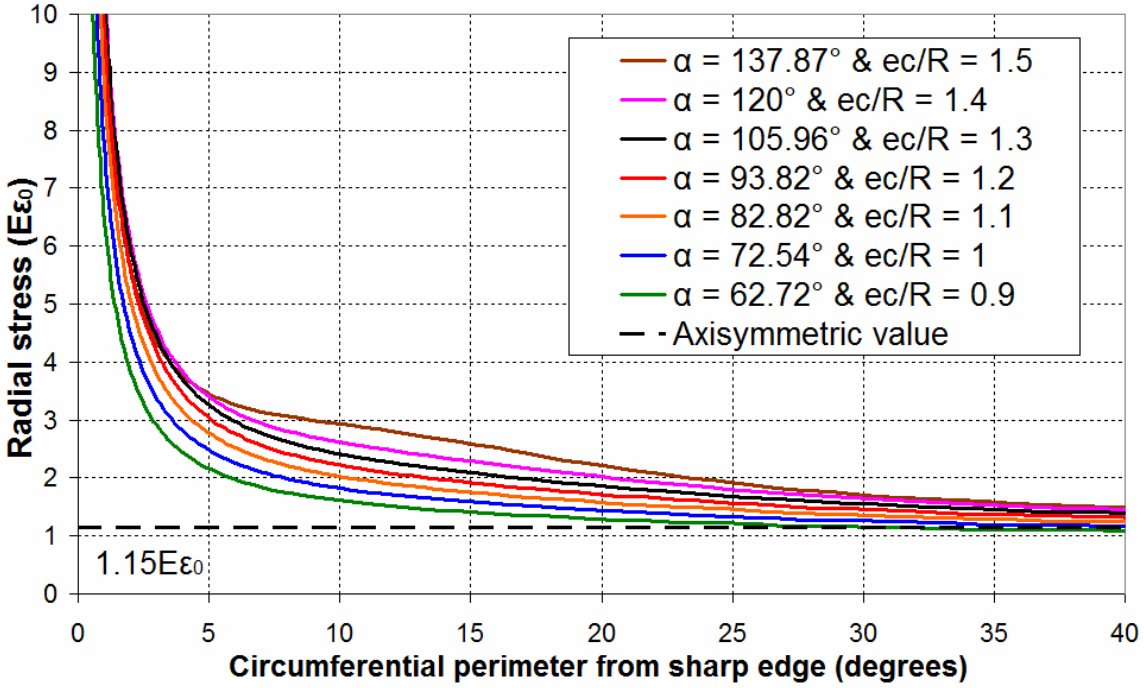

Fig. B.10 – Distribution of radial stresses around the outer circumference of the elastic body starting at the sharp edge, $r_c/R = 0.6$

The above result directly supports the finding of increased normal wall pressure adjacent to the edge of the flowing solid under eccentric pipe flow. The stationary solid, however, cannot exhibit infinite stress concentrations or sharp edges, as material would be lost into the flow channel and plasticity effects smooth out the normal pressure peak. Thus despite the assumptions inherent to this elastic analysis, the results are physically explainable and offer a valuable insight into the possible internal stress states within the granular solid under different conditions.